CITY UNIVERSITY LONDON

School of Engineering and Mathematical Sciences

Investigation of Cavitation inside Multi-hole Injectors for large Diesel Engines and its Effect on the Near-nozzle Spray Structure

B.Eng Adamantios Andriotis

This thesis is submitted for the fulfilment of the requirements for the Degree of Doctor of Philosophy

May 2009

Στην μητέρα μου, Μαίρη, στην θεία μου, Χριστίνα, στην γιαγιά μου Βιολέττα και στον παππού μου, Διαμαντή.

Σας ευχαριστώ για την αγάπη, την κατανόηση και την υποστήριξη που πάντα μου προσφέρετε ώστε να πετυχαίνω τους στόχους μου.

Table of Contents

List of Figures

List of Tables

Acknowledgements

Firstly, I would like to thank my supervisor, Dr. M. Gavaises, for his continuous professional and human support during the time towards the completion of my PhD. Furthermore, I am very grateful that he provided the opportunities, the freedom and the funding needed to pursue this research work as well as for widening my knowledge and expertise in areas different than cavitation. I am sure, that although he never liked my 'last minute' theory, we both managed our way towards a successful outcome.

I would also like to thank to my second supervisor, Professor C. Arcoumanis, for his support, guidance, ideas, and help with my research. Moreover, I would to thank him for giving the extra "push" forward to finish with my thesis when my motivation had started abandoning me.

In addition, I would like to warmly thank Dr. A. Theodorakakos for his support, help and patience all this time that I was 'experimenting' with the GFS code for my CFD simulations. Moreover, I would like to thank him and Fluid Research Co. for providing the precious computational resources needed.

I would also like to say a big thank you to Dr. J.M. Nouri, for his assistance, help and support on my experimental investigations as well as for his continues interest on my research outcomes and progress

For their technical support and help I thank Mr. J. Ford and Mr. T. Flemming. Without them everything would have been much more difficult or even impossible. For the same reasons I would also like to thank Dr. W.D. Gunawardana, Mr. J. Kenny and Mr. I. Wright.

Furthermore, I would like to thank Dr. D. Bouris for showing me the first steps into mesh generator software. Also, for the exchange of insight into various interesting numerical, theoretical and experimental issues, I would like to thank Dr. S. Tonini and Dr. H. Roth. Also, the help and assistance of Dr. N. Mitroglou and Dr. A. Marchi in the beginning of my experimental work as well as the useful discussions we had are highly appreciated. Thank you both guys!

A big and warm thank you goes also to my other friends and colleagues from the research group at City for being around and for helping me in one way or the other: Dr. P. Dellis, Dr. A. Dhunput, Mr. M. Hamid, Dr. J. Kashdan, Mr. K. Kinoshita, Mr. L. Liverani, Mr. K. Mori, Dr. T. Ous, Dr. S. Petropoulou and Mr. K. Wang.

Additionally I would like to thank Dr. E. Giannadakis, Dr. D. Papoulias and Ms. M. Spathopoulou for their help and support as colleagues as well as for being always on my side as friends. I would like you to know that many times you three gave me the missing courage to keep on walking.

Having spent in the beginning some of my time in NTUA, I would like to thank Professor G. Bergeles for his hospitality and for the provision of university resources. During my short stay I had the chance to enrich my CFD knowledge through interesting discussions; for this I would like to thank Dr. N. Nikolopoulos and Dr. G. Strotos. In addition, I would

like to thank Dr. G. Strotos for flooding our cold office with warm melodies coming from his radio; always tuned at ERA2 103.7fm (our favourite station).

At this point, I would like to say a warm thank you to Mr. S. Hatzigrigoris. Through his deep knowledge on marine diesel engines as well as been always interested on new research and technical improvement, he provided the link for sponsorship by the relative industry leader company and always provided the necessary help and support whenever it was needed. Moreover, I want to thank Mr. D. Styllianou, for providing me his house in London, for guiding me through my first steps abroad and for showing me what London can offer in order to make my stay more enjoyable.

I would like to acknowledge the financial support of MAN Diesel (ex. MAN B&W), who funded the first three years of my research work on marine fuel nozzles; in this context I would like to warmly thank and express my gratitude to Mr. D. Tsalapatis, for his personal interest in our research and ongoing collaboration. In the same spirit, I would like to thank CATERPILLAR, for the financial support of second part of my work with multi-hole Diesel injectors. ; in this context I would like to warmly thank Mr. A. Stockner and Mr. D. Ibrahim, for their interest in our research and ongoing collaboration.

A huge 'thank you' goes to the owner of G.M.T.H workshop in Piraeus, Greece, Mr. G. Kouvoutsakis. Without his personal interest and willing to sacrifice highly profitable ordinary production in order to make the precise and delicate job of nozzle model manufacture most parts of this work would have been impossible. Among his entire crew that showed interest to help on making these difficult pieces, I want to particularly thank Mr S. Beltzinitis and Mr. D. Kladis for providing all their experience, technique, knowledge, personal time and piece in order to manufacture the nozzles under time pressure and various uncontrollable situations. Thank you both!

Finally, on a personal level, I would like to thank my good friends Elena, Antonis, Semmy, Anastasia and Angelos for been next to me all these years. In addition, I would like deeply thank my cousins Dimitris and Giorgos for supporting me in various ways and for been my companion and advisors when stress levels were overtaking me. Moreover, a warm 'thank you' goes to my beloved Despina for reminding me that there are achievements that go beyond calculations and experiments.

Finally, I want to thank those that made me what I am. Those that always put my personal welfare and progress above their own lives. Those that flooded me with their loving support and took care of everything else in order for me to be solely concentrated on my research. My loving family! My mother Mary, my aunt Christina, my grandmother Violetta and my grandfather Diamantis who left before seen my work completed. Particularly for my aunt Christina, I want to mention that without her been with me during all these years in London, by putting aside her personal life to become my guardian angel, I would not have been able to do anything. Τα καταφέραμε!

Diamantis Andriotis
November 2009

Declaration

I hereby declare that the presented work in this thesis is my own or was developed in a joint effort with other members of the research group as it is stated and referenced in the text accordingly!

I grant powers of discretion to the University Librarian to allow this thesis to be copied in whole or in part without further reference to me. This permission covers only single copies made for study purposes, subject to normal conditions of acknowledgement.

London, _____

_____

(Adamantios Andriotis)

Abstract

The fuel injection system is considered among the most important components controlling engine's performance and exhaust emissions. The fuel nozzle is the component that determines to a large extend the structure of the emerging liquid spray. Cavitation forming inside Diesel injection nozzles enhances the break-up of the fuel and this results to better atomization. In order to establish the link between complex cavitation structures developing inside Diesel nozzles and their effect to the emerging spray, a series of experimental investigations were carried out along with the aid of RANS numerical simulations.

Two distinct types, based on the engine to be used, of nozzles were manufactured and investigated; a) nozzles used with large low-speed two-stroke marine Diesel engines and b) multi-hole nozzles used with automotive or heavy duty Diesel engines.

Different nozzle geometries were considered and large scale transparent model were manufactured in order to allow optical access inside the nozzle. Both cylindrical and tapered holed nozzles were fabricated in order to allow for hole cavitation effects to be investigated in detail.

The experiments included extensive digital imaging of the different cavitation structures developing in the injection holes, the dynamic or 'string' cavitation forming in the nozzle sac volume and the 'needle-seat' cavitation. Moreover, the near hole exit spray formation was also visualized in direct link with the nozzle's internal cavitating flow regimes.

CFD simulations showed that strong vortical structures exist in both marine nozzle sac volume and injection holes. The same was identified for multihole Diesel nozzle. In all times the pressure values at the core of the identified vortexes were only slightly decreased compared to the surrounding area. After comparison with experimental results it was proved that CFD simulations could accurately predict the internal nozzles flow and recirculation zones location variation with time.

Visualization in the marine nozzle replicas showed that string cavitation is almost always present in the sac volume of the nozzle. Moreover, it was found that the location of the string varies with time and affects different injection holes flow characteristic differently. Parametric studies revealed that cavitation number, CN, and needle lift are the dominant

factors that affect string cavitation. Similar findings were recorded also for multihole Diesel nozzles.

Visualization of the emerging near-hole exit spray structure along with nozzle internal flow for the marine injector revealed that string cavitation entering an injection hole can cause an increase of almost 20 degrees on the spray cone angle as well as a downward deflection of its direction.

In the multi-hole nozzle it was identified that hole-to-hole string cavitation is linked with metal parts erosion after comparing with SEM images. Moreover in the multi-hole nozzles, for low needle lifts and after comparing again with SEM images it was shown that needle seat cavitation is also linked with erosion of the metal parts.

With the aid of numerical simulations the pressure field, as well as the flow structure inside the investigated nozzles was identified and combined with digital image processing. A 3-D reconstruction method was developed and allowed correlation of the experimentally recorded vapour structures with the vortical flow developing inside the nozzle as well as the volume under tension. Out of this comparison it was found that strings are formed in the core of the recirculation areas. Also, for needle seat cavitation it was found that cavitation sites lye across region of volume under tension.

Investigation of nozzles with tapered, outwards converging holes, and combination with numerically identified flow field revealed that although recirculation zones exist strings are not formed. This finding along with experiments using air bubbles introduced in the flow field, showed that strings are formed by vapour from existing cavitation sited (hole cavitation) that is captured and transferred inside the strong vertical flow core.

Finally, for hole cavitation free tapered marine spraying nozzles, it was found that strings can form by trapped ambient air that is sacked inside the nozzle from the hole exit plane due to the strong vortex existing in the injection hole. Interestingly enough it was found that strings were developing in the opposite direction of the hole flow, travelling from the hole exit plane all the way upwards until they reach the sac volume. Similar results were also recorded for the multi-hole nozzles revealing the mechanism of string formation.

Based on the literature that was available and reviewed, the original contribution of the Thesis is the following:

1) Investigation on nozzles used in large two-stroke slow speed marine Diesel engines.
2) Quantitative analysis of string cavitation formation and characteristics along with simultaneous visualization of its effects on the internal nozzle flow and near hole exit spray structure.
3) Combined internal nozzle flow and spray structure investigation in enlarged transparent nozzle replicas with tapered holes and inlet rounding.
4) Mechanism of string cavitation formation in outwards converging tapered hole nozzles without geometric cavitation.
5) 3-D reconstruction of experimentally obtained string cavitation regimes and comparison with the local flow field obtained by CFD calculations.
6) Qualitative and quantitative analysis of needle seat cavitation and its link with erosion. Identification of string cavitation as a mechanism of erosion of the metal parts.
7) 3-D reconstruction of needle seat cavitation sites and comparison with the local flow field obtained by CFD calculations.

The aforementioned aspects will provide the future researcher with valuable results and conclusions in order to promote understanding of the complex phenomenon of cavitation.

Nomenclature

Abbreviations

2-D	Two-dimensional
3-D	Three-dimensional
ACEA	Association des Constructeurs Europeens d'Automobiles
BHP	Break Horse Power
BSFC	Break specific fuel consumption
BMEP	Break mean effective pressure
BTDC	Before top-dead-centre
BDC	Bottom-dead-centre
CCD	Charge cooling device
CFD	Computational fluid dynamics
CFC	Chlorofluorocarbons
CI	Compression-ignition
CIDI	Compression-ignition direct-injection
CO/CO_2	Carbon monoxide/dioxide
DI	Direct-injection
DISI	Direct-injection spark-ignition
DAQ	Data acquisition
ECM	Electrochemical machining
EDM	Electrical Discharge Machining
EU	European Union
EEA	European Environment Agency
EGR	Exhaust gas recirculation
FIE	Fuel injection equipment
GHG	Green-house gases
IMO	International Maritime Organization
HCFC	hydro-chlorofluorocarbons
HSDV	High-speed digital video
LDA	Laser Doppler Anemometry
LDV	Laser Doppler Velocimetry
LIF	Laser induced fluorescence
LIEF	Laser induced Exciplex fluorescence
LSD	Laser sheet drop-sizing
l-h-s	Left Hand Side
MEPC	Marine Environment Protection Committee
NO_x	Nitrogen oxides
N_2O	Nitrous oxide
PCB	Polychlorinated biphenyls
PDF	Probability density function
PIV	Particle Image Velocimetry
RMS	Root mean square
RANS	Reynolds-averaged Navier–Stokes

r-h-s	Right Hand Side
RPM	Revolutions per minute
SMD	Sauter mean diameter
SI	Spark-ignition
SECA	Sulphur Emission Control Area
SO_x	Sulphur oxides
SEM	Scanning Electron Microscope
SUV	Sport Utility Vehicles
TP	Tapered
TWC	Three-way catalyst
TDC	Top-dead-centre
VCO	Valve covering orifice
VOF	Volume of fluid

Roman Symbols

C_d	Orifice discharge coefficient	-
CN	Cavitation number	-
D	Injection hole diameter	m
	Bubble diameter	m
k	Factor determining behaviour of cavitation bubble content	-
	Turbulent kinetic energy	m^2/s^2
L	Injection hole length	m
n	Refractive index	-
p	Pressure	bar
p_{back}	Back pressure, pressure downstream of model nozzle	bar
p_G	Partial pressure of gas inside cavitation bubble	Pa
p_{inj}	Injection pressure, pressure upstream of model nozzle	bar
$p_{v,\ vapour}$	Vapour pressure of working liquid	Pa, bar
Re	Reynolds number	-
T	Temperature	K
U, V	Velocity	m/s
U_{inj}	Bulk velocity of flow through injection hole or channel of model nozzles	m/s
VF	Void fraction	-
We	Weber number	-

Greek Symbols

ε	Turbulence dissipation rate	m^2/s^3
λ	Relative air/fuel ratio	-
	Wave length	m
$\mu_{(L)}$	Dynamic viscosity of liquid	kg/m.s
$\nu_{(L)}$	Kinematic viscosity of liquid	m^2/s
$\rho_{(L)}$	Density of liquid	kg/m^3

Chapter 1
Introduction

1.1 Motivation

At the end of the first decade of the 21st century the first negative impacts of environmental pollution to the world climate are visible and affect the entire world. As it has been seen recently in Mediterranean countries flowers and fruits started to grow in the middle of the winter while hail has fallen during summer after a prolonged period of dryness. It seems that after, nearly, two hundred years since industrial evolution human concern regarding the environment has not been sufficiently grown. Although many attempts have been done to diversify energy production, with less polluting techniques, the so called 'renewable energy sources', fossil fuels are still the dominant way of turning chemical energy into mechanical work and heat.

Internal combustion engines have certainly been one of the factors that changed human life in the last 150 years. They made possible to produce high amounts of work from sufficiently smaller installation than steam power plants. The evolution in later years was even more exciting, this can be realized if consider that today a small size turbocharged engine, having 1.4 l capacity, can produce 170 BHP while still been reliable, fuel efficient, and environmentally friendly.

On the other hand, with today's manufacturing methods the cost of a car can be as low as 7000-8000 Euros which makes possible to a large portion of population to own and use them. This explains that there are currently over 500 million cars on the road globally, and analysts expect to reach 600 million by the end of 2020. According to the EEA, road transportation contributes to 20% of GHG emissions [1, 2], and even though certain measures, like the Kyoto protocol, are taken in order to reduce air pollution, it seems that economic growth of the Asia countries might cause further increase of such emissions.

According to the Oil & Gas Journal (2007) and the US Energy Information Authority, (2007), the already known oil reserves are sufficient for almost 80-90 years. Furthermore it is also expected that new explorations will increase those numbers even more. Taking into account the aforementioned figures it is reasonable to say that IC engines will most likely continue to be considered as first option for propulsion.

At the moment that this work is written oil prices are in the region of 100 dollars per barrel. Many attempts are made to turn into renewable energy sources. However, their cost, both in production and usage with the methods and the limitations that those technologies have today, is still higher that this of conventional fuels even at the current high rates. It is worthwhile to mention here that even in countries having sunshine throughout the year, like my native country Greece, the use of solar power for electricity generation is only used by few individuals and always in a state-supportive way.

After nearly 100 years of development, Diesel engines are considerably more efficient than gasoline engines and are as much "civilized" as their rival. However, as technology evolves, there is still room for further improvements. It is widely acknowledged that one of the most important parameters for IC engines is the fuel injection system. Use of the common rail concept has opened a new era to the DI Diesel engine. In common rail, high pressure generation is independent from engine load and fuel injection. This provides more freedom in the adaptation of the injection process to the engine requirements offering enhanced control of the injection profile at different loads. As a result it makes possible to develop quiet-running, economic engines featuring outstanding dynamic response and also increases the efficiency of combustion.

Fuel injection system is considered as the key component affecting engine's performance and emission characteristics. The amount of fuel that will enter the combustion chamber and the way it will be mixed with air almost solely depends on it. The injector nozzle in particular is the component that will affect the most this mixing process. The size of the injection holes, their number, their orientation with respect to the combustion chamber geometry, and the sac volume geometry will determine how and when fuel will be distributed. In order for the engineers to choose the correct nozzle design they must know its internal flow characteristics since they will affect the spray structure near the hole exit.

Cavitation has been identified as the key parameter affecting the emerging spray since it enhances atomization process. So far geometric induced cavitation inside the injection holes has been thoroughly investigated and is possible to be predicted with today's advanced CFD codes. However it has been observed that more complex and much more transient forms of cavitation can co-exist inside a nozzle. The fact that research on these forms of cavitation along with their effect to the spray structure is limited, and given the importance of nozzle flow on emissions and engine's characteristics, gave the motive to start this study.

This evolution over the years has been accompanied with a vast amount of research in injection equipment and techniques. From internal nozzle flow, to spray characterization two major pathways existed almost in parallel directions. First came the experimental investigations dating back to the early 1900, and at that point the first equations describing heat transfer and fluid motion were formulated as well as the chemical reactions taking place during combustion. Although these equations were proved to be accurate enough, they could not be used, but only for very simplified cases due to lack of computational power, therefore they remained practically unused. It was not before the 80's where the processor technologies started to evolve and today an average personal computer with a CFD solver can predict the flow inside a complex geometry. Also the experimental techniques have become much more sophisticated allowing for quantitative assessment of the various injection systems. Techniques such as LDV, HSDV and PIV that were developed in the last 20 years greatly improved the understanding on the complex flow structures that are present and also provided the necessary data for CFD code validation.

At this point it has to be stated that although there is a huge body of literature concerning fuel injection systems for car and truck size engines, there are very limited studies for large-scale low-speed two stroke Diesel engines. Such engines are mainly used for ship propulsion and are in the top list as far as efficiency is concerned. The fact that research was limited for such engines can be attributed to the reduced competitiveness between manufacturers since there are no more than four major builders, with the first two to share over 70 % of the market. Another reason is that the sales are limited to few hundred per year and therefore doing costly research for just few engines, for a particular model, was considered irrational. Finally the fact that the good working order of such engines assures

the lives of few thousands of people on board a large cruise liner, or the safe transportation of hundreds thousands tonnes of crude oil with a large tanker vessel, thus avoiding an environmental disaster, makes reliability the top perquisite. Therefore when a system is proved to be robust it is very difficult to pursue to change it to a more advanced solution, that came out of theoretical studies, with questionable, though, reliability. For all the above reasons research in this kind of engines has been very limited and usually not publishable. However over the last few years this is changing, the fact that emission regulations start to apply also for sea going vessels made manufacturers to start considering fuel injection research as a solution to meet the new standards.

Therefore since IC engines and fossil fuels will be the main way to produce power for the near and distant future, there will be always the need for further improvements. The current study is part of this ongoing development, for the special category of large Diesel engines, and will concentrate on both internal flow and spray formation, using advanced two-phase CFD solver simulations and extensive experimental investigations for a series of different nozzles with complex geometric characteristics. Particularly string-cavitation will be considered and investigated in detail as well as other transient forms of cavitation.

1.2 Air Pollution

As previously mentioned, the restrictions for the production of harmful GHG set by world governments and organizations are acting as a driving force to manufacturers to produce better engines. This is certainly appreciated by all, however it should be pointed that transportation is not the main producer of those gases. It is a fact that if one wants to make a proper review about emission and their effects will need probably the length of many theses. This section will give only some key information in order to help the reader to have a general view of today's status.

In order to support the above mentioned claim, Figure 1-1 shows the annual GHG emissions by sector. As it can be seen, transportation accounts for 14% of the total GHG emission. GHG, as can be realised is a group of gases that enhance the greenhouse phenomenon that leads to global warming. GHGs include water vapour, carbon dioxide,

methane, nitrous oxide, and ozone. Although it is not clear what is the exact contribution of each one of these gases to the greenhouse effect, carbon dioxide is considered the most important of all. Harmful gases are also Sulphur oxides, especially sulphur dioxide, and carbon monoxide, however they are not considered GHG but are included in the various directives that consider measures about air pollution from fossil fuels combustion.

The above mentioned figure, Figure 1-1, shows the relative fraction of man-made GHGs coming from each of eight categories of sources, as estimated by the Emission Database for Global Atmospheric Research version 3.2, fast track 2000 project. These values are intended to provide a snapshot of global annual GHG emissions in the year 2000. The l-h-s shows the percentage of all the GHG while the r-h-s only shows the carbon dioxide emissions. As it is shown, transport accounts for almost 20% of total carbon dioxide emissions globally. However, it is not clearly stated if the transportation section contains only land vehicles or it takes into account ships and airplanes. It also has to be considered that these values include countries or even entire continents where industrialisation is still under development and vehicle concentration is limited. Finally, as it was expected the greatest contribution to CO_2 emissions, almost 30%, comes from electric power generation plants.

The same trends apply also for the EU countries. As Figure 1-2 below shows, in a more recent investigation (2005), Emissions from domestic transport represent 21 % of total EU-15 GHG emissions while the carbon dioxide (CO_2) only from road transportation contributes by 19% to the total. As commented in the same report of the European Environment Agency more than 90 % of total domestic transport emissions are due to road transport.

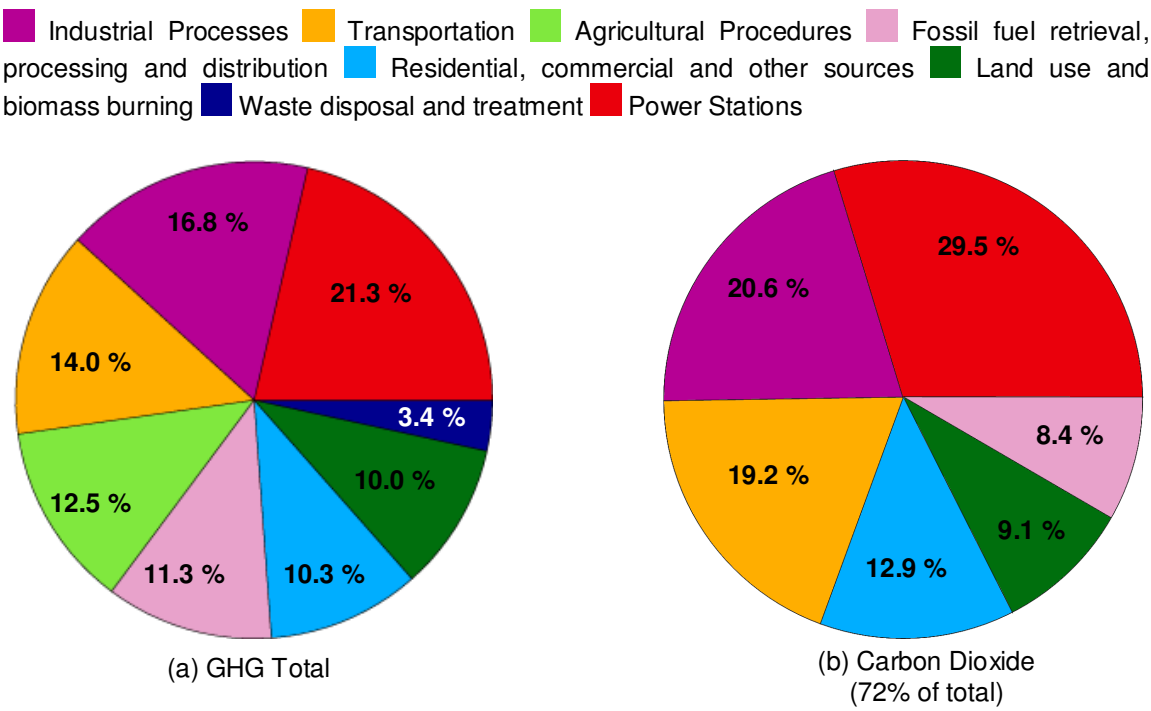

Figure 1-1: Relative fraction of man-made GHGs per category. [According to Emission Database for Global Atmospheric Research (2000)]

Between 1990 and 2005, EU-15 GHG emissions from domestic transport increased by 26 %. These figures are projected to be at about the same level by 2010 if only existing domestic policies and measures are used and to be at 18 % above 1990 levels if additional measures are taken. Emissions from the energy supply and use sector include emissions from energy supply industries, fugitive emissions, emissions from the industry and other emissions from energy use. Although transport emissions are energy related, they are shown separately. However, emissions from international maritime navigation and international aviation are not included.

It is well known that EU has set several emission standards regarding both passenger cars and heavy road vehicles. The European emission standards are sets of requirements defining the acceptable limits for exhaust emissions of new vehicles sold in EU member states. The emission standards are defined in a series of EU directives staging the progressive introduction of increasingly stringent standards.

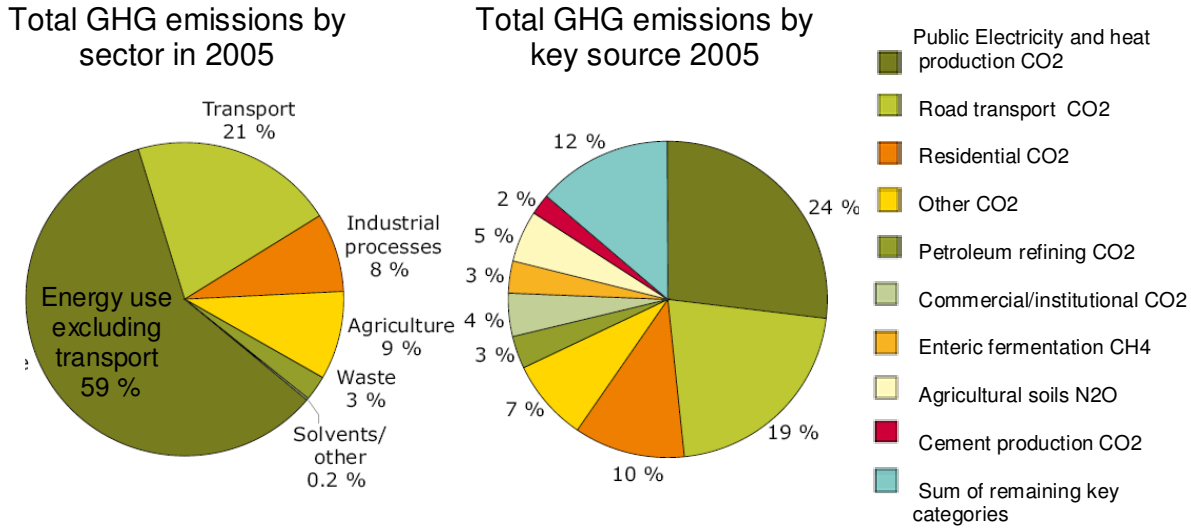

Figure 1-2: GHGs in Europe (EU-15 2005). Modified from [1]

Currently, emissions of NO_x, unburned HC, CO, and of PM which consists mostly of soot, are regulated for most vehicle types. This includes cars, lorries, trains, tractors and similar machinery, as well as barges. However it excludes seagoing vessels and aeroplanes since they are considered international. Another reason for this exemption might be that their negative impact was not realized at an early stage, however this is changing and there are international organizations that are setting strict standards for this kind of transporters as well.

For each vehicle type, which is determined by the usage and its size, different standards apply. the compliance to the standards is determined by running the engine at a predetermined test cycle. Vehicles that fail to comply cannot be sold in the EU, however new standards do not apply to vehicles already on the roads by the time that the new regulations become effective. Even though there are no specific instructions of which technology has to be used in order to meet the new standards, the committee takes into account the available technology, and their limitations, in order to set the standards.

The following Table 1-1 shows the evolution of those standards along with their limitations regarding emissions. Even if CO_2 is the most ubiquitous of the six GHGs, there are no, until

now, EU regulations to set the maximum permissible limits. Until now all the CO_2 limits are given in recommendation basis and not as restriction, however, as will be later mentioned there are certain thoughts in changing the current, rather soft, status. It is believed that passenger cars alone account for about half the transport-related CO_2 emissions in the EU while air transport accounts for 12% of the transport emissions of CO_2 in the atmosphere. Later in this section the contribution from sea-going vessels will also be presented.

Tier	Year	CO		HC+NOx		NOx		PM	
		Passenger Cars	Light Commercial Vehicles 1760-3500 kg	Passenger Cars	Light Commercial Vehicles 1760-3500 kg	Passenger Cars	Light Commercial Vehicles 1760-3500 kg	Passenger Cars	Light Commercial Vehicles 1760-3500 kg
		In mass per driven kilometre g/km							
EURO 1	1992	2.72	6.9	0.97	1.7	-	-	0.14	0.25
EURO 2	1996	1.0	1.5	0.7 (DI 0.9)	1.2 (DI 1.6)	-	-	0.08 (DI 0.1)	0.17 (DI 0.2)
EURO 3	2000	0.64	0.95	0.56	0.86	0.5	0.78	0.05	0.1
EURO 4	2005	0.5	0.74	0.3	0.46	0.25	0.39	0.025	0.06
EURO 5	2010	0.5	0.74	0.23	0.35	0.18	0.28	0.005	0.005
EURO 6	2015	0.5	0.74	0.17	0.215	0.08	0.125	0.005	0.005

Table 1-1: European emissions standards for Diesel passenger cars and Light commercial vehicles

It has to be stated that EURO 5 and 6 have been finalized in 2 July 2008. Moreover, limits equal to those listed for Diesel vehicles, will be set for DI gasoline engines as well, that until now did not have limits. Also, in order to fight against SO_x the maximum Diesel sulfur content in 2000 was set to 350 ppm and in 2005 to only 50 ppm. Regarding petrol (gasoline) the maximum sulfur content was set at 150 ppm in 2000 and 50 ppm in 2005. Finally "Sulfur-free" Diesel and gasoline fuels, having less than 10 ppm of sulphur, must be available from 2005, and will become mandatory from 2009. It has to be stated that all the above limits must be met, from EURO 3 and onwards, for 100,000 km or 5 years (whichever comes first). As a measure in order to encourage the development of more environmentally friendly engine, that also comply with future emission standards, EU member states may introduce tax benefits making these vehicles more attractive.

Even if, as also mentioned before, CO_2 is considered as the gas that mostly affects greenhouse effect, in the EU there are no obligatory limits for the vehicles that are emitting it. As it is shown in Figure 1-2 CO_2 is directly linked with industrialization, and since

burning of fossil fuel is the primary energy provider, it follows that the more 'developed' nations, that have more energy needs, have higher contribution into CO_2 levels in atmosphere. The well known Kyoto protocol was a global measure that was adopted in order to reduce CO_2 emissions along with the other GHG and since it is considered as a positive step into emissions reduction it will be explained later in this section.

Concerning the European automotive industry, the only obligation that since the year 2000 manufacturers have is to ensure that information relating to the fuel economy and CO_2 emissions of new passenger cars is available to consumers in order to enable them to make an informed choice. This practically means that all brochures and advertisements have to include information regarding the above mentioned quantities. However it is widely acknowledged that those labels were too complicated for consumers to understand, and usually they were deliberately undersized so they were practically unnoticed. United Kingdom was among the first to realize that and decided to adopt a color-coded label displaying CO_2 emissions on all new cars since September 2005, with a letter from A, for cars producing less than 100 CO_2 g/km, to G for cars producing more than 250 CO_2 g/km. This was later adopted by many EU member countries that were already familiar with such labels from EU Energy Label with respect to white goods energy efficiency.

Instead of having obligatory CO_2 limits, for emissions generated by vehicles, EU decided to make a voluntary agreement with automobile manufacturers, which is known as the ACEA agreement. In this voluntary agreement, that was signed in 1998, it was agreed that the fleet-average CO_2 emission from new cars sold in the EU has to achieve an average of 140 g/km of CO_2 by 2008 for new passenger vehicles sold by the association's cars in Europe. Considering the 1995 level of 186 g/km, this target represents a 25% reduction. This target has to be reached collectively by the members of the association, and the ultimate EU target to which these agreements are to contribute, is to reach an average CO_2 emission of 120 g/km for all new passenger cars by 2012. The fact that by year 2005 the average CO2 emission had only fallen to 160 g/km made EU commission, at the end of 2006 and after a new report by the European Federation for Transport and Environment documenting lack of progress on the voluntary targets, to consider adopting legal measures and obligatory limits in order to ensure that the target will be achieved. Actually, in February 2007 some drafts were published and, as expected, the automotive industry raised strong argues against them.

Since CO_2 emissions are related to engine size, manufacturers that have in their range mostly small engine cars are already close to those limits and have accepted the new regulations. While some more prestigious and larger car makers, mostly German, are still far away and therefore show skepticism against these strict levels. Also, the fact that the demand for bigger vehicles, like SUVs and big saloons that are considered safer, has risen it makes this target even harder to be reached. A promising fact is that over the last decade and with the evolution of Diesel engines, the sales of Diesel powered cars in Europe have been more than doubled. In fact today Diesel powered cars have overtaken gasoline, while in 1995 the ratio was 3:1 favoring gasoline engine cars.

U.S. has obligatory CO_2 limits by means of fuel efficiency expressed in miles per gallon. This means that if the average fuel economy of a manufacturer's annual fleet of car or truck production falls below the defined standard, the manufacturer must pay a penalty, which is currently set at 5.50 USD per every 0.1 mpg under the standard, multiplied by the manufacturer's total production for the U.S. market. Even if this is a good step, there are some exemptions, mostly for SUVs, light trucks, and vans of certain weight rating, that led more than half a million cars that did not meet the fuel efficiency standard to be exempted from the penalty. It is a strong belief that if something similar is adopted for the CO2 limits in EU the manufacturers that fail to comply will face severe profit loss and if they cannot cope they may pass this extra cost to buyers. Other thoughts considered imposing increased taxation to more polluting cars making them less attractive to buyers.

1.2.1 Ship Exhaust Emissions

Since the current study mostly involves investigations on marine two-stroke low-speed Diesel engine fuel injection system, a review regarding sea going vessel’s emissions has to be given.

According to the EU commission ships are fast becoming the biggest source of air pollution in the EU. Based on a report by the Clean Air for Europe impact assessment, it is believed that unless more action is taken they are set to emit more than all land sources combined by year 2020. Also according to the ship emissions assignment report (2005) in the year 2000 EU-flagged ships emitted almost 200 million tonnes of carbon dioxide which is significantly more than the emissions from EU aviation.

Although official results are not easily found it is said that seagoing vessels are responsible for an estimated 14% of emissions of nitrogen and 16% of the emissions of sulphur from fossil fuels uses into the atmosphere. According to an article, Published by BBC, in Europe ships make up a as much sulphur as all the cars, lorries and factories in Europe put together also it was mentioned that by 2010, up to 40% of air pollution over land could come from ships. It is mutually accepted that Sulphur in the air is responsible for acid rain which has a detrimental effect on vegetation, human health and buildings. Also, when inhaled, SOx are known to cause respiratory problems. The increased SOx emission is caused because marine fuels, bunkers, are oils of poor quality with high sulphur contents, however favourable due to their significantly lower cost. The amount of SO_x emissions is directly proportional to the sulphur content in fuel and to the fuel consumption since the sulphur entering the combustion chamber will be oxidized to form SO_x. Typical percentage of SO_2 in SO_x is 95% while SO_3 accounts for the remaining 5%. According to IMO the maximum allowance of sulphur content in bunker fuels globally is 4.5 %. However this percentage drops to 1.5% when ships navigate in SECAs (Baltic Sea, North Sea and English Channel). There are thoughts that these limits might have to reach 1% in 2010 and ultimately 0.5 % by 2015. Also the EU has set a 0.2% sulphur limit for ships in port and territorial waters. This practically means that the engine changes from burning Heavy fuel Oil to the more expensive Diesel oil. However according to a recent report of Prof. Kyrtatos of NTUA [3] in order to avoid demonization of shipping it was stated that manmade SO_x emission are about 10% of the Volcanic and that Ships SO_x are about 4% of the manmade.

Also regarding NOx emissions IMO has set limits that are function of engine's rated speed. Therefore for low speed engines running at up to 130 rpm the limit is 17g/kWh, for medium speed engines running at 130 to 2000 rpm is $45n$-0.2 g/kWh and for engines running at 2000 rpm and above 9.8 g/kWh. As per 2005 there are considerations for 10-30 % reduction by 2010 and 50-80% by 2015. Finally regarding PM and smoke there are no set limits at the moment, however some proposals are under review with possible inclusion in 2010 but limits have not yet been specified.

Regarding the CO_2 emissions the MEPC at its 55^{th} session in October 2006 agreed a work plan, with a timetable, to identify and develop the mechanisms needed to achieve the

limitation or reduction of CO_2 emissions from ships, noting that climate change caused by GHG emissions from the burning of fossil fuel is a steadily growing concern for most countries. The MEPC noted that shipping, although an environmentally friendly and fuel-efficient mode of transport, nevertheless, needs to take action on GHG.

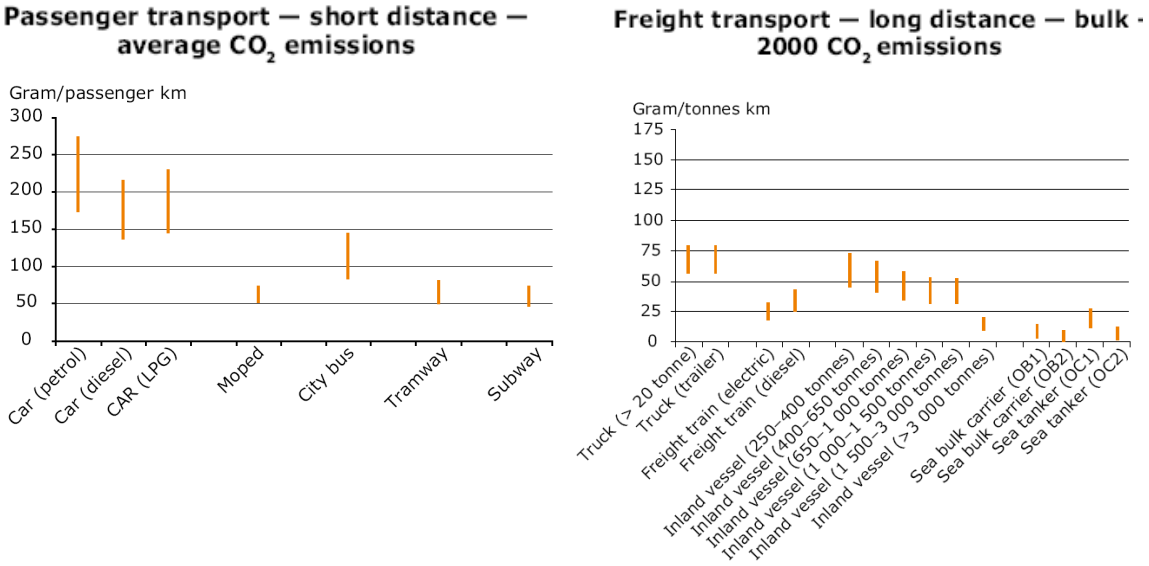

Figure 1-3: CO_2 Emissions in transport according to [4].(presented by European Environment Agency)

As it can be seen from Figure 1-3 above, large ship transportation has the lowest 'specific' CO_2 emissions, while, as expected, the use of cars as personal transportation method affects the environment the most. However, considering the huge loads that ships are carrying and their increased number, that analysts expect to rise more due to China's needs, together with the increased numbers of voyages, it is mandatory for obligatory limits to be set.

1.2.2 Kyoto Protocol

The Kyoto Protocol, that was negotiated in Japan from 1997 and was signed in 1999, is an agreement made under the UNFCCC. The Countries that ratify this protocol commit to reduce their emissions of GHGs, including CO_2, or engage in emissions trading if they maintain or increase emissions of these gases. Emission trading can be consider as a

pollution stock market where companies that pollute more have to buy allowance for emission from companies that are below the limits set by the protocol.

The Kyoto Protocol now covers more than 170 countries globally and more than 60% of countries in terms of global GHG emissions. As of December 2007, the US and Kazakhstan are the only signatory nations not to have ratified the act. This treaty expires in 2012, and international talks began in May 2007 on a future treaty to succeed the current one.

Industrialized counties that have signed the agreement are committed to reduce their collective emissions of GHGs by 5.2% compared to the year 1990 over the period of 2008-2012. Considering the emissions levels that would be expected by 2010, this limitation represents a 29% cut. The reduction of 5.2% represents an average which means that individual targets have been applied to different nations considering their contribution to global emissions, therefore national limitations range from 8% reduction for the EU and some others, 7% for the US, 6% for Japan, 0% for Russia, and also permitted increases of 8% for Australia and 10% for Iceland. The United States has neither ratified nor withdrawn from the Protocol. The signature alone is symbolic, as the Kyoto Protocol is non-binding on the United States unless ratified. The United States was, as of 2005, the largest single emitter of carbon dioxide from the burning of fossil fuels. Finally in 2004 China's GHG emissions reached 54% of the USA emissions, however it is now building on average one coal-fired power plant every week, and plans to continue doing so for years. Various predictions see China overtaking the US in total greenhouse emissions between late 2007 and 2010 and according to many other estimates, this already occurred in 2006. Despite those facts no numerical limitations were set.

Concluding this section it was made clear that unless drastic measures are taken, in the near future the climate changes are expected to have severe badly effects on world's population. Some pessimistic studies state that even if measures are taken, earth's climate has already been affected and these effects will need decades to be reversed. Certainly IC engine manufacturers will have to make significant efforts to meet the new standards towards a greener future. Until renewable energy systems substitute fossil fuels, research on fuel injection systems will always be needed in order to improve combustion characteristics.

1.3 The Diesel engine

1.3.1 History of the invention, components and early applications

At the end of the 18th Century the German inventor Rudolf Diesel, pictured in Figure 1-4 (a), started to materialize his vision towards an internal combustion engine having high efficiency. This can be considered as the beginning of the CI engine era.

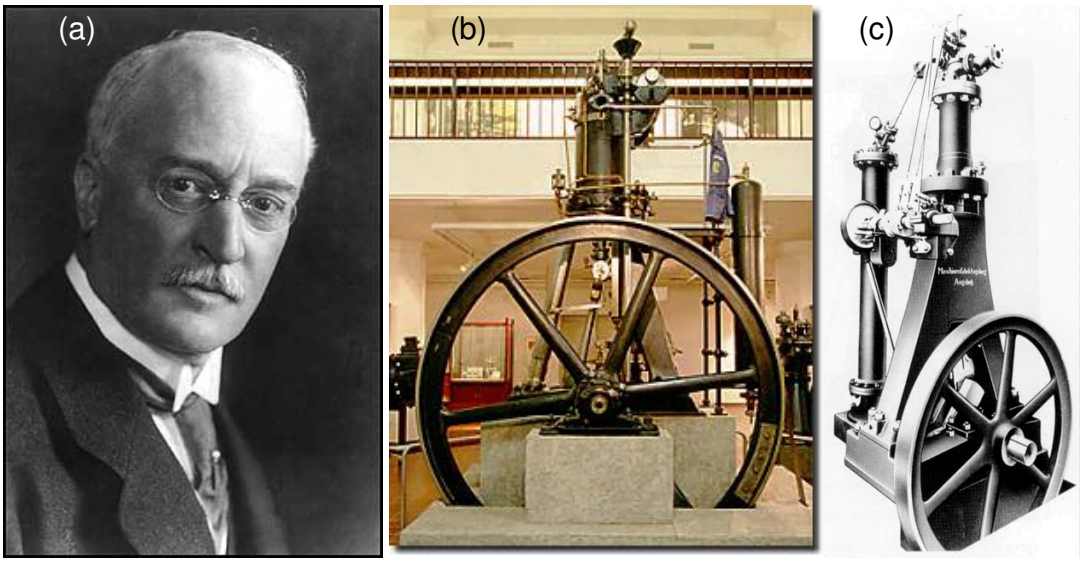

Figure 1-4: a) Rudolf Diesel (1858 – 1913). b) and c) first successful Diesel engine in 1897 (20hp, 172min^{-1})

Even though the patent for this innovative engine was issued in 1892, the first attempts of running the engine using coal dust were catastrophic, the engine after a while exploded and R. Diesel was severely injured. After almost three years, in 1895, he used oil to run his engine and the attempt was successful. Later on, in 1897 together with Maschinenfabrik Augsburg AG, later Maschinenfabrik Augsburg Nürnberg AG (MAN AG), he managed to produce the first commercial engine (Figure 1-4 b & c). At this point it has to be mentioned that in the form that the engine had at that time it could not be considered as a propulsion unit for any kind of vehicle. The fuels that had to use were mostly lamp, vegetable and peanut oil (ironically enough one century later we started considering using those agricultural waste as Biodiesel). However, once the petroleum industry realised the potential success of this kind of engine, it decided to label the by-products of gasoline distillation 'Diesel fuel' and make it widely available for use with CI engines. As the

concept was evolving the first small Diesel engines started appearing, and in 1908 a prototype truck featuring a CI engine was revealed.

In November 4, 1911 it was the beginning of a new era in sea transportation. That day the 6,800 dwt Selandia, the first oceangoing Diesel engine-powered ship, was launched at Burmeister & Wain, Shipyard in Copenhagen, Denmark. Delivered in February 1912, the 370 ft x 53 ft Selandia was one of three such ships ordered by the Danish trading firm East Asiatic Company for service between Scandinavia, Genoa, Italy, and Bangkok, Thailand. Propulsion power was supplied by two eight-cylinder, four-cycle, 1,250 hp Diesel engines in a twin-screw arrangement. The engine had both crossheads and piston rods. Figure 1-5 shows photos of the ship and its engine room.

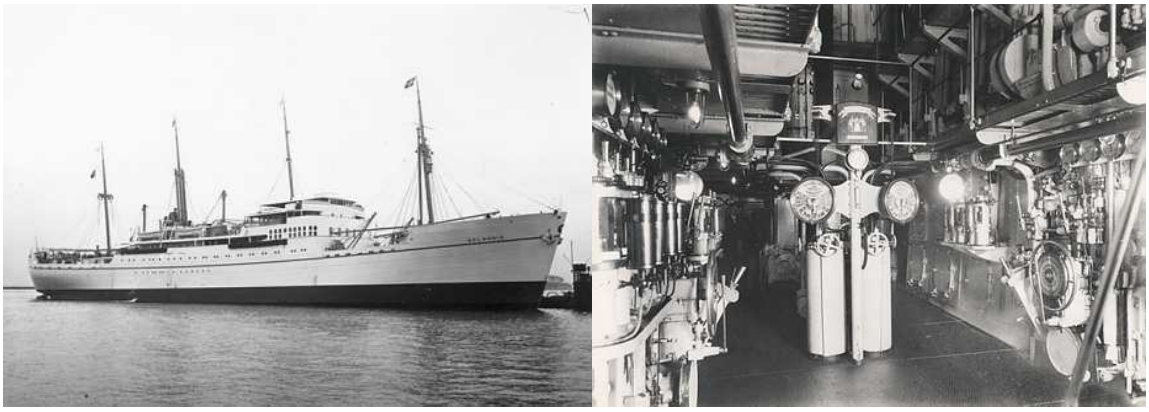

Figure 1-5: M/s Selandia 1912-1937. The first oceangoing ship powered by Diesel engines.[5]

Reporting on the sea trials of the Selandia in its April 1912 issue, International Marine Engineering said, "The future of the big motor ship is practically assured." After official acceptance tests, Burmeister & Wain, Shipyard, Copenhagen, was "inundated with orders for similar vessels from steamship owners who were aboard, and now has enough marine oil vessel contracts on hand to keep them busy for about three years.". That same year, manufacturers M.A.N., Messrs. Sulzer Bros., Krupp's Germania Yards, Vickers Sons & Maxim, and Messrs. Carels Freres were already busy testing high-power two-stroke marine engines, with as much as 2,000 hp per cylinder. Commenting on the tests, Dr. Diesel said, "If, as seems probable, these tests give satisfactory results, the era of very large Diesel engines has come." In fact nowadays low-speed two-stroke Diesel engines are the dominant

propulsion units for sea going vessel and after the acquisition of Burmeister & Wain from MAN the new company called MAN B&W is the leader in manufacturing of such engines having almost the 70% of the market.

The next main target was to reduce the size of CI engine in order to make possible to be fitted in light vehicles. To achieve that R. Diesel visited the Carl Benz AG in 1910. However there he realised that his idea had already spread and that in fact some new more technological advanced designs had made possible to produce compact engines. The pioneer was Franz Lang, also an inventor, who had already carried out first fruitful experiments with Diesel direct injection in 1906. The fact that his idea was over-taken had made R. Diesel to be depressed. He died in September 1913, vanishing during an overnight crossing of the English Channel. The reason of his death remained unknown and rumours included suicide or even assassination.

With the direct injection been established as the most suitable mechanism, in 1924 the first commercial Diesel engine vehicles, trucks from MAN, Benz and Daimler, were revealed.
The Daimler-Benz AG, Deutz AG and MAN AG produced satisfactory injection systems at that time. However they considered to consult Robert Bosch in 1921 to build Diesel injection systems since he had successfully done similar work with ignition systems for gasoline engines from 1902.

In fact the engineers at Bosch managed to develop a variety of injection pumps and injectors of high quality and efficiency over the years. Their main goal was to create a universal Diesel injection system able to be fitted in any engine irrespectively of who was the manufacturer. In 1927 his concept paid off by having Diesel injection pumps and nozzles available to be fitted in production cars. Nearly 10 years later in 1936 the first production passenger Diesel car was presented by Daimler-Benz AG. It was powered by a 4-cylinder engine, having 2.6L displacement and producing 45hp.

Later in the 1950s automotive manufacturer around the world started seeing the potential of Diesel powered cars and started getting actively involved into their production. After a prolonged period with limited action regarding research and development, in 1976 Daimler-Benz introduced the turbocharged version of Diesel car engines. In the early years and

particularly after the introduction of common-rail systems, almost every car manufacturer has a Diesel power option for his entire range of cars. Also the fact that Diesel engines are sufficiently more efficient than gasoline has dominated the commercial vehicle sector. Actually nowadays, in Europe at least, the number of passenger car sales that are Diesel powered is larger than those with gasoline.

Needless to mention that Diesel technology is always under development with vast amount of resources given towards a better end product. Finally, according to [6], for more detailed information regarding the work of Rudolf Diesel and his engine it is suggested to read the two books written by Eugen Diesel [7, 8], the youngest son of R. Diesel.

1.3.2 Diesel Engine Process

Diesel engines are auto-ignition, or compression ignition engines. Air at either atmospheric pressure or already pressurized through a turbocharger enters the engine and then is highly compressed. The fact that only air is compressed, and not an air/fuel mixture as in gasoline engines that are susceptible to knocking, allows for much higher compression ratios to be achieved. Since compression ratio is directly linked to efficiency it is not surprising that Diesel engines are much more efficient than gasoline engines.

As also in gasoline engine there are two cycles that these engines can run, the two-stroke and the four stroke. The two-stroke is mostly used in low-speed large engine while today almost all motor vehicles use four-stroke cycles. As expected the physical and chemical processes that occur during the operation of such engines are highly complex. The intention of this section is to give a short presentation of the fundamental processes that are occurring in the direct injection concept of Diesel engine operation, more details can be found in [9].

Utilizing the fuel injection system Diesel fuel enters the combustion chamber at the end of the compression stroke just before the desired start of combustion. The fuel is injected at high velocity through the injection holes located at the nozzle of the injector. This causes the fuel to be atomized due to break-up, and the resulted small droplets are spread into the combustion chamber. Due to the increased temperature the Diesel fuel start to evaporate and at the same time mixes with the compressed air due to the swirling motion. Only few

ms later the temperature and pressure inside the chamber are above the ignition point of the Diesel fuel and the portion of vapour fuel that has been mixed with air ignites. This rapid expansion increases the in cylinder pressure causing the remaining unburned fuel to rapidly burn, shortening the delay time for ignition. Depending on the load condition of the engine, the injection process continues until the required amount of fuel has entered the cylinder. The subsequent processes of atomization, vaporisation, air-fuel mixing and combustion continue until essentially all the fuel has passed through each process. Moreover, the mixing of the remaining air with burning or already burned gases within the cylinder carries on throughout the combustion and expansion processes. This last burning phase corresponds to around 50% of the overall combustion period in modern high-speed Diesel passenger car engines, whereas only a small amount of the injected fuel is burned during that period.

Start and rate of fuel injection and the atomisation and vaporisation of the liquid fuel not only influence the air-fuel mixing and combustion process but also control the exhaust gas composition of a Diesel engine. Moreover, the engine operating parameters such as load and speed have a major impact on exhaust gas emissions. Besides CO, unburned HC and NO_x the Diesel combustion process also produces noticeable amounts of PM. NO is the main part (>90%) of the total NO_x emissions of a Diesel engine while NO_2 is around 5%. Formation of SO_2 can nowadays be neglected due to the drastic reduction of the sulphur content in Diesel fuels over the last few years from 300ppm to less than 50ppm.

1.4 Modern Two-Stroke Marine Diesel Engine

1.4.1 Introduction

Nowadays, propulsion of most modern merchant ships, like crude oil carriers, containerships and iron ore carries, is performed by using the marine Diesel engine as propeller prime mover. Typical marine propulsion plants include a single, long-stroke, slow speed, turbocharged, two-stroke Diesel engine which is directly coupled to the vessel's propeller. Usually most vessels have only one propeller which is of large diameter (even in excess of 10 m) and has a fixed pitch. This configuration can reach very high power outputs and is considered very reliable due to the simplicity of its concept. It is interesting to

mention that the Largest Marine Diesel Engine in the world is a 14-cylinder RT-flex96C low-speed engine which entered into service on 1 September 2006 in a very large, fast container vessel. The engine was developed by Wärtsilä Corporation and has a cylinder bore of 960mm. The output of the engine was rated 80,080 kW (108,920 bhp) at 102 rpm.

Propulsion by mechanical means was first introduced in shipping in the mid-19th century. In early years, ships were propelled by side wheels or screw propellers that were powered by steam engines. Later, a slow transition to steam turbine power plants started and by the end of WWII had become the dominant technology.

Today the Diesel engine has become the industry standard for marine propulsion. This can be explained by looking at the following facts: (a) Diesel engines have superior thermal efficiency compared to other prime movers, (b) with the advance in engine cylinder lubrication and the use of alkaline oils, large marine Diesel engines can run on HFO which is cheap and widely available and finally (c) the fact that are slow-speed makes possible to be directly connected to the propeller without the need of gearbox or clutch while still are reversible. Currently, the major competitors of Diesel engines in ships are gas turbines. The reason is that gas turbines require a smaller engine room and this can be consider advantageous when extremely large power outputs are required. Despite the fact that Diesel engines have lower specific power per unit volume and weight it is most likely to continue be the first choice for ships.

1.4.2 Marine Engine Components and Operation

Having presented the brief introduction regarding marine Diesel engines, this section will present its layout, main components and principals of operation. As previously mentioned, this type of engine can burn very low quality fuel, such as HFO, much more easily than a medium-speed Diesel engine because the space and time available for combustion are significantly larger. The favoring trend in Slow-speed engines is to have small number of cylinders and increased bore. As a result there is a smaller number of moving parts, increasing engines reliability while reduces maintenance cost. A section of a large marine, two-stroke, turbocharged engine used for ship propulsion is shown in Figure 1-6.

The main parts of the engine are:

- Bedplate and crankcase: The bedplate supports the engine and ensures alignment of the shaft. The crankcase provides housing for the crankshaft. In large engines the crankcase and bedplate come in one piece.
- Crankshaft and flywheel: The crankshaft is one of the heaviest and costliest components of large marine engines. The flywheel ensures attenuation of the vibrations introduced by the discrete firings in each cylinder.
- Engine body: this part of the engine provides mechanical support for the engine cylinders and ensures the mechanical robustness and flexibility of the engine structure. Account is also taken that human access to the inner parts of the engine remains possible.
- Cylinder blocks and liners: In large marine Diesels each cylinder is contained in its own separate cylinder block.
- Pistons and connecting rods: Pistons consist of the piston crown, the piston rings and the piston rod. Their role is to deliver mechanical power to the crankshaft to which they are connected through the connecting rods.
- Cylinder heads and exhaust valves: the cylinder heads secure the top of the combustion chamber and provide mechanical support for two other engine components, namely the exhaust valves and the fuel injectors.
- Camshaft: the camshaft is one of the most critical engine parts because it ensures timing of exhaust valves opening/closure, as well as fuel injection.
- Fuelling system: this is comprised of the high-pressure fuel pumps, the high-pressure pipelines and the fuel injectors (there can be more than one for each cylinder).

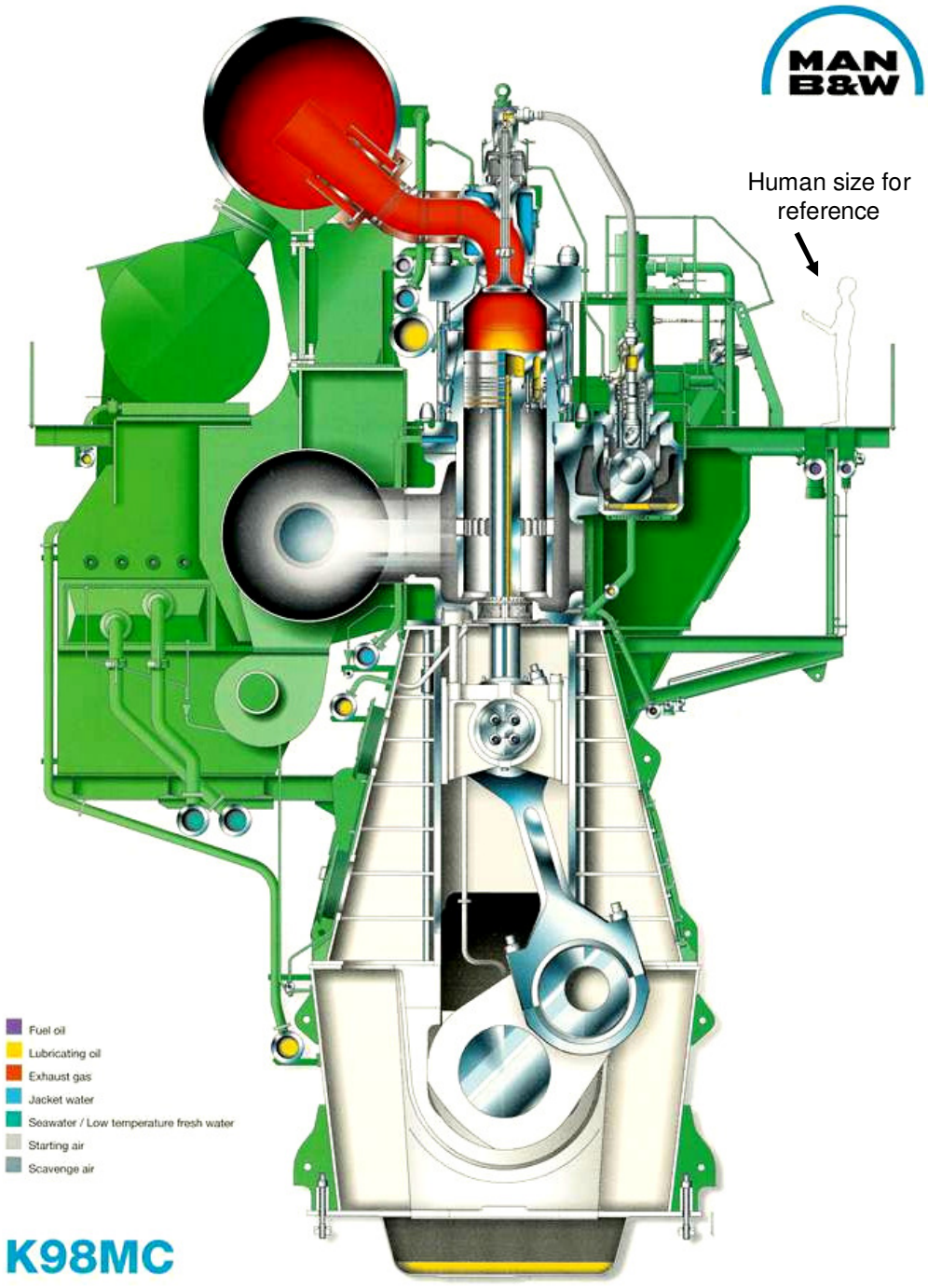

Figure 1-6: Cross section of MAN B&W K98MC-C Two-Stroke slow speed Diesel engine. [courtesy of [10]

Diesel engines used for ship propulsion are tuned in order to operate near-steady-state. Propeller power absorption characteristic can be modified during service due to a variety of factors such as sea conditions, wind strength, hull condition (roughness and fouling) and

vessel displacement. Generally, increased severity of any of these factors requires a power increase in order to drive the ship at the same speed. Therefore, allowances need to be made for the propulsion plant to be able to develop full power under less favourable conditions due either to weather deterioration, deeper draught or hull fouling. This concept of difference in performance introduces the term "sea margin", in order to ensure that the ship propulsion plant has sufficient power available in service and throughout the docking cycle.

Steady –state engine load is expressed in terms of power rating, i.e. as a fraction of MCR power. However, the operating point of the engine is controlled through the position (in mm) of the fuel index (rack) at the fuel pumps, which in most cases is provided in dimensionless form [0%,100%]. The steady-state fuel index position is directly proportional to steady-state engine power, if the engine's mechanical losses are neglected. This implies that the fuel pumps of marine Diesel engines are designed in order to provide linear operation in terms of generated power.

Today's high-power-output engines are both long-stroke and very-large-bore. Piston stroke for these types of engine is typically larger than 2m and cylinder bore above 900mm. BMEP of large marine engines has reached peak values of 18-18.5 bar. Limitation to further increase of BMEP originate from the fact that increasing BMEP leads to increasing in-cylinder Pmax. Indeed, BMEP of 18 bar corresponds roughly to Pmax values of about 130-140bar. A great amount of research effort is nowadays invested in material's technology in order to manufacture combustion chambers able to withstand even higher values of P_{max}. This will enable a further increase of BMEP and engine power output.

Most commonly, large two-stroke marine engines are built in arrangements of 6-12 cylinders according to requirements of propulsion power, engine room availability and mechanical vibration considerations. As the number of engine cylinders increases, a larger engine room is required along with modifications on the turbo-charging system as the intake and exhaust manifolds grow longer. Often a larger number of engine cylinders may be prohibitive due to limitations on crankshaft length and weight.

Finally, marine propulsion engines are always turbocharged. Large two-stroke marine engines use constant pressure turbo-charging systems. In this type of system the exhaust

ports of all cylinders are connected to a common receiver, whose volume is sufficiently large to damp the exhaust pressure pulses. Then one or more turbochargers with a single turbine entry can be used. The main advantages of the constant pressure system are the simple exhaust receiver configuration and the almost steady conditions at the turbine inlet. The disadvantages are inadequate boost pressure at part engine loads and slow system response and the engine becomes more sensitive to torque demand fluctuations. Additionally, the linear relationship between engine torque and fuel index may cease to hold if the turbo-charging system fails to deliver adequate air mass to the combustion chambers leading to incomplete combustion.

1.5 Cavitation

Liquid flow takes place almost everywhere in industry and nature. Usually the flowing liquid is not the only component in a flow. Certain impurities, trapped air or even another liquid may exist. When a liquid is heated, at constant pressure, and once its temperature reaches its boiling point any extra heat that will be given it will cause the liquid to change phase and become vapour, this process is commonly referred as boiling. However the same phase change can occur if, statically or dynamically under constant temperature, the pressure of the liquid is reduced. The latter process is termed cavitation, [11-14] and will be later described as the key element that can affect liquid flow. Therefore cavitation can be described as the formation of a two-phase mixture of vapour and liquid, which occurs when the liquid pressure drops below the vapour pressure. However, it has to be mentioned that most fluids can withstand high values of tension before this phase change starts occurring [11-14].

When liquid and gas/vapour coexists the flow is termed two-phase flow with the gaseous bubbles being the second phase and significantly influencing the liquid flow itself. If the gaseous phase is a result of cavitation it is important to identify and have knowledge on the dynamic behaviour and the cavitation structures in order to understand what will be the effect on the equipment, both structural and also on its performance, and the flow itself.

Going further into analysing how two-phase flow occurs, cavitation is associated with the process of nucleation, which is the initial condition in order to have bubbly flow

phenomena. In general two forms of nucleation mechanisms exist in hydraulic machinery that is subjected to cavitation. Homogeneous nucleation is one of the two. In this case the thermal motion produced by the molecules in the liquid makes some microscopic voids which act as nuclei that will then cause the rupture of the liquid and will later form macroscopic bubbles. The second form is that of heterogeneous nucleation. In that case, trapped gas in the form of microscopic bubbles or solid impurities within the liquid can lead to inception of cavitation by acting as nuclei. It has to be mentioned that if the degree of gas concentration and impurities is high, it will drastically affect cavitation formation by increasing the number and size of nuclei. Also the dissolved gas and impurities can concentrate on the surface of the nozzle where crevices exists increasing locally the nuclei formation. Therefore it can be concluded that the roughness of the walls as well as their temperature (higher temperature – increased crevices) can affect nucleation. Finally in both types of nucleation, nuclei will grow to form cavitation bubbles, which then oscillate, coalesce with other voids, or collapse according to their surrounding contiguous pressure field and the liquid properties[11-14].

Usually for the majority of hydraulic applications it is not desirable to have cavitating flow inside the machinery, since the collapse of cavitation bubbles can affect the integrity of the equipment that it occurs in, through the mechanism of erosion which, in many cases, can be catastrophic [11, 12]. Another major disadvantage of cavitating flows is that the efficiency of the equipment is reduced due to the lower overall density of the fluid-vapour mixture. Finally cavitation increases the noise of such machinery which can be potentially annoying; in fact there are several methods to investigate cavitation through the induced noise levels and frequencies [15-17].

Contrary to the above mentioned concerns, cavitation in the engine fuel injection systems such as multi-hole Diesel injectors and particularly inside the injection holes of the nozzle is considered beneficial. This is because as the more volatile components of the Diesel fuel enter to regions, of relatively low temperature, having pressure below that of vapour cavitation bubbles start appearing and this is recognised as a possible mechanism for improved atomisation of Diesel sprays. This is due to the fact that the primary break-up and subsequent atomisation of the liquid fuel exiting the nozzle can be improved by the enhanced turbulence and inherent instability caused by the cavitation patterns within the

flow [18-22]. In addition, the dynamics of the cavitation structures inside the injection holes are expected to enhance fuel atomisation through generation of smaller size droplets which will vaporise more rapidly, thus enhancing the fuel/air mixing and reducing ignition delay. Finally the improved spray development is believed to lead to a more complete combustion process, lower fuel consumption and reduced exhaust gas and particulate emissions.

However, the fact that cavitation is a mechanism that improves the spray formation, it does not eliminate the disadvantages that may have in the fuel injection equipment. Multi-hole nozzles in particular are suffering from severe erosion problems that in some cases lead to complete failure with disastrous results. Even though today engineers are provided with improved models able to identify such unwanted behaviour, this cannot always apply. In fact, there are many modern design nozzles, particularly those used with high pressure common-rail systems, that exhibit significant damages even after few hundred hours of operation.

Another key note is that cavitation might be desirable but there is always the need to be able to predict it and control it. After years of experimental investigations and numerical simulations it can be said that geometrically induced cavitation, occurring inside the injection holes, is well understood and can be modelled and calculated with advanced CFD codes. This also makes possible to predict the spray structure out of such cavitating nozzles and do some fine tuning in order to achieve the best combustion characteristics. However, as it will be presented in this study, the lately identified string (or vortex) cavitation [23] has been proved to be very unstable and since its formation mechanism has not yet been identified, it is not possible to be predicted by the current CFD codes. This makes it potentially an even greater problem if one considers that it can have great impact on spray formation. It has to be mentioned that even though ‘strings’ are accounted as a form of cavitation, it has been found numerically that the regions where they form have sufficiently higher pressure than the vapour pressure of the liquid. This finding can lead to the consideration that although vapour string exists it has not been formed in that region following the conventional principal of cavitation formation. Instead, it is believed that what is observed is the transfer of already existed bubbles (made in a negative pressure region; usually the injection hole inlet) through a strong vortical flow structure. The high

magnitude of vorticity existing at the core of this structure can be strong enough to deform the bubbles and make vapour have a 'string like' shape [24]. Although this theory is well justified based on known physics rules and numerical results, it still needs to be confirmed. A major doubt regarding the aforementioned mechanism was raised when string cavitation was found to form inside nozzles with no geometrically induced cavitation [25]. These results were obtained in outwards converging tapered nozzles and will be shown later in this study. All these concerns regarding "string cavitation" formation will be presented and addresses in detail in the next chapters.

Throughout this thesis in order to perform the macroscopic characterisation of cavitating nozzle flows, a number of important non-dimensional parameters will be used; these are listed below in order of significance:

1. Cavitation number, $CN = \frac{p_{in} - p_{back}}{p_{back} - p_{vapour}} \approx \frac{p_{in} - p_{back}}{p_{back}}$, where p_{in} is the pressure upstream of the injection hole (usually the injection pressure), p_{back} the downstream pressure (usually the hole exit pressure) and p_{vapour} is the vapour pressure of the liquid. Increasing cavitation number signifies an increase in cavitation intensity as well.

2. Reynolds number, $\mathrm{Re} = \frac{\rho \cdot U \cdot L}{\mu} = \frac{U \cdot L}{\nu}$, where U is the mean bulk velocity of the flow through the injection hole and L is the characteristic length, which for nozzle flow often is the diameter of the injection hole. When considering the flow inside a typical injection hole the turbulent region would have started after Re = 5,000 or even lower.

3. Discharge coefficient, $C_d = \frac{U}{U_{Bernoulli}} = \frac{U}{\sqrt{\frac{2(p_{in} - p_{back})}{\rho}}}$, where ρ is the density of the liquid and $U_{Bernoulli}$ is the velocity of the liquid due to the pressure difference. According to [26] discharge coefficient is the ratio of actual flow rate to theoretical flow rate. Therefore, the discharge coefficient characterizes the amount of losses in a real flow with respect to the theoretical limit. Decreasing discharge coefficient means that losses are increasing in the flow. Usually nozzle designs with high C_d are desirable.

1.6 Thesis outline

The present thesis consists of eight chapters including the introductory *Chapter 1*, where the motivation of this research work is outlined along with a brief description of air pollution background knowledge. Moreover, some information is provided regarding the Diesel engine concept along with some technical details of the particular category of large low-speed two-stroke Diesel engines and their injection components. Finally a summarised description of the cavitation phenomenon and its effects is also given.

Chapter 2 reviews relevant publications in the area of measurement techniques, experimental cavitation and engine investigations along with publications dealing with numerical simulation of bubbly and cavitating flows. Emphasis has been given to publications having combined numerical and experimental results particularly in large scale geometries using transparent nozzles. Moreover, description of different nozzle geometries and how they affect atomization is also provided along with the methods that are used for their manufacture. Finally the relation between cavitation and erosion is also briefly reviewed through a number of studies.

Chapter 3 presents the equipment and the various experimental techniques used for investigating the internal fluid flow and the near hole exit spray structure through a series of different enlarged nozzles. Also the nozzle model geometries are presented in detail along with a brief description of the manufacturing techniques that were used to produce them. Finally an extensive description of the image processing tools that were developed for the analysis of the experimental results is also given.

Chapter 4 presents the numerical simulations that were carried out for the marine engine nozzles. This includes also parametric studies for different nozzle geometries, transient simulations, two-phase flow calculations as well as validation of various CFD code parameters and their effect on fluid flow. Full results are given for both real-size operating condition and for large-scale experiments along with extensive discussion and analysis.

Vortex core location and the flow path inside the nozzle sac-volume are particularly investigated.

Chapter 5 presents the experimental results from the internal nozzle flow investigation in marine nozzles along with detailed quantitative analysis. These are results from 9 different marine nozzle designs including nozzles with tapered injection holes (outwards converging). The analysis of the results includes 2-D spatial probability of vapour in the sac volume for different flow conditions as well as 3-D reconstruction of vapour strings. Parametric studies include, apart from different designs, different injection and ambient pressures, different flow rates as well as different needle lifts. This chapter gives the needed information in order to understand the mechanism of string cavitation formation.

Chapter 6 presents the experimental results from the near nozzle exit spray structure emerging from marine nozzles. Both real size and large scale nozzle models are investigated including different designs and tapered injection holes. Similar parametric studies as for internal nozzle flow are presented and analyzed. The main part of spray analysis presented is the monitoring of the upper and lower spray angles throughout the test period and their link with internal nozzle flow characteristics. Moreover the 2-D probability of liquid presence in air is calculated for different operating conditions. This Chapter emphasises to provide the effect of string cavitation on near hole exit spray structure.

Chapter 7 Having seen the results from marine nozzles investigations in the previous chapters, this chapter presents experimental results from the internal nozzle flow investigations in conventional Multi-Hole injectors, both VCO and SAC type using large-scale transparent models with both cylindrical and tapered injection holes. Similarly to the marine nozzle3 investigation, various parametric studies are presented emphasizing on the effect of flow conditions to string formation and geometric characteristics. More over emphasis is given in showing the string formation frequency. Apart from string cavitation, interesting results for needle seat cavitation are also presented and thoroughly analyzed. Finally 3-D reconstruction for both string cavitation and needle seat cavitation is performed in order to define the link between the flow field and the experimental observations.

Chapter 8 concludes the Thesis with the summary of the major findings, whereby Chapter 2 through Chapter 7 have their own brief summaries. Recommendations for further work in the area of experimental and computational cavitation research are also given in the same chapter.

Chapter 2
Literature Review

2.1 Introduction

The following literature survey provides an overview of research carried out on relevant to the current thesis work. At the end a summary of the most important findings will be given along with explanation on how it contributed to the development of the current study. The overview mainly focuses on: large-scale and real-size nozzle investigations, characterisation of direct injection sprays, as well as on some general engine experiments regarding air/fuel mixing and performance considerations. Also many of the reviewed investigations include numerical simulations and there are also some reviews on purely computational work. Later on, the discussion includes cavitation and erosion and the effect of nozzle geometry on internal nozzle flow, including cavitation structures, and what is the subsequent effect on the spray formation. Apart from the literature that is listed in this section during the thesis there will be a numerous of other investigations that will be claimed for reference.

2.2 Internal nozzle flow and spray investigations

One of the mostly used methods of nozzle investigation is to manufacture transparent large-scale nozzles (10x-20x) from transparent material in order to allow visualization of the internal nozzle flow and the cavitation structures. Moreover, if the liquid medium that is used has the same refractive index as the transparent material of the nozzle then it is possible by using LDV to determine the velocity distribution inside the injection holes and the nozzle. An early investigation that utilized this technique was that of Arcoumanis et al. 1992 [27]. In this study a Steady-state flow test rig with enlarged model injector (transparent single-hole nozzle) was used along with Refractive index matching and LDV.

Among the major findings was that simulating Diesel fuel with a mixture of hydrocarbons having the same refractive index as the acrylic model nozzle was proved to be a useful tool in characterising the internal flow in Diesel injectors since it made possible for 3-D components of mean velocities and RMS values to be measured for Re = 18800. Through a series of parametric studies, the measured flow field provided insight into the dependence of the injector flow on nozzle geometry, needle lift and injection pressure. These results were concluded to be useful for validating multi-dimensional CFD models.

Similarly to the previous investigation, Soteriou et al. 1993 [28] used a steady-state flow rig with large-scale model nozzles, transient injection test rig with various real-size nozzles and injection into liquid as well as into gas. In this study still imaging of cavitation in transparent large-scale and simplified real-size nozzles was presented as well as still imaging of spray from real-size and model nozzles. Finally detailed pressure measurements made possible to calculate nozzle discharge coefficients. One of the most important conclusions was that investigation of large-scale nozzle flow and spray characteristics is a valuable tool when cavitation and Reynolds number are matched simultaneously to those found in real-size flows. Overall, results from investigations in large-scale and real-size nozzles were found in good agreement. Cavitation in injection holes was found to be the predominant mechanism causing spray atomisation. Moreover, higher turbulence levels in nozzle flow were identified as a possible measure to prevent occurrence of hydraulic flip phenomenon which is believed to cause unequal sprays from VCO nozzles. Eccentricity in VCO nozzles was found to produce hollow cone sprays. Finally it was concluded that discharge coefficient only depends on cavitation number and not on Reynolds number and moreover cavitation characteristics do not change beyond a specific cavitation or Reynolds number and above a certain pressure.

Later on He and Ruiz 1995 [20] used Enlarged two-dimensional channel flow rig with liquid into liquid injection having water as the working liquid. The used techniques were LDV along with flow rate measurements. The most interesting conclusions were that Cavitation has strong influence on velocity profiles across the flow area near the channel inlet and that turbulence after cavitation zones was found to be higher that after recirculation zones. Similarly, Arcoumanis et al. 1998 [22] used a steady-state flow test rig with enlarged model injector (transparent 6-hole conical mini-sac type nozzle) combined

with Refractive index matching technique, LDV, flow rate measurements as well as imaging of cavitation structures with CCD and high-speed camera and CFD calculations for non-cavitating conditions. Among the key conclusions was that even for symmetric nozzle conditions the individual hole flow rates can vary noticeably due to small differences in hole size, wall roughness and hole inlet shape. Moreover, CFD calculations confirmed that manufacturing tolerances in the geometry of the nozzle from its nominal geometric characteristics result in unequal flow distribution between the injection holes. Further to the above, LDV results from measurements of local mean velocities and RMS values were used to validate CFD calculations; predictions are generally in good agreement with experimental values, but do not capture well the recirculation zone at the hole inlet.

Using the well known techniques of Refractive index matching, LDV, pressure measurements and Laser light sheet illumination along with still imaging of cavitation, Soteriou et al. 1998 [21] investigated scaled up plain orifice nozzle; injection with un-submerged and submerged outlet, attached on a steady-state flow test rig. One of the major findings of this investigation was that downstream, close to orifice inlet, is a strong flow recirculation area and separation of the boundary layer for non-cavitating flow conditions that strongly influences the cross-sectional velocity profiles. Furthermore it was seen that formation of hole cavitation structures depends on Reynolds number of flow upstream of orifice; Laminar flow allows large voids to form while Turbulent flow encourages formation of small bubbles. On the spray characteristics it was found that cavitation within attached boundary layer causes emerging spray to become slightly bushy and increases the spray angle. Moreover, when plug cavitation extends to orifice outlet the angle and bushiness of spray increases significantly and flow in cavitating plug is more turbulent than non-cavitating flow which is believed to be a reason for improved spray development. In the same spirit, Yule et al. 1998 [29] used large-scale axisymmetric models of VCO nozzle orifice, with sharp and rounded orifice inlet edge, under transient flow conditions due to fast valve (needle) movement utilizing various working fluids. With the aid of high-speed video imaging of the developing orifice flow for different injection pressures and atmospheric back pressure it was concluded that atomisation occurred more rapidly for the orifice with sharp inlet edge compared to the rounded one under the same pressure conditions.

Another key study on nozzles was that of Afzal et al. 1999 [30]. The nozzles investigated were a transparent enlarged 6-hole conical mini-sac and a VCO type nozzle. The experiments showed that Discharge coefficient decreases asymptotically to its minimum value for increasing cavitation numbers. Over a wide range of nozzle operating conditions significant transient pressure variations (5-10% of the mean) have been recorded for the difference between upstream and downstream pressure. Most importantly it was shown that initiation and development of cavitation structures inside the injection holes and nozzle volumes have different patterns in terms of spatial and temporal development of the cavitation bubbles as a function of needle lift and needle eccentricity. Following, Soteriou et al. 2000 [31] conducted experiments using a steady-state flow test rig with transparent 20x scaled up models of plain orifices employing either variable throttling of the injection hole exit or the hole inlet always injecting into atmosphere. This investigation showed that flow through throttled model orifices and emerging jets/sprays are significantly different compared to those produced by conventional sac or VCO type nozzles. Moreover, fan-shaped jets, horseshoe-shaped jets and quasi-normal sprays were observed for decreasing degrees of exit throttling. It was found that cavitation is suppressed for most of the investigated conditions. In the case of hole entry throttling, hollow non-circular sprays were identified with progressive opening of the hole. Finally, cavitation occurred at reduced levels compared to normal nozzles and produced bushy opaque sprays in some cases.

A very comprehensive study is also the one of Roth et al. 2002 [32]. In this study a steady-state and quasi transient flow test rig with large-scale transparent models of 6-hole conical mini-sac and VCO type injectors was used along with LDV, refractive index matching and HSDV imaging of the cavitation structures. It was among the first studies where it was found that Vortex flow inside nozzle tip volume is prerequisite for string cavitation and that cavitation strings in the nozzle tip volume can induce hole cavitation. At higher needle lift cavitation flow structures for both nozzle types are more stable. Interestingly enough, turbulence levels increase in lower part of injection hole with increasing cavitation numbers at moderate flow rates. Also at moderate as well as increased flow rates the normalised RMS are higher at low needle lifts compared to those at high needle lifts due to bottleneck effect. Finally it was found that close to the hole exit the averaged TKE decreases asymptotically to the turbulence level of the non-cavitating flow due to cavitation bubble break-up. Further to the above, Scholz et al. 2003 [33] utilized a steady state flow test rig

with large scale model of a slit nozzle injector along with PIV and Double Pulsed backlit photography of free liquid films near the nozzle exit. This made possible to determine that the development of turbulent boundary layers stabilises the liquid film, as long as the turbulence intensity is not too strong. Finally it was shown that energy transfer or/and velocity equalisation between core flow and liquid film surface at the nozzle exit plays an important role in the promotion of liquid film disturbances, which lead to rough liquid film surface and detachment of big droplets. Later on, Nouri et al. 2005 [34] conducted experiments on a large scale outward opening gasoline direct injector model attached on a steady state flow test rig. The techniques used were LDV and HSDV/CCD imaging of the internal nozzle flow patterns and cavitation structures. The results revealed four jet-like flows internally and upstream the valve seat due to the design configuration of the model. In the mixing chamber of the four jet-like flows just upstream the valve seat, four pairs of counter-rotating vortices were identified with highly unstable patterns. The aforementioned instability could be seen downstream the valve seat on the spray itself. Finally existence of cavitation was confirmed initiating on the valve seat. Moreover, Sou et al. 2007 [35] showed that liquid jet atomization near the nozzle exit depends on cavitation regime, i.e., ligament formation and spray angle depend on the normalized cavitation length. The nozzles investigated were large scale 2-D transparent models of single-hole nozzles with variable geometries. The techniques used were imaging of internal nozzle flow patterns, cavitation structures and near hole exit spray structure with HSDV and LDV measurements inside the nozzle hole. Among other findings, an interesting relation between cavitation and spray structure was defined. Cavitation in 2D nozzles and liquid jet are classified into the following regimes: 1 – no cavitation, wavy jet; 2 – developing cavitation, wavy jet; 3 – super cavitation, spray; and 4 – hydraulic flip, flipping jet. Furthermore it was shown that cavitation and a liquid jet near the nozzle exit are not strongly affected by the Reynolds number but by the cavitation number. Finally it was concluded that strong turbulence induced by the collapse of cavitation clouds near the exit plays an important role in ligament formation.

Focusing on real size nozzle investigations, Stegemann et al. 2002 [36] conducted experiments on High pressure Diesel fuel piezo-electrically controlled common rail injection test rig multi-hole Diesel injector. Using a rapid compression machine ensured engine like chamber conditions. the technique used was ultra high speed spray imaging

combined with accurate control of all injector operating parameters such as needle lift and needle speed. Results indicated a significant influence throttle effects at the needle seat on the spray characteristics. Effects generated by pressure drop at the needle seat have a much bigger influence than a variation of injection pressure. Furthermore, throttle effects at the needle seat show a distinct influence on the spray angle. Finally pressure drop due to partial needle lifts generate cavitation phenomena that move into the sac hole and influence the flow inside the injection holes. As a result spray breakup and dispersion were significantly influenced. Another interesting study on real size nozzles has been done by Blessing et al. 2003 [37]. The equipment used were conventional common-rail and pump-line-nozzle Diesel injection systems with transparent and metal 1-hole and transparent 6-hole mini-sac nozzles in real-size geometry. The investigation included imaging of cavitation structures with CCD camera, measurement of micro cone angle of fuel spray close to nozzle exit, spray tip penetration measurements, needle lift measurements, combustion imaging with soot formation measurements inside optical engine and, finally, cavitation investigation with a commercial CFD package results of which were compared with experimental results. One of the key findings was that conical shape of injection hole (K-factor, defined as K=(Di-Do)/10) influences cavitation behaviour and thus micro cone angle and spray break-up with 1-hole nozzles. The higher K is, the smaller is the micro cone and spray angle, the less cavitation formation & spray break-up and the more tip penetration can be observed. Furthermore, influence of K onto cavitation formation was also reproduced with CFD simulations. Comparison of experimental and CFD results for 6-hole nozzle investigations showed fairly good agreement regarding cavitation pattern distribution and development. Concluding the review of investigations in real size nozzles, Arcoumanis et al. 2001 [38] used closed loop common-rail injection test rig with optical accessible real-size mini-sac injection nozzle as well as large-scale steady-flow test rig with mini-sac model nozzle. This study included imaging of cavitation structures inside real-size injection hole with high magnification CCD camera and imaging of cavitation in sac and injection hole of large-scale nozzle with CCD camera. As it was shown, in order to initiate hole cavitation in the real-size nozzle it is required to get into higher cavitation numbers relative to the enlarged nozzle. More over regarding cavitation structures characteristics, it was concluded that the thickness of cavitation film does not seem to scale with hole size and also that for sufficient high cavitation and Reynolds numbers Cavitating two-phase flow extends all the way to the hole exit. Finally it was shown that string cavitation is more apparent at higher needle lifts

inside real-size nozzle and strings interact with hole cavitation and create cavitation bubble clouds in both real-size and enlarged nozzle holes.

2.3 Nozzle and injection hole geometries

There are many studies regarding multi-hole nozzles used either for Diesel or for gasoline injection systems. In what follows, a brief description of the manufacturing techniques used in order to achieve unique internal flow and spray structure characteristics in multi-hole nozzles is given.

The VCO design brings the needle seat very close to the injection holes. This leaves almost no sac-volume left when the needle is fully closed and therefore minimizes the quantity of fuel that can enter inside the combustion chamber without been atomized (dribbling). From this point of view, the VCO nozzle is superior to the sac-type nozzle. However, due to the fact that when the needle is fully open, it is still at a short distance opposite to the injection holes, special constructive actions must be taken in order to suppress any radial eccentricity of the needle tip. In fact, the manufacturing of the needle is considered a high precision process and mainly involves CNC machinery with sub micron precision (rectification) and temperature controlled environments. Another common solution to this problem can be given by introducing some guides upstream of the needle tip, on the needle body. However this is also not easy to do since a non appropriate positioning of the guides can lead to opposite results. Placing the guides at a great distance from the tip might have limited effect on needle eccentricity. Placing the guides too close can lead into uneven flow distribution in the injection holes, since there might not be enough length for the flow to develop after the guides.

Finally the tolerance between the needle guides and the nozzle body is also crucial. Minimizing the gap between the guides and the body will most probably result into increased wear of the moving parts with unpredictable results. Contrary to that, a larger space might constraint the positive effect of the guides. It should be stated that even a perfectly concentric needle, from the manufacturing perspective, can still experience eccentricity due to the difference in the pressure distribution in the flow annulus. This

mainly happens during the opening of the needle although it may exist at full lift but with minimized effects.

Even a slight degree of eccentricity directly results in an uncontrollable variation of the discharge through the nozzle holes and, thus, strongly deteriorates the overall spray quality. Figure 2-1 shows a schematic describing the above mentioned behaviour which has been the subject of many investigations.

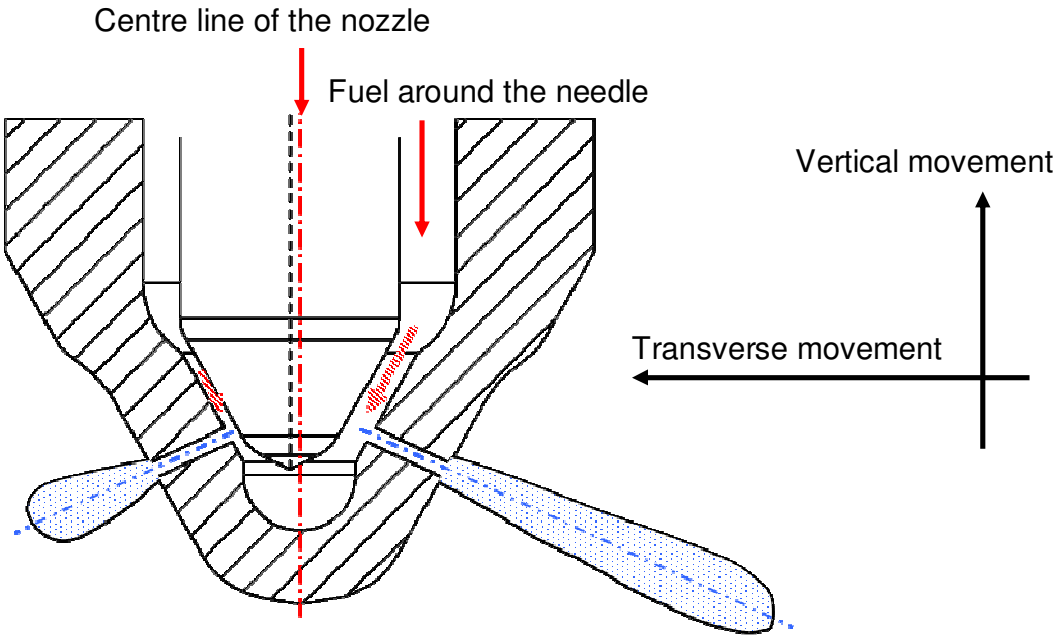

Figure 2-1: Schematic of needle eccentricity effect in a multi-hole VCO nozzle (modified from [39])

In a recent study of [39] through a series of investigations the effects of needle transverse motion on spray structure were revealed. The above mentioned study [39] reports a parametric investigation in an attempt to identify how various injection parameters, including the number of holes of the injector, affect the needle eccentricity. Figure 2-2 shows images of the spray structure from a 3-hole VCO injector nozzle, for exactly the same injection and ambient conditions, in a pressurized chamber, at three different injection cycles at the same time after start of injection. From this figure it can be concluded that there are hole-to-hole and also cycle-to-cycle variations that are clearly indicated by the different spray structures exiting each individual hole. The two main characteristics that can be seen are the penetration length and the spray cone angle, which as shown, are not

consistent. Such behavior has been observed also in [40] where similar experiments were reported. While hole-to-hole variations might be accounted to manufacturing imperfections, the fact that there are cycle-to-cycle variations suggests, according to [39], a transverse movement of the injector needle, and a variation in the magnitude of the needle oscillation. However, it has not been mentioned that the needle movement, which can exist, might trigger complex and unstable vortical structures, such as string cavitation [41], that can lead into such irregularities.

This has been presented in the numerical study of [42], where a VCO nozzle is utilized to monitor the variation of the flow field at the nozzle exit plane. The simulation takes place during transient needle operation, having the transverse motion of the needle as a function of the lift (i.e. vertical movement see Figure 2-1). The velocity profiles at the hole exit plane were then used as input for the spray calculations.

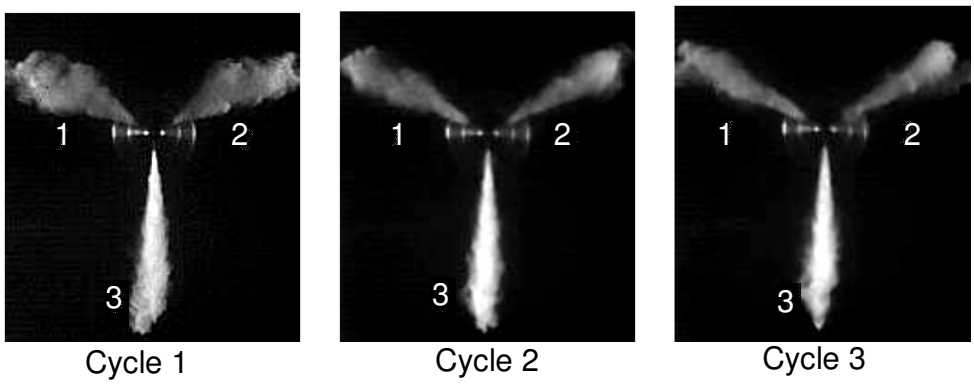

Figure 2-2: Hole-to-hole and cycle-to-cycle variation from a 3 –hole VCO single guided nozzle. [20 kg m^{-3} in-cylinder density, 2 MPa in-cylinder pressure, 60 MPa injection pressure, the images are captures 0.17 ms after first sight of fuel]. (by courtesy of [39])

Observing the upper row of Figure 2-3(a & b) it can be seen that for the tested 5-hole VCO nozzle, the hole-to-hole variation in spray penetration and particularly the spray cone angle is evident during the initial (a), and final stages of injection stage (b). According to [39], this phenomenon occurred regardless of the injection or the in-cylinder pressure. In a multi-hole nozzle, a small imperfection in the injection hole geometry, such as a slightly smaller diameter, will make the pressure distribution on the needle, as it moves upwards to allow flow into the injection holes, to become asymmetric. At the side of the smaller injection

hole the pressure will be increased, this will make the needle to move in the transverse direction towards the opposite side. The needle's dislocation will temporarily reduce, or at first stage when the needle lift is low even totally block, the flow in the injection holes of that side allowing the main portion of flow to exit freely through the defective (smaller) hole side. At a later stage, as the needle lift increases the radial distance between the needle and the nozzle body also increase and the pressure distribution becomes more stable. Finally, at later stage when the needle reaches its fully open position and all the injection holes are uncovered the flow entering into the holes becomes almost uniform. The effect of the needle eccentricity, which by now has been significantly reduced and was mainly due to manufacturing reasons, is minimized. This is indicated by more uniform penetration lengths and spray cone angles between the injection holes, compared to the great differences in the first stages.

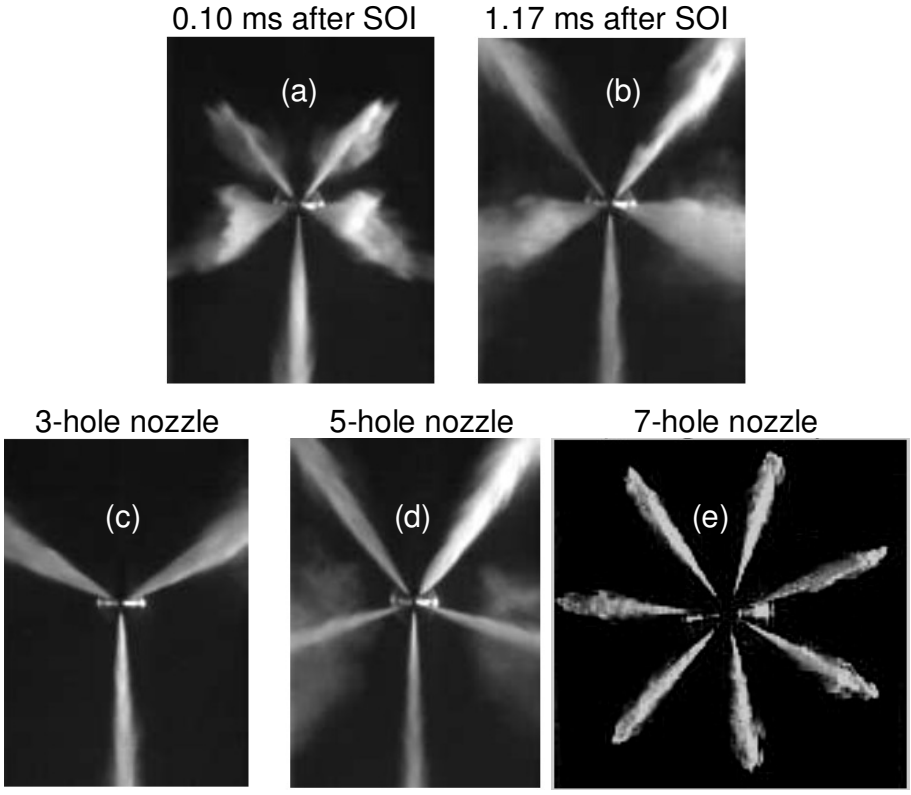

Figure 2-3: Effect of injection time on hole-to-hole spray variations for a 5-hole VCO nozzle (a & b) [P_{inj}=140 MPa, P_{back}=1MPa]. Effect of number of injection holes on hole-to-hole spray variations for a 3-hole, 5-hole and 7-hole VCO nozzle (c, d & e respectively) [P_{inj}=60 MPa, P_{back}=1MPa]. (by courtesy of [39])

Finally, by comparing the spray formation in multihole injectors with different number of holes, it was found that as the number of holes of the nozzle increases the pressure

distribution on the needle becomes more balanced, without meaning that oscillations in the transverse direction are not still present. This conclusion is visually confirmed by observing the lower row of (c, d & e). As it can be seen the 7-hole VCO has the smaller hole-to-hole variations regarding both penetration and spray angle, evidence of the more uniform pressure distribution and the reduced oscillations of the needle.

As previously mentioned precision in nozzle manufacturing is a key element to have successful fuel injection and predictable fuel distribution inside the combustion chamber. As technology evolves the designers have the ability to produce more complex nozzle geometries in order to achieve the exact injection characteristics needed for the particular application of the engine that they will be used on. It has to be clear by now that on the injection system side, and particularly the nozzle, the most important parameter that affects the near hole exit spray structure is cavitation. The most common injection hole designs that are used today are shown schematically in Figure 2-4 .

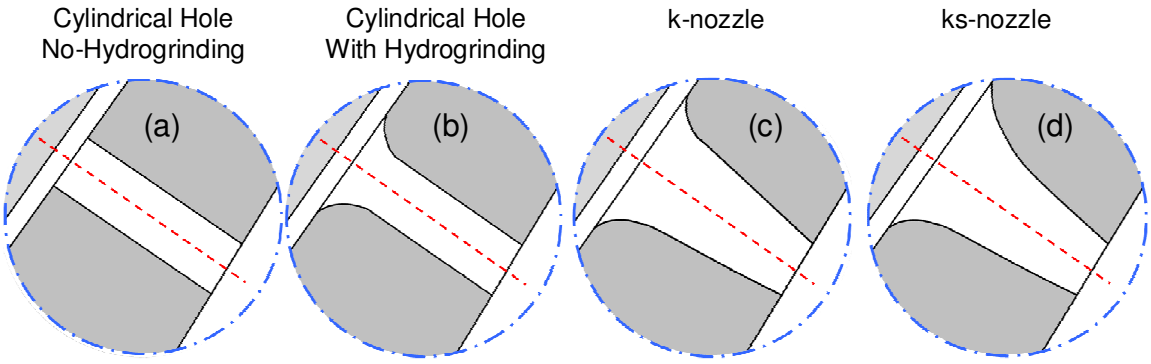

Figure 2-4: Typical examples of different injection hole geometries. (Modified from [28])

In (a) the simplest form of injection hole is presented. A cylindrical hole with sharp inlet edges can, depending on the diameter and the nozzle material, to be made either by conventional drilling or by EDM [43, 44]. The cylindrical hole produces the strongest cavitation and results in an increased spray break up with a large spray divergence near the nozzle. In (b) Hydro-Erosion grinding is used in order to produce rounded hole inlets, in order to enhance the inflow conditions and to produce abrasion in advance, which would otherwise occur during operation and change the spray characteristics. Smoothening of the edges will allow the flow to turn into the hole more gradually, reducing detachment, and

significantly suppressing cavitation by reducing the volume under tension, i.e. region of pressure below vaporization pressure of the fluid. Moving to (c) the axis-symmetric conical geometry further reduces cavitation inside the injection hole by gradually reducing the effective cross-sectional area along the hole. The sprays from outwards converging conical holes usually show an increased penetration. The degree of conicity, the so-called k-factor [45], is defined by Bosch as:

$$k = \frac{D_{inlet}[\mu m] - D_{exit}[\mu m]}{10}$$

Where D_{inlet} is the hole inlet diameter and D_{exit} is the hole exit diameter all given in μm. It follows that conical injection holes with a negative conical shape factor (k) have an increasing diameter towards the nozzle exit. Contrary to that, positive values of the conical shape factor (k) suggests that the diameter decreases towards the exit, i.e. outward converging. In a relatively recent study of [46] fully transparent real-size injecting nozzles with different k factors were manufactured and tested at the cavitation test rig using a Common Rail injection system and a rail pressure of 800 bar and a chamber pressure of 1 bar. In this study it was shown that negative k factors make cavitation structures inside the injection holes stronger. As the k factor becomes positive cavitation is suppressed and for higher values, ≈2.5 for the given geometry and operating condition, is totally eliminated. Apart from the internal nozzle flow the effect of injection hole conicity on the emerged spray was also examined. However, a more quantitative study focusing more on the spray structure from various nozzle design is that of [47]. One of the conclusions of this study is presented in Figure 2-5. As it can be seen, as the k-factor increases the spray cone angle decreases. This is attributed to the fact that as the k-factor increases cavitation inside the injection hole is reduced. As previously mentioned, cavitation enhances the liquid break-up and therefore the result is a better atomized fuel. It follows that cavitating nozzles will produce wider sprays than non cavitating conical nozzles. On top of the above conclusion, the difference in the spray cone angle between the injection holes for the same nozzle shows that the nozzle might experience some eccentricity effects, as previously described, or has some manufacturing imperfections or there is an unstable flow pattern inside the sac volume, which however is not mentioned.

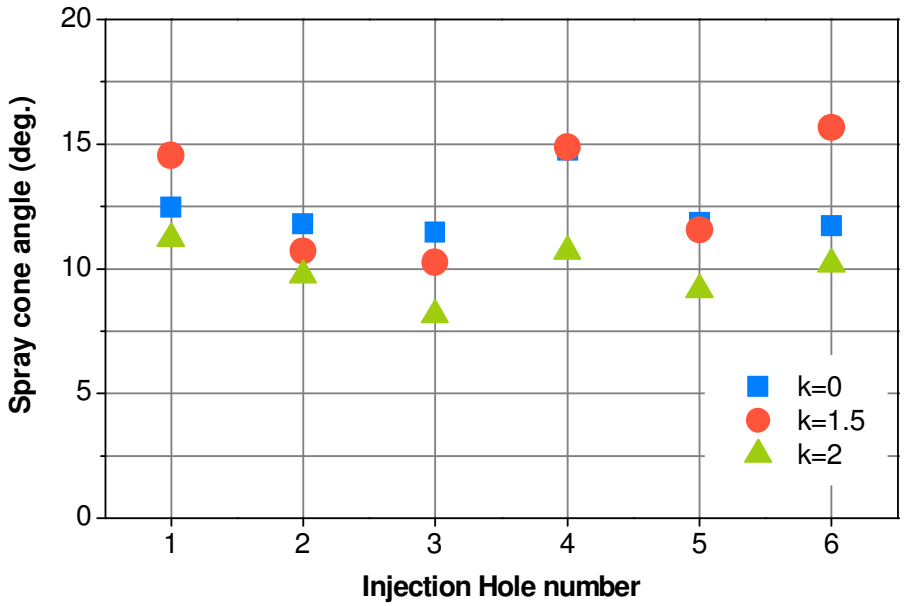

Figure 2-5: Effect of k-factor on spray cone angle from individual holes for a 6-hole VCO nozzle.[P_{Inj} =1200 bar, $P_{Chamber}$=15 bar](modified from [47])

The last type of geometry is shown in (d). Nozzles belonging to this group are those with conical holes that have been flow optimized, commonly referred as ks nozzles (German: Konisch strömungsoptimiert). In this kind of nozzles, the reduction of cross-sectional area across the injection hole is dependent on the distribution of mass flow, and are designed in such way in order to suppress cavitation completely. For a conventional VCO nozzle where the main portion of the flow entering into the injection hole is coming from the upper side, the cross-sectional area and the degree of rounding will be sufficiently larger for this side of the injection hole (i.e. upper side), where geometric cavitation is more likely to exist. The sprays generated by these nozzles are characterized by small spray cone angles, especially near the nozzle, and large penetration lengths. References and reviews of detailed optical investigations of the effect of different nozzle hole geometries on the primary spray structure can be found in [48], where the work of many researchers is presented.

2.3.1 Review of manufacturing methods for nozzle injection holes

In order for the previously mentioned nozzle geometries to be manufactured, certain innovative techniques were developed. EDM is one of these and allows metal to be cut by electrolysis. Instead of having a conventional cutting tool, an electrode having a high current touches the nozzle and as it moves inwards it 'drills' a hole without needing heavy machinery but only a very good positioning control. EDM represents today, the preferred method to form the spray injection holes with high precision having sub micron tolerances. In order for those narrow tolerances to be achieved the manufacturing process control has to be highly sophisticated along with close and continuous supervision of the manufacturing process as well as product quality is required. Apart from confirming the geometric characteristic of the injection holes, such as the diameter, conicity or the surface quality, it is also required to perform also hydraulic quality control. It is a fact that for many years, when the only method for drilling holes was by mechanical machinery, those injection nozzles were only manufactured with cylindrical holes. Also today for large injection hole diameters, such as those in marine nozzles, and cylindrical hole shape mechanical drilling is still used. However, the EDM technique allows a spray hole diameter to decrease in the flow direction (i.e. outward converging), with a defined taper with very low tolerances of few μm. This process depends on electrode guidance mechanism, the electrode material and the electric current which has to adjust accordingly as the electrode proceeds for the conical shape to be formed accurately. This conical shape combined with rounded inlet edges make possible to have different flow pattern inside the injection hole and therefore modified spray structure. The higher discharge coefficient of the injection holes, due to the reduced or eliminated cavitation, leads to a smaller injection hole exit diameter for the same injected fuel quantity since now the effective area (area that is not occupied by vapour as is normally the case in cavitating nozzles) of the hole has been increased. Based on empirical results of [45], when considering combustion chamber development and nozzle layout design, this tends to be highly beneficial especially in passenger car cylinder volumes.

The other technique that has to be used for the manufacturing of most modern nozzles is the HE grinding, commonly also referred as hydro-grinding. This process is applied after the

opening of the injection holes either by EDM or mechanical drilling. In this process the nozzle is attached on a closed loop flow rig where a fluid containing erosive particles is pumped through. This leads to an erosion at the inlet edges of the injection hole where the local flow velocity is at its peak. As the inlets become rounded, the flow rate is increased due to the increased discharge coefficient. This continues until the desired value of 'hydro grinding' is reached. The magnitude of hydro-grinding is the 'HE' value which defines the percentage increase in flow rate relative to the non grinded nozzle hole inlets, and is given by the following equation.

$$HE = \frac{flow\ after\ HE - flow\ before\ HE}{flow\ before\ HE}$$

Hydro grinding has three main advantages which directly affect spray formation and engine performance. Firstly, the same nozzle can be adjusted to have different flow conditions, such as higher discharge coefficient, in order to be suitable for a different engine application (fine tuning). Secondly, it reduces the flow tolerance caused by small geometry imperfection between holes, and finally it produces some wear at the spray hole entrance purposely introduced at the manufacturing stage which results in a higher stability and consistency of the nozzles performance throughout its operational lifetime. In order for hydro-grinding to be beneficial, it has to be correctly implemented.

In the stages of the above mentioned process is given schematically, as a function of time, along with its effect on the discharge coefficient of the nozzle. Starting from a sharp edged conical hole, produced by EDM and presented by the green lines, Phase I rounds the edges and this is associated with a rapid increases on the discharge coefficient. This is highly appreciated with passenger vehicle applications due to the resulting flow characteristics.

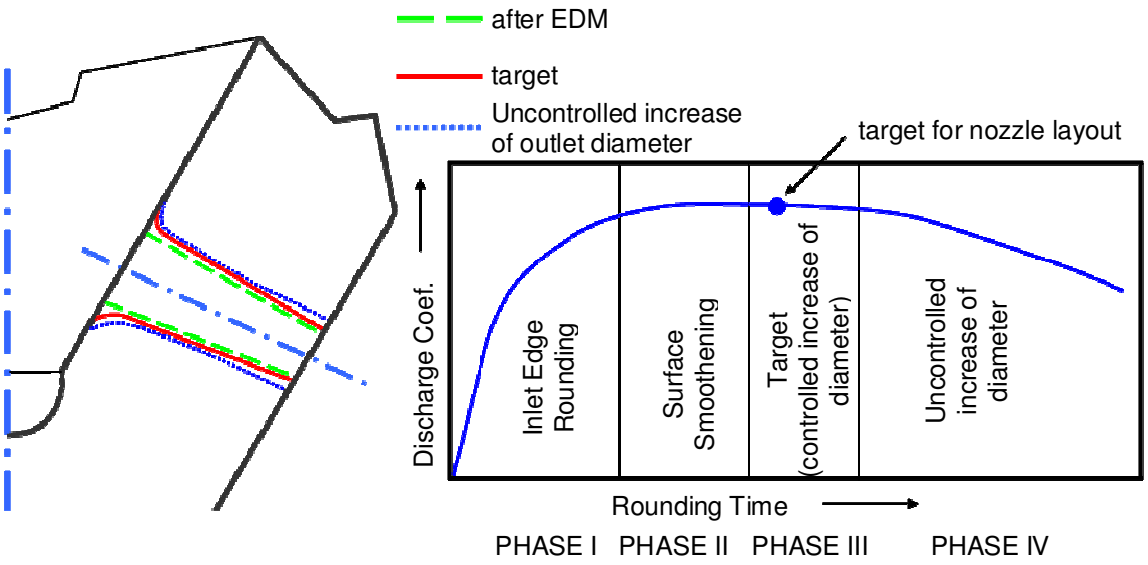

Figure 2-6: Hydrogrinding Phases and its effect on Discharge coefficient. (modified from[45])

Phase II leads to a highly smoothened surface which improves the discharge coefficient even further. In Phase III , presented by the red line, the diameter starts to widen. This is the stage where the flow rate of the nozzle will be determined (i.e. final tuning) and is very important to be precisely controlled. Finally attention has to be given in order for Phase IV of this process to be avoided since at the highest rates of hydro grinding, the local velocity peaks vanish together with the spatial orientation of the grinding. Consequently, this would lead to an uncontrolled hole widening and therefore asymmetric hole geometries as indicated by the blue dotted line. It can be concluded that an optimum geometry and stable hydraulic characteristics of a nozzle are achieved through the closely linked processes of EDM and HE grinding and today these new developments of the above spray hole manufacturing processes deliver nozzles discharge coefficients of up to 0.92 in combination with a k-factor of 1.5 [45].

2.4 Vortex Cavitation

The subject of vortex cavitation has received great attention in the literature, particularly in propellers, hydraulic turbines and hydrofoils, with relevant studies those of [49], [50], [51] and [49] among many others. Cavitation is linked with undesirable effects such as sharp

reduction in performance, increased noise and vibrations as well as surface erosion. Fundamental cavitation bubble dynamics theories are also well documented, for example in [11]. Non-spherical bubble dynamics simulation models have been employed in predicting vortex cavitation in [49], but so far, such models have not been applied to nozzle flows. A recent review paper on experimental techniques and simulation models for cavitation is reported in [52]; still, this study refers to flow environments far from those realised in automotive injector nozzles.

The main differences arise from the nozzle geometric configuration and operating conditions. In fuel injectors huge pressure drops are encountered within very short distances, while the life time of the formed vortical structures is usually only a fraction of the injection period (abt 1 ms for typical engine operating conditions). This is why, the formation and development of such vortical structures has only be studied in enlarged nozzle models operating under steady-state conditions.

The complex geometry is the main reason for not having sufficient information available regarding the formation, of vortical structures and their link to cavitation, in nozzles as we can have in theoretical works like [53] [54]. In any case, research on Diesel injector nozzles is continuously evolving and there have been many attempts to identify and understand the mechanism of strings and their subsequent effect. Some of the first studies that clearly identified cavitation in such nozzles into two district forms of geometric-induced and vortex or string cavitation, are those of [30], [22] and [32]. According to these investigations string or vortex cavitation has been observed in the bulk of the liquid of sac or mini sac-type nozzles. At this region the volume available may allow formation of large-scale vortices relative to the nozzle geometry. Typically, in nozzle flows, two possible flow separation regions exist. These can be realised in Figure 2-7: where the flow field inside a typical Diesel injector along with total velocity vectors are shown.

In order to locate the vortical flow structures, which are shown as transparent tubes in this figure, an iso-surface of the swirl number, which is a non-dimensional parameter, has been used.

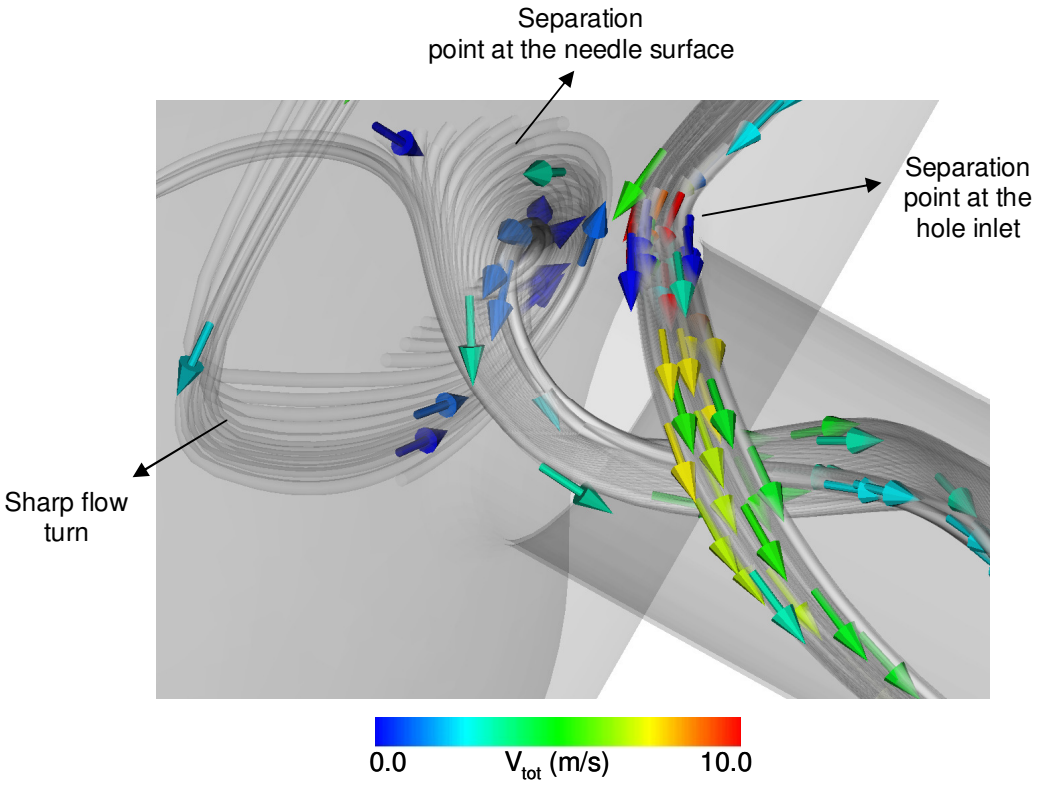

Figure 2-7: Visualisation of flow separation points present in typical Diesel automotive injector nozzles. Velocity vector coloured with the magnitude of velocity showing locations of sudden deceleration.

As it is clearly shown, two distinct structures can be observed. The first one originates from inside the sac volume upstream of the injection hole. As the flow turns in order to enter inside the injection hole, it forms a separation region near the needle seat area and forms a clearly indicated vortex. Then, as it enters into the nozzle hole passage, it forms a clearly identified vortex. The second flow detachment point is located at the top or side surface of the hole inlet where a clear vortical structure can also be identified. It has to be mentioned that a small eccentric placement of the needle will promote the asymmetric entrance of the flow in the discharge channels. More recent studies have shown similar behaviour in various types of multi-hole nozzles as reported by [55], [56] and [57]. However, no evidence for the existence of string cavitation has been reported so far for valve covered orifice (VCO) nozzles, which are known to reduce engine unburned hydrocarbon emissions in modern Diesel engines.

Parallel to the continuing efforts to obtain better experimental information under as realistic conditions as possible, there is an increasing demand for developing and validating CFD models able to predict cavitation. This has been done with relevant success and results have been presented in various publications such as those of [58] [59] [60] [61] [62]. Experimental validation of computational models is essential for assisting to the understanding of the flow processes in complicated nozzle geometries and ultimately, to the design of new nozzle designs. However, the difficulty in manufacturing real-size transparent nozzles that may allow direct visualization of cavitation under realistic conditions imposes simplifications to be made to the design of the nozzle itself and the transient operation of the needle. Complications related to the physical properties and the quality of the working fluid comes to add even more difficulties. Nevertheless, experimental data obtained in large-scale injectors can be valuable for the development and validation of cavitation models applicable for fuel injectors. The aforementioned models have been applied so far in simulating the geometric-induced cavitation. Unfortunately, there is no study reported on the prediction of string cavitation in fuel injection equipment. This is mainly due to the lack of experimental data available for the relevant flow phenomena and thus, the incomplete physical understanding of the process.

2.5 Cavitation and erosion

It is quite well known that the implosion of cavitation bubbles causes, given sufficient time, severe erosion on the material surface of the hydrodynamic equipment [11, 12]. Depending on its structure, the material is locally deformed, loosened and eventually eroded in particles in various ways. The mechanism that is believed to cause this phenomenon is the frequent strain arising from the pressure waves created partly by the microjet and partly by the local shockwave that are induced by bubble collapses. Which of the two phenomena is the primary cause for the inflicted damage is a debatable topic, since some studies have suggested that the local shockwave is the dominant mechanism [63], whereas others support that it is the local micro-jet induced by the asymmetric bubble collapse near solid boundaries that causes the wear of the material [64, 65]. Cavitation erosion is generally subdivided in terms of evolution into three periods [66]. The first period, which is known as the incubation period, is characterized by non-measurable material weight-loss. In the

second period the erosion rate is almost constant, and the areas and depths of the material erosion increase with time. In the third period the surface that is already strongly fractured reduces the probability for an implosion close to the surface, and so in a way erosion is impeded. During this last period the material erodes at a much slower rate. In terms of material behavior, which is essential to know for engineering hydrodynamic applications [6], during the incubation period the surface of ductile metals undergoes only elastic deformation and then plastic deformation. This causes the creation of dents and bulges, with their number increasing with time. After the deformability of the material is exceeded at the end of the incubation period, fractures occur and individual particles start to break off. The deformation phase does not take place to a great extent with brittle metals, due to the high density of dislocation obstacles. As a consequence, internal tensions form that exceed the material strength at the end of the incubation phase. Fractures and ruptures occur that cause an increasing weight loss. In all materials, surface roughness in the area where the bubbles collapse leads to a significant increase in material erosion since the machining notches promote bubble implosions; moreover, the ridges of the roughly machined surfaces resist the imploding bubbles less than even surfaces would. Due to the aforementioned detrimental effects of cavitation on hydrodynamic equipment, most of experimental research has focused over the years on methods with which cavitation damage could be quantified and linked to measurable material properties. For example, in [67] a new pressure detector was developed, able to measure simultaneously cavitation impact load and erosion damage in terms of indent size and volume loss, in order to establish a reliable quantitative link between the two phenomena. From their measurement data they concluded that there was a linear relationship between impact load and indent area for most metal specimens they utilized. As expected, they found that there is a critical impact load above which an indent is formed. This critical impact load increases linearly with the dynamic hardness of the material. Finally, they also found that there is linear relationship between the accumulated summation of squares of impact loads, the equivalent to the impact energy, and the volume loss of the material. In [68] a pit count measurement technique was developed, based on CCD images and computer-aided image-processing. Subsequently, in [69] this technique was further extended by utilizing a white-light-interferometer, with which a three-dimensional map of the eroded specimen area could be obtained.

In studies concerning Diesel injectors, it is well known that today's modern fuel injection systems operate at pressures exceeding 200 MPa. Under these operating conditions and depending on the design of the injector nozzle and holes, cavitation can be present [30, 70, 71]. This cavitation is predominantly of geometric type, although vortex type or sting cavitation is also encountered. For this reason, Diesel nozzles are susceptible to cavitation erosion and fatigue, given the fact that these phenomena can lead to catastrophic failure of the injectors [72]. Moreover, the fact that vortex cavitation can also inflict damage on hydraulic equipment [73] makes imperative the assessment and improvement in terms of erosion resistance of materials that could be used for the manufacturing of such equipment. Carbon steels, for example, are the most frequently encountered material for such applications, therefore the work of reported in [74] can be considered extremely useful. In this work correlations were also produced for some cases, connecting cavitation resistance with Vickers hardness [75], an easily measurable material property. Similar works were also reported in [76] and [77]. The issue of surface hardness was also investigated in [78], who found that with decreasing grain size the cavitation resistance of steel would improve. Another relevant study [79], explored the potential that Cr–N surface coating has towards the improvement of cavitation resistance. From their experiments it was found that with the coating the incubation time of the specimen was increased up to 50%, but after the incubation period was over a higher erosion rate was observed, when compared to the uncoated specimen. In concluding with material properties and performance, it should be noted that the working temperature has an effect on erosion as well. In [80] this effect was investigated systematically and found that for the combination of water with pure copper and pure aluminum the erosion rates increased with liquid temperature and reached a peak, followed by a decrease. The observed increase is a result of the increased number of bubbles based on vapour pressure change, and the decrease is due to the thermodynamic effect of a bubble collapse.

2.6 Cavitation and emerging spray structure

Cavitation occurs inside some type of injector nozzles; this is generally accepted as one of the most important parameters affecting fuel spray atomization [32, 81-83]. It is known that nozzle cavitation is a transient phenomenon even under steady-state operating conditions, but its effect on the spray structure is still not well understood. Laser-based experimental techniques have been extensively applied as diagnostic tools in characterizing the transient development of high-speed sprays; a representative study of the author's group has been presented in [32] while many others have published numerous data for different kind of injectors and examples can be found in [84]. However, these studies do not provide an instantaneous link between the spray and the nozzle flow. Due to the very short time scales of the underlying processes, the frequently unknown details of the nozzle design and the very large number of droplets present, the link with the internal nozzle flow during the injection period remains still a gray area. Few studies have provided measurements of the spray angle as function of the nozzle design [85, 86]. A number of recent studies have linked atomization with the two-phase flow forming inside the nozzle [87-92] including imaging, x-ray measurements and phenomenological atomization models. However, simultaneous imaging of the internal nozzle flow and the spray is very difficult; as a result, up to now the relevant information is mainly based on empirical models which effectively provide phenomenological quasi-steady-state correlations for the droplet size and/or the spray angle for specific nozzle designs, for example [22, 93, 94]. In addition to the difficulty in obtaining experimental data for the nozzle flow and the atomization process, achievements in the understanding of the nozzle flow have been published only recently, starting from the early and more recent works of [31, 82, 95] in large scale nozzle replicas while others have looked into real-size injectors but with simplified nozzle designs [37, 96-99] or with Diesel marine nozzles [100]. Some of the recent studies have investigated the effect of hole shape (cylindrical versus tapered) as well as the effect of hydro grinding on cavitation and atomization [37, 83, 101]. A number of publications from the author's group have been reported in this area, including visualization in enlarged models and real-size transparent nozzles [32, 102, 103] and, more recently, investigating the effect of multiple injections [104]. Despite these efforts, there is still no quantitative –rather than qualitative- study linking cavitation with the initial dispersion of the spray plume formed just at the

nozzle exit. On top of all the difficulties, some studies [56, 105] have indicated that cavitation can be also associated with hole-to-hole and cycle-to-cycle variations. Geometric-induced cavitation gradually becomes a relatively well-known phenomenon but another form of cavitation has been identified recently as a possible flow mechanism responsible for those instabilities. This is referred to as 'string' or 'vortex' type cavitation [32, 56]. These cavitation structures are found usually in the bulk of the liquid, in the area where vortical structures exist. Although different studies have shown similar behaviour in various types of multi-hole nozzles, their formation process has been found to be relatively irregular while their interaction with the mean flow is still poorly understood.

The reason that hole cavitation can be useful is due to the fact that the primary break-up and atomization of the fuel jet can be improved by the increased turbulence levels and also from the instability that is caused within the flow from the cavitation patterns. Also cavitation presence inside the injector holes results into a reduction of the hole effective area for liquid to pass through, leading to higher fuel velocity. Finally cavitation bubbles inside the nozzle holes are expected to generate smaller fuel droplets that subsequently will vaporize more rapidly improving the air-fuel mixture within the combustion chamber.

With today's trend of increasing injection pressure, particularly in common rail injection systems that are operating in excess of 1500 bar even achieving 2000 bar, the fuel velocity, especially when considering small injection holes diameters, can reach very high levels in excess of 500 m/s. such high velocities will make cavitation patterns extend from their starting point, hole inlet, to the hole exit increasing their influence on fuel atomization. Having an improved spray dispersion can lead into a better mixture that will subsequently result into a more complete combustion, increased fuel economy and reduced emissions.

2.6.1 Background knowledge on Fuel Atomization

The need to investigate the link between nozzle flow, cavitation structures and spray formations was identified in the middle of 20^{th} century. Following is a short summary of the first historic experiments and how they have developed into modern investigations.

A pioneering investigation on cavitation and nozzle flow was that of Bergwerk [106] in 1959 that set the path for all the subsequent investigation on that field. For this investigation Perspex real-size and large-scale replicas of a single hole nozzle were used. It was found that for large-scale nozzles, which were more accurately manufactured, with increasing cavitation number there would be a transition into a 'hydraulic flip' state and the spray would emerge smoothly resembling a glass-like appearance. For the real-size nozzle, where manufacturing imperfections caused asymmetries, such effect was not observed. Instead with increasing cavitation number the emerging spray was becoming more ruffled confirming the effect of hole cavitation on fuel atomization. Finally it was found that once cavitation is present the discharge coefficient of the nozzle mainly depends on the cavitation number and is independent of the Reynolds number. This is a fundamental finding that allows experiments to be done by matching the operational cavitation number and not the Reynolds number that would have been harder.

A similar study is that of Spikes and Pennington [107]. In that study a steady –state flow rig was used and the discharge coefficients of partly transparent small submerged orifices were measured. The investigation resulted into the same conclusion that the discharge coefficient is only dependent to cavitation number, once in the cavitation flow regime. During the investigation various inlet hole edge geometries were tested. Orifices with small L/d (length-to-diameter ratio) were found to be desirable due to their higher discharge coefficient, but not always practicable. Finally it was found by having rounded inlet edges larger L/d ratios were possible without negative effect on the discharge coefficient of the nozzle.

Closing this historic review Nurick [108] performed experiments with various sharp-edged single-hole orifices that were made of Lucite (a material similar to Perspex used for visualization of the flow), stainless steel and aluminum. Both circular and rectangular orifices were tested. Increasing the upstream pressure cavitation appeared at the channel inlet of the orifices, forming a *vena contracta*. This is essentially restricting the flow of the liquid and resembles a venturi-like shape. At this point there were cavitation pockets attached to the hole walls at small distance after the hole inlet. After this region the flow fully reattached and the emerging spray would become bushy in appearance, indicating that an additional distortion was present. By further increasing the cavitation number the flow

changes into a hydraulic flip condition. Nurick also developed a model with which the discharge coefficient of the orifice can be estimated as a function of cavitation number, the hole inlet curvature and the hole L/d ratio.

Technology evolution led into more sophisticated investigation helping even more to the understanding of the effect that cavitation has on spray formation. A description of those studies and their conclusions can be found in Chapter 2 however following some key points of those investigations will be mentioned below.

The study of Arcoumanis et al. [27] was one of the first in 1992 to use the refractive index matching technique in an enlarged acrylic model of a production Diesel injection Nozzle. This technique uses a unique mixture of hydrocarbons which has the same refractive index as the acrylic material used for the nozzle replicas. This allows the laser beams to travel in the flow without distortion from the nozzle geometry. Using a steady-state flow test-rig and an LDV system velocity measurements were taken across the injector body.

Following, the studies of Soteriou et al. [28, 82] were among the first to use large-scale transparent Diesel injector nozzles to visualize cavitation and sprays. By studying the spray behavior in both real-size and large-scale nozzles and also the cavitation patterns inside the injection holes it became clear that once the Reynolds and the cavitation number were matched simultaneously, between real-size flow conditions and large-scale ones, the same transition flow regimes and the same dependence of the discharge coefficient on cavitation number were observed. This was an important finding, establishing a link between large-scale and real-size nozzle cavitation. Among other it was found that real-size multi-hole nozzles have some unavoidable geometrical asymmetries that lead into different partial hydraulic flip at the absence of needle that produced asymmetric sprays. Finally it was found that in the presence of cavitation sprays were observed to atomize right at the hole exit, confirming that cavitation enhances the atomization process.

In 1995 Chaves et al.[96] used transparent real-size single-hole axis-symmetric nozzles to study hole cavitation and spray atomization. In order to clearly demonstrate the enhancing effect of cavitation on atomization a nozzle with different surface roughness at the hole entrance was used. At the upper part the hole entrance was well polished and on the lower

part it was ruffled. The spray that was emerging from the upper part of the hole, where there was no cavitation, was smooth. Contrary the spray that was emerging from the lower part, where there was cavitation, the spray was wrinkled. Finally velocity measurements using cavitation bubbles as tracers have confirmed that the liquid jet velocities at the nozzle exit are higher than those deduced from volumetric discharge measurements, which implies that the effective hole exit area is smaller than the geometric area due to the presence of cavitation bubbles and structures [109].

2.7 Summary of literature review

In this chapter a comprehensive volume of publicly available literature has been reviewed in order to provide the foundations to understand the result of the current study that will be later presented. At this point it should be stated that the presence of a chapter like that in a thesis is considered by many, including the author at an early stage of this journey, as complimentary formality. However, it turned to be good opportunity for further consideration and also provided, in many cases, confidence about the drawn conclusions. Following is a brief, yet complete, summary of the previously reported conclusions and an explanation of how they affected the current study. Four main topics will be considered along with the approach that was followed by the different investigators in order to resolve them. These are, the internal nozzle flow, the developed cavitation structures within (including dynamic cavitation), the link of cavitation regimes with the near hole exit spray structure and finally the link between cavitation and injector metal erosion.

It turned out that there are three distinct types of nozzle geometries that can be utilized in order to investigate the internal flow:

1) The first approach seems to neglect the exact internal nozzle geometry as well as the hole-to-hole interactions that are present in a multi-hole nozzle. Therefore, it focuses on single-hole axisymmetric nozzles, mostly real-size or slightly magnified but in some cases even 100x when 2-D, which are made from transparent material and are subjected to realistic operation conditions.
2) The second approach is to replicate the exact nozzle geometry, including all the injection holes, by making a real-size transparent model which is then fixed on a

real injector and through a common rail system supplied with the typical injection pressure.

3) The third approach is to use enlarged transparent nozzles to provide information about real-size multi-hole nozzles used in production Diesel engines through flow similarity.

The first type of nozzles is unable to represent the complex flow patterns present in multi-hole nozzles. This includes failure to reproduce string or vortex cavitation (dynamic cavitation), which is transiently formed in the sac volume usually between holes (but also between the needle and the hole). However, such nozzles are relatively easy to manufacture and can be very useful for CFD models validation regarding geometrically induced cavitation.

The second bring us as close to reality as possible. Having the complete geometry reproduced, even hole inlet rounding and conicity, while still having optical access inside the nozzle is highly beneficial. However, such nozzles are very difficult to be manufactured, which translates into great amounts of time and high cost.

Finally with the third type it is possible to identify both geometric and dynamic cavitation patterns and it is more convenient to be manufactured. Also it is mounted on a constant flow rig with manually controlled needle which makes possible for detailed investigations under fixed operating conditions. However it is unable to represent the flow velocities present in nozzles under engine operating conditions and, thus, residence times of the formed bubbles within the nozzle holes.

After considering the above mentioned aspects of investigations it was decided that the first step into identifying the internal nozzle flow would have been through numerical studies (CFD). Then after considering the results the proper experimental investigation would have been chosen. CFD studies, as literature suggested, can be an excellent tool to predict the flow field inside the nozzle and in more advanced codes accurately predict the two phase flow. Certainly there is always the need for further improvement, however, accurate quantitative results are already a reality. The in-house CFD code which uses a Lagrangian

discrete bubble method, as shown by the group and third party studies, is reliable both for single phase calculations and for cavitation prediction.

Another conclusion that was drawn from the review is that although geometric cavitation has been extensively investigated, both numerically and experimentally, together with its effect on the spray structure yet dedicated studies on string cavitation inside nozzles do not exist. String cavitation has been mentioned in many investigations, but the mechanism of formation and its effect on spray has not been identified. It also became clear that there are extensive studies on conventional nozzles either for Diesel or gasoline injection however mostly concentrate on passenger vehicle engines or medium speed Diesel engines. Very limited studies have been done on injection equipment used by large two-stroke marine Diesel engines and usually are not published.

Finally it was chosen to investigate nozzles from all kind of Diesel engines, including high speed four-stroke ones used in passenger vehicles, medium-speed four-stroke and slow-speed two-stroke mainly for marine applications. Also it was decided to concentrate only on the enlarged fully transparent nozzle approach, been exact replicas of the real geometry, with different injection hole shapes, including rounding and conicity. These nozzles would have been made both for closed-loop flow and also for injection into ambient air. The main objective is to link the cavitation structures inside the different kinds of nozzles to the near hole exit spray structure.

A common conclusion of the majority of the reviewed papers in the open literature that examined the influence of cavitation on the flow exiting the nozzle of diverse design and the emerging spray structure, is that cavitation can improve the spray characteristics by enhancing the primary break-up and the subsequent atomisation of the liquid fuel. It was also reported that cavitation may increase the levels of flow turbulence within the nozzle. The development of the different stages of cavitation inside the nozzle holes has been typically connected with decreasing nozzle discharge coefficients and increasing velocities in the non-cavitating flow regions. Another general conclusion has been that the hole inlet geometry plays the dominant role in controlling geometric cavitation and that sharp-edged (no hydro grinding) orifices cavitate the most under a given flow condition. Also outwards converging tapered nozzles have increased spray penetration and reduced cavitation. The

L/d ratio has been also identified as a key parameter affecting cavitation and the emerged spray suggesting that low L/d ratios increase the discharge coefficient of the nozzle.

Chapter 3
Experimental Techniques & Equipment

3.1 Introduction

As mentioned above, it is very useful to examine the flow through scaled up injectors, particularly when those models are exact replicas of real-size production, or research injectors. Real-size injectors are also of interest. However the experimental rig is much more complicated and it is also extremely difficult to make them transparent. This is purely because of manufacturing limitations regarding the transparent material, which is usually Perspex, and the very small injection hole diameters which are of the order of few hundred μm, typically 100-300 μm for multi-hole Diesel injectors. When investigating real-size injectors, researchers mostly focus on the injected spray structure since they use production nozzles made from metal making impossible to visualize the internal nozzle flow. Ideally a transparent real-size nozzle would combine both, thus, improving the understanding of hole internal nozzle flow, including the forms of cavitation developed within, and its effect on spray structure.

In the current study, only transparent large-scale nozzles were investigated except from one case where a transparent real-size marine injector was tested in order to investigate the spray formation. However, a real-size marine Diesel engine injector is almost ten times larger than other conventional nozzles as was mentioned and explained in section 1.4. Finally for all investigations a steady flow rig was used and the flowing liquid was water at room temperature.

It can be considered as an advantage that due to sufficient funding from various companies a total of twelve (12) different transparent nozzle body where manufactured along with a total of eight (8) different injector needles. As mentioned before, the investigated nozzles were exact replicas which include injection hole inlet rounding and also tapered injection

holes, converging outwards. Investigated nozzles

3.1.1 Large scale marine nozzles for internal nozzle flow

A marine nozzle for large two-stroke Diesel engines, as described in section 1.4, is totally different from conventional multi-hole nozzles. The injection hole diameter is between 1.5-1.8 mm allowing for the huge amount of fuel to fill the extremely large combustion chamber. The hole arrangement is also different since the holes are concentrated in a 90^{o} section only in a non axis- symmetrically arrangement. This is due to the position of the valves on the cylinder head. The low speed two-stroke Diesel engines, presented in section 1.4, have the exhaust valve at the centre of the cylinder head. This forces the injectors to be placed circumferentially in order to distribute the fuel evenly inside the combustion chamber. The internal design is also different and is almost cylindrical allowing to the sliding needle to be always in surface contact with the nozzle body, thus leaving no sac volume left to be filled with fuel once the injector is closed eliminating 'dribbling'. A 3-D schematic of a marine nozzle and its needle is presented in Figure 3-1.

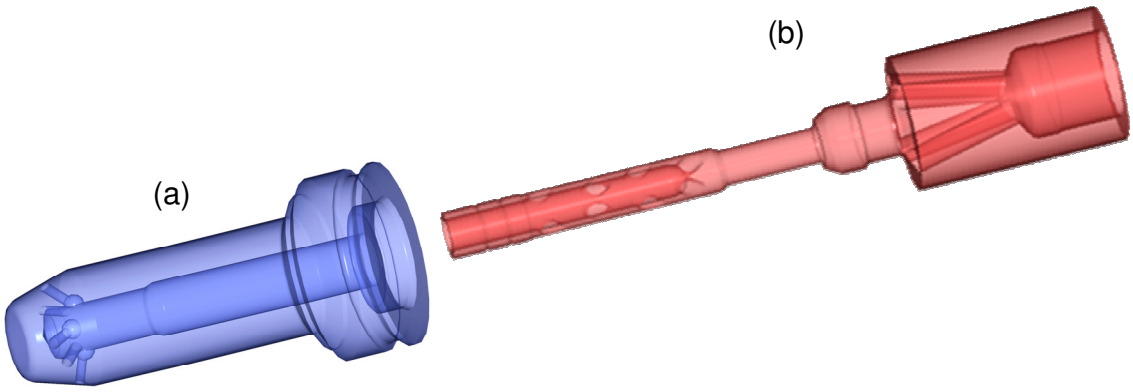

Figure 3-1: 3-D schematic of a) a marine nozzle and b) the injector needle (also referred as cut-off shaft)

Once the cut-off shaft is placed inside the nozzle body it forms a complicated flow path which is illustrated in Figure 3-2 and can be divided into four distinct sections. The flow is coming from a cylindrical annulus which belongs to the body of the needle and is illustrated in section (A). Then enters into four cylindrical channels (holes) which are symmetrically

arranged in a cross shape and are presented in section (B). It then goes through those channels, into a common volume shown in section (C). This volume is formed outside of the nozzle body and is the gap between the main injector body and the needle. In the middle of this volume is the needle seat where the flow seals. Right after the needle seat the diameter is reduced and flow passes between the gap of the nozzle body and the needle. This leaves a hollow cylinder passage of 9mm external diameter and 6mm internal. Then the flow is entering into section (D), which is contained inside the nozzle body and where the flow passage is further reduced since the needle diameter has been increased from 6 to 7.5 mm. Then the flow is directed through 4 pairs of holes, as indicated by the blue arrows, into hollow part of the needle and through this to the sac volume and finally to the five injection holes.

A special feature of this kind of marine nozzles is that 3 of the 5 injection holes, hole number 1, 3 and 5, have a semi-spherical inlet with a diameter of 1.7mm. These cavities are formed by a technique called ECM. ECM is similar in operation with EDM however the electrode, carrying the high current, does not come in direct contact with the metal since the entire process takes place within an electrolyte. Therefore there are no mechanical but also no thermal stresses to the material. This technique enables to machine extremely hard metals in very short time [43, 44]. Even though extensive numerical investigations were conducted in this nozzle design (see Chapter 4) it was requested from the industrial not to represent this feature in the transparent model. Actually, this kind of nozzles is common to differentiate across the same engine type, even the same model, depending on the special needs and condition under which the engine will operate. A more detailed analysis of the variation that such kind of nozzles might have is given in section 1.4.

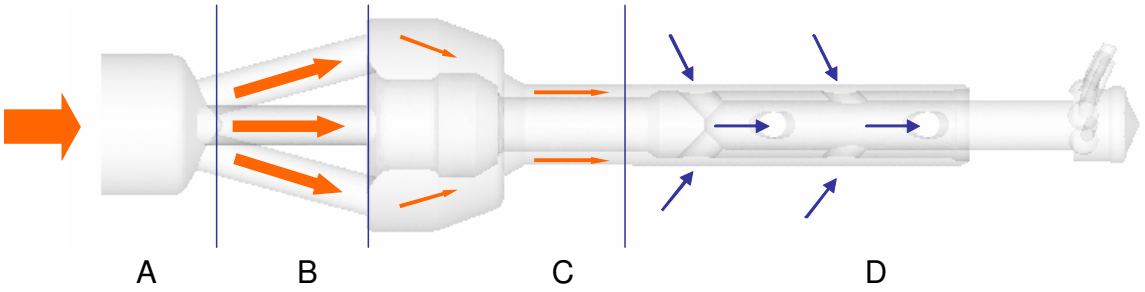

Figure 3-2: Schematic of the internal marine nozzle flow pattern

The previous discussion reveals that both the geometry of the nozzle and the needle are rather complicated compared to conventional automotive injectors. On top of the difficulties due to the complex geometry, the enlarged nozzle model has been manufactured in such a way to fit with the existing steady flow rig; the latter is manufactured to accommodate enlarged conventional multi-hole injectors. Except from design constraints implemented by the rig, there were also time and cost/time & equipment limitations. Therefore after consideration and suggestions from other members of the group and also some numerical simulations; it was decided a simplified geometry to be manufactured with minimum effect on the flow field. The simplification was done in the upstream section of the original geometry, i.e. (A), (B) and (C) in Figure 3-2, leaving section (D) almost unchanged. The only change in section (D) is that the four pairs of holes on the needle that were arranged with 90^{o} twist between them, where replaced by two sets of four holes arranged symmetrically and without any twist between them. The model needle has a large male thread at its upper end and thus can be fixed into the lower end of the enlarged metal needle part through a corresponding female thread. A photograph of the large scale needle parts is shown in Figure 3-3. These sets of holes are positioned, in the vertical direction, where the two middle pairs were in the original design. This design change was done for two reasons. First, to decrease the height of the model and second, and most important, in order to achieve a uniform velocity profile for the downstream flow, since the needle position relative to the nozzle cannot be controlled with the current rig. Also, in the real injection system the position of the needle relative to the nozzle is also random and is also possible to change during the operation of the engine since there are no guides to fix its circumferential location.

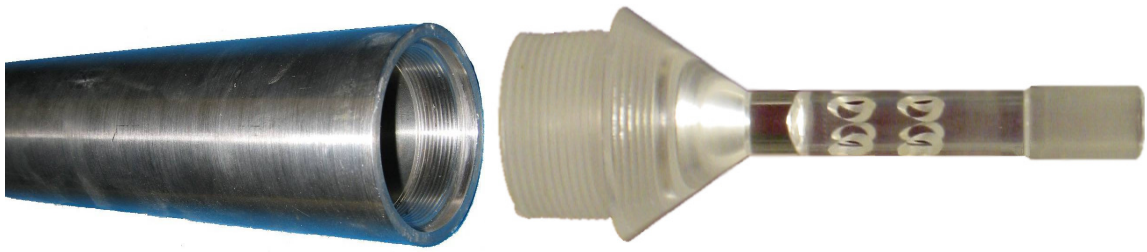

Figure 3-3: Enlarged transparent and metal needle parts

In order to fit the large-scale model to the flow duct of the test rig an adaptor had to be manufactured in order to match the two different diameters. The adaptor, actually been a

simple cone, would have been incorporated to the transparent model in order to avoid extra connections that could potentially cause leakages and eccentricity. The schematic of the adaptor is shown in section (A) of Figure 3-4. This design required a very thick block of Perspex which is not available commercially. Indicatively, the required thickness was 200mm while Perspex sheets are available with 80-100 maximum thickness, and even those are difficult to be found in small pieces thus making necessary to buy the entire sheet having 1000 x 1000 mm dimensions.

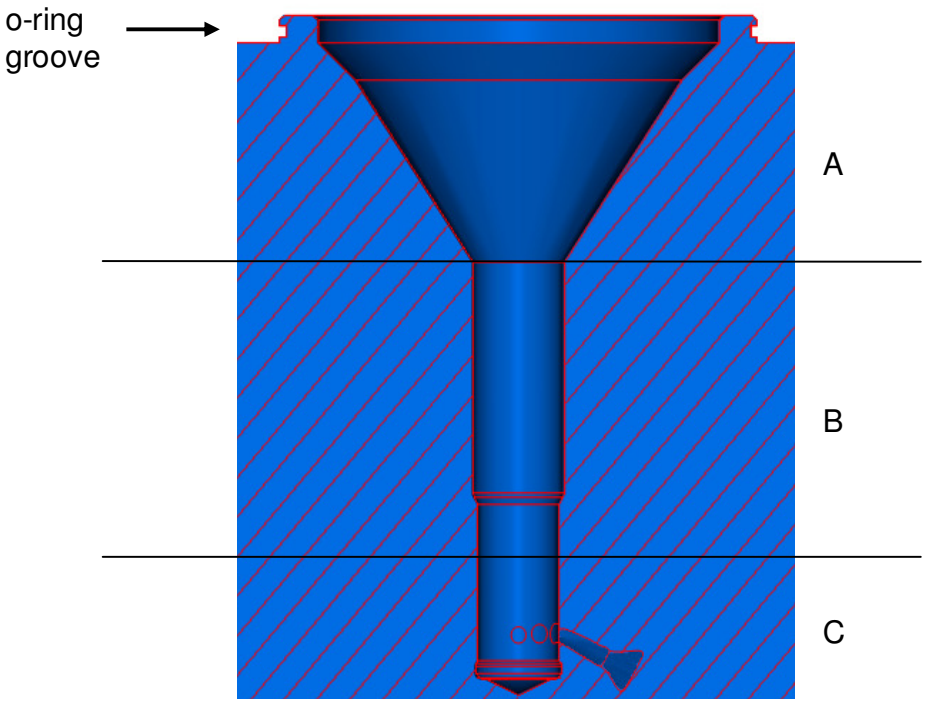

Figure 3-4: schematic of the cross-section of the large-scale nozzle model used

Therefore the designs were given to a special workshop able to cast acrylic material in custom dimensions and then complete the manufacture by shaping the internal geometry with high accuracy. Unfortunately, due to the complexity of the geometry, the first attempt was not successful. With over one month of delays and less than ten days to start taking measurements certain modifications had to be considered. It seemed that the most time consuming and difficult process was to cast the acrylic block. By increasing the leakage possibility and totally loosing visibility of the flow entering through the needle holes, section A and B (Figure 3-4) where chosen to be manufactured as a separate non-transparent piece. Aluminium was chosen in order to be lightweight, yet strong, and rustproof.

An o-ring seal in a groove on the flat bottom surface of the aluminium adaptor was fitted to prevent leakages (Figure 3-8). In order for the pieces to be aligned a female groove was manufactured on the acrylic block with the corresponding male geometry on the aluminium block (Figure 3-5 & Figure 3-8).

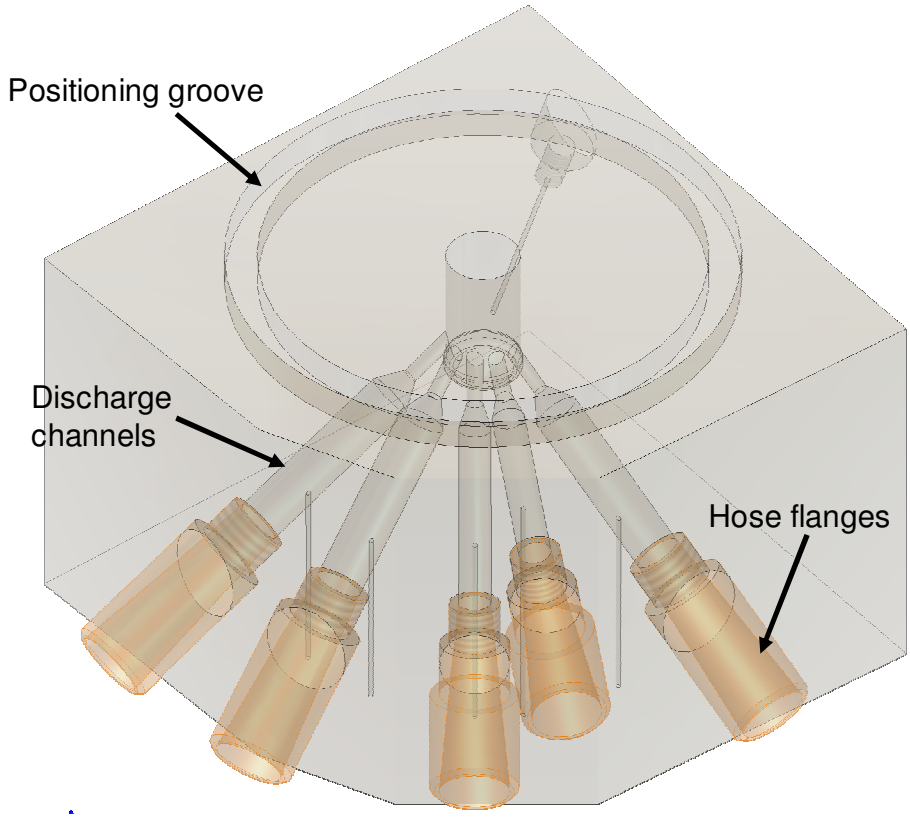

Figure 3-5: 3-D schematic of the large-scale transparent marine nozzle

It can be seen in Figure 3-5 that specially designed discharge channels had to be manufactured allowing injection into liquid without restricting the upstream flow in the nozzle's injection holes. In this way splashing of the liquid on the outer surfaces is prevented and thus, clear images of the internal nozzle flow can be obtained.

These discharge channels, which are 3-4 times larger in diameter than the injection holes, collect the emerging liquid and direct it into the tubes leading to the suction pump (see Section 3.2). The flow is directed to the suction pump through flexible hoses. The fittings for those hoses were chosen to be push-fit type in order to avoid having large threads on the acrylic block since they produce lot of tension thus increasing the risk of having the model

cracked as had happen with other models in the past. The fittings were made out of stainless steel to prevent from rusting. Two o-ring where fitted to each hose fitting in order to avoid leakages. (Figure 3-7)

Pressure tapings of 1mm diameter were manufactured in order to get measurements of the inlet pressure and the back pressure of each individual hole. Thread type fittings, with o-ring seal, were chosen for the pressure tapings hoses in order to avoid leakages. (Figure 3-7 & Figure 3-8).

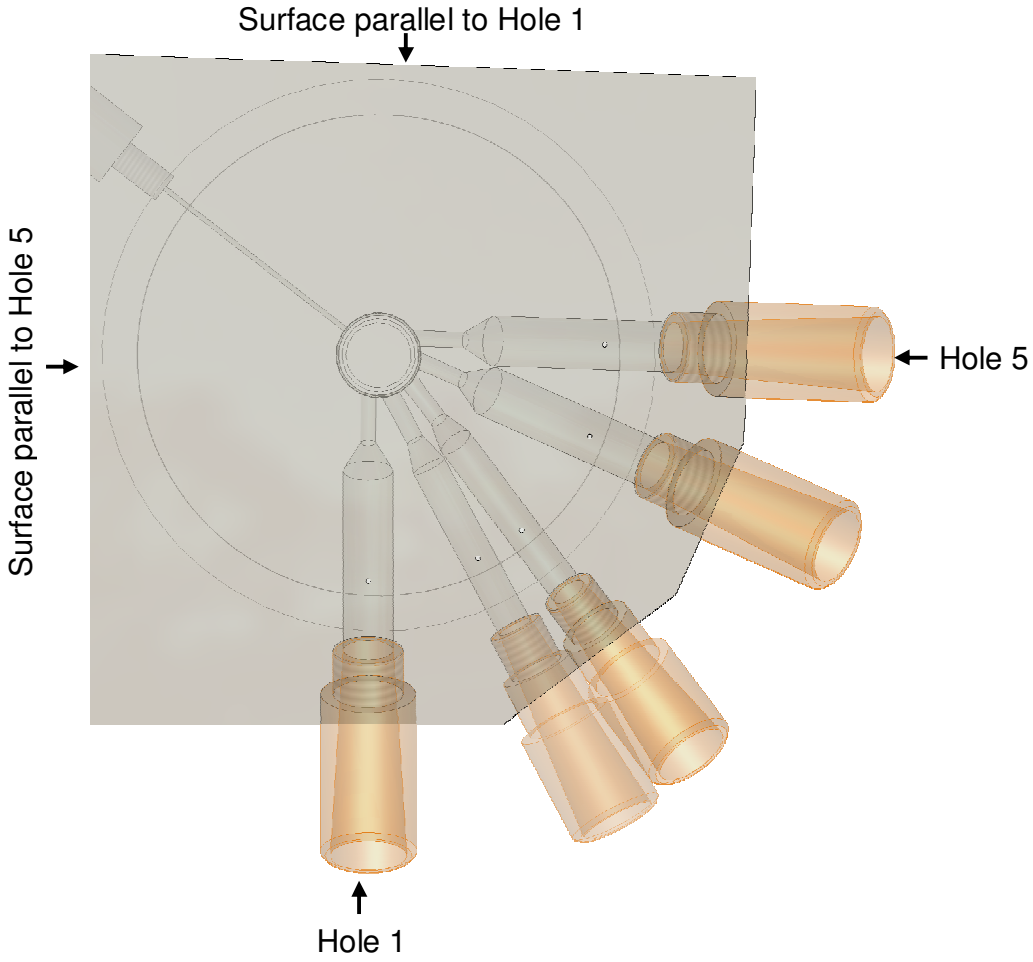

Figure 3-6: 3-D schematic of the large-scale transparent marine nozzle. (Top-View)

Since all the holes are concentrated in a 90 degree sector the holes with the best view are hole 1 and 5, which are the side (outer) holes. As shown in Figure 3-6 parallel surfaces, to those holes, where manufactured in order to avoid deflections and allow good visibility of the cavitation structure inside the injection holes as well as inside the sac volume. All the

holes can be, visually, accessible through the bottom flat surface. An O-ring between the flow duct and the nozzle body provides sufficient sealing (Figure 3-4) provided that the model is properly tightened. The enlarged nozzle was kept attached to the rig by applying pressure from below through 4 screws and a metal plate as illustrated in Figure 3-7.

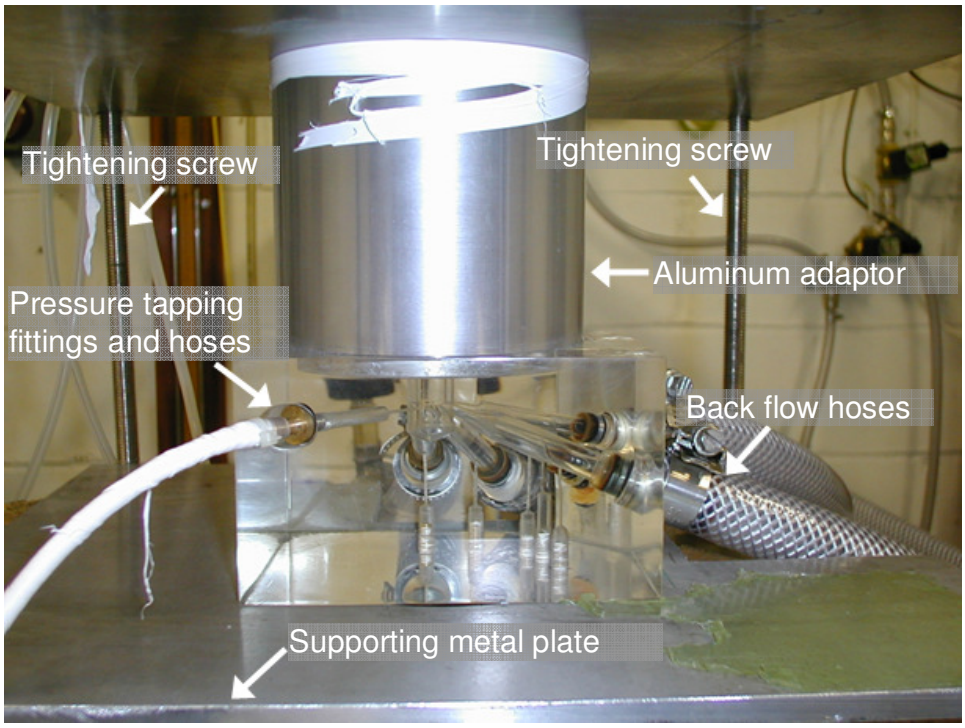

Figure 3-7: Photograph of the large-scale marine model fitted on the test rig.

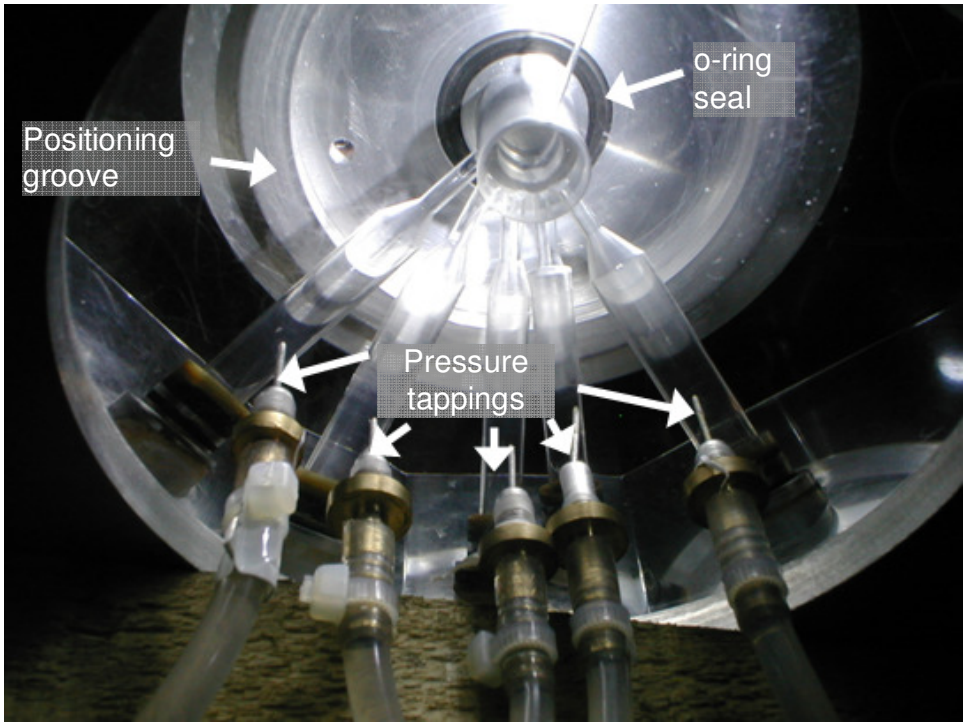

Figure 3-8: Photograph of the large-scale marine model fitted on the test rig. Bottom view

3.1.2 Manufacturing methods

The manufacturing process was supervised and partly conducted by the author and certain methods have been tested in order to achieve better finishing inside the holes and the sac volume. In order to minimize vibrations the drilling bits were chosen to be made of cobalt. The most important concern was to keep the temperature of the drill and the model as low as possible in order to avoid surface cracks, particularly inside the injection holes which had only 3mm diameter, while been 80mm inside the Perspex block. An example of defective injection hole is presented in Figure 3-9. In this figure, it can be seen that except from surface cracks, that heavily reduce the visibility inside the injection hole, there is a big step in the geometry which was caused by the combination of high temperature, that soften the plastic, and the inappropriate, higher, feed rate of the drilling tool.

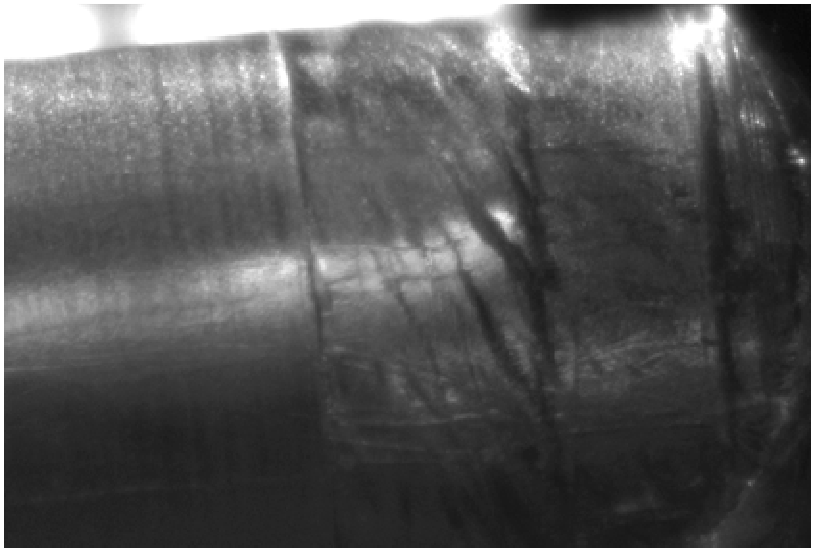

Figure 3-9: image showing a defective injection hole of the large scale marine nozzle model.

In order to keep temperature at low levels, the drill feed rate was set almost to minimum moving only 0.2 mm per move. By doing that the cut material flakes were removed quickly avoiding blockage in the hole which prevented the cooling liquid to convect the heat caused by cutting. A key factor affecting the material flake removal and also, as later proved by the result, the surface finishing is the shape of the cutting edges of the drilling bit. It was proved that drills used for manufacturing of aluminium parts give much better finishing and remove the flakes much faster. This is due to the coarser arrangement of the spiral cutting edges.
In order for the groove inside the sac volume (Figure 3-15 & Figure 3-16) to be accurately manufactured, special tools had to be designed and manufactured since there were no suitable tools commercially available.

Once the manufacturing of the nozzle was finished, the model was polished in order to become fully transparent. For the outer surface a high speed cotton brush was chosen combined with a special polishing 'soap' for acrylic material. The most important, and as proved the most difficult and time consuming, was to polish the injection holes. The need to preserve the exact geometry features was an additional difficulty. The two most important features for this nozzle were the sharp edges at the injection hole inlets and the same diameter for the entire hole length, preventing tapering effects either suppressing or enhancing cavitation formation. Therefore, power tools were not possible to be used as was done for the outer surface. Instead it was chosen to wrap a small piece of cotton wool

around a drilling bit, soaked with special fine Perspex polish paste and by hand polish the holes following a helical movement. The end result was more than satisfactory.

3.1.3 Large scale marine injector nozzle for internal nozzle flow investigation with tapered injection holes

After completing the first experiments on the internal nozzle flow with the large scale marine nozzle model, with cylindrical holes, it became evident that in order to understand the mechanism of string cavitation formation geometric cavitation inside the injection holes had to be eliminated. The most common method to suppress hole cavitation is to make conical, tapered, holes converging toward the hole outlet. This will cause a pressure recovery sufficient to prevent the injection hole from cavitating. For real size operating nozzles, which are made out of metal, tapering is achieved by electrogrinding [43, 44]. However, such machining does not apply to Perspex. Also due to the small hole diameter there were no tools commercially available to start machining a larger inlet diameter and gradually decreasing it toward the injection hole exit.

After an accidental crack, on the outer surface of the large scale cylindrical transparent nozzle, the broken Perspex piece was reattached by using a commercially available Cyanoacrylate adhesive, which is typically sold under trademarks like ‘Superglue’ that was used as the bonding agent. Few hours after restoring the broken piece it was almost impossible to locate the crack location. This proved to be a key element for the manufacturing of very complicated geometries at reasonable cost and time scales.

After some research and several tests a specialized adhesive, indented for Perspex material, was found having the property to bond strongly while retaining the transparency of the material. When applying this adhesive great caution had to be given in order not to leave the glue to come in contact with the surfaces not intended to be bonded. The fact that the glue was relatively thin was making the process more difficult. When the adhesive was applied on the surface the Perspex was dissolved, this was mainly the reason why the bonded pieces where keeping the original transparency and clarity. After 10-14 hours, depending on the temperature, the material was polymerized again and the work piece was ready. Maintaining

a high, relatively, temperature (approx. 35-40 C^o) was favorable and was achieved by placing heating units in the proximity of the Perspex piece right after the bonding. The pieces also had to be kept together by applying some pressure by using common woodworking jigs.

After the first attempt to glue two pieces of machined Perspex, it was found that even with great caution licks of glue were unavoidable. The effect of the glue on a clean Perspex surface was to dissolve it causing it to become blurry and rough. In order to restore the finishing the piece had to be re-machined removing at least 0.3mm of material. This is 0.6mm in diameter for a shape like the sac volume of the nozzle which is unacceptable regarding precision. Therefore it was decided that a draft machining to be done on the piece leaving the final geometry to be shaped after bonding. An offset of at least 0.5 mm was kept for all geometries. However this was not possible for the injection holes since after the bonding of the pieces there was no access from the inlet side in order for the conicity to be shaped. Therefore once the holes were machined to their final dimensions, they were then cleaned with pure ethanol in order to remove any remaining grease on the hole's surface. Then some cotton was inserted towards the injection hole outlet. Then hot wax was poured in leaving the injection hole completely isolated from any possible glue leakage.

In Figure 3-10 and Figure 3-11 photographs of the large scale transparent tapered marine nozzle model is shown. The red parallelograms in the two corresponding views define the section that was removed in order for the conicity, inside the injection holes, to be shaped with the specially made tool shown in Figure 3-12. After machining, the removed section was glued back and as it can be seen it has been completely integrated with no visible edges or internal markings and the transparency is the same as in the solid piece. The outer surfaces of the model where also replenished. A close-up view of the five tapered, outwards converging, holes is given in Figure 3-13.

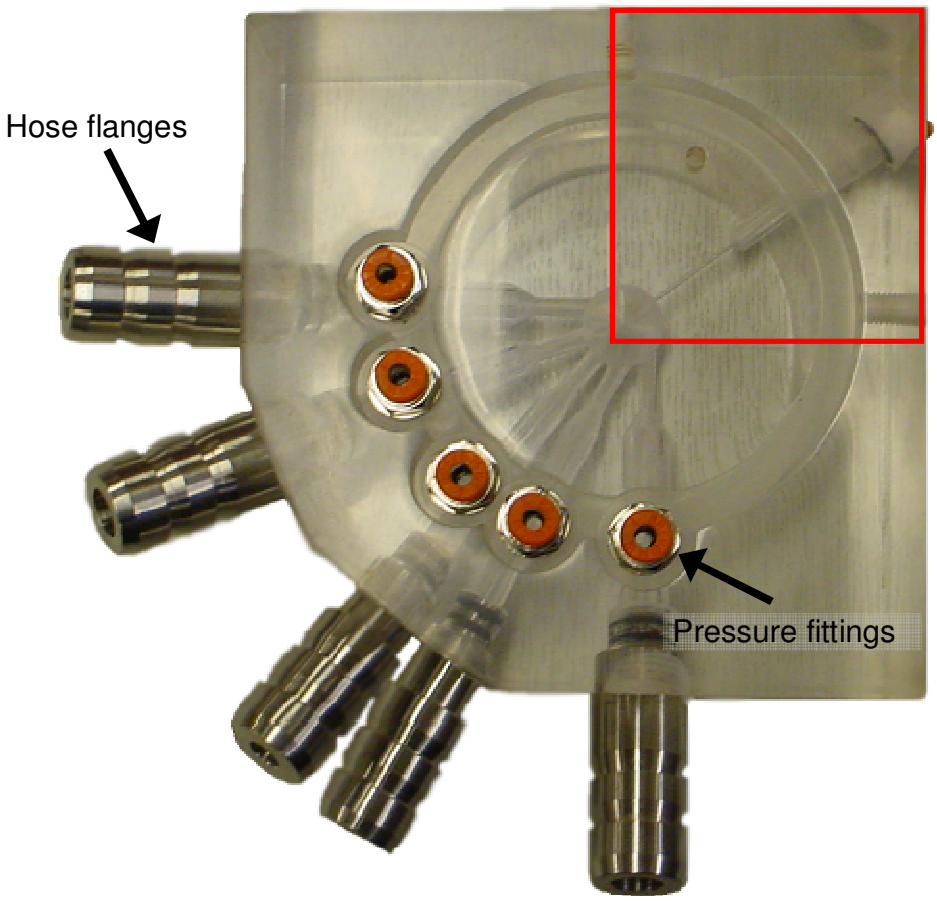

Figure 3-10: Photograph of the large scale marine tapered nozzle model. Bottom-view.

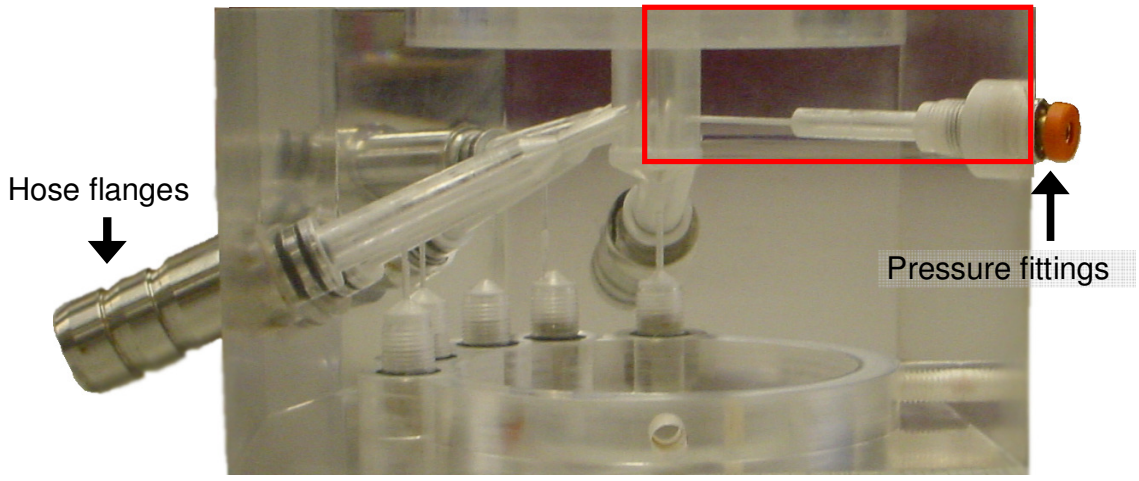

Figure 3-11: photographs of the large scale marine tapered nozzle model. Side-view.

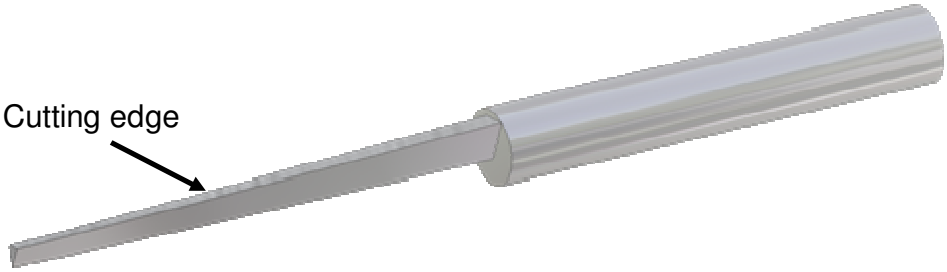

Figure 3-12: specially made cutting tool for manufacturing of the tapered injection holes (outward converging) of the large scale marine nozzle model.

All the injection holes have 4^{o} degrees total cone angle and are followed by discharge channels having the same size as those in the large scale transparent cylindrical marine nozzle model described before. The geometry of the sac volume was also kept unchanged as well as the grooves for the aluminum adaptor to fit the model to the rig.

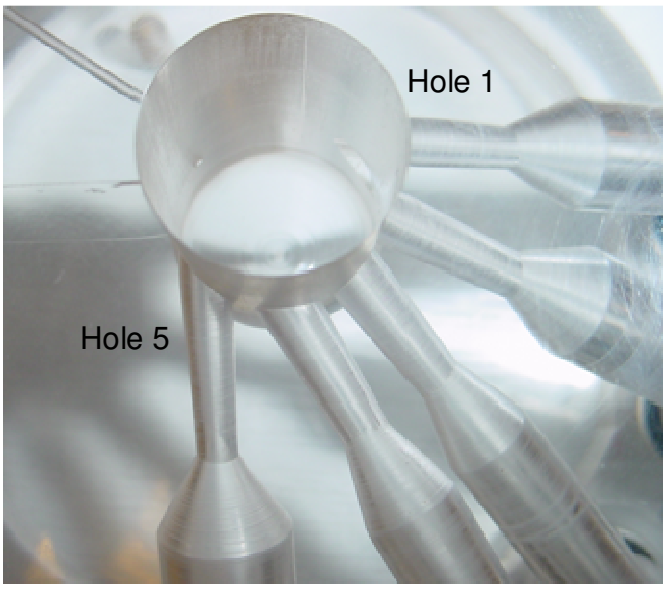

Figure 3-13: Close-Up view of the tapered injection holes of the large scale transparent marine nozzle model.

The hose flanges were redesigned in order to correct leakage issues that had arisen after the first experiments. The sealing mechanism on the model side was kept unchanged, but instead of one, two o-rings per flange were fitted.. The pressure fittings were also changed and instead of using the specially made brass ones, new commercially available 'quick-release' stainless steel and Teflon fittings, used with medium pressure pneumatics, were installed. This was a major improvement since it eliminated leakages as well as air suction

in the discharge channels and dramatically reduced the installation time of the model to the rig. All the models that followed had this type of pressure fittings which were also fitted on the corresponding rig equipment.

3.1.4 Transparent marine nozzles for spray and internal flow visualization

As previously mentioned, it is widely acknowledged that important results can be obtained from flow visualisation inside enlarged three-dimensional and fully transparent model nozzles. However, in most cases, what is of great importance is to visualize how the internal nozzle flow affects the near hole exit spray structure. Studies have shown that apart from the well understood geometric (or hole) cavitation, dynamic forms of cavitation, commonly referred to as string cavitation, have great effect on the atomization process of the emerging spray. [30, 32, 56, 102, 110-116]

This has lead many researchers to investigate the internal flow in enlarged models while using original real-size (non-transparent) nozzles for high pressure spray characterization. Then by utilizing the flow similarity, they are trying to link the effects observed in the spray with a change that they have seen in the flow inside the large scale nozzle. Ideally, some have tried to manufacture transparent real size injectors, capable to work at close to operational flow conditions, and thus enabling the simultaneous monitoring of the internal flow and the near hole exit spray structures. Usually that involves the addition of a quartz window after cutting part of a real-size metal injector [114], however, the end result is not very reliable, leading to failure of the quartz window, and even for those nozzles that withstand the high liquid pressure the image quality is poor, mainly due to insufficient lighting.

For the two-stroke low speed marine Diesel engine nozzle even if the manufacturing of a real-size transparent replica was easy, since its size is almost ten times the size of a multi-hole Diesel injector, there would have been no possibility, at least with the equipment available in the testing facilities of the university, to achieve actual pressure levels due to the huge flow rates that would be needed.

Taking that for granted, a real-size fully transparent, Perspex, real-size nozzle was manufactured in order to be fitted on the same rig as the large-scale nozzle model. Usually, in the real-size spray testing facilities, the injector is placed inside a pressurized chamber able to achieve pressures similar to those that exist inside the engine cylinder while injection takes place. However, in the large-scale internal flow model, the back pressure is controlled from the suction pump that reduces the pressure inside the discharge channels; this allows for higher cavitation numbers to be achieved. However, none of these techniques could be used here. Therefore, it was decided to keep the injecting nozzle in real-size dimensions, thus reducing the required flow rate, but achieving cavitation numbers close to those existing at real operating conditions. An extra reason for making a real size nozzle was also to confirm if the internal flow characteristics that were found in the large-scale model, including both geometric and string cavitation, would be present and in what frequency. Even if this is well established for conventional multi-hole Diesel nozzles there were no literature references for those used in marine engines.

.

Due to the large hole diameter of the real-size injector it was impossible to provide the flow rate needed in order to achieve actual pressure field levels with the equipment available in the university. Moreover the mass (or volume) flow rate of the liquid leaving each injection hole could not be measured. Therefore the discharge coefficient from the large-scale nozzle investigation would be used when needed assuming that, for similar flow conditions, is the same for the real-size nozzle.

An acrylic adaptor was manufactured in order for the real-size injecting nozzle to be fitted on the rig, having the same o-ring groove as the large-scale internal flow nozzle. Since it was not possible to hold the transparent model against the adaptor by the metal plate that was used before, female threads were manufactured on the adaptor with corresponding male threads on the nozzle model in order to connect the pieces together (Figure 3-17 section (A)). This was proved to be a very useful design making nozzles to be attached or removed very easily on the rig enabling testing of different nozzles geometries to be much more convenient. Finally an o-ring was fitted between the two pieces in order to prevent leakages.

As in the large-scale nozzle, two surfaces parallel to hole 1 and 5 were shaped in order to provide the necessary optical access inside the injection holes and the sac volume (Figure 3-14). These surfaces were necessary since there is no visual access from the bottom surface of the nozzle due to water splashing. The upstream nozzle geometry was kept unchanged compared to the large scale model, i.e. omitting sections A, B and C (Figure 3-2) assuming the flow to be uniform as it comes down the flow duct.

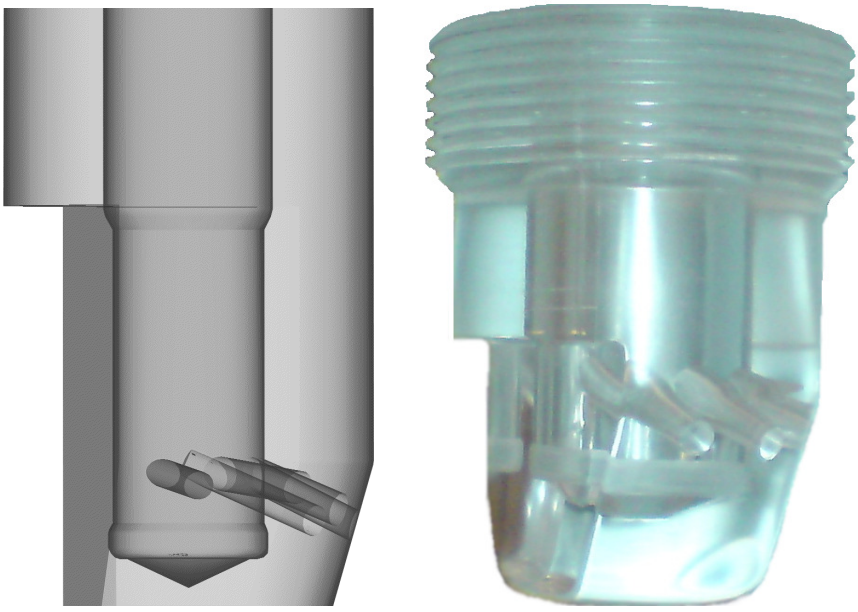

Figure 3-14: 3-D schematic and photograph of the transparent marine injecting models.

The injection hole diameters were between 1.5 and 1.8 mm. The fact that all the injection holes are concentrated on a 90-degree sector leaves limited space between them on the inlet side. That practically means that few 1/100ths of a millimetre error at the drilling bit positioning can lead to the injection holes been merged, eventually destroying the entire piece. It also has to be mentioned that a major concern was the strength of the model since the thickness of the material, particularly at the two side holes and the corresponding parallel surfaces, was about 0.25mm. Since it was very difficult to predict the forces which the nozzle can withstand without breaking, two more nozzles with thicker walls were also manufactured. In those nozzles part of the hole was not optically accessible.

Again, as in the large-scale model, special tools had to be designed and manufactured in order to shape the sac volume accurately. The most difficult was to replicate the groove located below the hole inlets. For that reason a tool was designed to have exactly the same profile (male geometry) as the groove, including the rounding, the inclined and straight edges within less than 2 mm space as shown in Figure 3-15.

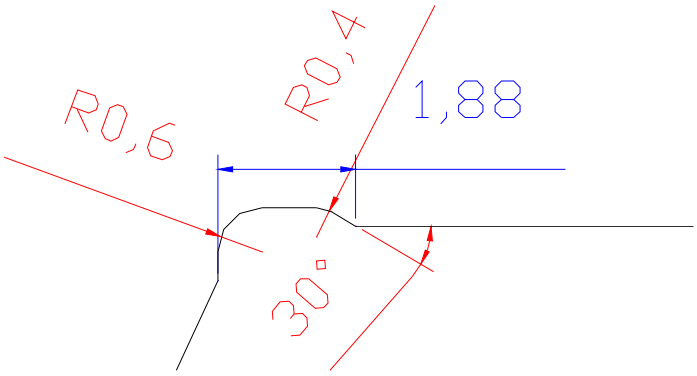

Figure 3-15: real-size marine nozzle sac volume detail

The design of the tool was prepared and was uploaded to a highly accurate and sophisticated CNC machine capable of handling complex geometries. In order for the tool to be sharp and with the least possible vibration (deflection under load) when it would be used to cut Perspex, a high carbon content steel was chosen. Upon manufacturing the next stage was to sharpen the cutting edges. This was done by grinding the tool using a rectifying machine with special grinding stones. Finally, it was heated and then cooled in oil in order to harden. The finished tool was then attached to the CNC machine in order to shape the groove in the sac volume. The tool that was manufactured was used for all other marine nozzles that were made. The end result was considered satisfactory as can be seen in Figure 3-16. The groove for the large-scale model has been manufactured in exactly the same way.

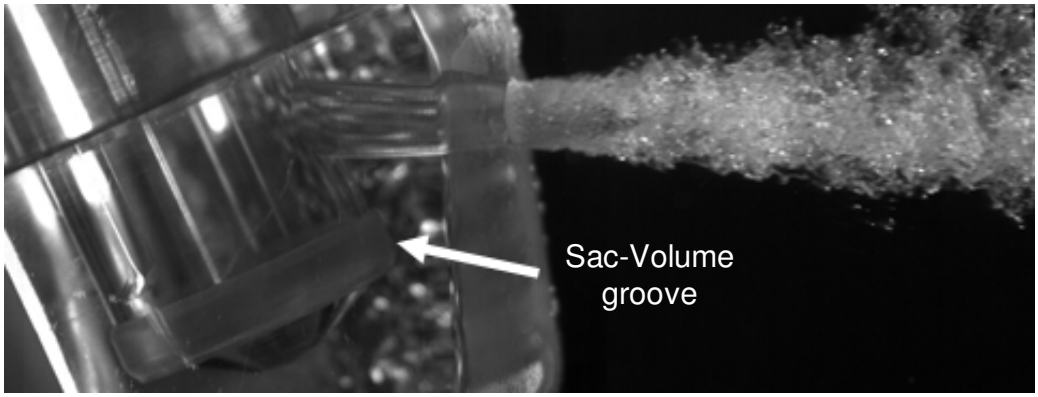

Figure 3-16: Photograph of injecting marine nozzle model sac volume detail

Again the manufacturing process had been supervised and assisted by the author, using the previously acquired experience from the manufacturing of the large-scale model; the process followed was exactly the same. However, in this case even lower feed rates have been used in order to achieve the best possible finish inside the holes and the sac volume.

3.1.5 Large-scale transparent marine injecting nozzles

After completing the first set of spray experiments with the real-size transparent injectors it became evident that the optical access in the sac volume and the injection holes was limited. The need also to make more complex geometries such as outward converging tapered holes, led to the manufacturing of large scale (2:1) fully transparent marine nozzles. This was also assisted by an upgraded delivery pump able to supply the increased flow rate needed. The internal nozzle geometry was kept exactly the same as well as the concept of attaching the nozzles on the rig. Apart from the enlarged dimensions (2:1) and the fact that the adaptor was made from aluminium the arrangement was the same as the one illustrated in Figure 3-17.

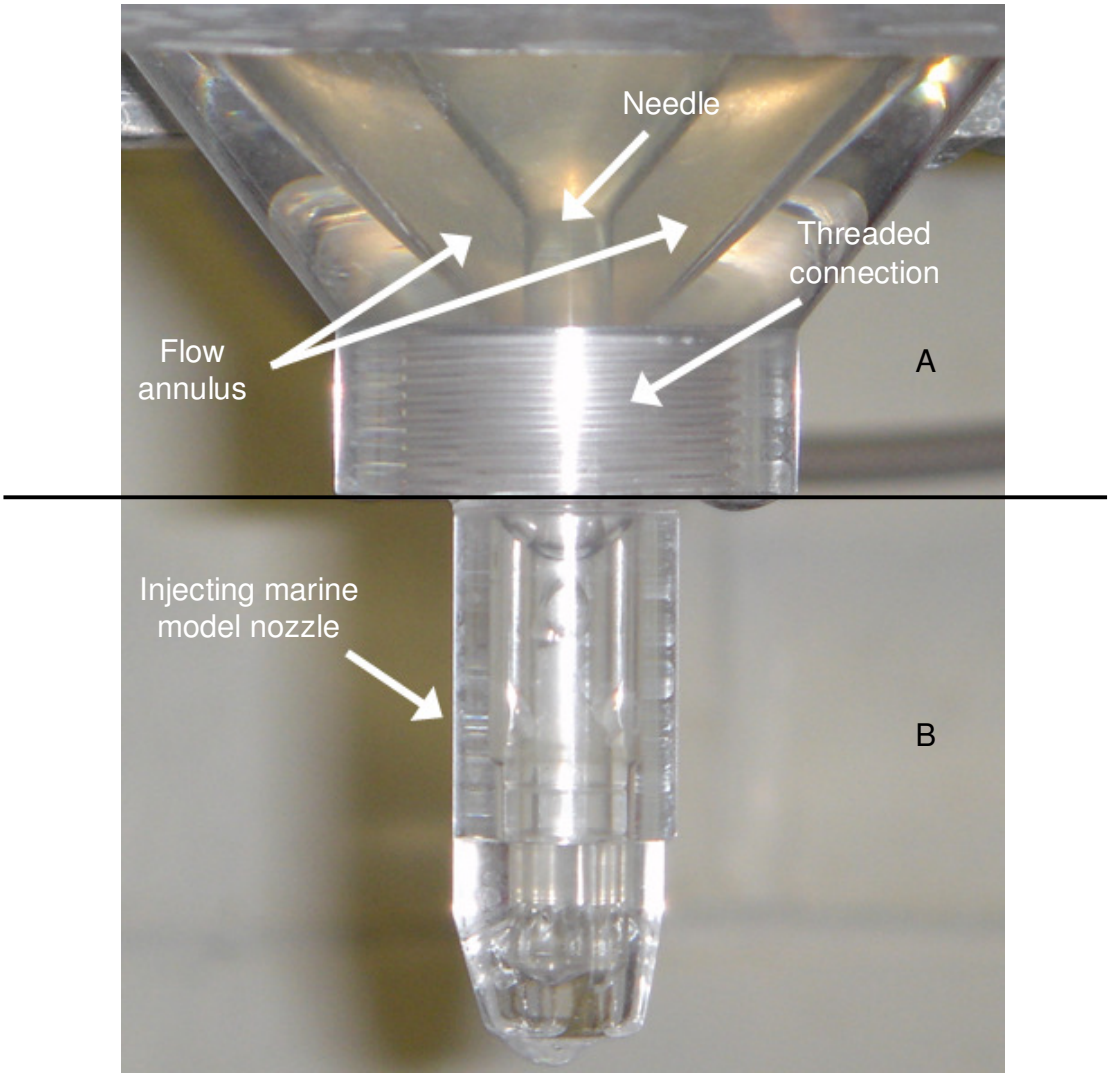

Figure 3-17: Photograph marine nozzle model fitted on the test rig used for spray visualisations

Six different large-scale nozzles were manufactured all having the same sac volume geometry. These are: a) five-hole cylindrical, b) two-hole cylindrical, c) one-hole cylindrical, d) five-hole tapered, e) two-hole tapered and finally one-hole tapered nozzles. Schematics of all the six designs can be seen in Figure 3-18. Tapered nozzles were manufactured using the same technique as the one described in the previous section, for the large-scale nozzle model. The total cone angle was also the same, i.e. 4^{o} degrees.

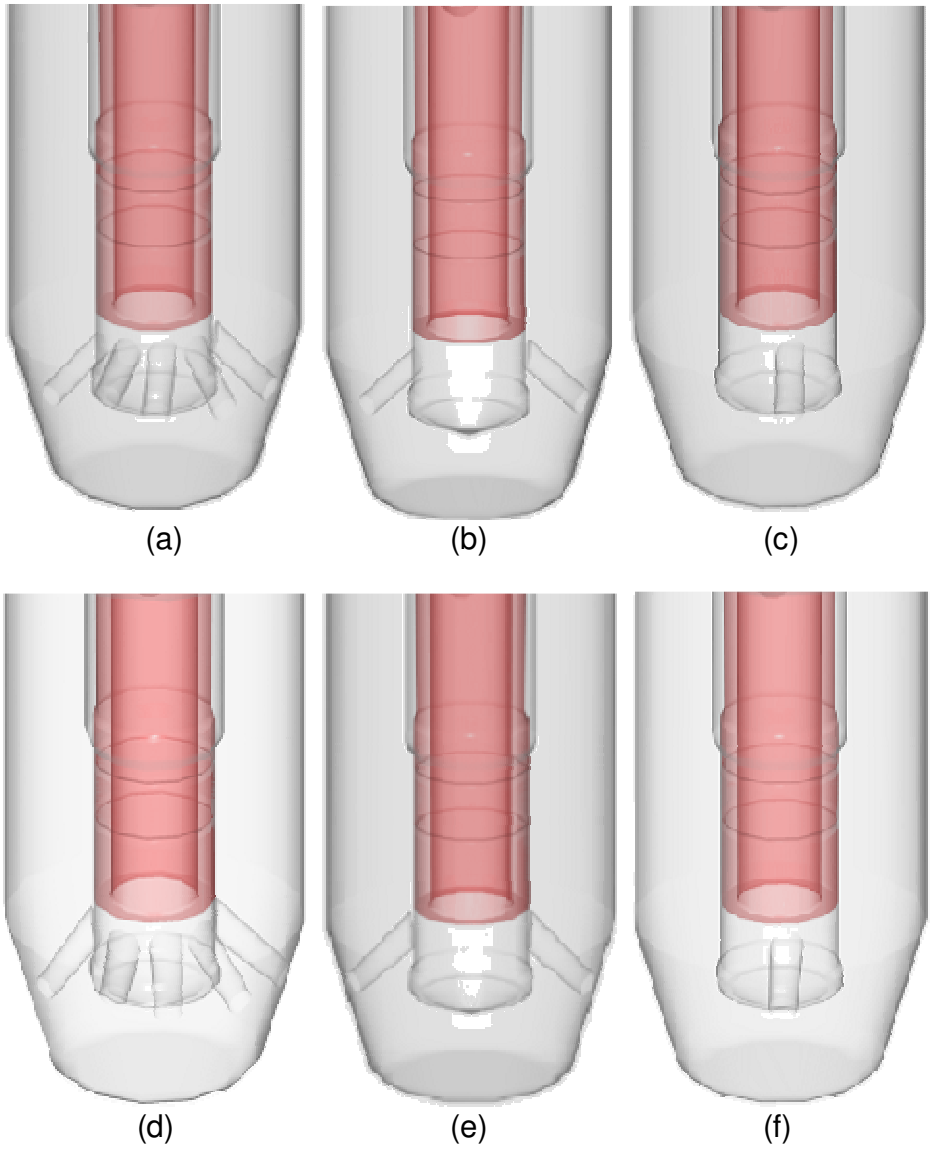

Figure 3-18: 3-D schematic of all marine nozzle models used for spray visualization. a) 5-hole cylindrical (real & large scale), b) 2-hole cylindrical (large scale), c) 1-hole cylindrical (large scale), d) 5-hole tapered (large scale), e) 2-hole tapered (large scale) and f) 1-hole tapered (large scale).

The large-scale five-hole cylindrical injecting nozzle was made in order to have direct comparable results with the internal nozzle flow nozzle previously presented and also correlate the spray structure with the real-size injecting nozzle that was investigated before. The two-hole cylindrical nozzle was made in order to produce geometry with relatively steady string cavitation as this was suggested by the internal nozzle flow investigation findings. The single hole cylindrical nozzle was intended for quantitative spray cone analysis which was not possible, at least not in a fully automated way, with the five hole

nozzle since the sprays were interacting. The tapered injecting nozzles were made in order to isolate the effect of geometric cavitation on the spray formation. Also as the investigation in the large-scale transparent tapered nozzle has shown that at high cavitation numbers string cavitation can be formed inside the nozzle without visible hole cavitation. However, after some further analysis it was concluded that the string was formed because bubbles from the throat of the expansion tubes were sucked inside the vortex core, thus forming a string like cavitation structure. Since these nozzles would not have expansion tubes it was interesting to see whether any visible string cavitation structure would form inside the sac volume. Moreover, if such structure was found, it would made possible to understand how it was formed and how it affected the near hole exit spray structure. Finally, the number of holes that each tapered nozzle would have, was determine with the same criteria as for the cylindrical nozzles mentioned before.

3.1.6 Manufacturing methods of injecting nozzles

Similar to the previous transparent models, the main objective for the spraying injector models was to have a good surface finishing on the inside of the injection hole and sac volume surface while maintaining the precision in the geometry. As previously mentioned high strength steel or cobalt drills were used for opening the holes. However, it was concluded that even though the drill has to be new, it is much better before the first use on acrylic to be used to open some holes on soft metal. This will remove any sharp edges, that have been developed during the drill's manufacture, from the cutting edge of the tool. If the cutting edge of the tool has such impurities it will produce heavy scratches on the injection hole's surface. High rotation speeds result into better surface finish as long the temperature is kept low. Every time that the drill is moving inwards to open a hole, it has then to come out in order to remove the flakes of the cut material. This might be time consuming but is much safer than risking to increase the temperature of the tool. Finally, even with small feed rates, when drilling small and deep holes there is always possibility for the material flakes to stack. Then these flakes will start rotating with the drill and if not removed burn the hole surface. To prevent this to occur, each time the hole was filled with some liquid in order for the heat to be convected. There are many liquids commercially available used to lubricate and cool both the cutting tool and the component been machined but usually are designed to

be used with metals. Since acrylic may react with some of the substances of these products, it was chosen to use just plain water or water-oil emulsion both giving satisfactory results.

3.1.7 Large scale conventional multi-hole nozzles

Within the framework of the collaboration with a major Diesel engine manufacturer it was decided to include investigations of the flow through large-scale multi-hole VCO and sac-type Diesel nozzles. As with the marine nozzle models, these transparent nozzles were manufactured from Perspex. Both nozzles were six-hole; the magnification factor was 15x for the VCO and 10x for the sac-type. Three-dimensional schematics of the transparent nozzles are shown in Figure 3-19. These types of nozzle have their main difference in the way they seal off the high pressure region, upstream of the needle seat, from the injection holes.. In the case of the sac-type nozzle there is only a line contact between the needle and the needle seat which is located well above the injection holes. This distance along with the presence of the sac causes a relatively large amount of fuel to remain in the "dead volume" of the nozzle tip after the end of injection leading to dribbling. On the other hand, in the VCO nozzle there is virtually no sac volume left to be filled with fuel, since the needle is in surface contact with the needle seat covering the injection holes completely. Figure 3-20 shows photographs of the enlarged 6-hole VCO nozzle.

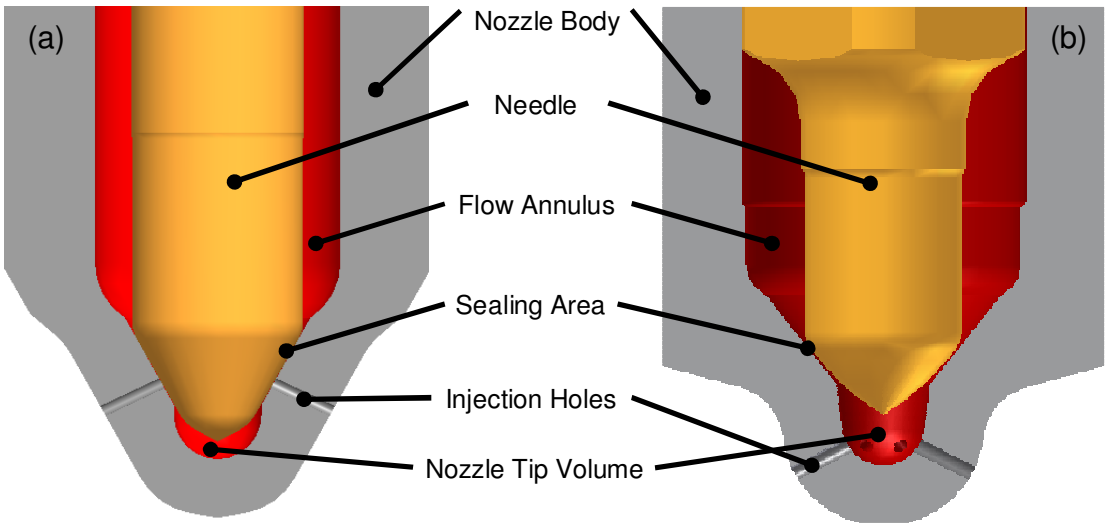

Figure 3-19: Geometry of the VCO nozzle (a) and sac-type nozzle (b) investigated.

Figure 3-20: Photographs of large-scale VCO nozzle.

The hole diameter of the cylindrical VCO nozzle is 195μm, which results to a nominal hole size of 3mm in the large-scale model. For the sac-type nozzle the injection hole diameter is about 320μm which gives 3.2mm in the large-scale model.

In total three large-scale transparent multi-hole nozzles were manufactured. The VCO nozzle was made with both tapered and cylindrical holes. The sac-type nozzle was made with cylindrical holes only. All the nozzles in their original design had rounded hole inlet edges. This is a feature that was required to be modelled. As it has been explained previously in this chapter, rounding of the hole inlet edges can change dramatically the behaviour of the fluid flow. Although a number of studies have been made on rounded nozzles both numerical [117] and experimental [96, 118], most involve simple single hole nozzles. Having tested the technique of bonding Perspex blocks while preserving their strength and transparency, the same method was used for manufacturing nozzles with rounding and tapered holes. A photograph of the sac-type nozzle is shown in Figure 3-21 .

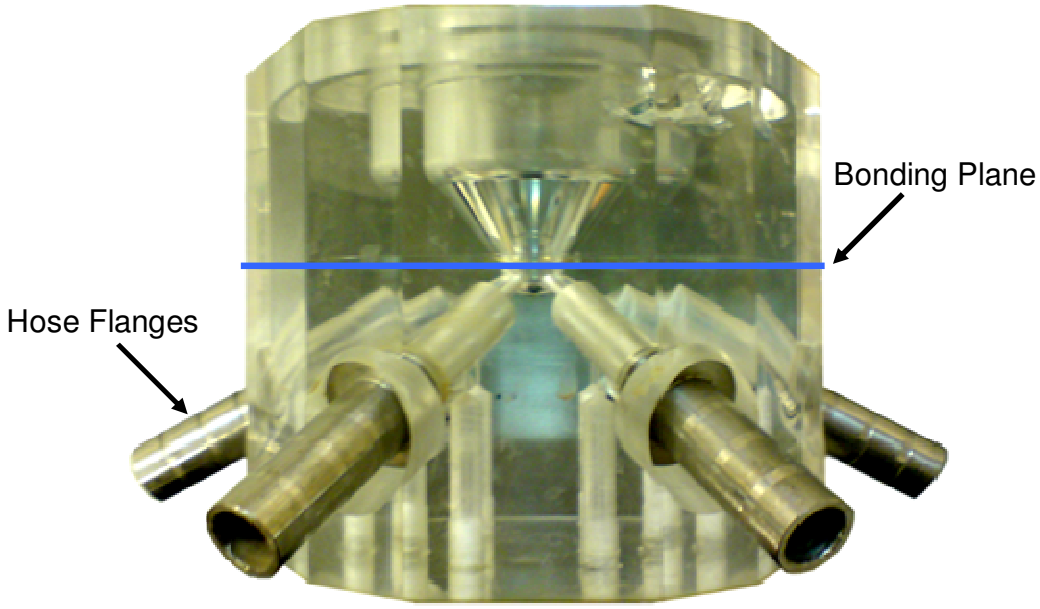

Figure 3-21: photograph of the large-scale transparent model of the sac-type nozzle. (Side view)

For the hole inlet edges a special tool made of carbide was made having the male geometry of the rounding. Then with a standard drilling bit the cylindrical hole was shaped as in the marine nozzle. The first block of Perspex included only the section of the nozzle geometry starting at 5mm above the injection holes and below. As it is shown in Figure 3-22 this provided the necessary access to the special rounding tool to be positioned opposite to the hole inlet. Then, the tool was aligned and moved inside the hole enough for the rounding to be formed. This was the common method for manufacturing all the three multi-hole nozzles. For the tapered VCO between the opening of the cylindrical hole and the rounding an extra step was added in order to shape the conicity by using a similar tool as the one shown in Figure 3-12. The shape factor for the conical VCO nozzle was k=2; this means the equivalent exit hole diameter of the real-size nozzle would be 20μm smaller than the inlet one. The rounding of the edges were specified in radius of curvature, instead of percentage increase in flow rate compared to the sharp edged nozzle (% 'HE'). The equivalent radius of curvature of the real-size nozzle would be 20μm for both VCOs and 25μm for the sac-type nozzle. A schematic of the injection hole geometry of the VCO nozzles is given in Figure 3-23.

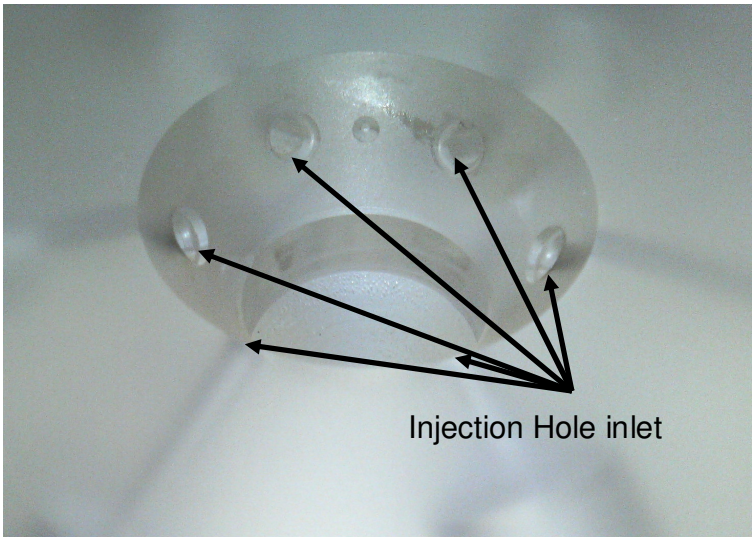

Figure 3-22: Perspex block of the large-scale transparent VCO Tapered nozzle, with injection holes before bonding.

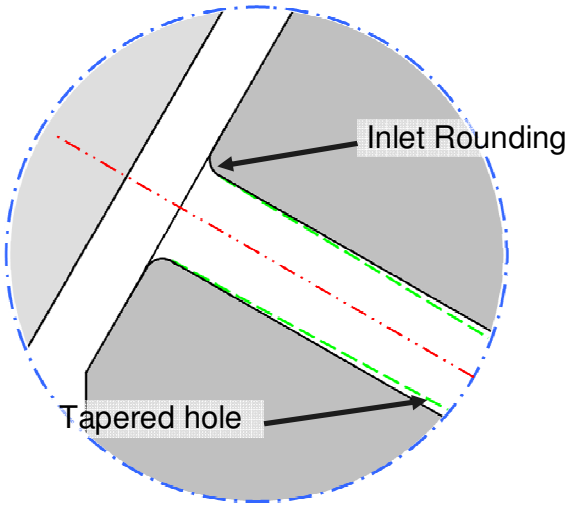

Figure 3-23: Schematic of the injection hole geometry of the investigated VCO nozzle.

The second block of Perspex was added and glued with a special adhesive. Once bonded, the completed piece was transferred to the CNC lathe for the internal nozzle geometry to be shaped. Pressure tappings and hose fittings were also added as with the large-scale marine nozzles. The enlarged nozzles had discharge channels downstream of the injection holes in order to collect the emerging liquid and direct it into the tubes leading to the suction pump of the closed flow circuit (see Section 3.2). These discharge channels were almost 4 times greater in diameter than the injection holes. As in the marine nozzle model flat outer surface were shaped to insure undistorted optical access inside the injection holes and the sac volume of the nozzle. All three nozzle models were manufactured in such a way that the

details of the nozzle geometry were represented until the final cylindrical shape reaching to the needle shoulder.

The existing rig which was made to model the geometry of a conventional Diesel nozzle includes the geometry of the flow passages upstream of the nozzle (Figure 3-24). This was accomplished by enlarging the real-size geometry from the volume around the needle shoulder downstream to the nozzle, except that the length of the flow passage along the needle was shortened slightly, due to overall size limitations. Nevertheless, this has allowed the flow inside the enlarged needle annulus to fully develop until it reached the nozzle annulus[114].

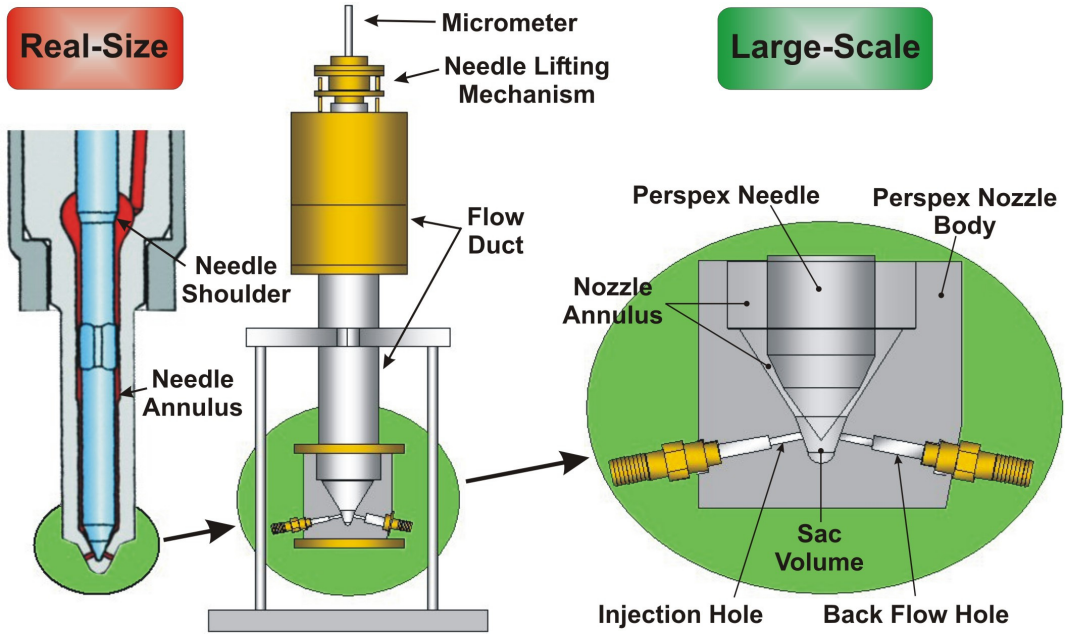

Figure 3-24: From real-size to large-scale injector. (as shown in [114])

As explained in Chapter 2 needle eccentricity can strongly affect the internal nozzle flow and cavitation formation and distribution in the nozzle. For the VCO nozzle it was requested to take measurements with deferent degrees of needle eccentricity. It should be stated that although the needle body has guides in order to reduce needle transverse motion, the tolerance between the nozzle body may allow for sufficient eccentric shifting.

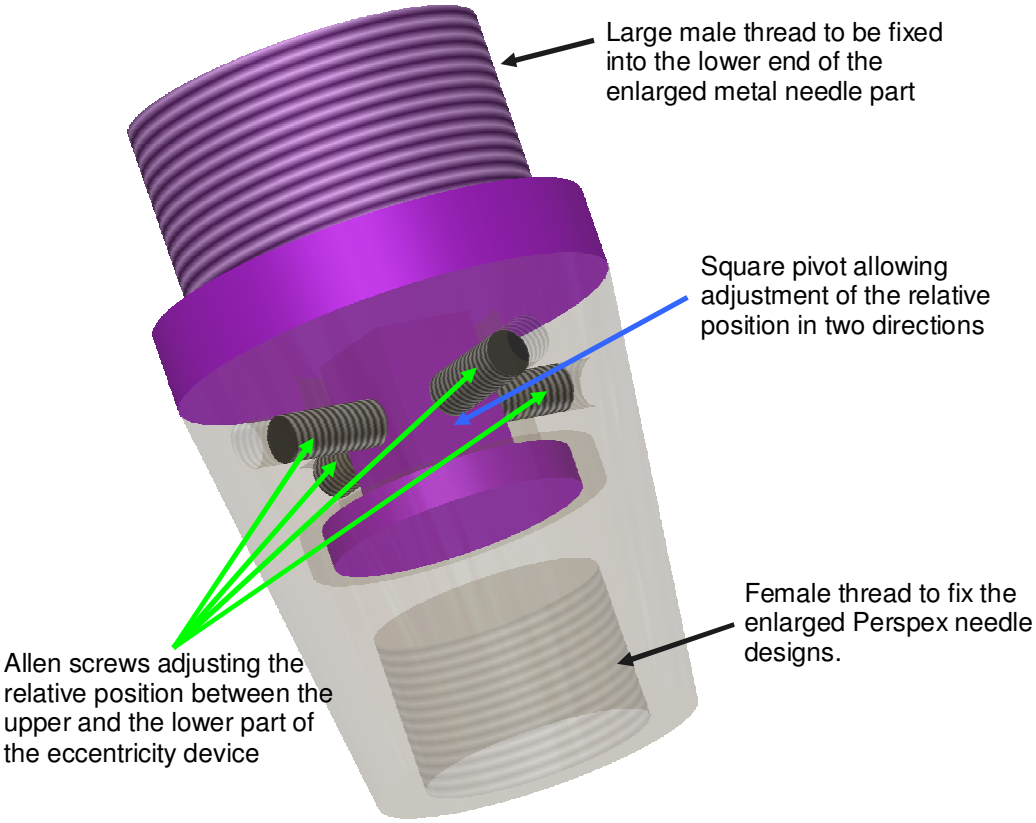

Figure 3-25: 3-D schematic of the eccentricity mechanism for the large-scale multi-hole nozzles.

The above Figure 3-25 shows a 3-D schematic of the eccentricity device. This mechanism was made from aluminum and consists of two parts. The upper part (shown purple) was fixed into the metal needle shaft of the rig. Then, the lower part (shown transparent), which was split in two pieces in order to be possible to dismantle it, was placed around the upper part. Once the two pieces of the lower part were fixed by some pins, it could have a relative radial displacement of 2mm compared to the upper part. Four Allen-type screws where adjusting the eccentricity by touching on the square pivot belonging to the upper part. Once the required eccentricity was set, the Perspex needle model was fixed on the lower part using the corresponding female threads.

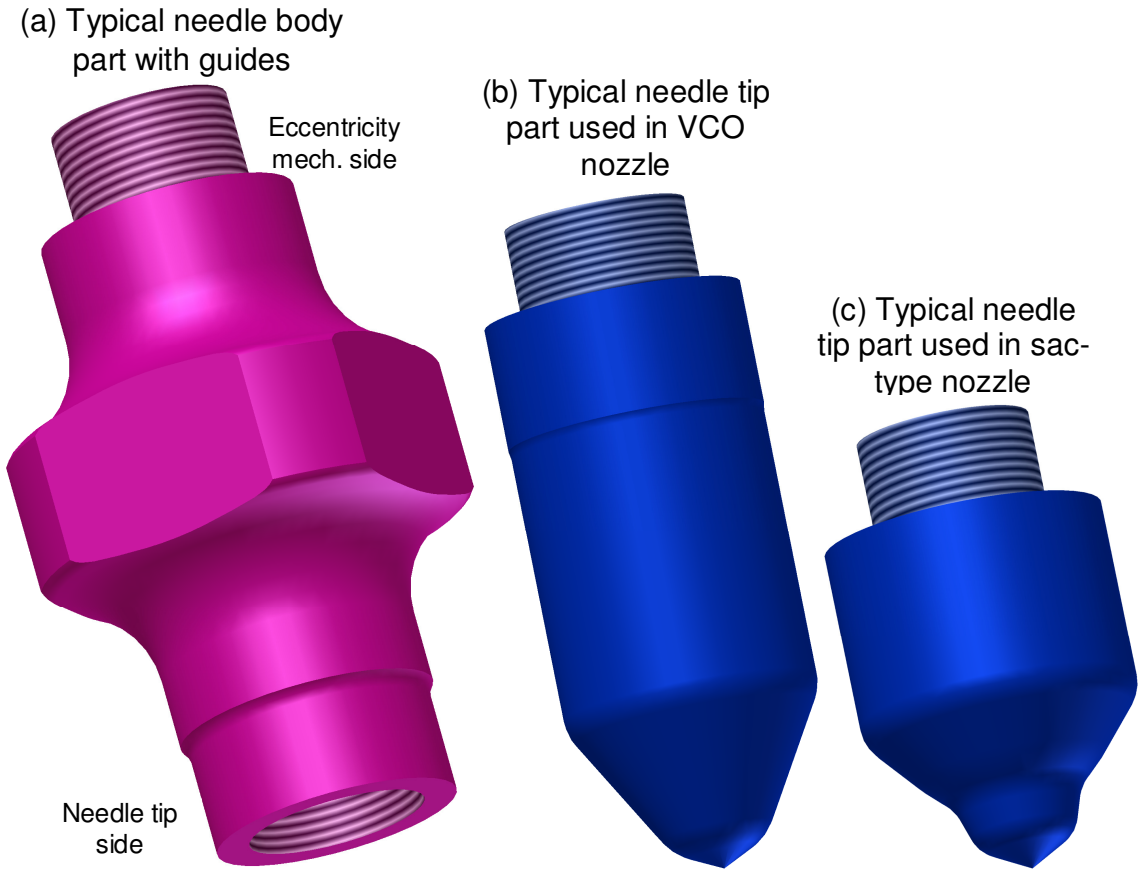

Figure 3-26: 3-D schematics of the Perspex needle models used with the large-scale multi-hole models.

Figure 3-26 shows 3-D drawings of needle parts fitted after the eccentricity mechanism. The needle body part that contains the guides was made both for the VCO and the sac-type nozzles. All have similar layout but different tolerances with respect to the needle body. The needle tips where fixed on it using the corresponding threads. In total four different needle guide parts were made and eight different needle tips, 2 for the VCO and 6 for the sac-type. A typical image of those Perspex needle parts is shown in Figure 3-27.

Figure 3-27: photographs of selected enlarged transparent needle parts used with multi-hole nozzles.

3.2 Continuous flow test-rig

An improved version of the refractive index matching test rig available in the university facilities, with water been the working fluid, was used in order to investigate the transparent nozzle models. The experimental setup of the system is shown in together with the L-S model nozzle. The rig incorporates stronger pumps with variable speed control. The overall flow rate can be adjusted over a wide range directly through the pumps in addition to the fine adjustment by means of the various flow and bypass valves. The incoming flow rate is measured by using a two-channel ultrasonic flow meter which provides the individual flow rates through one or two flow pipes with high accuracy. The flow pumps generate heat which, after long periods of continuous flow, may increase the water temperature. To prevent the water temperature to exceed 25ºC, a water-cooling flow loop was fitted in the 90 litre storage tank and was connected to the water supply of the test cell

For the L-S model, the flow rate collected through the flexible hoses from each of the injection holes was also measured simultaneously with the incoming flow rate. The fluid is then directed via the suction pump into the tank in order to close the flow loop. Also inlet and outlet pressures were monitored and measured with highly accurate digital pressure gauges through the pressure tappings on the L-S model. In order to reach sub-atmospheric back pressures and therefore higher cavitation number, a suction pump was installed in addition to the main feed pump. This pump is connected to the back flow hoses collecting the liquid from the discharge channels of the nozzle model.

For the spraying nozzles only the feed pump was used. The spray exiting the injection holes was collected and directed to the tank.

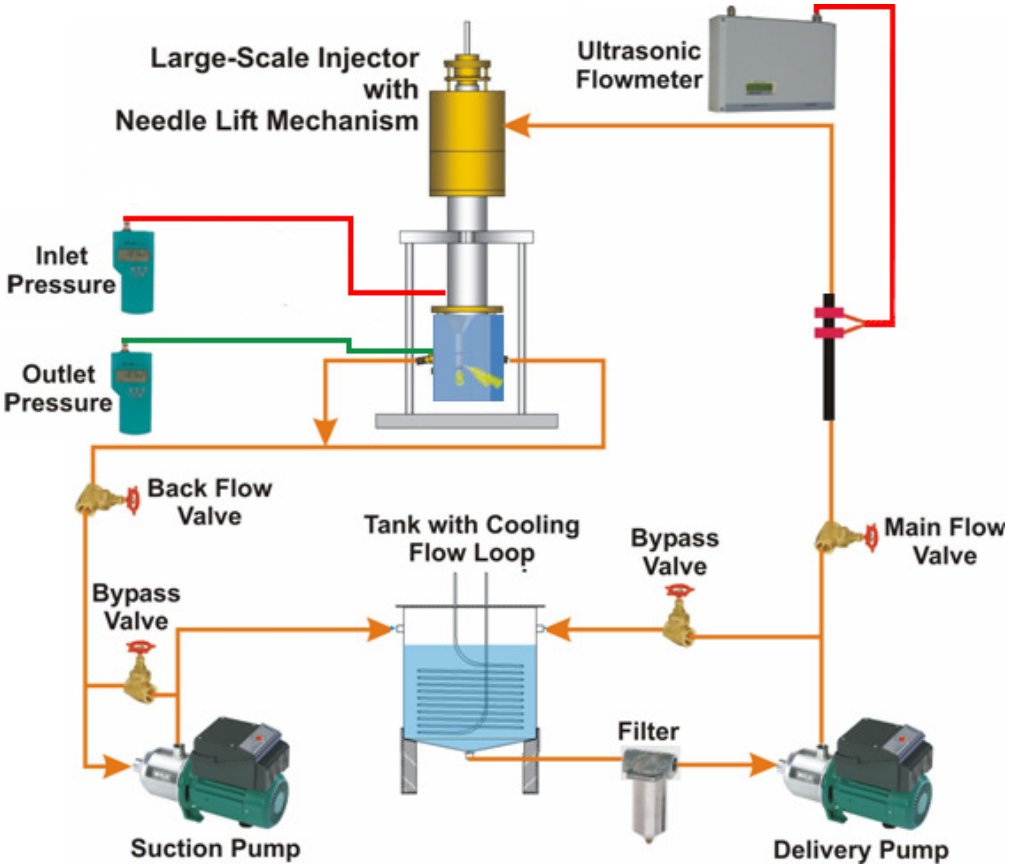

Figure 3-28: Schematic of the improved refractive index matching flow test rig with incorporated Large-Scale model nozzle

3.3 Imaging techniques

3.3.1 Imaging in large scale nozzles with expansion tubes and injecting

Since the fuel flow through the injector nozzles, especially through the holes, is highly turbulent, all flow features can be expected to behave transiently and with short time-scales. This behaviour is virtually impossible to capture with still images, or an image sequence taken with a conventional CCD camera. Since it is important to gain knowledge about the dynamics of the cavitation inception and formation processes for various flow conditions, two high-speed digital video systems, in conjunction with the refractive index matching test rig (Section 3.2), were set up and synchronised in order to capture the cavitating structures from two views simultaneously, as shown in Figure 3-29 .

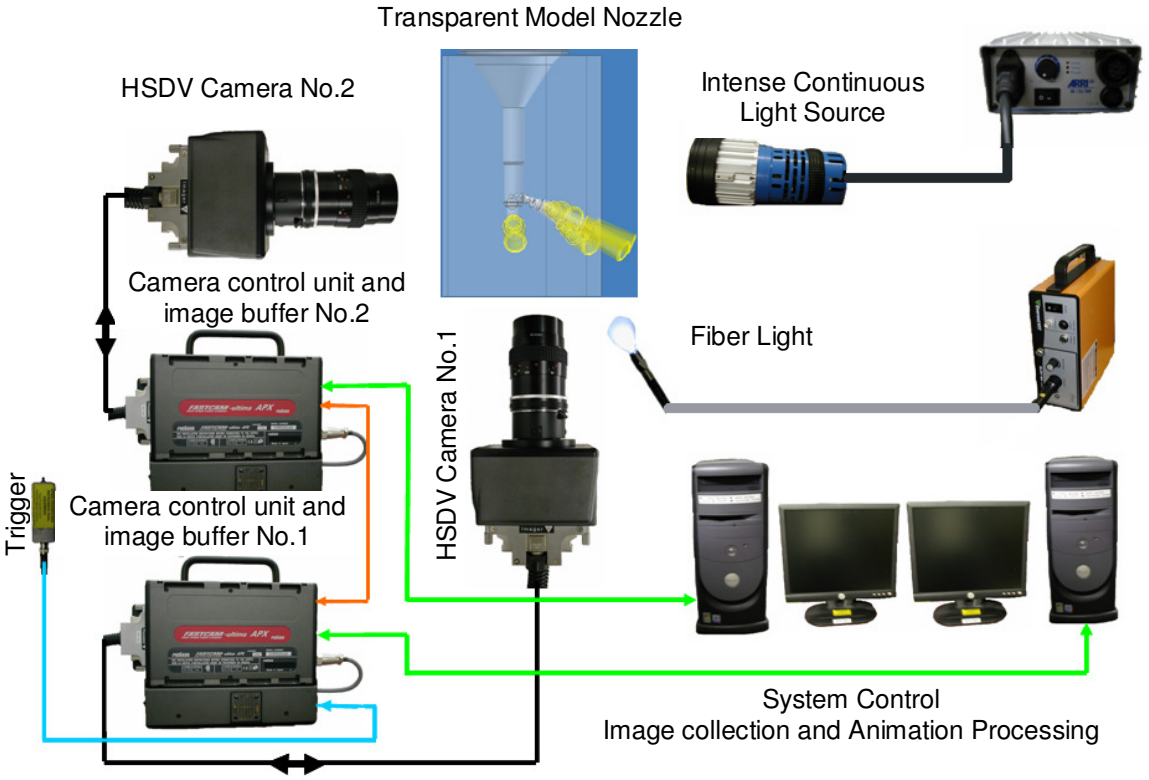

Figure 3-29: Schematic of HSDV imaging in large-scale 3-D model nozzle

This has allowed 3-D reconstruction of the cavitation strings. With simultaneous use of the numerical grids used for the CFD analysis, the spatial and temporal average locations of the strings have been calculated in the 3-D space. At the same time, superimposing of images obtained from the bottom view only has allowed for time- and spatial averaging over the whole nozzle volume depth of the projected 2-D images. This can provide a relatively fast way for comparing between different cases where the cavitation strings form at different locations on the X-Y plane within the nozzle volume. It has to be noted that although imaging from the bottom view can capture the flow structure in all injection holes and the nozzle sac volume simultaneously, imaging from the side view is restricted only to one or two holes depending on the positioning of the camera, together with the nozzle flow.

The Photron FASTCAM-ultima APX cameras used are able to take up to 120,000 frames per second (fps) with an exposure time as low as 4μs and a maximum resolution of 1024×1024 [119]. For the particular cases investigated here, usually 6,000 to 16,000 fps where sufficient to capture the temporal development of cavitation using a shuttering time of 30μs. In total up to 4,000 images were collected for a particular case.

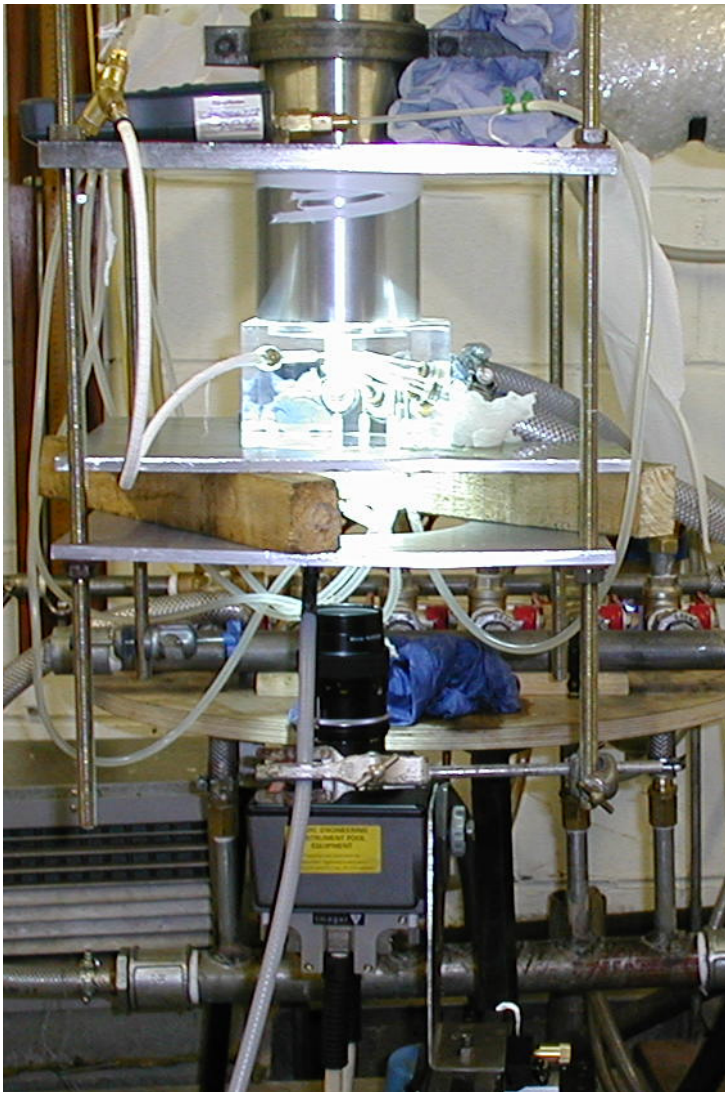

Figure 3-30: Photograph of HSDV imaging in large-scale 3-D nozzle (Bottom)

A strong gas discharge spotlight, with variable focus, together with a fiber light from below were necessary to provide enough light for the intensified CCD video chip in combination with the high frame rates. The main advantage of this kind of light is that is extremely strong without producing a lot of heat. Therefore only one such light was enough, making the environment much more work friendly and also allowing for great periods of continues run since there was no problem for the model from high temperature as with other light sources.

The cameras were triggered and controlled with the image processor unit via a remote control. In the image processor's memory the single video frames of one imaging sequence could be stored in digital form.

The same equipment has been also used for spray visualization investigations along with the setup explained in the following section.

3.3.2 Spray visualization

The real-size transparent model of the marine nozzle was incorporated into the refractive index matching test rig, which was described previously in Section 3.2. Since the model is transparent, the aim is to establish a direct link between hole and string cavitation structure, and its effect on near hole exit spray structure. The main reason for using this setup was the capability of the camera to be combined with microscopic lenses while maintaining a high resolution making possible to focus both inside the nozzle as well as to spray.

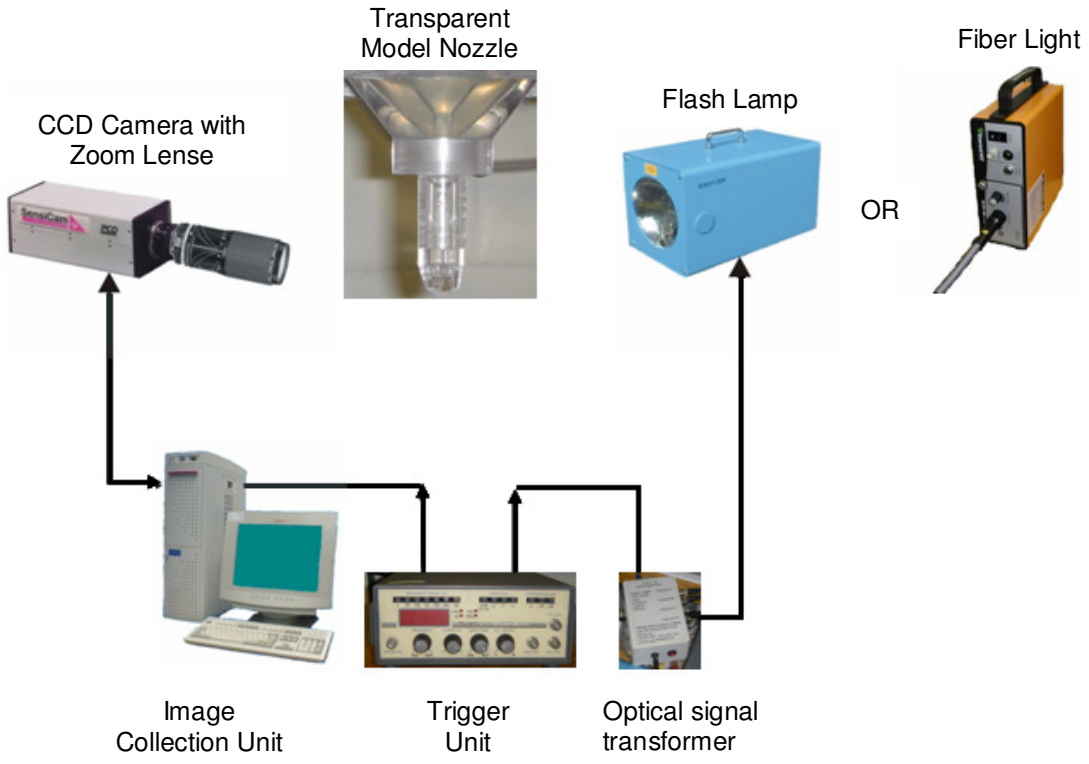

Figure 3-31: Schematic of CCD imaging in Real-Size nozzle

In Figure 3-31 a schematic of the setup for simultaneous imaging of the cavitation and spray structures inside the transparent three-dimensional model nozzles is shown. The CCD

camera used was a 12bit fast-shutter Sensicam [120] with a resolution of 1280 x 1024 pixels and a minimum exposure time of 100ns. It was fitted with a zoom lens and connected to a PC via an image acquisition card. The PC had a timer card installed that could trigger both the camera and the flash lamp illumination through an optical signal transformer. All internal camera settings could be adjusted with the image acquisition software and the obtained pictures were downloaded onto the PC.

Different lighting sources and positions were tested in order to gradually improve the quality of the acquired images. A main concern was the water spray splashing on the nozzle surface, particularly for high CN numbers, that created light deflections and block the optical access to the sac volume. Different lenses were also used as well as different focal points. Figure 3-32 shows a typical arrangement of the CCD camera and the flash lamp.

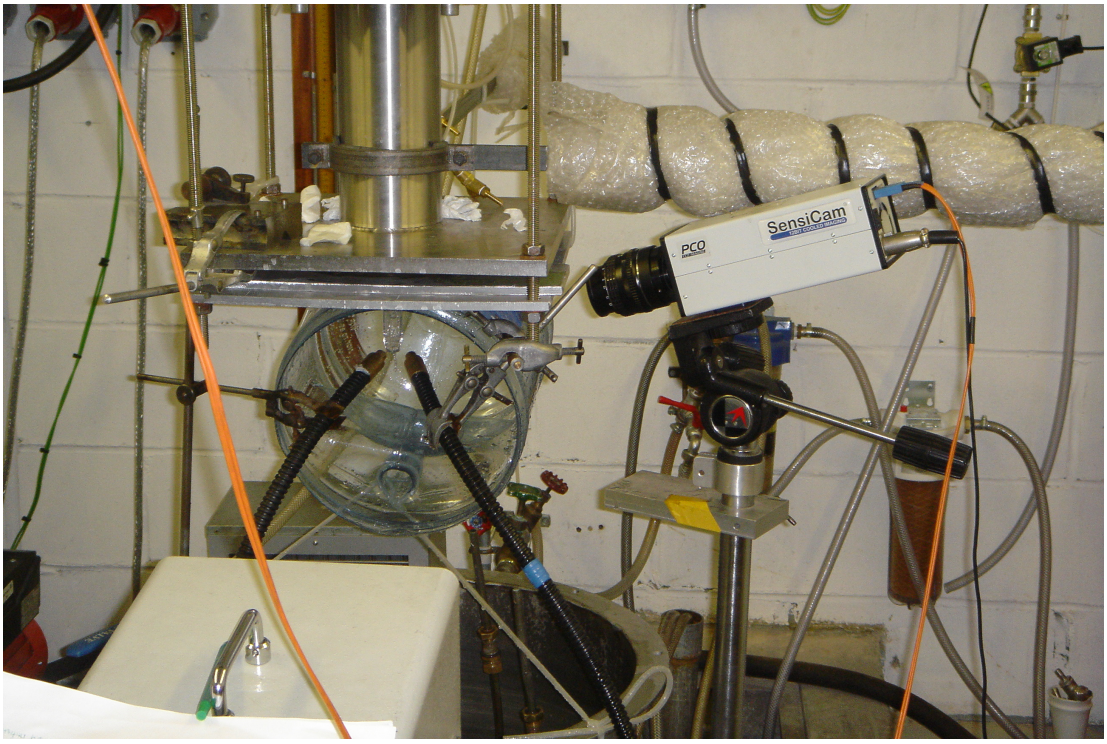

Figure 3-32: Photograph of typical arrangement of the equipment

3.4 Image Processing tools

3.4.1 Mean image calculation

Having sequences of more than 4000 frames per case makes image processing a valuable tool. Image processing was extensively developed and used in order for the raw data, obtained from the numerous experimental investigations, to be processed and exploited towards the better understanding of the various phenomena associated with the internal nozzle flow and the near nozzle spray characteristics. At this point it should be stated that all the image processing has been done through MATLAB [121], which is considered as a reliable and convenient tool for such studies.

Detailed observation of each image obtained may be inevitable, for example when small changes regarding the morphology of cavitation structures have to be investigated. However, for the present investigation this was not a major concern. The main task was to find how string cavitation was affected by differences in geometry, nozzle needle lift or injection hole arrangement, or flow parameters, such as CN and Re. Then, how it affects the flow inside the injection holes and spray structures exiting through the holes. Therefore, in order to monitor such changes effectively, the whole sequence of the collected images has to be presented in convenient and clear way in order for those effects to be determined. A common well established method, used by many researchers including [6, 115, 116, 122, 123], in order to present a sequence of frames as a single image is to perform temporal and spatial averaging.

A digital image is practically an array of data. Each pixel corresponds to a member of that array. When an image is obtained in grayscale is called an intensity image. Depending on imaging equipment and the output format the ‘depth’, bit number, of the image is different. In this investigation the high speed video system was using an 8bit format. The CCD system that was used for part of the spray characterization investigation was acquiring still images with a 16bit sensor. After adjusting the properties of the acquired images, such as contrast, gamma correction, brightness, etc, the images were saved in 8bit, uncompressed, tagged image file format (.tiff) sacrificing some information, gaining however valuable space and processing time. Therefore each member of the matrix can take values from $0\text{-}2^8$ or 0-256. Since the images are in gray scale there is only one array per image.

When considering the internal nozzle flow for the large scale marine nozzles, presented in section 3.1.1, the most interesting features that needed to be investigated was string cavitation mainly inside the sac volume but also inside the injection holes, whenever possible. For the L-S conventional Diesel multi-hole nozzles, presented in Section 3.1.7, except from the hole-to-hole strings that were thoroughly investigated, it was also interesting to explore the needle seat cavitation, since this type of cavitation is claimed to cause severe erosion problems in some types of nozzles. Finally, for the real-size and L-S spraying marine nozzles, presented in section 3.1.4, the goal was to find the spray dispersion angle variation with time.

In order for the post-processing method to be explained, the L-S marine nozzle will be used as an example; however, the same process was also followed for all other nozzles. For the L-S marine nozzles internal nozzle flow investigation the structure that had to be isolated in order to be studied in detail was string cavitation. A typical bottom-view image of the string inside the sac volume is given in Figure 3-33 (a). Figure 3-33 (d) is the same image as Figure 3-33 (a); however a color map has been applied through MATLAB [121] promoting the contrast differences . As it can be seen, within the red circles there is some noise mainly due to light reflections, different materials and the nozzle's geometry. These impurities will prevent from properly isolating the area of interest. In order to improve the quality and the accuracy, a background image, such as the one shown in Figure 3-33 (b) or (e), was obtained for every investigated flow condition and was then subtracted from the entire frame sequence. The result of this operation is shown in Figure 3-33 (c) or (f) where the string cavitation structure has been enhanced.

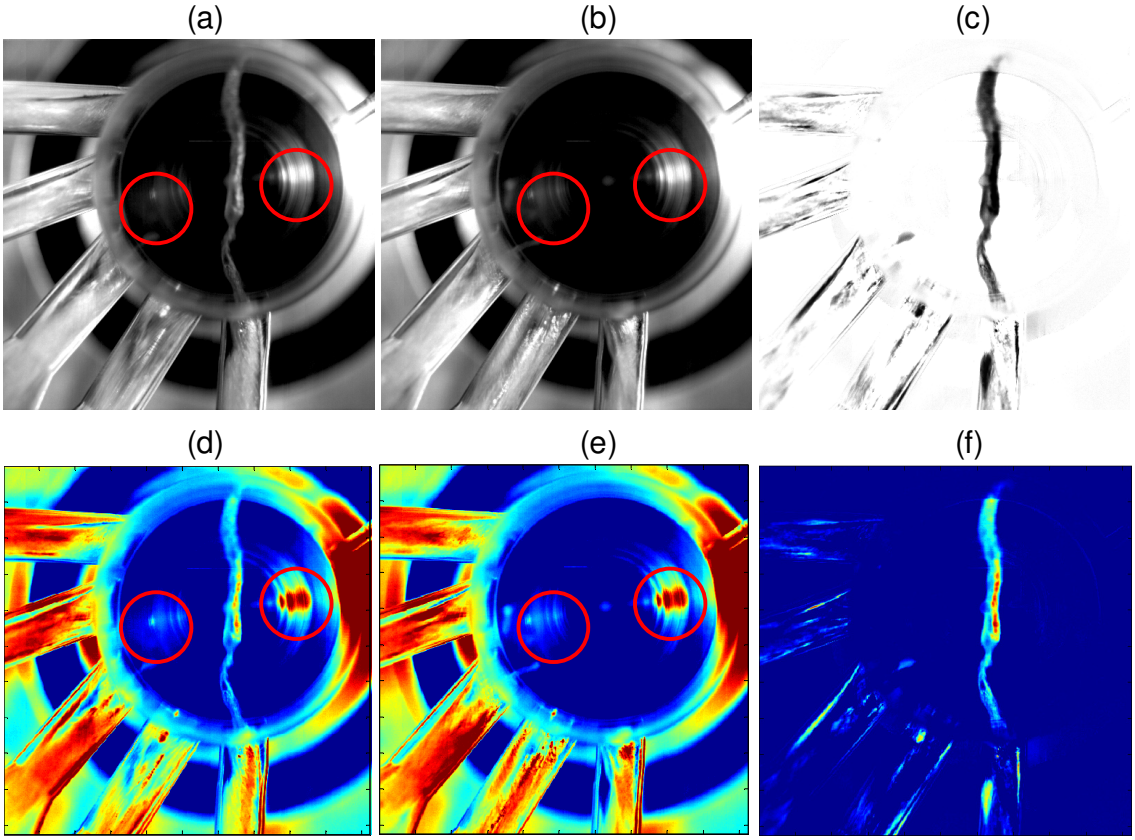

Figure 3-33: a) image with string, b) background image, c) subtraction of (a) with (b), d), e) and f) same as (a), (b) and (c) but with 'jet' color map to increase image contrast.

Until this point, the images are still indexed, i.e. intensity images. The next step is to transform the images into logical arrays, giving 0 values to the background pixels and 1 when string, needle seat cavitation or spray respectively are present. This is done relatively easy after thresholding Figure 3-33 (c), or (f). The result is presented in Figure 3-34 (a). As it can be seen there are also some other objects, apart from the string, however for this kind of processing these do not cause any problems.

Adding all the thresholded images for every case and then dividing by the number of processed images the probability of string cavitation appearance on the projected 2-D bottom view plane is obtained. A representative calculated mean image is shown in Figure 3-34 (b). Finally, purely for presentation reasons, the sac volume area is isolated and is superimposed on a 3-D schematic of the nozzle geometry, Figure 3-34 (c).

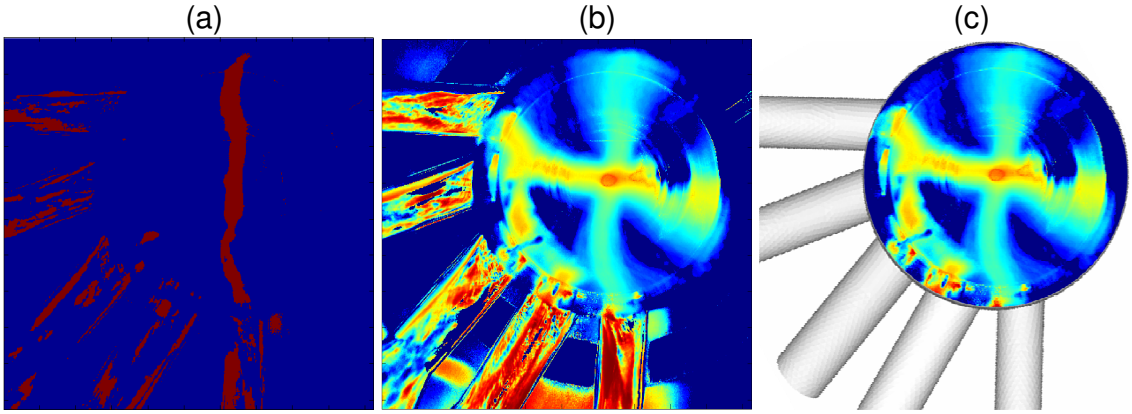

Figure 3-34: a) Figure 3-33 (c) after thresholding, b) a typical mean image calculation result and c) same as (b) superimposed on a 3-d schematic of the nozzle.

3.4.2 String Cavitation 3-D reconstruction

During the current study of the internal nozzle flow visualization in large scale models a huge amount of successive images where acquired for each operating condition. This was done for both the marine nozzles used in two-stroke slow speed Diesel engines and also for the VCO and sac-type nozzles used with medium speed four-stroke Diesel engines. The average number of acquired images was between 5000 and 6000 frames; in a limited number of cases 30000 images were acquired. As previously mentioned, there was a clear need of developing fast, reliable and automated image processing tools in order to enhance and fully explore the acquired data. Except from calculating the mean image for each condition, which is fairly easy and well established in previous studies, an attempt was made to develop a reconstruction algorithm in order to find the 3-D orientation and shape of the cavitation structures inside the sac volume of the nozzles. For that purpose, two HD cameras were arranged in such a way that normal views (bottom & side) were captured simultaneously. A simplified schematic of the camera arrangement together with two sample images are presented in Figure 3-35.

Following, a short description of the steps involved in order to perform the string cavitation reconstruction is given.

The reconstruction tool was developed and operates in MATLAB. It uses purpose developed functions as well as ready function from the standard image processing toolbox

of MATLAB [121]. The function which is used to extract the string boundary in ordered form, in the 2-D image plane, is a custom modified version of the function 'boundaries' found in [124].

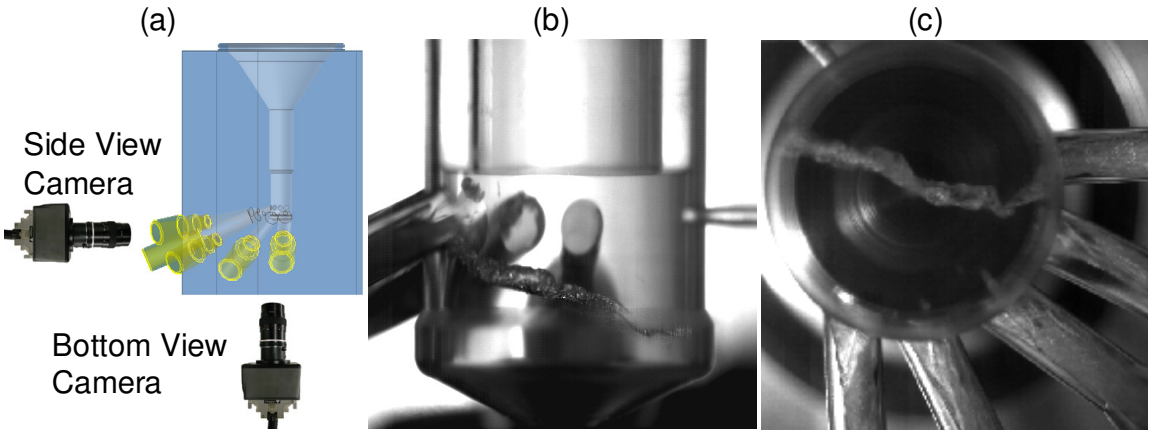

Figure 3-35: a) Schematic showing the cameras position with respect to the nozzle, b) typical side view image and c) typical bottom view image.

Figure 3-35 (b) & (c) show respectively bottom and side view images of string cavitation obtained using the synchronized HSDV systems. Following will be described the process used in order to isolate string cavitation from the acquired images. The bottom view image will be used as an example; however the same procedure was also followed for the side view.

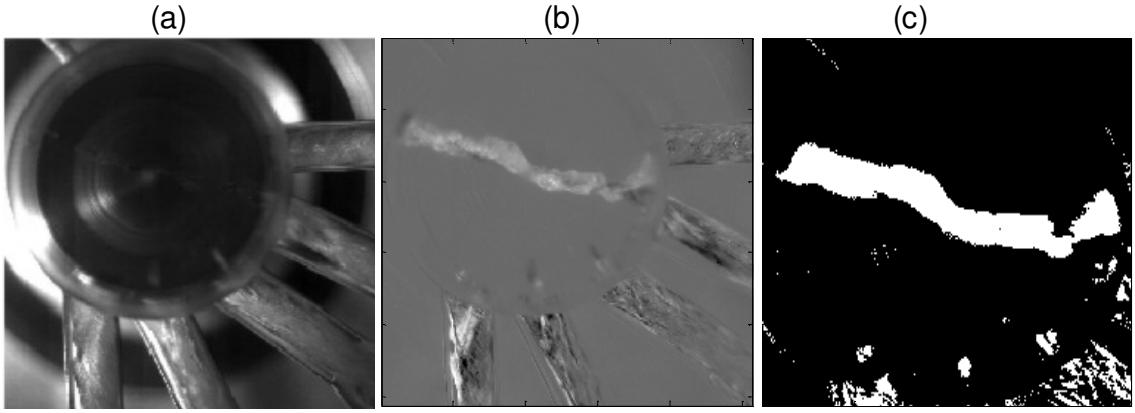

Figure 3-36: a) Bottom view background image, b) indexed image after subtracting Figure 3-36 (a) from Figure 3-35 (c) and c) Figure 3-36 (b) converted to binary.

For each flow condition, a background image, as the one presented in Figure 3-36 (a), is acquired. This background image is subtracted from Figure 3-35 (c) and this subtraction

results to the image shown in Figure 3-36 (b) which is an indexed image with values from 0 to 255. After having the background noise removed, a global thresholding is applied in order to convert the indexed image into binary having values of either 0 or 1. Until this step, the procedure followed is the same as the one used in order to calculate mean images as described in section 3.4.1. As it can be seen in Figure 3-36 (c) there are some artifacts, noise, that are mainly located in the hole cavitation sights and to less extent inside the sac volume. A more careful observation shows that, especially inside the sac volume, there are some single pixels that have values of 1, that if they are not removed they will cause confusion to the automated boundary detector subsequently leading into a wrong reconstruction. Even though a background image was taken before every visualization of different flow conditions, it was unavoidable to have such artifacts. The main reason for this is the slight variations in electric current that affect lighting, as well as the dynamic reflections caused by string cavitation. Therefore, in order to eliminate this remaining noise, it was necessary to apply further processing. It has to be mentioned that if these artifacts remained, the string continuity in the thresholded image could have been interrupted as well as the boundary would have been very wavy and poorly defined.

The image processing toolbox of MATLAB has a number of operations under the 'bwmorph' function that perform morphological operations on binary images. When using this function there are two inputs that have to be specified. The first is to choose the operation that has to be applied and second is the number of times (n) that the operation will be applied. Number (n) can be either a real integer or it can be set to 'Inf', in which case the operation is repeated until the image no longer changes. The first operation that is performed on the thresholded image is called 'majority'. This operation sets a pixel to 1 if five or more pixels in its 3-by-3 neighbourhood are 1's. Otherwise, it sets the pixel to 0. This will eliminate the very small 1's areas however the bigger ones will still be present.

The next step is to improve the shape of the string, mainly on its boundary, and also restore its continuity. Again this can be done through the image processing toolbox of MATLAB by using the 'fspecial' function in combination with the imfilter' function. The 'fspecial' function creates predefined 2-D filters. There are several choices of filters and the result of this function is a correlation kernel in the appropriate form in order to be used with

'imfilter'. A Gaussian low pass filter has been chosen as shown, magnified, in Figure 3-37 (a).

Having chosen the appropriate filter the 'imfilter' function is used in order to filter the multidimensional array, i.e. the string image after the 'majority' operation, with the multidimensional filter. The image can be a nonsparse numeric array of any class and dimension. The resulted filtered image has the same size and class as the original one.

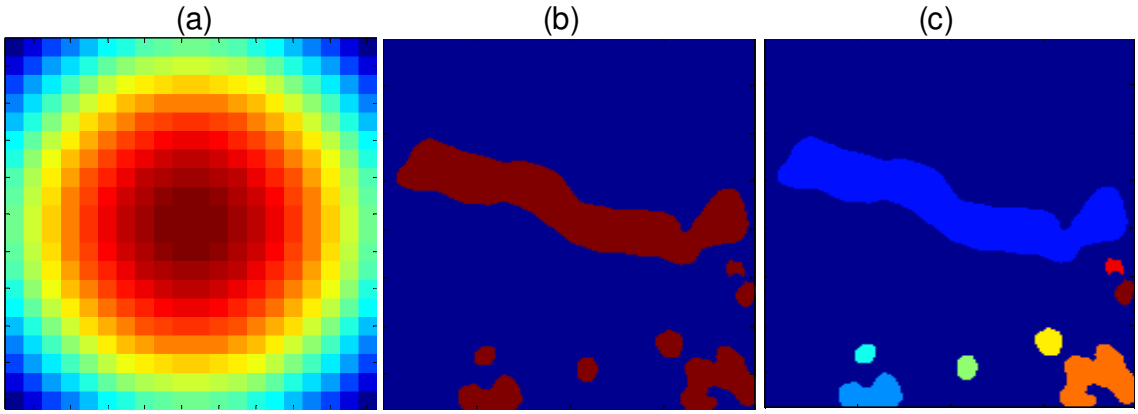

Figure 3-37: a) Gaussian low pass filter used, b) Figure 3-36 (c) after applying filter and c) after labelling all image features.

After having the filtered image the 'graythresh' function [121], that uses Otsu's method, which chooses the threshold to minimize the intraclass variance of the black and white pixels, is used in order to compute a global threshold that will be used to convert the resulted filtered, blurred, image to a binary image with 'im2bw' function [121]. The result after this operation is the binary image shown in Figure 3-37 (b) where all the features are slightly oversized. At this stage the string is continuous and its boundary is well defined, however there are also 1's areas from geometric cavitation that have to be eliminated.

The function 'bwlabel' [121] returns an array, of the same size as the binary image, containing labels for the connected objects in the binary image. This function can check for connectivity in either 4 or 8 directions. The elements of the resulted array are integer values greater than or equal to 0. The pixels labelled 0 are the background. Then each region of pixels that define an object are given deferent labels, i.e. the pixels labelled 1 make up one object, the pixels labelled 2 make up a second object, and so on. The resulting image after

this process is given in Figure 3-37 (c) where each object is represented by a different colour.

It then becomes obvious that the most distinct difference between the string cavitation and the other objects in the image is its size (area). Using the 'regionprops' function [121] a set of properties for each labelled region in the labelled image can be measured. As mentioned before, the 'area' was chosen, out of the predefined properties, as the most interesting property and was found for every object in the image. Then the index of the region with the maximum area was isolated and all the other where discarded. The result after this operation is an image only containing the string cavitation structure inside the sac volume of the nozzle, this is shown in Figure 3-38 (a). Finally the 'imfill' function [121] is used in order to fill holes, if present, inside the string area. A hole is a set of background pixels that cannot be reached by filling in the background from the edge of the image. Then the 'bwmorph' function [121] with the 'thin' operation is used in order to restore the size of the object that was increased due to the blurring when it was filtered. After completing these operations the string is isolated with a well described boundary. The final result is shown in Figure 3-38 (b).

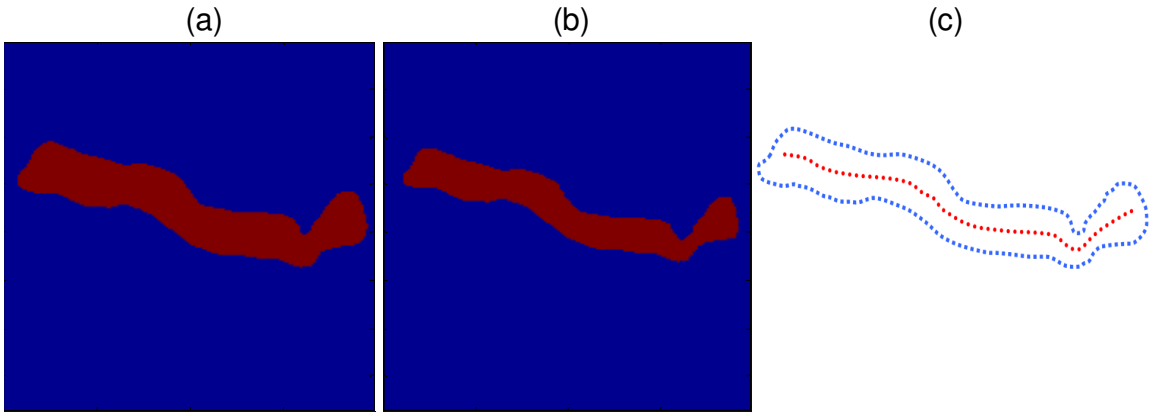

Figure 3-38: a) image of the isolated object of interest (i.e. string), b) image of string after filling of internal gaps and after restoring the string size and c) image of the string boundary and centreline.

Until this point the string is only given as an image and not in a form that can be used to extract the 2-D coordinates of its location. The modified function 'boundaries' found in [124] was used in order to trace the exterior boundaries of the string in the final binary image of Figure 3-38 (b). The outcome of this function is an array of Q-by-2, each row of

which contains the row and column coordinates of a boundary pixel. Q is the number of boundary pixels of the object. The boundaries are traced in the clockwise direction, by default, although it is also possible to reverse the direction. There is also an option to define if the boundary will have 4 or 8 directions connectivity. The centreline of the string is also required for the reconstruction and was found by using the MATLAB function 'bwmorph' and the 'skel' operation. Skeletonization removes pixels on the boundaries of objects but does not allow objects to break apart. The pixels remaining make up the image skeleton. This option gives as outcome an image of connected pixels forming the centreline of the string. In order to have the coordinates of the pixels of the line in an ordered form, a custom algorithm was developed by the author based on the minimum allowable distance between that two consecutive line points can have taking also into account the slope of consecutive segments.

The final result are two ascii files for each view containing the pixel coordinates of the boundary and the centreline of the string. A graphic representation of the outcome is given in Figure 3-38 (c) (not in scale). The dotted blue line represents the boundary pixels and the red is the centreline.

The next step is to transform the pixel coordinates into spatial coordinates. This is done by scaling with a known dimension of a feature in the image, which for the current study was the diameter of the sac volume. Then the centrelines in the two views are redistributed over the same number of uniformly spaced points, which for the current study was set to 150. After setting up the rotation matrix the centreline of the string is reconstructed and is defined in the 3-D space.

In order to introduce the experimental string cavitation location into the computational grid that has been used for the CFD flow simulations, the string had to be represented as spherical vapour pockets. Although the string's shape is a continuous vapour filled tube, this compromise regarding the shape was used in order to have limited modifications to the in house CFD code while still been able to get helpful results. In order to define the void pocket's diameter the diameter of the string had to be found at each point of the centreline, ideally, on both views. However the side view image due to distortion from the sac volume geometry was considered unreliable. Therefore the diameter was defined only by the

boundary of the string in the bottom view image. This was done by finding the minimum distance between each point of the string line with the segments of the boundary line, in both directions. This means that for each point, two distances, one for each side of the boundary with respect to the centreline, were found representing the radius of the string at the current location. Since the real shape of the string is closer to a cylinder a correction had to be made in order for the spherical vapour pocket to have the same volume as the cylindrical vapour segment. The spherical pockets started from the first point of the reconstructed centreline, however in order for the pockets not to overlap the next location of the pocket was found with respect to the radius of the previous one. The result is a series of non overlapping spherical vapour pockets lying on the reconstructed centreline of the string and having the same volume as the 'cylindrically' shaped string. A typical result of this process is given in Figure 3-39 where an experimental string cavitation structure is placed inside the computational grid.

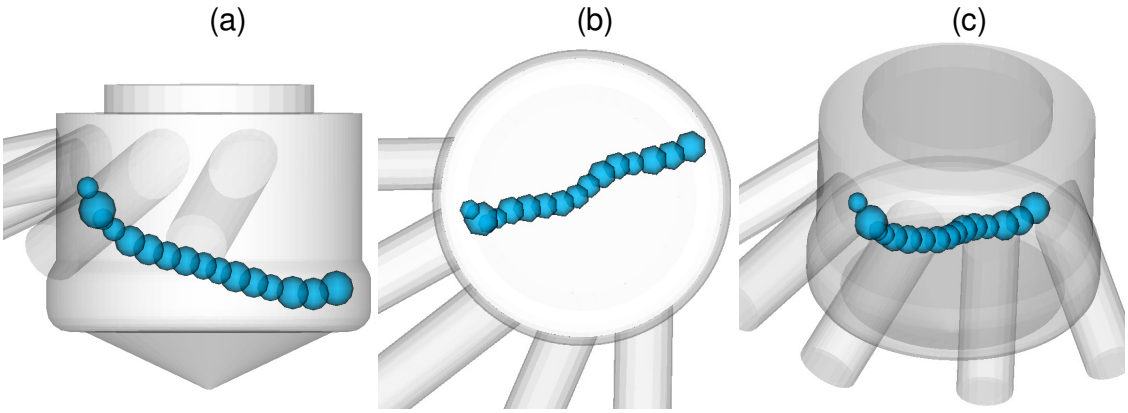

Figure 3-39: 3-D reconstructed string a) side view, b) bottom view and c) stereoscopic view.

The string was reconstructed for each set of image pairs and was imported in the computational grid in order for the vapour fraction in liquid to be calculated. This was repeated for the entire acquired sequence of each flow condition adding each time the obtained vapour pockets. The total vapour fraction is then averaged with respect to the number of frames that had string cavitation and the result is a 3-D temporal and spatial probability of string cavitation presence inside the sac volume of the nozzle. By performing this averaging, apart from string cavitation probability, it was possible to establish a relation

between the internal nozzle flow and the string location. This is of great importance since it will help to understand the string formation mechanism.

Finally it should be stated that the same technique was applied to the conventional multi-hole nozzles in order to reconstruct the hole-to-hole strings present inside the sac volume.

3.4.3 Spray Cone Angle calculation

The last two sections, 3.4.1 and 3.4.2, described the image processing techniques used to calculate the spatial probability of various cavitation structures, the spray dispersion angle and the 3-D reconstruction of string cavitation inside the large scale nozzles used for internal nozzle flow visualization. In this section it will be presented the processing that was developed, always using MATLAB, in order to calculate the spray cone angle for every frame of the spray investigation sequence.

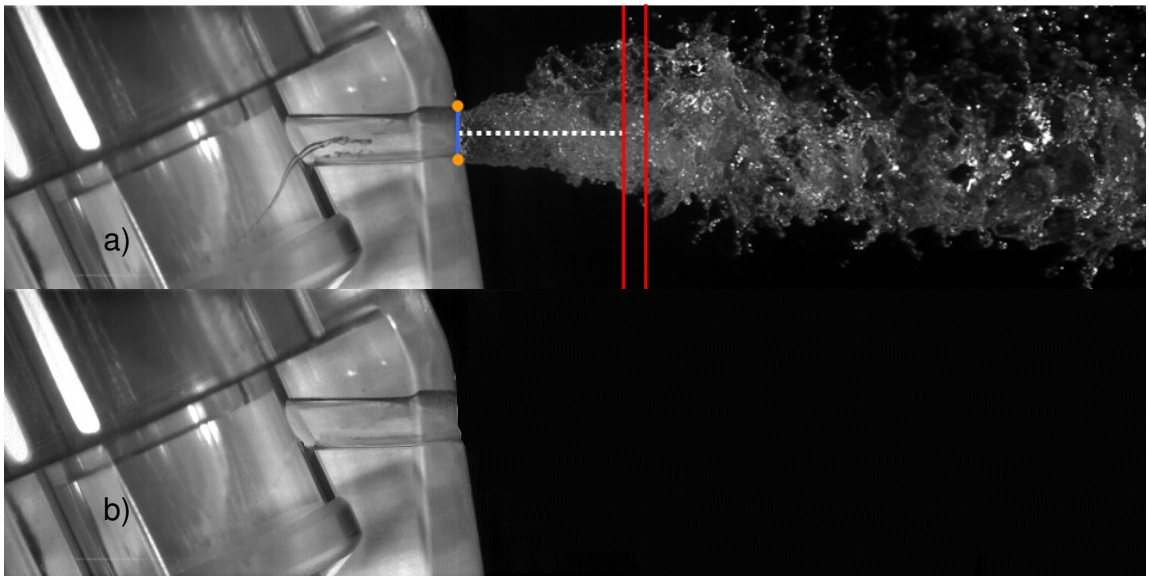

Figure 3-40: a) typical spray image from the single hole cylindrical nozzle and b) the corresponding background image.

A typical spray image is shown in Figure 3-40 (a). Although the spray is injected at a clear background, with no reflections or geometry effects, it was chosen to subtract a background image in order to account for the light distribution and the distortion of the camera sensor. By making the nozzle body transparent the internal flow is also visible. This is an excellent

way to monitor how cavitation, and particularly dynamic forms of it such as string cavitation, affects the injected spray. For that reason, the background image that was chosen to be subtracted was from an instance without string cavitation. This made possible to get both the string cavitation and the spray dispersion probability.

After subtracting the background image a global threshold is applied in order to convert the indexed image into a logical array of 0's and 1's. This process returns an image like the one shown in Figure 3-41 (a). As it can be seen, the thresholded image is cropped since the spray cone angle is calculated within one injection hole length, represented in both figures by the dotted line, starting from the hole exit plane, represented by the blue line. This almost reduces the image processing time to half purely because the image processing software performs calculations for less pixels.

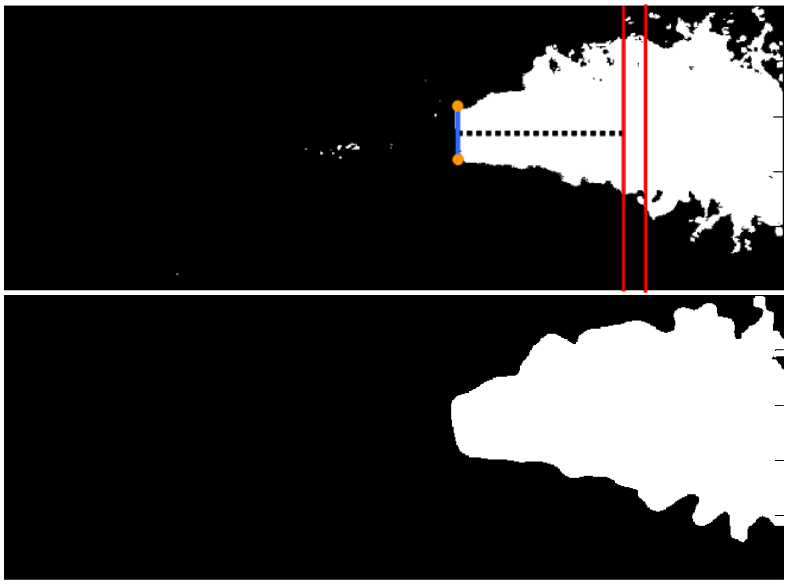

Figure 3-41: a) thresholded section of the original spray image Figure 3-40 (a) before processing and b) after image processing.

Due to the fact that the thresholded image includes many isolated droplets, that bounce from the main body of the spray, and due to the sharp fishbone shaped edges, which result into a wavy and non uniform boundary, further processing was necessary.

In order to remove these artifacts, that will cause false angle measurements, the 'bwmorph' function was used with the 'majority' operation in the same way as described before in

section 3.4.2. Then the 'fspecial' and the 'imfilter' function was used, with a Gaussian filter similar to the one used in the string reconstruction, in order to smooth the spray boundary. The final result of this process is shown in Figure 3-41 (b). A direct comparison between the original spray image and the spray boundary after processing is shown in Figure 3-42. It can be concluded that the resulting edge is describing the spray with good accuracy while been smooth enough for reliable cone angle measurements.

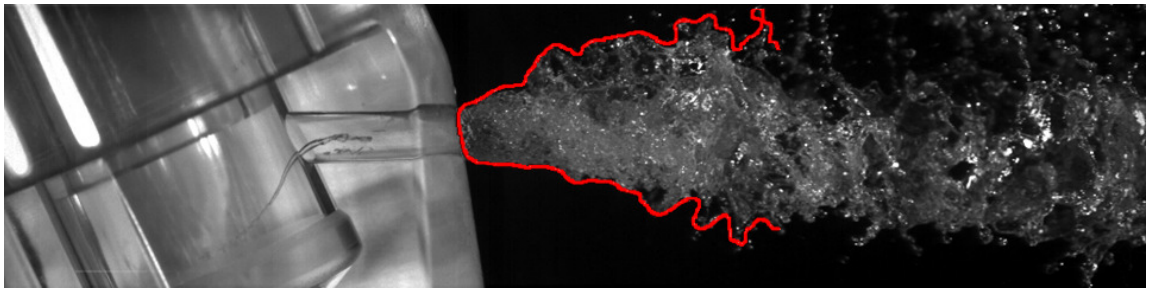

Figure 3-42: Original spray image with the boundary, after the processing, superimposed for comparison.

Once the image processing is finished the next step is to find the upper and the bottom spray cone angle. As previously mentioned the angle is measured at a distance of one injection hole length starting from the hole exit plane. Since the spray is dynamically changing, finding the slope over the hole spray edge would have been like averaging any effect seen due to the internal nozzle flow. Therefore ideally the angle measurement should have been taken only by one point. However this would have made the measurement extremely sensitive to any image impurity or artefact. Also due to the fishbone structure of the spray, the probability of taking a wrong measurement of the angle is increased. In order to minimise the possibility of error the slope is been found over a 15 pixel range indicated by the two red vertical lines shown in Figure 3-40 (a) and Figure 3-41 (a).

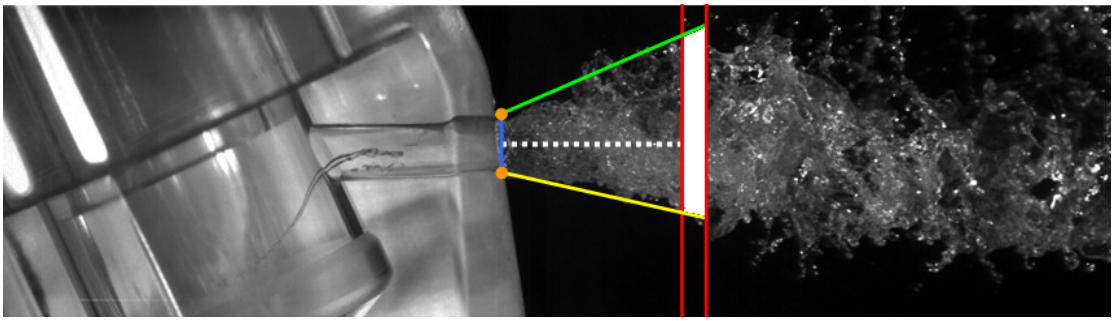

Figure 3-43: Schematic showing the spray cone angle measurement.

Figure 3-43 illustrates this method. The two red lines define the range over which the outer pixels will be found, in the black and white image (Figure 3-41 (b)). This is done by scanning vertically the pixel values and keeping the first pixel having the value of 1 starting from the upper and the lower side of the image. Then every boundary pixel, depending on which side of the spray is found, is connected with the corresponding starting point, indicated with the orange dots, which are interactively placed by the user with the aid of the pointing device. This results into 15 possible slopes, since there is a 15 pixel range, for each side of the spray. The green line indicates the upper angle and the yellow line indicates the bottom angle. Then the angle is found by averaging the 15 values at each side. It has to be mentioned that there is also a safety feature such that it will discard a measurement if is too far from the average value.

It should be stated that the only user input are the two starting points at the hole exit plane which for a series of investigations, and while the camera has maintained its original position, do not change. However, this is always checked before every angle calculation and is properly adjusted when needed.

3.4.4 String cavitation sequence and radius measurement

As with the instantaneous spray cone angle measurements, previously explained, it is important to be able to measure not only the average location and probability of having string cavitation, but also how it develops. This was done with the 3-D reconstruction processing; however, that refers to string cavitation structures that were fully developed.

After the first experiments of the internal flow of the multi-hole models it became evident that a quick, yet reliable, method had to be found in order to be able to instantly identify string cavitation presence at selected locations within the nozzle. Having this information at every time instance of the investigation it will provide information for the sequence and frequency of the event.

As done before with the other image processing techniques, the first step is to remove the light reflections and the geometry generated artifacts in order to get an image free of noise. A background image is chosen and it is subtracted from every frame of the time sequence. Then a global threshold is applied in order to produce a binary image. Taking as an example the L-S VCO nozzle with tapered holes the above process is presented graphically in Figure 3-44.

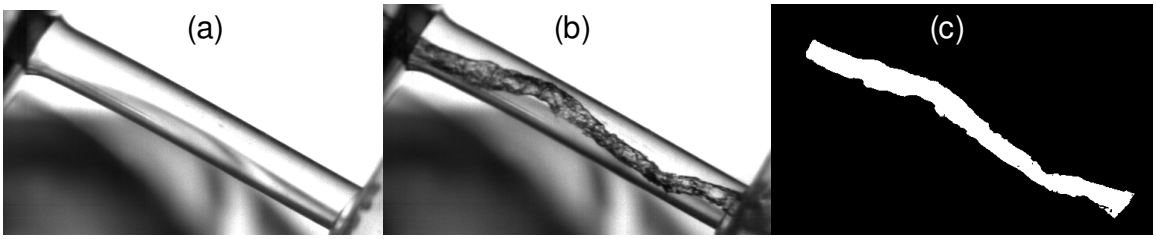

Figure 3-44: Large-scale VCO nozzle with tapered injection holes. a) background image, b) image with string and c) thresholded image.

For this particular case it was important to identify how the string inside the hole is developing. It could be a string to initiating from the inlet side and move all the way towards the hole exit or a string starting form at the hole exit and evolve until the middle length of the hole. In order to capture the string motion, the hole was divided in 16 regions, having a resolution of almost 1mm. Each one of these regions was assigned with a different index number. The regions chosen and their corresponding index for this case are shown in Figure 3-45.

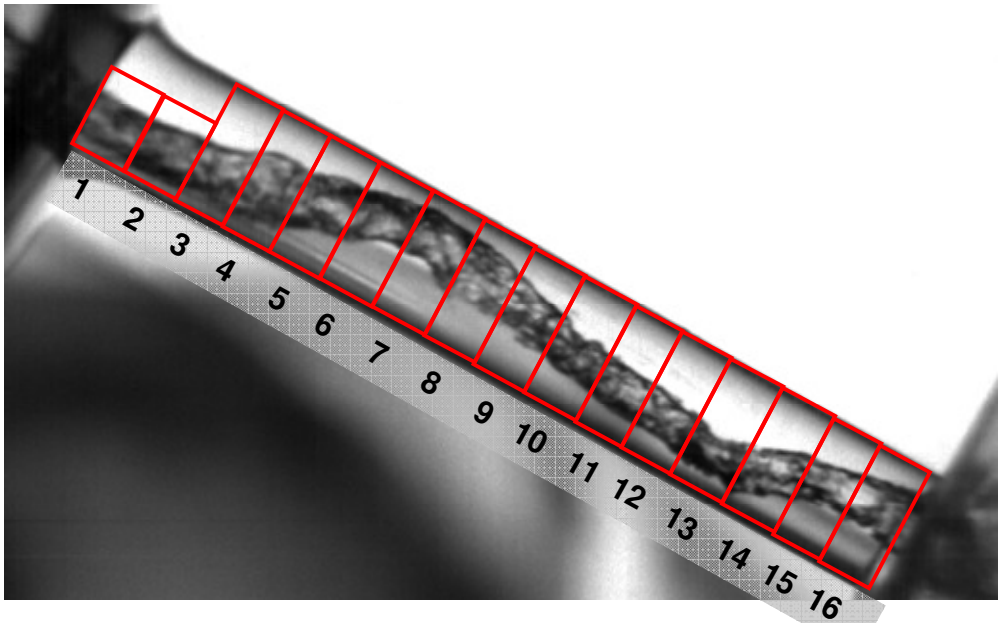

Figure 3-45: selected regions for the tapered VCO nozzle model

As it can be seen the first two regions (1 & 2) are shorter in order not to take into account geometric cavitation that may occur at high CN and low needle lift. Each of these regions has a given area which is measured in number of pixels. Once the thresholded image, only containing 1s and 0s, is available, the percentage of volume that have value of one is calculated with respect to the total area of the region. If this fraction is above a predetermined value it gives a flag that the current region is partly occupied by the string. These readings from all the regions are recorded in an array with the number of columns being equal to the number of regions, and the number of rows being the number of processed frames. As expected, this array has values of 1s, when string is present and 0 when the fraction is not above the predetermined value, denoting that no string is present. Assuming that the string will fully occupy the length of the region that is present and that for that relatively short length can be consider parallel to the hole direction, it follows that the fraction of area can be translated into fraction of diameter of the string compared to the hole diameter at the current region.

Similarly to what it was described above, the following Figure 3-46 & Figure 3-47 show typical region arrangements that were used throughout this investigation for different nozzles and string cavitation structures.

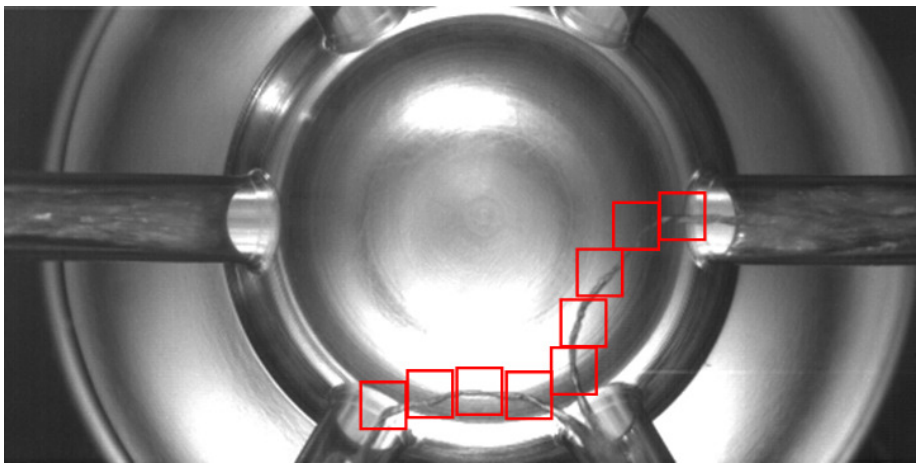

Figure 3-46: selected regions for hole-to-hole string cavitation in large-scale multi-hole nozzle models.

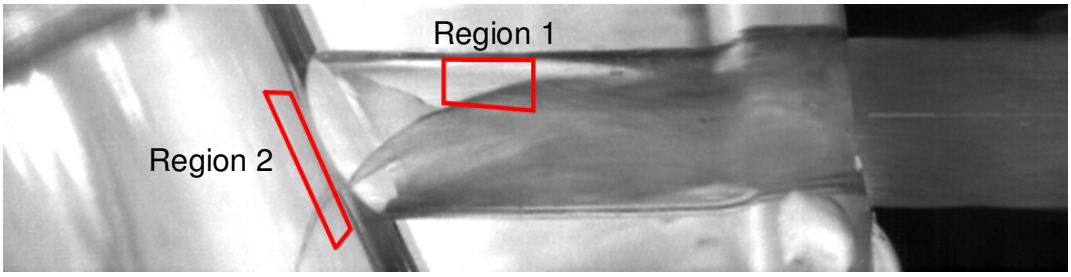

Figure 3-47: Selected regions for string cavitation in large-scale marine injecting nozzles.

3.4.5 Needle seat cavitation sequence and intensity measurement

The same technique, by introducing control boxes, was also used for post-processing the results acquired for low-lift cases from the internal nozzle flow visualization of the multi-hole nozzles. For these particular cases the dominant cavitation regime was the so called needle seat cavitation. In order to better understand the complex and highly transient characteristics of the flow, the entire needle seat area of the nozzle was divided in 1 deg radial sectors as shown in Figure 3-48. This ensured that the resolution would have been good enough to allow for quantitative analysis between different cases. As for the previously presented cases, once the background image was subtracted, the image was thresholded and the percentage cavitation occupation in each sector was recorded for every frame. The results of this analysis were able to provide an overview of the entire run case in a single figure, providing also information regarding the position change of the cavitation pockets.

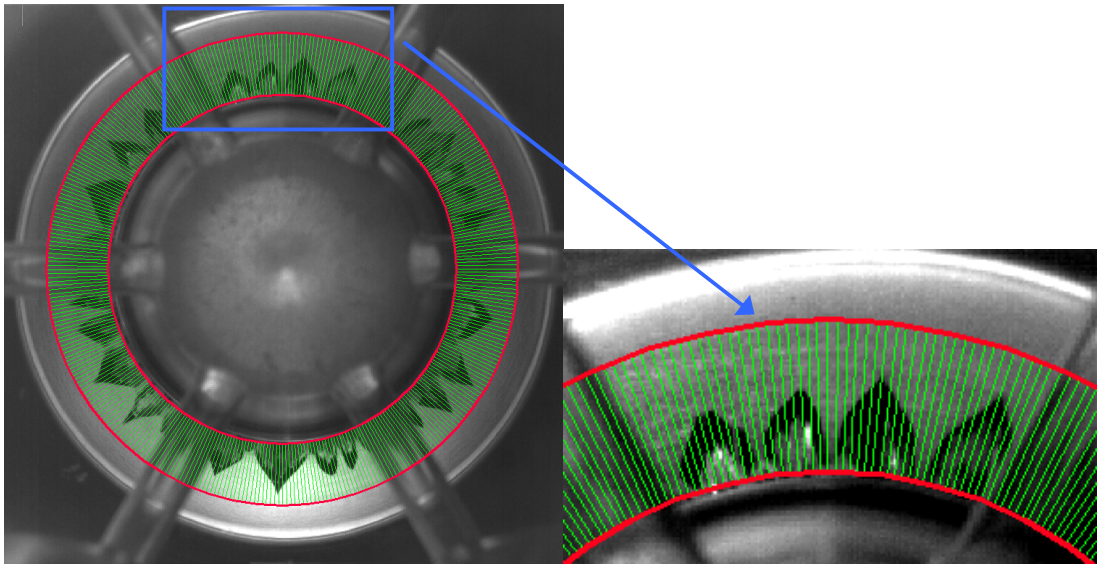

Figure 3-48: Selected regions for Needle-Seat cavitation in large-scale Multi-hole internal flow nozzles.

3.5 Discussion and quantification of experimental errors and uncertainty

Experimental errors and uncertainty in most cases inevitable and has to be taken into consideration. For the current study the systematic errors are associated with the instruments used to take flow rate and pressure measurements. Both instruments were digital with LCD displays, eliminating any parallax errors which are common in dial gauge instruments. The accuracy according to the maker was ± 0.01 litre/s and ±0.05bar respectively. These errors are within the acceptable range and will not influence the conclusions to be drawn from the analysis of the results. Moreover it has to be mentioned that after every flow rate alteration it was given an adequate time for the reading to stabilize before recording it. For the pressure meter, and particularly for the back pressure measurements downstream of the injection hole outlet where cavitation was causing the reading to fluctuate, a median was recorder. Apart from the instrument errors, other errors and uncertainties are associated with the needle lift control mechanism, which was manually adjusted and checked by a micrometer and the camera, and the eccentricity mechanism which was also manually adjusted and was verified by the camera. The error in the needle lift was estimated to ± 0.02 mm and the error in eccentricity values was estimated to ± 0.1mm. As previously mentioned, these errors were within the safety limits for valid results and conclusion to be drawn. Finally, regarding errors of instruments and equipment used, the precision of the

replicated nozzle geometries must also be considered. Due to the fact that all nozzles where manufactured by highly sophisticated CNC machines and experienced technicians under close supervision, the error in nozzle geometry was estimated to ± 0.01mm which is practically negligible for large-scale nozzles.

Apart from the errors associated with equipment and instrument, there are also errors and uncertainties associated with the interpretation of the results particularly for internal nozzle flow visualization where hole and string cavitation inception had to be determined. For this kind of uncertainty to be minimized the results were thoroughly examined many times and when necessary a second opinion was requested. Same as with equipment error, any uncertainty arising from human error was minimal and further decreased by performing extensive Digital image processing over large frame sample.

Overall, all possible sources of errors and uncertainties, were properly identified and measures were taken in order to keep them within the minimum acceptable values.

3.6 Summary

Concluding this chapter a large number of large-scale transparent models of different types of Diesel injectors were manufactured. String cavitation was of particular interest and an extensive number of processing methods were developed in order to make a quantitative analysis and further understand the mechanism of their formation as well as their effect on the emerged spray. Advanced manufacturing methods were used in order to replicate complex geometries including hole inlet rounding and outward converging tapered injection holes (positive k factor).

The link between needle eccentricity and cavitation was also considered by designing a simple controllable eccentricity mechanism for the large-scale multi-hole nozzle models with different needle guide designs and tolerances. With the same equipment a link between needle seat cavitation and erosion would also be investigated.

High speed digital video systems were used in order to capture the small time scales of the phenomena. Combination of two systems provided the necessary input in order to reconstruct the location and form of strings in the 3-D space.

Chapter 4
Numerical investigation results

4.1 Introduction

In the following sections a series of flow calculations were performed for different nozzle geometries under both cavitating and non-cavitating conditions. These were conducted in order to become familiar with the special nozzle characteristics and, later, help to understand the experimentally obtained results. The in-house GFS RANS flow solver, as modified by [62], has been used to simulate the flow inside the nozzles tested. This model is able of simulating the geometric-induced hole cavitation but not string cavitation; thus, model predictions can be used only complementarily to the experimental results.

Moreover, an extensive parametric investigations was conducted in order to determine the dependency of the nozzle's flow to various changes mostly in geometry. Among other, the effect of sac volume geometry as well as conicity of the injection holes was revealed.

It has to be mentioned that although a complete set of results will be presented, the main feature of the flow that was thoroughly investigated were recirculation zones. As mentioned before these recirculation zones are possible locations for string cavitation occurrence and therefore need to well understood and monitored.

These numerical studies will also serve as input data for spray dispersion simulations which compared with the experimental results of near-nozzle spray structure will assist for the development of the spray model by providing the necessary correlations. Having these correlations for large-scale conditions it will be possible to apply them for real operating conditions making a powerful tool in predicting spray dispersion inside the cylinder. Spray calculations and model development are part of the work of another research group member.

Finally it should be mentioned that special data visualization software were used in order to produce the plots that will be presented throughout the current study. Two of the software

are commercially available [125]& [126] while [127] is a dedicated postprocessor of the in-house CFD code.

4.2 Marine nozzle internal flow overview

The internal nozzle geometry has been descritized with a 3-D mesh using a commercial grid generator [128]. As shown in Figure 4-1 for the single phase steady-state or transient numerical simulations the inlet boundary condition has been flow rate or pressure, as function of needle lift and time. At the exit plane of the injection holes the outlet boundary condition was set by constant static pressure. Figure 4-1 also reveals a special feature of this kind of marine nozzles. Three of the five nozzle holes have a semi-spherical inlet which are made by ECM

Each injection hole has different flow characteristics (flow rate, velocity distribution, discharge coefficient etc), due to the asymmetric nozzle design. Therefore mean properties have been estimated.

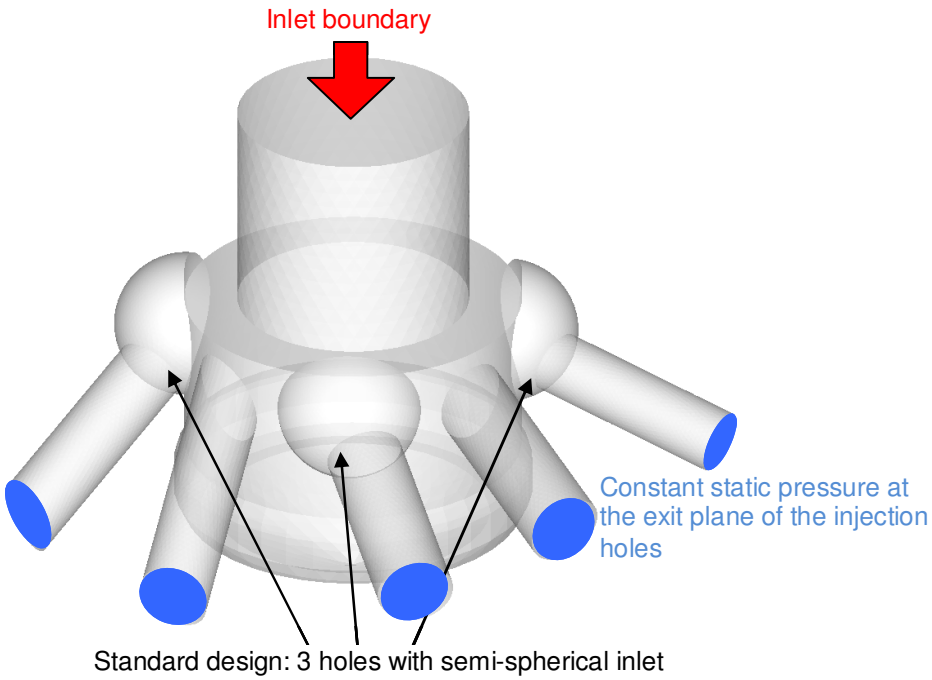

Figure 4-1: 3-D standard geometry for numerical investigation

4.3 Effect of grid

As previously mentioned the investigated nozzle is used in a two-stroke marine Diesel engine. Given the description of such an engine, as presented in section 1.4, the dimensions are totally different to those of a conventional automotive Diesel engine or even engines used in locomotives or for medium scale power generation. Having an engine with dimensions similar to those of a small country house it follows that the injection equipment will be proportional.

Having to fill a cylinder of almost 1m diameter and 2.8m long the three nozzles will have to supply heavy fuel oil at a rate of 2.14 l/s. to achieve this flow rate with inlet pressure of around 500 bar the nozzle holes diameters are between 1.5 and 1.8 mm, depending on the hole number.

Provided that the diameter of the injection holes of a typical Diesel injector is 140-170μm, the current design of the marine nozzle is almost 10-15 times larger. Therefore it can be considered as 'L-S'. One of the most important findings from numerous experimental studies is that cavitation cannot be scaled. Large-scale cavitating flows are also much more sensitive to pressure distributions. Due to its unique size and time scales there are significant differences in the flow patterns and regimes that occur in large-scale and real-size geometries [103]. However at this stage of the investigation only single phase simulations will be considered.

It is well-known that the computational cell size, or the density of the grid , that is used to discretize a geometry is very important for the accuracy of the flow calculation results [129]. Using a very coarse grid with low cell density will probably fail to capture essential flow characteristics. This will be even more critical in regions of the flow where large gradients are present. Finally a 'non-proper' grid will lead into miscalculation of the viscous losses resulting into wrong flow rate and discharge coefficient calculations.

Using the same cell size as with other conventional nozzle would have resulted into a multi million cell grid making impossible any kind of simulation because of computational power limitations. The density of the grid which can be considered as a non-dimensional number would have been a more reasonable approach.

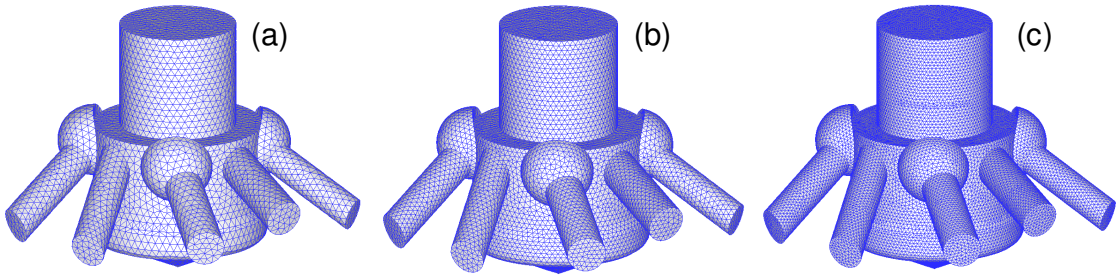

Figure 4-2: 3-D Mesh of Standard Geometry for Numerical investigation. (a) 67,000 cells, (b) 164,000 cells and (c) 460,000 cells

Three different fully unstructured grids were created in order to find the optimum grid size to be used for the rest of the numerical calculations. Three fully unstructured computational grids where created having 64,000, 164,000 and 460,000 computational cells respectively. A 3-D schematic of the grids can be seen in Figure 4-2. Cross-sections of the 3-D grids at the centre of Hole 3 can be seen in Figure 4-3.

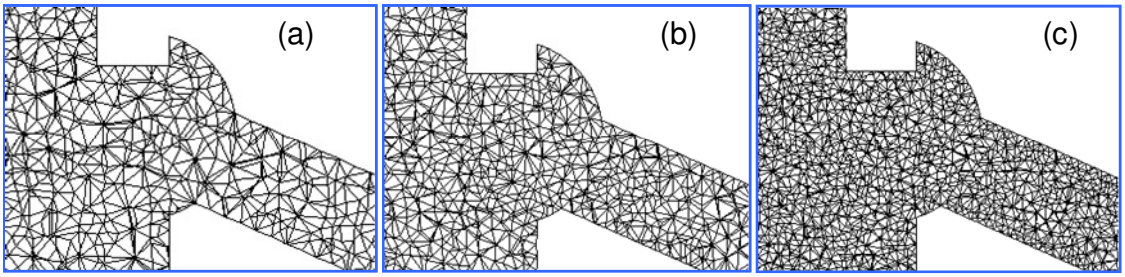

Figure 4-3: 3-D Mesh of Standard Geometry (Hole 3 Cross-section). (a) 67,000 cells, (b) 164,000 cells and (c) 460,000 cells

The boundary conditions where injection pressure Pinj of 550 bar and backpressure Pback of 120 bar. The working fluid for this investigation and for all the other real-size simulations is Diesel since Heavy Fuel Oil properties vary considerably and therefore no consistent data could be provided by the engine manufacturer. The Diesel properties, as found in [130], were kept constant throughout the investigation and are presented in

Table 4-1.

Liquid Density ρ_L	Vapour Density ρ_V	Vapour Pressure p_V	Dynamic Viscosity μ	Surface Tension σ
830 kg/m^3	~ 0.1 kg/m^3	~ 1000 Pa	3.32x10^{-3} kg/m.s	~ 0.02 N/m

Table 4-1: Properties of the Diesel Fuel Used for Real-Size simulations

4.3.1 grid effect on pressure distribution and cavitation prediction

The pressure distribution inside the nozzle is among the most important parameter that have to be predicted with good accuracy in a simulation. As it can be seen in Figure 4-4 all the three grid sizes used gave similar pressure distributions and the differences are so small that cannot be realized at first sight.

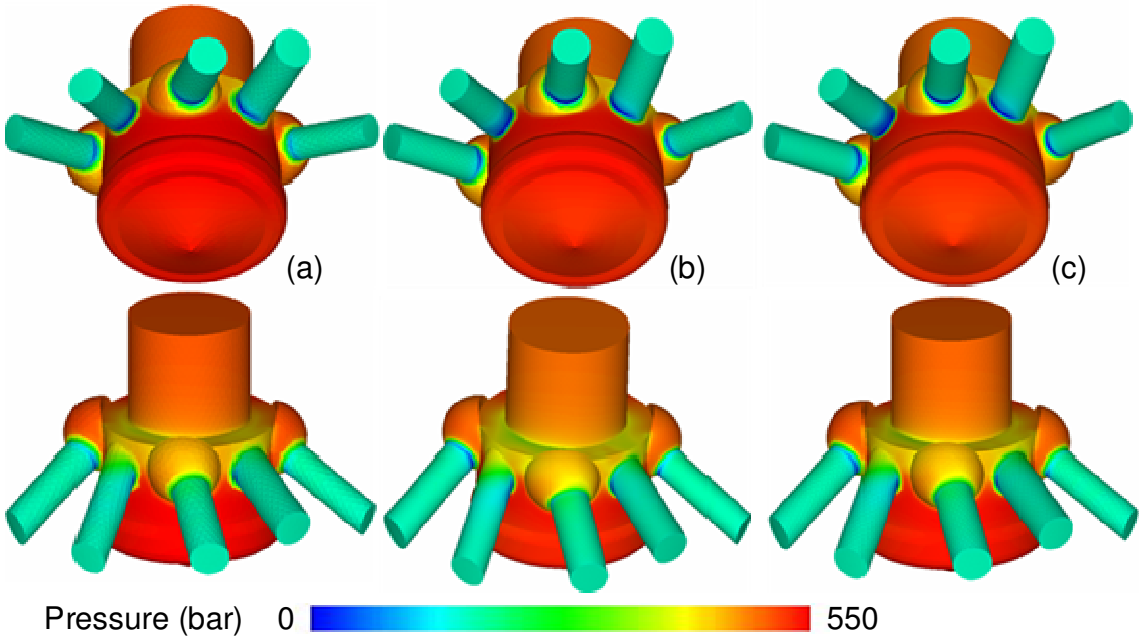

Figure 4-4: Grid Effect on Pressure Distribution. (a) 67,000 cells, (b) 164,000 cells and (c) 460,000 cells

Although the pressure distribution appears to be the same, it is of great importance to be able to predict accurately the possible cavitation sites. As it can be seen in Figure 4-5 the volume under tension is predicted in the bottom of the injection hole inlet. Given that the flow is coming from upstream it would be expected, from previous experience in nozzle

calculations, that negative pressure would be found in the upper hole entry region. Provided the current distribution it can be concluded that for this kind of nozzle the flow is mainly coming from below due to recirculation in the sac volume. It can also be seen that there is uneven distribution of tension volume from hole-hole, indicating that each hole is likely to cavitate with different intensity and result into different void fraction distribution.

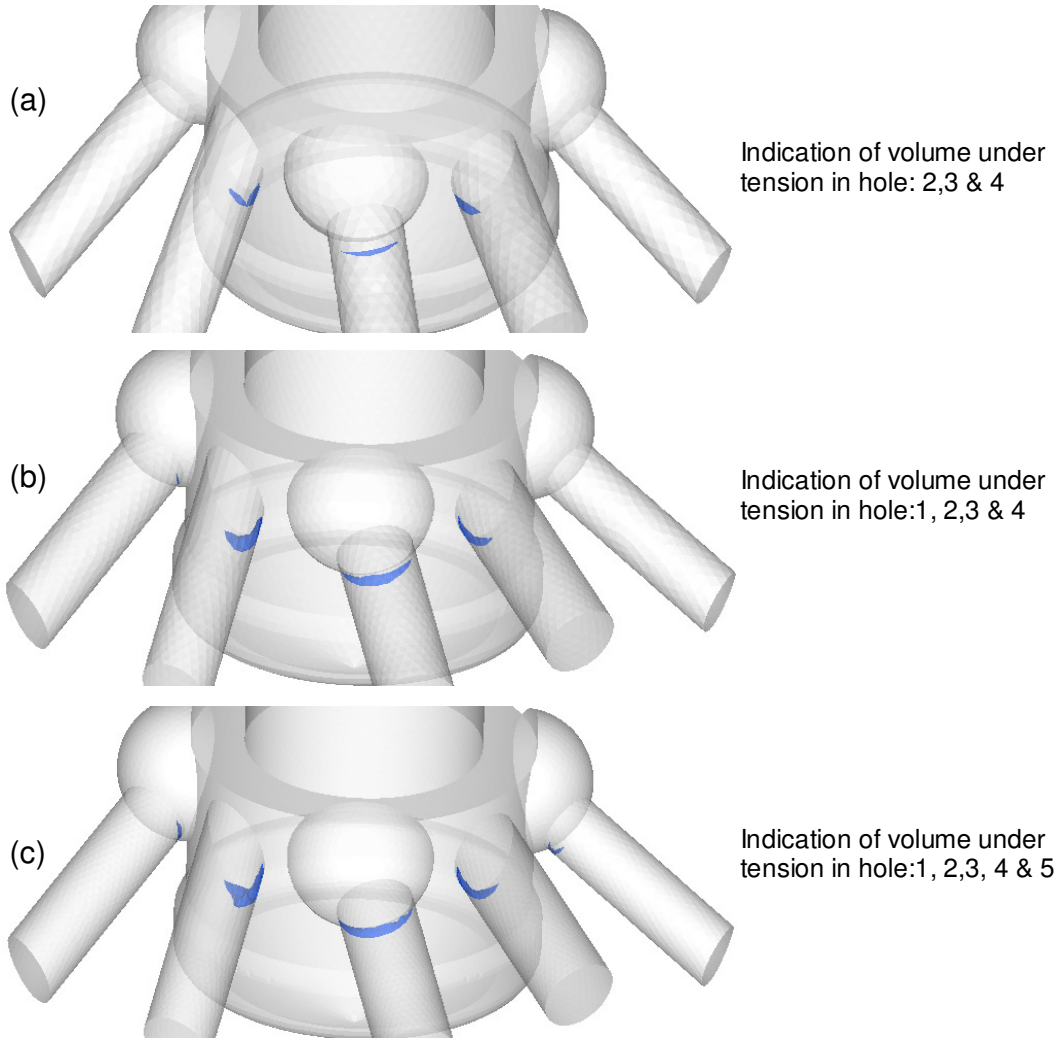

Figure 4-5: Grid Effect on Cavitation Prediction, Steady State results. Single-Phase Tension. (a) 67,000 cells, (b) 164,000 cells and (c) 460,000 cells

As shown in Figure 4-5 single-phase tension prediction is the most sensitive regarding grid density. This was expected since the hole entry is one of the regions with large gradients. Moreover it was found that the total velocity distribution varies between the three grids and particularly at the wall boundary of the nozzle. This was also expected since the number of cells within a certain diameter will influence the calculated velocity profile.

4.3.2 Grid Effect on Flow Rate, Discharge Coefficient and Mean Exit Velocity

The effect of grid size in calculating the viscous losses at the nozzle wall can also be seen from Figure 4-6 and Figure 4-8 where the coarse grid has the lower discharge coefficient and the lower mean hole exit velocity.

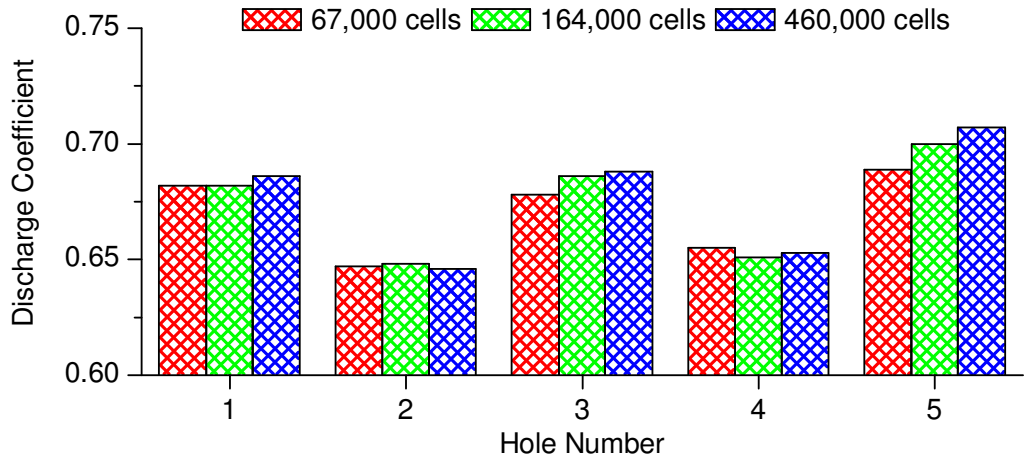

Figure 4-6: Grid Effect on Discharge Coefficient of Individual Holes. Steady State results.

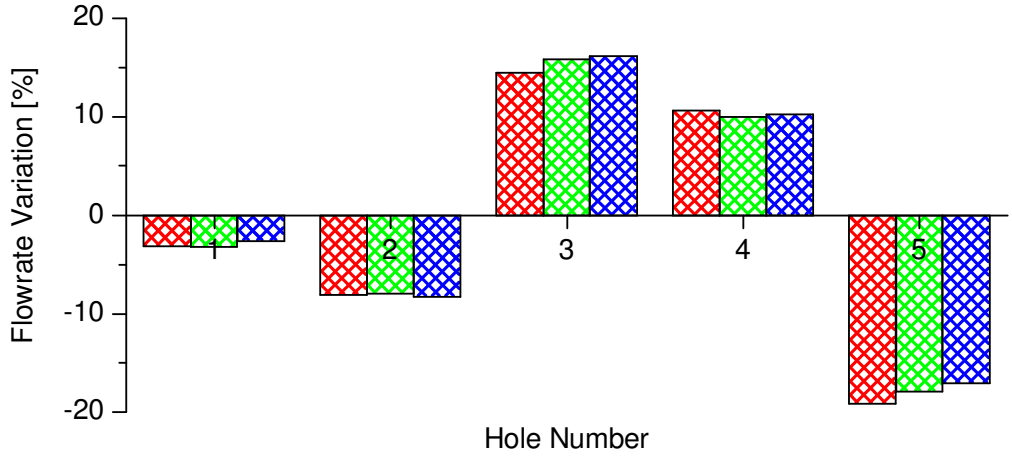

Figure 4-7: Grid Effect on Flow rate Variation of Individual Holes. Steady State results.

As previously mentioned the asymmetry in the design of the nozzle was expected to result into an asymmetric flow, from Figure 4-7 it is shown that all the three grids predict the

same trend regarding flow rate variations of individual holes, although some minor differences exist. Finally from Figure 4-9 is shown that the dense grid (460,000) predicts the greatest overall variation in mean exit velocity, however the differences are negligible.

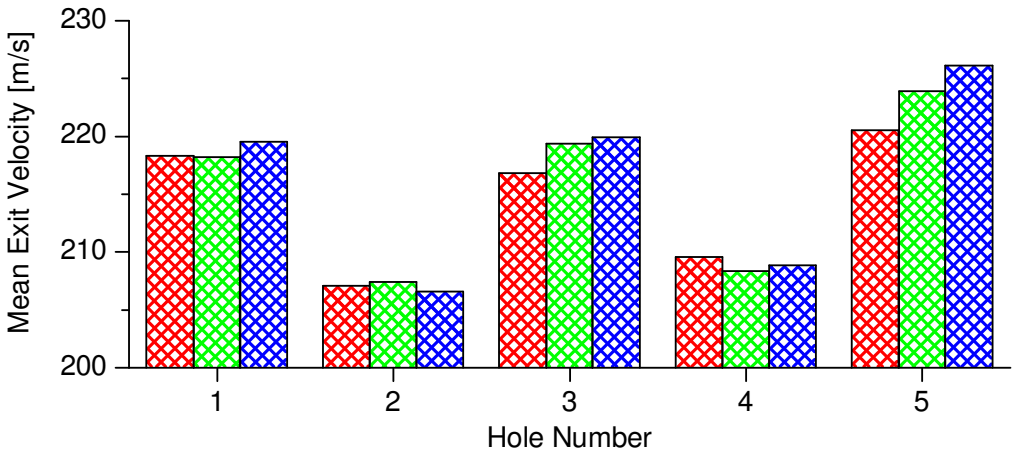

Figure 4-8: Grid Effect on Mean Exit Velocity of Individual Holes. Steady State results.

Concluding the results it was found that the grid size affects the calculated flow characteristic, although giving small differences in most parameters except from the volume under tension. Therefore it is necessary, at least for multi-phase simulations (cavitating) where negative pressure volume will be the site where bubbles will be forming, to use a dense grid.

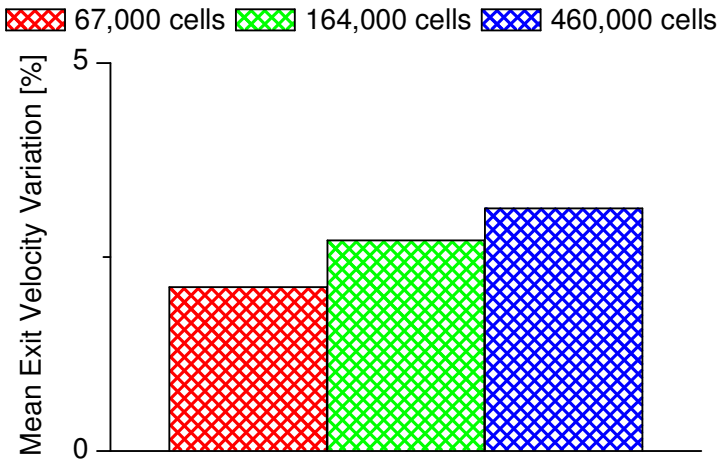

Figure 4-9: Grid Effect on Mean Exit Velocity Variation. Steady State results.

4.4 Effect of needle lift

As mentioned in section 3.1.1 the current nozzle has a slide-type needle, which when closed completely isolates the injection holes from the sac volume. It is well known from previous experimental work [30, 37, 96, 99, 118, 131-133] that the position of the needle plays an important role in the internal nozzle flow and cavitation regimes inside the injection holes.

Needle motion during injection occurs either from the change in lift, which is the normal operation of the nozzle, or due to the transient pressure throttling on the needle body and tip by the flowing liquid, particularly during opening and closing. This will cause an uncontrollable deflection leading to the needle to become eccentric.

However due to the current design of the nozzle the needle is always in contact with the nozzle wall and therefore it is not possible for the needle to have lateral movement. So for this design needle lift is the only parameter that can be investigated.

The nozzle manufacturer provided the needle lift profile for normal operating conditions and also the fuel flow rate as a function of crank angle which was converted to time. For the steady-state simulations four grids were created at Full, 80%, 60% and 40% lift.

Lower lifts were considered of no importance since even at 40% one of the holes is fully covered and at 35% all the five holes are closed. A schematic of the four grids can be found in Figure 4-10.

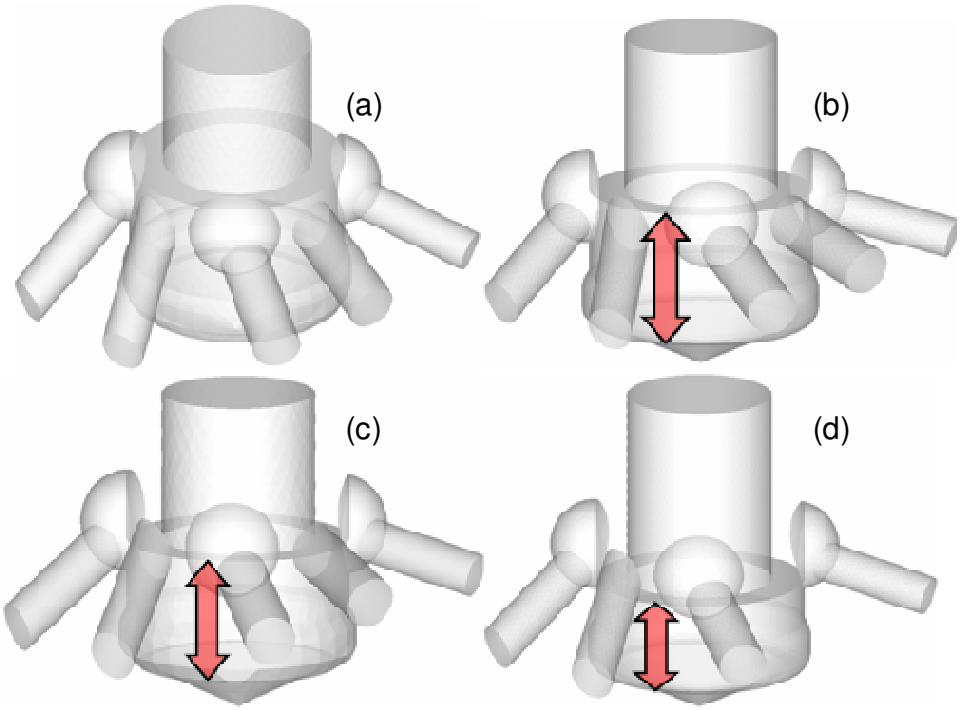

Figure 4-10: 3-D schematic of Full (a), 80% (b), 60% (c) and 40% (d) Needle Lift Nozzle Geometry for Steady-State simulations

A brief summary of the calculated results including the inlet flow rate, the inlet pressure the maximum injection velocity, the mean exit velocity and the discharge coefficient of the fully open nozzle can be found in Table 4-2: Summary of calculated parameters for Needle Lift Effect.

CASE	Flow rate		Pressure (bar)		Velocity (m/s)		Discharge coefficient
	m^3/s	kg/s	Min	Max	Max	Mean	
Full Lift	2.4096E-03	2.000	-100	460	269	216	0.76
80% Lift	1.0843E-03	0.900	70	200	126	97	
60% Lift	1.0482E-03	0.870	29	255	175	95	
40% Lift	2.0000E-04	0.166	100	182	101	23	

Table 4-2: Summary of calculated parameters for Needle Lift Effect

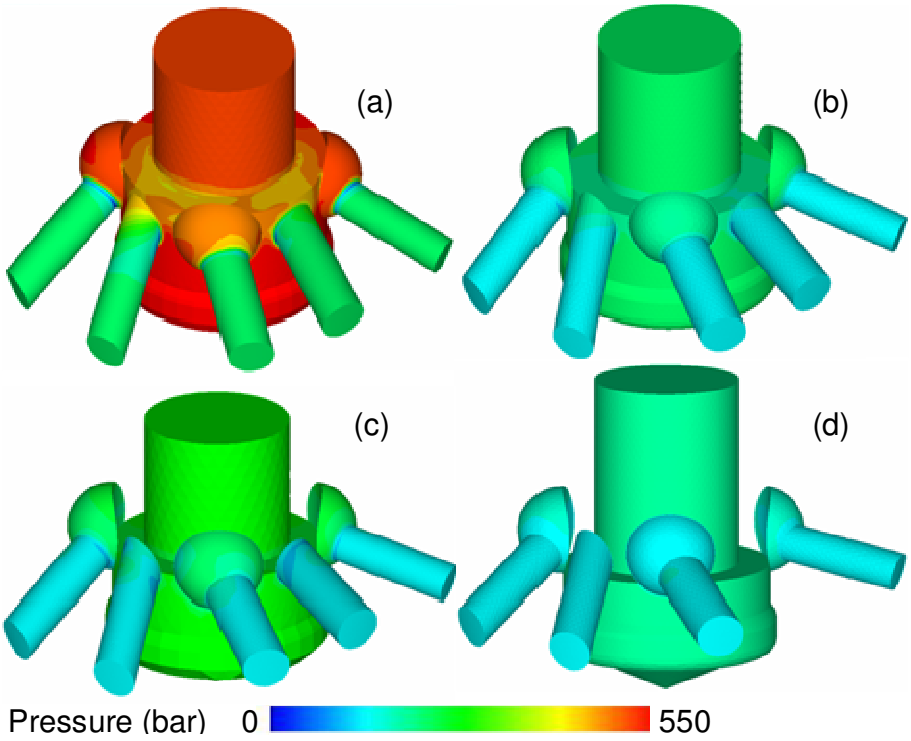

Figure 4-11: Needle Lift Effect on Pressure Distribution @ Full (a), 80% (b), 60% (c) and 40% (d) Lift. Global Scale

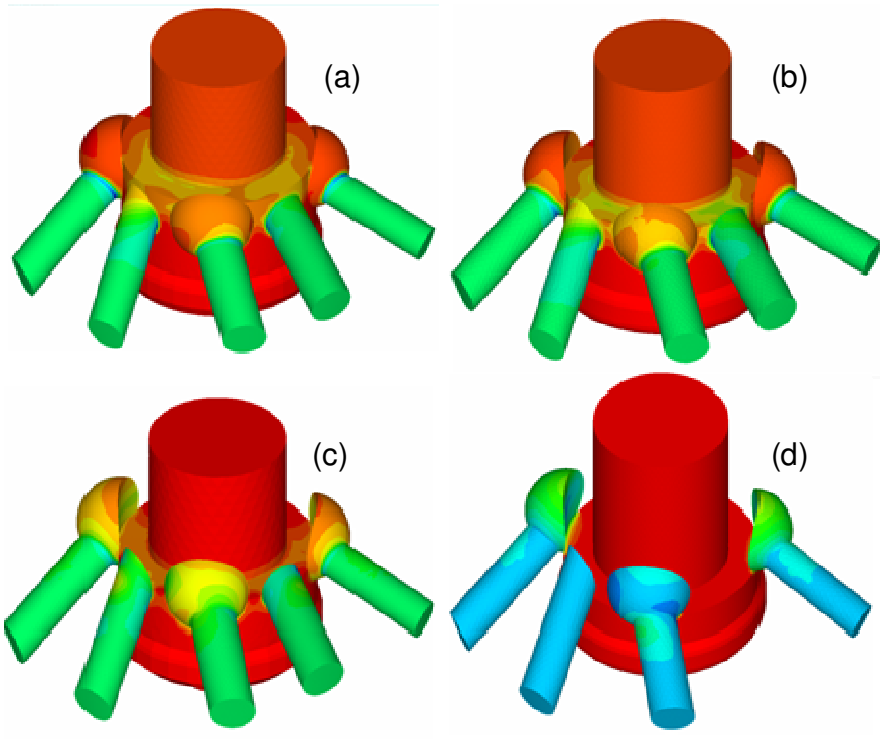

Figure 4-12: Needle Lift Effect on Pressure Distribution @ Full (a), 80% (b), 60% (c) and 40% (d) Lift. Local Scale

The most interesting finding can be seen in Figure 4-13, Figure 4-14, and Figure 4-15. The predicted flow structure shows that there is a large recirculation zone inside the sac volume, located opposite to the hole inlets, mostly affecting the two side-holes, 1 and 5, where the main proportion of the flow is coming through that zone.

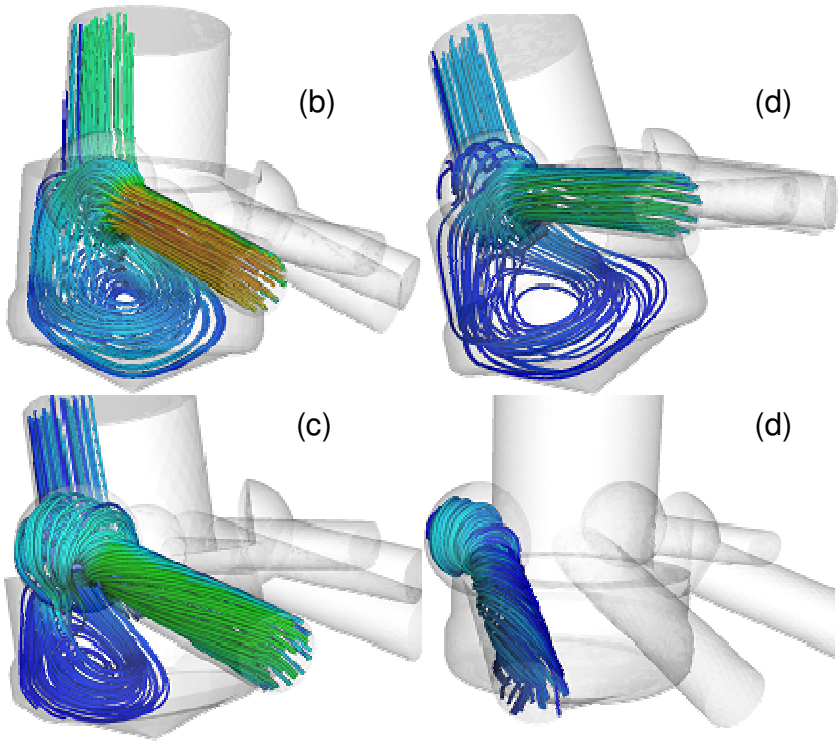

Figure 4-13: Needle Lift Effect on Predicted flow structure inside the nozzle volume and the injection holes @ Full (a), 80% (b), 60% (c) and 40% (d) Lift. (Hole 1)

As mentioned before such recirculation zones can enhance string-cavitation which is undesirable since it is difficult to be predicted and controlled. Contrary to that, the flow entering into the middle holes, 2, 3 and 4, is mostly coming directly from upstream and are not associated with the afore mentioned recirculation zone. It can also be seen that swirling motion is present inside all holes with rising intensity as lift decreases.

From Figure 4-16 and Figure 4-17 it can be seen that as needle lift increases the differences between the flow rates of the holes decreases. This was expected since the holes are positioned in different heights and also because of the semi-spherical inlets that allow more flow to pass through for greater needle lift range.

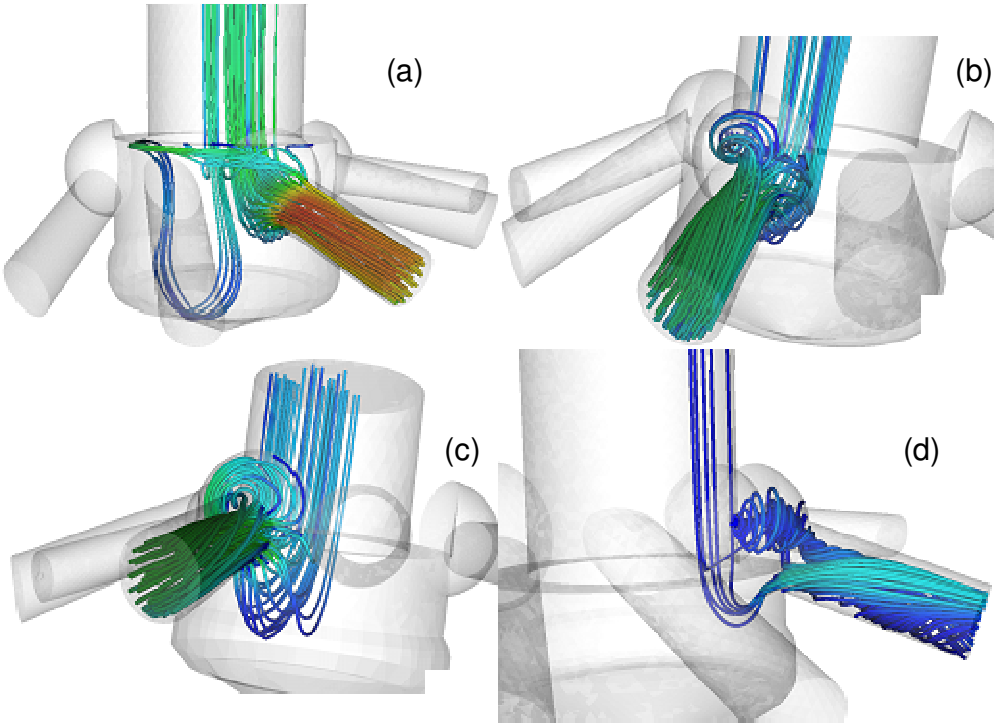

Figure 4-14: Needle Lift Effect on Predicted flow structure inside the nozzle volume and the injection holes @ Full (a), 80% (b), 60% (c) and 40% (d) Lift. (Hole 3)

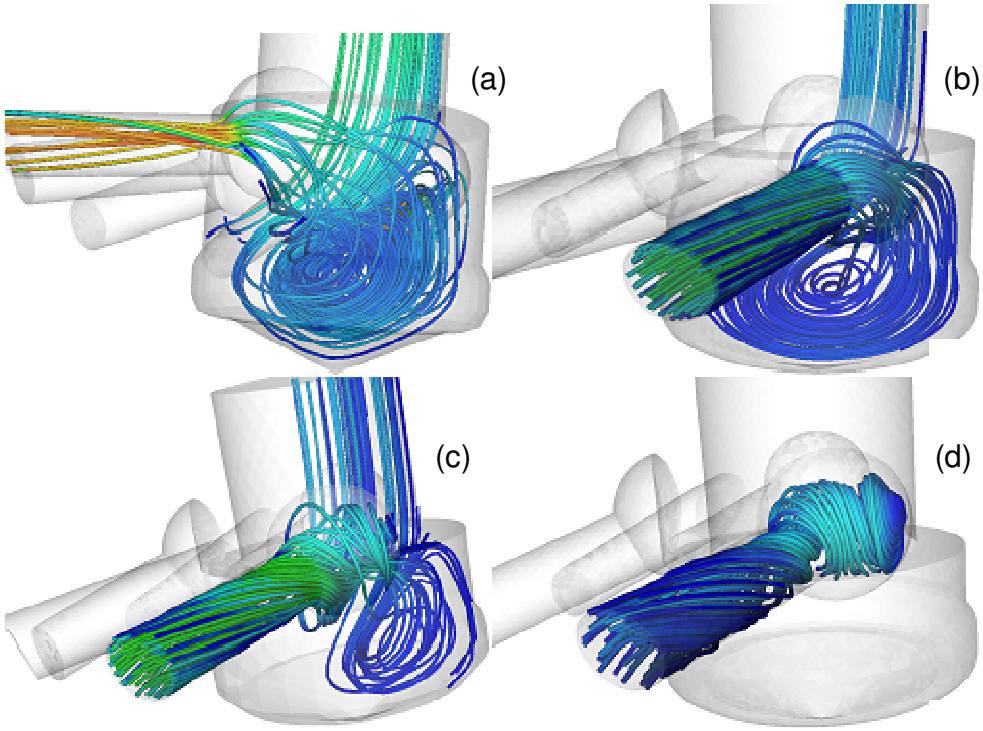

Figure 4-15: Needle Lift Effect on Predicted flow structure inside the nozzle volume and the injection holes @ Full (a), 80% (b), 60% (c) and 40% (d) Lift. (Hole 5)

That is why holes 1, 3, and 5 are, at least at low lifts, are gaiting larger proportion of the flowing liquid. The same applies for differences in mean exit velocity since is directly proportional to flow rate.

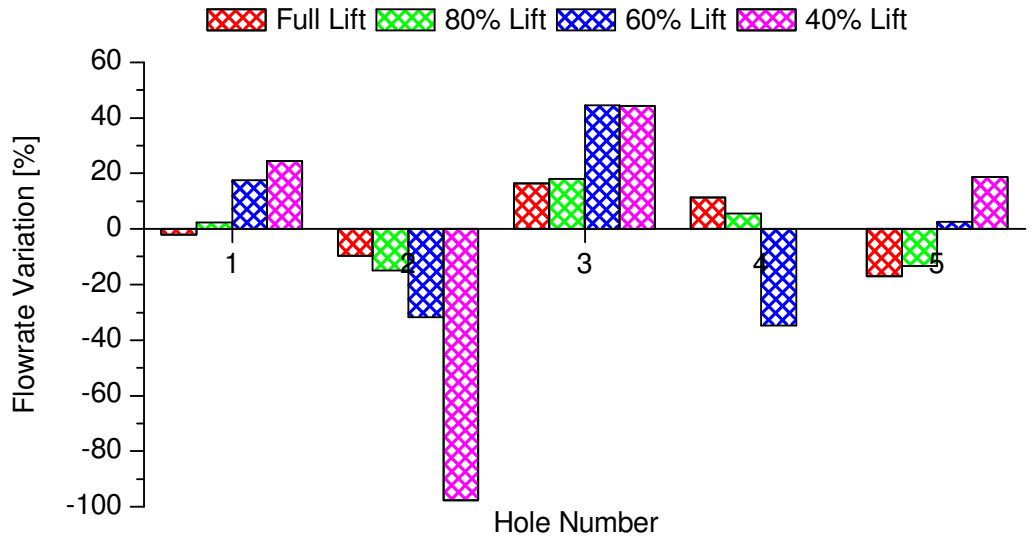

Figure 4-16: Needle Lift Effect on Predicted Flow rate Variation [%] of Individual Holes @ Full, 80%, 60% and 40% Lift.

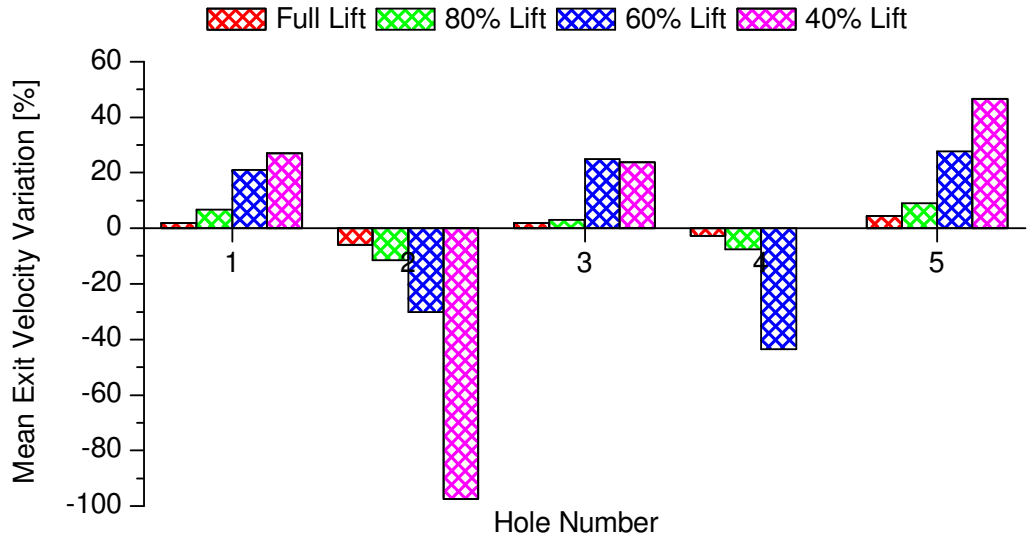

Figure 4-17: Needle Lift Effect on Predicted Mean Exit Velocity Variation [%] of Individual Holes @ Full, 80%, 60% and 40% Lift.

Finally it can be seen from Table 4-2 when the needle is not fully open, i.e. at 80%, 60% and 40% lift, and with the corresponding inlet pressure and flow rate given by the

manufacturer there is no indication of volume under tension, negative pressure, in any of the five holes. This behaviour has been reported also in studies by [114, 117, 134] and was attributed to the increased levels of turbulence that characterize low needle lift flows.

4.5 Parametric studies

4.5.1 Effect of upstream needle geometry

Previous studies presented in section 4.3 and 4.4 revealed important hole-to-hole differences and also large vortical structures in the sac volume. When considering fuel atomization and spray dispersion in cylinder such behaviour is not desirable. So, further simulations had to be done focusing into finding the dominant parameters that produce the aforementioned undesired flow behaviour.

So far the simulations presented were focusing at the lower part of the nozzle ignoring the upstream geometry. As mentioned in section 3.1.1 and as can be seen in Figure 3-1 the needle geometry is very complex. It follows that in order for the obtained results to be accurate a highly dense grid would be required, leading into a much increased computational time.

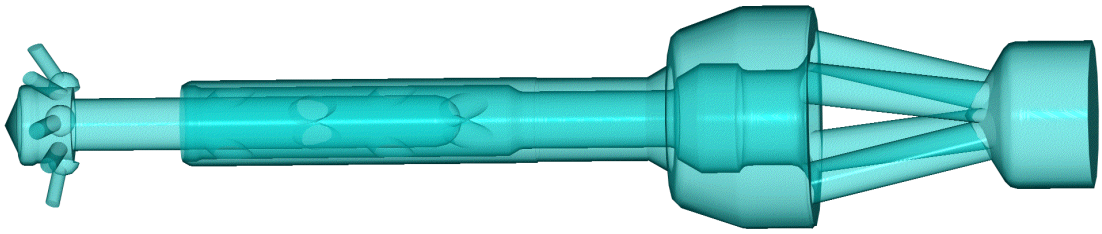

Figure 4-18: 3-D Schematic of full lift complete geometry grid

Combining the needle (or cut-off shaft as usually referred), schematic of which can be seen in Figure 3-1 (b), and the entire nozzle body, as presented in Figure 3-1 (a), results into the so-called ‘complete geometry’ which is presented in Figure 4-18.

The resulting geometry was discretized with more than 1 million computational cells in order to compare the results of the short version simulations. The comparison of the results

will show the effect of the needle geometry on the various flow characteristics and help into improving the understanding for the flow irregularities.

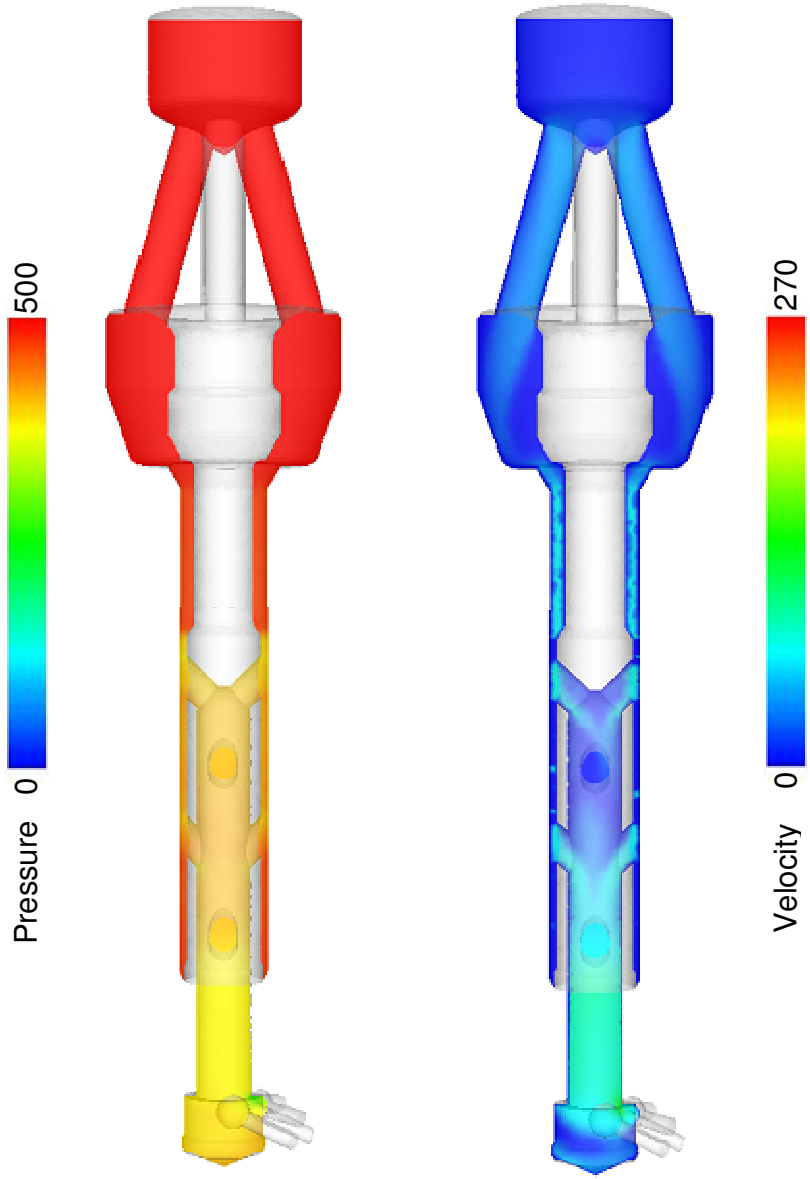

Figure 4-19: Complete Geometry Pressure and Velocity Distribution @ XZ Plane. Full Lift.

The flow simulations showed that the needle geometry effect on pressure distribution is not significant for the current conditions. However, as shown in following Figure 4-20 the holes that seem to be mostly affected are the side ones, 1 and 5.

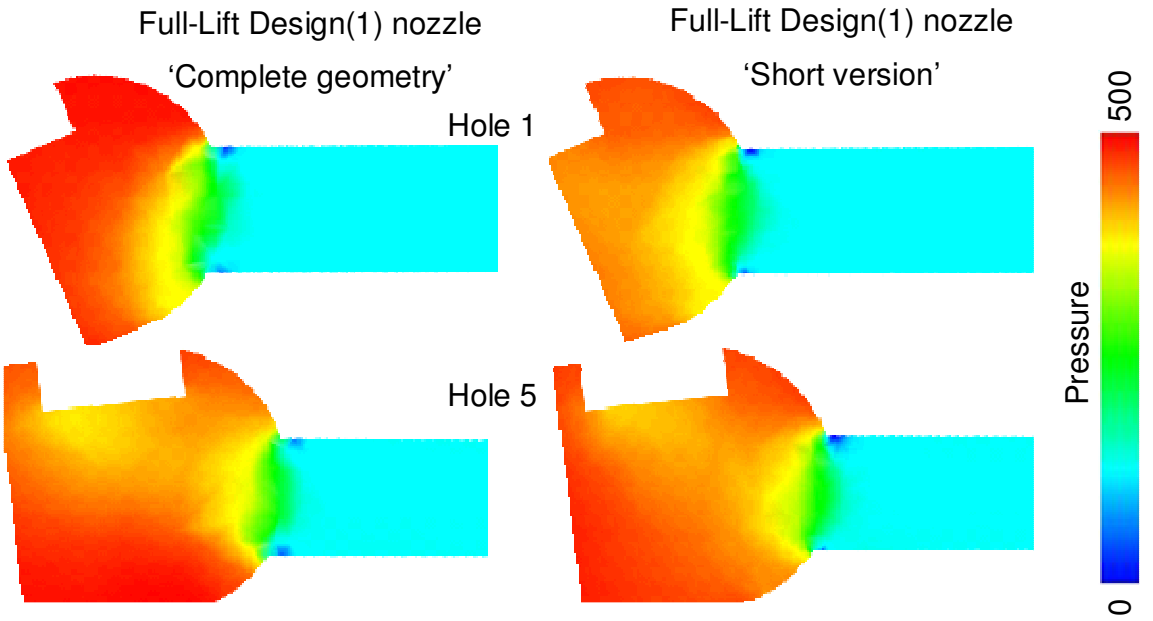

Figure 4-20: Contour plots of pressure distribution at hole cross-section. Complete Vs short geometry. Full lift.

Also in Figure 4-21 is shown that velocity distribution is mostly affected inside the sac volume of the investigated nozzle while inside the injection holes the differences are not notable.

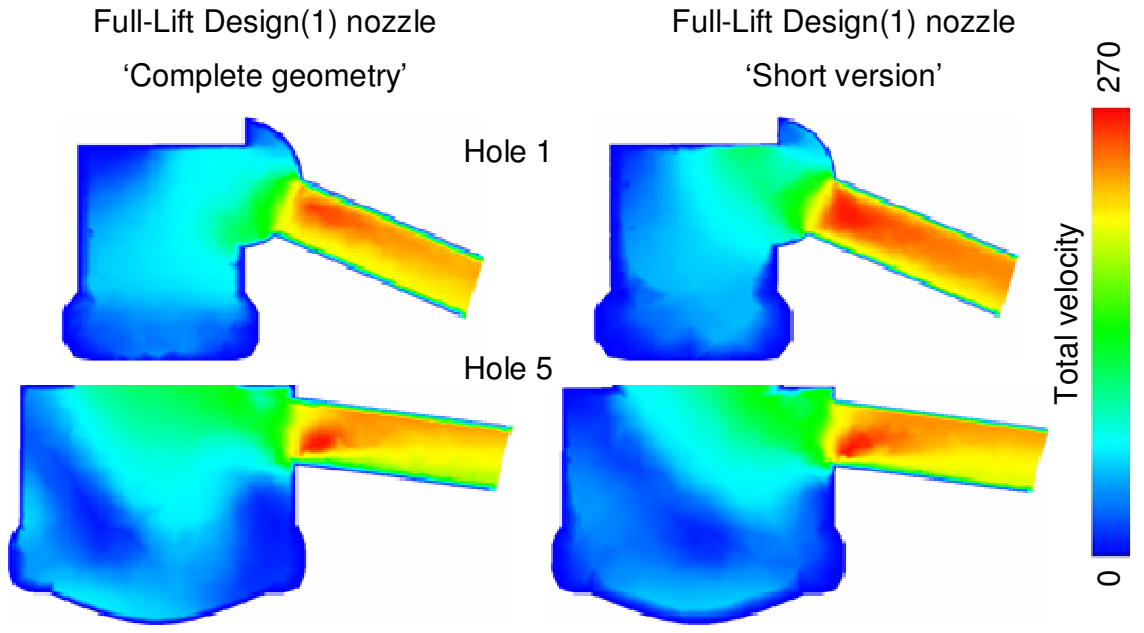

Figure 4-21: Contour Plots of Velocity Distribution at hole cross-section. Complete Vs Short Geometry. Full Lift.

Combining the results shown in and Figure 4-23 it can be seen that the existence of the upper needle geometry shifts the flow towards Hole 5, this results into having lower flow rate entering to Hole1. This in turn makes Hole1 to have lower exit velocity as seen in Figure 4-22. The change, in flow rate distribution between the holes, is also clearly indicated by noting that the blue region, representing lower velocities, opposite to the holes is shifted towards Hole 1.

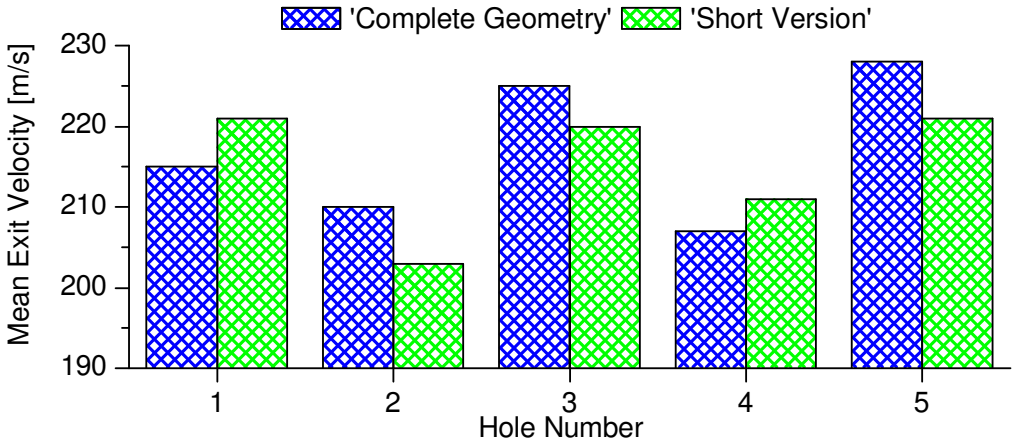

Figure 4-22: Needle geometry Effect on Mean Exit Velocity. Complete Vs Short Geometry. Full Lift.

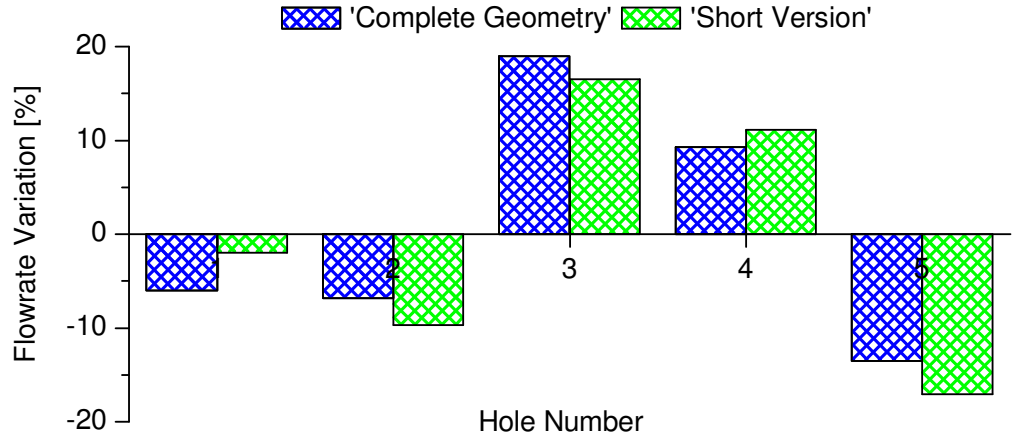

Figure 4-23: Needle geometry Effect on Flow rate Variation [%] of Individual Holes. Complete Vs Short Geometry. Full Lift.

As previously mentioned the needle geometry resulted into differences of the various predicted quantities, however not very significant. In contrast what seems to be affected significantly is the recirculation zone inside the sac volume. As it can be seen in Figure 4-24 the main proportion of the flow entering Hole 5 in the short version of the nozzle is coming from the recirculation zone inside the sac volume.

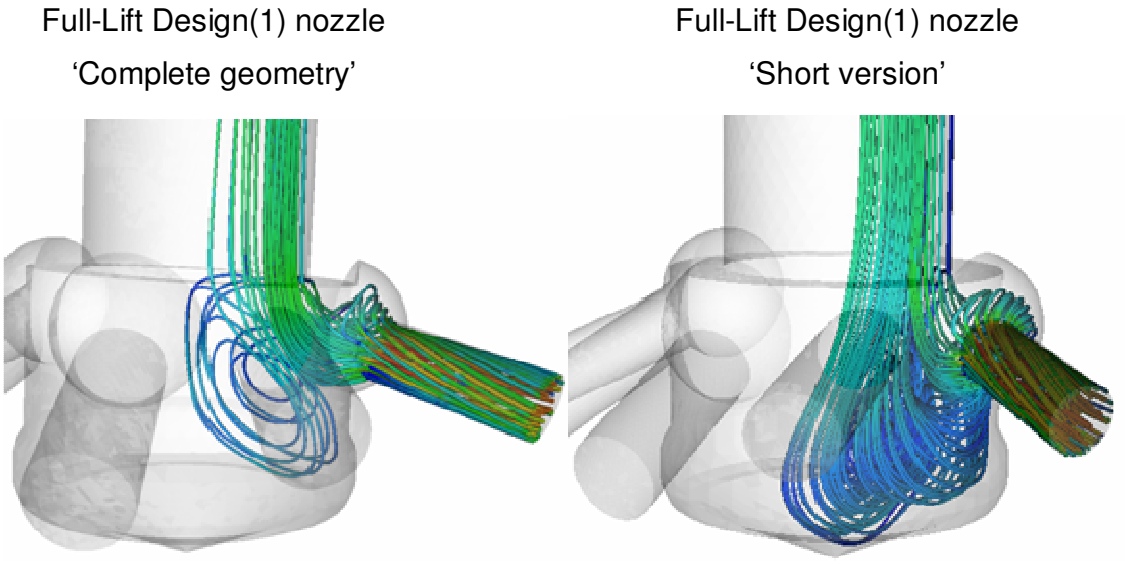

Figure 4-24: Needle geometry Effect on Predicted flow structure inside the nozzle volume (Hole 5). Full Lift.

While in the complete geometry of the nozzle, where the needle geometry has been accounted, the flow is mostly coming directly from upstream, living only a small recirculation zone opposite to the hole inlet. Even though for steady simulation these structures can not change the flow characteristics dramatically, previous investigations have shown that areas with high recirculation may initiate, as previously mentioned, 'string' or 'vortex' type cavitation [30] [32] which has been recently identified as a possible flow mechanism responsible for significant instabilities of various flow parameters as well as effecting the structure of the spray exiting the hole.

Those cavitation structures are usually formed in the bulk of the liquid, which implies that they are induced by the local flow turbulence or larger scale vortical structures rather than the pressure drop at sharp corners.

Although different studies have shown similar behaviour in various types of multi-hole nozzles, their formation process has been found to be relatively irregular while their interaction with the mean flow is still not purely understood.

4.5.2 Effect of nozzle geometries

The two major findings, so far, were that the flow rates between the holes have relatively large differences, even though the nozzle was designed in order to have a uniform distribution, and that large vortical structures exist in the sac volume mostly affecting the side Holes i.e. Hole 1 and 5 as clearly seen in Figure 4-25.

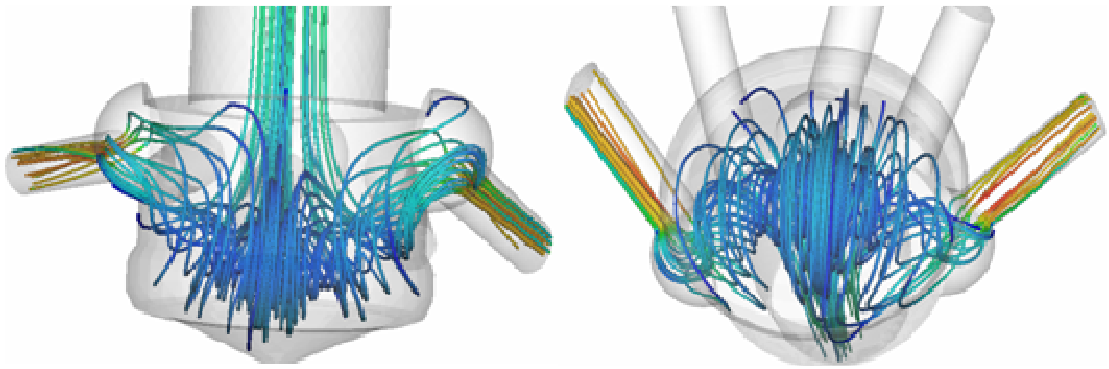

Figure 4-25: Predicted flow structure inside the nozzle volume. Design(1) nozzle, Short Version. Full Lift

Continuing the investigation and considering the undesired effects that this recirculation can cause a series of different nozzle designs where created in order to observe how the internal nozzle flow structures are affected. Having examined the effect of the needle geometry it was decided not to include the needle for those studies. Firstly because there were only minor changes in the predicted quantities, and secondly, because the required computational time would have been considerably higher, at least 5 times longer than the time required for the short version, limiting the amount of conceptual designs.

Even if there was a significant change in the flow structure between a new design and the short version of the standard nozzle, the difference would have been the same as if both had the needle geometry included.

All the simulations of the conceptual nozzle designs where conducted under steady-state boundary conditions at full needle lift. In order for the results to be comparable with the short version of the standard nozzle design the number of holes, the hole diameter and the hole direction were kept unchanged.

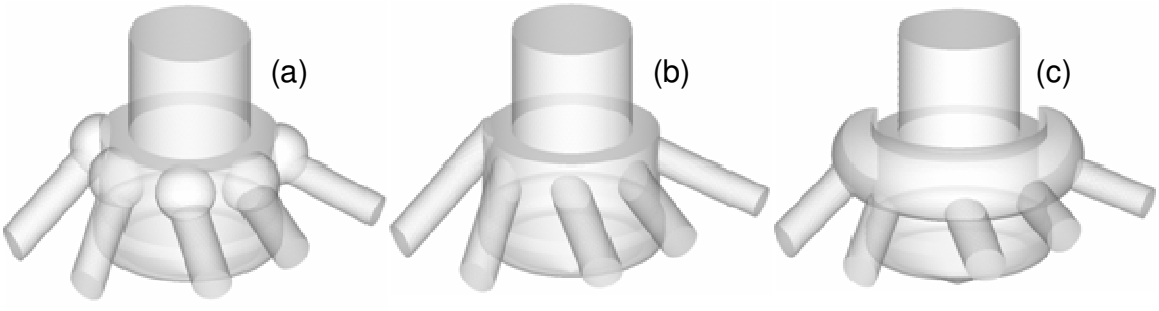

Figure 4-26: 3-D schematic of Conceptual Nozzle Designs (Uniform Flow). (a) 5-Spheres, (b) Without Spheres and (c) Single Groove designs.

The concept of the three designs presented in Figure 4-26: 3-D schematic of Conceptual Nozzle Designs (Uniform Flow).Figure 4-26 was to make the flow entering the holes uniform. Therefore instead of having spherical inlet in three of the five holes it was chosen to make 5 spherical cavities of smaller diameter. Then another obvious change would have been to remove all the spheres from the holes inlet and finally to substitute the spherical inlets with a single groove and observe the changes to the flow.

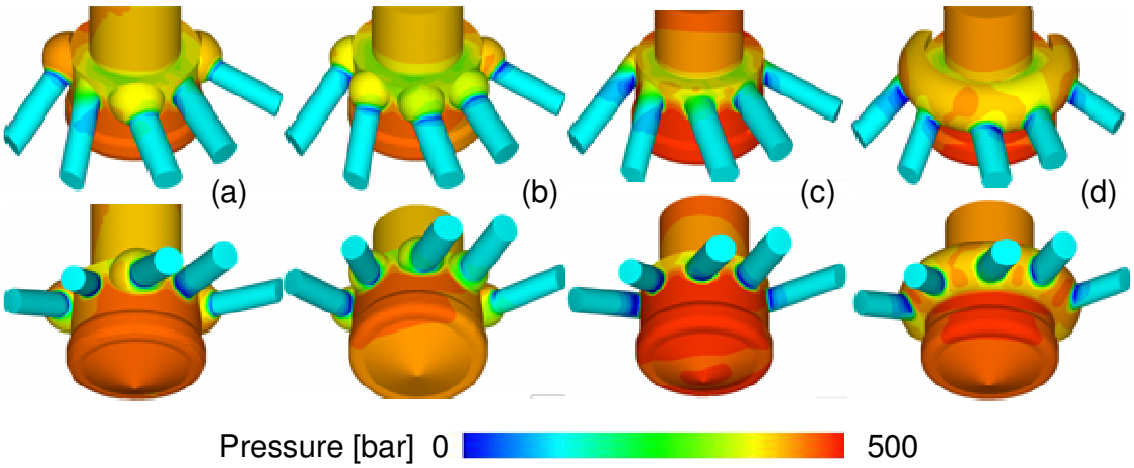

Figure 4-27: Pressure Distribution of Conceptual Nozzle Designs Vs Standard Design. (a) Standard, (b) 5-Spheres, (c) Without Spheres and (d) Single Groove designs.

It should be mentioned that at this point there were no concerns regarding whether the new designs would have been possible to be manufactured and operated in the engine. Although the hole diameters and directions were unchanged.

Figure 4-27 shows qualitatively the effect of the different designs on the predicted pressure distribution. However in order for safe conclusions to be drawn, further more quantitative analysis was required. Following shows the calculated parameters of the simulations.

CASE	Flow rate		Pressure (bar)		Velocity (m/s)		Discharge coefficient
	m3/s	Kg/s	Min	Max	Max	Mean	
Standard	2.4096E-03	2.000	-100	460	269	216	0.76
5-Spheres	2.4096E-03	2.000	-33	457	264	215	0.75
Without Spheres	2.4096E-03	2.000	-86	495	288	215	0.72
Single Groove	2.4096E-03	2.000	-65	366	270	215	0.73

Table 4-3: Summary of calculated parameters for Conceptual Nozzle Designs Vs Standard Design

As it can be seen in the above graphs, Figure 4-28 and Figure 4-29, it is clear that the new designs still have relatively large variations in flow rate between the injection holes and that the geometry with the higher discharge coefficient is still the standard original one.

However, since the flow rates of the holes have changed further plots of the calculated results were created in order to visualize the internal flow structure. As previously mentioned what was of interest was to see if these changes in nozzle geometry would affect the recirculation zone inside the sac volume of the nozzle.

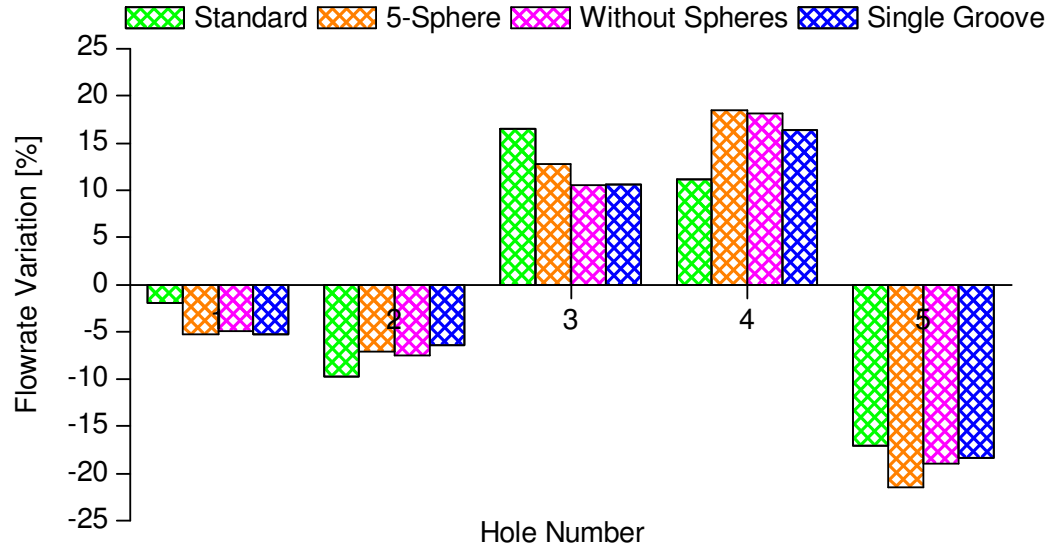

Figure 4-28: Flow rate Variation [%] of Conceptual Nozzle Designs Vs Standard Design

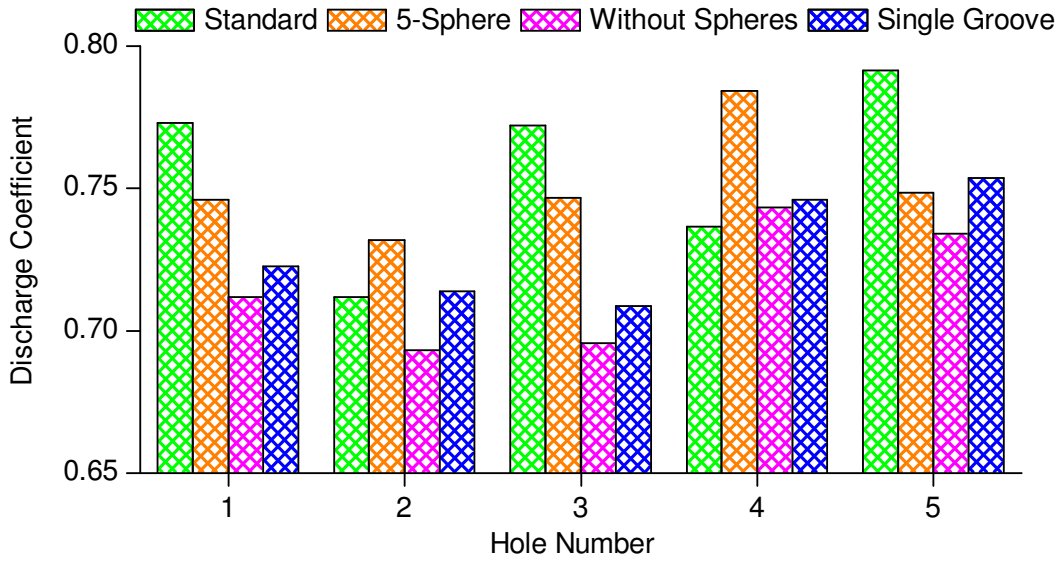

Figure 4-29: Discharge Coefficient of Conceptual Nozzle Designs Vs Standard Design

It has to be clarified that at this stage of the investigation there was no experimental evidence of this vortical structures in the nozzle volume and no indication that they affect the flow rates of the injection holes or the emerging fuel spray. As reported from Salvador et al. [135] a force sensor, equipped with a piezo-electric pressure sensor, would have made possible to measure the mass and momentum flux of the injected spray that would impinge on its surface. This provides the response time of the equipment was fast enough could have provided the distribution of flow rate across the injection holes. Even in steady

flow test rig this would have been very useful in a time average basis. However such data were not available. However the standard design concept, according to the manufacturer, was to have the same flow rate exiting the injection holes.

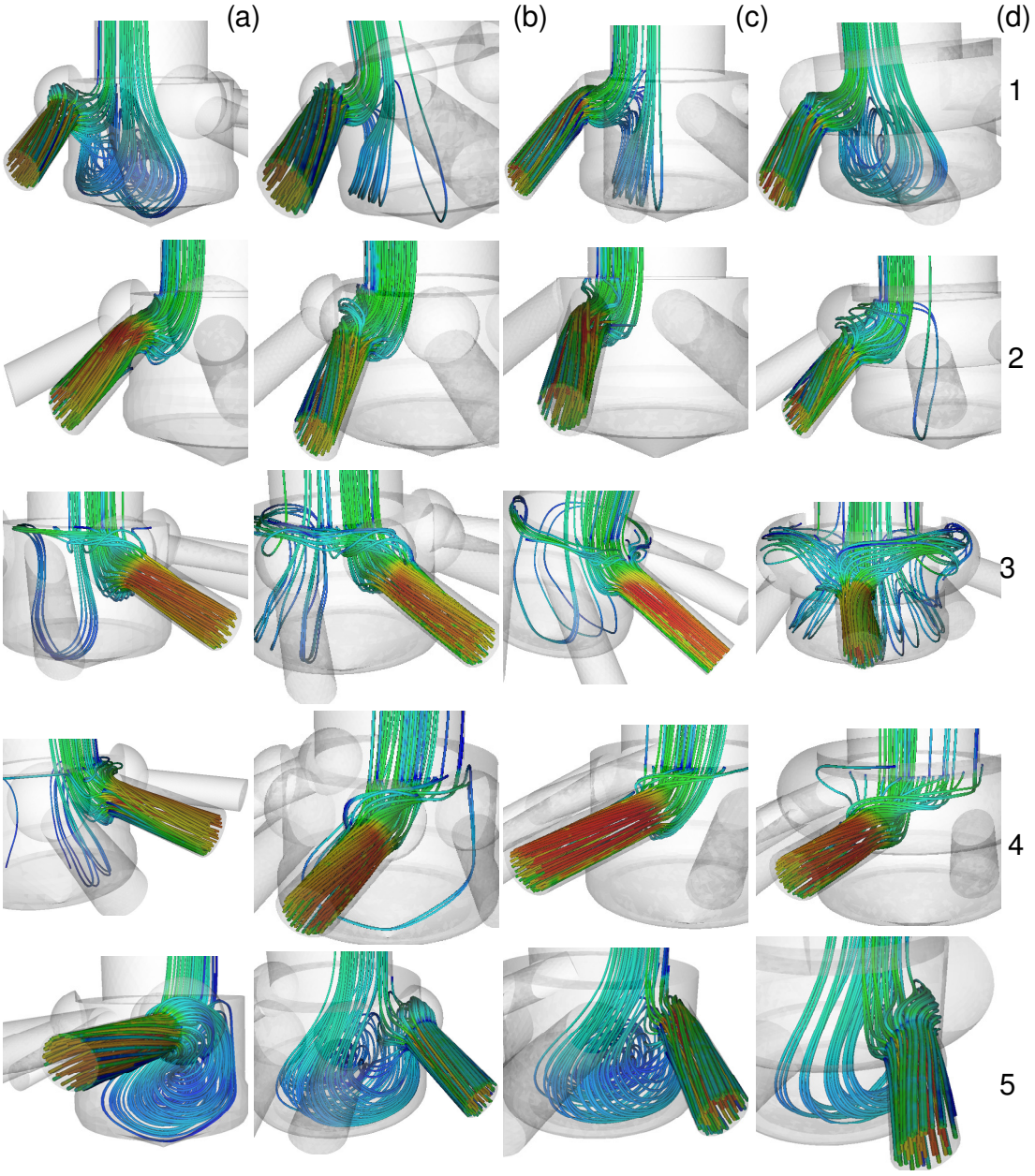

Figure 4-30: Predicted flow structure inside the nozzle volume. (a) Standard, (b) 5-spheres, (c) without spheres and (d) single groove.

In Figure 4-30 it can de seen that all the new designs tend to reduce the vortices in the sac volume. It can also be seen that Hole 5 is the one with the most flow coming from the

recirculation zone, and is also the hole with the smallest changes, in flow structure, except from the single groove design where the recirculation has been significantly reduced. What can also be seen is that for the middle holes i.e. 2, 3 and 4 almost all the flow is coming directly from upstream and enters into those holes directly without forming any recirculation along its path towards those injection holes. Again for the single groove design it can be seen that flow is entering into hole 3 through the recirculation in the sac volume and also from both directions within the groove.

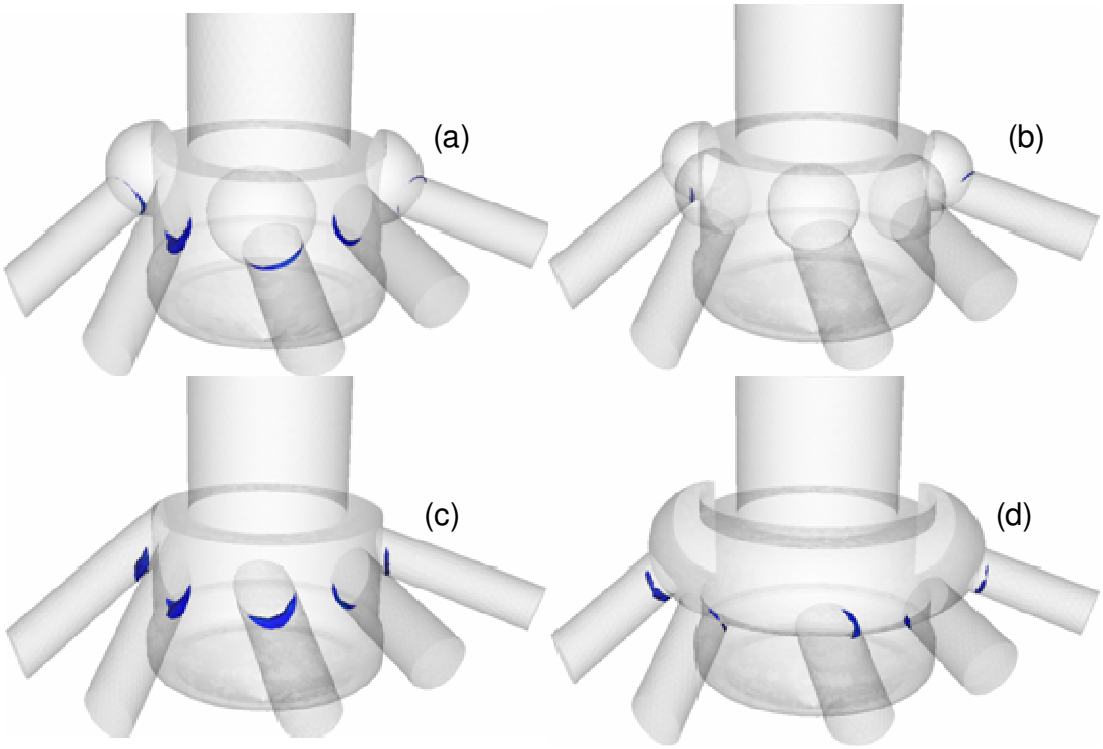

Figure 4-31: Predicted Single-Phase Tension. (a) Standard, (b) 5-spheres, (c) without spheres and (d) single groove design.

What can be seen in Figure 4-31 is that the 5-Spheres design has the lowest negative pressure, therefore is expected to cavitate in higher CN values than the other designs. In fact this can also be seen in Figure 4-31 where the 5-spheres design has the smallest amount of volume under tension, and which also for those particular conditions hole 2, 3 and 4 no negative pressure region is predicted.

What can also be seen in Figure 4-30 is that there is a swirling motion inside the holes. Swirl in the injection holes can affect the spray angle and also the injection direction.

Therefore it was also interesting to see what are the velocity vectors at the hole exit. What was also of interest was to see the velocity distribution inside the holes in 3-D rather than at the middle cross-section of the hole, which would give a qualitative view of the swirl effect on velocity distribution.

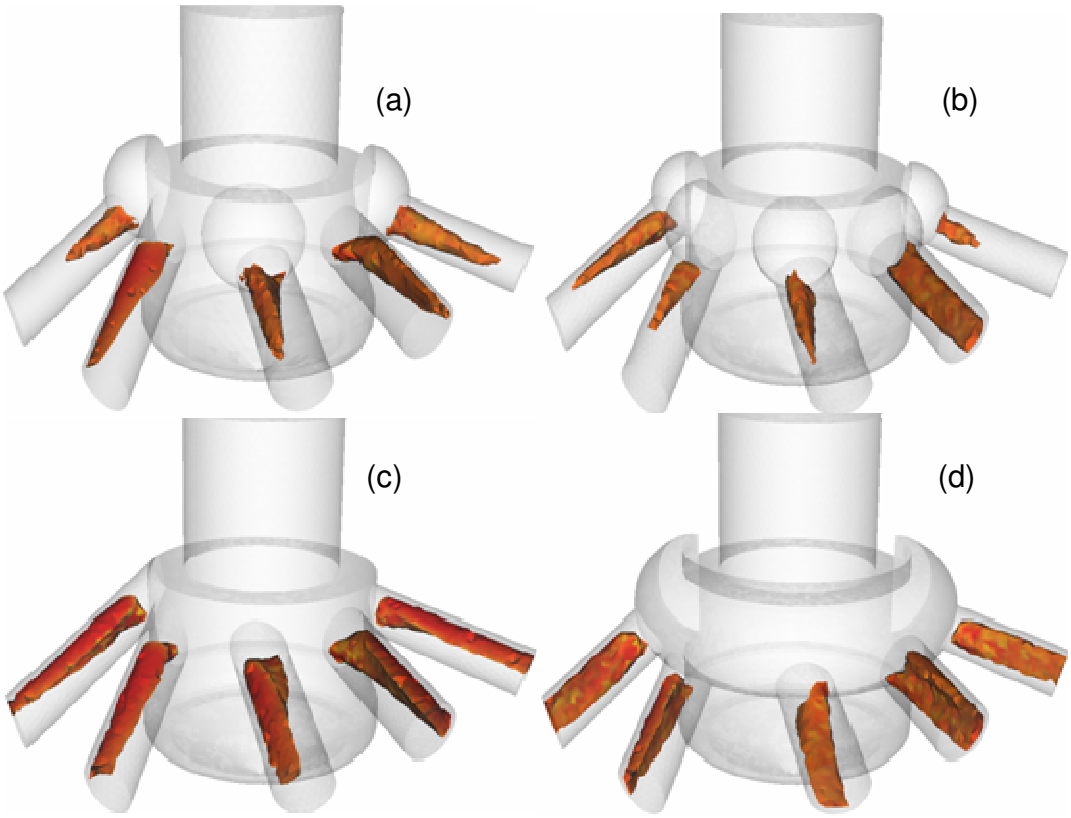

Figure 4-32: Isosurface plots of predicted velocity @ 240 m/s. (a) Standard, (b) 5-spheres, (c) without spheres and (d) single groove design.

It can be seen in Figure 4-32 that velocity distribution inside the injection holes is highly asymmetric. Not only between holes but also within the same injection hole, possibly this can be attributed to the swirling motion of the flow that was presented before. The same asymmetric, structure is expected to be found to the dispersion of the cavitation bubbles inside the injection holes. What can also be seen is that the 5-speres design has developed lower velocities inside the holes, particularly in hole 5 which is associated with vortices.

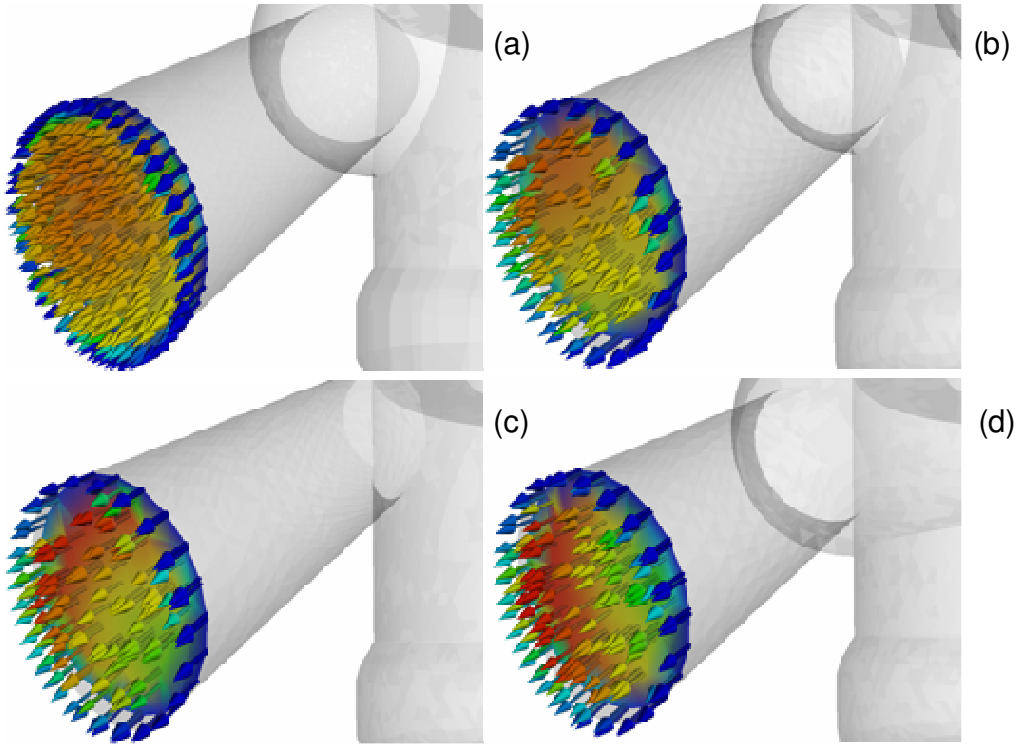

Figure 4-33: Predicted velocity vectors on the nozzle exit plane, indicating that the liquid may be deflected relative to the hole axis orientation (Hole 1). (a) Standard, (b) 5-spheres, (c) without spheres and (d) single groove design.

As can be seen in Figure 4-33 the velocity vectors at the nozzle exit plane clearly indicate a swirling motion and an uneven flow distribution inside the injection hole. This can result into a deviation of the spray injection direction from the nominal one (hole direction) which may cause undesirable effects on the liquid distribution and fuel/air mixing within the combustion chamber. Similar vector directions and distributions were found in all injection holes.

It follows that the velocity vectors and profiles on the hole exit plane had to be further examined since it was expected to affect significantly the spray structure. Results of this investigation will be presented later in this chapter, in section 4.6.3.

Until this point the new designs where aiming into a more even flow distribution. The following designs presented in Figure 4-34 were aiming to change the flow structure in the nozzle sac volume (a), inside the injection holes (b) and also to prevent geometric cavitation (c). Once again it was not considered if the new designs would have been

possible to be manufactured and work under the engines operating conditions; however the hole diameters and direction were kept unchanged.

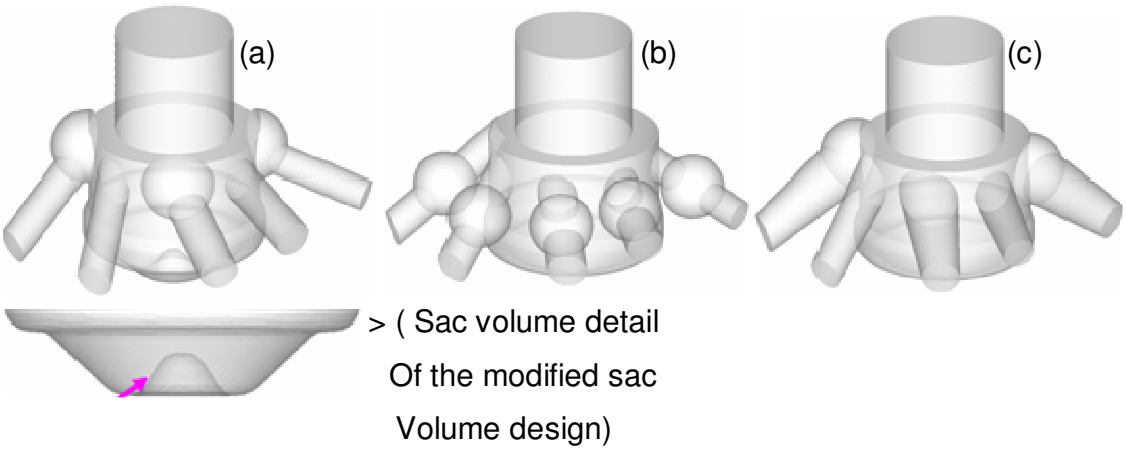

Figure 4-34: 3-D schematic of further conceptual nozzle designs. (a) Modified sac volume, (b) Middle-hole spheres and (c) Tapered holes designs.

The "modified sac volume" design has a small "hill" at the bottom of the nozzle sac volume. This change was expected to change the flow direction and affect the recirculation zones inside. Although the holes are concentrated on one side of the nozzle it was chosen to put that hill in the middle for simplicity. In order not to have a severe change to the nozzle design the height of that 'hill' was set to 1mm only.

The "middle-hole spheres" design is perhaps the most unconventional design of all the others. Basically this design came by combining the without spheres design and the 5-spheres design, except that this time the spheres were placed at the middle of the holes. What was expected to see was a change in the flow structure not in the sac volume but inside the injection hole. By having those spherical cavities at the middle of the hole it would have been as the flow was undergoing a sudden expansion and shortly after a contraction. At the time that this design was created it was not clear how this will affect the flow, but certainly it would result in a notable change in flow structure and also in the location of the tension volume.

Finally, it is well known from previous investigations, such that of Blessing et al. [37], that the conical shape of the injection holes (also known as K-factor of the nozzle) influence cavitation behaviour and thus cone angle and spray break-up significantly. Positive K-factor means that the hole would have a larger diameter at the inlet than at the exit and a negative factor will be the opposite. The more conical (tapered) the hole towards the exit the higher the K-factor (or conicity). A high K-factor was found to cause smaller spray angles, and less cavitation formation. This was reasonably well predicted with CFD simulations too. In a purely numerical investigation of Payri et al. [136], no cavitation was observed for the conical hole nozzles and it was attributed to the smooth pressure distribution along the hole.

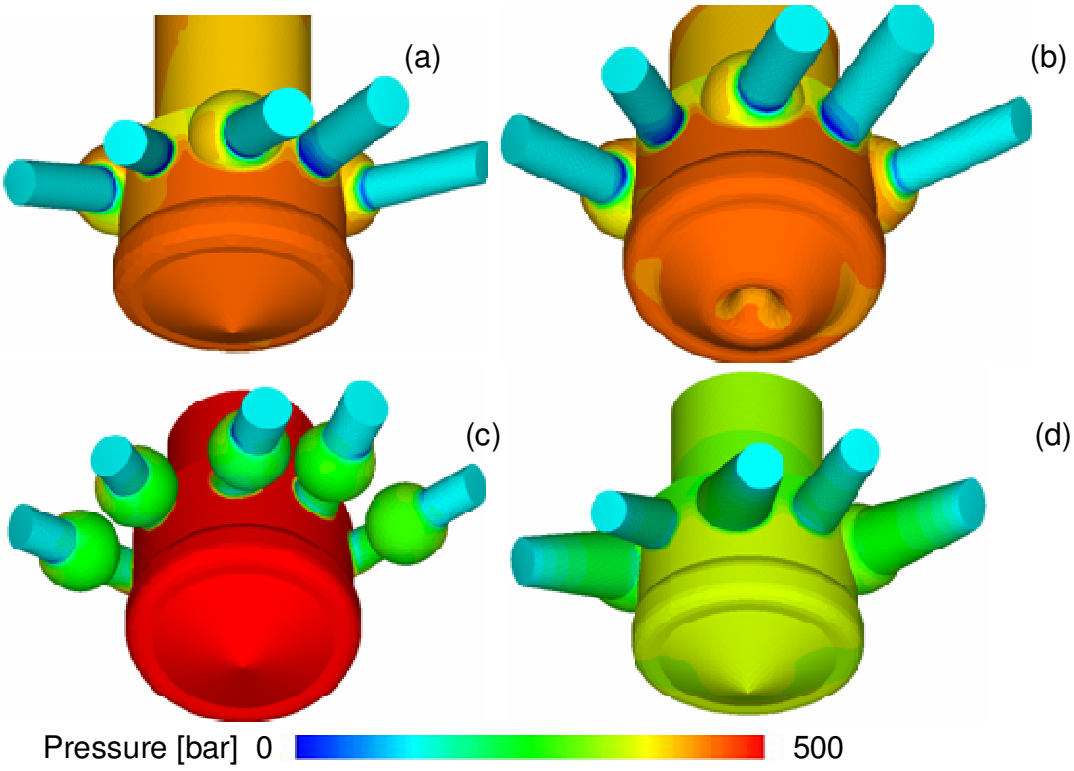

Figure 4-35: Pressure Distribution (Global Scale-Bottom View) of Standard (a), Modified Sac Volume (b), Middle-hole spheres (c) and Taped Holes (d) Designs

Since the aforementioned investigations and theory suggested that conical holes, or tapered holes, are expected to reduce geometric cavitation or even eliminate it, it was decided to create a conical hole design. Therefore, the standard nozzle design was kept unchanged, except from the semi-spherical inlet of hole 3, and the holes were changed from cylindrical

to conical. A high conicity was chosen, 4o deg total cone angle, in order to ensure that no negative pressure regions will appear. In order for the results to be comparable with the original design the exit diameter of the injection holes were kept unchanged. Therefore the inlets had to increase. The physical limitation was that if the hole inlets were significantly increased, then the holes would have collided. That is why the middle spherical inlet had to be removed in order to allow a sufficient space between the holes inlets.

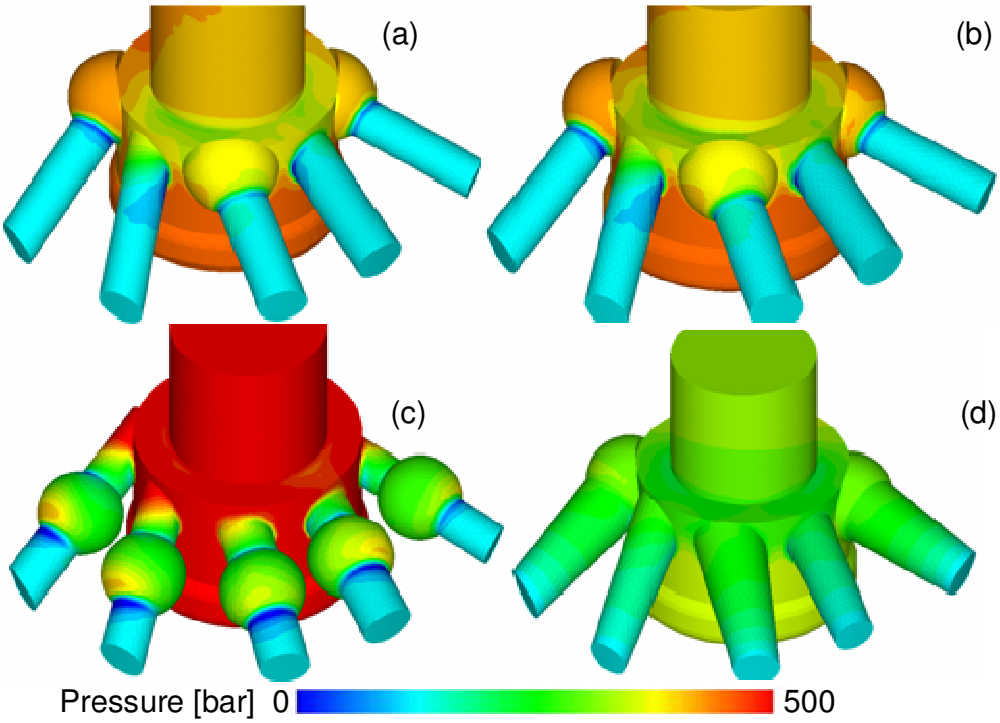

Figure 4-36: Pressure Distribution (Global Scale-top View) of Standard (a), Modified Sac Volume (b), Middle-hole spheres (c) and Taped Holes (d) Designs

As it can bee seen in Figure 4-35 and Figure 4-36 the Modified sac volume design does not have a dramatic effect on pressure distribution within the nozzle. This was expected since this modification was only aiming to change the direction of flow and not its characteristics.

Contrary to that, the placement of spherical cavities at the middle of the holes acts as a blockage. Therefore, the pressure has been significantly increased in the sac volume while starts to drop at the hole inlet.

Finally as expected the taped holes design has much lower pressures and also no indication of volume under tension i.e. negative pressure which is indicated with dark blue colour. Following is a more quantitative investigation based on the previous qualitative approach.

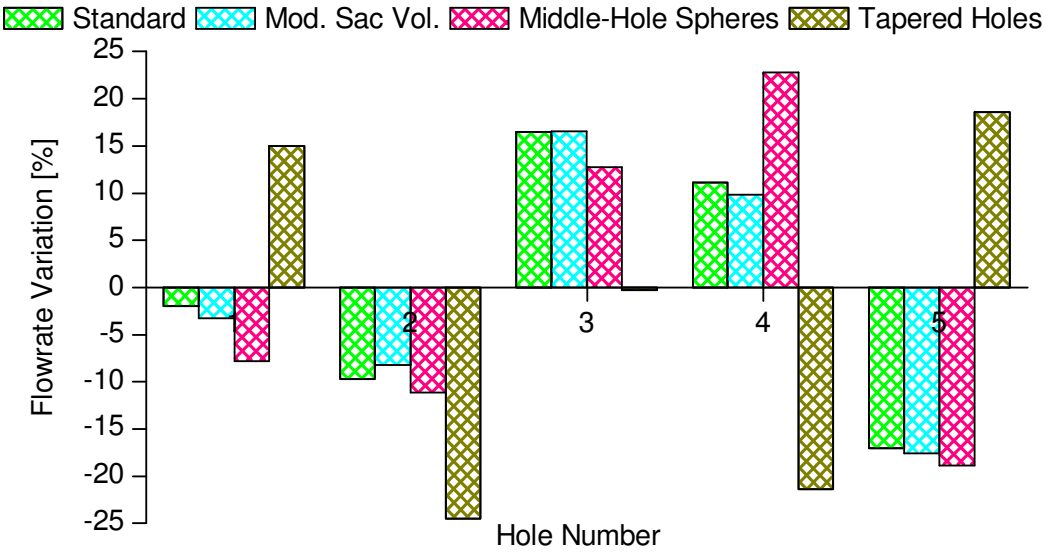

Figure 4-37: Flow rate Variation [%] of Conceptual Nozzle Designs Vs Standard Design (2)

It can be seen in Figure 4-37 that for the modified sac volume design that the changes in the flow rate of the holes are negligible. For the middle-hole design the changes are more noticeable however the trends are still the same. In contrast, the tapered holes design is totally different with variations of over 15% except from hole 3 which seems to get almost the exact amount of fuel according to each nominal hole exit area.

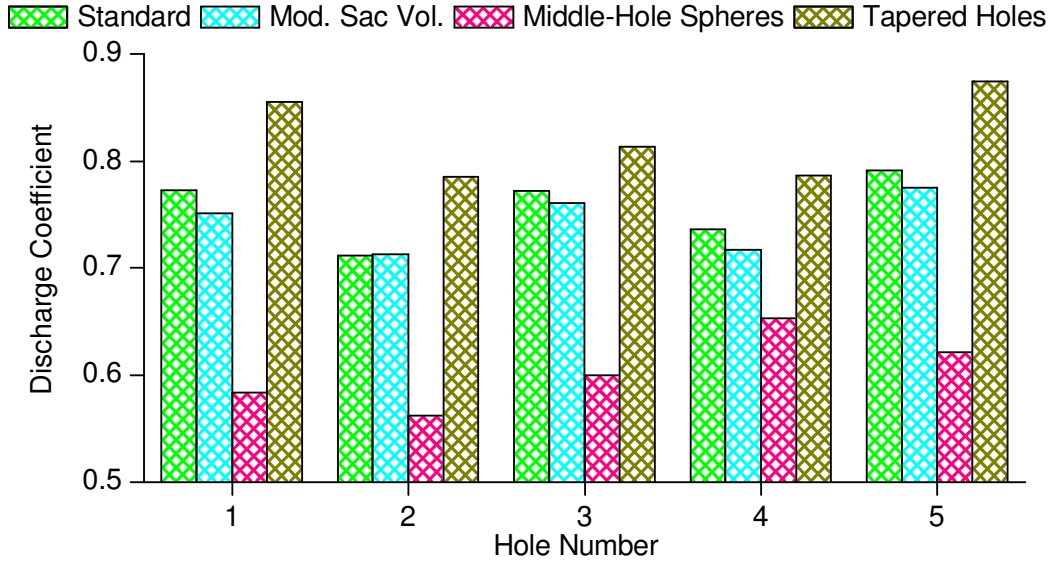

Figure 4-38: Discharge Coefficient of Conceptual Nozzle Designs Vs Standard Design (2)

Furthermore, it can be seen in Figure 4-38 that the discharge coefficients of the injection holes of the modified sac volume design are almost identical to those of the standard design. The middle-Hole spheres design has much lower discharge coefficients since the spheres at the middle block the flow and increase the pressure difference. Finally as expected from theory and previous investigations, such that of Payri et al. [136], the taped holes design has appreciably higher discharge coefficients than any other design having cylindrical holes.

From Figure 4-39 can be drawn that the standard and the modified sac volume design have similar negative pressure levels and locations (hole inlets) while the middle–hole sphere design has indications of tension volume at the sphere exit. That might be due to the fact that is the region with the most sudden pressure change across the injection hole. Finally the tapered holes design is free of any negative pressure regions, as expected

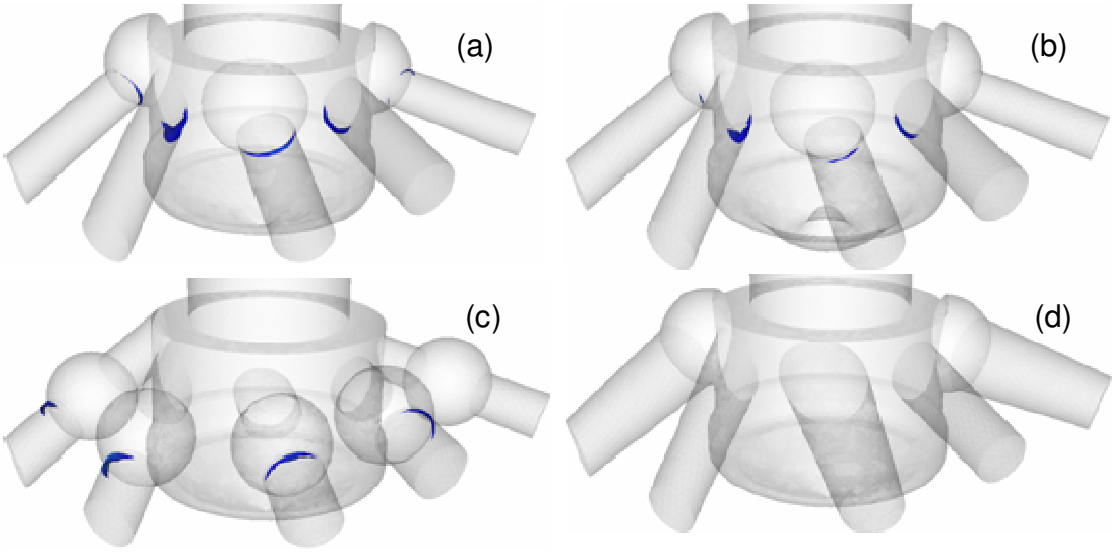

Figure 4-39: Predicted Single-Phase Tension. Standard (a), Modified Sac Volume (b), Middle-hole spheres (c) and Taped Holes (d) Designs.(2)

As it can be seen in Table 4-4 the middle-hole spheres design has the higher maximum pressure and also the higher maximum velocity. The tapered holes design has the lowest maximum velocity of all, while the modified sac volume is almost identical to the standard one. However, what is interesting is that the mean velocity for all designs is roughly the same. Therefore it can be concluded that the tapered holes design has the most uniform velocity distribution inside the injection hole than any other design investigated.

CASE	Flow rate		Pressure (bar)		Velocity (m/s)		Discharge coefficient
	m3/s	kg/s	Min	Max	Max	Mean	
Standard	2.4096E-03	2.000	-100	460	269	216	0.76
Modified sac volume	2.4096E-03	2.000	-85	470	272	216	0.74
Middle hole spheres	2.4096E-03	2.000	-82	645	311	215	0.60
Taped Holes	2.4096E-03	2.000	94	366	221	215	0.82

Table 4-4 Summary of calculated parameters for Conceptual Nozzle Designs Vs Standard Design (2)

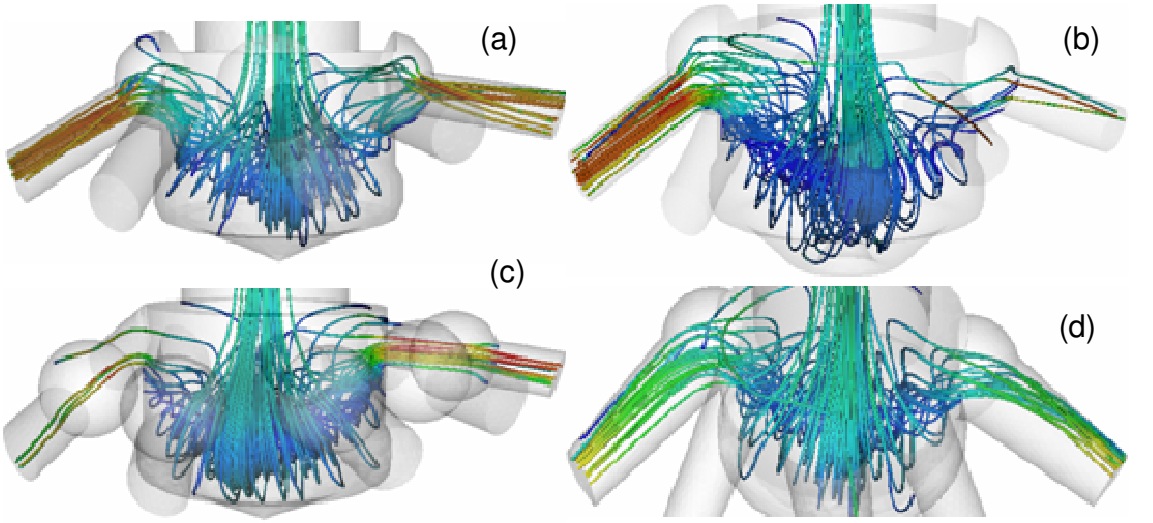

Figure 4-40: Predicted Flow structure inside the nozzle volume. Standard (a), Modified Sac Volume (b), Middle-hole spheres (c) and Taped Holes (d) Designs. (Overview)

As it can be seen in Figure 4-40 the flow structure is similar for all designs. The main characteristic is the recirculation zone in the sac volume, entering mostly into holes 1 and 5, however in order to fully identify the special characteristics of each modified design, the flow structure of each individual hole has to be visualized.

Figure 4-41 provides the necessary evidence in order to conclude how those three new designs affected the flow structure inside the nozzle. Comparing column (a) and (b) only minor changes can be identified. In fact the flow seems not to be affected by the change in the sac volume. Therefore such a small change in the geometry of the nozzle sc volume can not produce notable results. However the concept of modifying the sac volume geometry could have given different flow pattern if the modifications were more emphasized.

The middle-hole spheres design affected both the hole and the sac volume flow structure. By comparing column (a) and (c) it can be seen that the swirling motion inside the injection holes has been significantly reduced. Also in the sac volume vortices are only entering into hole 5 while the flow in hole 1, which was traditionally associated with vortical structures inside the sac volume, is coming directly from upstream.

Finally the tapered holes design, column (d), when compared to the standard design shows similar flow structures. However the amount of flow that is coming directly from upstream into hole 1 and 5 has been significantly increased. The swirling motion in the injection holes can also be identified.

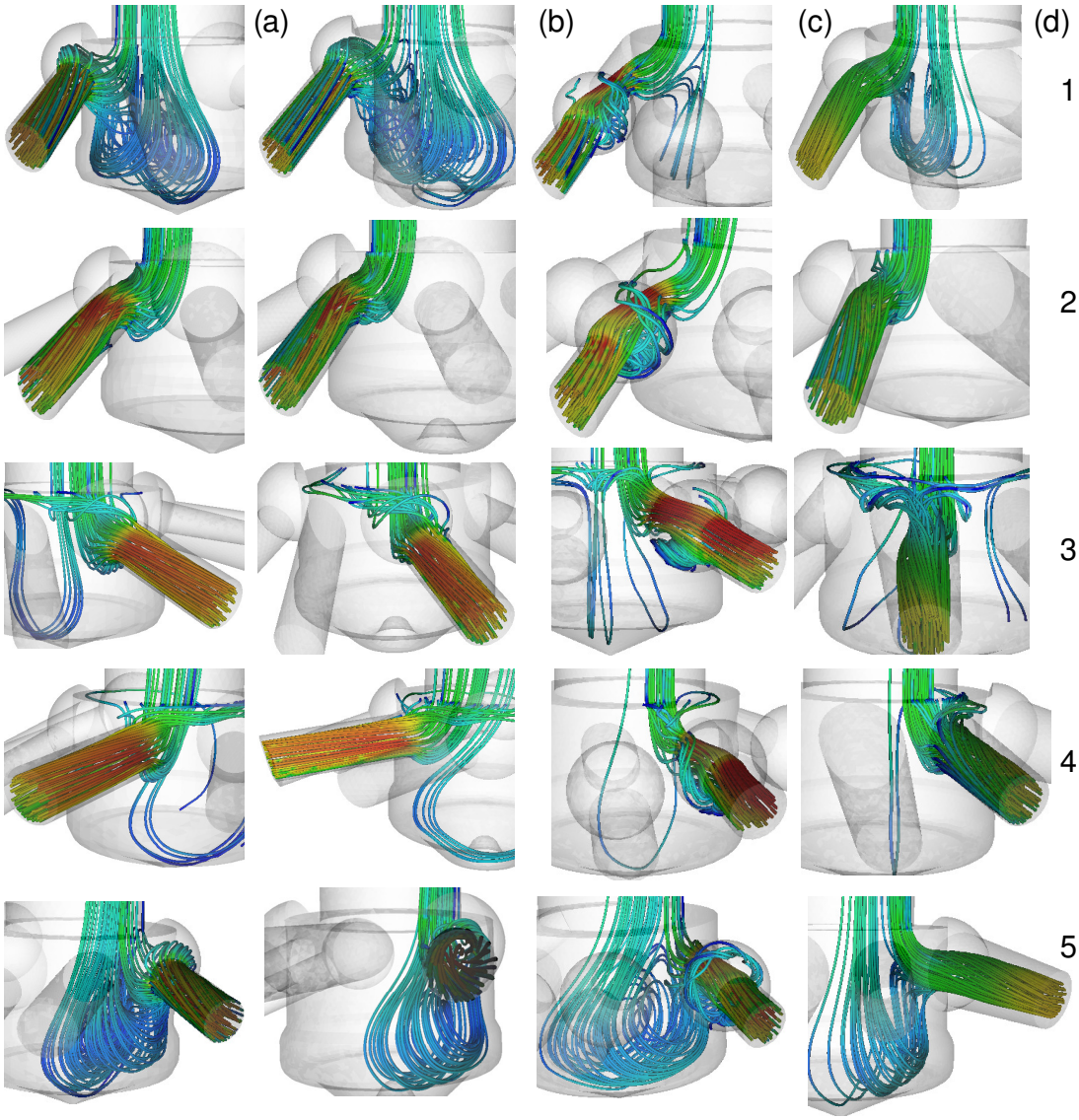

Figure 4-41: Predicted flow structure inside the nozzle volume. Standard (a), Modified Sac Volume (b), Middle-hole spheres (c) and Taped Holes (d) Designs.(2)

4.6 Real-Size test cases

4.6.1 Transient flow inlet boundary

In order to estimate the injection pressure at which cavitation initiates for each injection hole a transient flow rate inlet boundary has been used. The back pressure was kept unchanged and the needle was fixed at full lift position.

What was also possible to be determined was the transient variation of the discharge coefficient. Two designs were chosen for this investigation, the standard original design and the 5-sphere design which in the steady-state results showed the lowest amount of volume under tension.

Cavitation number is defined in Chapter 1 and is the injection pressure minus the back pressure over the back pressure minus pressure of vaporization of the flowing liquid.

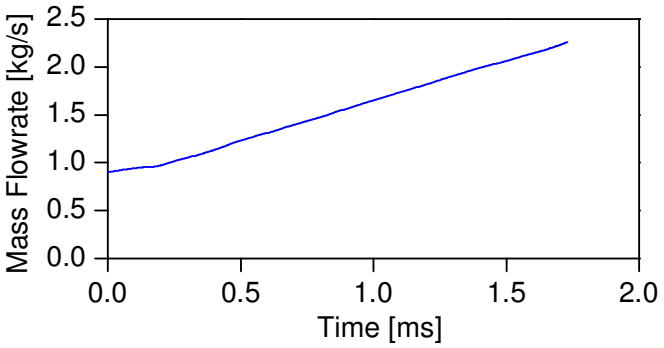

Figure 4-42: Mass flow rate Vs Time (Standard Design - Short Version)

Figure 4-42 shows the mass flow rate as a function of time. Zero time is defined as the time when the needle has just reached the full lift. Flow rate is linearly increased and is not following the same profile as in the real engine operating conditions. The end time of simulation is when the needle starts to close.

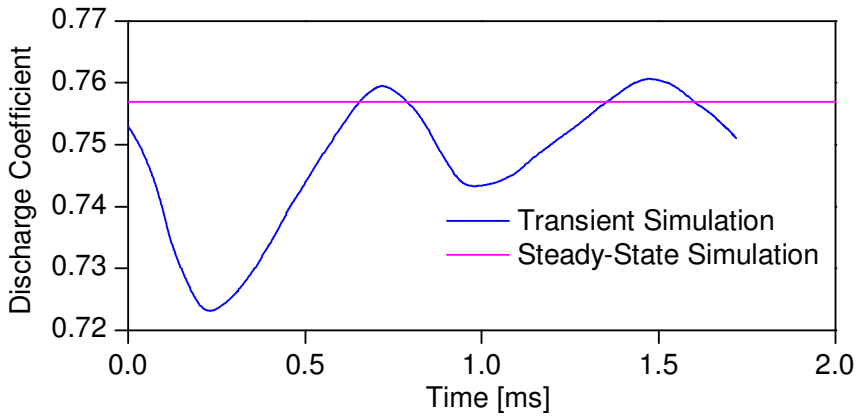

Figure 4-43: Discharge Coefficient Vs Time (Standard Design – Short Version)

In Figure 4-43 the Discharge Coefficient calculated from the transient simulation is plotted against time. The discharge coefficient shown in the figure is the nozzle's discharge coefficient which is the average of the individual holes discharge coefficients. The blue line represents the time history of the discharge coefficient of the nozzle from the transient simulation while the purple line shows the value of discharge coefficient of the steady-state simulation. It can be seen that as discharge coefficient fluctuates it gradually tends to converge with the steady state predicted value. This is a behaviour stated in theory and previously confirmed in other investigations including Giannadakis [117].

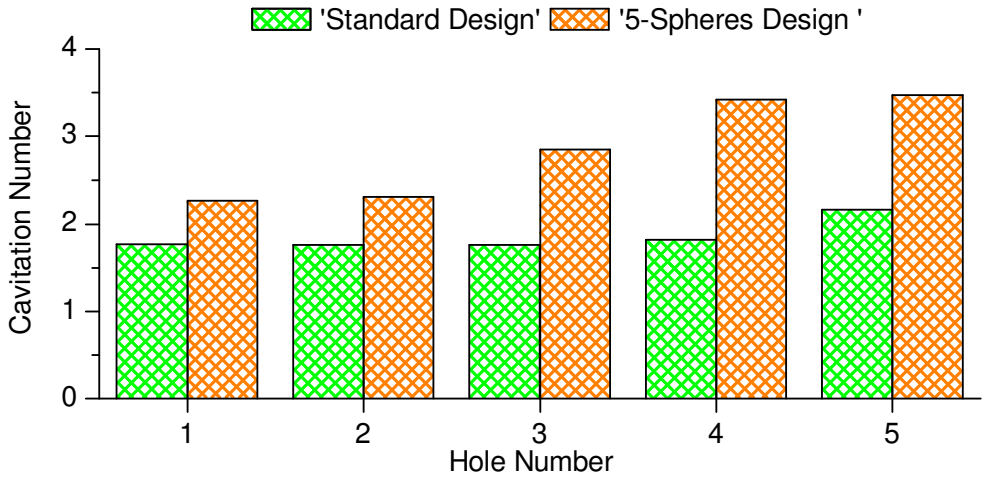

Figure 4-44: Cavitation Number of each hole at which tension regions are predicted. Transient Simulation. Original Vs 5-Spheres design.

It can be seen in Figure 4-44 that the 5-Sphere design will start to cavitate at higher injection pressure than the standard original design. This was expected from the steady-

state results previously presented in this chapter. What can also be seen is that hole 5 will cavitate last in both designs. Also holes 1, 2, 3 and 4 will start to cavitate almost at the same injection pressure in the standard nozzle design.

4.6.2 Preliminary Nozzle Hole Cavitation Modeling Results

In this section the first calculations of the cavitating flow of the original design nozzle are presented. The in house RANS flow solver, description of which can be found in Chapter 1 and [117], was implemented. This model is able of predicting only the geometric-induced hole cavitation. This solver uses the same in-house continuous phase flow solver that was used for all the single phase simulations, previously presented in this chapter.

The continuous phase flow is numerically solved on the Eulerian frame of reference by the typical conservation equations taking into account the effect of the dispersed phase volume fraction α_L and the momentum exchange source term between the two-phases. A pressure correction method using the PISO algorithm is used to solve for the continuous phase flow-field.

As previously mentioned in single-phase calculations of nozzle flows the location of cavitation inception is identified from the locations inside the flow-field where the pressure falls below vapour pressure (negative pressure).

The volume of all the Eulerian grid cells in which pressure is below vapour is referred to as ‘tension volume’ and it is a quantitative indication of how much liquid is stretched due to the flow.

Cavitation is initiated and then further develops by the existence of small spherical bubble nuclei in the liquid. The model is based on the Eulerian-Lagrangian approach, by which the liquid phase is modelled as the continuous phase and the cavitation bubbles as the dispersed one. Many of the fundamental physical processes assumed to take place in cavitating flows are incorporated in the model.

These include bubble formation through nucleation, momentum exchange between the bubbly and the carrier liquid phase, bubble growth and collapse due to non-linear dynamics, bubble turbulent dispersion and bubble turbulent/hydrodynamic break-up. The effect of bubble-to-bubble interaction on momentum exchange and during bubble growth/collapse is also considered.

Finally fixed pressure boundary conditions have been applied corresponding to the steady-state single phase simulations previously presented. It has to be noted that modelling of cavitation itself is transient even for fixed boundaries and non-moving geometries and is referred as pseudo-steady state flow. This will be proved an important feature of the simulation code which will lead to some useful conclusions regarding the nozzle flow structure.

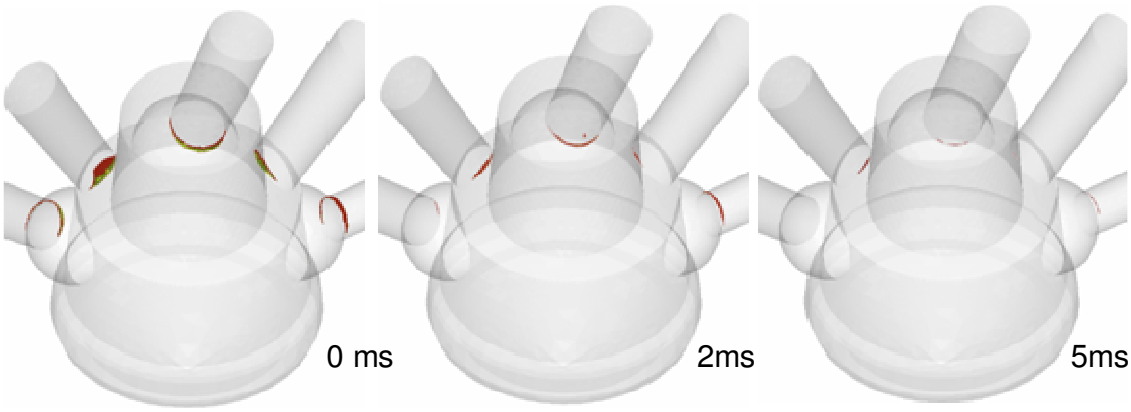

Figure 4-45: 3-D schematic of the predicted tension regions time history. Standard Design.

Vapour is produced at the area under tension (negative pressure) through the nucleation process. Then the bubbles grow and collapse, as they are convected towards the exit of the nozzle holes. At the same time, they are undergoing turbulent break-up and they exchange momentum and turbulent kinetic energy with the surrounding liquid.

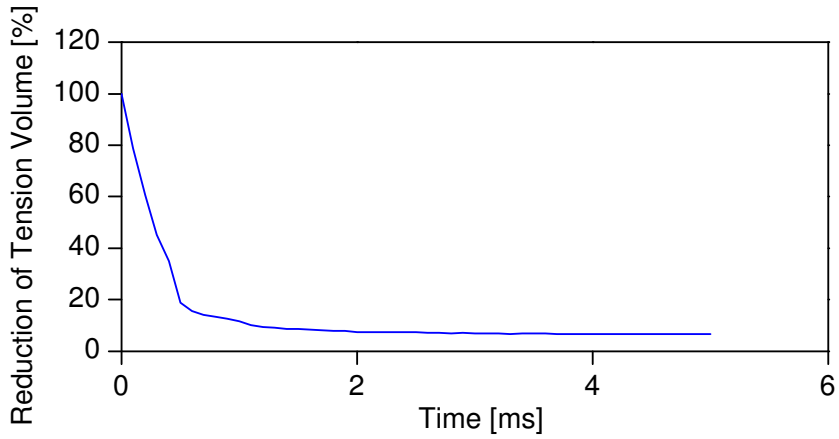

Figure 4-46: History of the predicted tension volume reduction. Standard design.

It can be seen in Figure 4-45 and Figure 4-46 that due to the vapour produced, the volume under tension is reduced significantly and the negative pressure recovers. When quasi-steady-state condition is obtained, there is a small volume (of the order of 5% relative to that of the single-phase calculation) which remains under tension and produces cavitating bubbles in a transient fluctuating mode.

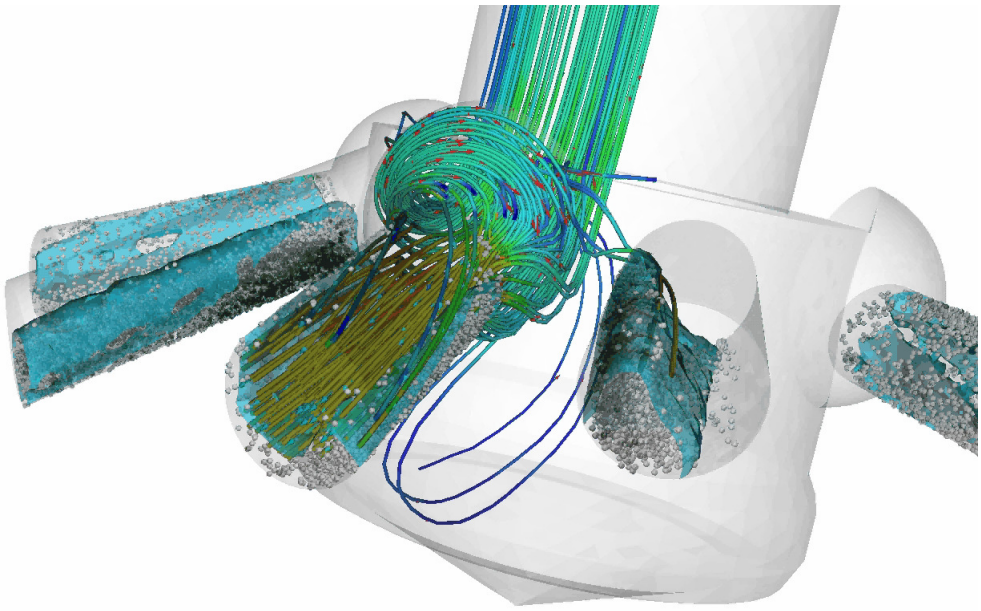

Figure 4-47: 3-D view of calculated cavitation bubbles inside the injection holes, vapour-liquid inter-phase and flow structure (Hole 3 only). Standard Design.

As show in Figure 4-47, the cavitation bubbles inside the injection holes and also the vapor-liquid inter-phase, which are formed at the bottom of the holes, are having a canopy

shape. This is due to the swirling motion inside the injection holes which was identified earlier in this chapter.

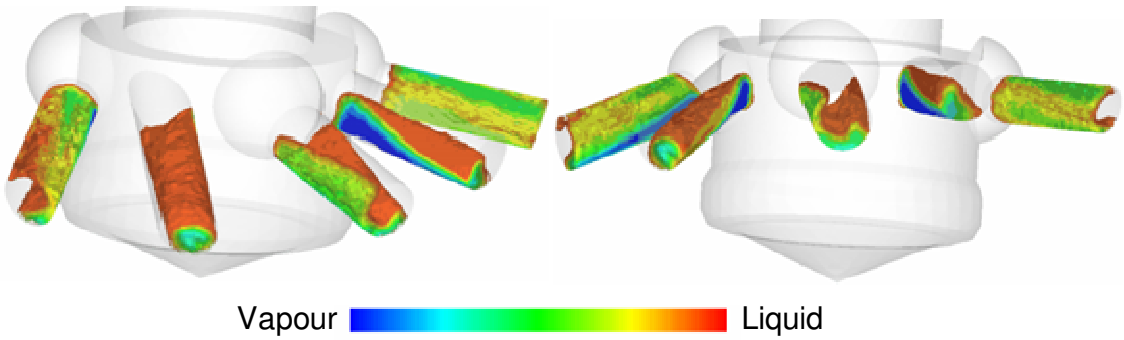

Figure 4-48: 3-D Void Fraction Distribution (different views). Standard Design.

In Figure 4-48 the predicted void distribution inside the holes is illustrated. When close to the cavitation initiation area the vapour phase is dominant. Moving towards the hole exit the liquid phase increases. As a result of the vapour volume present in the injection hole, the discharge coefficient of the nozzle is reduced, the flow rate decreases while at the same time a significant percentage of the hole exit cross sectional area is occupied by cavitating bubbles, which exit from the nozzle. This can be seen in Figure 4-49 where the time history of the reduction of flow rate and hole effective area are plotted.

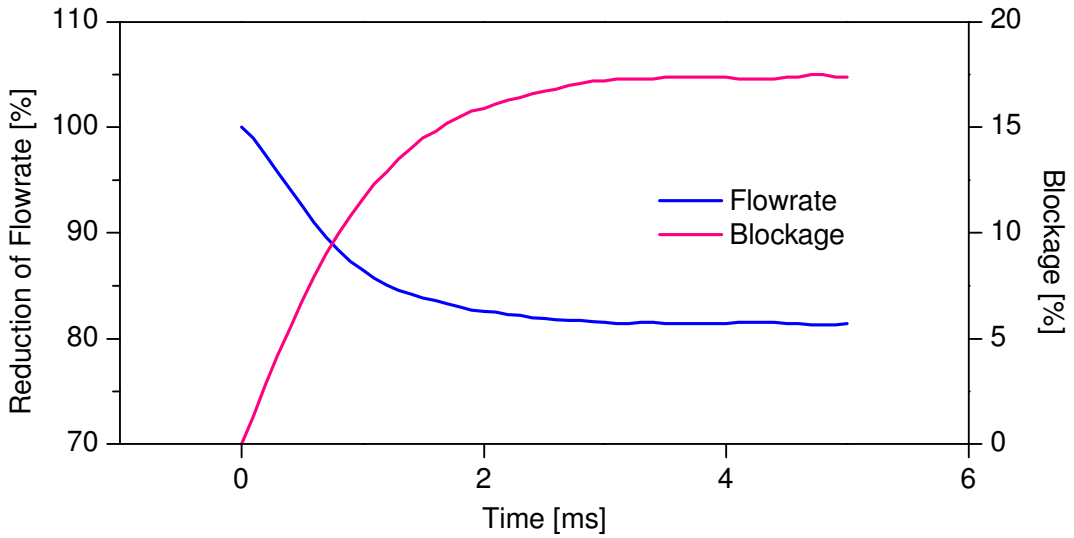

Figure 4-49: Time History of the Flow rate Reduction and Blockage. Standard Design

4.6.3 Further Numerical Analysis: Velocity Profiles

Having completed a series of flow simulations in the standard design as well as in several other conceptual designs it became clear that the velocity profiles and flow direction at the hole exit plane had to be investigated more thoroughly. This investigation had also to be presented in a way that the result between different designs and condition would have been easily comparable.

During the discretization process an index is given to the cells belonging to the hole exit plane. Each hole has each own index. The injection hole direction vectors were found using a commercial design software. Then a post-processing tool has been added to the in-house CFD code in order to transform the calculated velocity components according to each injection hole's direction. The coordinate system was shifted in order the Axis start point 0, 0, 0 to be at the center of the hole exit plane. Then the axis system was rotated in order for the Z-Axis to be parallel to the injection hole direction and the Y-axis to pass throw the point with the maximum Z-value in the original Coordinate System. Then the velocity profiles of each hole where exported as scatter plots. The tangent velocity component is represented with vectors. Figure 4-50 illustrates a 3-D graphic representation of the above mentioned coordinate system translation.

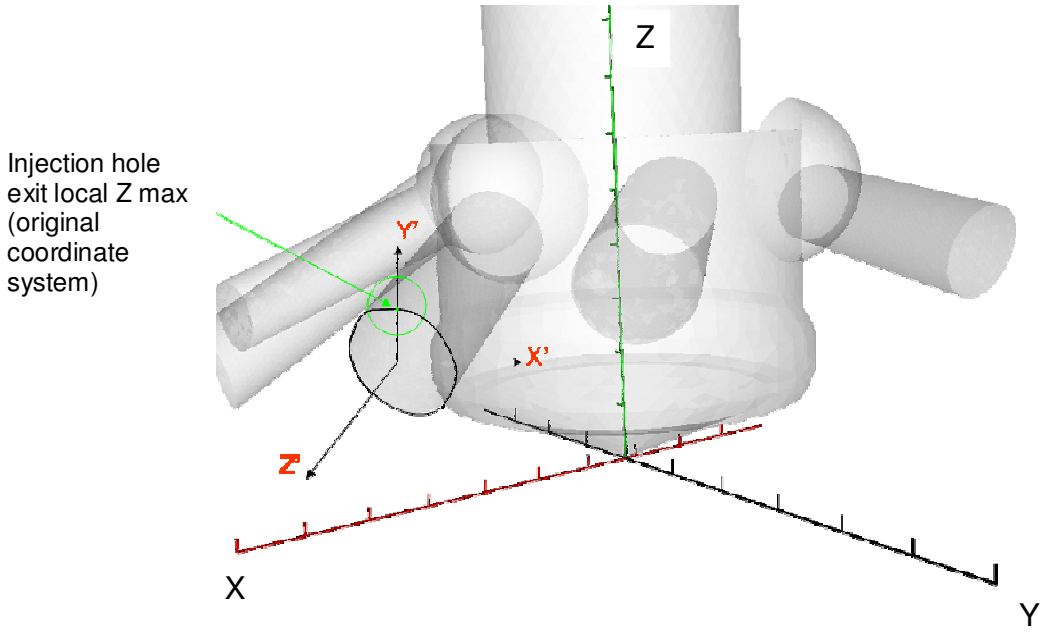

Figure 4-50: Coordinate system translation for velocity profile calculation.

After the transformation of the velocity components the axial velocity is the Z component of the newly defined coordinate system. The tangential velocity component is given by (4-1).

$$\text{Tangent Velocity} = \sqrt{\left(U^2_{\text{radial}} + U^2_{\text{circumferential}}\right)} \qquad (4\text{-}1)$$

The resulting velocity profiles produced by this investigation can be used as input for the future spray simulations. Since the velocity profile at the hole exit plane is expected to be highly asymmetric, it might lead into a deviation between the actual and the designed injection direction, which is defined by the geometric orientation of the injection hole. Also the fact that there is a strong swirling motion inside the injection hole will certainly affect the initial spray cone angle. However due to high back pressure at the time of injection these differences might be suppressed. At a later stage these profiles will also include information regarding the Void distribution at the hole exit. With the knowledge acquired from the experimental investigations, presented in Chapter 5, the initial spray conditions will account not only for geometric cavitation but also for vortex cavitation.

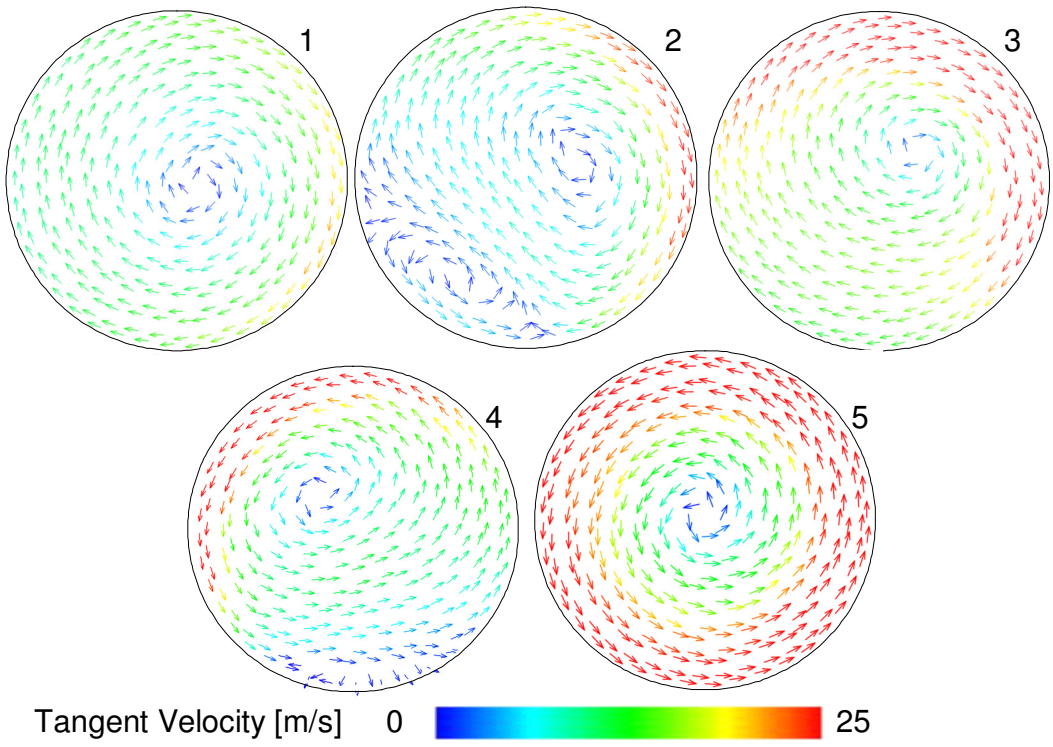

Figure 4-51: Tangent velocity vectors. Standard design different holes

As it can be seen in Figure 4-51 all the injection holes of the standard nozzle design are associated with high swirling motion at the exit which reaches up to 25m/s. Although these results represent one time instance, it can be seen that each hole has different behaviour regarding both the magnitude and the direction of the tangential velocity. As expected, the tangent velocity component increases as the distance from the swirl centre increases. However for the current time frame the swirl centre does not coincide with the geometric injection hole centre. Provided that tangent velocity affects the initial spray cone angle such uneven distribution is expected to result into deflected spray dispersion.

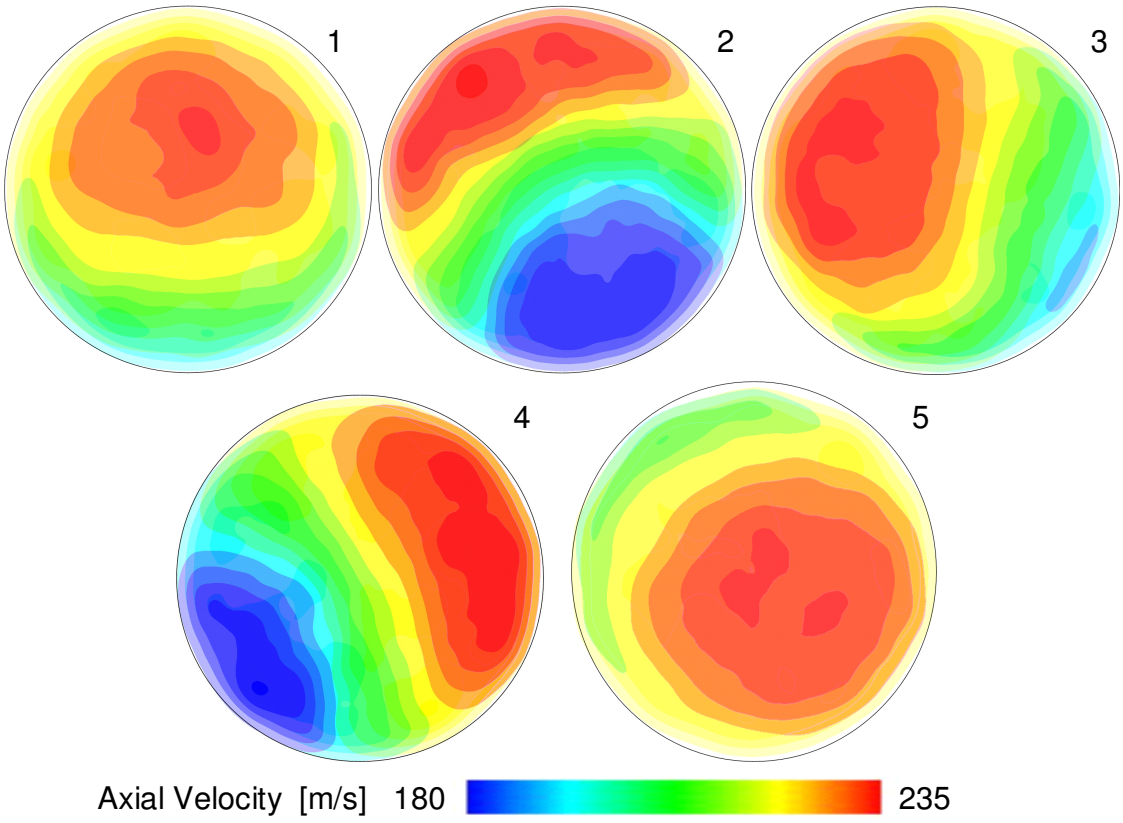

Figure 4-52: Axial velocity Distribution. Standard design different holes

Figure 4-52 represents the axial velocity distribution at the injection hole exit plane. The velocity distribution inside the hole is asymmetric and also the velocity profile varies from hole-to-hole. This hole-to-hole variation in the velocity profiles will lead into hole-to-hole spray variation. The fact that velocity is not uniformly distributed will also lead into different spray density due to the differences in the mass flux.

4.6.4 Hole Interaction Effect

After the first discussion of the numerical results what was requested was to find what is the effect of the interaction between the hole flows. In order to investigate the interaction, the boundary conditions of the four holes were changed to be considered closed, allowing the flow to exit through only one hole. This was repeated for all holes and then comparison was made with the default case.

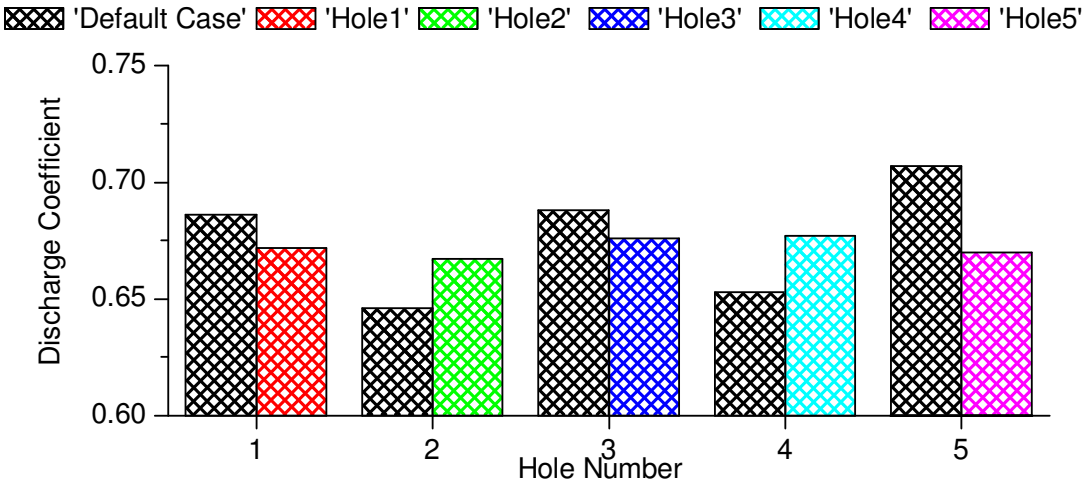

Figure 4-53: Hole interaction effect on discharge coefficient

It can be seen that for the holes without spheres i.e. 2 and 4 the discharge coefficient is higher when the flow is exiting only from one hole. For the holes with spherical inlet i.e. 1, 3 and 5 the discharge coefficient is higher when all the holes are open.

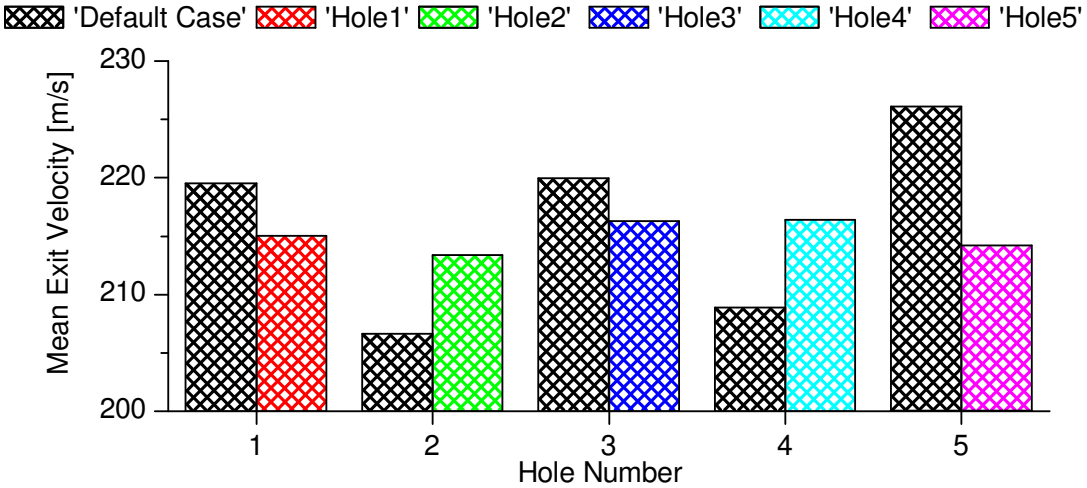

Figure 4-54: Hole interaction effect on Mean exit velocity

It can be seen in Figure 4-54 that the holes without spherical inlet have higher mean exit velocity when simulated individually. The holes having spherical inlet have lower mean exit velocity when simulated individually.

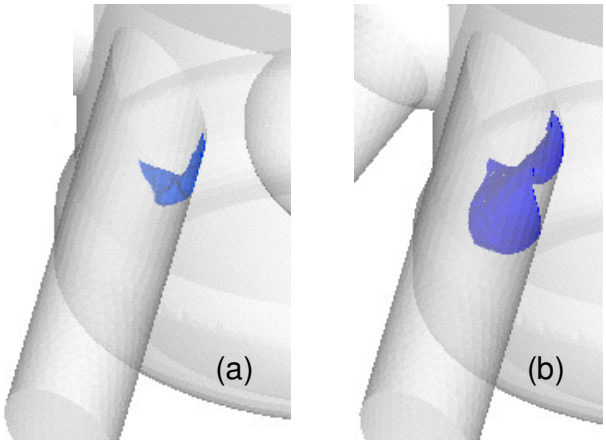

Figure 4-55: Hole interaction effect on Tension Volume. (a) Default Case and (b) Only Hole 2 open

It can be seen in Figure 4-55 that the location of negative pressure is roughly the same for both cases. Although for the single hole simulation more fluid seems to be under tension.

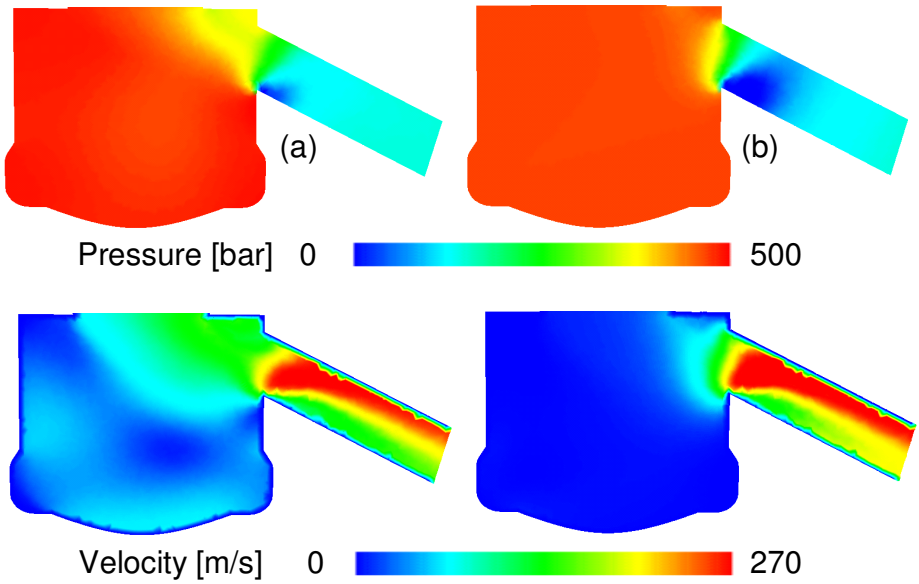

Figure 4-56: Hole interaction effect on Pressure and total velocity Distribution. (a) Default Case Hole 2 and (b) Only Hole 2 open.

Figure 4-56 shows that hole interaction mostly affects the flow within the sac volume and not as much the flow inside the nozzle hole itself.

As previously shown, Hole 2 has never been associated with vortical structures in the sac volume, for all the tested designs.

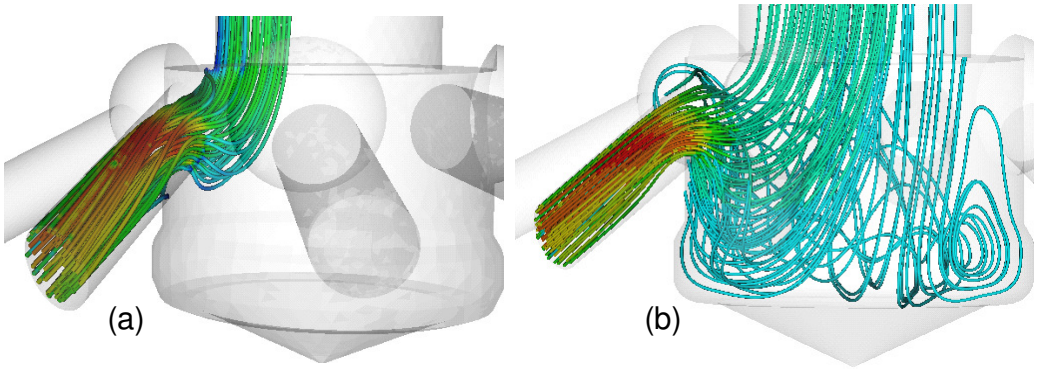

Figure 4-57: Hole interaction effect on Predicted flow structure inside the nozzle volume. (a) Default Case and (b) Only Hole 2 open

It can be seen in Figure 4-57 that while in the default case the whole flow is coming directly from upstream in the single hole simulation a portion of the flow is coming from the recirculation zone inside the sac volume. Perhaps this is the most significant change between the two cases. Swirling motion inside the hole can still be identified.

4.6.5 L/d Effect

What was also of interest was to find how the hole length affects the flow. For that reason a nozzle with holes having two times the original length was designed and investigated. The numerical grids used in this investigation can be seen in Figure 4-58.

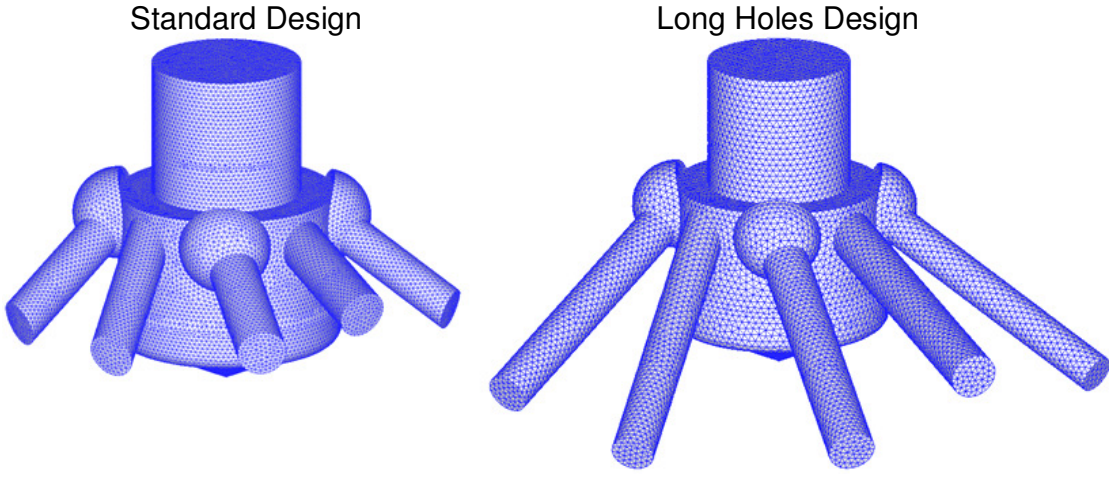

Figure 4-58: 3-D numerical grids used in the Hole Length effect investigation

It can be seen from Figure 4-59 and Figure 4-60 that the hole Length has minor effect on the discharge coefficient and the mean exit velocity.

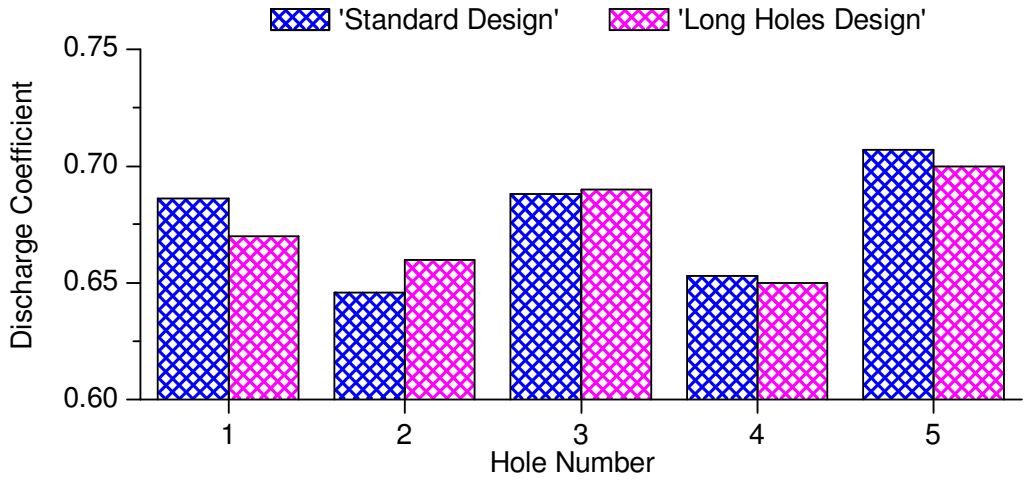

Figure 4-59: Hole Length effect on discharge coefficient

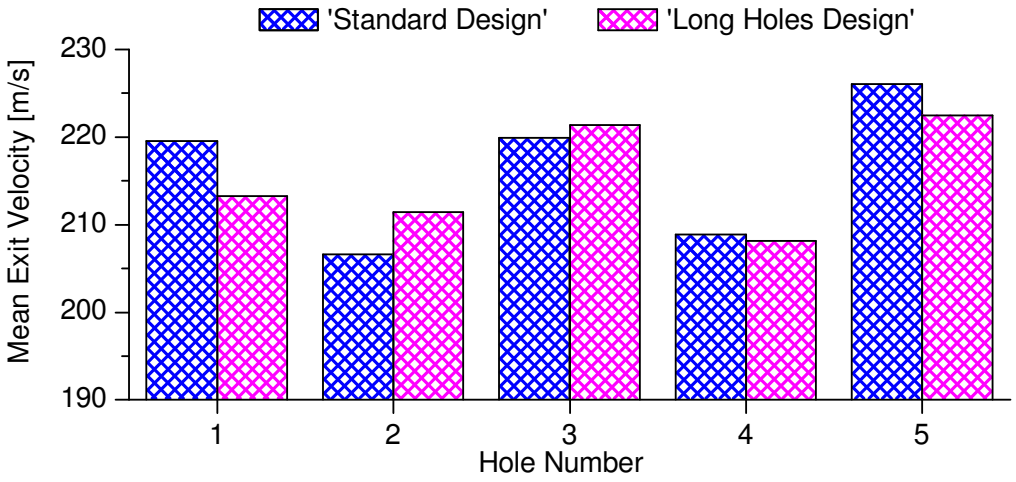

Figure 4-60: Hole Length effect on Mean Exit Velocity

Furthermore, hole length effect on pressure distribution is not notable. However the velocity distribution in the injection hole has changed significantly. The greater length allows the flow to normalize that is why the velocity at the hole exit of the long holes design is uniform.

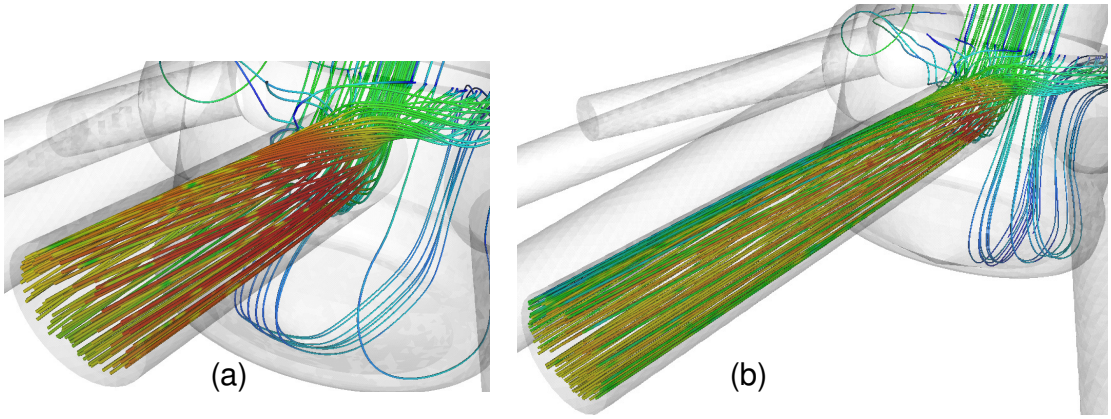

Figure 4-61: Hole length effect on Predicted flow structure inside the nozzle volume. (a) Standard Design and (b) Long Holes Design. Hole 4

It can be seen in Figure 4-61 that the length of the hole does not affect the flow structure in the sac volume. However the flow inside the Injection has changed notably. The difference is that in the Long Holes design the swirl inside the injection hole has been significantly reduced.

4.7 Large scale marine nozzles simulations

4.7.1 Effect of turbulence model and grid size on vortex core prediction

As previously mentioned the path lines of the flow inside the sac volume of the marine nozzle had clearly shown large vortical structures associated mainly with holes 1 and 5. However the conclusions that one can make by examining the path lines can often be sensitive to the visualization parameters of the software that has been used to produce the lots. What is of scientific interest is to predict the core of the vortex that is formed. An extensive body of literature exists on predicting the core of a vortical flow and relating it to vortex cavitation, like those of [111, 112], and even though represent a promising theoretical background, they have not yet been applied to nozzle flows. The in-house CFD code has implemented a model which calculates the swirl intensity, which according to [137] is a parameter frequently used to locate and track vortical flow structures. As in every computational model that is intended to be used for turbulent flows, high Reynolds number, a series of parametric studies had to be done in order to identify the dependency of the swirl intensity parameter to the turbulence model and the computational grid size.

There are four different turbulence models implemented in the in-house CFD code. The classical k-ε model of [138], the RNG k-ε as suggested by [139], the non-equilibrium k-ε by [140] and the k-ω model presented in [141]. The classical turbulence models are too momentum-dissipative in contrast to the RNG and the k-ω. Also the non-equilibrium model instead of having constant coefficients, it depends them on the local turbulence production, and is considered preferable for predicting flows with large vortices. All four models were tested with both grids totaling eight transient simulation of the single-phase flow inside the large-scale marine nozzle with cylindrical holes. All cases had a time dependant inlet pressure boundary condition and a fixed pressure boundary at the outlet. The time step of the continuous phase was 1e-03 s and the fixed outlet pressure was 0.7 bar. The computational domain with the boundaries is shown in Figure 4-62 along with the inlet pressure diagram as a function of time.

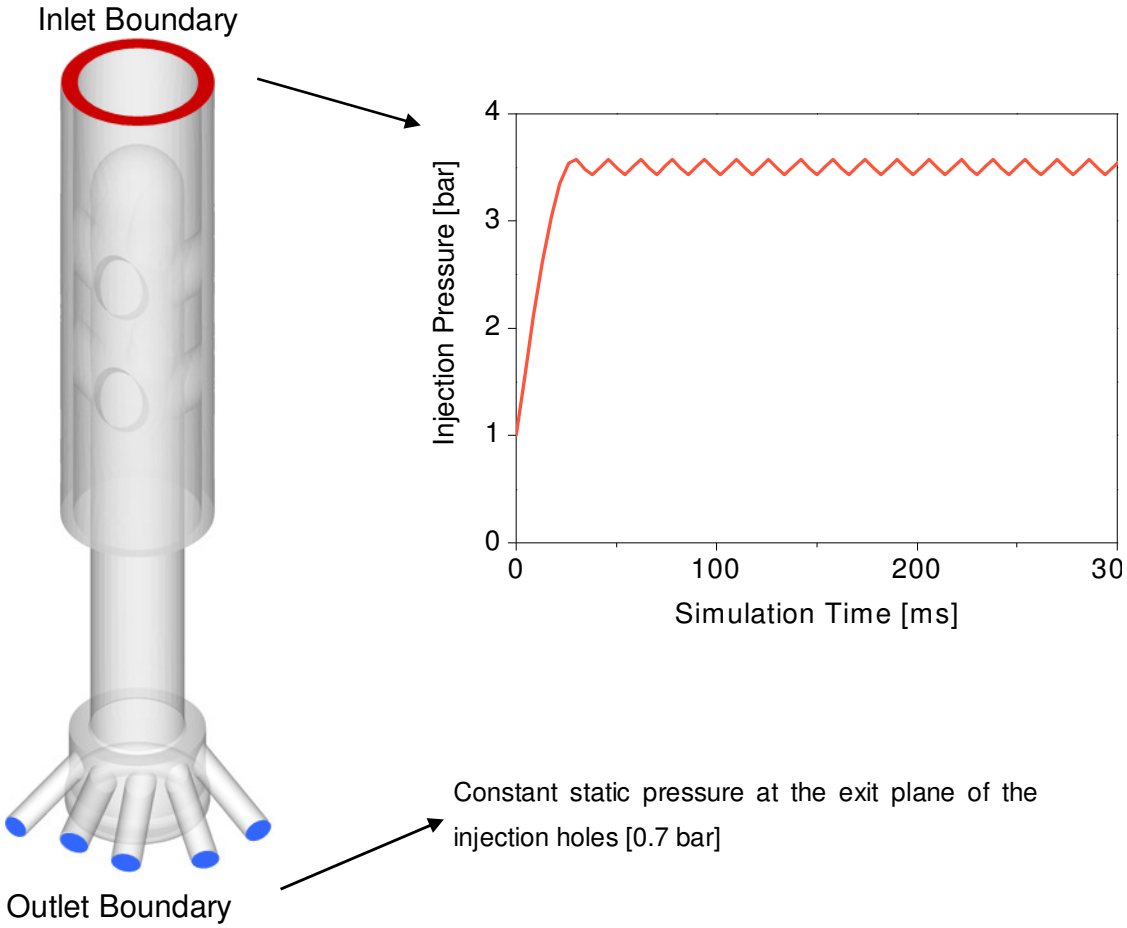

Figure 4-62: Computational parameters for the turbulence model effect investigation.

As mentioned above the effect of grid size was also to be investigated for all four turbulence models. Since the subject of this study are the vortices generated inside the sac volume and the corresponding injection holes, the upstream grid structure was kept the same for both cases. Therefore only the mesh in the lower part of the computational domain was refined. Starting from the default grid, each of the injection holes is discretized by 5,000 hexahedral cells, while the sac volume contains 65,000 tetrahedral cells. The average cell size for the lower part of the nozzle including the injection holes, for the default grid is 0.48 mm. For the dense grid the structured mesh inside the injection holes consist of 25,000 hexahedral cells. The unstructured mesh of the sac volume contains roughly 210,000 tetrahedral cells, and the average computational cell size is 0.15 mm (also for the injection holes). All the computational grids used for this investigation, and all the computational work presented in this study, have been made by using a commercially available mesh generation software [128]. The two grids are presented in Figure 4-63 below.

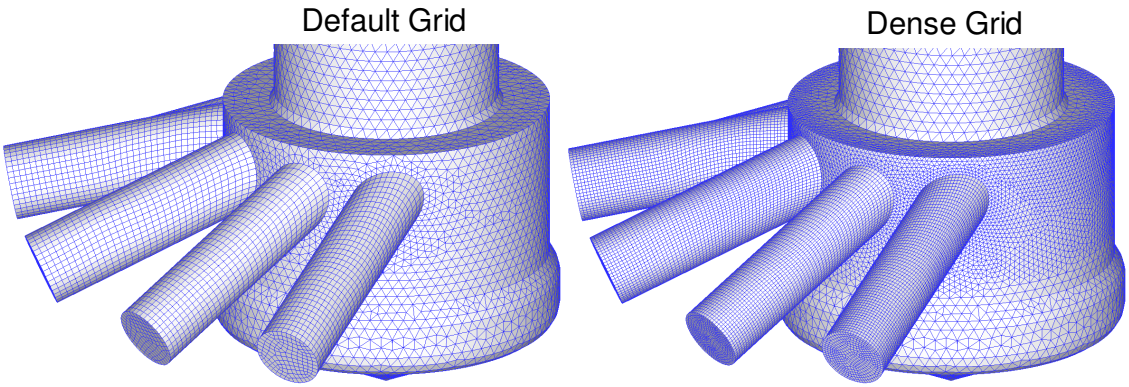

Figure 4-63: Computational grids for the turbulence model effect investigation

In order to visualize the transient development of the vortices inside the sac volume of the nozzle, iso-surface plots of the swirl intensity in the sac-volume have been produced for every time step of the time dependant calculation. The iso-surface plots inside the injection holes are of the 90% of the maximum total velocity that has been developed in the nozzle. This combined with vortex core presented in the same plot will give an indication of how those vortical structures affect the flow inside the injection holes. Finally the iso-surface plots of the swirl intensity have been colored with the axial velocity component of the incoming liquid, in order to highlight the change in the direction of the flow, and the iso-surface plots of total velocity inside the injection holes are coloured with helicity.

It has also been seen that the location of the vortex inside the nozzle affects the instantaneous flow rate of the injection holes. assuming that the total incoming flow rate has to be distributed evenly to the injection holes according to their crossectional area a nominal instantaneous flow rate for every injection hole was calculated. Then the actual calculated flow rate was divided with the nominal for every time step of the solutions thus providing a line plot of the flow rate percentage variation with time as a result of the internal flow. Such plots are used throughout this study since they have proved to be very useful for understanding the complimentary pattern of the injection hole flows.

In order to make possible the comparison of the vortex development inside the sac volume for different operating (simulation and experimental) conditions and different nozzle scales a non-dimensional time had to be implemented and is given from the equation below:

$$\tau = \frac{t}{t^*} \quad \text{where the normalisation time scale used is equal to} \quad t^* = \frac{D_{SAC}}{U_{SAC}} \qquad (4\text{-}2)$$

Where U_{SAC} is the mean axial velocity entering into the sac (nozzle) volume and D_{SAC} is the diameter of the nozzle. With this time scaling, it is possible to identify the frequency of vortex formation inside the sac volume and, thus, the Strouhal number of the recorded periodic flow pattern.

As it can be seen from Figure 4-64 the orientation of the vortex structure inside the sac-volume of the nozzle changes with time and it is attached mainly to holes 1 and 5. what can also be seen is that the time interval between successive string appearances, (holes 1&5) is of the order of $\Delta\tau \approx$40-50 and cavitation strings re-appear in front of the same injection hole about every $\tau \approx$ 90-100.

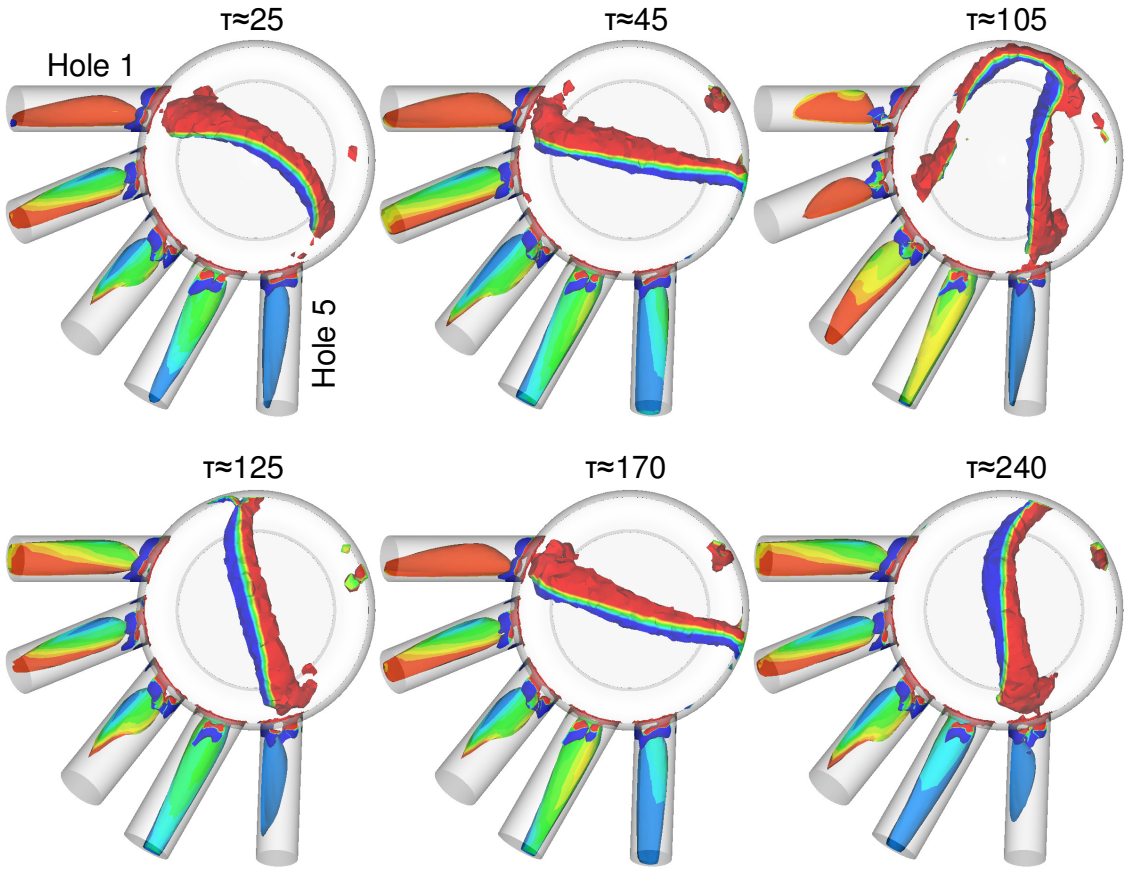

Figure 4-64: iso-surfaces of swirl intensity inside the core of the nozzle volume vortex coloured with the axial velocity component of the liquid. [Default grid, Std. k-ε]

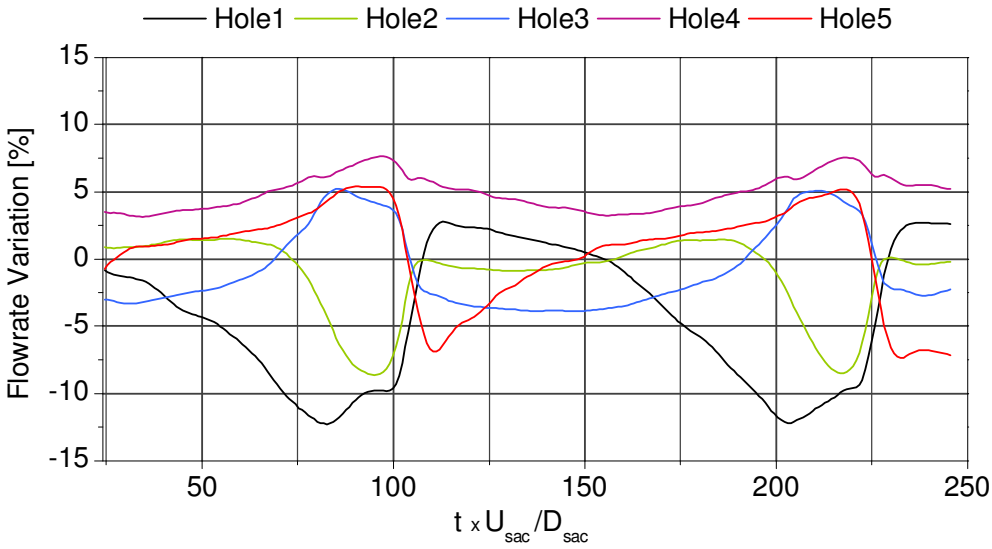

Figure 4-65: Predicted temporal variation of hole-to-hole flow rate. [Default grid, Std. k-ε]

During the simulation time, starting from the instance where the inlet pressure has come to its maximum value (i.e. after the first time steps), model predictions suggest at least 3 events of string cavitation formation. Also from the same figure it can be concluded that the vorticity direction, radial motion, stays the same throughout the simulation, it rotates clock-wise, and that the vortex core changes orientation only in the x-y plane. Finally when a vortex is attached to an injection hole the iso-surface area of the 90% maximum total velocity is significantly reduced, suggesting that the flow inside the injection hole is reduced.

The latter, the effect on the flow rate, it can be seen from Figure 4-65 where the calculated instantaneous flow rate from each of the five injection holes is plotted with respect to the non dimensional time, as it has been explained previously. From this plot it is clear that during the given time window, that the vortical structure changes its location, Hole 1 exhibits the highest flow rate variation with flow rate peaking when the nozzle vortex is facing the opposite hole 5 and dropping when the vortex enters it. Similarly, but with smaller variations, the flow of hole 5, also fluctuates been dependent on the vortex location. The fact that the flows of these particular holes have this complementary, but opposite, behaviour suggest that, for this particular test case, the vortices associated to Hole 1 do not overlap with those of Hole 5.

The maximum calculated flow rate reduction for Hole 1 is ~10% and the average flow rate reduction for the time window during which the nozzle flow vortex is attached to this particular hole is ~4-6%. Finally it is interesting to see that Hole 4 that is not associated with vortices, always receives more than the nominal flow rate. It can be thus concluded that the measured flow rate reduction in the presence of a string can be attributed to the reduced liquid quantity entering the hole when the flow vortex is attached to it.

The next series of figures will provide the same information as taken from the different turbulence models and grid size simulations.

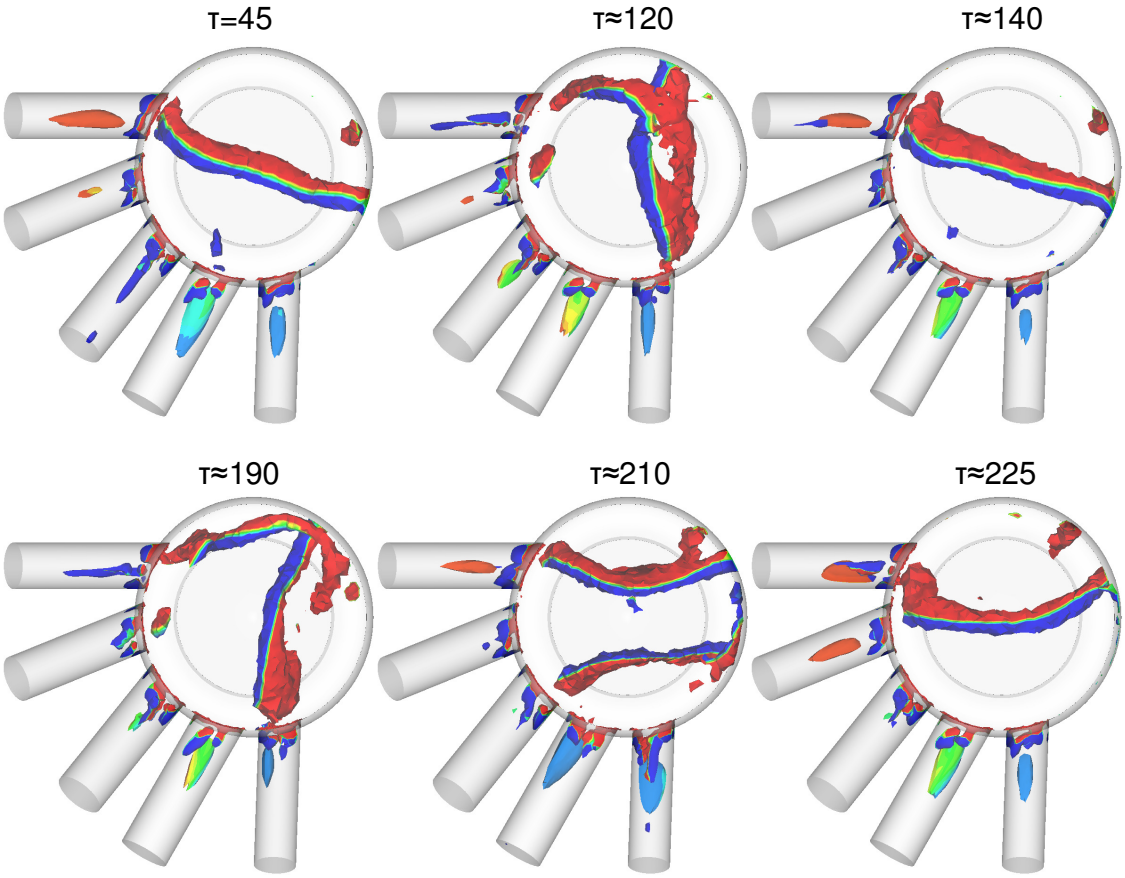

Figure 4-66: iso-surfaces of swirl intensity inside the core of the nozzle volume vortex coloured with the axial velocity component of the liquid. [Default grid, Std. k-ω]

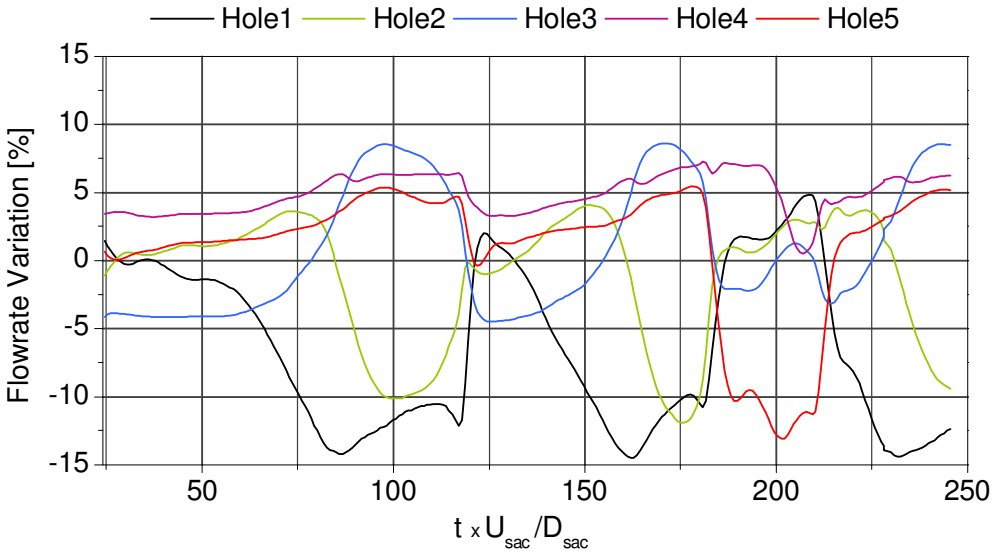

Figure 4-67: Predicted temporal variation of hole-to-hole flow rate. [Default grid, Std. k-ω]

τ=40 τ≈100 τ≈140

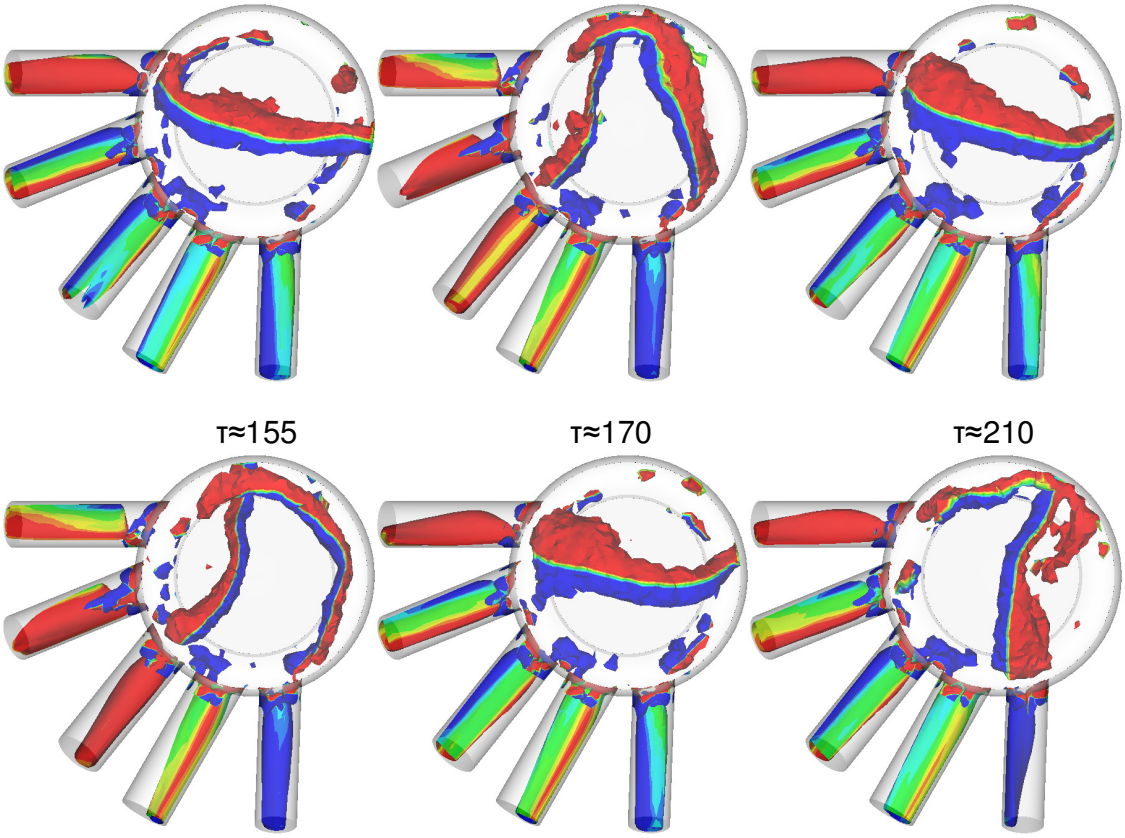

Figure 4-68: iso-surfaces of swirl intensity inside the core of the nozzle volume vortex coloured with the axial velocity component of the liquid. [Default grid, RNG k-ε]

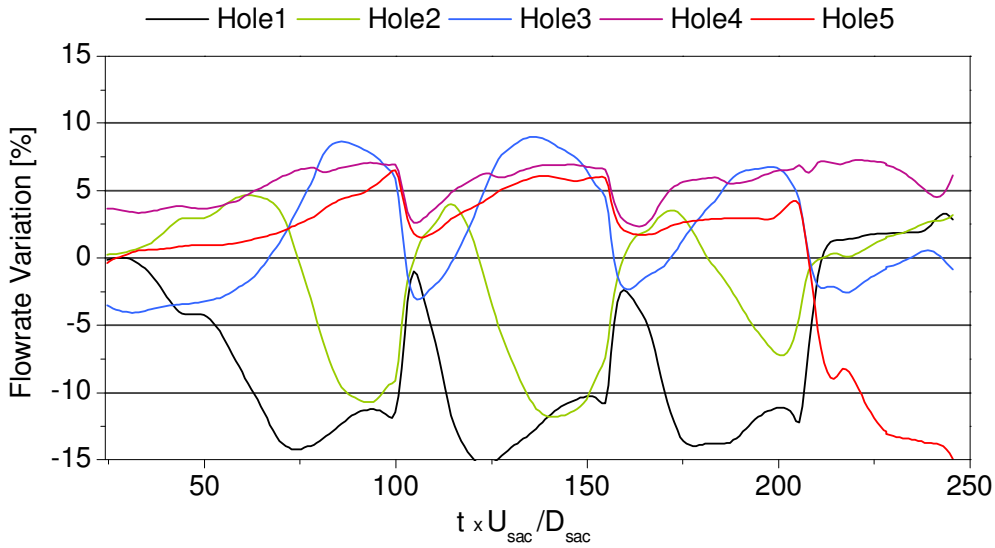

Figure 4-69: Predicted temporal variation of hole-to-hole flow rate. [Default grid, RNG k-ε]

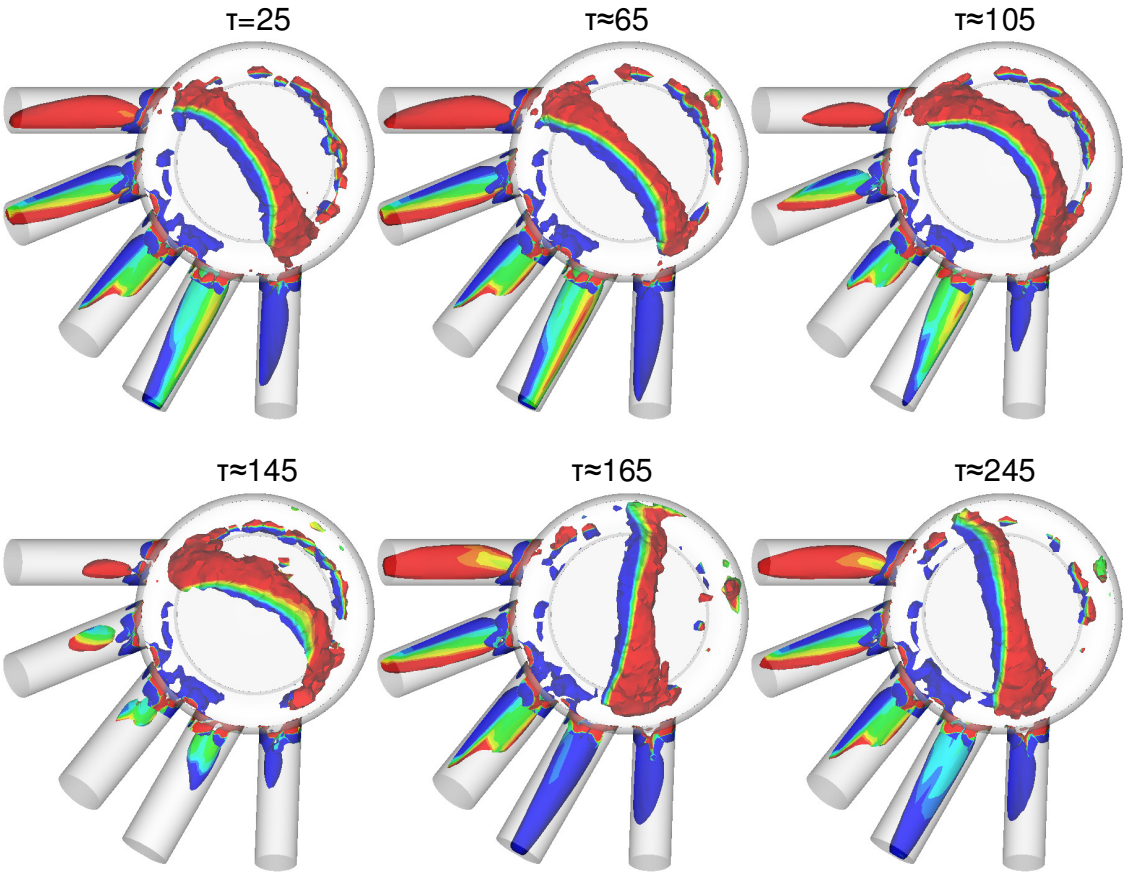

Figure 4-70: iso-surfaces of swirl intensity inside the core of the nozzle volume vortex coloured with the axial velocity component of the liquid. [Default grid, Neq. k-ε]

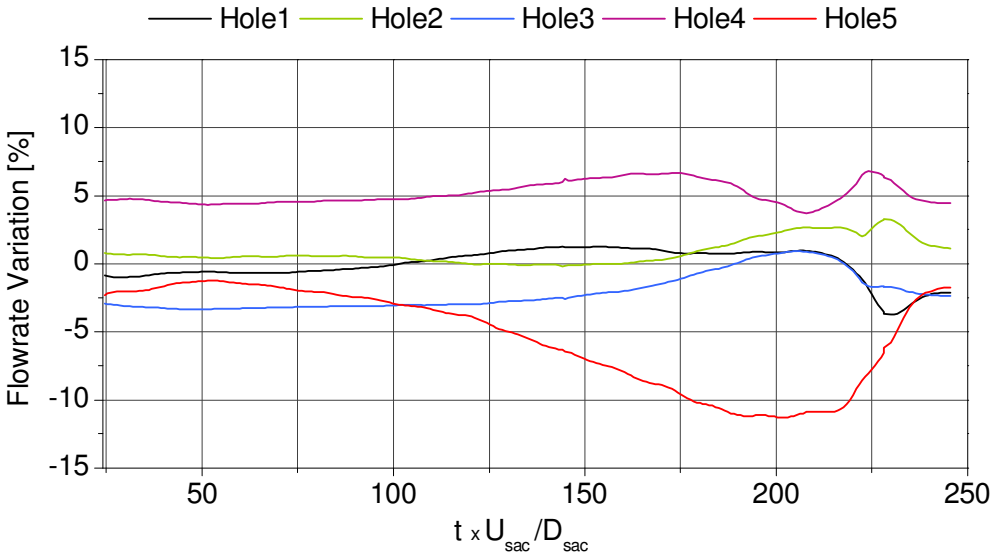

Figure 4-71: Predicted temporal variation of hole-to-hole flow rate. [Default grid, Neq. k-ε]

All the previous results were obtained with the default grid. As it can be seen there are no big differences between the different turbulence models, except the non equilibrium k-ε where even though the same vortical structures are present, there are not so many changes in their location. Finally as the flow rate variation plots suggest the same patterns are followed between the injection holes and also the percentage reduction, or increase, is closely comparable between the different models. The results that were obtained with the dense grid simulations are given below in a more compact form, however results from more time-steps can be found in the appendix.

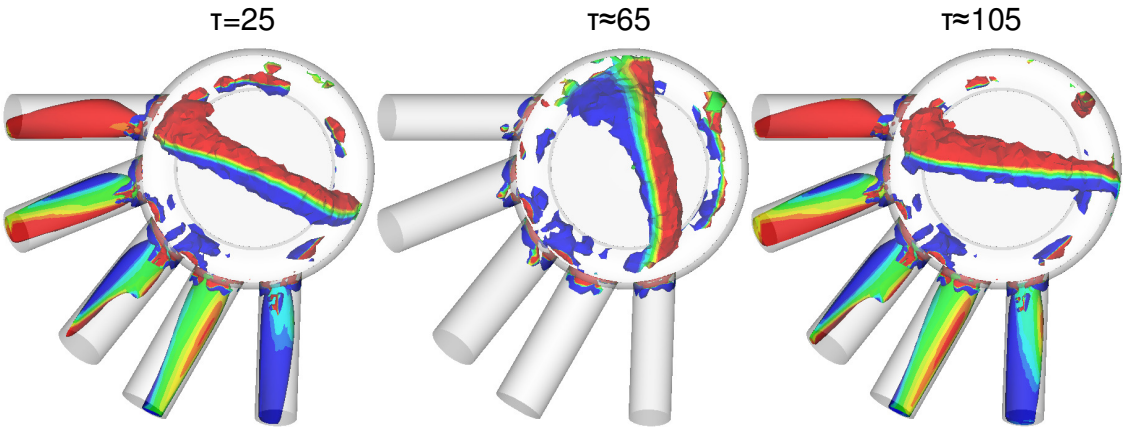

Figure 4-72: iso-surfaces of swirl intensity inside the core of the nozzle volume vortex coloured with the axial velocity component of the liquid. [Dense grid, Std. k-ε]

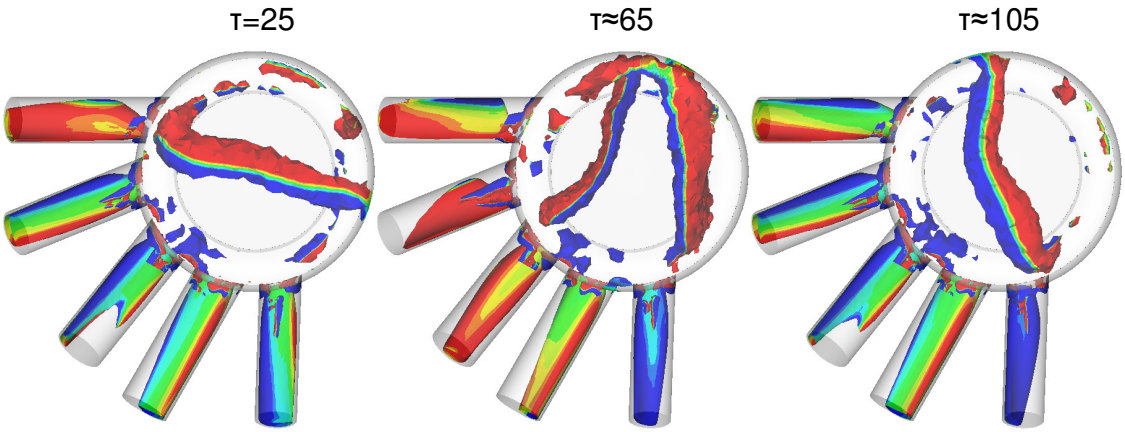

Figure 4-73: iso-surfaces of swirl intensity inside the core of the nozzle volume vortex coloured with the axial velocity component of the liquid. [Dense grid, Std. k-ω]

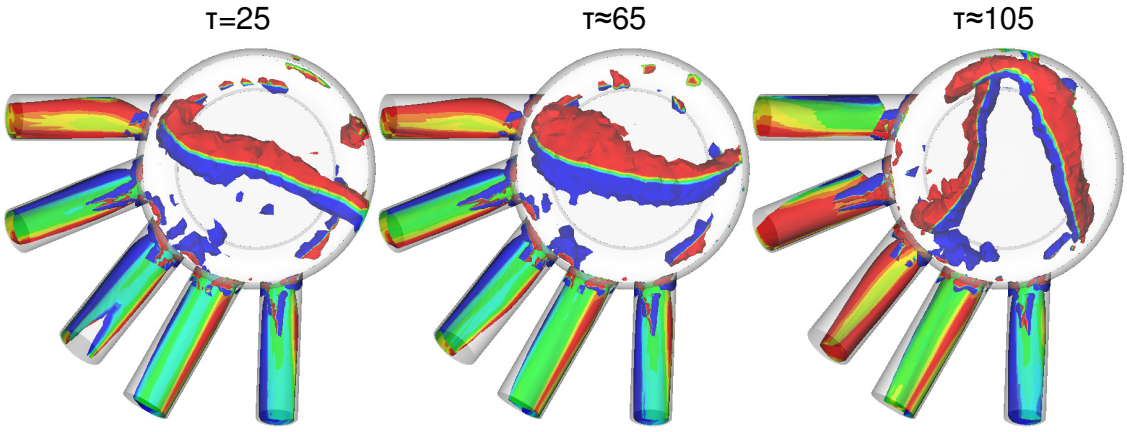

Figure 4-74: iso-surfaces of swirl intensity inside the core of the nozzle volume vortex coloured with the axial velocity component of the liquid. [Dense grid, RNG k-ε]

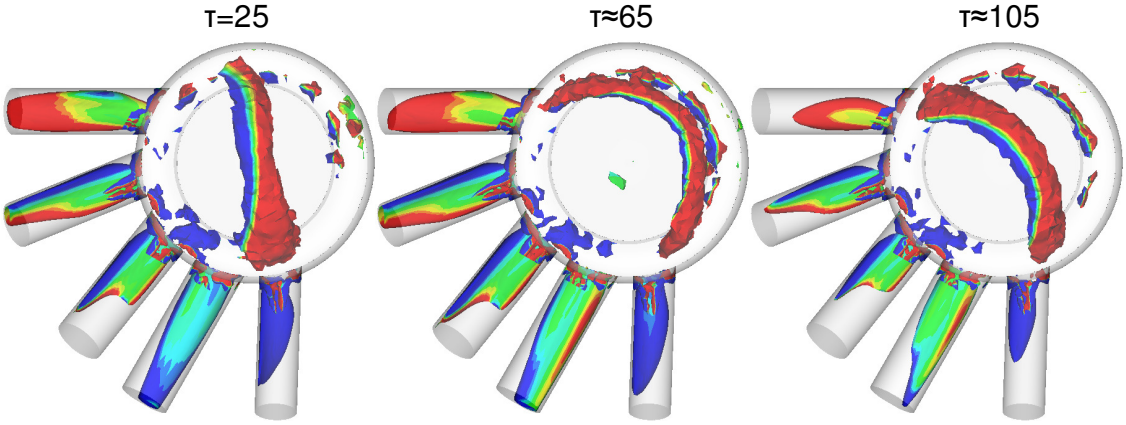

Figure 4-75: iso-surfaces of swirl intensity inside the core of the nozzle volume vortex coloured with the axial velocity component of the liquid. [Dense grid, Neq. k-ε]

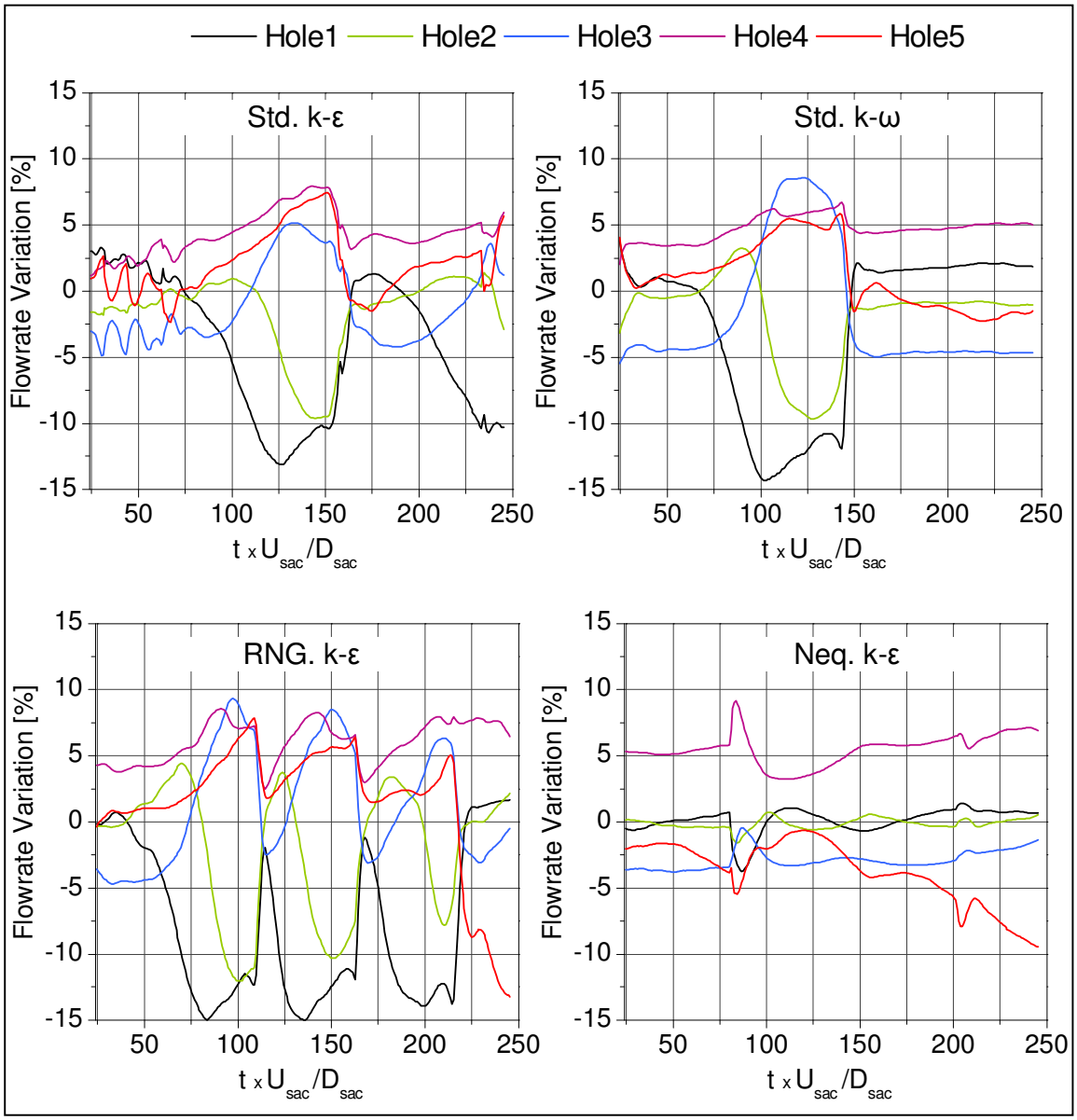

Figure 4-76: Predicted temporal variation of hole-to-hole flow rate. [Dense grid]

It can be concluded by observing Figure 4-72 through Figure 4-76, which are the plotted results for the dense grid cases, that similar vortical structures have be seen in the nozzle sac-volume. Although there are differences in the sequence of formation, these are limited and the presence duration of vortices along with their orientation are not dramatically affected. therefore it has been safely concluded that model predictions are not sensitive to these parameters with respect to the formation and development of the nozzle vortical flow structures.

4.8 Simulation Work: Conclusions

The needle geometry effect was investigated and it was found that it can change the inside nozzle flow structure significantly.

Six new geometries were created and were compared with the standard nozzle design.

Negative pressures were found in all holes at the bottom of the inlet indicating initiation of the hole cavitation.

Differences in the flow rates and the mean exit velocities of the holes were found. Under these working conditions some holes are over-fuelled and some are under-fuelled.

A large recirculation zone is formed inside the sac volume which indicates the possibility of vortex (string) cavitation to be present in the sac volume.
Swirling motion inside the injection holes was identified with tangent velocities having magnitudes of 15%-20% of the axial velocity.

The axial velocity profile at the hole exit plane is not symmetric which indicates that there might be a deviation from the designed injection direction.

The hole interaction effect was investigated and it was found that when only one hole is allowed to inject, a portion of the flow is coming from the recirculation zone inside the sac volume even for holes that have never been associated with vortices in the sac volume.

Finally the effect of hole length was investigated and was found that as the hole length increases swirl is reduced and the velocity distribution at the hole exit plane becomes uniform and symmetrical.

Chapter 5
Experimental Results-Internal flow in Large scale marine nozzles

5.1 Introduction

As mentioned in Chapter 2, Cavitation inside the nozzles of Diesel injectors can be investigated by employing transparent model nozzles, which represent the enlarged three-dimensional geometry of production nozzles. The models provide the necessary optical access for qualitative visualisation investigations of all flow regions of interest and also measurements of various nozzle characteristics such as discharge coefficient and how the flow rate is distributed to the holes. These investigations provide information for improving the physical understanding of the cavitation phenomenon and its dependencies on various parameters, such as nozzle geometry and flow conditions.

Since the fuel flow through the injector nozzles, especially through the holes, is highly turbulent, all flow features can be expected to behave transiently and with short time-scales. This behaviour is virtually impossible to capture with still images, or an image sequence taken with a conventional CCD camera. Since it is important to gain knowledge about the dynamics of the cavitation inception and formation processes for various flow conditions, two high-speed digital video systems were set up and synchronised in order to capture the cavitating structures from two views simultaneously as seen in Chapter 3. Usually until recently there was a trade of image quality and frame rate. However with the current video system very high image quality could be achieved for frame rates able to capture the highly transient phenomena.

At the current stage of the investigation, and given the results obtained from the numerical investigation as presented in chapter 4, there was no particular interest to examine the various hole cavitation structures and regimes in detail. This has been done many times in

the past with interesting and validated results which were presented in the literature review section presented in Chapter 2.

Instead of that what will be presented in this chapter is the link between hole and string cavitation and the flow structure in the marine injector nozzle and how they affect the various flow parameters.

For the investigation presented in this Chapter four different transparent replicas were used. This replicas have been presented in Chapter 3 along with various details regarding their manufacture. The first manufactured large-scale model was that of the Five-Hole Cylindrical Marine Nozzle, shown in Figure 3-5, fitted with expansion tubes in order to facilitate high cavitation numbers by reducing the back pressure below atmospheric. Then the same nozzle design with the same scaling factor was manufactured with tapered holes, outwards converging, as shown in Figure 3-10. Finally two large-scale singe hole marine nozzles were manufactured, having identical internal geometry as with the five-hole ones. Again the first such model features a cylindrical hole while the second a tapered with the same dimensions and arrangement as hoe number 3 of the five-hoe nozzle. Both these nozzles are shown in Figure 3-18

Throughout the chapter, and in order to both enhance the understanding of the experimental results and in order to validate the in house CFD code, the experimental results will be compared by numerical results obtained for the Large-Scale Nozzle by using the same RANS flow solver [142] as in chapter 4 in order to simulate the flow inside the nozzle. This model is able of modelling the geometric-induced hole cavitation but not the string cavitation.

The following tables show the experimental conditions investigated along with sample pictures indicating the viewpoint for every set of results. As can be seen, they refer to cavitation numbers between 0.5 and 15, which is similar to those of the real-size injector operating under engine operating conditions. However, the much lower injection pressures used restrict the experiment into flow rates (and Reynolds numbers) much lower than those of the real operating conditions.

Case Index	CN	Re ≈	P_{inj} [bar]	P_{back} [bar]	Flow Rate [litre/s]	Frame Rate [1/s]	Needle Lift
1	1.52	41,000	2.2	0.90	0.55	15,000	100%
2	2	41,000	2.23	0.79	0.55	15,000	100%
3	2.5	41,000	2.22	0.65	0.56	15,000	100%
4	3	41,000	2.24	0.58	0.55	15,000	100%
5	4	41,000	2.23	0.48	0.56	15,000	100%
6	3.15	56,000	4	1	0.75	15,000	100%
7	4	56,000	4	0.84	0.75	15,000	100%
8	5	56,000	3.96	0.7	0.75	15,000	100%
9	6	56,000	4	0.61	0.75	15,000	100%
10	7	56,000	4	0.54	0.75	15,000	100%
11	8	56,000	4	0.49	0.75	15,000	100%
12	14	56,000	3.95	0.30	0.75	15,000	100%
13	4	70,000	6.1	1.27	0.935	15,000	100%
14	5	70,000	6.05	1.05	0.935	15,000	100%
15	0.57	28,000	1.39	0.9	0.37	15,000	100%
16	0.65	28,000	1.41	0.87	0.36	15,000	100%
17	0.7	28,000	1.4	0.84	0.36	15,000	100%
18	0.75	28,000	1.39	0.82	0.37	15,000	100%
19	0.8	28,000	1.38	0.78	0.37	15,000	100%
20	0.9	28,000	1.36	0.73	0.38	15,000	100%
21	1	28,000	1.34	0.7	0.38	15,000	100%
22	1.1	28,000	1.34	0.66	0.38	15,000	100%
23	1.2	28,000	1.33	0.63	0.38	15,000	100%
24	1.3	28,000	1.32	0.6	0.39	15,000	100%
25	1.4	28,000	1.31	0.57	0.39	15,000	100%
26	1.6	28,000	1.32	0.53	0.39	15,000	100%
27	1.8	28,000	1.32	0.5	0.39	15,000	100%

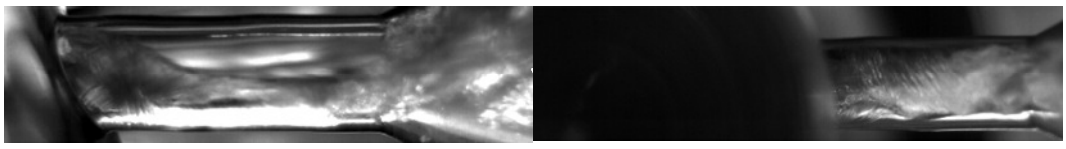

Side View Bottom View

Table 5-1: Flow conditions inside the large-scale cylindrical marine model nozzle and representative results for hole 5 side and bottom views.

Case Index	CN	Re ≈	P_{inj} [bar]	P_{back} ≈ [bar]	Flow Rate [litre/s]	Frame Rate [1/s]	Active Injection Holes
28	2.6	41,000	2.6	0.76	0.55	6,000	2, 3, 4 & 5
29	2.6	27,000	2.6	0.76	0.36	6,000	3, 4 & 5
30	2.6	19,000	2.6	0.76	0.25	6,000	4 & 5
31	2.6	11,000	2.6	0.76	0.15	6,000	5
32	2.6	12,000	2.6	0.76	0.16	6,000	4
33	2.6	13,000	2.6	0.76	0.17	6,000	3
34	2.6	11,000	2.6	0.76	0.15	6,000	2
35	2.6	11,000	2.6	0.76	0.15	6,000	1
36	2.6	20,000	2.6	0.76	0.27	6,000	1 & 3
37	2.6	29,000	2.6	0.76	0.39	6,000	1, 3 & 5
38	2.6	20,000	2.6	0.76	0.26	6,000	3 & 5
39	2.6	20,000	2.6	0.76	0.26	6,000	2 & 4
40	2.6	35,000	2.6	0.76	0.47	6,000	1, 2, 3 & 4
41	2.6	36,000	2.6	0.76	0.7	6,000	All

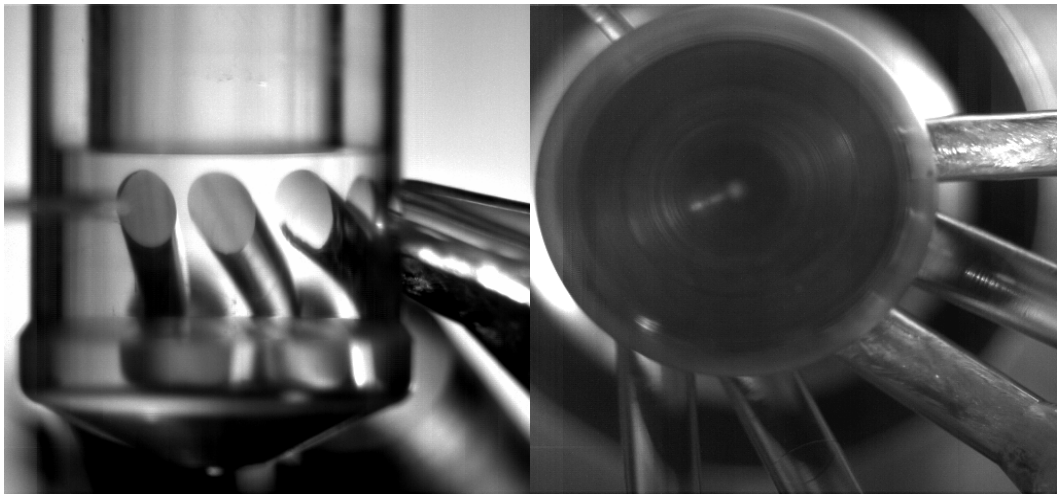

Side View Bottom View

Table 5-2: Flow conditions inside the large-scale cylindrical marine model nozzle and representative results for hole 5 side and bottom sac volume view. [Full Lift]

Case Index	CN	Re ≈	P_{inj} [bar]	P_{back} [bar]	Flow Rate [litre/s]	Frame Rate [1/s]	Needle Lift
42	4	68,00	3.4	0.72	0.9	6,000	100%
43	2.5	32,00	1.5	0.47	0.45	6,000	80%
44	4	53,00	4.3	0.89	0.7	6,000	80%
45	5.7	49,00	4.4	0.7	0.65	6,000	70%
46	5.4	53,00	4.2	0.7	0.56	6,000	90%
47	4.3	60,00	3.8	0.76	0.8	6,000	120%

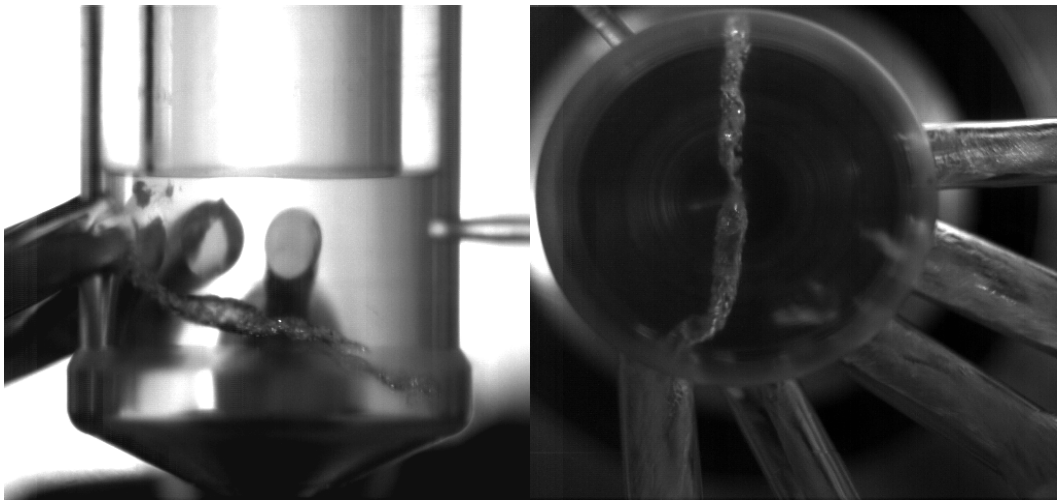

Side View Bottom View

Table 5-3: Flow conditions inside the large-scale cylindrical marine model nozzle and representative results for hole 1 side and bottom sac volume view.

Case Index	CN	Re ≈	P_{inj} [bar]	P_{back} [bar]	Flow Rate [litre/s]	Frame Rate [1/s]	Needle Lift
48	3	53,000	3.4	0.85	0.7	6,000	100%
49	4	53,000	3.4	0.72	0.7	6,000	100%
50	5	53,000	3.3	0.64	0.7	6,000	100%
51	2	53,000	3.3	1.16	0.7	6,000	100%
52	0.8	53,000	3.3	1.79	0.69	6,000	100%
53	0.8	37,000	2.2	1.26	0.51	6,000	100%
54	0.9	35,000	2.3	1.22	0.47	6,000	80%
55	1	34,000	2.4	1.22	0.45	6,000	70%
56	1.2	31,000	2.5	1.17	0.41	6,000	60%
57	1.4	25,000	2.7	1.14	0.33	6,000	40%

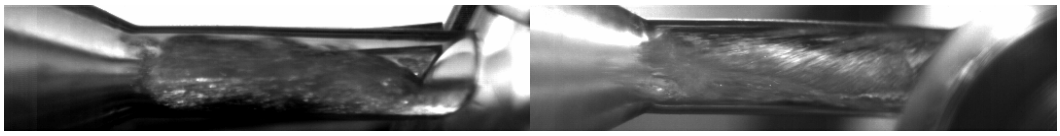

Side View Bottom View

Table 5-4: Flow conditions inside the large-scale cylindrical marine model nozzle and representative results for hole 1 side and bottom view.

Case Index	CN	Re ≈	P_{inj} [bar]	P_{back} [bar]	Flow Rate [litre/s]	Frame Rate [1/s]	Needle Lift
58	0.5	31,000	1.8	1.15	0.40	6,000	100%
59	0.57	32,000	1.89	1.18	0.43	6,000	100%
60	0.6	35,000	2	1.21	0.46	6,000	100%
61	0.66	36,000	2.11	1.24	0.48	6,000	100%
62	0.68	38,000	2.17	1.25	0.5	6,000	100%
63	0.74	39,000	2.31	1.28	0.52	6,000	100%
64	0.84	44,000	2.56	1.35	0.58	6,000	100%
65	0.9	47,000	2.75	1.42	0.62	6,000	100%
66	1	50,000	3	1.46	0.66	6,000	100%
67	1.1	53,000	3.3	1.51	0.7	6,000	100%
68	4.25	53,000	3.25	0.63	0.7	6,000	100%
69	1.15	20,000	0.64	0.32	0.27	6,000	100%

Bottom View

Table 5-5: Flow conditions inside the large-scale cylindrical marine model nozzle and representative results for bottom sac volume view.

Case Index	CN	Re ≈	P_{inj} [bar]	P_{back} [bar]	Flow Rate [litre/s]	Frame Rate [1/s]	Active Injection Holes
70	0.56	31,000	1.8	1.15	0.40	6,000	All
71	0.62	32,000	1.89	1.18	0.43	6,000	All
72	0.68	35,000	2	1.21	0.46	6,000	All
73	0.67	36,000	2.11	1.24	0.48	6,000	All
74	0.73	38,000	2.17	1.25	0.5	6,000	All
75	0.9	39,000	2.31	1.28	0.52	6,000	All
76	1	44,000	2.56	1.35	0.58	6,000	All
77	1.1	47,000	2.75	1.42	0.62	6,000	All
78	1.7	50,000	3	1.46	0.66	6,000	All
79	5	53,000	3.3	1.51	0.7	6,000	All
80	1.8	31,000	1.75	0.59	0.41	6,000	All
81	2.3	28,000	1.88	0.56	0.37	6,000	1,2,3 & 5
82	2.7	24,000	1.99	0.54	0.32	6,000	1, 3 & 5
83	3.5	17,000	2.22	0.49	0.22	6,000	1 & 5
84	3.2	9,800	2.34	0.6	0.13	6,000	1
85	2.1	16,000	2.2	0.74	0.21	6,000	1 & 2
86	2.9	18,000	2.17	0.6	0.24	6,000	2 & 3
87	2.5	18,000	2.16	0.65	0.24	6,000	3 & 4
88	2.5	17,000	2.18	0.66	0.22	6,000	4 & 5
89	2	24,000	1.98	0.7	0.32	6,000	2, 3 & 4
90	2.6	9,800	2.6	0.77	0.14	6,000	2
91	2.6	11,000	2.6	0.77	0.16	6,000	3
92	2.6	12,000	2.6	0.77	0.16	6,000	4
93	2.6	12,000	2.6	0.77	0.13	6,000	5
94	2.6	9,800	2.6	0.76	0.13	6,000	1
95	0.56	23,000	2	1.3	0.31	6,000	1, 3, 4 & 5
96	0.7	26,000	2.3	1.37	0.35	6,000	1, 3, 4 & 5
97	0.67	27,000	2.25	1.37	0.36	6,000	1, 2, 3 & 5

Table 5-6: Flow conditions inside the large-scale cylindrical marine model nozzle and representative results for bottom sac volume view. [80% needle lift]

Case Index	CN	Re ≈	P_{inj} [bar]	P_{back} [bar]	Flow Rate [litre/s]	Frame Rate [1/s]	Needle Lift
98	0.4	28,000	1.8	1.15	0.37	12,500	100%
99	0.44	26,000	1.89	1.18	0.34	12,500	80%

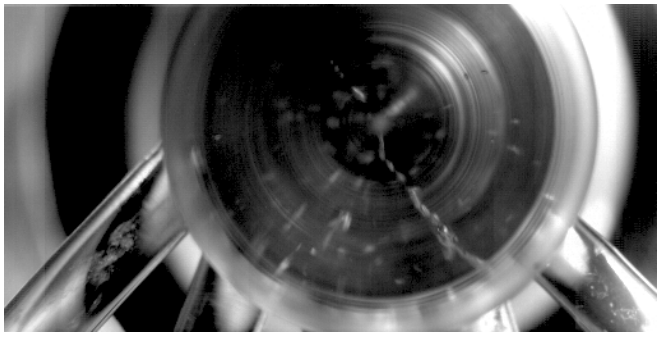

Table 5-7: Flow conditions inside the large-scale cylindrical marine model nozzle, with air bubble seeding, and representative results for bottom sac volume view.

The flow conditions for all the experimental investigation that were conducted for the large scale model of the cylindrical marine nozzle are given in Table 5-1 through Table 5-6. The CN values that are indicated are averaged values from the individual holes. The reason for having those slight differences is mainly due to the back pressure differences. As mentioned in the transparent model description every injection hole is followed by a discharge channel or expansion tube as also referred. These back flow holes, which are larger in diameter than the injection holes, collect the emerging liquid directly after the injection hole exit and direct it into the tubes leading to the suction pump. Due to the different injection hole diameters and the asymmetric arrangement of the holes there is a difference ± 2mm over a 12mm expansion tube diameter. This, along with the different flow supply that each injection hole is receiving, also due to the fact that are of different diameter, leads into these slight variations which are around 4%. Reynolds number values are also rounded within ± 1.5% in order to make easier comparisons between different CN values under the same incoming flow rate.

During this investigation more than one hundred (100) cases were recorded including: different cavitation and Re numbers, different needle lifts, different viewing areas and frame acquisition rates and finally different injection hole arrangements. The last one was achieved by struggling the flow at the end of the expansion tube of each individual hole. Although the relative position of the holes was unchanged it was possible to reduce the

number of injection holes of the injector and also try many combinations of open-close arrangements. This had also been desired by the sponsoring company since, and not very rarely, due to cock concentration an injection hole could be blocked while operating in the engine with many undesirable effects.

In Table 5-7 are the flow conditions of two cases where air bubbles were introduced upstream, in the nozzle annulus, through a valve that was connected by a flexible tube to the compressed air network of the testing facilities. The main reason for having air bubbles in the flowing liquid was to visualize the flow patterns mainly inside the sac volume, actually using the air bubbles as tracking particles. However, and this will be clearly shown later in this chapter when investigating the large scale marine nozzle with conical or tapered injection holes, air bubble seeding will be extremely helpful into identifying the mechanism of formation of 'string' or vortex cavitation which until this study was questionable.

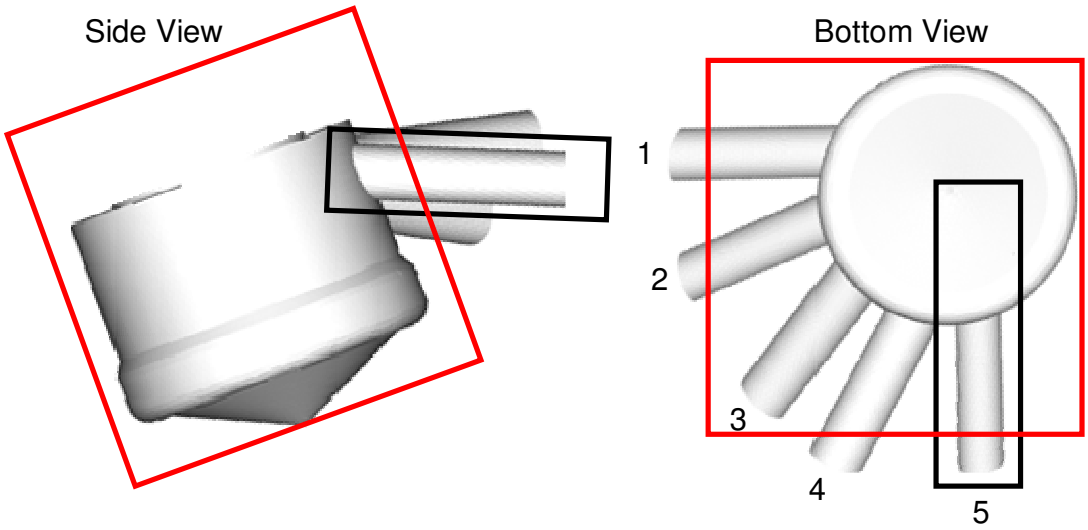

Figure 5-1: Schematic showing the viewing area of the camera for the side and bottom view focusing in the hole (black rectangle) and in the sac volume (red rectangle).

5.2 Results - Internal Nozzle Flow marine cylindrical injector - Hole cavitation

As mentioned in Chapter 4 at normal operating conditions, that typically is CN=4, all the injections holes of the nozzle were expected to cavitate. However it is always extremely important for a CFD code to predict the correct cavitation sight, i.e. the location where the pressure drops below the vaporization pressure of the flowing liquid subsequently leading to bubble formation, and also the correct flow path of the generated bubbles until the hole exit. Having those correctly calculated then a correct void distribution can be derived allowing safe conclusions for the performance of the nozzle. A correct prediction of the two-phase flow is always a key element in order to get a correct spatially resolved nozzle hole exit flow distribution, that will then be used as input for complex asymmetric spray calculations such as those presented in [42, 143].

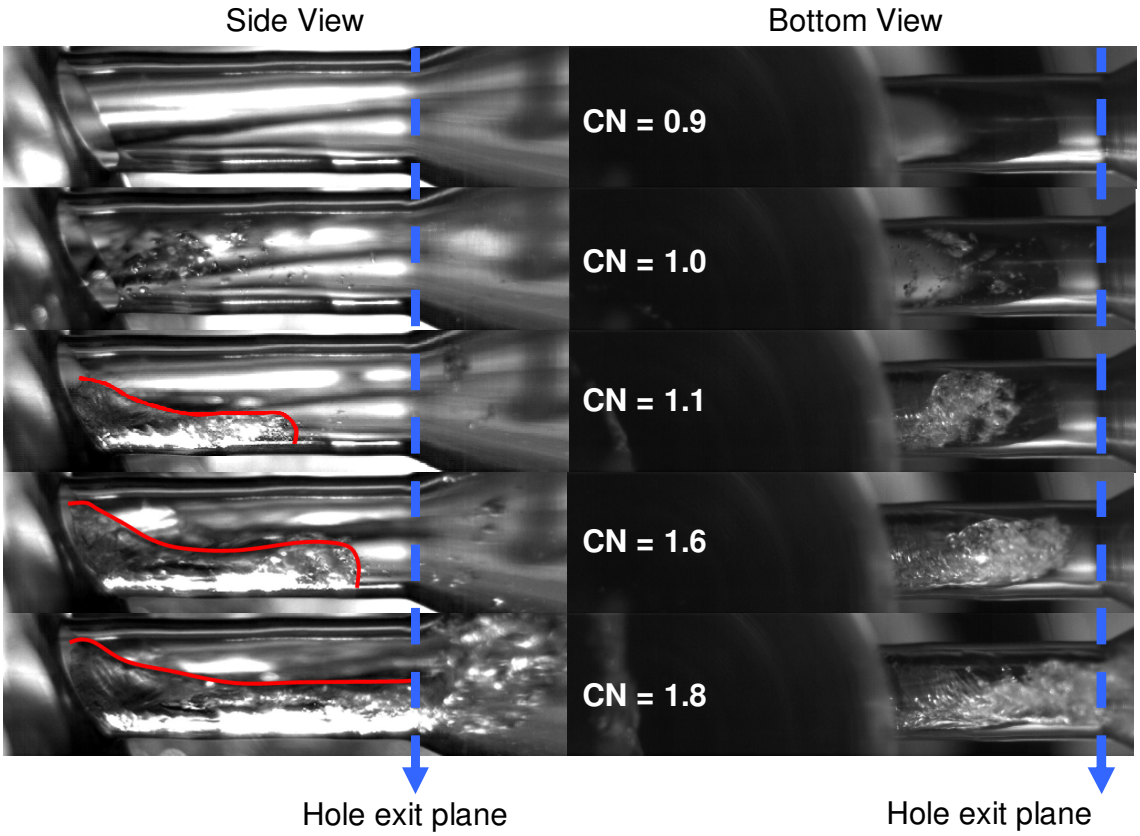

Figure 5-2: Cavitation structure and its variation with CN inside hole 5 for side and bottom view [Case: 20, 21, 22, 26, 27]. Red line describes the boundary of cavitation inside the injection hole.

In Figure 5-2 a series of typical images of the cavitation structures inside the injection hole 5 is presented for nominal needle lift. The viewpoints used are those indicated by the black rectangles shown in Figure 5-1 with the imaging equipment arrangement being described in Figure 3-29. As it can be seen from top to bottom the CN increases for the same Reynolds number. The first observation to be made is that the cavitation sites are at the same location as the predictions had shown in Chapter 4 (e.g. Figure 4-5). The second observation to be made is that the hole cavitation was highly non-symmetric and different from hole to hole, due to the highly swirling motion of the flow entering through individual injection holes. As will be shown later this had also been successfully predicted through a serious of two phase calculations that were performed using the in house CFD code described briefly in section 4.2. Finally by comparing the images for different CN numbers it can be confirmed that by increasing CN the cavitation structures inside the injection become stronger and occupy a larger portion of the hole. As will be shown later in this chapter, and as has been reported to other similar investigations, the increased fraction of vapour will significantly affect the discharge coefficient of the hole. Often, particularly when dealing with the spray initial condition, it is of great importance to determine if the cavitation bubbles/cloud reach the hole exit without breaking and mixing with the injecting liquid. For this particular nozzle it was determined that for CN values greater of 1.8 the cavitation structure evolve all the way from the hole inlet to its exit.

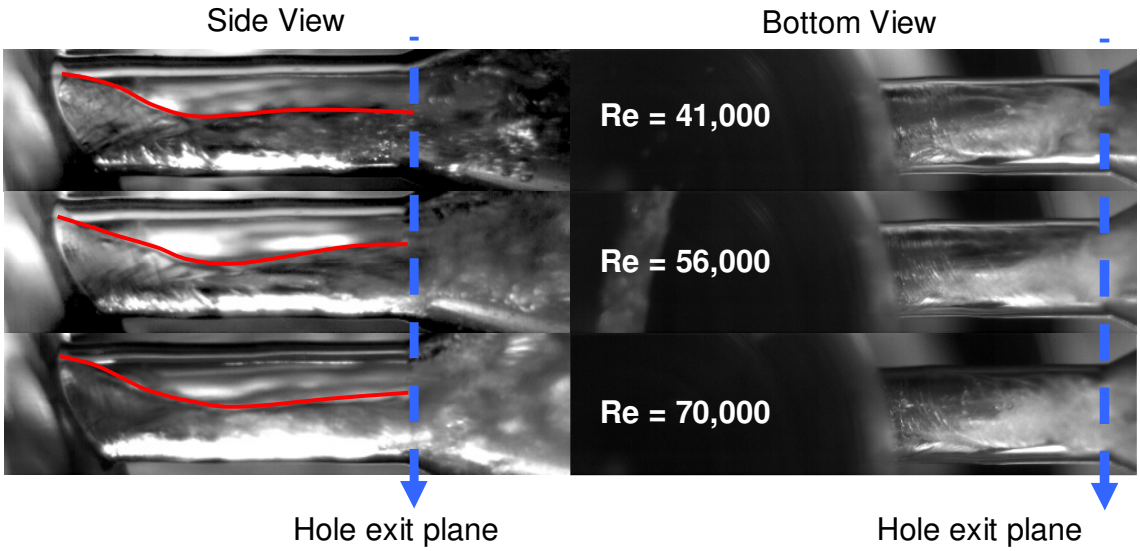

Figure 5-3: Cavitation structure and its variation with Re inside hole 5 side and bottom view [Case: 4, 7, 13] (CN=4). Red line describes the boundary of cavitation inside the injection hole.

Having explored the effect of cavitation number on the flow structure inside the nozzle's hole, Figure 5-3 shows what is the effect of Re number at a constant CN. Determining the effect of Re number on cavitation development is the prerequisite in order to conclude if a Large-scale experiment can provide valuable results, since flow images can be obtained only at low injection pressures relative to those used in real injectors. As also past studies, such as those of [30, 103, 104] comparing cavitation in large-scale and real-size nozzles, have shown, Reynolds number is of least importance compared to the effect of CN. This conclusion can be further supported by Figure 5-4, which presents the measured nozzle discharge coefficient as function of the cavitation number for different Reynolds numbers and three different needle lifts. As it is evident, the overall volumetric flow rate of the nozzle is function only of the cavitation number for a fixed needle lift, and not of the Reynolds number. In agreement with previously reported data, when the cavitation number is large enough to produce fully developed cavitating flow, the volumetric flow rate effectively reaches asymptotically to its minimum value. This flow behaviour is closely associated with the formation of a fully developed flow regime where the cavitating structures exit from the injection hole and where no further change in the flow topology is expected with further increase of the injection or the back pressure.

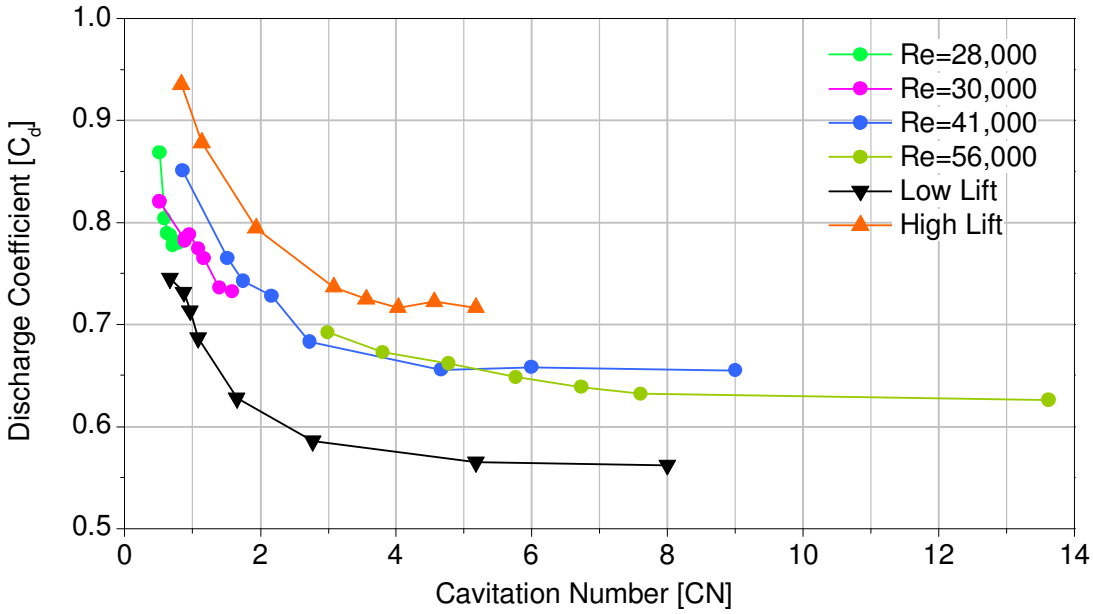

Figure 5-4: Measured nozzle discharge coefficient as function of cavitation number for different Reynolds numbers and needle lifts.

Therefore, in order to conclude, Figure 5-2 through Figure 5-4 have shown that the macroscopic structure of the two-phase flow formed inside the injection holes as well as the overall volumetric flow rate of the nozzle, for a fixed needle lift, are mainly a function of the cavitation number and not of the Reynolds number. This comes in agreement with previously reported data of [144] & [56] as well as model predictions presented in the current study. It has to be mentioned that the Reynolds number used in this study has been defined on the basis of the mean flow rate and the average hole diameter and has been followed throughout this work.

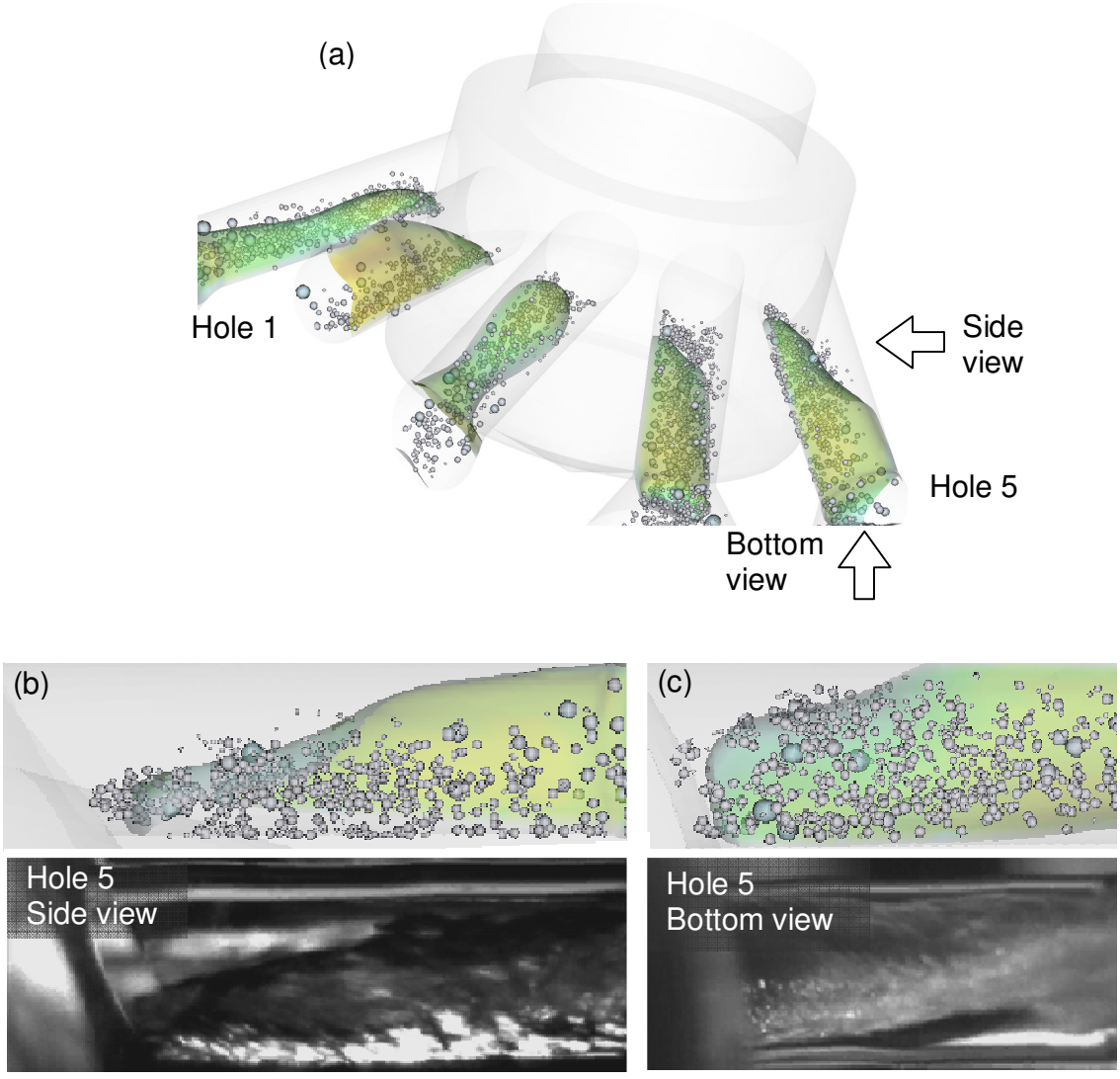

Figure 5-5: (a) 3-D view of calculated cavitation bubbles inside the injection holes and vapour-liquid inter-phase, (b) comparison between cavitation model predictions and CCD images of cavitation inside hole 5 from the bottom-view and (c) comparison between cavitation model predictions and CCD images of cavitation inside hole 1 from the side-view [Case 7]. (colour scale not significant)

Having established the correlations between Reynolds, CN, Cd and cavitation structures inside the injection holes, the next to be established is the ability of the in house CFD code to predict cavitation intensity as well as distribution inside the injection hole. Although preliminary results were presented in Chapter 4, they were not compared against experimental images. To provide a visual evidence of the model prediction for the hole cavitation, Figure 5-5 is presented. Figure 5-5(a) shows a 3-D view of the computational bubbles forming inside the 5 injection holes, superimposed with a void iso-surface indicating the boundary between the pure liquid flow and the bubbly flow regimes inside the injection holes. For this particular injection condition, close-up images of the nozzle flow have been obtained with the same visualisation system used for the nozzle flow investigation. Those images, together with the corresponding model predictions are presented in Figure 5-5(b) and (c). Although this is not sufficient to fully validate the two-phase flow model, it can be claimed that the cavitation model predicts reasonably the dispersion of the cavitation bubbles inside the injection hole and therefore its results can be further exploited.

5.3 Results - Internal Nozzle Flow marine cylindrical injector - String cavitation

Until this point the experimental results presented refer to geometrically induced cavitation. However, as it was also mentioned at the beginning of this chapter, the dominant and most interesting cavitation structure that was identified in the marine nozzles was the vortex (or often called ‘string’) cavitation. Before the presentation and detailed analysis of the obtained results, it is mandatory to have a brief introduction, been a synopsis of some of the studies mentioned in Chapter 2, in order to recap what is the current extend of knowledge on this field.

As mentioned before, the geometric-induced cavitation is a relatively well-known phenomenon initiating at sharp corners where the pressure may fall below the vapour pressure of the flowing liquid. The second form of cavitation has been observed, and referred to as ‘string’ or ‘vortex’ cavitation by [30] and [71]. These two-phase flow structures are usually found in the bulk of the liquid, in the areas where large-scale, relative

to the nozzle geometry, vortices exist. Although more recent studies have shown similar behavior in various types of multi-hole nozzles, for example [145], their formation process has been found to be relatively irregular while their interaction with the mean flow remains poorly understood. Other studies on cavitation performed in venturi-type nozzles, for example see [146] and [147], have employed laser diagnostics to provide insight into the mechanism of bubble entrapment into vortical flow structures, but the complexity of the geometry of Diesel injectors makes it difficult to obtain such measurements. Furthermore, because of the difficulty in obtaining real-time measurements during the injection process, most of the reported experimental studies refer to experimental devices simulating operating conditions relevant to those of Diesel engines. Nevertheless, simplifications to the design of the nozzle itself or to the transient operation of the needle are unavoidable, which has implications on the very short injection durations and the very high liquid velocities, of the order of 400 m/s in production injectors. Parallel to the continuing effort to obtain better experimental information under as realistic conditions as possible, there is an increasing demand for developing and validating computational fluid dynamics models to predict cavitation. Despite the effort devoted to developing cavitation models applicable for fuel injectors, all of those applied so far have focused on geometric-induced cavitation. It can be argued that there is no model yet capable of predicting string cavitation in fuel-injection equipment. This is mainly due to the lack of experimental data available for the relevant flow phenomena and, thus, the incomplete physical understanding of the process. As it will be revealed later in this paper, the aforementioned models are, in principle, incapable of simulating string cavitation inside injector nozzles. Some studies on vortex cavitation, for example [111] and [112], which represent a promising theoretical background to this problem, have not yet been applied to nozzle flows.

Having finished the aforementioned short introduction, The presentation of the results starts from a general description of the flow distribution inside the specific nozzles investigated. As in section 4.7.1, where it was also defined, the non-dimensional time τ will be used, wherever needed. with this scaling approach, it will be possible to compare the vortex development inside the sac volume for different operating flow rates through the nozzle.

Figure 5-6 shows typical images of the string cavitation formed inside the nozzle sac volume at a nominal needle lift, CN =4 and Re=68 000, at two time instances with $\Delta\tau$~100. Images are presented from both the bottom and the side views (red rectangles in Figure 5-1). It can be seen that well inside the nozzle sac volume, a relatively thick and long vapour structure is formed, this two-phase flow structure will be referred to from now as 'string cavitation'.

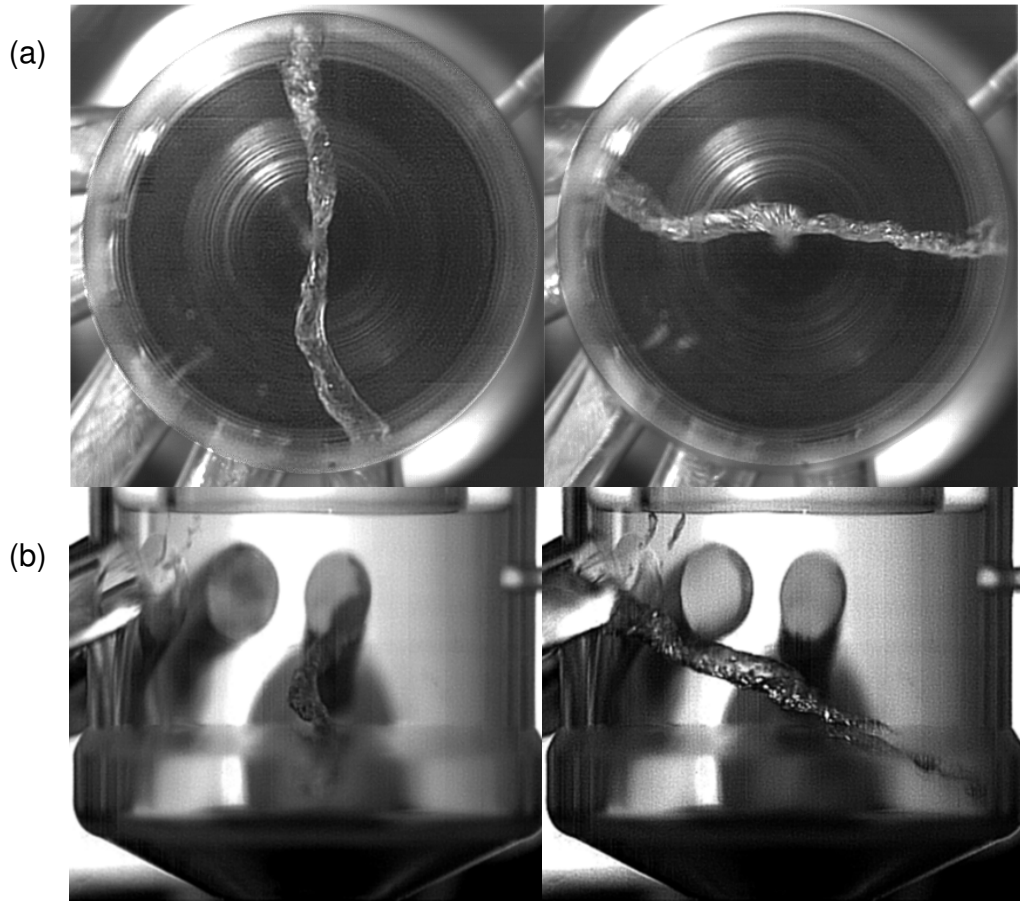

Figure 5-6: Typical image of string cavitation formed inside the nozzle sac volume at two different time instances with $\Delta\tau$~100 (a) bottom view and (b) side view [nominal needle lift, CN =4.0, Re =68 000].

In the area where these structures are formed, it is expected that the pressure of the flowing liquid is almost equal to the feed pressure, which is much higher than the vapour pressure of the liquid. This can also be seen in Chapter 4 , Figure 4-19, where the pressure distribution across the nozzle for similar conditions is plotted.

Despite that, cavitation has been identified to form and develop in a transient mode. The location of the string seems to change considerably, since it may exit either from hole 1 or from hole 5, as images taken at different time instances reveal. Collection of thousands of images has allowed capturing of the frequency of the formation of those strings as well as their motion inside the nozzle volume. Before presenting those results, it was considered equally important to investigate the local flow field where the strings are formed with use of the CFD model. The following results to be presented are part of the extended calculations, form the previously reported numerical investigation that was presented in Chapter 4. this time the initial conditions have been adjusted to the experimental ones and the numerical grid is based on the large scale manufactured geometries. A typical grid used for these simulations is presented in Figure 5-7 below.

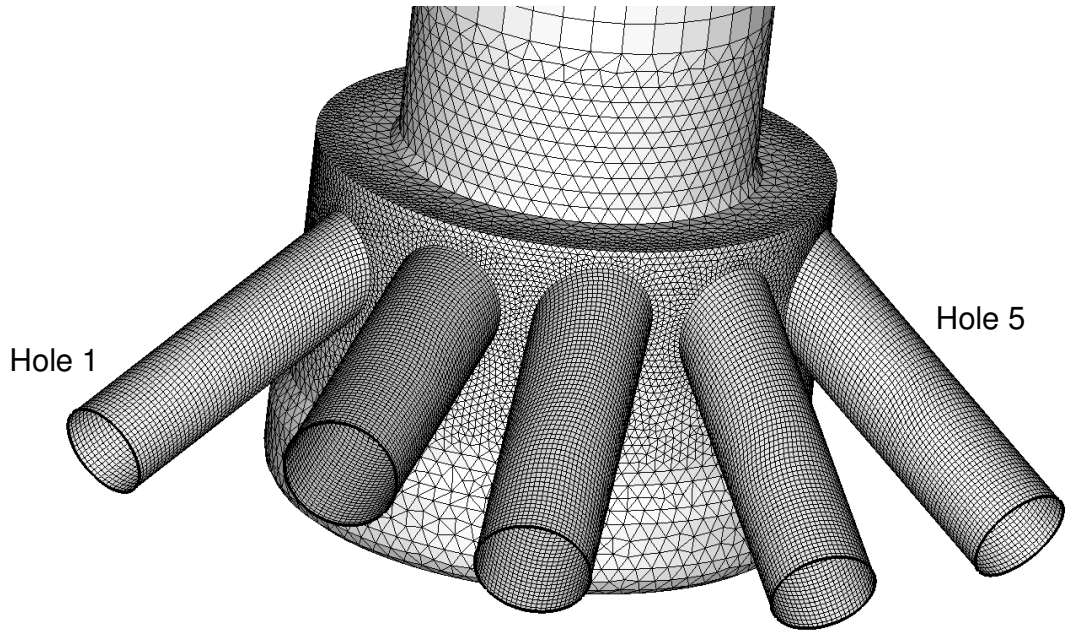

Figure 5-7: unstructured computational grid for the 5-hole nozzle with local refinement upstream and at the entry to the injection holes.

Figure 5-8 presents the model predictions for similar operating condition as those of the images of Figure 5-6 presented above. For those calculations transient simulation was performed although the boundary conditions and the geometry were fixed. The aim of this figure is to visualize the flow field inside the nozzle, as well as its possible variation with time. Figure 5-8 (a) presents flow lines inside the sac volume exiting only from holes 1 and 5, been viewed by a position opposite to the hole inlets. It can be seen that as the flow

enters from upstream into the nozzle volume, it turns around 90° in order to exit from the nozzle holes. As a result, strong recirculation zones are formed inside the nozzle volume. By performing Time-dependent predictions it was revealed that for specific operating conditions this vortex may be rather unstable and move inside the nozzle volume.

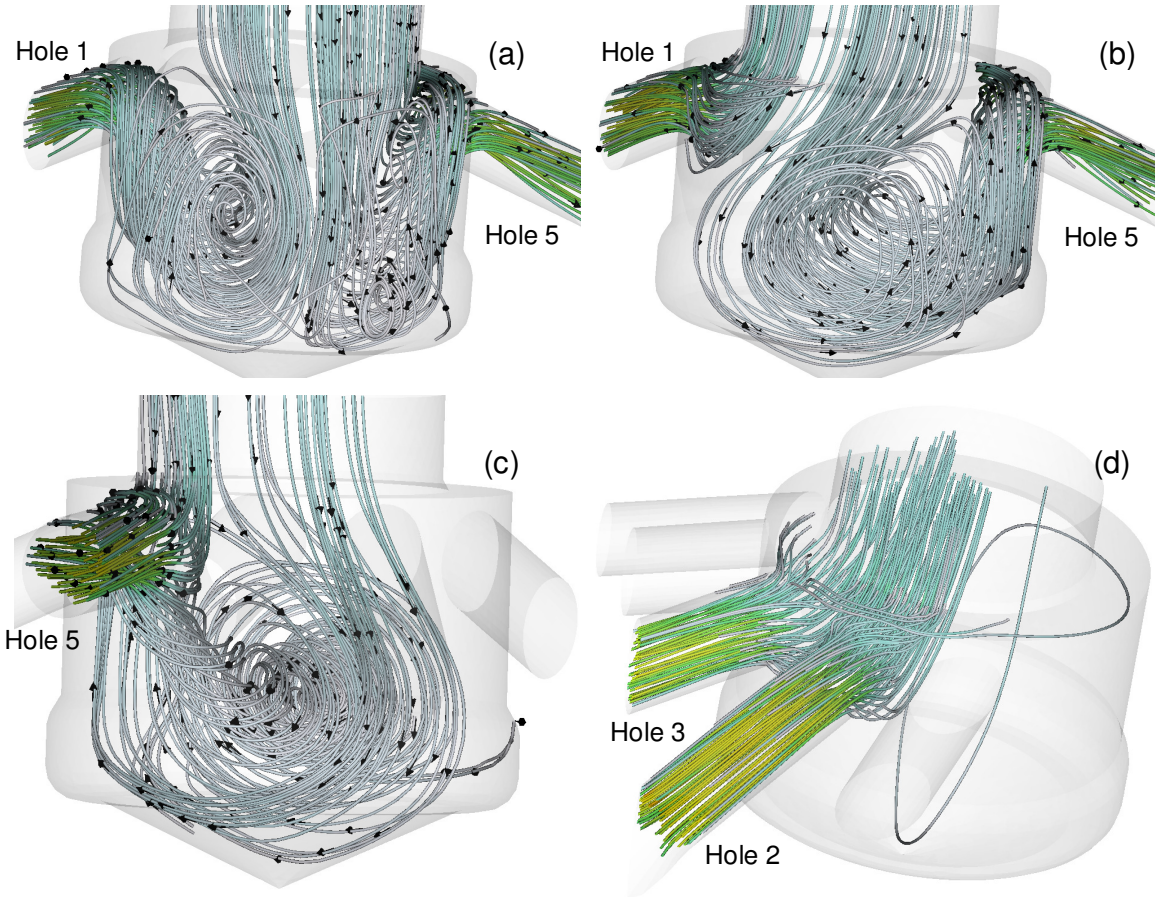

Figure 5-8: Predicted flow structure inside the nozzle volume and the injection holes (a) flow structure with two large vortices entering in holes 1 and 5, (b) flow structure with a large vortex entering in hole 1 (c) the same flow structured as seen from the front view and (d) flow lines entering into string cavitation-free holes 3 and 4. (color scale not significant)

Having identified this instability, Figure 5-8 (b) shows the flow entering in hole 5 been associated with a large vortex, occupying almost half of the nozzle volume, while flow entering to hole 1, now comes directly from upstream. This again changes in Figures 2-8 (c) where flow entering in hole1 is linked to a strong vortex. Finally figure 2-8 (d) shows the flow entering into the middle holes. as it can be seen for these holes the flow is entering

directly from above and are not associated with vortical structures. This is not a random result, after many test cases examined, it was found that for this particular needle lift these holes where always free of vortex flow and no recirculation zones were attached to them. Although the above presented figure is shown as an introduction to the various phases that the flow undergoes inside this kind of nozzles, following figures will show that this variation in string location follows a time pattern which was found in compliance with experimentally acquired results. It also has to be mentioned that this vortex movement inside the nozzle volume was identified both for cases where the cavitation model was turned off, single phase runs, as well as in two-phase ones with nucleation to take place in regions under tension. Such results are presented below, in Figure 5-9 where the streamlines plotted, coloured with the axial velocity component of the incoming liquid, show that this vortex is connected in the first instance to hole 5 and in the second to hole 1.

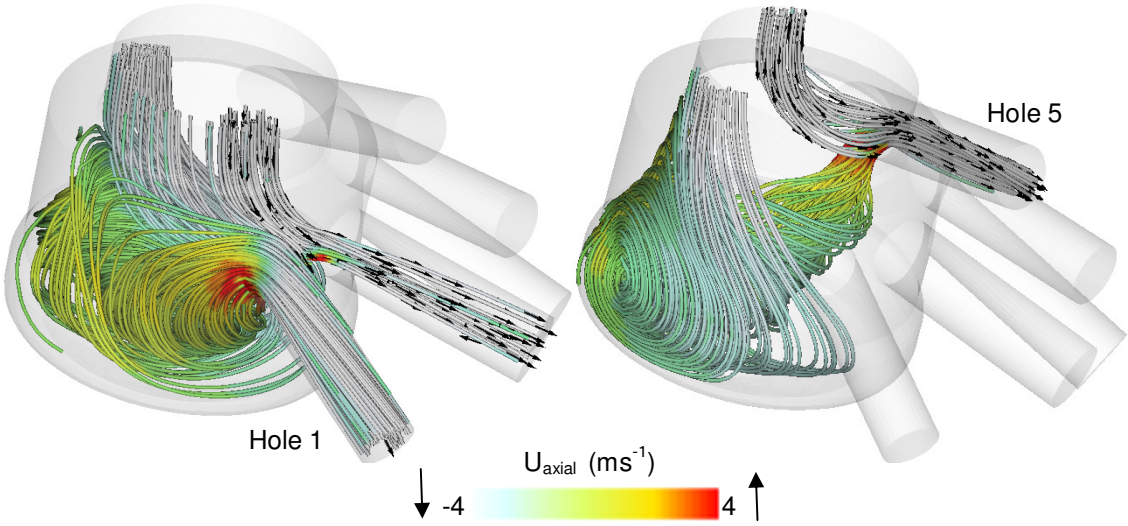

Figure 5-9: Prediction of flow structure inside the sac volume (*a*) path lines of vortex in front of hole 1, (*b*) vortical structure at $\Delta\tau$~100 relative to previous flow, showing the vortical structure located in front of hole 5.

As it can be seen the flow patterns are similar both to those presented in Figure 5-8, as well as to those previously shown in Chapter 4. Later in this chapter the location of vortex as well as the frequency of its appearance will be further analyzed, both by experimental results and predictions.

Irrespective of the vortex motion upstream of the injection holes, as the flow enters through the sharp corner entry hole, the pressure drops locally below the vapour pressure of the

flowing liquid, thus initiating cavitation. Since each hole has a different orientation relative to the nozzle, cavitation initiates at a different location relative to the corresponding hole entry and develops inside in a rather asymmetric three-dimensional shape, which is in compliance with the experimentally obtained images and has been also shown in Figure 5-5. what the following figure intends to show, is the link between the recirculation zone location and the cavitation initiation sites. Although the model does not predict string cavitation, it is interesting to see how the vapour concentration inside the hole changes, when a vortex is attached to the hole.

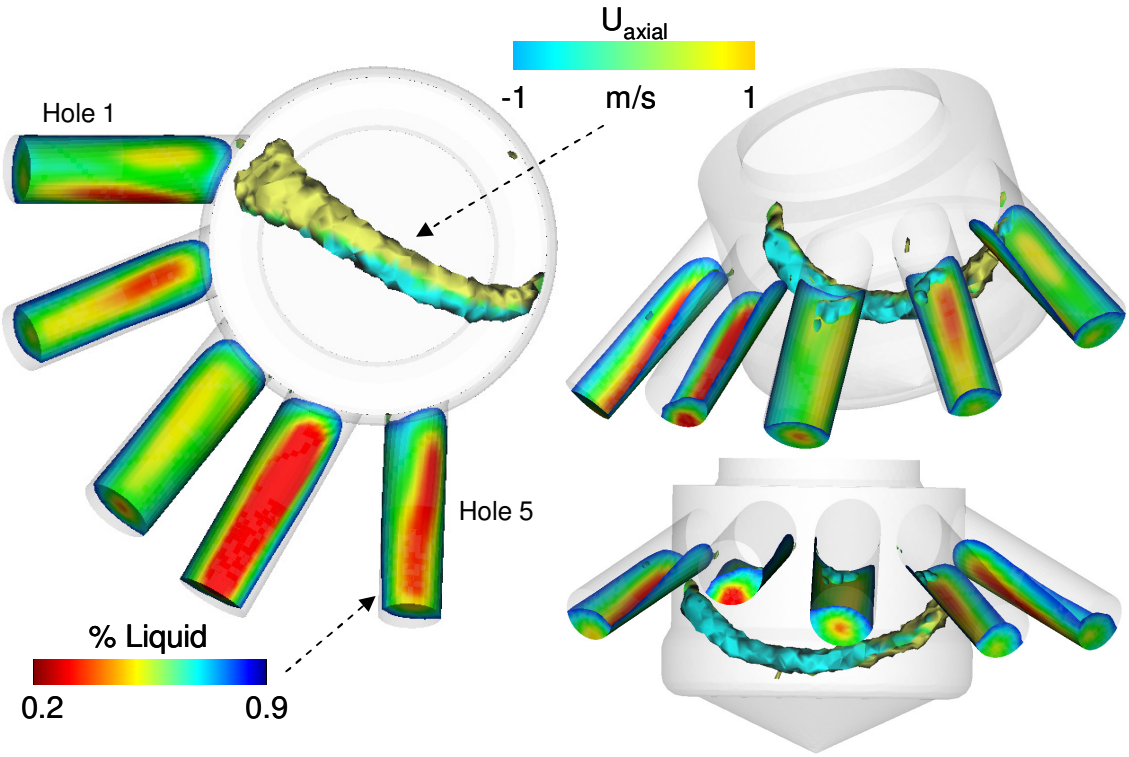

Figure 5-10: Predicted cavitation vapour volume fraction iso-surfaces inside the nozzle holes and core of the nozzle volume vortex colored with the axial velocity component of the incoming liquid, as seen from two different views [nominal needle lift, *CN* =4.0, Re =68 000].

Figure 5-10 shows views of an instantaneous cavitation pattern as predicted by the model in all five holes, together with the predicted core of the nozzle volume vortex. The core of the vortex can be identified from the isosurfaces of the swirl intensity, which is a parameter frequently used to locate and track vortical flow structures according to [137]. The swirl intensity calculation has been implemented to the in-house CFD code and is part of the

work of a group's member, and is defined as the ratio of the convective time t_{conv} (the time for a fluid particle to convect through the region of complex eigenvalues) to the orbit time t_{orbit} (the time for a fluid particle to return to the same angular position):

$$t_{conv} = \frac{2\pi}{|\mathrm{Im}(\lambda c)|} \qquad t_{orbit} = \frac{L}{|V_{conv}|}$$

Where: Im(λc) is the imaginary part of complex pair of eigenvalues (deformation matrix $\rightarrow \nabla \otimes \vec{V}$) and $\vec{V}_{conv} = \vec{V} - (\vec{V} \otimes \vec{n})\vec{n}$, whrere V is the velocity vector and n is the unit vector normal to ω or to the real eigenvector (Deformation matrix). Hence V_{conv} is the projected velocity which is aligned along the axis of the vortex core. Similar to the streamlines presented above the the selected iso-surface is colored with the axial velocity component of the incoming liquid in order to highlight the change in the direction of the flow. As it can be seen from the bottom view (Left), the vapour distribution inside the middle holes, although different compared between them and the side ones, is almost symmetric. Then looking at hole 5 it can be seen that at the hole inlet the concentration is shifted to the right, and towards the hole exit, where the effect of the initial flow conditions at the hole inlet are minimized, it normalizes and follows a symmetrical pattern similar to the middle holes. However, hole 1, which in this particular time instance is associated with a strong vortex, has a totally asymmetric distribution, showing that the vapour concentration has been shifted to the right, and this extends all the way to the hole exit. Considering also the direction of rotation of the vortical flow, by looking the direction of axial velocity, it can be clearly seen that the strong vortex has shifted the direction of the predicted bubbles to the direction of the flow, causing this asymmetric distribution. It naturally follows that this change in VOID distribution will result in a much different initial spray structure compared to the other holes. However this is to be thoroughly investigated in Chapter 6.

Although with the so far results, the link between string cavitation, as presented in Figure 5-6, and the recirculation zones inside the sac volume of the nozzle, as predicted by the various numerical simulations, has been adequately proved, the next series of figures will help in order to further correlate the experimentally observed string cavitation structures with the flow distribution inside the nozzle volume. In order to do that the experimental and the numerical results should be combined into a common domain. By doing that the

accuracy of the aforementioned link would be present graphically making possible to validate also the CFD predictions for such complex flows.

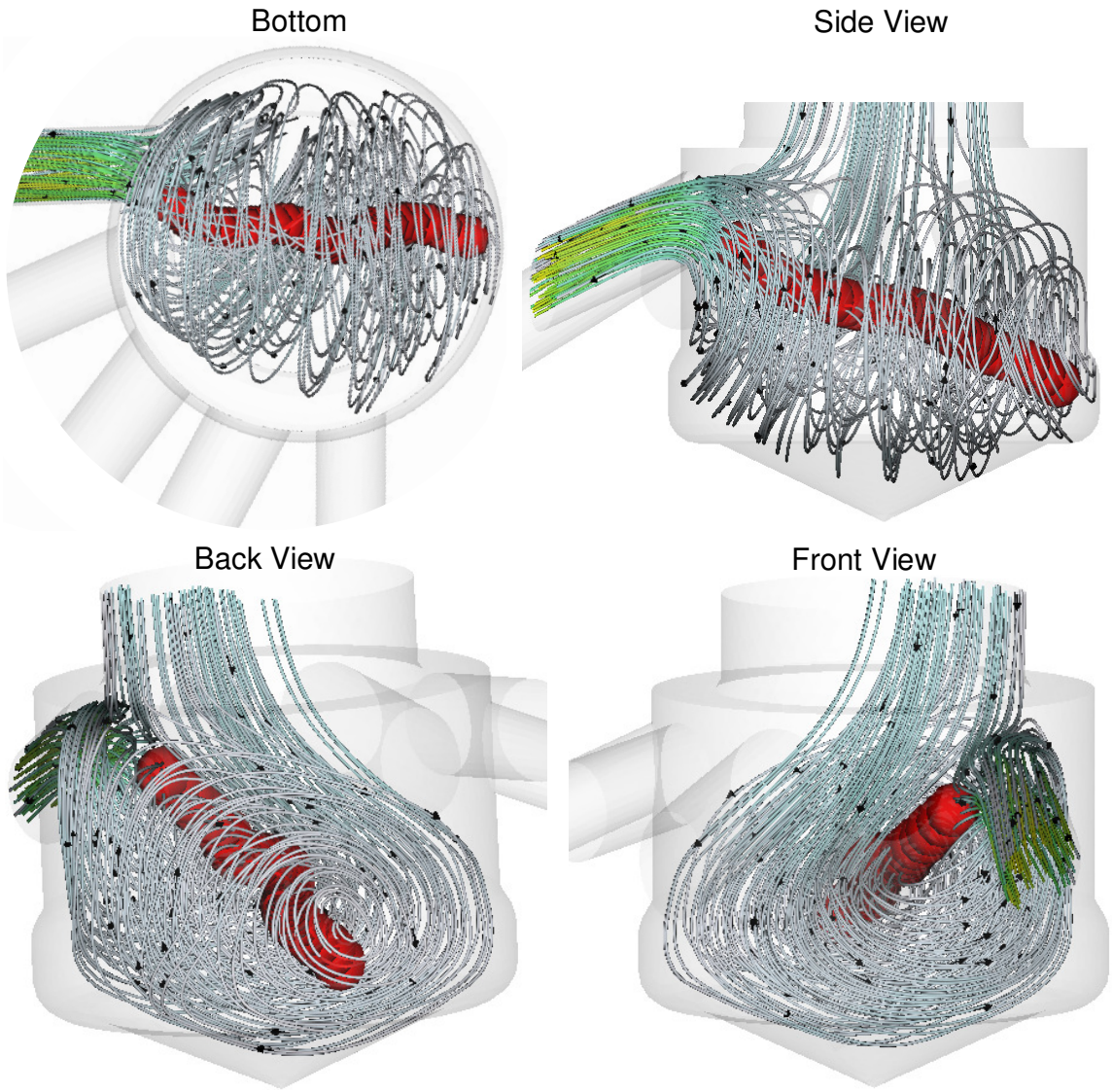

Figure 5-11: 3-D reconstruction of cavitation string inside the nozzle volume superimposed with predicted flow lines exiting from hole No 1 [Case 7]. (colour scale not significant)

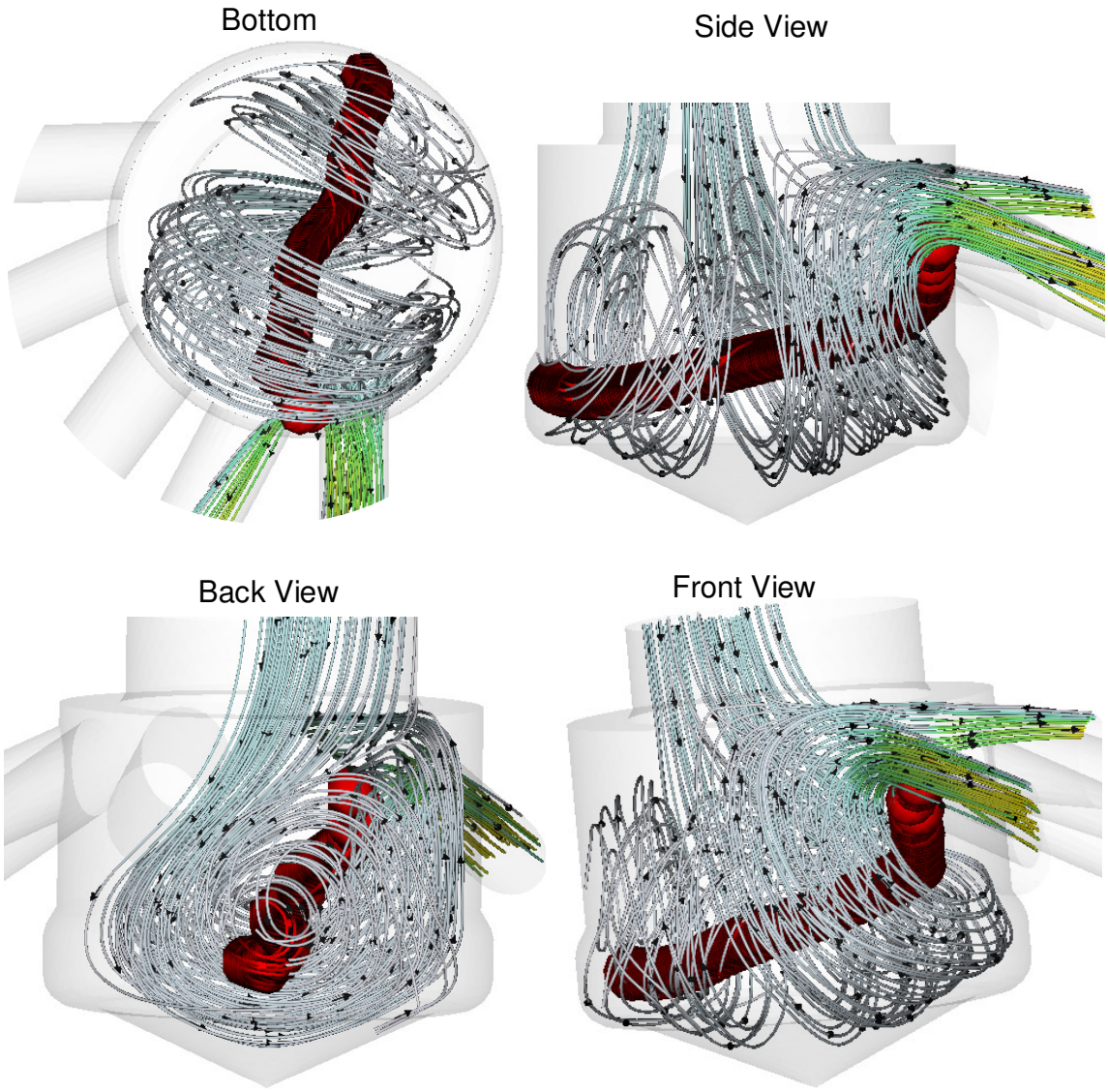

Figure 5-12: 3-D reconstruction of cavitation string inside the nozzle volume superimposed with predicted flow lines exiting from hole No 5 [Case 7]. (colour scale not significant)

In order to combine the predicted flow field and the experimentally observed strings the CCD images, which have been obtained simultaneously from two perpendicular views (bottom and side), have been used to reconstruct the string in the three-dimensional space inside the nozzle volume. The long string was then discretized into a sufficient number of vapour pockets along the string centerline and with radius equal to that of the actual string. Those experimental or 'virtual' vapour pockets, which have the same total volume as the actual string, could be numerically handled as numerical bubbles and inserted into the numerical grid only for visualization purposes, but not for actual multi-phase flow

calculations in this area. Detailed description of all the steps involved in this purpose developed process can be found in Chapter 3, section 3.4.2.

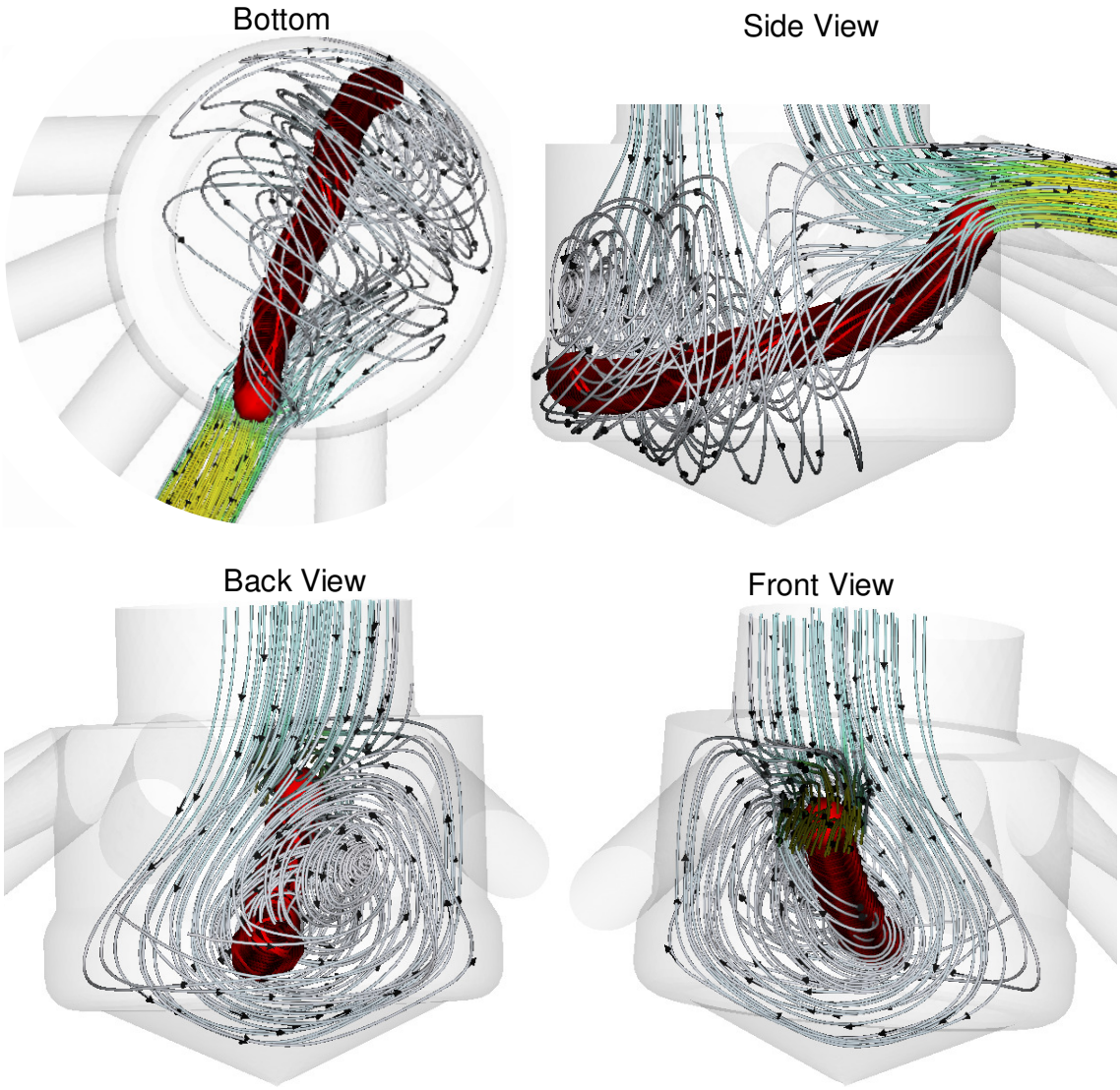

Figure 5-13: 3-D reconstruction of cavitation string (red) inside the nozzle volume superimposed with predicted flow lines exiting from hole No 4 [Low needle lift, CN=4, Re=53,000]. (colour scale not significant)

Figure 5-11 and Figure 5-12 present typical results combining the string cavitation images with the calculated flow field inside the nozzle volume for string been connected to hole 1 and hole 5 respectively. Four plots are presented, corresponding to four different views in order to enhance understanding. As obvious, the results confirm that the observed cavitation strings are formed at the core of the large-scale recirculation zones developing

transiently inside the nozzle volume.

Figure 5-13 shows a similar set of predictions and cavitation string reconstruction, but this time for the low needle lift case where the string is connected to hole 4 only and not to holes 1 or 5, as for the nominal needle lift case. It can thus be expected that the position of the needle affects the formation of the recirculation zones formed inside the nozzle. The effect of needle lift as well as of various flow parameter will be presented later in this chapter.

Having identified the location of the cavitation strings inside the nozzle volume, we can proceed to the presentation of various cases aiming to identify the effect of geometric and operating parameters on the string cavitation structure. Since cavitation strings develop in a highly transient mode and are not always present at the same operating condition (e.g. during the image collection process a significant number of them are string-cavitation-free), it was considered useful to derive mean images.

It has to be noted that from the reconstruction, not only can the string location be correlated with the local flow field, but also their volume can be estimated. However, it is a much simpler approach to derive a mean image only from the bottom view images. The images obtained from the bottom view are superimposed with each other and the pixels where cavitation string is present are identified and averaged for all obtained images. Temporal and spatial averaging includes not only the time steps where string cavitation is present, but also those where it is absent. Since the raw images provide only a projection of the string on the camera plane, the averaged image effectively corresponds to a mean projected view rather than to a full three-dimensional representation. Further details regarding the various processes involved in this technique can be found in Chapter 3. As the following discussion of the results will show, this approach has proved useful in comparing different cases. The following figures to be presented in this section refer to 2-D string cavitation probability plots on the same projected view.

One aspect of this investigation was to experimentally determine at what cavitation number each holes starts to cavitate. Unfortunately, with the enlarged injector it is not possible to simulate the fast opening of the needle, which occurs in a real-size production injector at

the start of injection. The needle in the model nozzle was set to full lift position and the flow rate was increased very slowly by controlling the pump and the valves of the rig, previously described in Chapter 3. Figure 5-14 presents three sets of results corresponding to the initial development of both hole and string cavitation for the low needle lift case.

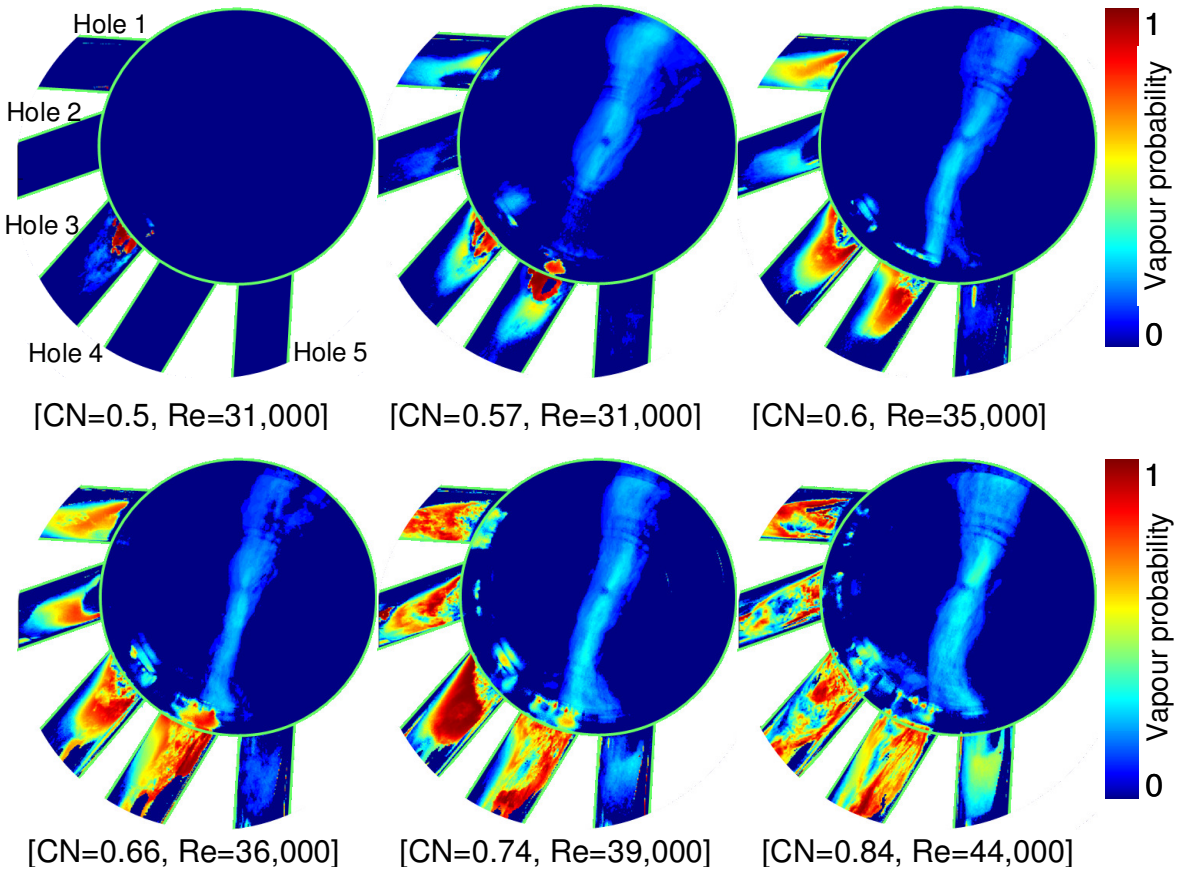

Figure 5-14: Effect of increasing flow rate on two-dimensional temporally and spatially averaged images of string cavitation probability, showing the initial stages of the development of hole and string cavitation. [Low needle lift]

At low cavitation numbers, around 0.5, no string is evident and only hole 3 starts to cavitate. With a slight increase of the cavitation number to about 0.6, all holes start to cavitate, but not continuously, while a string appears to develop inside the nozzle volume and exits mainly from hole 4 and very few times from hole 5. Since the maximum level of the mean image corresponds to about 20% according to the attached scale, and since the observed string is only present more or less in the same location and exits always from hole 4, it can be deduced that string cavitation is actually formed during only 20% of the time of

the whole flow process. A further increase in the cavitation and Reynolds numbers results in a higher probability of string formation. At the same time, hole cavitation seems to become well established in all holes, reaching the exit of holes 3 and 4, but within holes 1, 2 and 5 it disappears before reaching the exit. For cavitation numbers above 0.9, all holes cavitate continuously and the string is entering more frequently in hole 5.

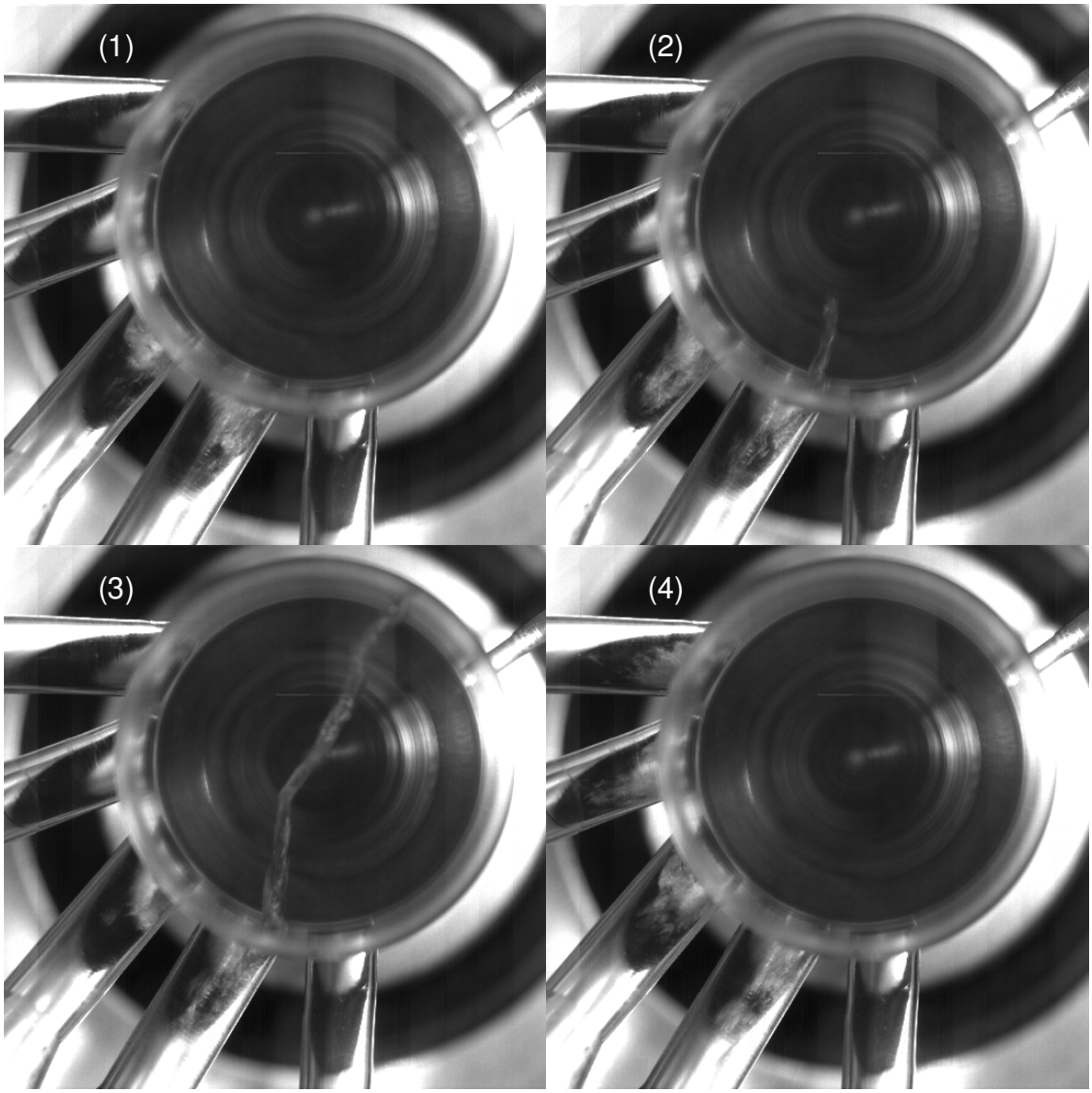

Figure 5-15: Sequence of images showing string induced hole cavitation [Nominal needle lift, CN=0.6]

Following the previous discussion of results regarding cavitation inception, by observing the image sequence in Figure 5-15 for a constant low CN (0.6) and Re it can be seen that: at

the beginning holes 3 and 4 have developed geometric induced cavitation (Image 1). When the vortex flow in the volume becomes strong enough to create the necessary low pressure in its core region, nuclei for the string cavitation in the form of already existing vapour bubbles are sucked out of the cavitating zone of one of the holes (Image 2) into the vortex's core. There the bubbles begin to form the continuous vapour string (Image 3), which extends rapidly along the vortex's low pressure region, i.e. the whole sac volume length. Since the string is in the region of hole 4 and 5 more flow is directed two the other holes i.e. this increase in flow rate makes those holes to cavitate (Image 4) not continuously though. From those results it can be concluded that cavitation initiation is an unstable process triggered by local pressure fluctuations and transient vortices formed inside the nozzle volume and to the entry of the injection holes.

The six images of Figure 5-16 show the effect of cavitation at constant Reynolds number for a test case where cavitation strings appear either in hole 1 and hole 5 side and corresponding to the instantaneous images such as those presented in Figure 2-6. As can be seen, hole cavitation is presented in all holes for these cases. Increasing the cavitation number while keeping the same flow rate (and thus the same mean velocity) results to higher probability of string formation and presence within the nozzle volume. Another interesting feature that can be seen regards the location of these strings within the nozzle volume.

As we can see the end of the string that is attached to the hole, either hole 1 or 5, is more 'tied' than its free end which seems to move more freely in the nozzle volume. This results is a sort of triangular region where string is probable to appear. It also has to be noted that as the CN increases the range of movement of the string also increases.

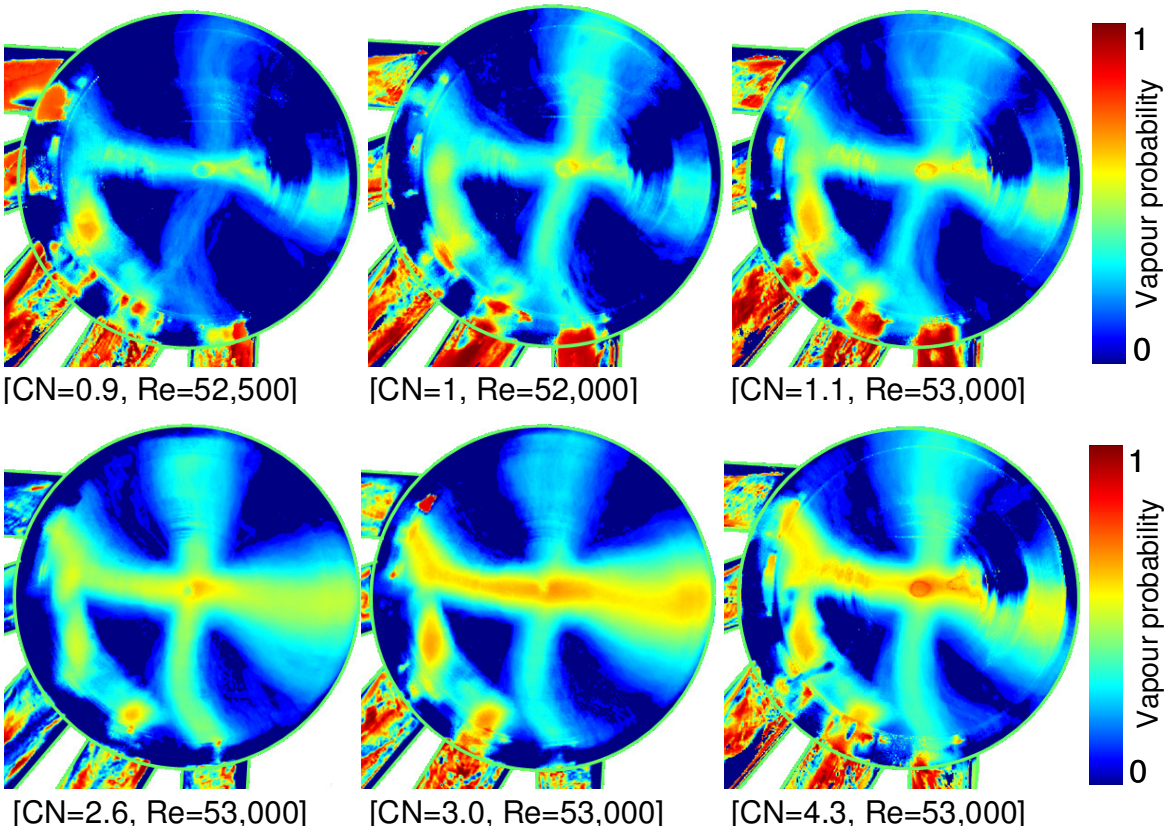

Figure 5-16: Effect of cavitation number on two-dimensional temporally and spatially averaged images of cavitation string probability [nominal needle lift, Re ~53 000]

Further analyzing the figure, it can be said that strings are more frequently attached to hole1, however as CN increases the probability is equally distributed between them. As the mean image for CN=4.3 suggests, the peak of the scale is almost reaching 50% at the centre of the nozzle volume, implying that a string is always present in this location. Considering that the probability of finding a string exiting through hole 5 is about 25%, implies that strings, and thus vortices, which are formed almost with the same probability, do not exist simultaneously. Interestingly enough the region where max probability occurs, i.e. the centre of the crossing string probabilities, lies at the geometric centre of the nozzle, suggesting an interesting symmetry.

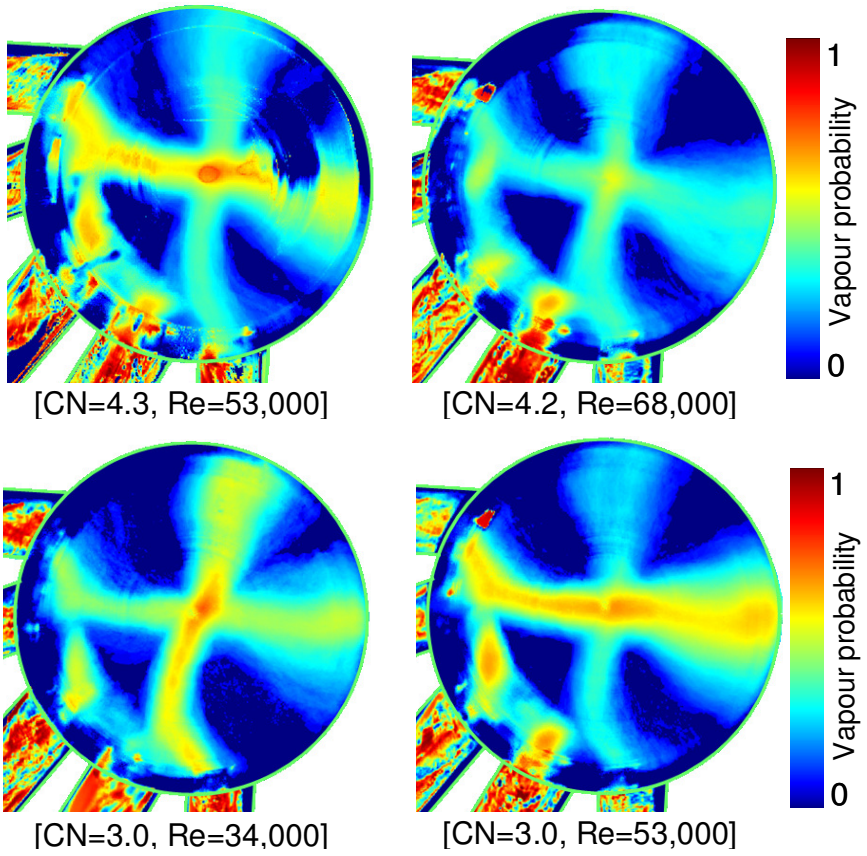

Figure 5-17: Effect of Reynolds numbers on two-dimensional temporally and spatially averaged images of cavitation string probability [Full lift].

Having investigated the effect of CN in string cavitation, Figure 5-17 will help in order to identify the effect of Reynolds number. As we have seen earlier in the chapter, the effect of Reynolds number in hole cavitation was negligible, although for hole cavitation there were extensive experimental and numerical data supporting this finding.; however, there was no relative information regarding string cavitation. The top row shows two mean images of cases having the same CN and different Reynolds numbers. The same stands for the bottom row, for another CN. Comparing the left and right column it can be seen that an increase in the Reynolds number while keeping the same cavitation number may result to a slightly reduced probability of string presence while diffusion (or vapour spreading) is increasing at the same time. Also focussing at the bottom row, we can see that the probability of having a string attached to hole 1, has been increased at the increased Reynolds case, while respectively the probability to have a string attached to hole 5 was reduced. In any case, the differences documented can be considered minor, since the overall probability of having a string in the nozzle volume remained almost unchanged, thus confirming the CN has been

the dominant factor for string formation as well as for hole cavitation. As we will see later on in this chapter, the two cavitation regimes are closely linked.

Having presented the first set of processed data, by performing time and space averaging, one can notice that apart from geometric cavitation existing inside the hole and string cavitation, in the form of a long cylindrical structure extending from the hole inlet up to the opposite sac volume side wall, there are some other spot marks in front of, almost, all holes which vary in presence probability, similarly to the other cavitation structures. These are not artefacts, resulting from image background noise, but are smaller cavitation structures appearing at the space between the sharp edge of the needle and the hole inlet. This can be clearly realized by looking at Figure 5-18, where a CCD image and geometry graphic hybrid is presented.

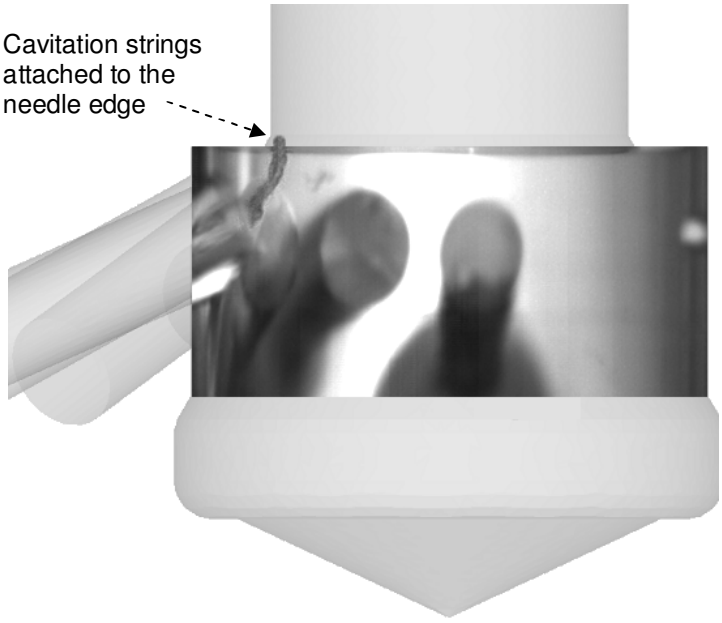

Figure 5-18: CCD image of cavitation structures formed in the space upstream the inlet of the injection holes and the edge of the needle [Nominal needle lift, CN=4.0, Re=53,000].

Although such interactions between the needle and the injection holes have been seen in previous investigations of L-S nozzles [9,117] it was not expected to have similar behavior in this nozzle. What was expected though was that needle lift would have had a strong effect on these structures. As it was found, when the lift was reduced, minimizing also the

gap between the hole's inlet and the needle edge, these form of small strings are also reduced, sine the available space in order for them to evolve is limited. Also when the lift increases from nominal, the needle edge is moving away from the hole's inlet and therefore the geometry becomes smoother, minimizing the small vortices that cause these strings. Following figures to be presented will show this interesting behavior.

So far from the results presented by using the averaging technique, it can be concluded that for the range of parameters tested in this experiment, it was not possible to identify important differences in string appearance frequency and location once the flow was becoming fully developed (after CN=1 for nominal needle lift) for a particular operating point.

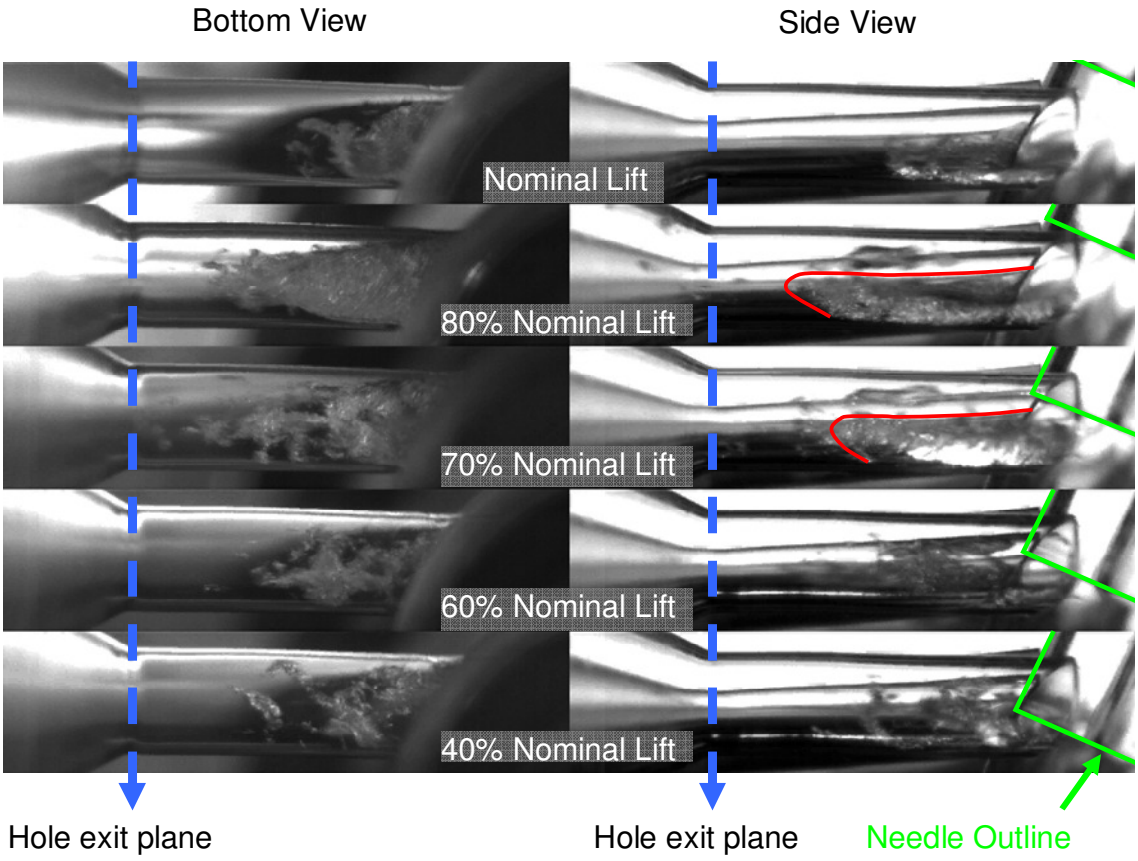

Figure 5-19: Hole Cavitation structure, and its variation with needle lift, inside Hole 1. Side and Bottom View [CN~1, Re~32,000]. Red line describes the boundary of cavitation inside the injection hole.

The next parameter that was investigated was needle lift. Before presenting the effect of needle lift on string cavitation formation, its effect on hole cavitation is shown in Figure 5-19. in this figure fine different needle lifts are shown for similar flow conditions. the hole investigated is hole 1 and the green lines show the outline of the needle in order to highlight its position compared to the hole. Starting from the top row, nominal lift, it can be seen that cavitation is established, however it only reaches up to the first third of the hole and then breaks up. The next row correspond to an 80% lift, and as it can be seen cavitation has become stronger extending to almost 2/3 of the hole length. At this lift the needle's edge is in line with the upper corner of the hole inlet. Moving to the next row the lift has been further reduced to 70% of the nominal. As it can be seen the flow is suppressed and as a result the restricted flow causes cavitation to shrink. The last two rows, corresponding to 60 and 40 % lift respectively, show significantly reduced cavitation, with bubbles breaking up few millimetres after the hole inlet. With needle covering almost 80% of the hole, the flow has to turn into a very steep corner in order to enter the hole. This causes deceleration which in turn reduces the regions of negative pressure and thus cavitation.

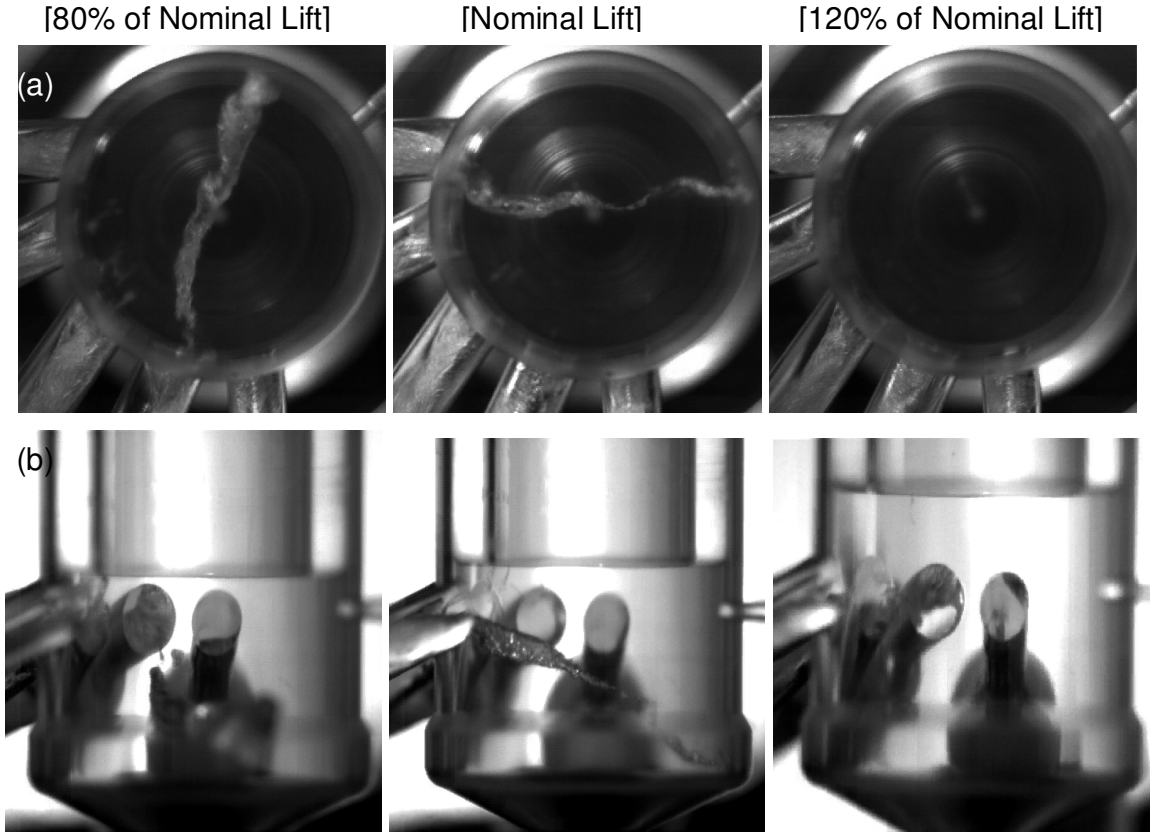

Figure 5-20: Typical image of string cavitation formed inside the nozzle volume at three different lifts (a) bottom view and (b) side view [CN =4.0, Re =53,000].

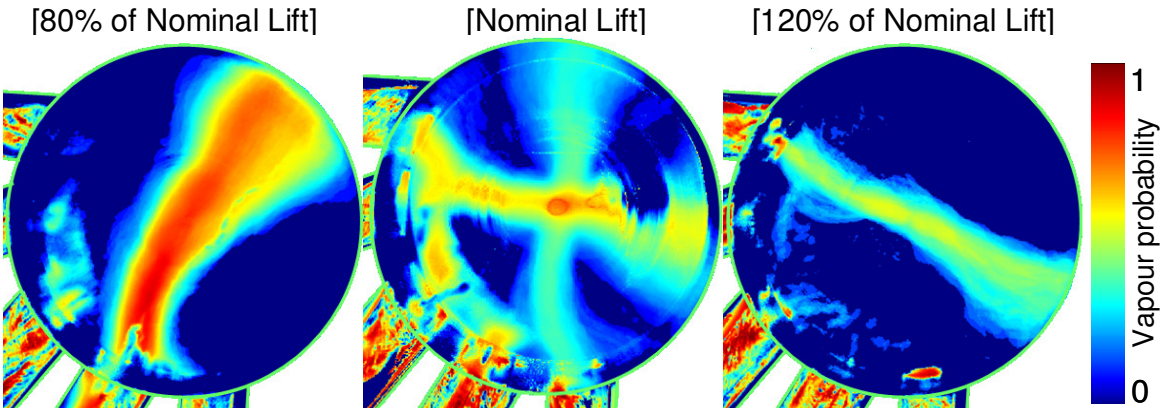

Figure 5-21: Effect of needle lift on two-dimensional temporally and spatially averaged images of cavitation string probability [CN=4, Re=53,000].

Having presented the effect of needle lift on hole cavitation, the next step was to find the effect of lift on string cavitation. The effect of the geometry was found to play a much more important role than CN and Reynolds. This can be seen in Figure 2-20, which presents again the probability of string presence on the same projected 2-D plane. Three mean images are presented corresponding to 80% of the full lift, full lift (defined from the actual needle stop position of the real injector) and 120% of full lift. It is evident that those small needle lift variations result to a huge change of string location. For the low needle lift case, string is exiting only through hole 4 and it is consistently present. Increasing the needle lift to its nominal full stage, the two-string structure is taking place, as described above. A further increase of the needle lift results to the completely disappearance of the hole 5 string. In this case, strings are exiting only through hole 1 but with a reduced probability, as the significantly reduced maximum levels indicate.

Having seen the probability in the 2-D projected space for various operating conditions, the next step would be to define the probability of string formation in the 3 dimensional space. The approach of reconstructing the experimentally obtained strings by combining the two projected views, has been presented in section 3.4.2 and the first results were shown in Figure 5-11 through Figure 5-13. however the presented results corresponded to particular time instances and although the shape of the string could be visualized accurately, its variation and movement inside the nozzle volume was still to be found. In order to do that a series of reconstructions were performed for all the strings obtained within a set of selected

cases. This meant an average of 500-800 string per case expressed as spherical vapour pockets having a x,y,z coordinate and radius.

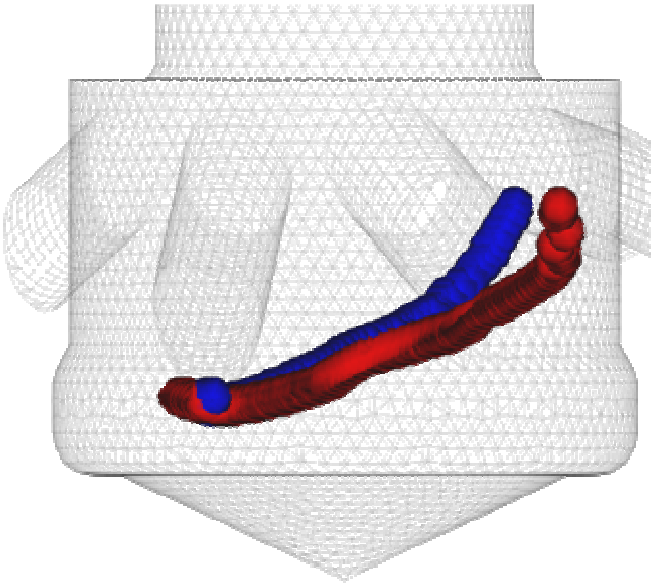

Figure 5-22: 3-D schematic showing two strings corresponding to different time instances in the nozzle sac volume.

Having the string discretized, these sets of virtual pockets were inserted into the discretized nozzle volume, as shown in Figure 5-22 and by performing Spatial and temporal averaging of a sufficient number of strings it was allowed to estimate the probability of finding a string present in the 3-D space.

A typical result from the aforementioned process is shown in Figure 5-23a and Figure 5-23b for the Full lift and the Low needle lift cases, respectively. On these plots, three iso-probability surfaces are plotted. The first one depicts the most remote location where strings may reach as they transiently move inside the nozzle volume, which practically means the boundary after which no vapour in the sac volume was found. The second iso-surface value plotted for the low needle lift case (Figure 5-23b), where strings have been found to be continuously present, corresponds to the boundary where strings are present 50% of their life time.

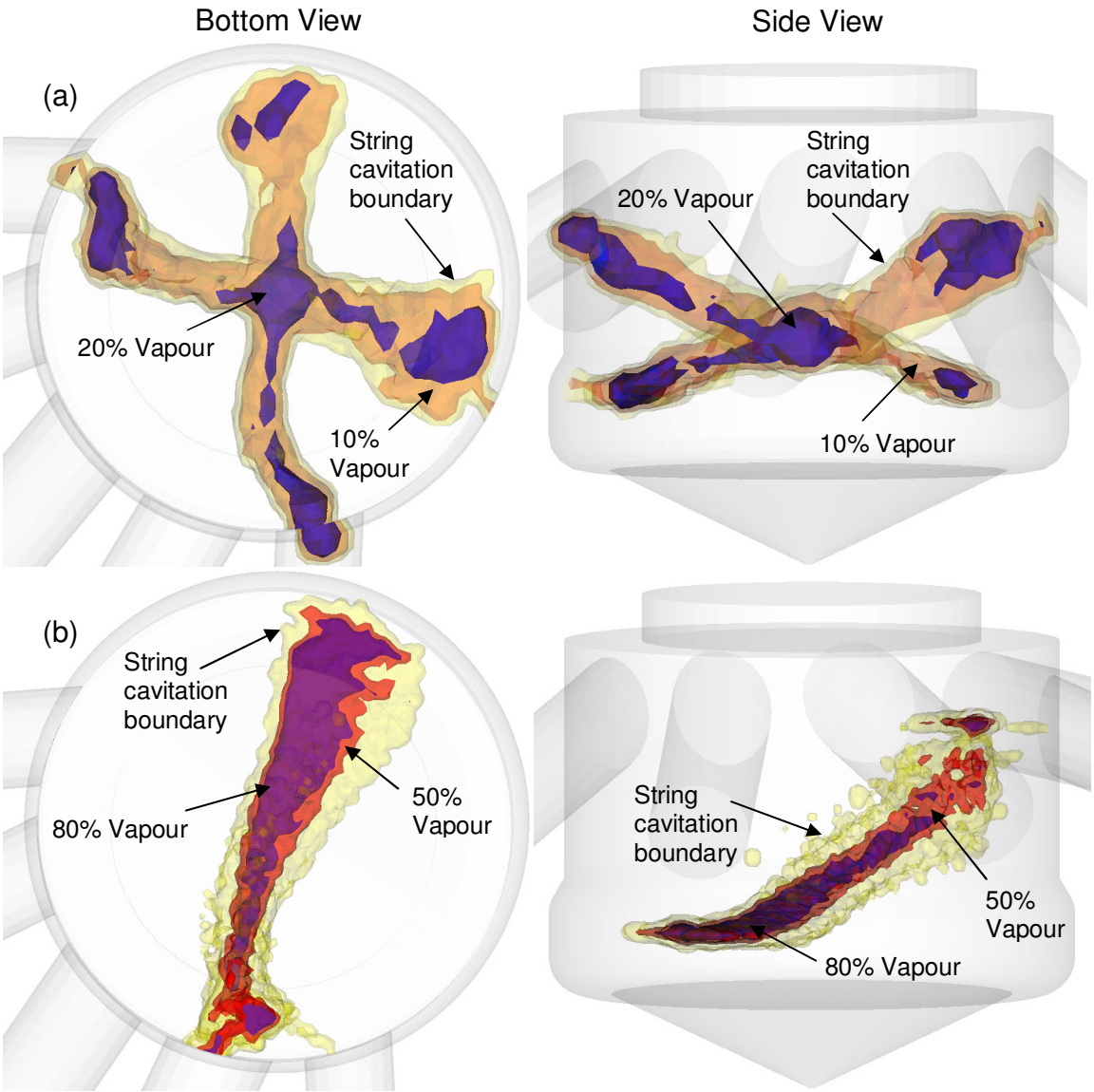

Figure 5-23: Three-dimensional iso-surfaces of cavitation string cavitation probability for (*a*) low lift and (*b*) nominal lift [CN=4, Re=53,000].

Finally, the last one on the same figure shows the iso-surface of 80% vapour, which can be interpreted as the volume always occupied by cavitation strings. For the nominal needle lift case, strings are observed less than 50% of the running time and they are attached either to hole 1 or hole 5 and never overlap with each other. This implies that the maximum calculated probability value should be less than 25%; the 10 and 15% iso-surfaces plotted reveal the string structure for this particular operating condition. As it can be seen the results obtained in the 3 dimensional space match those previously presented in the

projected averages and additionally provide information regarding the movement and variation of the strings in the axial direction. The interesting observation from these figures is that while the location of the string varies a lot in the x-y plane, by changing hole position, its movement in the z-axis is limited. It can also be seen that the string are always attached to the groove present in the sac volume, and thus make almost a 45^0 degree angle in order to get to the injection hole, and the possibility of some sort of interaction had to be further investigated. As it will be shown later this orientation depends on the internal flow and not to the geometric characteristics of the groove.

As we have seen so far the location of the strings was thoroughly invested and their probability of appearance inside the nozzle has been also shown both in 2-D and 3-D space. Moreover, it was found that the strings are associated with the vortical structures inside the nozzle volume, which are well predicted by the in-house CFD code. Since For the nominal needle lift case it was shown that the position of the string changes between the two side holes, it was considered useful to register the time sequence of appearance of cavitation strings. The following figures to be presented show the time history of the string presence for the nominal needle lift case for various flow conditions. On these plots, three bar values are plotted on the *y*-axis, corresponding to string attached to hole 1, to hole 5 and no cavitation string. The *x*-axis corresponds to the dimensionless time τ introduced previously. With this scaling, it is possible to identify the frequency of vortex formation inside the sac volume and, thus, the Strouhal number of the recorded periodic flow pattern. Such graphs were also shown in Chapter 4 in order to investigate the effect of different grid sizes and turbulence models on vortex location movement.

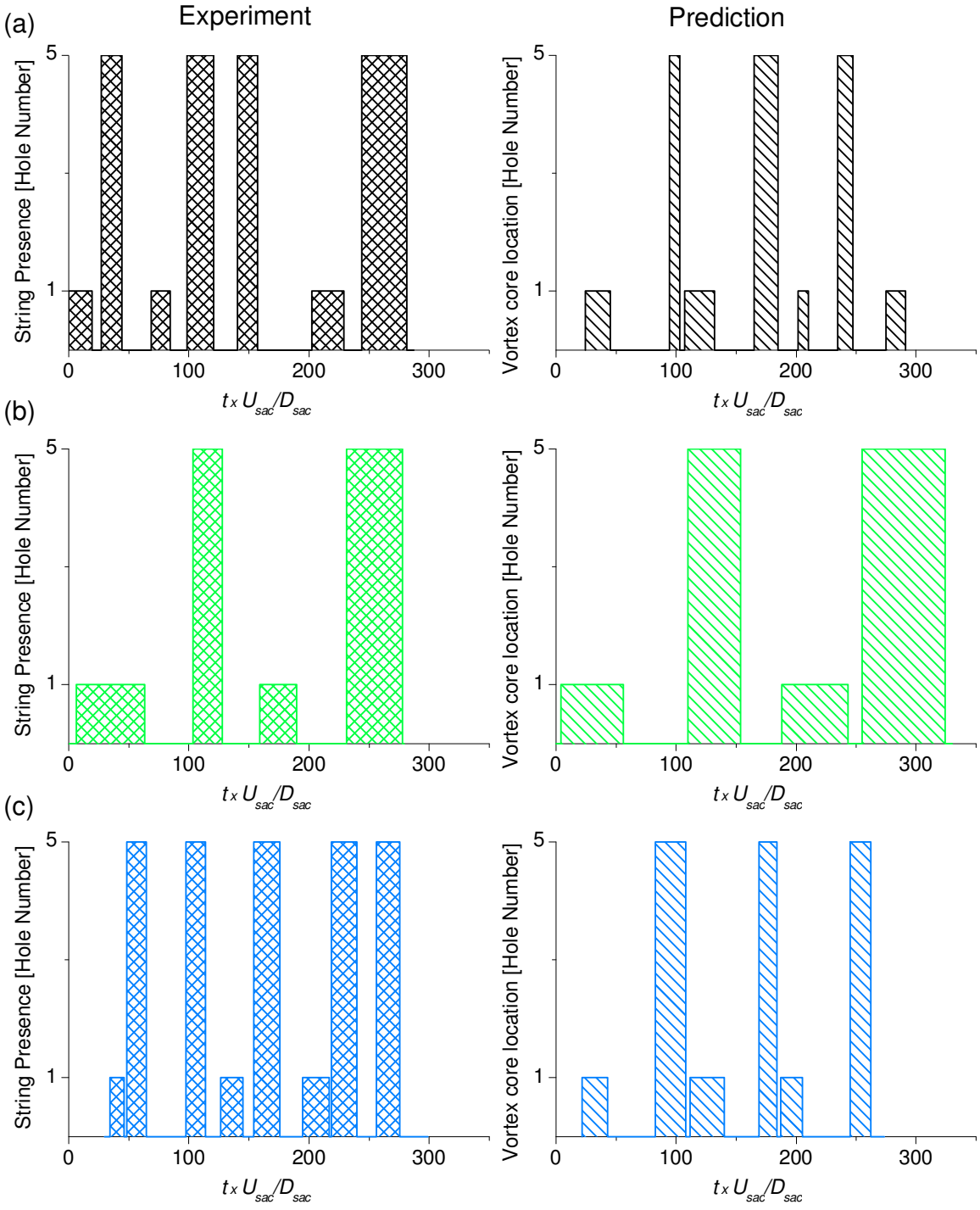

Figure 5-24: Comparison between measured temporal development of string cavitation presence next to holes 1 and 5 and predicted vortex core presence attached to these holes for (a) Re =68,000, with expansion tubes, (b) Re =53,000, with expansion tubes, (c) Re =68,000, without expansion tubes. [CN ~4.0, nominal needle lift]

Figure 5-24 is comprised by six (6) plots showing the string appearance frequency from three different experimental cases, left column, and the vortex core location movement frequency for the same experimental conditions, right column. Regarding Figure 5-24 (a), from the experimental results, it can be observed that there is no string overlapping period while the time interval between successive string appearances is almost the same as their lifetime; the latter is of the order of $\tau \approx 15–20$ for this particular operating condition. Cavitation strings reappear in front of the same injection hole about every $\tau \approx 70–80$. A similar set of predictions, this time for the presence of the vortex core in front of the corresponding injection hole are shown in the right column plot. The core of the vortex can be identified from the iso-surfaces of the swirl intensity shown previously in figure 2-10. it has to be mentioned that the iso-surface used has been selected in such a way as to have the same diameter as that of the observed strings near the inlet to the injection holes. Note the close similarity between the observations and model predictions.

Moving to Figure 5-24 (b), we can see a similar set of plots as in (a) but for a lower Re number. As it can be seen for this case the time interval between successive string appearances has been increased but also the string/vortex lifetime has been increased. This also explains why the mean images for different Reynolds numbers were almost the same, since the overall lifetime of the observed strings for both cases was almost the same.

Soon after the first experimental results obtained using the close loop flow rig and the enlarged nozzle model having expansion tubes after the injection holes exit, as shown in Figure 3-8, in order to collect the emerged liquid, there was the need to investigate if the results would have been the same for spraying nozzle, i.e. without expansion tubes (Figure 3-17). As it might be thought, since the following step of this investigation would have been to visualize the near hole exit spray structure, it was of great importance to verify this similarity since such an information had not been presented in open literature before. As it can be seen Figure 5-24 (c) correspond to the same operating conditions as Figure 5-24 (a) but without the existence of expansion tubes. A quick comparison of the results verify that the existence of liquid collectors does not affect the formation of vortices and strings inside the nozzle. This finding provides an additional proof that the string formation mechanism inside the sac volume is caused by the internal nozzle flow field.

Concluding Figure 5-24, model predictions reveal that the vortical structure formed inside the nozzle volume is moving with a low-speed circumferential velocity component relative to the nozzle axis. Cavitation strings appear when the core of the vortex is attached to an injection hole. The combined experimental finding for the string lifetime and the predicted flow pattern lead to the conclusion that cavitation strings appear when the nozzle volume vortex is attached to an injection hole. This is an important conclusion and will be further supported in the following section of this chapter when the origins of cavitation strings will be investigated.

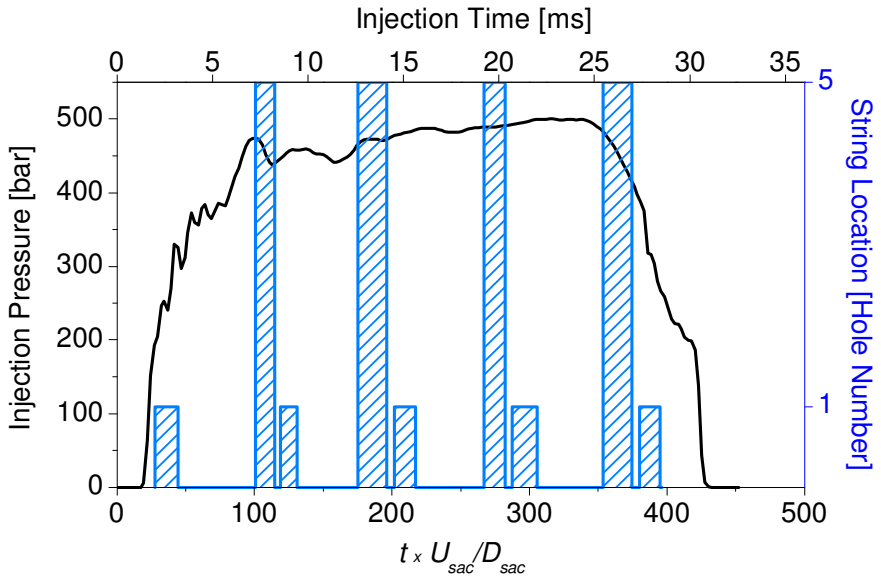

Figure 5-25: Input pressure boundary condition used for the simulation of the internal nozzle flow for the real-size injector operating under engine conditions with superimposed the predicted temporal evolution of the vortex presence in holes 1 and 5; the similarity with the large-scale nozzle presented in figure 2-23 (c) is evident.

It naturally follows that the next to be confirmed was whether similar patterns in string/vortex frequency would have been found for real operating conditions. Figure 5-25 shows similar to the previous figure predicted vortical structure presence in front of holes 1 and 5 for realistic operating conditions that may provide evidence for the appearance of strings during engine operation. On the same plot, the injection pressure profile used is shown. this pressure profile has been provided by the engine maker and is used by production engines, the pressure is measured under engine operating conditions just upstream of the nozzle inlet. It is clear that model predictions suggest at least 3 events of string cavitation formation even for the much shorter injection event. The vortex develops

during the same normalized time τ with almost the same frequency, thus the same Strouhal number; thus this scaling can be used to extrapolate results from the transparent but low flow rate nozzles to the actual injectors operating at much higher pressures.

It has to be mentioned that similar computational results have been obtained for a wide range of parametric studies, which can be found in Chapter 4, which have addressed the effect of spatial and temporal discretization methods, including first- and second-order ones, the effect of the time step which has been reduced down to two orders of magnitude, the effect of the number of computational cells which has been increased four times as well as the effect of different turbulence models, including different realizations of the k-ε model, the k-omega and the Reynolds stress one. Out of these studies, it has been safely concluded that model predictions are not sensitive to these parameters with respect to the formation and development of the nozzle vortical flow structures.

5.4 Results - Internal nozzle flow marine tapered injector - String cavitation

Although until this point we have seen the dependence of string cavitation on various flow parameters, we have still not positively identified the mechanism of their formation. The next set of results to be reported will help to find the origin of the cavitation strings. As already mentioned, the location of the string has been correlated with the core of the vortex formed inside the nozzle volume. Furthermore, it has been argued that one mechanism for the appearance of cavitation strings is associated not only with the existence of the vortex, but with its direct link with a cavitating site formed at the hole inlet. Formation of vortex cavitation as a result of the pressure drop within the core of the vortex has been abandoned as a mechanism on the basis of model predictions which indicate pressure levels much higher than the vapour pressure of the flowing liquid. In other words, combination of experimental observations and model predictions has indicated that cavitation strings form from pre-existing cavitation sites.

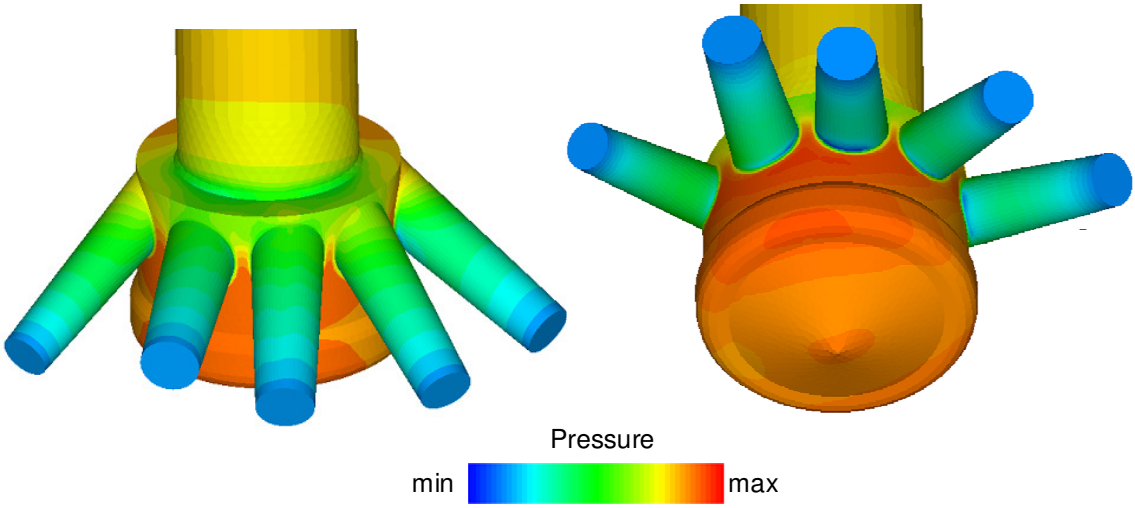

Figure 5-26: Predicted pressure distribution inside the tapered large-scale 5-hole nozzle [High needle lift, CN=3.0, Re=53,000]

This means that if the vapour formed by geometric cavitation inside the injection holes comes into contact with a vortex, then vapour may be trapped inside the vortex core and form the observed string cavitation structures with the high-speed camera. It follows, that if this assumption is correct at no cavitation conditions there would have been no strings. Actually this could be confirmed by the low cavitation results shown earlier in Figure 5-14, however one could say that the fact that there were no strings was due to the low flow rates.

Therefore in order to provide adequate support to this hypothesis a nozzle had to be manufactured that would have been free from hole cavitation even at high CN and Reynolds numbers. For this reason two transparent nozzles with tapered (converging) holes have been manufactured, as explained in detail in section 3.1.3. As it can be seen in Figure 3-10 the first nozzle incorporates expansion tubes and the second, Figure 3-14, does not, while the rest of the geometry was kept identical to the original nozzle design with the cylindrical holes. As preliminary model predictions have shown in Chapter 4, hole cavitation should not be expected for this nozzle since the pressure distribution at the hole inlet is greatly modified by the hole shape. Therefore conical holes create a much smoother pressure gradient, also shown in Figure 5-26 for the large scale conical nozzle, and do not cavitate even for much higher pressures relative to the cylindrical ones due to pressure recovery downstream of the hole inlet. This is a well-known characteristic for such nozzles which also exhibit a higher discharge coefficient, as reported by [148] and will be further

supported in later chapters where the flow inside tapered multi-hole nozzles will be presented.

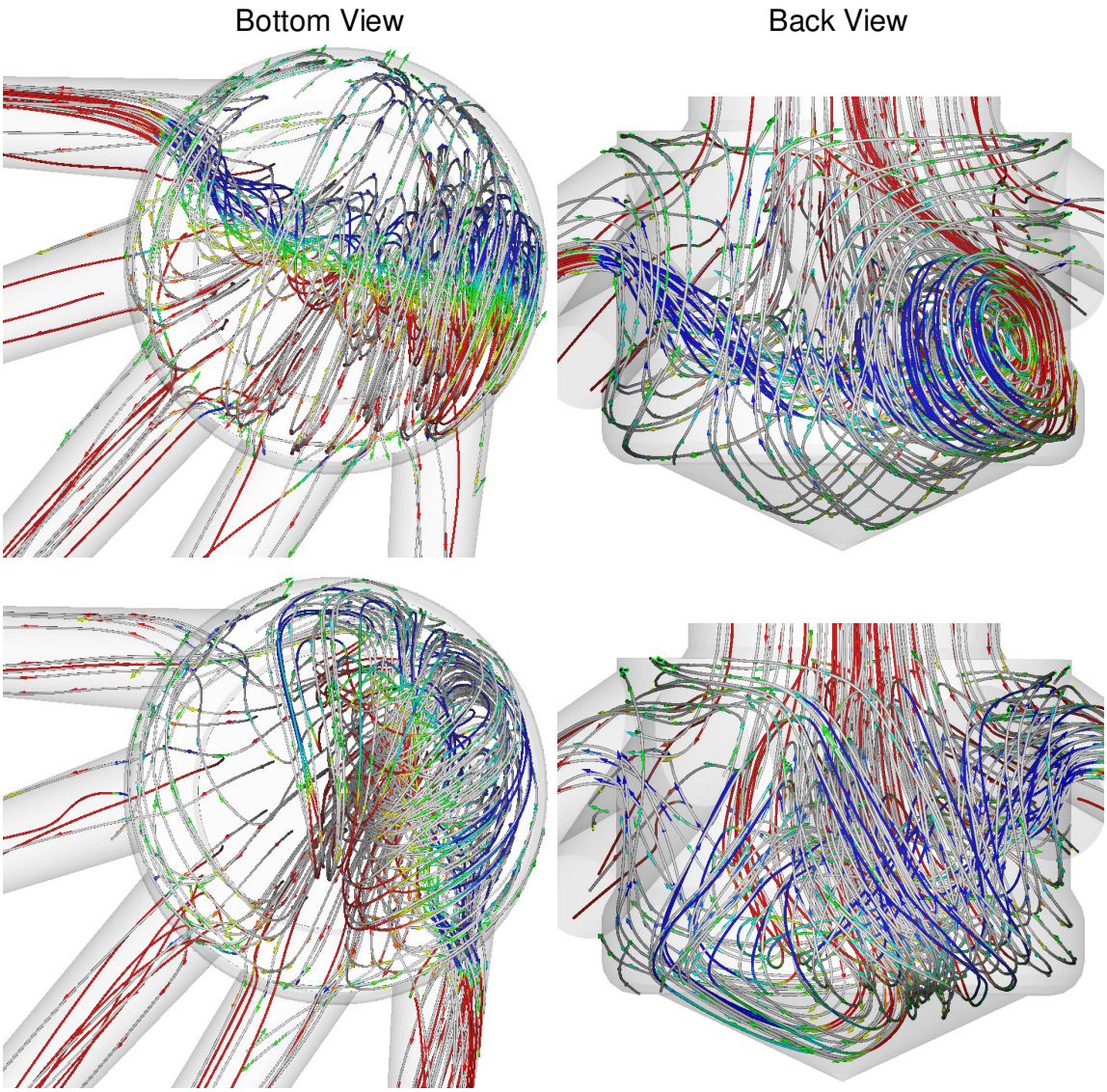

Figure 5-27: Prediction of flow structure inside the sac volume of the tapered large scale nozzle (*a*) path lines of vortex in front of hole 1, (*b*) vortical structure located in front of hole 5. (color scale not significant)

Although the conical nozzle design was expected to be free of hole cavitation, it was required to also have similar flow distribution as the one existing inside the sac volume the nozzle with cylindrical holes. As preliminary predicted flow results, reported in Chapter 4, had shown the vortical structures were also existed inside the tapered nozzle and further evidence is shown in Figure 5-27 where the simulated flow field for the large scale tapered nozzle is shown.

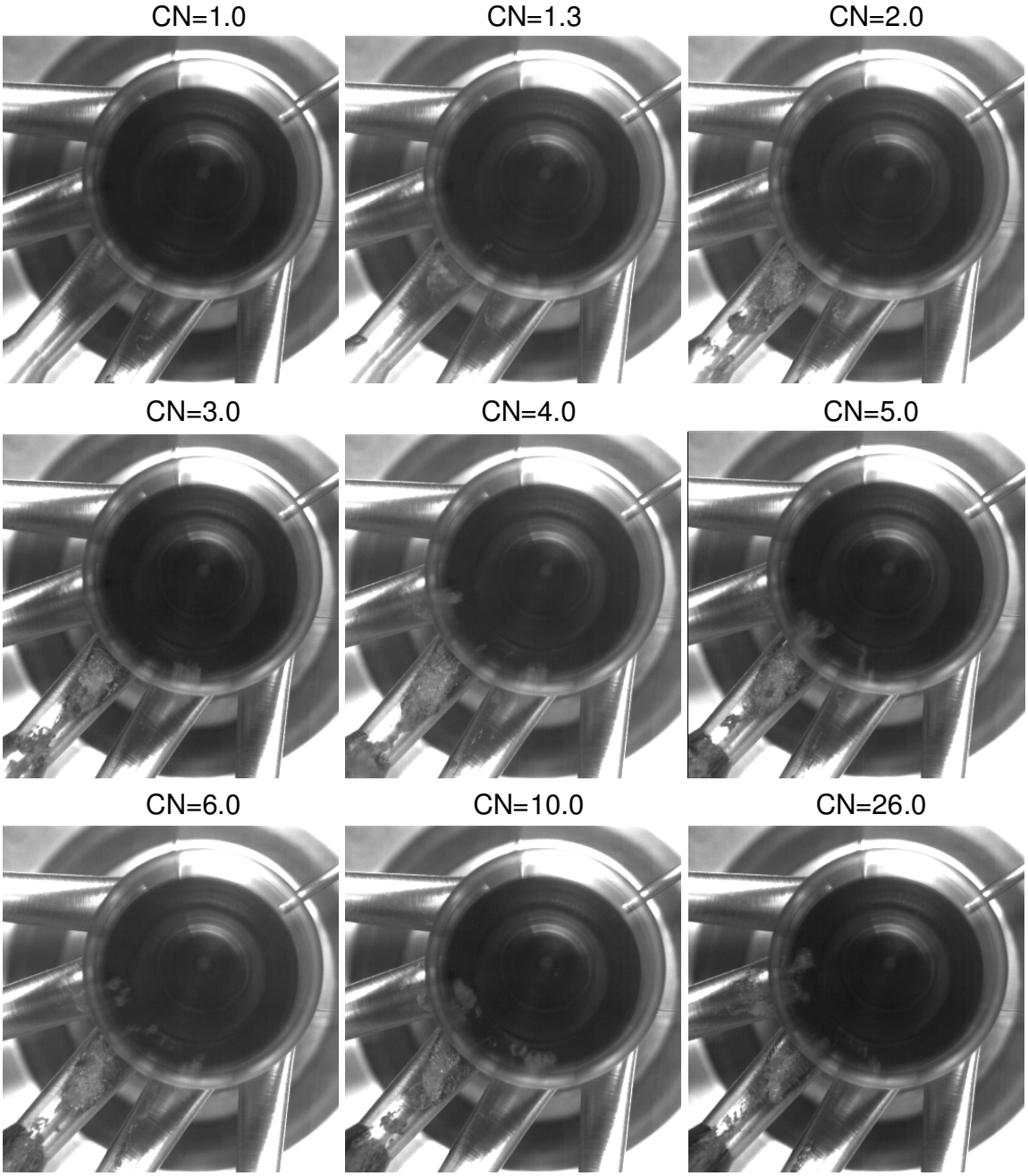

Figure 5-28: Representative images for the tapered 5-hole large scale nozzle for different CN values, showing no string cavitation. [Nominal needle lift, Re ~55,000].

As it can be seen, the vortical structure inside the nozzle is still present and follows a similar pattern of motion as in the previous nozzle for the same needle lift. However, some differences do exist and will be reported in the following section where detailed processed results will be shown. Before we proceed into presenting experimentally obtained results, it

has to be mentioned that due to the increased inlet hole diameter of the tapered injection holes, in order to have the same exit diameter, the needle position had to be reallocated. This means that in order for the upper part of the injection hole inlet of the tapered nozzle to have the same distance from the needle edge of the cylindrical holes one, the lift was sifted almost 20% upwards. This practically means that the nominal needle lift of the tapered nozzle corresponds to the high lift of the cylindrical one. This deviation is not expected to play a role in string formation since it is the relative position that affects the flow and not the actual one.

Visualisation of the flow inside the nozzle with the expansion tubes, which is the case for injection of liquid into liquid, has revealed that this design was string-cavitation free. Figure 5-28 shows typical images of bottom-view CCD for the nozzle operating at high Reynolds number and various CN numbers. The needle was set at high lift corresponding to the same hole to needle distance as in the nominal lift for the cylindrical nozzle. As it can be seen at CN=1 the nozzle is free from any form of cavitation, it has to be reminded that as Figure 5-16 suggests for the cylindrical nozzle there was both hole and string cavitation. As the CN increases it can be seen that Hole 3 starts to cavitate. Also a further increase in CN enhances the small strings caused by the needle edge interaction similarly to what we have seen in Figure 5-18 before. It also interesting to observe that even at very high CN values (CN=26) cavitation collapses within the injection hole before cavitation bubbles could reach the hole exit, whereas in the cylindrical hole nozzle after CN=4 there was fully developed cavitation in all holes that was extending all the way to the hole exit. Most importantly it is shown that the nozzle for this particular lift condition is free of string cavitation. This observation combined with the internal nozzle flow and the fact that the holes associated with vortices were free of hole cavitation further supports the previous stated assumption that if the vortex does not come in contact with an existing vapour site, string cavitation will not occur.

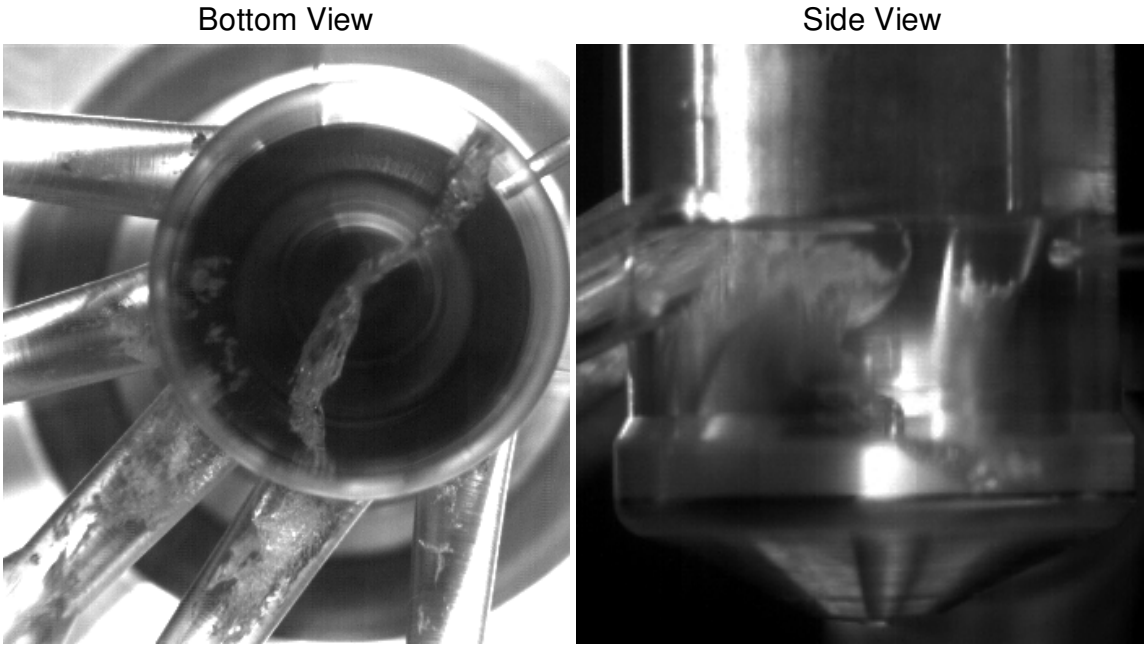

Figure 5-29: Representative images for the tapered 5-hole large scale nozzle at low needle lift showing presence of string cavitation next to hole 4 [CN=2.0, Re =52,000].

As it was shown in the previous figure, due to their position and the closer distance with the needle edge as well as due to the smaller gap between them, the middle holes showed evidence of cavitation initiation. Therefore it was interpreted that a lower lift will enhance this hole – needle interaction and possibly could lead into well established cavitation inside the holes that had been associated with vortices at lower lifts, i.e. hole 4.

Figure 5-29 shows typical bottom and side CCD images from a low needle lift case. As it can be seen at this lift hole 4 has developed hole cavitation and since the vortices are now also attached to that hole, a thick string of cavitation is also present in front of it, similarly to the results that have been obtained in the cylindrical nozzle. It also has to be mentioned that at the same needle lift and a further increase in CN the string position changed to hole 2, while still being steadily attached to one hole and not fluctuate in position as in full lift conditions presented before. Although the mechanism that triggered this event is not clear, it can be interpreted that due to the change in hole cavitation intensity, the vortical structures inside the nozzle have changed orientation. As we will se later there is a direct link between hole flow rate, cavitation and string/vortex location. The result obtained at low needle lift and higher CN can be seen in Figure 5-30 below. It also interesting and useful to observe that as CN increases, thus increasing vapour available inside the injection

hole, the thickness of the string also increases. This will also be confirmed in Chapter 7 where the flow inside a tapered hole multi-hole transparent model will be investigated.

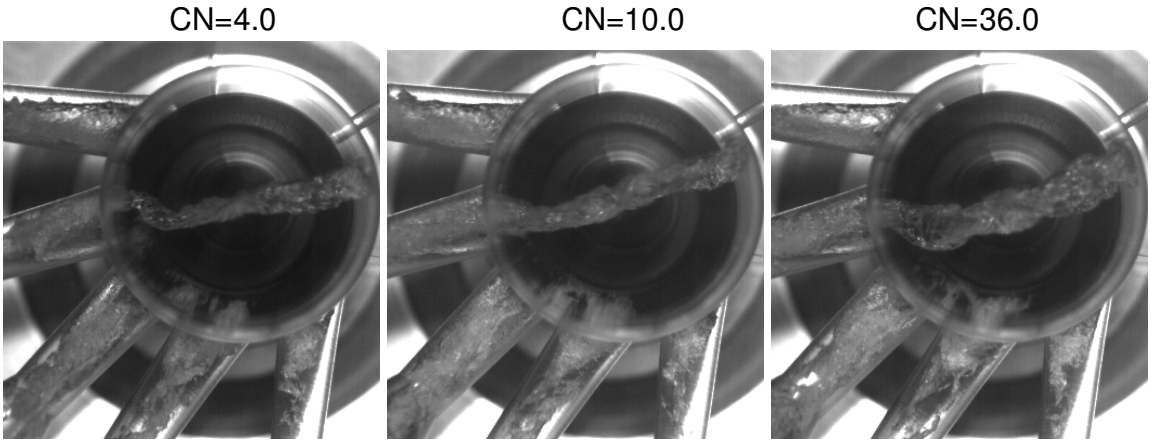

Figure 5-30: Representative images for the tapered 5-hole large scale nozzle at low needle lift and high CN showing presence of string cavitation next to hole 2 [Re ~53,000].

It has be seen so far that for the full needle lift cases the nozzle was string cavitation free. It naturally follows that for high lift cases it would have also been free of strings as well as hole cavitation. This was in principal correct however for the first time in this investigation it was observed another interesting feature of this complex flow. As the images in Figure 5-31 show, for CN=4.5 and a high Reynolds holes 1 and 5 are free of geometric cavitation. However as it can be clearly seen from the bottom view images, there is a clear string-like structure that extends from the hole exit, where cavitation exists at the connection with the expansion tubes, runs all the way upstream the injection hole and enters the nozzle sac volume. Later in this chapter results obtained from tapered nozzles without expansion tubes will provide a further evidence of how string cavitation is formed.

As we have seen so far there are strong evidences that string cavitation is formed by existing vapour pockets that are sucked inside the vortical structure present in the nozzle. Therefore it was considered useful to see if the introduction of air bubbles in the liquid would have had the same effect as the vapour existing at the hole inlet of cavitating holes. It has to be mentioned that air seeding had been also used in the cylindrical hole nozzle in order to verify the vortical flow that had been obtained in the predictions.

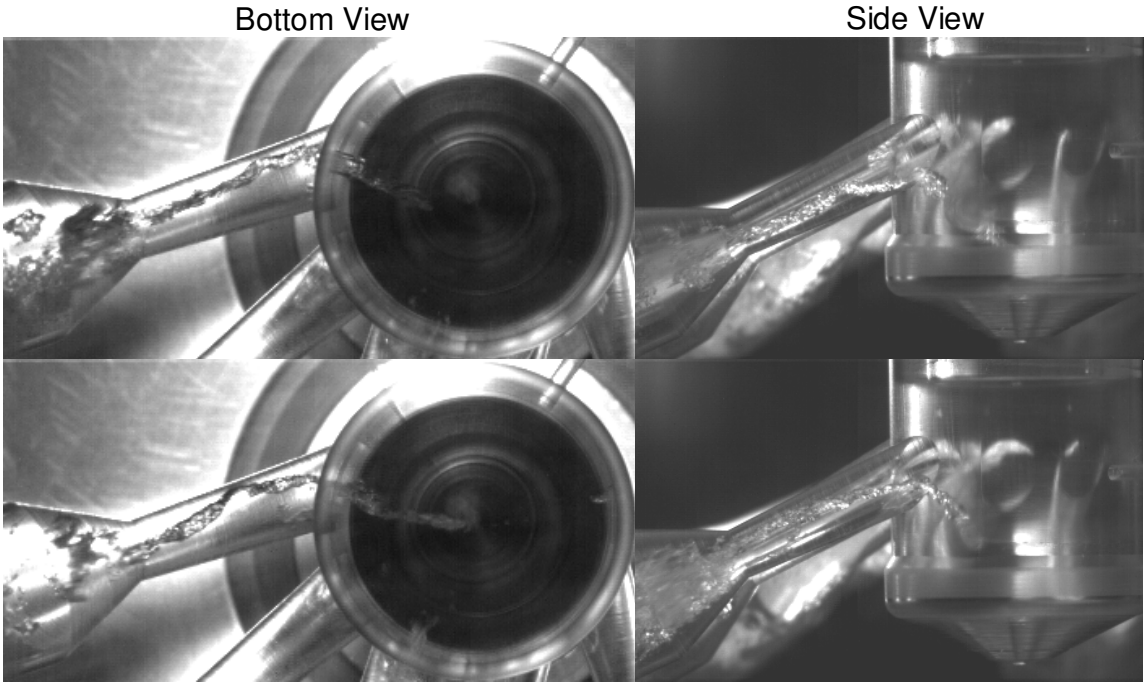

Figure 5-31: Representative images for the tapered 5-hole large scale nozzle at high needle lift showing presence of string cavitation exiting through hole 1 [CN=4.5, Re =68,000].

So far with the existing arrangement of the rig the bubbles could be introduced only upstream the injection holes (more than 1 meter inside the flow annulus), resulting into a fine bubble cloud inside the water, however a slight modification in the pressure tapings distributor made possible for the first time to inject bubbles directly inside the sac volume of the nozzle. Figure 5-32 shows an image of the flow rig and the taping used to inject the air bubbles. The compressed air used was regulated through a sensitive rotary valve in order to avoid excessive supply of air.

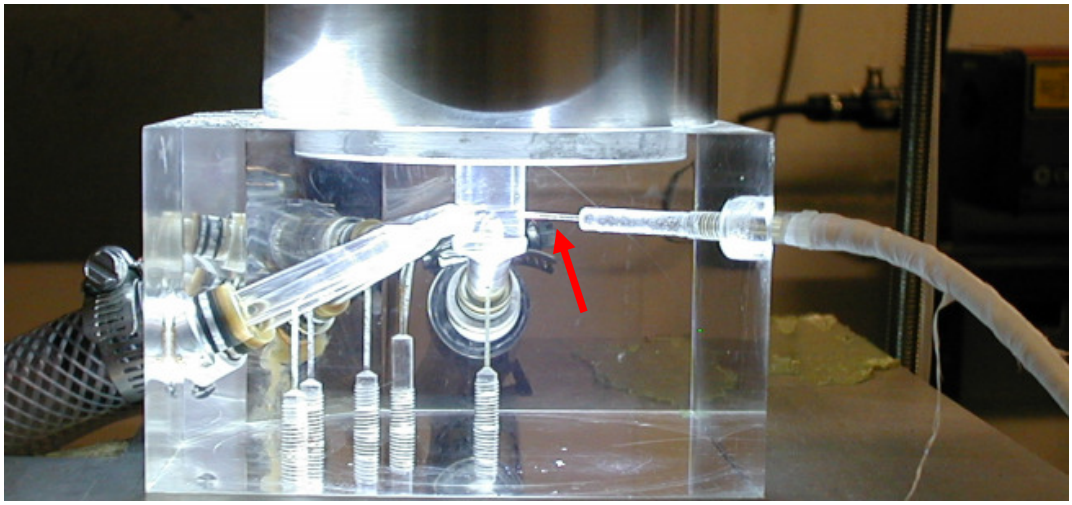

Figure 5-32: Pressure taping used in order to introduce air bubbles directly inside the sac volume of the large scale tapered marine nozzle

The following figure shows that when such bubbles are trapped in the vortex forming within the nozzle volume, their initially spherical shape could develop into the string-like structure as the sequence of images in Figure 5-33 reveals.

As it can be seen in Figure 5-33 (a) in the absence of air bubbles the nozzle is free from both hole and string cavitation. Once bubbles start to be introduced (b) they are captured inside the vortical flow and start to concentrate inside the core of it. As more bubbles are introduces this effect starts to be more evident (c). At a later stage more bubbles have been concentrated inside the core of the vortex and now a clear string like structure is present in the volume of the nozzle similar to the ones we have previously seen in the cylindrical hole nozzle. It has to be also noted that this vortex directs the bubbles towards the hole that is attached to and therefore for this particular case the main volume of bubbles exit through hole 1 even though hole 5 is much closer to the pressure tapping where bubbles are coming from (d) & (e). Finally in (f) when bubbles have stopped been injected in the sac volume, it has to be noted that the string does not disappear instantly. Instead, the disintegrated bubbles seem to be trapped inside the vortex core for a sufficient time period. This observation can be useful since it introduces a lag that has not been identified with the previous presented results.

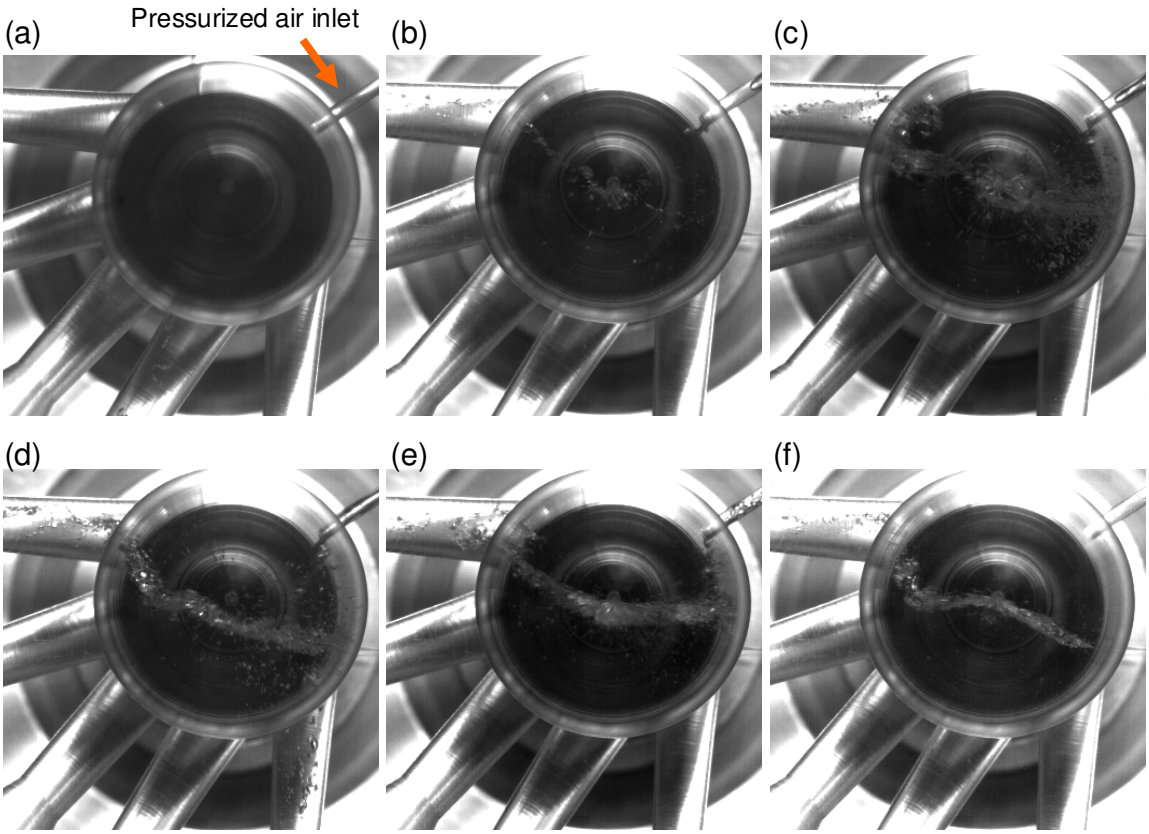

Figure 5-33: Representative image for the geometric hole cavitation-free tapered 5-hole nozzle with air bubbles introduced into the sac volume in the area of the vortex development at high needle lift, resulting to an induced string-like two-phase flow structure [CN=3.0, Re=53,000].

It can thus be argued that the observed cavitation strings do not contain vapour produced at the core of the vortices, but rather vapour originating from pre-existing cavitation sites and trapped within the core of the vortices formed upstream of the injection holes.

5.5 Results - Internal nozzle flow marine injector - String cavitation effect on hole flow characteristics

Having identified the mechanism leading to the formation of cavitation strings and their dependence on geometric parameters and operating conditions, it was considered important to investigate their effect on the hole flow structure. As already described, the geometric-induced cavitation is taking place in the injection holes, as both flow images and model

predictions have indicated. It should be also recalled that hole cavitation was highly asymmetric and different from hole to hole, which is due to the highly swirling motion of the flow entering through individual injection holes, as shown in Figure 5-5.

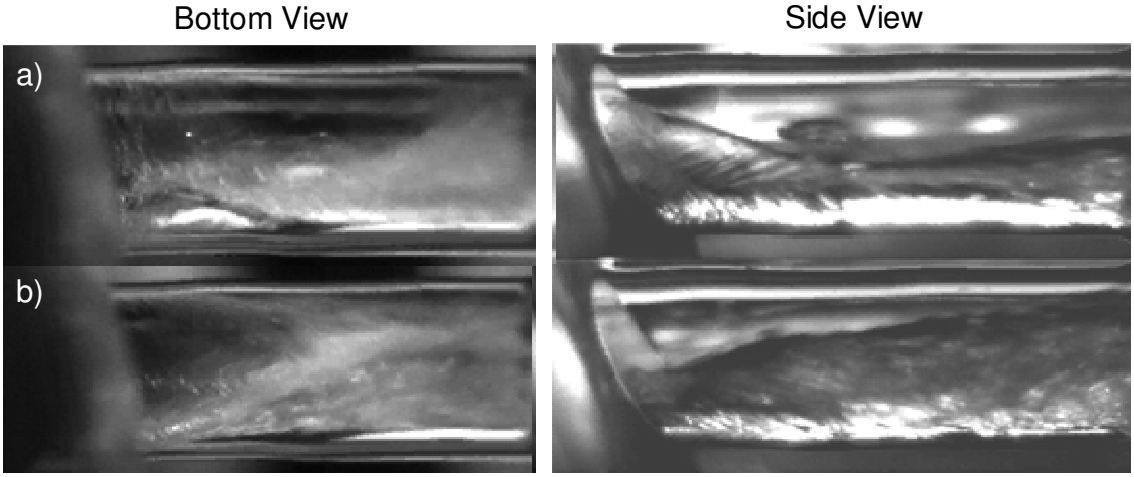

Figure 5-34: Effect of string cavitation on the flow distribution inside the injection hole, as seen from the side view (*a*) with string cavitation and (*b*) without string cavitation (nominal needle lift, CN=4.0, Re =53 000).

Figure 5-34 shows a side view CCD image of the cavitating structures developing inside injection hole 1 in the absence and in the presence of a cavitation string. These images give a clear indication that once a cavitation string enters the injection hole, the two separate cavitation structures become indistinguishable and a much larger cavitation cloud dominates the flow; this extended cavitation cloud seems to occupy the full cross-sectional area of the injection hole in the presence of string cavitation. However as will be shown later on in Figure 5-36 the position of the string inside the hole may also change and have an effect in its flow distribution.

So far we have visually shown what is the effect of string cavitation and/ or vortex location to the flow inside the nozzle volume as well as inside the injection hole itself. The next section of this investigation will try to provide a more quantified approach on what is the effect on the flow rate of each hole.

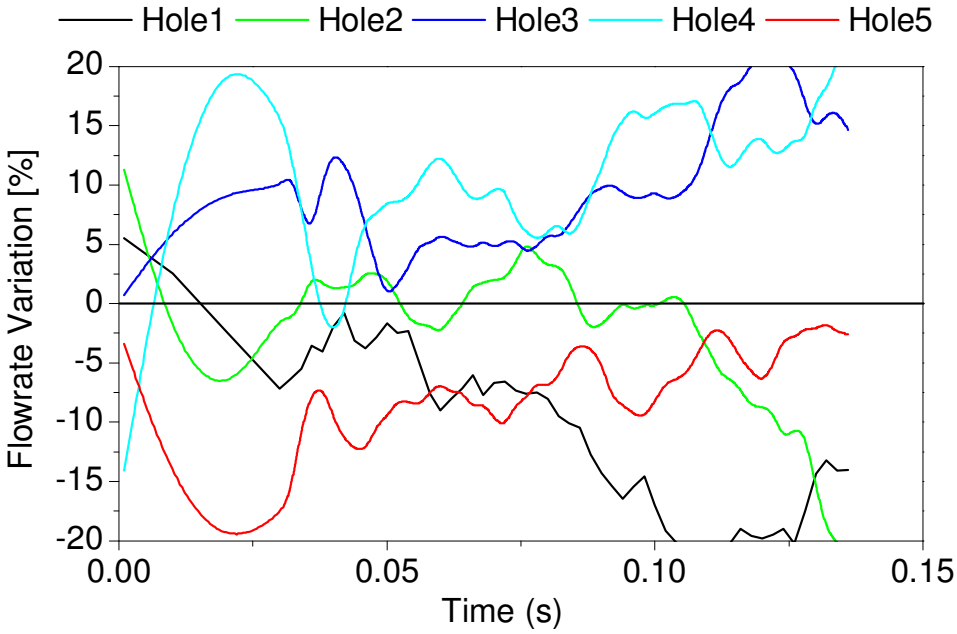

Figure 5-35: Predicted temporal hole-to-hole flow rate variation [CN=4.0, Re=53,000].

Figure 5-35 presents the percentage variation from the mean of the individual hole flow rate during the simulation period. It can be seen that holes 3 and 4 always inject more liquid that the rest while they exhibit the smaller fluctuation. However, holes 1 and 5, which are the two side holes of this particular nozzle geometry, seem to follow a 'complementary' flow pattern. When more fuel flows through hole 1, then less fuel flows through hole 5, as can be seen by concentrating between 0.55 and 0.8 ms. this indicates that individual injection holes interact with each other through the geometrically-induced hole cavitation. This is an important conclusion not properly addressed in past studies on nozzle cavitation. It seems that this transient flow development changes the flow structure inside the nozzle volume, which, in turn, results to the formation of transient vortices, depending on the local flow field and geometry details.

It should be mentioned that such complementary paths have been seen in the experimental investigation as well. Following is a graph that has been made by monitoring the instantaneous flow rate exiting through each one of the five injection holes of the cylindrical five hole nozzle. The flow rates obtained for a series of cases having the same needle lift and Reynolds number is presented below. The data points have been deliberately put in such an order to promote the complimentary path between the two side holes. as in the predictions the flow rate has being normalized by the flow rate that each one hole such

have been getting due to their different cross-sectional area. A typical graph showing the flow rate percentage for various full lift cases at Re=53,000 is presented in Figure 5-36.

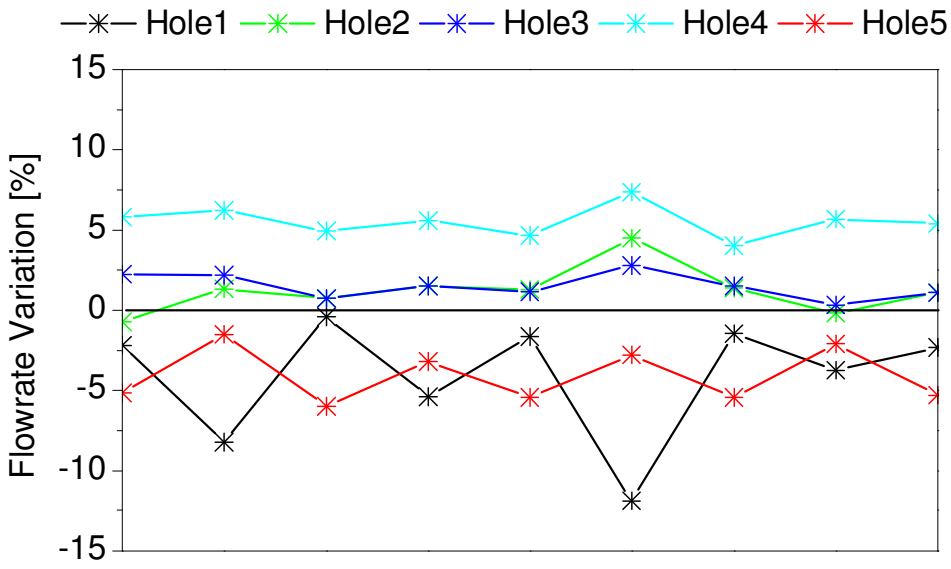

Figure 5-36: Experimental hole-to-hole flow rate variation for a set of measurements [Re=53,000].

To further understand the influence of the presence of string cavitation on the mean flow characteristics, the individual hole flow rate was measured in their presence as well as in their absence. Those results are presented in Figures Figure 5-37 and Figure 5-38, for the full lift and the low lift cases, respectively. Figure 5-37a shows the individual hole-to-hole mean flow rate variation prior to the initiation of either hole or string cavitation. It can be seen that hole 4 is the only over-fuelling hole while hole No 5 is the under-fuelling one. Measurements where then repeated in the case of fully developed string cavitation while string cavitation was exiting only through hole 1. Those results are presented in Figure 5-37b. It is evident that in this case this particular hole injects about 10% less fuel compared to the average value. Figure 5-37c shows a similar result for the case where the string cavitation enters either to hole 1 or hole 5, which corresponds to the full needle lift case. Again, it can be seen that those two holes are strongly influenced by the presence of the string over a long period of time.

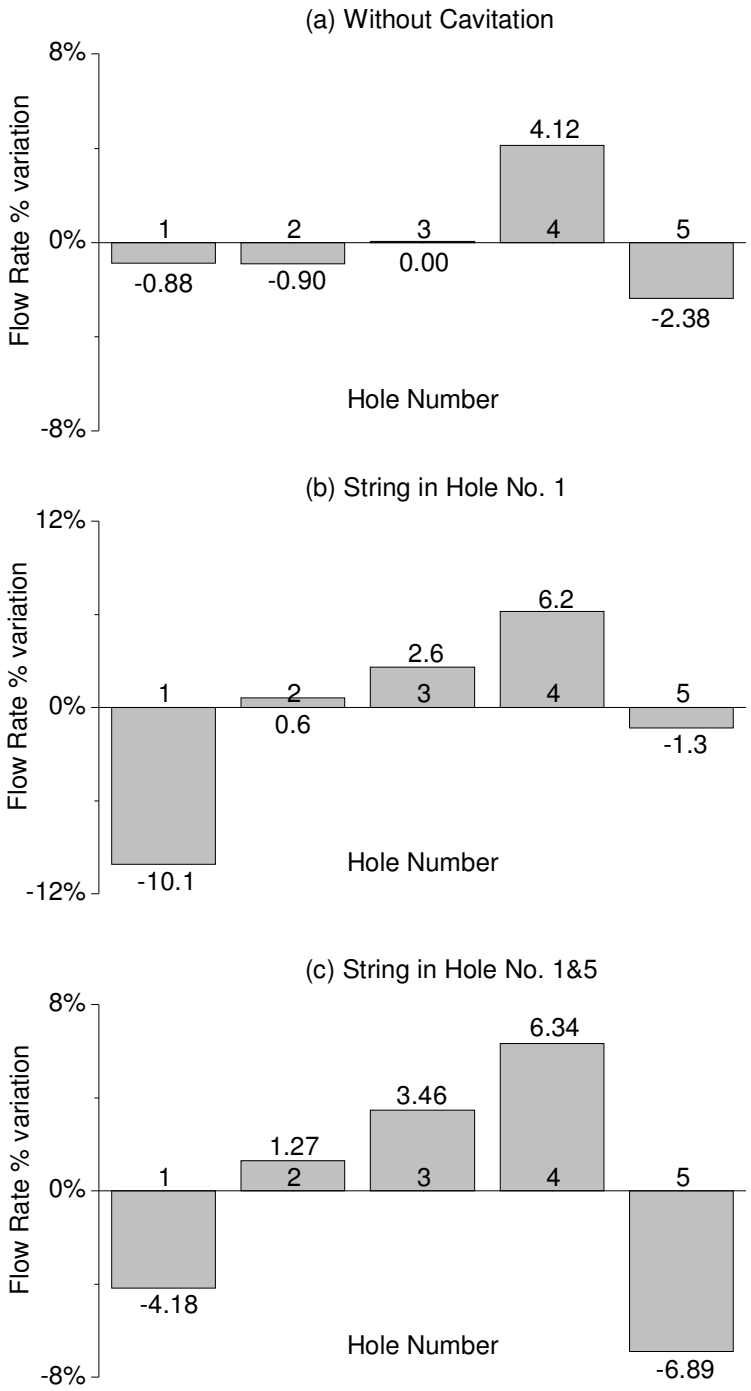

Figure 5-37: Measured mean hole-to-hole flow rate variation (a) without strings, (b) with string in hole 1 only and (c) with strings in holes 1 and 5 [CN=4.0, Re=53,000, Full lift].

Thus, the conclusion from that experimental result is that string cavitation has a significant effect on the fuel injected from individual injection holes. At present, it is not possible to

distinguish if this effect is related to the flow distribution upstream of the injection hole or it is simply the effect of the increased vapour volume present inside the injection hole in the presence of a cavitation string. It seems like an 'egg and chicken' cause and result! Finally, Figure 5-38 further confirms the above conclusion for the low needle lift case, where the string exits mainly from hole 4. This time, an approximately 8% reduction of the flow rate has been measured for the over-fuelling hole 4 of the non-cavitating case.

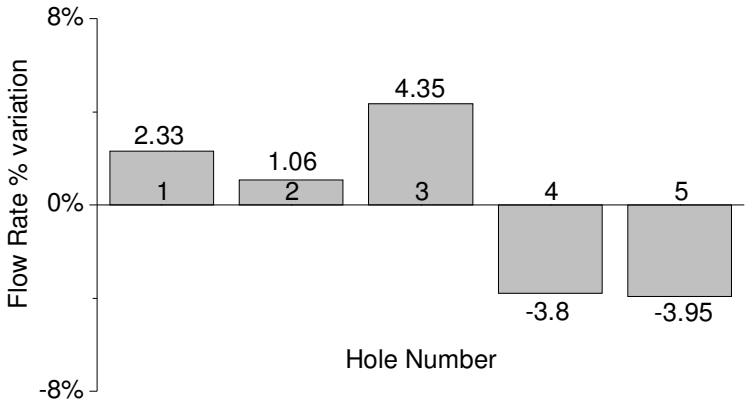

Figure 5-38: Measured hole-to-hole flow rate variation at low needle lift, with strings always present in holes 4 and 5 [CN=4.0, Re=53,000].

Therefore as the above presented figures suggest, around 10% reduction of the hole flow rate is associated with the presence of a cavitation string attached to an individual injection hole. However, in that study, it was not possible to distinguish from the experimental data whether this effect is related to the flow distribution upstream of the injection hole or is simply the effect of the increased vapour volume inside the injection hole in the presence of a cavitation string. Evidence of this can be provided by the CFD model. Figure 5-39(*a*) and Figure 5-39 (*b*) show the calculated instantaneous flow rate from each of the five injection holes for the cylindrical and the tapered nozzle holes, respectively. These predictions have been obtained with the needle at its nominal lift and within a time window during which the vortical structure changes its location from hole 1 to hole 5 for both cases simulated here. It is clear that hole 1 exhibits the highest flow-rate variation with flow rate peaking when the nozzle vortex is facing the opposite hole 5 and dropping when the vortex enters it.

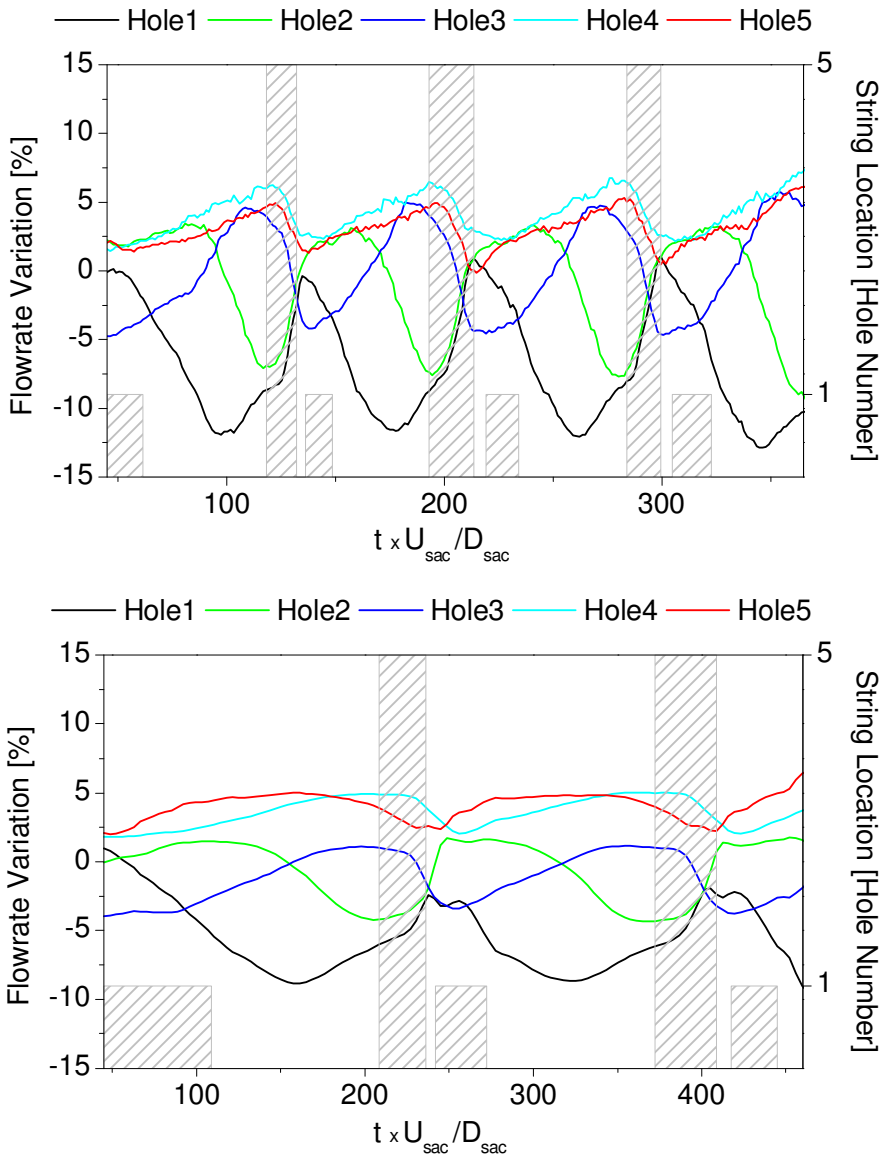

Figure 5-39: Predicted temporal variation of hole-to-hole flow rate for (a) cylindrical 5-hole nozzle and (b) tapered large-scale 5-hole nozzle [Nominal needle lift, CN=4.0, Re=68,000].

The maximum calculated reduction is ~10% in the case of the cylindrical holes and ~8% in the case of tapered holes; the average flow-rate reduction for the time window during which the nozzle flow vortex is attached to this particular hole is ~5–7%. It can be thus concluded that the measured flow-rate reduction in the presence of a string can be attributed to the reduced liquid quantity entering the hole when the flow vortex is attached to it. The rest of the observed flow rate reduction can be attributed to the modified cavitating flow structure inside the injection hole in the presence of the increased cavitation vapour. Comparing the

predicted temporal flow-rate variation between the cylindrical and the tapered holes, it can be concluded that the nozzle vortex switches from hole 1 to hole 5 faster for the case of the cylindrical holes, confirming that the nozzle flow development is sensitive not only to the needle lift, but also to the geometric characteristics of the nozzle.

5.6 Results - Internal nozzle flow marine injector - effect of hole interaction on string cavitation

Having a better understanding on string formation mechanism, which was also the main objective of this investigation, the following section will present some additional results mainly showing what is the effect of hole interaction.

This was done by isolating individual injection holes and investigating what is the effect on the string presence probability. As both images and CFD calculations have revealed, the formation of the strings within the nozzle volume is sensitive to the vortical structure formed and developing transiently within the nozzle volume. Isolating individual holes simply changes the internal nozzle flow and results to formation of strings at different locations, implying that small modification to the number of holes or their location at the nozzle volume is expected to change the string cavitation pattern within the nozzle volume.

Figure 5-40 shows how the string location changes by sequentially closing the flow of the hole that the string was present. In order to have the string permanently in one hole the investigation was done for low lift where when all the holes are open the string in hole 4. Time averaged images are shown in order to account for changes in frequency as well.

(a) All Holes Open

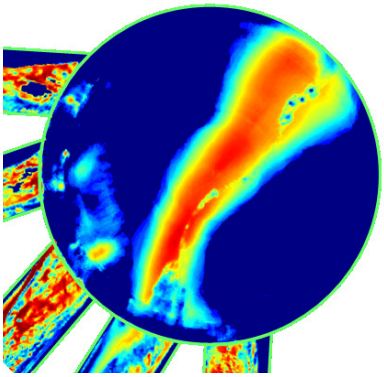

(b) Hole 4 Closed

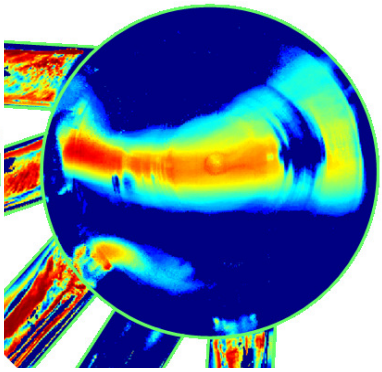

(c) Hole 4&2 Closed

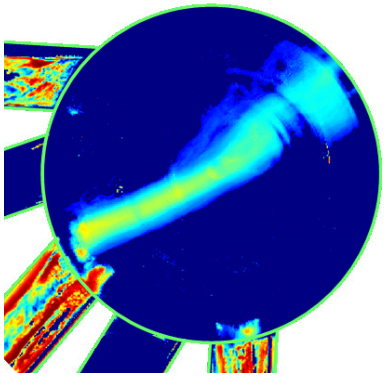

(d) Holes 1&5 Open

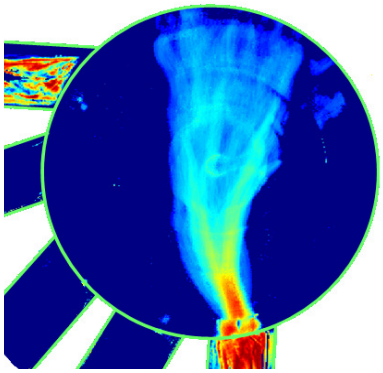

(e) Hole 1 Open

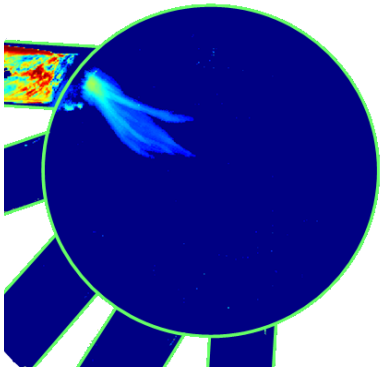

(f) Hole 2 Open

(g) Holes 3 Open

(h) Hole 4 Open

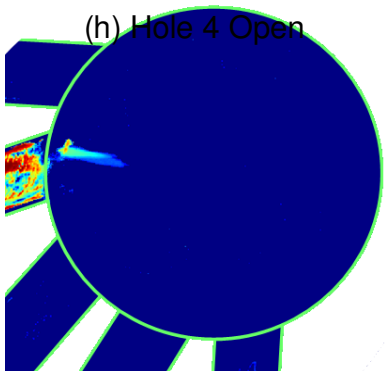

(i) Hole 5 Open

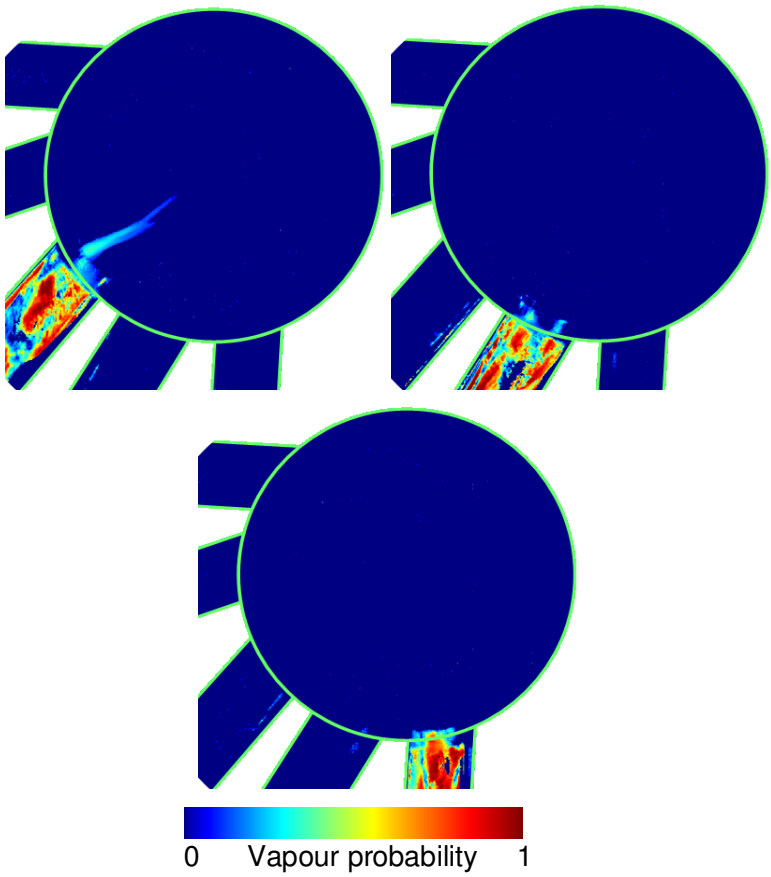

Figure 5-40: Two-dimensional spatially averaged images of cavitation string probability or different scenarios of hole combination blocking [Low needle lift, CN=2.6, Re~20,000)

As it can be seen in figure 1-40 above, at low lift and when all the holes are open the string is constantly attached to hole 4 (a). Closing the exit flow valve of hole 4 will make the string to attach to hole 2 (b). at this stage we can also see a smaller string like structure exiting through hole 3 while its other end seems to be entering hole 5. Isolating hole 3 (c) the string moves to hole 5 (d). then leaving only hole 1 open the string, much weaker now and without been extending to the full length of the sac volume as before, continues to exist. The rest of the mean images show that the string is gradually fading as the remaining holes are investigated. However what we have shown with this figure is that it is almost inevitable in this type of nozzle to avoid having strings.

As mentioned before it was also found string cavitation between two holes. Such structures have been previously seen in symmetrical multi-hole car Diesel injectors between adjacent injection holes, and will also be further examined Chapter 7. In the case of the marine nozzle investigated this form of string cavitation was found between hole 1 and hole 3 when the hole between them was blocked as seen in

Figure 5-41.

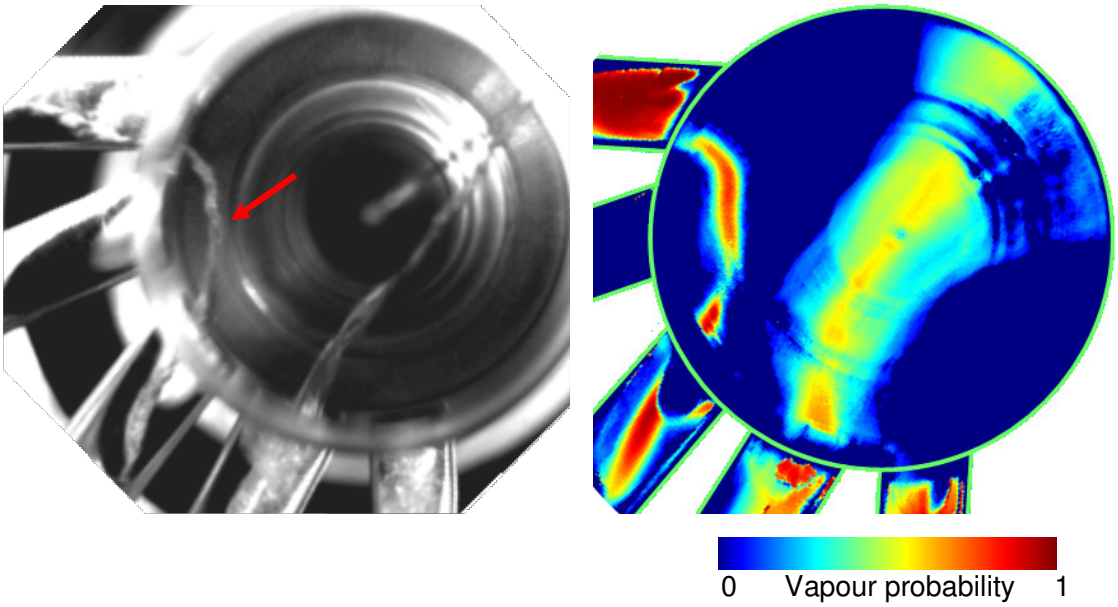

Figure 5-41: typical CCD image and Two-dimensional spatially averaged image of cavitation string probability having hole 2 blocked [nominal needle lift, CN=2.6, Re =45 000]

As it can be seen for this particular case hole 2 was closed, therefore no flow was allowed to pass through it. String cavitation was developed between hole1 which had geometric cavitation, and hole 3 which only had the string entering in it. Except from those two holes, string cavitation was also present in hole 4 together with geometric cavitation.

Finally it has to be mentioned that due to the fact that even by having one open hole vapour strings continue to form inside the nozzle's sac volume, the investigation was also conducted for the nominal needle lift. As

Figure 5-42 shows, the strings attached to a single open hole are much thinner than those previously observed. As it can be seen the string probability even close to the hole does not

exceed 40%. Even when a string is present the probability to be present in all the length of the sac volume is around 5%. In any case once again the simulation results have been proved reliable.

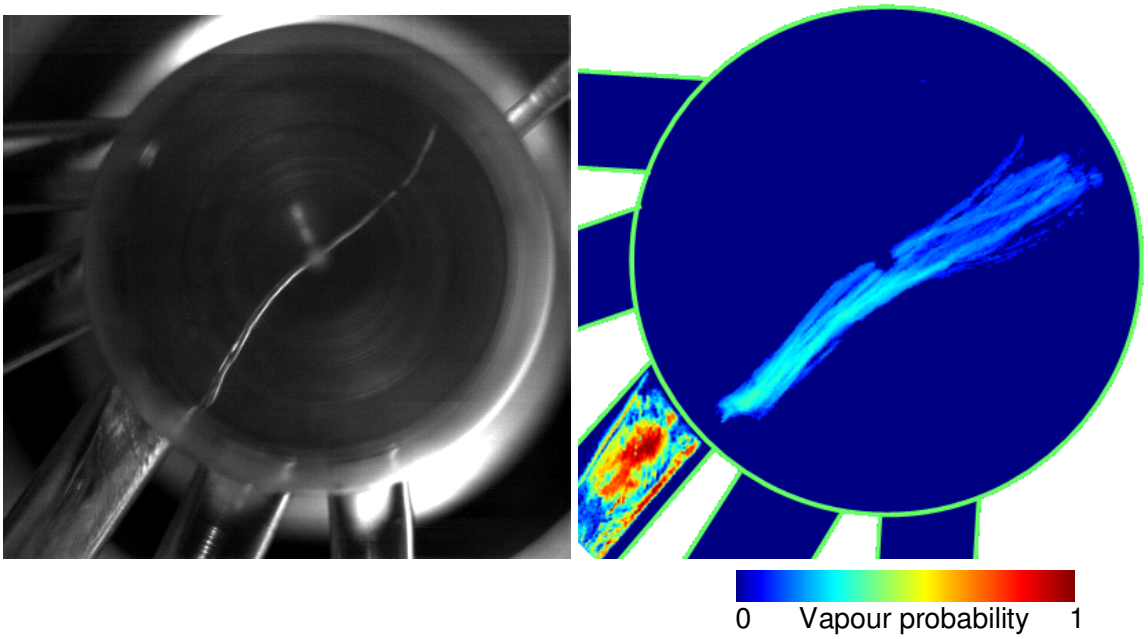

Figure 5-42: typical CCD image and Two-dimensional spatially averaged image of cavitation string probability having only hole 3 open [nominal needle lift, CN=2.6, Re =13,000]

5.7 Internal Nozzle Flow marine injector – Understanding the mechanism of string cavitation formation

Having detected the complex internal nozzle flow as per the previously shown results, and having identified that the string formation was independent of the number of injection holes, it was decided to further investigate the string formation mechanism, which is still poorly understood, by focusing only in single-hole nozzles. Single-holes nozzles would provide better view access inside the injection hole, since from the previous investigations there were indications that string cavitation was formed by existing vapour from geometrically induced hole cavitation that was sucked by the strong vortex inside the sac volume of the nozzle. Furthermore these large-scale single hole nozzles were injecting in

atmospheric condition, instead of having a closed looped by directing the injected liquid in expansion tubes as done before. This made possible to visualize both the nozzle flow and the emerging spray end establish a better understanding of the string cavitation effect to the near hole exit spray characteristics. The results of the spray visualization results are presented in Chapter 6. In this section only internal nozzle flow results will be presented focusing only on characterising the various flow regimes related to the formation and development of string cavitation in the injection hole and the sac volume.

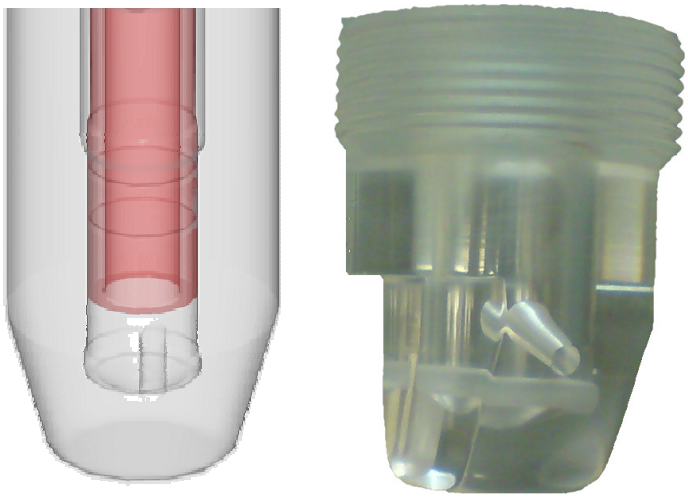

Figure 5-43: Single-Hole Large-Scale marine nozzle replicas schematic and photo

As previously mentioned, in order to focus on the cavitating flow structures forming inside the nozzle, the geometry has been simplified to a single-hole one, as shown in. these fully transparent nozzle replicas provided optical access inside the nozzle volume upstream of the injection holes, inside them as well as at the sprays formed at the nozzle exit. Image collection over sufficient duration period has provided information on the string frequency of appearance and life time. The nozzle designs tested have included cylindrical as well as tapered holes converging towards the nozzle exit.

5.7.1 Description of test cases

Table 5-8 summarises the range of operating conditions investigated for the visualisation studies. As mentioned, both cylindrical and tapered injection holes have been made. Cylindrical holes with sharp inlet corners promote formation of geometry-induced

cavitation, while tapered holes (i.e. holes with conical shape converging towards the nozzle exit) suppress or even eliminate formation of cavitation at the hole inlet. The flow conditions refer to cavitation numbers between 1 and 7, which is similar to those of the real-size injector operating under nominal engine running conditions. However, the much lower injection pressures used restrict the experiment into flow rates (and Reynolds numbers) much lower than those of the real operating conditions. Since the fuel flow through the injector nozzles, especially through the holes, is highly turbulent, all flow features can be expected to behave transiently and with short time-scales.

The Photron FASTCAM-ultima APX cameras, having a similar set-up as the one described in section 3.3, along with the continues flow test rig, as described in section 3.2, were used with a frame rate between 6,000 to 16,000fps; this was considered sufficient to capture the temporal development of cavitation using a shuttering time of 30μs. In total 3000 to 12,000 images were collected for a particular case. Furthermore, superimposing of images has allowed for time- and spatial averaging over the whole nozzle volume depth of the projected 2-D images. Imaging was performed for various combinations of the cavitation and Reynolds number and for different needle lifts. The cases to be reported here correspond to the 'full' lift, which is defined as the nominal stop position of the needle in the real injector. The 'low' lift case corresponds to a needle lift at about 80% of the full one. In this case, the slide is just uncovering the injection holes. Finally, the 'high' lift case corresponds to 120% of the full lift position. Finally, for most of the cases to be presented here, the cavitation number has been kept constant at CN=4 and the Reynolds around 60,000 unless it is stated otherwise.

Nozzle Design	Needle Lift	Injection Pressure [bar]	Flow rate [litre/s]	CN Number	Re Number
Single Hole Cylindrical	Low, nominal & high	2,3,5, 8	0.12 0.15 0.20 0.24	1,2,4,7	39500 49400 65900 79050
Single Hole Tapered	nominal	3, 5	0.18 0.25	2.0 4.0	63500 88250

Table 5-8: Flow conditions inside the large-scale cylindrical and tapered single-hole marine model nozzle.

5.7.2 Cavitation regimes in the cylindrical-hole nozzle

Due to the specific characteristics of the nozzle geometry investigated, geometric-induced cavitation is forming at the lower part of the injection hole and stays attached to its bottom surface up to the nozzle exit, this is the same location as the for the five-hole nozzles, results of which were presented before in Section 5.2. The aforementioned regime can be clearly seen in Figure 5-44 (a), corresponding to the nominal needle lift and a cavitation number equal to 2, which as mentioned in Section 5.2 is sufficient enough for fully developed cavitating conditions to be reached.

As expected from the results obtained in the first investigations with the 5-hole marine nozzles, in addition to the geometric-induced cavitation, vortex or string cavitation is also forming even in this simplified nozzle geometry. Typical images of that can be seen in Figure 5-44 (b), (c) and (d).

Cavitation strings are developing upstream of the entry to the injection hole well inside the nozzle's sac volume and extend up to the nozzle exit. Their formation and life time varies with the operating and flow conditions (i.e. needle lift, Reynolds and cavitation numbers).

(a)

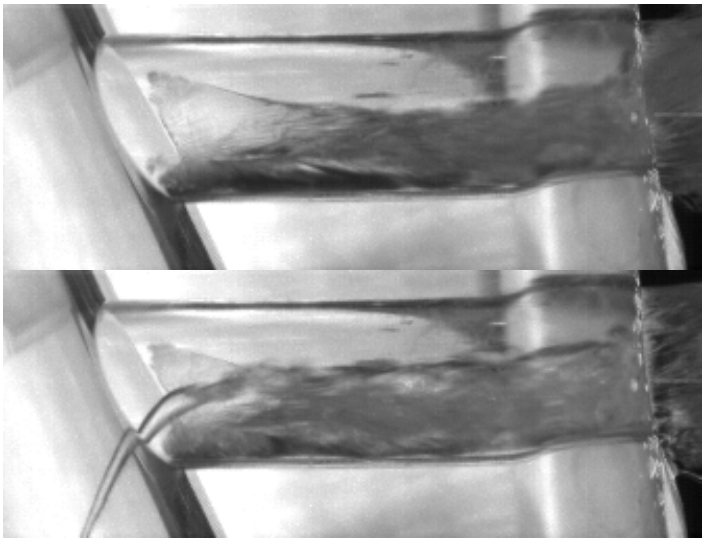

(b)

(c)

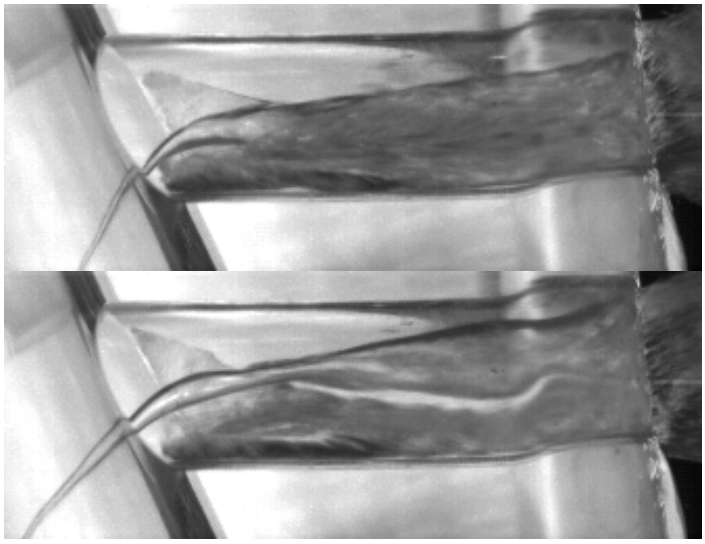

Figure 5-44: Images showing four distinct cavitation patterns inside the injection hole of the single-hole cylindrical nozzle, a) only geometric cavitation, b) string cavitation at the lower part of the injection hole, full mixing with geometric cavitation, c) string cavitation at the centre of the hole, partially mixing with geometric cavitation and d) string cavitation at the upper part of the injection hole, string cavitation separated from geometric cavitation [CN=2, Re=52,950]

Until this point the focus was on whether a hole is associated with a string, without thoroughly investigating what is the effect in the flow regime inside the hole, at least not in detail. However this was the main target of this investigation and at this point, it is worth noticing that the development of string cavitation inside the injection hole can be found in three distinct locations relative to the cavitation cloud present at the bottom of the injection hole. As the three last images of Figure 5-44 reveal, string cavitation can be mixing fully with the geometric hole cavitation (Figure 5-44b), being clearly separated and flowing above it (Figure 5-44d), or found near to its boundary and thus been partially mixing with it (Figure 5-44c). It is also worth noticing that, depending of the area of its development, the flow conditions at the hole exit cross sectional area are greatly modified since in the first case the upper part of the injection hole is occupied by liquid while in the last case it is occupied also by cavitation bubbles. This difference in the flow characteristics at the crossectional exit plane of the injection hole, can be identified as an additional parameter affecting the initial spray structure formation even for periods where a string is constantly attached to an injection hole. This effect, on a both qualitative and less quantitative way, will be further examined in Chapter 6.

5.7.3 Cavitation formation in the cylindrical-hole nozzle

In the previous sections of this study, there was no clear evidence on how these complex cavitation regimes that were identified inside the marine nozzles, were formed. By using sequences of high speed images, even up to 30,000 fps, the formation process of geometric and string cavitation inside the cylindrical hole nozzle was revealed. There were more than 35 cases focusing only in the understanding of this mechanism. However, since the results were similar, leading to the same conclusions, only two operating conditions have been selected to be presented, been the most characteristic ones. The first case corresponds to low cavitation number where bubbles are just start forming. In the second, a fully developed cavitation cloud at the hole bottom exists. High speed image sequences of these cases can be seen in Figure 5-45 and Figure 5-46, respectively.

Concentrating first on the low CN number case (Figure 5-45), one can seen cavitation bubbles rarely forming at the bottom edge of the hole inlet and transported towards the hole exit; this is the so-called incipient cavitation regime. At some time instances, highlighted with a circle superimposed on the images, an elongated and rather large bubble structure appears to travel in the direction opposite to the main hole flow. This is forming and collapsing a few times until it may become a long cavitation string structure propagating well inside the nozzle's sac volume; its life time is only a fraction of the ms.

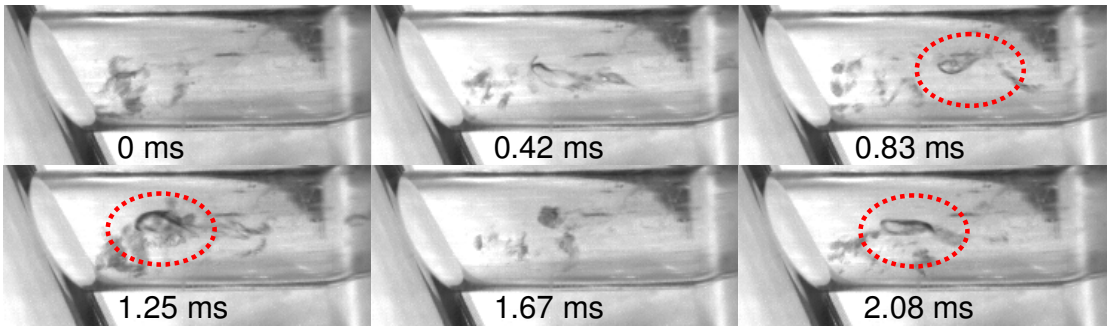

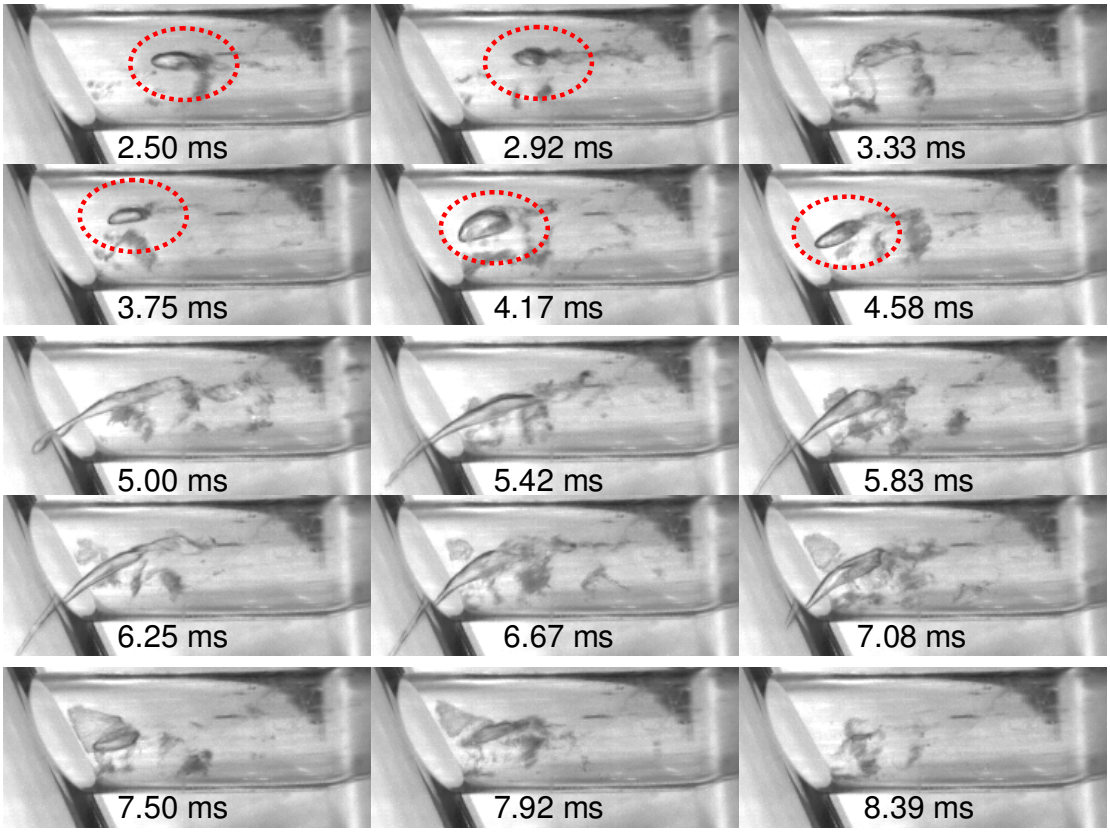

Figure 5-45: Sequence of high speed images showing the formation of string cavitation inside the single-hole cylindrical nozzle at low cavitation number [CN=1, Re=52,950]

A similar flow behaviour is realized with increased Reynolds and cavitation numbers; this can be seen in the following Figure 5-46. Although the mean hole liquid velocity is expected to be higher in this case, it seems that the cavitation string again propagates in the direction opposite to the hole flow while it appears to originate either from the hole exit or from its mid distance between the inlet and the exit. Once formed, it is not possible to distinguish any motion towards or upwards the hole exit. However, on the other side of the hole inlet, initially the string is moving inside the sac volume but at later stages its movement reverses its direction and moves towards the injection hole exit. In the area close to the hole inlet, the two cavitation structures are clearly separated while they mix around half hole length. Later in this chapter a quantitative analysis will be presented in an attempt to identify how string cavitation formation and movement is affected by different flow condition and needle lifts.

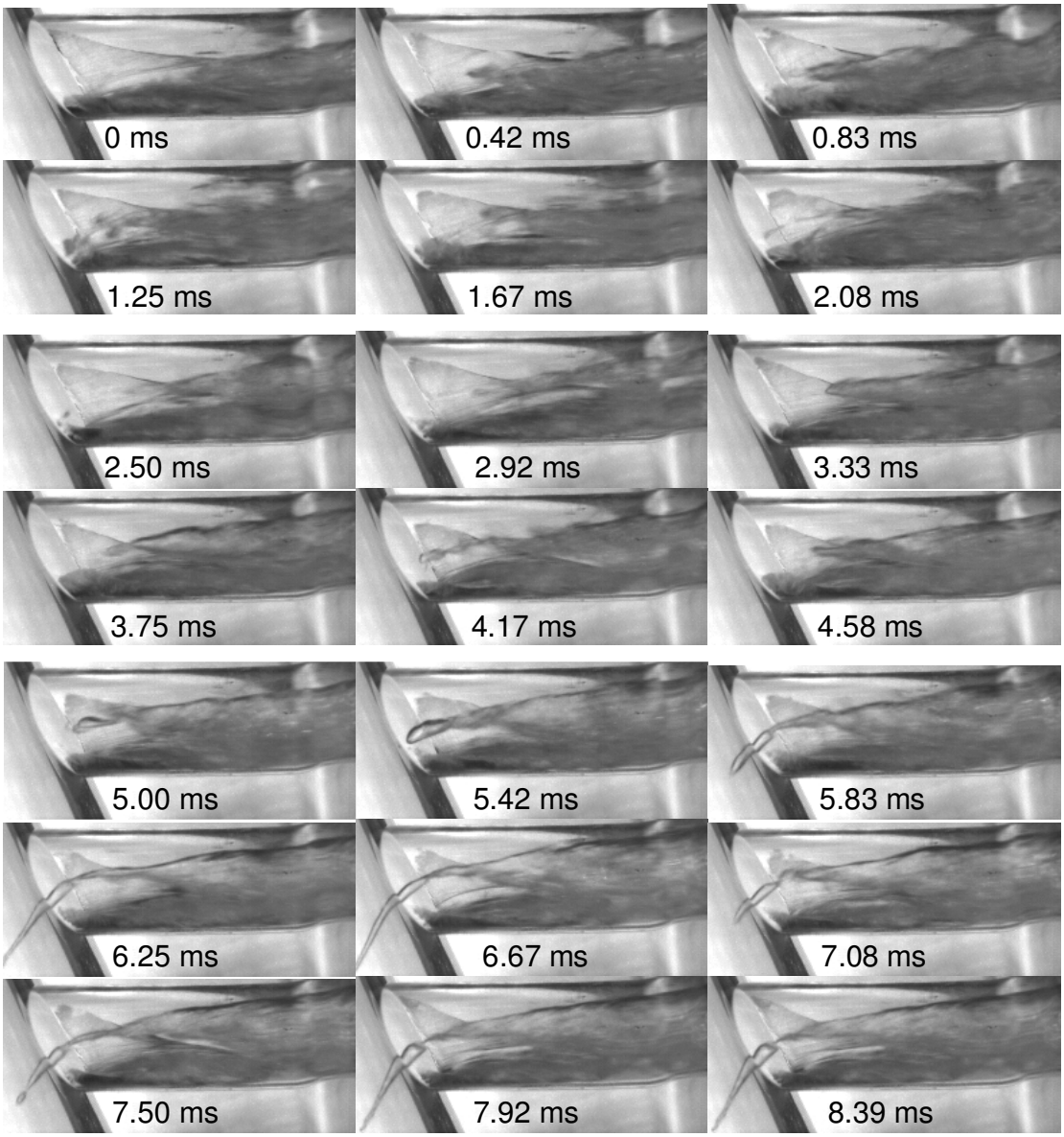

Figure 5-46: Sequence of high speed images revealing the formation of string cavitation inside the cylindrical single-hole cylindrical nozzle at nominal cavitation number [CN=4, Re=70,600]

5.7.4 Cavitation formation in the Tapered-hole nozzle

The area of formation of cavitation strings raises some questions since they appear to develop in the direction opposite to the hole flow. Relevant recent findings in this area suggest that cavitation strings develop inside vortical structures present in the flow [149]. Furthermore, they have been found to originate from pre-existing cavitation sites. Like the previously presented internal nozzle flow investigation on the tapered hole marine nozzle, it

was interesting to observe string cavitation forming in the tapered hole nozzle which is geometric-cavitation free. As before the aim of repeating the experiment by using a single hole nozzle was to focus on the formation mechanism and letter to observe the emerging spray behaviour to the different flow regimes.

Representative post-processed images of the temporal evolution of string cavitation for the tapered-hole nozzle are shown in Figure 5-47 and Figure 5-48, that correspond to two different cavitation numbers of 2 and 4, respectively.

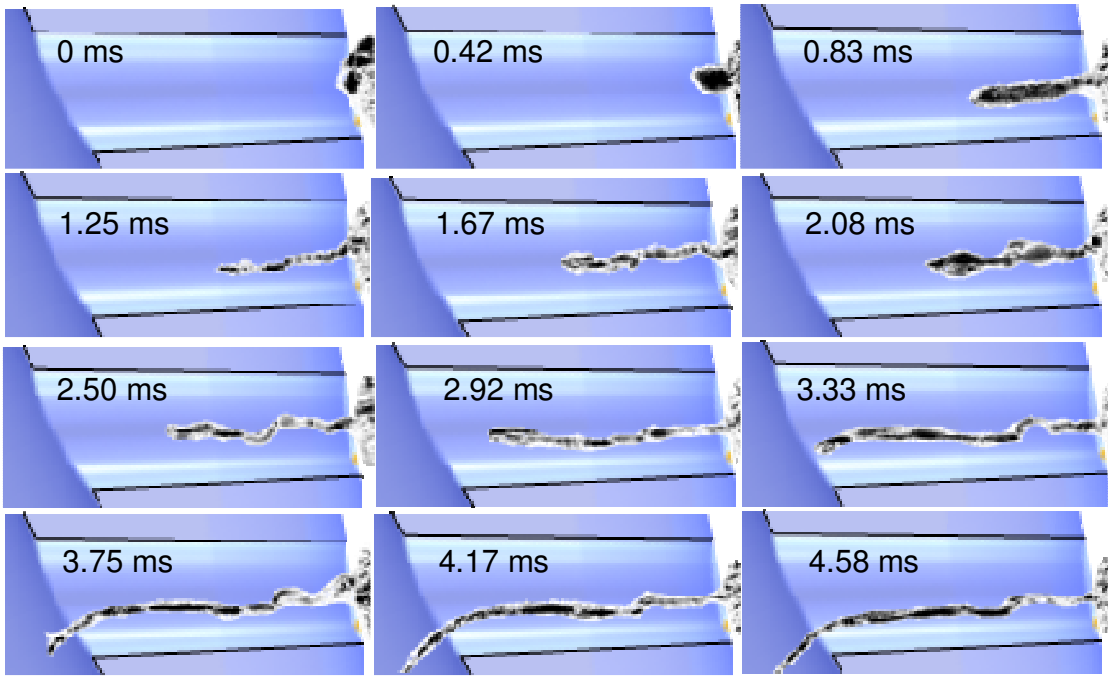

Figure 5-47: Post-processed high speed images revealing the formation of string cavitation inside the tapered single-hole nozzle [CN=2, Re=70,600]

The images indicate that due to the vortical flow present inside the injection hole (described in more detail in [150]), cavitation strings may initiate from downstream air, trapped in the low pressure region present up to the hole exit and propagating upstream inside the nozzle hole; a similar and well known case is that of the air-core surrounded by liquid film at the hole of pressure-swirl atomisers. Comparison between Figure 5-47 and Figure 5-48 reveals faster formation with increasing cavitation number.

In the next section, the frequency of appearance and area of formation/development are quantified for a representative range of operating conditions tested.

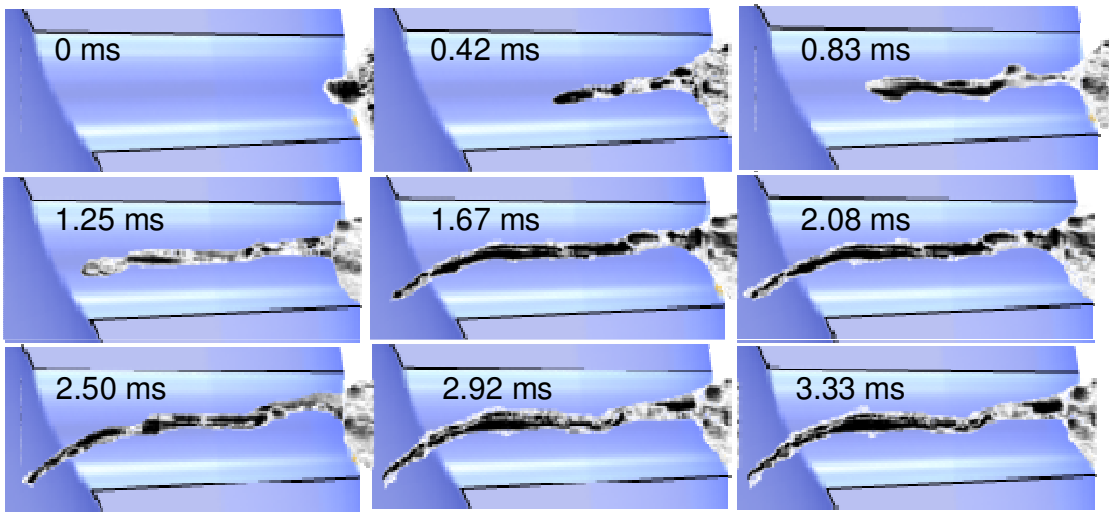

Figure 5-48: Post-processed high speed images revealing the formation of string cavitation inside the tapered single-hole nozzle at increased cavitation number [CN=4, Re=91,770]

5.7.5 Quantitative string cavitation characterization

In this section, results obtained from post-processing, by using the technique described in section 3.4.1, of the acquired images are presented. It has been considered useful to elaborate more on the tapered-hole nozzle, where more clear images have been obtained in the absence of geometric-induced hole cavitation. The result of Figure 5-49 shows the time-averaged probability of finding cavitation string in a particular location inside the injection hole. There is clear indication that the string is rather stable with respect to its location inside the injection hole. The frequency of appearance is again about 50% over the whole hole length while it decreases significantly upstream of the injection hole entry. Effectively, this implies that ~50% of the time strings are present while 1/5 of them manages to enter inside the nozzle's sac volume, as the light-blue values on the colour scale of this plot indicate.

Spray side

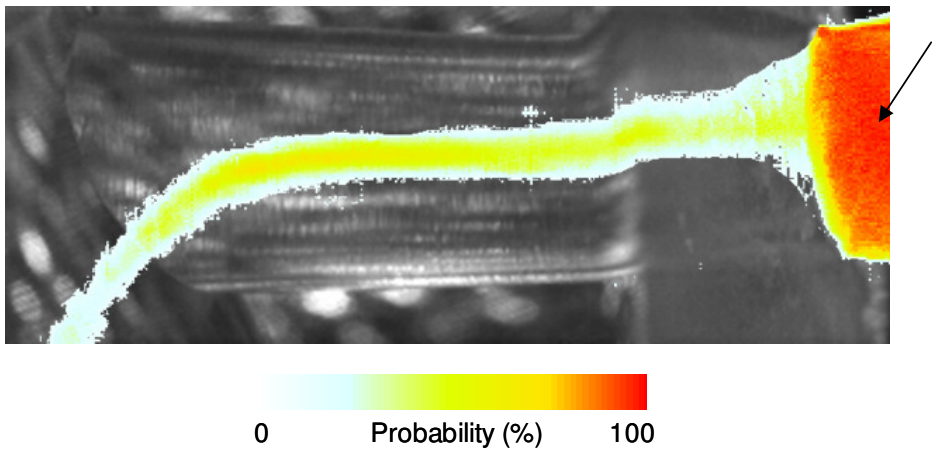

Figure 5-49: Spatial probability of string cavitation location inside the tapered single-hole nozzle [CN=2, Re=70,600]

Unfortunately, it has not been possible to produce mean images for the cylindrical hole nozzle since due to geometric cavitation there were differences that could not be only attributed to the existence of string cavitation. A more detailed analysis on string cavitation inside tapered multi-hole nozzles can be found in Chapter 7.

For the cylindrical hole nozzle a kind of similar information with respect to the appearance of cavitation strings inside the injection hole and the sac volume has been obtained with the post-process described in section 3.4.4 and the regions shown in Figure 3-47

This figure shows a representative image of the cavitation pattern where both hole and string cavitation co-exist. Since the cavitation string appears and disappears, it has been considered useful to capture the temporal evolution of its formation at two distinct locations indicated as 'Region 1' and 'Region 2', respectively, in Figure 3-47. The former one indicates the presence of a cavitation string inside the injection hole while the latter one indicated the presence of the cavitation string inside the nozzle's sac volume.

Corresponding results are presented in the last two Figure 5-50 and Figure 5-51; the y-axis on these graphs takes only two values of 0 and 1 indicating the presence or absence of the cavitation string from the area of interest, respectively.

(a) (b) (c)

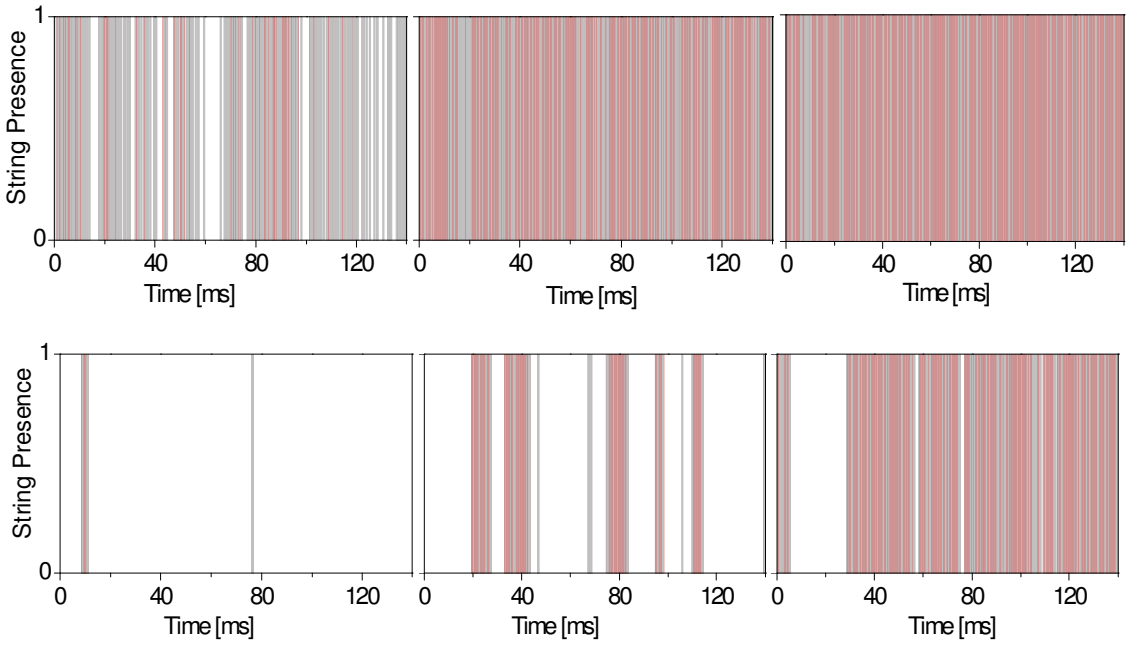

Figure 5-50: Effect of cavitation number on string appearance sequence for the cylindrical single-hole nozzle at high needle lift (a) CN=1, Re=49,400, (b) CN=2, Re=52,950 and (c) CN=7, Re=88,250. Top row corresponds to region 1 and bottom to region 2 of Figure 3-47, respectively.

In Figure 5-50 results are plotted for three different cavitation numbers by keeping the same needle lift while in Figure 5-51 results reveal the effect of needle lift by keeping the same cavitation and Reynolds numbers; for both figures, the top row refers to 'Region 1', i.e. inside the injection hole while the bottom row to 'Region 2', i.e. inside the nozzle's sac volume.

It is interesting to notice that increasing cavitation number results to continuous presence of the cavitation string inside the injection hole. Its appearance inside the sac volume is also enhanced with increasing CN (or equivalent, flow rate) conditions, confirming also the results of the internal nozzle flow investigation that were presented in section 5.3. On the other hand, it seems that the increasing or decreasing needle lift plays a less important role to the presence of string cavitation both inside the sac volume and the injection hole, which is not the same as happening to the five-hole nozzle, which string formation seemed to be more affected by the needle lift.

(a) (b)

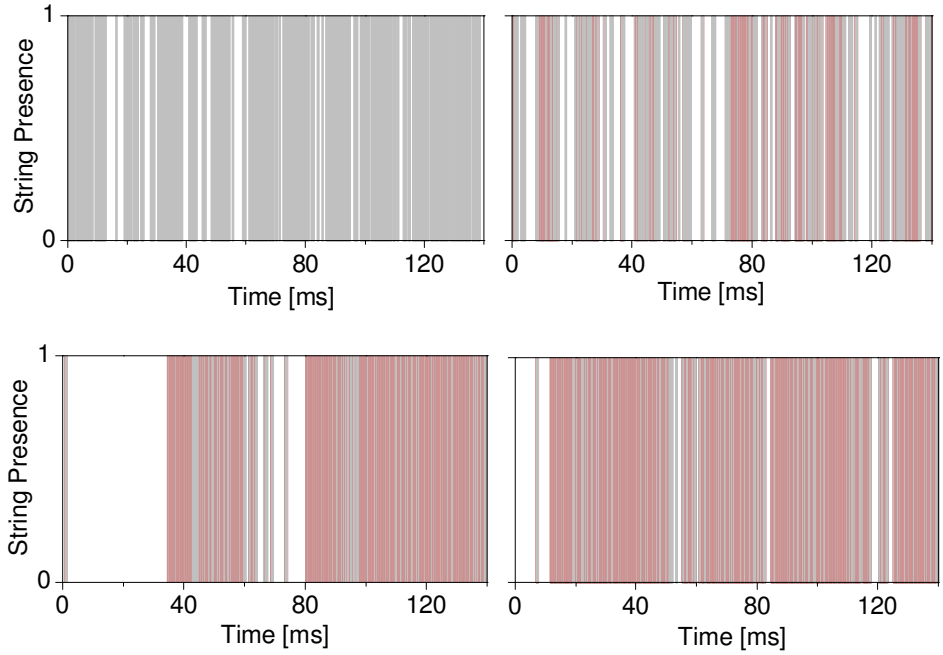

Figure 5-51: Effect of needle lift on string appearance sequence for the cylindrical single-hole nozzle at nominal cavitation number (a) CN=4, Re=70,600, nominal lift & (b) CN=4, Re=67,060, low lift. Top row corresponds to region 1 and bottom to region 2 of Figure 3-47, respectively.

5.8 Internal Nozzle Flow marine injector – Conclusions

Concluding this investigations, it can be said that formation of cavitation strings is enhanced with increasing flow rate (and thus increasing cavitation number) while it is less sensitive to needle lift, although for multi-hole nozzles the effect can be significantly larger.

Also clear evidence was provided that cavitation strings may travel upstream the injection hole entry well inside the nozzle's sac volume but with a reduced frequency of appearance compared to their presence inside the injection hole.

Finally, interestingly enough, it was found that even when now existing vapour pockets exist inside the injection hole, the vortex can become strong enough to sac air from the injection hole exit, which then forms the same kind of string cavitation shape.

Cavitation formed in the nozzle of fuel injection equipment for passenger car and marine Diesel engines has been identified as one of the main parameters affecting the nozzle discharge coefficient, the momentum of the injected liquid and the spray dispersion angle. The understanding of the flow mechanisms taking place in such nozzles is a prerequisite for the design of advanced systems which require accurate control to minimize spray-to-spray and shot-to-shot variations. Previous studies have categorized the observed cavitation structures forming inside injector nozzles as geometric-induced and dynamic-induced or string cavitation. Although adequate data exist for geometric-induced cavitation, limited information is available for the dynamic one. The present study has provided experimental data confirming the presence of string cavitation and addressing unresolved questions about its origin, area of formation, lifetime and influence on the nozzle hole flow. The visualization method employed has made simultaneous use of two high-speed cameras observing the two-phase flow structures forming inside transparent replicas of nozzles used in low-speed two-stroke Diesel engines. Interpretation of the obtained images has been assisted by computational fluid dynamics predictions of the nozzle and hole flow. The specific designs tested included five-hole nozzles with cylindrical as well as tapered holes operating at different fixed needle lift positions; nevertheless, the conclusions drawn for the observed flow mechanisms can be extrapolated to other nozzle designs where string cavitation is also present. Images have revealed formation of an unsteady vapour structure upstream of the injection holes inside the nozzle volume, referred to as ‘string cavitation’. From the images, it has been possible to reconstruct the location of the observed structures inside the nozzle volume. Combination of images with the simulated flow field has revealed that cavitation structures are found at the areas of flow circulation and they originate either from pre-existing cavitation sites forming at sharp corners inside the nozzle where the pressure falls below the vapour pressure of the flowing liquid, or even from suction of outside air downstream of the hole exit. This has been made possible by the manufacturing of nozzles with tapered holes which suppress the formation of geometric cavitation and thus have enabled data of string cavitation in controlled combination or in the absence of geometric cavitation to be obtained. Processing of the acquired images has allowed estimation of the mean location and probability of appearance of the cavitating strings inside the nozzle volume space, as a function of needle lift, cavitation and Reynolds numbers. The frequency of appearance of strings has been correlated with the Strouhal number of the large-scale vortices developing inside the nozzle volume; the latter has been

found to be sensitive to the geometric characteristics of the nozzle, including the needle lift and the shape of the injection holes. Large variations in the instantaneous fuel injection quantity of individual injection holes have been recorded when a cavitation string is observed inside them. Combination with model predictions has revealed that the observed reduction in the individual hole flow rate is partially attributed to the increased vapour fraction inside the hole when a string is present; the vortex flow developing upstream of the hole entry is the main reason for the observed trend. Extrapolation based on model predictions for real-size injectors operating at realistic injection pressure indicates that cavitation strings are expected to appear within the time scales of typical injection events.

Chapter 6

Near Nozzle Hole Exit Spray Structure Visualization

6.1 Introduction

As mentioned previously in Chapter 1 cavitation in hydraulic equipment is in principal not desirable since it causes power and efficiency losses, noise and also mechanical wear which in many cases might be catastrophic[11, 12]. Later on, an experimental investigation regarding the undesirable effects of cavitation in the form of mechanical wear will be presented in Chapter 7.

Contrary to the above mentioned approach, cavitation in fuel injection equipment is considered beneficial since it can enhance the development of the fuel spray. This also has to be clarified since inside a multi-hole Diesel injector there might be several types of cavitation structures which are not always desirable. In general what engineers regard as useful for fuel atomization is the so-called geometric or hole cavitation which takes place inside the injector nozzle holes and can be controlled and simulated with good accuracy.

In attempt to study the individual effect of various parameters on cavitation structures and liquid atomization many authors have used simpler geometries than Diesel nozzles. This allowed for safer conclusions to be drawn out of more quantitative investigations.

Having identified the flow characteristic of the nozzle through the Large-scale model and also the influence of string cavitation on the cavitating hole flow structure and the reduction of the individual hole flow rate, it was considered important to investigate the near hole exit spray structure.

The aim of this chapter is to investigate the quantitative effect of string cavitation in various Diesel injectors on the near nozzle spray dispersion angle. The near nozzle spray is defined at a distance of about four hole diameters (one hole length for the particular injectors

investigated here) downstream of the nozzle exit plane; due to the asymmetry of the formed spray plumes two dispersion angles are defined, as shown in section 3.4.3, above and below the hole axis of symmetry, respectively.

Such information has been achieved by manufacturing a number of fully transparent nozzle replicas, which have provided optical access inside the nozzle volume upstream of the injection holes, inside them as well as at the sprays formed at the nozzle exit. The designs tested have included one, two and five cylindrical as well as tapered (converging) holes as shown along with detailed information in section 3.1.5. Simultaneous use of two high-speed cameras allowed for estimation of the location of string cavitation in the 3-D space inside the nozzle volume and characterisation of their frequency of appearance and development, as function of the needle lift and operating conditions. At the same time, use of an in-house CFD model which incorporates a geometric-induced cavitation model [142, 151] has provided information about the local flow field at the location where strings develop as well as the temporal variation of the nozzle flow exit conditions, spatially resolved on the hole cross sectional area. Image collection over sufficient duration period has provided information on the string frequency of appearance and life time simultaneously with the temporal variation of the spray angle.

From the images it has been possible to derive the distribution density function of the formed spray angle for different cases which reveal both the effect of geometric-cavitation and string cavitation. Information is also provided for the time-averaged probability of finding liquid at a specific location on the camera viewing plane. Again, the clear link with the internal nozzle flow conditions has allowed for quantitative information to be obtained for different two-phase nozzle flow structures.

Due to the limited ways to control the flow through the real size nozzle that was fitted on the continues flow test rig described in Chapter 3, the only parameters that could be controlled in order to identify changes between spray structure was the inlet flow rate and the needle lift.

The flow rate was converted to CN using the discharge coefficients determined with the large scale nozzle. What will be presented in this chapter is spray cone angle as a function

of CN for different lifts, the probability of void fraction in 2-D, the deflection angle as a function of CN and lift and finally how all these are affected by string cavitation. It should be noted that since geometric-induced hole cavitation is taking place continuously in all injection holes at fully developed flow conditions, any differences in the acquired images will isolate and reveal the effect of string cavitation clearly.

So far in the previous chapters we had only investigated the five hole design. This time it was decide to manufacture also nozzles with less holes in order to be able to get more clear images for automated image processing and massive quantitative analysis. Therefore in addition to the five-hole nozzle, that was made both in large-scale (2X) and in real size, the two-hole nozzle incorporates only the two side-holes of the five-hole nozzle while the middle-hole is only present in the single-hole nozzle. Most nozzles have been made to 2:1 scale, in order to be in direct comparison with the conditions investigated in the internal flow experiment, while for all designs identical versions exist with cylindrical as well as tapered (outwards converging) holes. The nominal injection hole exit diameter, which varies between holes, has been kept identical for all nozzles and while the tapered holes incorporate a 4^o degress full cone angle, same as the conical nozzle used for the internal nozzle flow investigation. The hole length to diameter ratio is 4.

The nozzles were attached to the same steady-state flow rig, described in section 3.2 with water at 25^oC as working fluid. The flow rate was controlled by a valve in the pipe downstream of the feed pump and measured by an ultrasonic flow meter. The injection pressure was recorded with a pressure transducer installed in the nozzle volume just opposite of the injection holes while injection was taking place into ambient air at room temperature. The pressures tested here are again much lower compared to that of the nominal operating conditions of such injectors (~600bar); unfortunately the scale of the in-line pump (~3m height) and the resulting huge flow rates of the actual nozzles do not allow for measurements at realistic conditions to be obtained. Nevertheless, it is known from past studies that for fully turbulent flow conditions [103], the cavitation structures, which are believed to control the near-nozzle spray atomisation process, as well as the discharge coefficient of the injector, are mainly function of the cavitation number for cylindrical hole nozzles. Re number has been defined on the basis of the mean flow rate and average hole diameter as also done previously. The fuel flow through the injector nozzles, especially

through the holes, is turbulent (Re>40,000). Cavitation numbers tested here take values up to 7, which is greater than that of the nominal operating conditions of the actual nozzles, which is around 4 to 5.

The operating conditions tested and presented here are summarized in Table 6-1 and Table 6-2. Imaging was performed for various combinations of the listed parameters and for different needle lifts. Similarly to the previous results the 'full' or 'nominal' lift corresponds to the nominal stop position of the needle in the real injector; the 'low' lift case corresponds to a needle lift at about 80% of the full lift, where the needle-slide is just uncovering the injection holes, while the 'high' lift case corresponds to 120% of the full lift position.

Since it is important to gain knowledge about the dynamics of cavitation inception and spray processes for various flow conditions, the Photron FASTCAM-ultima APX camera was used, which is able to take up to 120,000 frames per second (fps) with an exposure time as low as 4ns and a maximum resolution of 1024×1024. Throuout the investigation different lighting, shuttering time and frame rates were used in order to extract the valuable information out of the series of images acquired.

For most cases investigated here, usually 16,000 fps where sufficient to capture the temporal development of cavitation and the spray using a shuttering time of 30μs. In total up to 4,000 images were collected for a particular case. A strong halogen floodlight together with some halogen spotlights were necessary to provide enough light for the intensified CCD video chip in combination with the high frame rates. A detailed description of the equipment used and the layout of the rig can be found in Chapter 3. Similar to Chapter 5, where the internal nozzle flow results were presented, temporal averaging of sufficient number of instantaneous spray images has provided a mean spray image, projected on the 2-D viewing plane, which has been interpreted as the probability of finding liquid within the spray cone angle formed just at the nozzle exit. The fact that the formed sprays do not exhibit a symmetry relative to the hole axis has limited the resulting mean spray images to 'upper' and 'bottom' spray angles, indicating the dispersion of liquid above or below the horizontal axis, respectively; the latter coincides with the hole axis of

symmetry, as explained in more detail in section 3.4.3.

More than one hounded cases have been investigated during this experiment, including different viewing positions and light techniques. The lists of the investigated cases are given in the tables below.

Nozzle Design	Needle Lift	Injection Pressure [bar]	Flow rate [litre/s]	CN	Re ≈
Single Hole Cylindrical	Low Nominal High	2,3,5,8	0.12, 0.15, 0.2, 0.24	1,2,4,7	39500, 49400, 65900, 79050
Two-Hole Cylindrical	Low Nominal High	3,5,8	0.24, 0.31, 0.37	2,4,7	48300, 62380, 74450
Five-Hole Cylindrical	Low Nominal High	2,3,5	0.47, 0.65, 0.85	1,2,4	35390, 48950, 64000
Single Hole Tapered	Low Nominal High	3,5,8	0.18, 0.25, 0.33	2,4,7	63500, 88250, 116500
Two-Hole Tapered	Low Nominal High	2,3,5,8	0.2, 0.27, 0.36, 0.51	1,2,4,7	40250, 54340, 72450, 102600
Five-Hole Tapered	Low Nominal High	3,5	0.71, 0.96	2,4	53460, 72290

Table 6-1: Range of operating conditions for all L-S nozzles investigated

Case index	CN	Exposure [μs]	Light Source	Notes	Representative Picture
3	2	700	Continuous	Front view	
4	2	700	Continuous	Back view	
5	2	700	Continuous		
7	2	1000	Continuous	Back view Distant lense	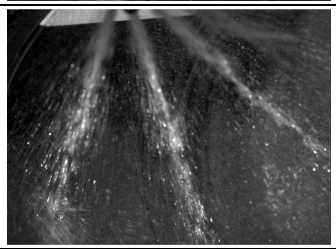
8	5	1000	Continuous	Hole 1 view	
9	2	30	Continuous	Macroscopic lense	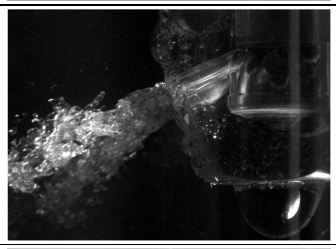
10	2	30	Continuous	Hole 1 view	
11	4				
12	5				
13	7				

Case index	CN	Exposure [μs]	Light Source	Notes	Representative Picture
14	2	100	Continuous	Hole 1 view	
15	2	5	Continuous	Hole 1 view	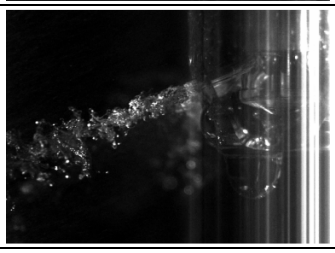
16	2	5	Continuous	Hole 1 view	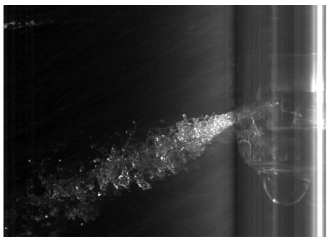
17	2.5				
18	3				
19	3.5				
20	4				
21	5				
22	7				
23	8				
24	10				
25	15				
26	15			High lift	
27	1.5	0.5	Spark light	Hole 1 view	
28	2				
29	2.5				
30	1	0.5	Spark light	Hole 1 view	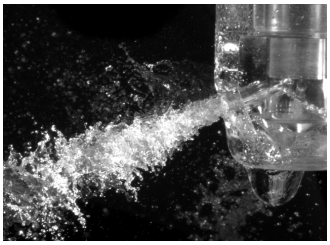
31	1.5				
32	2				
33	3				
34	3.5				
35	5				
36	15				
37	2			High lift	
38	15				

Case index	CN	Exposure [μs]	Light Source	Notes	Representative Picture
39	2	300	Continuous	Hole 4 view	
40	3				
41	4				
42	5				
43	10				
44	15				
45	2	10	Continuous	Hole 4 view	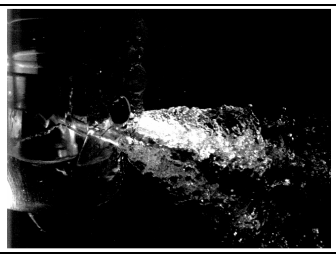
46	4				
47	15				
48	2	0.5	Spark light	Hole 4 view	
49	3				
50	15				
51	16				
52	0.5 -2				

Table 6-2: Flow and visualization conditions used with the R-S model nozzle and representative results.

6.2 Spray investigation -Predicted flow field of the nozzles

Before presenting the results obtained from the experimental observation of the emerging spray and the internal nozzle volume flow, it is important to identify the flow field existing inside these injecting nozzles by the use of the in house CFD code. So far we have seen results from both real size and large-scale nozzle simulations for various flow conditions, and the main flow feature that was identified to practically all cases was the large recirculation zone attached to the injection holes, occupying in some cases half of the nozzle's sac volume.

Although most of the simulations so far referred to the five-hole nozzle, it was considered useful to explore the flow inside the same nozzle having different number of holes. As we

have seen before in literature, often, when spray was to be investigated, it was considered more useful to manufacture simple single hole nozzles, in order to be able to isolate the effect of cavitation while having a much more confined space where the spray would be monitored. In this investigation, and due to the unusual nozzle design, the holes that had the best possible view from the side, where hole no 1 & 5. However as the first series of results showed, the sprays that were emerging from the middle holes, were forming a fluctuating background which was very difficult to be isolated, and given also the reduced contrast between the sprays, it was difficult to automatically identify the boundaries of the liquid emerging form these particular holes.

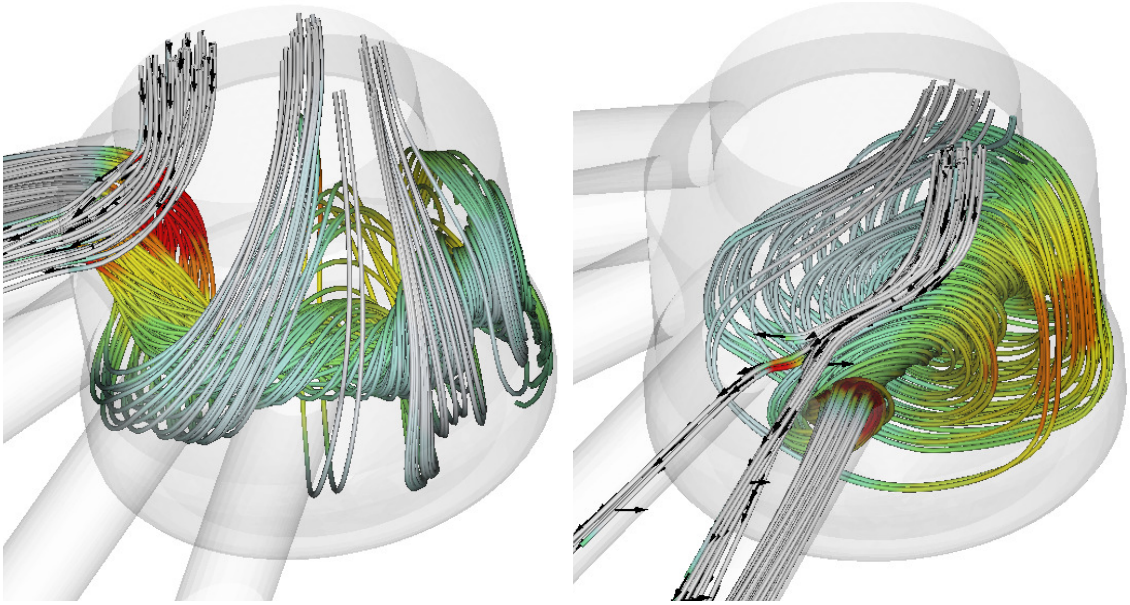

Figure 6-1: CFD calculation of the flow structure inside the sac volume of the cylindrical five-hole nozzle, showing the main flow path entering into the upper part of the hole and the secondary vortical flow structure forming inside the nozzle volume and entering into the injection hole from the bottom part [CN=4, Re≈65,000, Nominal Lift]. (color scale not significant)

This inconvenience gave thoughts of making injecting nozzles with less holes, in an attempt to get more clear results without losing the unique flow characteristics that make this type of nozzles particularly interesting to be investigated. As mentioned before, the arrangements that were chose to be investigated were, a two-hole one including only the side holes (1&5) of the five-hole nozzle and the single-hole one including only the middle hole of the original design (i.e. hole 3).

Since the main target was to identify the effect of string cavitation on the near hole exit spray structure, it had to be confirmed that the single and two hole designs would have had similar internal nozzle flow as the five-hole ones. Evidence of that was provided by performing a series of simulations, both single and two phase (cavitating), which typical sample of results are presented in Figure 6-1, Figure 6-2 and Figure 6-3 for the five-, two- and single-hole nozzles, respectively.

As it can be seen from Figure 6-1, the five hole injecting nozzle (without expansion tubes) has similar flow field with the nozzle used for the internal nozzle flow investigation. This was expected since preliminary studies, prior to the experimental nozzle manufacture, had shown that the addition of expansion tubes has minor effect to the internal nozzle flow structure. Moreover CFD simulations also showed that the location of the string cavitation is changing in a similar way as the experimental observation, presented in the previous chapter, had shown.

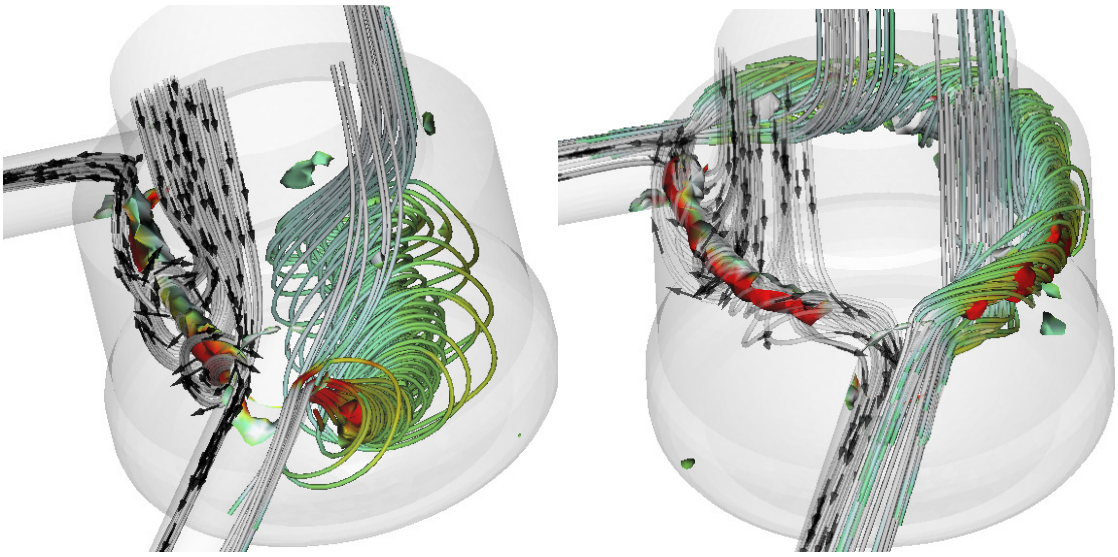

Figure 6-2: CFD calculation of the flow structure inside the sac volume of the cylindrical two-hole nozzle, showing the main flow path entering into the upper part of the hole and the secondary vortical flow structure forming inside the nozzle volume and entering into the injection hole from the bottom part [CN=4, Re≈65,000, Nominal Lift]. (color scale not significant)

As shown for two different time instances when the vortex is attached to one of the injection holes, the main portion of the flow enters the hole by the recirculation zone that exists inside the sac volume, while only a small portion enters directly from upstream. The two different frames show a vortex attached to hole 1 and 5 respectively.

As mentioned before apart from the five hole nozzle it was decided to manufacture a two hole nozzle having only the two side holes in order to reduce the background noise produced by the emerging spray from the three middle holes. During the experimental investigation of the internal nozzle flow it was attempted to examine the flow for different injection hole arrangements. This was practically done by not allowing the flow to exit through some of the expansion tubes, practically simulating a nozzle with fewer holes. as shown in Figure 6-2, even with only the two side holes existing the main flow characteristics do not change and follow the same trends observed in the five-hole nozzle.

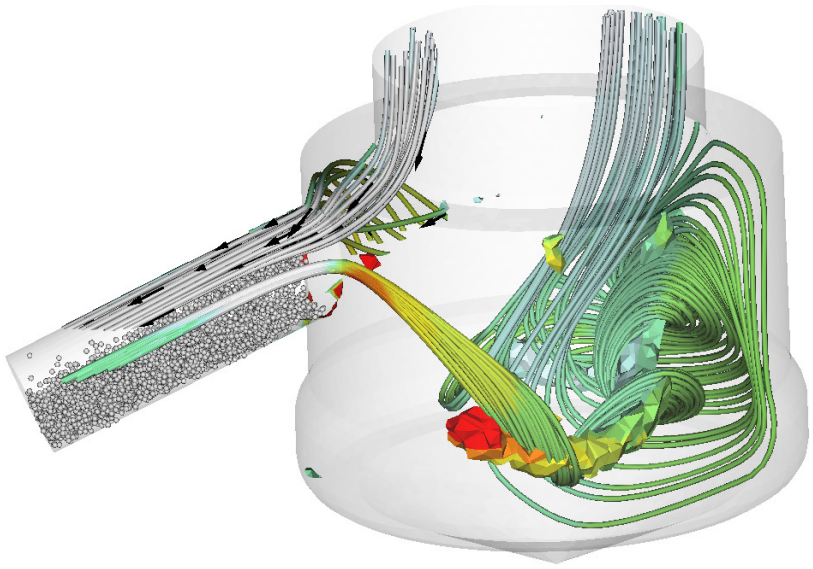

Figure 6-3: CFD calculation of the flow structure inside the sac volume of the cylindrical single hole nozzle, showing the main flow path entering into the upper part of the hole and the secondary vortical flow structure forming inside the nozzle volume and entering into the injection hole from the bottom part [CN=4, Re≈65,000, Nominal Lift]. (colour scale not significant)

Having presented the flow field of the five and two hole nozzles, Figure 6-3 shows the CFD simulation for the single hole one. As it can be seen even with only one injecting hole, the

flow inside the sac volume forms a recirculation zone which carries a significant amount of flow towards the hole inlet. This was expected since previous experimental results with only one hole open, such as those presented in

Figure 5-42, had shown vapour strings inside the sac volume of the nozzle irrespective of which one the holes was active. Moreover the vortex inside the sac volume was changing location with time and for some periods it was becoming very weak, making almost the entire portion of the flow to come directly from upstream.

6.3 Spray investigation –Discharge coefficient of the injecting nozzles

Before presenting the results of the investigation, it is worth looking to the measured discharge coefficient of the different designs tested; these measurements are shown in Figure 6-4 and the discharge coefficient has been averaged for each nozzle design for three needle lifts (nominal, low and high). At low cavitation numbers (low flow rates), the flow inside the nozzle is still relatively undeveloped and the discharge coefficient takes its maximum value. Once the vortical structures as well as geometric-induced cavitation start to develop, then the discharge coefficient drops until it reaches asymptotically a minimum value. This is realised for value above 5. Finally, it is worth mentioning that the single-hole nozzle exhibits the largest discharge coefficient among the two and five hole designs, while the tapered nozzles are about 20% more efficient compared to the cylindrical ones. These losses in the volumetric efficiency are attributed to geometric-induced cavitation.

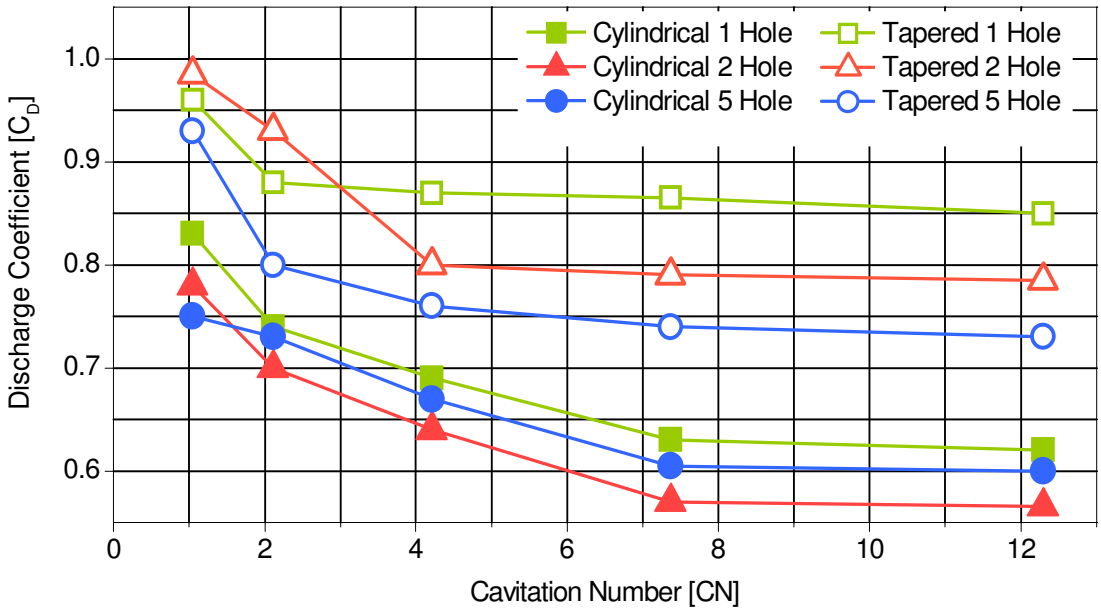

Figure 6-4: Averaged (over three needle lifts) measured discharge coefficient for all nozzle designs tested

Also the fact that the single hole nozzles exhibit the largest discharge coefficient combined with the fact that the vortices seen inside the sac volume were much weaker than those seen in the 5-hole ones, can lead to the conclusion that the vortex itself, even without forming a vapour string, causes a considerable restriction to the flow which is realised by a reduced flow rate coming out of the injection holes. this is in line with previous studies both in nozzles and duct flows.

6.4 Spray investigation –effect of the sac volume geometry on string cavitation location

When the internal nozzle flow was investigated, it was found that the strings formed inside the sac volume where attached to an injection hole, at one end, and their other end was attached to the sac wall inside the groove that is formed in order to improve the wear rate of the needle. At that time it was considered that it might be an interaction between the groove and the flow field, which could enhance the formation of vortices. Therefore it was decided to manufacture also a nozzle without having this groove and monitor if the string location/orientation will also be the same for that case.

Figure 6-5: Image showing string location inside the no-groove five-hole nozzle.

After an extensive range of acquired images, typical sample of which can be seen in Figure 6-5, it was concluded that the groove has a minimal effect on string cavitation location. The fact that the effect of the groove to the flow is not so important can be further supported by the discharge coefficient values which are close to the original nozzle.

Finally as it can be seen from Figure 6-6, the correlation between needle lift and discharge coefficient is similar for all nozzles. A low lift will restrict the flow resulting to a low Cd while an increased lift will have the opposite result.

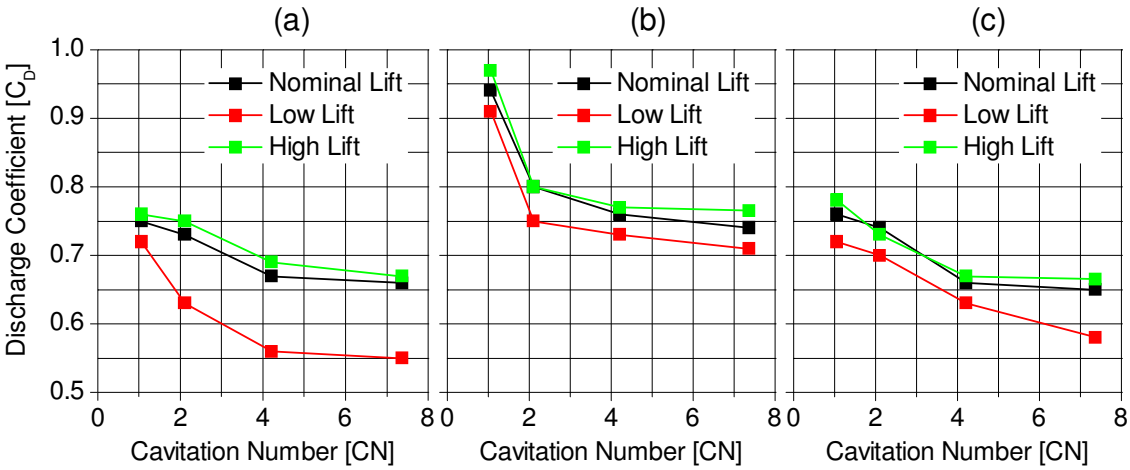

Figure 6-6: Measured discharge coefficient for five-hole a) Cylindrical, b) Tapered and c) No groove design nozzle for different lifts.

6.5 Spray investigation –string cavitation effect on spray structure for both cylindrical and tapered injection holes

The macroscopic structure of the geometric cavitation formed inside the injection holes differs from hole-to-hole and from injector-to-injector. It exhibits a three-dimensional shape originating from the bottom and/or side part of the injection hole and growing to a vapour cloud attached to the bottom part of the hole; that can be seen in all following images to be presented. The two-phase flow structure within the injection hole can be significantly altered by the presence of cavitation strings. When a cavitation string is present inside the injection hole, then towards the hole exit most of the cross-sectional area may be occupied by vapour. Two different scenarios have been observed; in the first one the cavitation string mixes directly with the pre-existing hole cavitation while in the second it is concentrated to the upper part of the injection hole without interacting with the hole cavitation structures. The above description is valid for all nozzle designs tested here. Furthermore, for the multi-hole nozzle designs large variations in the instantaneous fuel injection quantity of individual injection holes have been recorded when a cavitation string is observed inside them. Combination with model predictions has revealed that the observed reduction in the individual hole flow rate is partially attributed to the increased vapour fraction inside the hole when a string is present; the vortex flow developing upstream of the hole entry is the main reason for the observed trend.

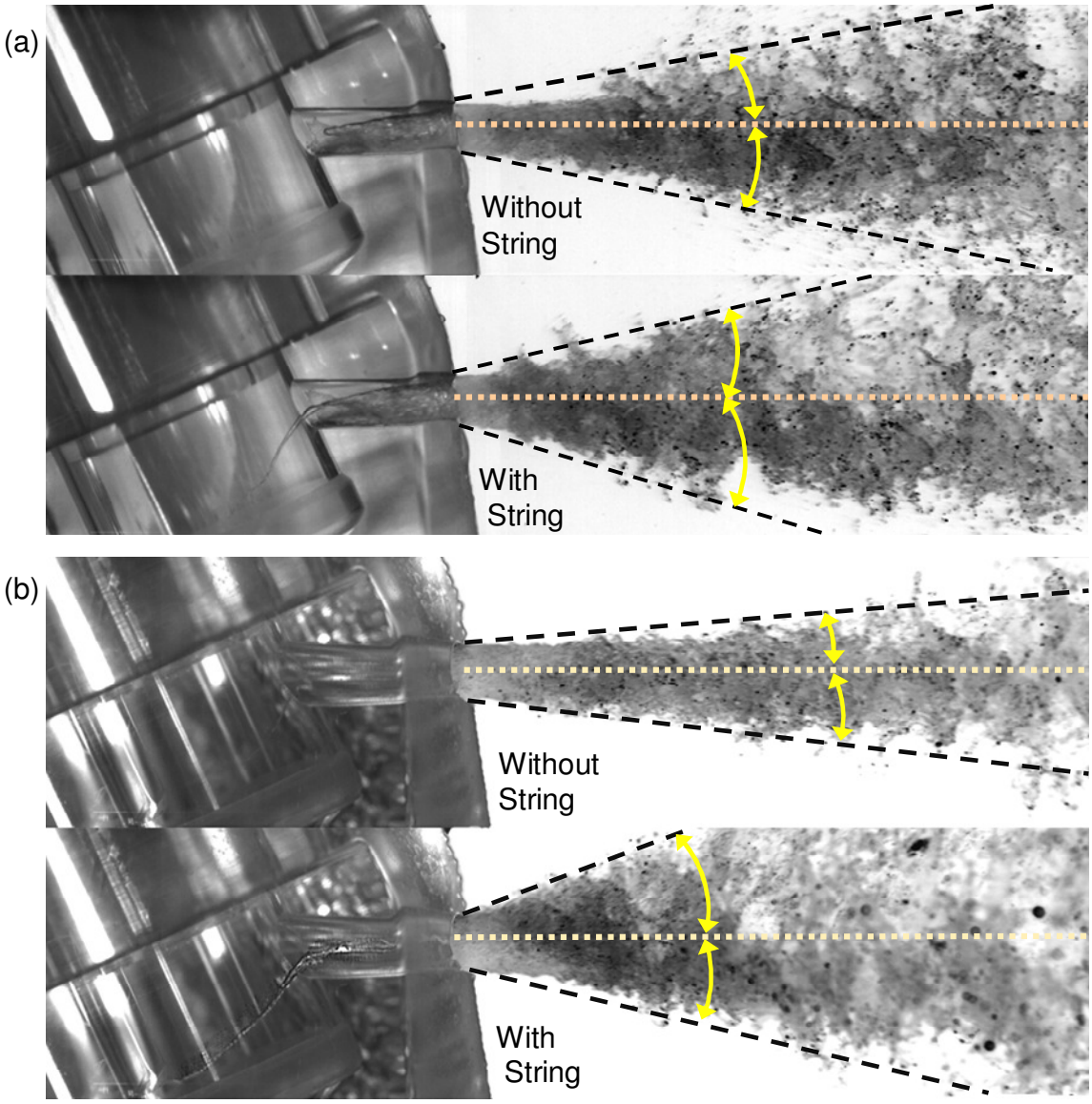

Figure 6-7: Spray images from the (a) cylindrical single-hole nozzle at Re=65,900 and (b) tapered single-hole nozzle at Re=88,250. The images show the near-nozzle deflection angle above and below the hole axis of symmetry attributed to the presence of string cavitation [CN=4, Nominal needle lift].

As it has been already mentioned, in this section, sample spray images will be presented, revealing the effect of geometric-induced cavitation as well as string cavitation on the near-nozzle spray formation for all nozzle designs investigated. Figure 6-7(a) shows the cavitation inside the cylindrical single-hole as well as the spray formed just at the hole exit. Two images are presented; the top one corresponds to a time instant where string cavitation is not present while the bottom image corresponds to a frame where string cavitation is also

forming and exiting from the nozzle hole. For this injector, geometric-induced hole cavitation is always present while the opposite is the case on the spray images shown in Figure 6-7(b). These refer to the tapered single-hole nozzle where geometric cavitation is suppressed at the full needle lift condition shown. From these images, the effect of geometric-induced cavitation and string cavitation can be qualitatively appreciated. In all images, the upper and bottom spray angles relative to the hole axis of symmetry are indicated. With the specific view selected, this orientation also coincides with the area of development of hole cavitation, which, as explained previously, is always found in the bottom part of the injection hole. The biggest difference between images is realised in the upper spray angle in the presence of string cavitation. It is clear that for both nozzles when the string is present the spray angle is substantially increased. Comparison between the string-cavitation free images of the two nozzles reveals the effect of geometric cavitation. It is evident that the cylindrical cavitating nozzle exhibits wider angles relative to the tapered one. However, these differences become smaller or even disappear at specific frames when the string cavitation is present. It is thus concluded that in relative terms, tapered nozzles may be more sensitive to cycle-to-cycle variations in their angle.

6.6 Spray investigation –string cavitation in hole orientation effect on spray structure

The fact that the effect of string cavitation is linked with geometric cavitation can be further supported from the following Figure 6-8 which shows the nozzle flow as well as the spray formed at the exit of one of the cylindrical two-hole nozzle. Three images are presented while next to them the predicted vapour volume fraction is indicated. These predictions have been made possible using a recently developed and validated cavitation model [142],[62] and correspond to the expected location of geometric-induced cavitation vapour exiting from the nozzle hole. The circle superimposed on these predictions indicates the location of the cavitation string, as approximately observed from two different views. The upper spray angle is again much higher in the case where string cavitation is present. It seems though that this influence is much bigger when the string is exiting from the part of the hole which is geometric-induced cavitation free. In other words, when vapour appears suddenly in a part of the hole that only liquid is present, a substantial increase in the spray

angle should be expected. When the string cavitation 'hits' and mixes with the pre-existing hole cavitation structures then the relative increase in the observed spray angle is smaller.

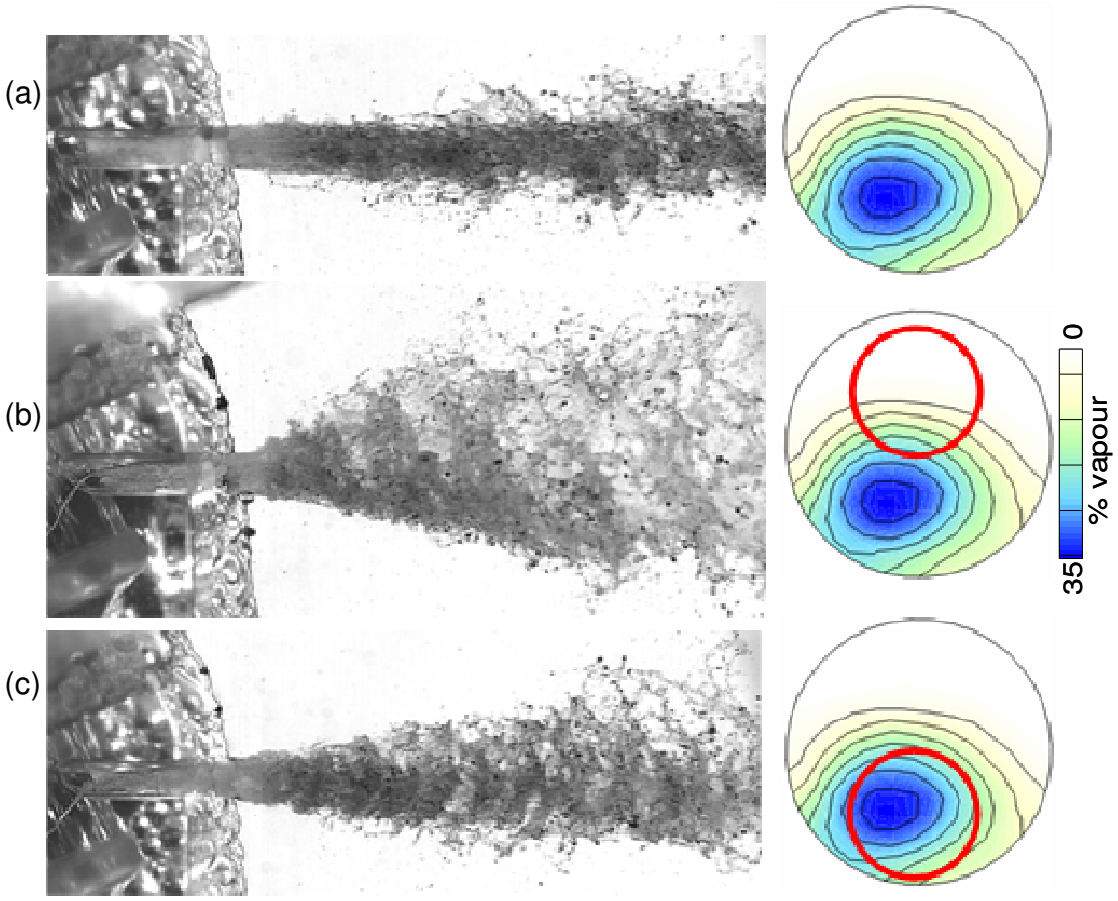

Figure 6-8: Effect of string cavitation exiting location on the near nozzle spray angle of the cylindrical two-hole nozzle (a) without string cavitation, (b) cavitation string exiting from the upper part of the injection hole and (c) cavitation string exiting from the bottom part of the injection hole [CN=2, Re=48,300, Low needle lift].

6.7 Spray investigation –spray structure of five hole nozzles

Consistent conclusions have been also drawn for the effect of string cavitation on the sprays formed at the exit of the tapered and cylindrical five-hole nozzles; two sample images of the observed spray injected from the cylindrical hole 5 in the absence and presence of string cavitation can be seen in Figure 6-9. Again, the upper spray angle is greatly influenced by string cavitation.

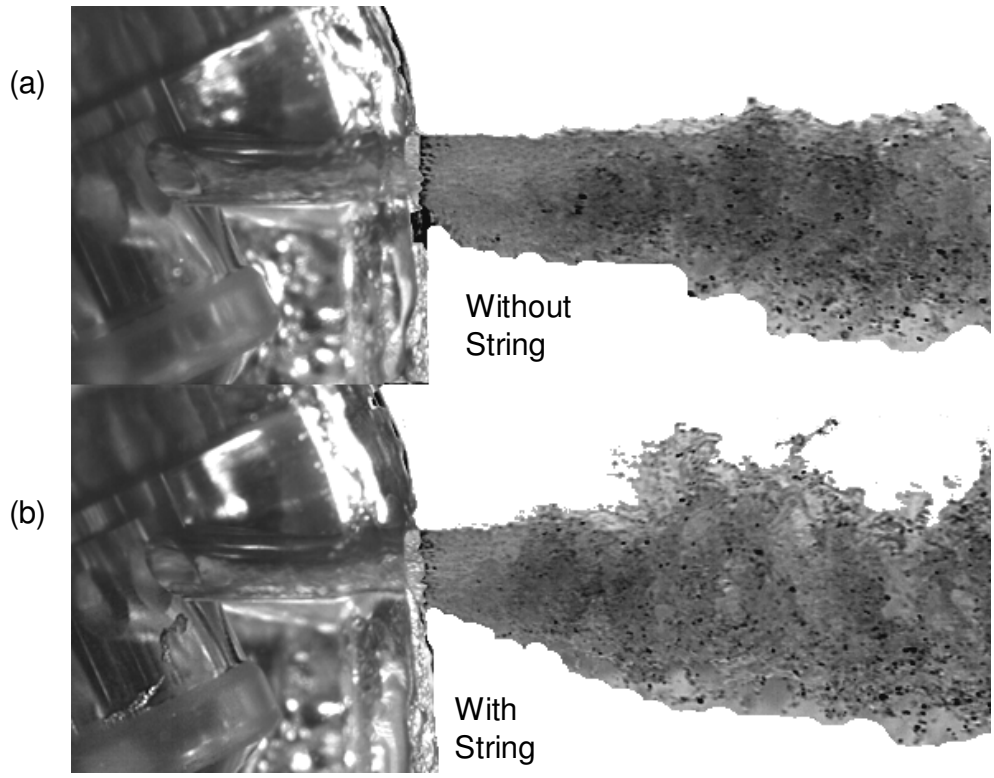

Figure 6-9: Effect of string cavitation on near-nozzle spray angle of the No. 5 hole of the cylindrical 5-hole nozzle (a) without string cavitation and (b) with string cavitation [*CN* = 4, Re = 64,000, nominal needle lift].

6.8 Spray investigation –effect of string cavitation intensity on spray structure

Having identified qualitatively the effect of geometric-induced and string cavitation on the angle of the spray formed at the exit of the injection hole, we proceed now to quantification of the observed trends. Figure 6-11 shows the measured temporal variation of the upper and bottom spray angle for the tapered single-hole nozzle. The time history of string cavitation inside the nozzle hole has been recorded simultaneously, and presented as a three-mode event, referred to as 'no string', 'non-exiting string' and 'exiting string'.

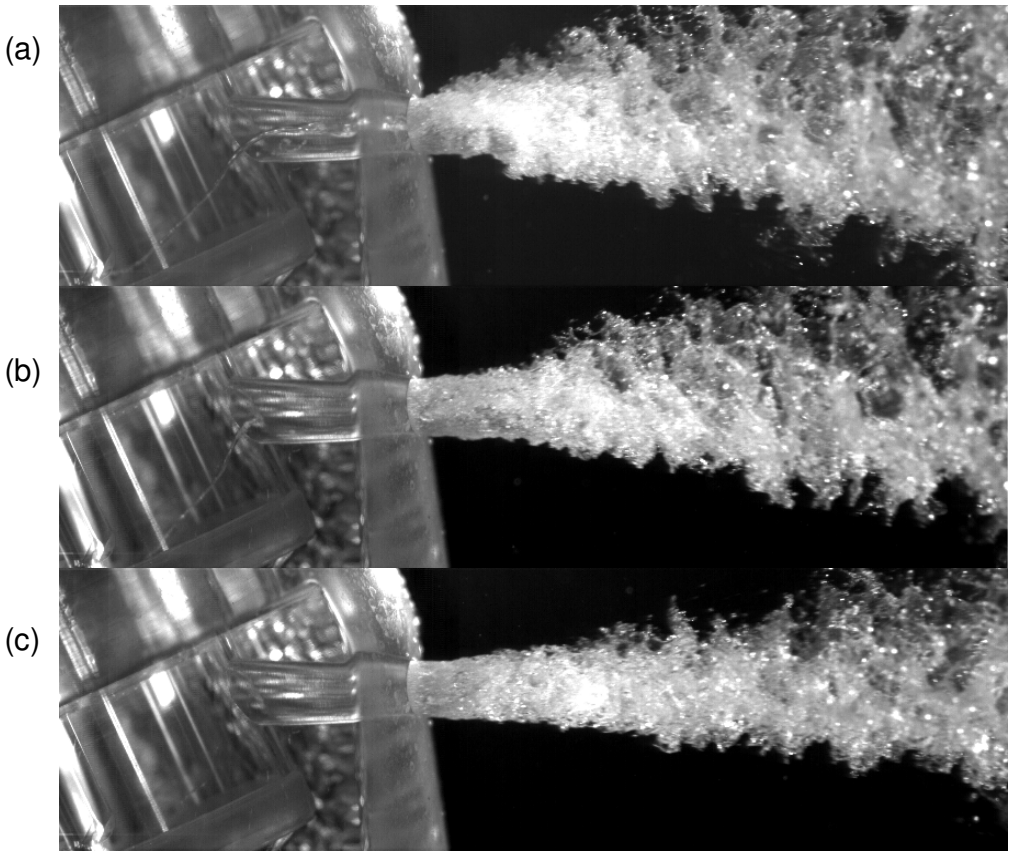

Figure 6-10: Effect of string cavitation extent on the near nozzle spray angle of the Tapered single-hole nozzle (a) 'exiting string' (b) cavitation 'non-exiting string' (c) 'no string' [CN=4, Re=68,000, Nominal needle lift]

The correlation between large deflection of the upper spray angles and string attached to the nozzle exit is evident. When a string is visible inside the injection hole then the relative

increase in the spray angle may reach values between 10-15degrees. It is also clear that the bottom spray angle, which has not been spatially correlated with the location of the string inside the injection hole, is almost independent from string cavitation. It is also of interest to observe an intermediate range of upper spray angle values, which correspond to the time frames indicated as 'non-exiting string'. These correspond to a number of images in which string cavitation has been observed inside the nozzle volume upstream the injection hole but not inside them. Figure 6-10 shows typical images of those three different string cavitation modes in order to enhance the understanding of what was observed.

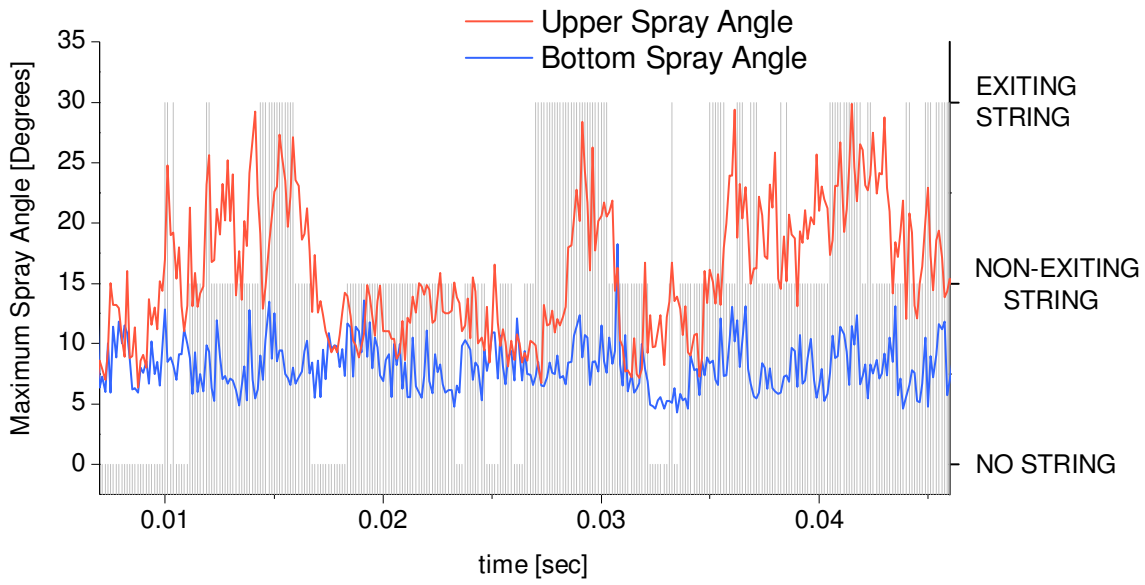

Figure 6-11: Measured temporal variation of the upper and bottom spray angle for the tapered single-hole nozzle. The presence of string cavitation inside the nozzle hole recorded simultaneously with the spray angle is also indicated [CN=4, Re=68,000, Nominal needle lift]

Model predictions indicate that the large-scale vortices formed inside the nozzle are not stable. In the case of two- and five-hole nozzles, their location relative to the entry of the injection holes changes periodically. In the case of the single-hole nozzle, the strength of the rotational motion is also following a periodic pattern. As also mentioned earlier, the origin of string cavitation in the case of tapered nozzle holes has been correlated with suction of surrounding air present downstream of the hole. Although it has not been possible to correlate the strength of the swirling motion inside the nozzle and the injection

hole with the formation of strings, it seems that the observed spray angles are function of this flow motion.

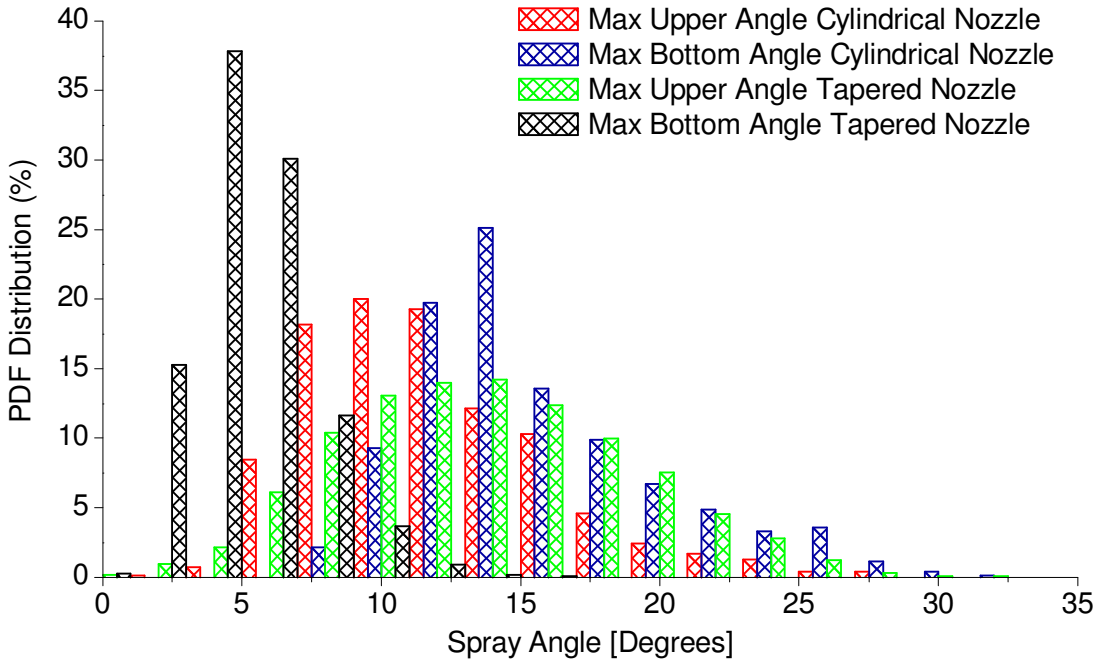

Figure 6-12: Measured probability distribution function of the maximum deflection spray angle above and below the hole axis of symmetry for the cylindrical single-hole nozzle at Re=65,900 and tapered single-hole nozzle at Re=88,250 [CN=4, Nominal needle lift].

In the related literature, numerous experimental data as well as model predictions have provided indications of the spray angle for different injection nozzles. The common practise is to give a 'single' value for the maximum spray angle, which may be function of the operating condition (for example, the injection pressure) and the nozzle design. Analysis of the data obtained during the present investigation suggests that a range of spray angles that follow a distribution function even at steady-state operating conditions is observed. From the temporal evolution of the upper and bottom spray angles it has been possible to derive the probability density function of maximum spray angles observed. These data for the cylindrical as well as the tapered single-hole nozzle can be seen in Figure 6-12.

The range of values referring to the bottom angle of the tapered hole reveal that even in the absence of cavitation, still a range of angle values is recorded. However, this range is rather

narrow compared to that of the cavitating cases, with more than 70% of the collected frames exhibiting values between 5-6degrees and more than 95% falling in the range between 3-8degrees. Comparison with the corresponding values from the cylindrical hole nozzle reveals the influence of geometric-induced cavitation. This time, a much wider range of values is observed with the maximum being at around 10% and peak values reaching even 25degrees at few time instances. Still, around 60% of all values recorded seem to be in the range of 12-16degrees.

It is also interesting to notice that the smallest angle observed for this case is ~7degrees, while the smallest angle of the tapered hole was as low as 1 degree, implying almost a jet leaving from the nozzle rather than an atomised liquid; it has to be noted though that hydraulic flip has not been observed.

On the same graph, the recorded values for the upper spray angle are also indicated; as described, this angle allows quantification of the effect of string cavitation on the atomisation angle. The data plotted reveal that string cavitation may result to angle values as high as those attributed to geometric-induced cavitation. This time the values plotted are more uniformly distributed within the observed range of spray angles. However, this time the relative influence is more in the case of the tapered nozzle, since the peak of the distribution function is around 15degrees for the tapered nozzle and around 10degrees for the cylindrical one. The mechanism for that, as explained earlier, is related to the location of the string cavitation relative to geometric-induced cavitation.

6.9 Spray investigation –five-hole nozzles spray structure and spray angle parametric investigation

As mentioned in the introductory part of this chapter, one of the aims of this investigation was to examine how different lighting and camera settings may affect the drawn conclusions out of the raw images.

As it can be seen in Figure 6-13, a relatively high exposure value was chosen making the emerging spray to be visualized like a cloud rather than discrete bubbles. Been consistent to

the previously shown results, the effect of the string entering into the injection hole No 4 can be realized by the widening of the emerging spray cone angle, which was increased by 20° degrees.

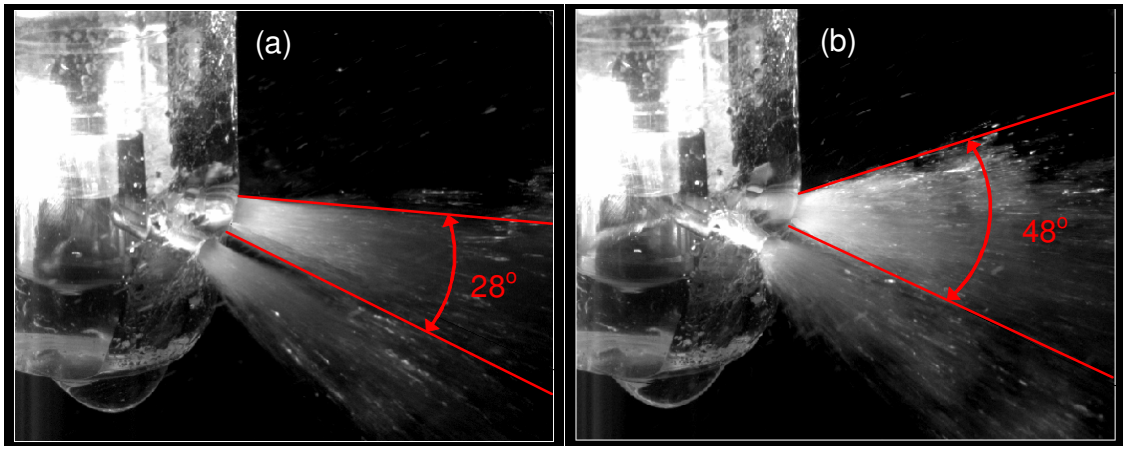

Figure 6-13: CCD images of the spray injected from hole No 4, taken at 300μs exposure time at CN=4. (a) Without String and (b) with string. The effect of string cavitation on near-nozzle dispersion angle is revealed.

It is also worth mentioning that these images were acquired using the real-size transparent nozzle replicas, further confirming that scaling does not affect the conclusion to be drawn for real operating conditions, provided that the correct flow similarities have been chosen.

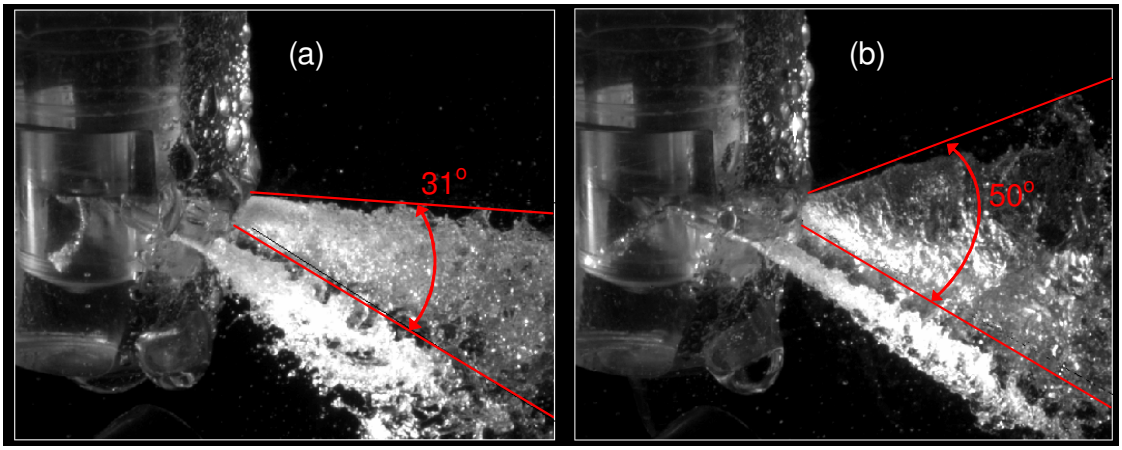

Figure 6-14: CCD images of the spray injected from holes No 4 and 5, taken at 0.5μs exposure time at CN=4. (a) without String and (b) with string.

Following the results presented above, Figure 6-14 shows the effect of string cavitation for the same operating conditions as those shown in Figure 6-13 however this time the

exposure time was set to 600 times smaller than before. This allows to freeze the spray and this can be realized by looking at the watermarks shown on the emerging liquid.

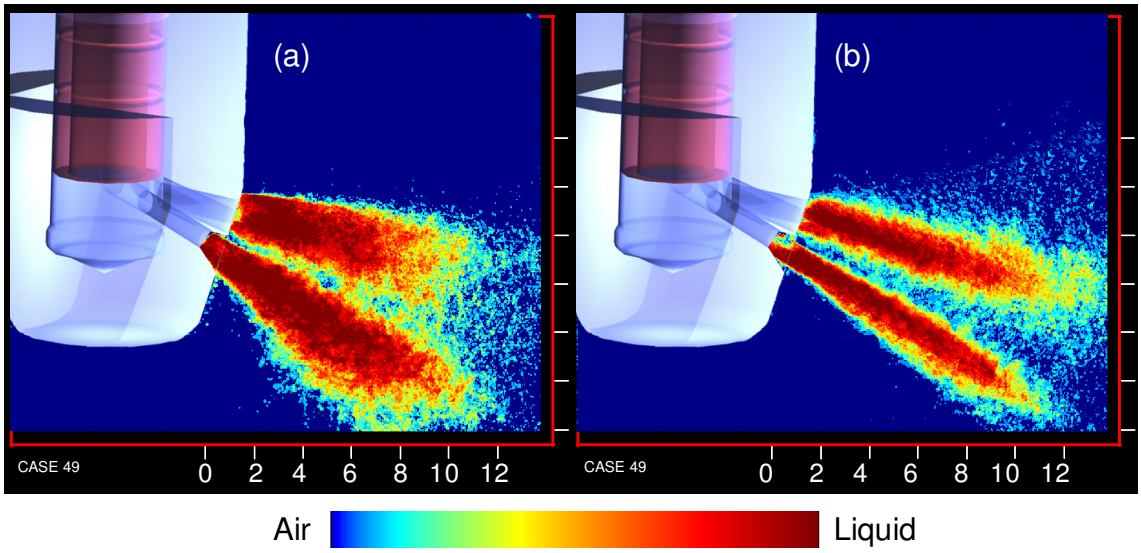

Figure 6-15: 2-D liquid probability, averaged over 300 spray images and showing the effect of cavitation string on spray cone angle of holes No 4 and 5 [CN=4]. (a) without String and (b) with string.

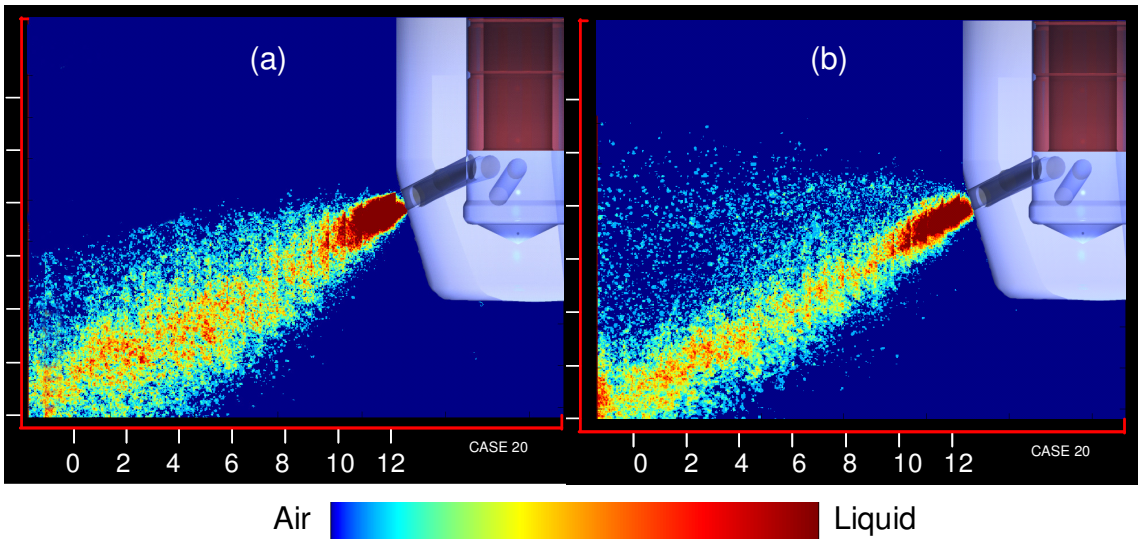

Figure 6-16: 2-D liquid probability, averaged over 300 spray images and showing the effect of cavitation string on spray cone angle of hole No 1 [CN=4]. (a) without String and (b) with string.

As it can be seen the measured cone angle is the same as the one found with the much higher exposure for both string cases. Furthermore, as it can be clearly seen in figure 1-10b,

with the smaller exposure it becomes evident that once the string enters the injection hole, the mass distribution of the resulting spray is not uniform. In other words the produced spray appears to be hollow, clearly showing that its upper part, which is also the part that is mostly influenced by the strings, is much coarser than the bottom. It has to be mentioned that similar findings have been reported in [31, 152-155] while examining the spray structure produced by VCO nozzles.

Further quantification of the effect of nozzle flow on the spray angle formed just at the nozzle exit can be provided by deriving the temporal and spatial averaged spray images. Since the shuttering time of the high-speed camera is fast enough to freeze the motion of the injected liquid, each image can be considered representative of finding liquid at each location of the viewing plane of the camera. This function takes values of one in any pixel covered by liquid and zero in pixels with air. At the core of the spray there is always liquid present, so temporal averaging and normalisation with the number of frames will always result to value of 1 for the possibility of finding liquid at this location. Similarly, the value of zero will be calculated at the locations of the edge of the spray. The most interesting part is in between these two regimes which are partially occupied by liquid as a result of the changes to the spray angle caused by cavitation. Such mean images can be seen in Figure 6-15 and Figure 6-16 for the cylindrical five-hole nozzle operating at its nominal lift. Figure 6-15 (a) & Figure 6-16 (a) show the derived mean spray image for the frames where string cavitation is absent while Figure 6-15 (b) & Figure 6-16 (b) show the derived image for the time instances where string cavitation is present. It is clear that the dispersion of the atomised liquid is different in the two images. However, for the five-hole nozzle, interaction between the injected sprays does not allow a clear comparison between the individual sprays to be made. Alternatively, the single-hole nozzle is ideal for quantifying with precision the effect of nozzle flow on this probability function. At this stage is worth mentioning that similar techniques of image processing and averaging have been used in many other relative studies such as those of [115], [116] as well as [57, 156-161] which have shown that the ratio of hole-length over hole-diameter (L/D) affect, to a large degree, the characteristics of generated sprays.

In order to perform some parametric studies, it was chosen to replace the continues light by a spark light, setting the exposure time to 0.5 μs which combined with the high-speed

camera was fast enough to 'freeze' the motion of the liquid spray.

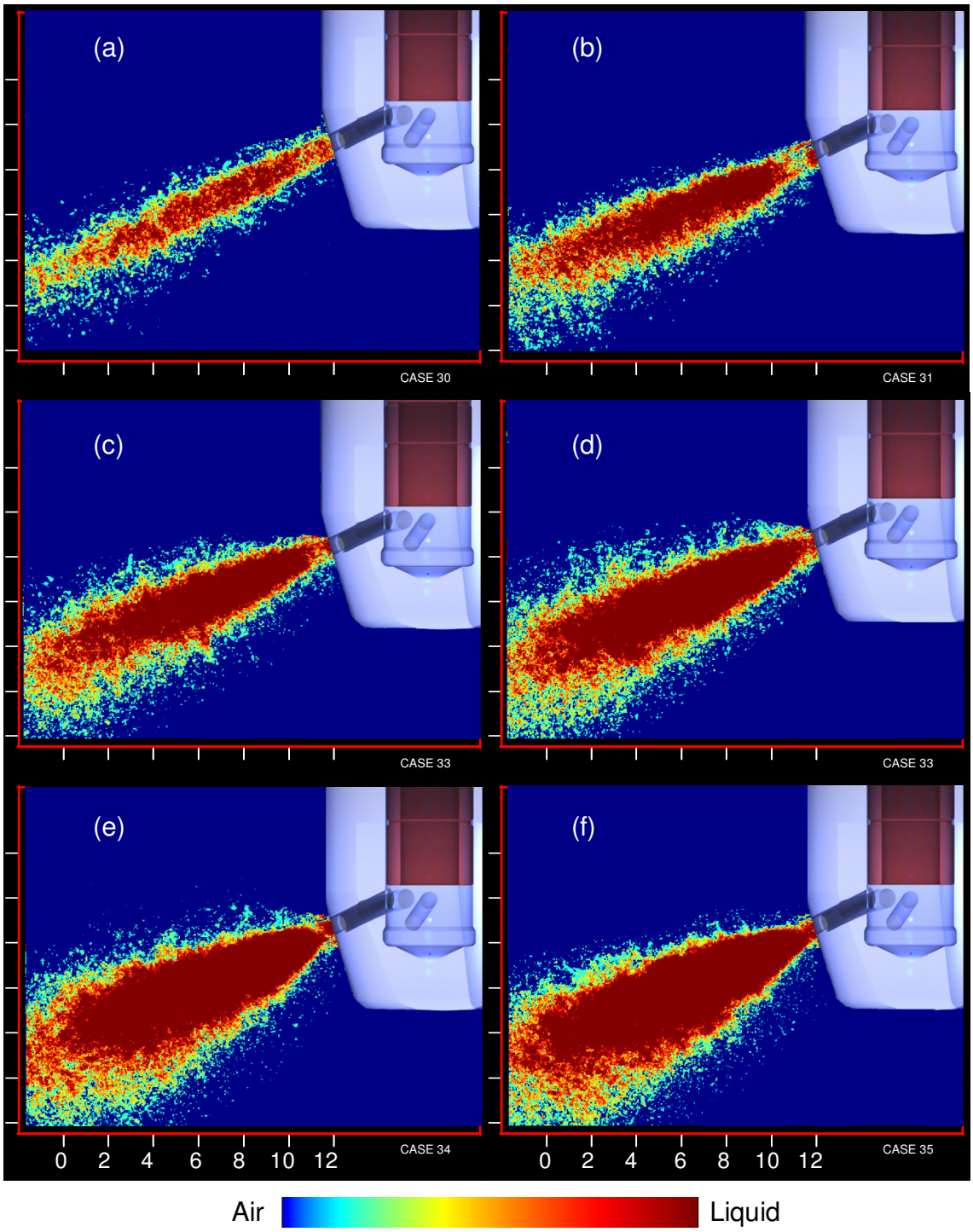

Figure 6-17: 2-D liquid probability, showing the effect of CN on spray dispersion for Hole No 1. (a) CN=1, (b) CN=1.5, (c) CN=2, (d) CN=3, (e) CN=3.5 and (f) CN=5.

As can be seen in Figure 6-17 which gives the liquid probability for different CN numbers

after an initial increase associated with the increase of the flow rate and the transition from the non-cavitating nozzle flow to the fully developed hole cavitation flow, the spray cone angle does not change significantly. Considering that geometric induced cavitation enhances atomizitation, the aforementioned conclusion is in order with previous reported work. It has to be mentioned that for the nozzle investigated cavitation bubbles were occupying the entire hole length for CN values greater than 3 which is considered a low value compared to modern common rail Diesel injectors that often work at CN=100.

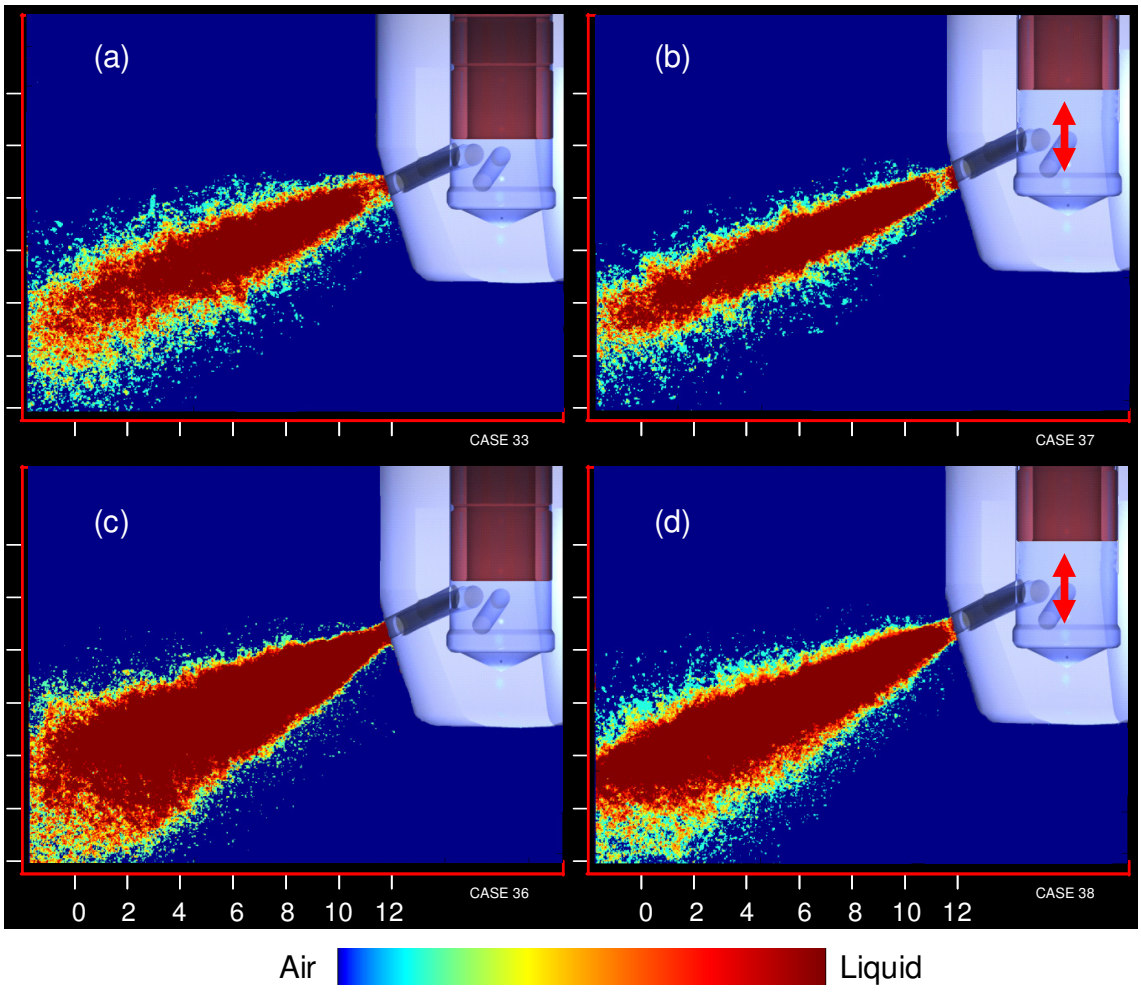

Figure 6-18: 2-D liquid probability, showing the effect of Needle Lift on spray Dispersion for Hole No 1. (a) CN=2, (b) CN=2, High Needle Lift, (c) CN=15 and (d) CN=15, High Needle Lift.

Figure 6-18 gives the liquid probability for the nominal and the high needle lift for two different CN numbers. What can be concluded is that at higher lift the spray cone angle

becomes smaller. Which can be attributed to the reduced interaction beteen the hole inlet and the needle's edge, which at high lift have a considerable space in between.

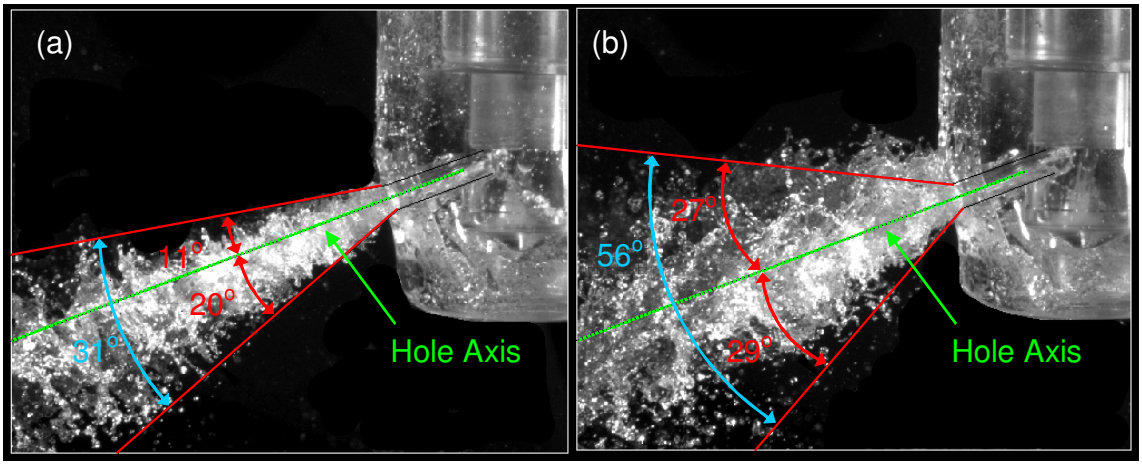

Figure 6-19: CCD images of the spray injected from holes No 1, taken at 0.5μs exposure time at CN=3. The spray deviation from the hole axis is revealed. (a) without String and (b) with string.

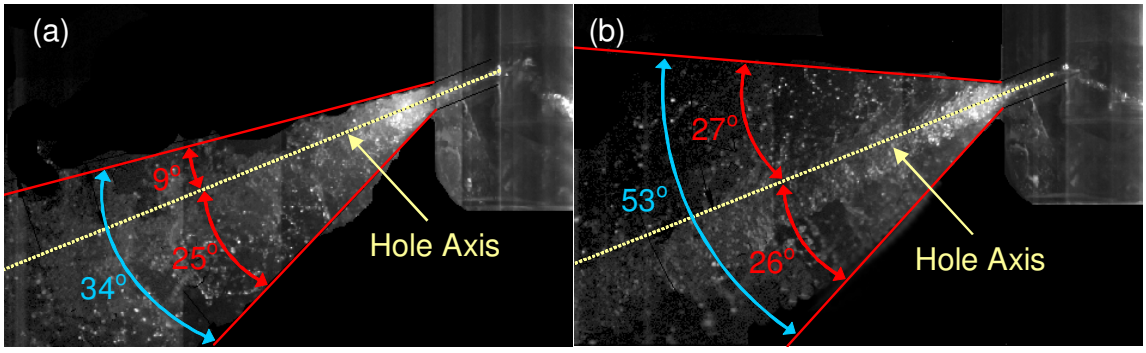

Figure 6-20: CCD images of the spray injected from hole No 1, taken at 5μs exposure time at CN=4. The spray deviation from the hole axis is revealed. (a) without String and (b) with string.

Figure 6-19 and Figure 6-20 above, shows typical acquired images as those used for averaging and in order to investigate the effect of CN and needle lift to the liquid dispersion probability. The reason for presenting these images is to show that at the absence of a cavitation string entering the injection hole, the emerging spray is shifted downwards. In other words if the theoretical spray direction was in line with the hole axis (Green line), the actual emerging spray has a greater bottom side cone angle suggesting a deviation which

might be an undesirable situation unless it has been predicted during the design phase of the nozzle.

In order to summarize the results obtained for hole 1 spray Figure 6-21 shows mean values over many individual images for cone and deflection angles of the spray as function of CN . Two lines depict the spray cone angle as a function of cavitation number for both case of string cavitation absence and presence. After an initial increase associated with the increase of the flow rate and the transition from the non-cavitating nozzle flow to the fully developed hole cavitation flow, the spray cone angle reaches asymptotically a maximum value. This angle becomes approximately 20degrees larger when string cavitation is present. The other two lines plotted correspond to the spray deflection angle from the axis of this particular injection hole. As can be seen, for the non-string case, the deflection angle is of the order of 5 to 10degrees, which can be high enough to cause undesirable effects on the liquid distribution and fuel/air mixing within the combustion chamber.

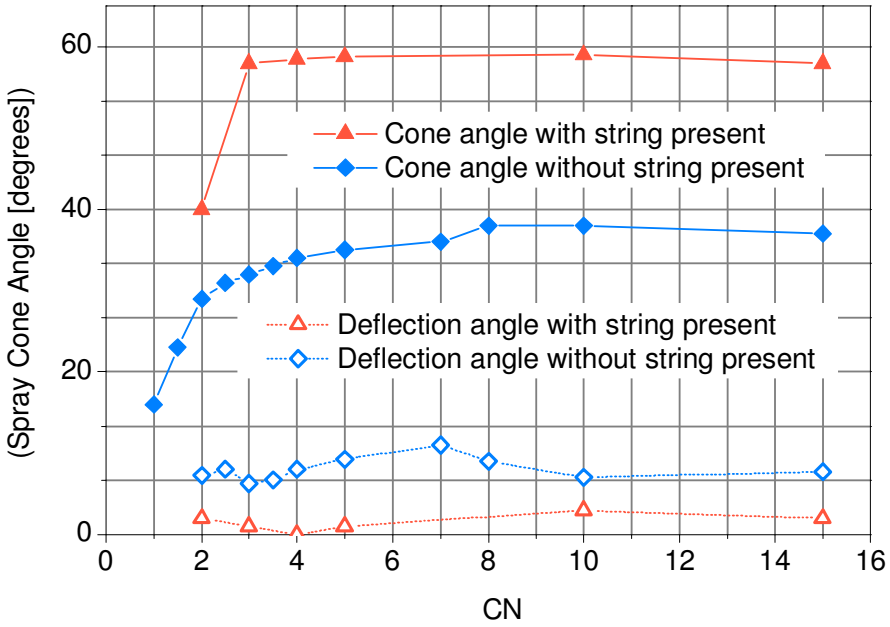

Figure 6-21: Measured spray cone angle and deflection angle from the axis of injection of hole No 1 as function of cavitation number.

Similarly to the above, Figure 6-22 shows mean values over many individual images for cone angles of the spray as function of CN this time for hole 4 . since the hole axis of that hole can not be clearly identified, since it is obstructed by hole 5, there was no recording of

spray deflection angle. It is interesting to mention that although hole 4 and hole 1 have different diameters as well as their orientation with respect to the nozzle body is totally different, they produce similar spray cone angles and are even affected in a similar way once a string in attached to them. This observation will be significant once the results from the single hole nozzle will be presented. It practically means that irrespectively of what injection hole is chosen to be investigated, the results obtained will be, within a reasonable daubt, comparable for the others.

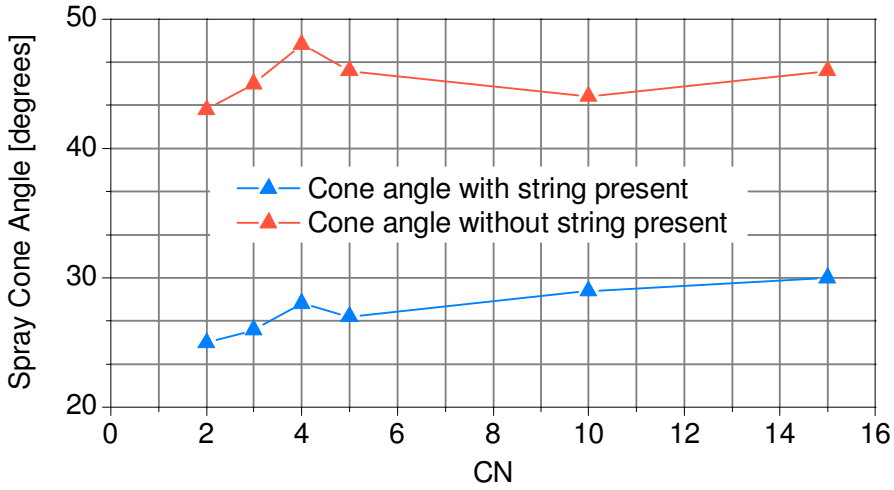

Figure 6-22: Measured spray cone angle of hole No 4 as function of cavitation number for 300μs exposure time. Spray cone angles in the presence and absence of string are indicated by the two different lines.

6.10 Spray investigation –five-hole nozzles spray structure and spray angle parametric investigation

As mentioned before for the five-hole nozzle, interaction between the injected sprays does not allow a clear comparison between the individual sprays to be made, at least not by been able to use automated image processing since the background is constantly changing. In order to quantify with precision the effect of nozzle flow on the near nozzle spray structure, the single-hole nozzle is the ideal solution.

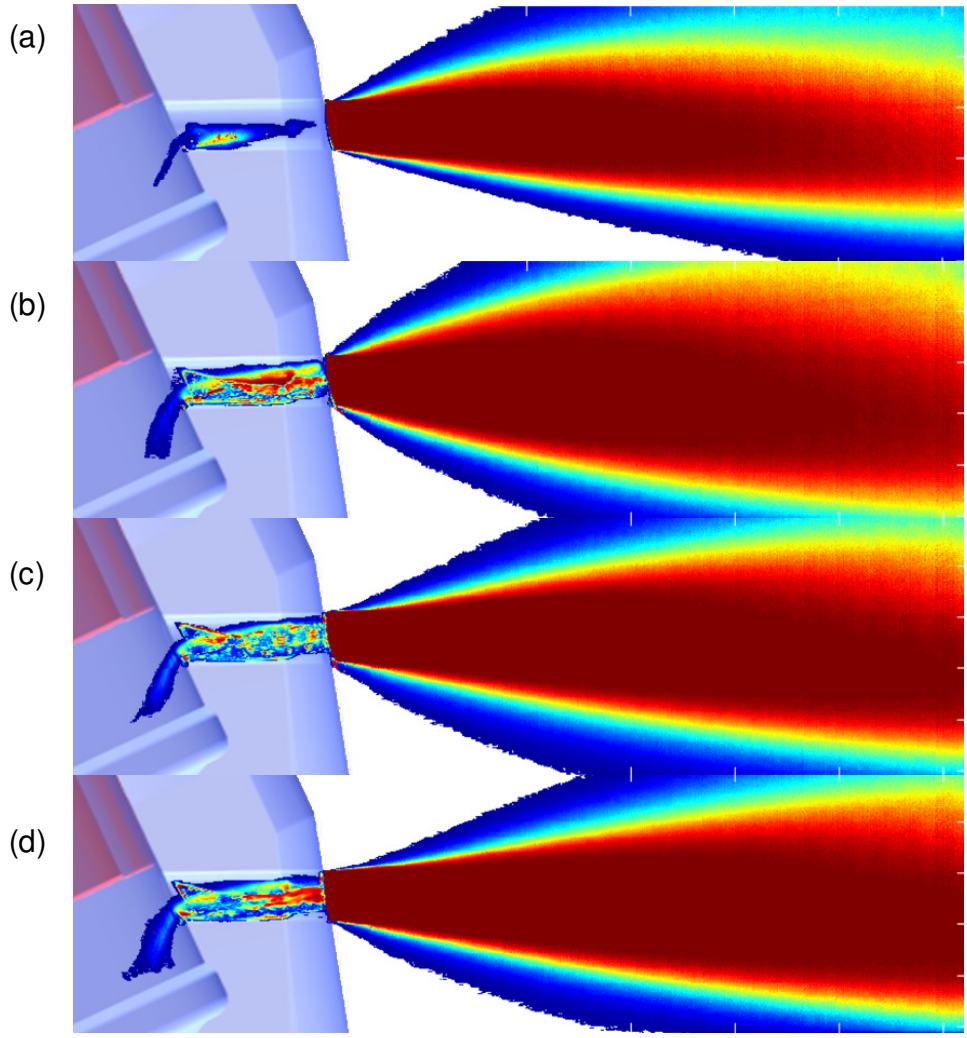

Figure 6-23: 2-D liquid probability, showing the effect of CN on spray dispersion for the Single Hole Cylindrical Nozzle. (a) CN=1, (b) CN=2, (c) CN=4 and (d) CN=7.

Figure 6-23 shows the 2-D liquid probability for the single hole cylindrical nozzle for different CN. It has to be mentioned that these averages have been calculated by using all the available frames from each case considered. On average this means that more than 8,000 frames have been processed, including both periods where a string was present inside the hole as well as frames where only hole cavitation existed. This allows having what will be the mean spray distribution during an injection where both flow conditions will exist. Looking at Figure 6-23(a) it can be clearly seen that for a low CN (CN=1) where hole cavitation is not fully developed, as we can confirm by focusing to the relatively small region that is occupying inside the injection hole, the spray is mostly distributed to the upper region. This is in line with the previous results that have shown that geometric

induced cavitation affects liquid atomization, particularly when the vapour cloud is running to the entire length of the hole.

Once the CN is increased such as the entire hole length is constantly filled with vapour, the spray spreads also to the lower part of the region near the injection hole exit. By observing Figure 6-23 (c) & (d) it can be seen that a further increase of the CN has only limited effect on the liquid distribution, which again comes in line to the previously reported results. It also has to be mentioned that by increasing CN the probability of string cavitation also increases and as a result the liquid probability on the upper part of the area near the hole exit also increases. So far the results reported where averaged for every case investigated. The use of single hole nozzles has allowed to monitor the instantaneous upper, bottom and total spray cone angle for every single frame recorded.

The plots shown in Figure 6-24 correspond to the same cases the mean probabilities of which were presented in Figure 6-23. Starting from Figure 6-24 (a), where CN=1, it can be clearly seen that the range of values for the bottom spray cone angle is between 10 and 20, with the majority of values been between 13 and 18 degrees. This relatively small fluctuation, suggest that the flow inside the bottom part of the hole is stable since hole cavitation is negligible.

Contrary to the bottom angle, the upper one has a much wider spread ranging between 5 and 32 degrees. It can also be seen that the upper spray angle varies considerably between frames suggesting that the flow inside the part of the injection hole affecting that angle is highly fluctuating. This observation combined with the previously reported results, where it was shown that string cavitation mostly affects the upper spray angle, can lead to the conclusion that recirculation region inside the sac volume, and consequently inside the injection hole, can lead to highly fluctuating sprays that are often not desirable since their predictability is limited.

Looking at Figure 6-24(b) through (d), it can be seen that as CN increases te bottom spray angle values are considerably increased, gradually reaching higher values than the upper spray cone angle.

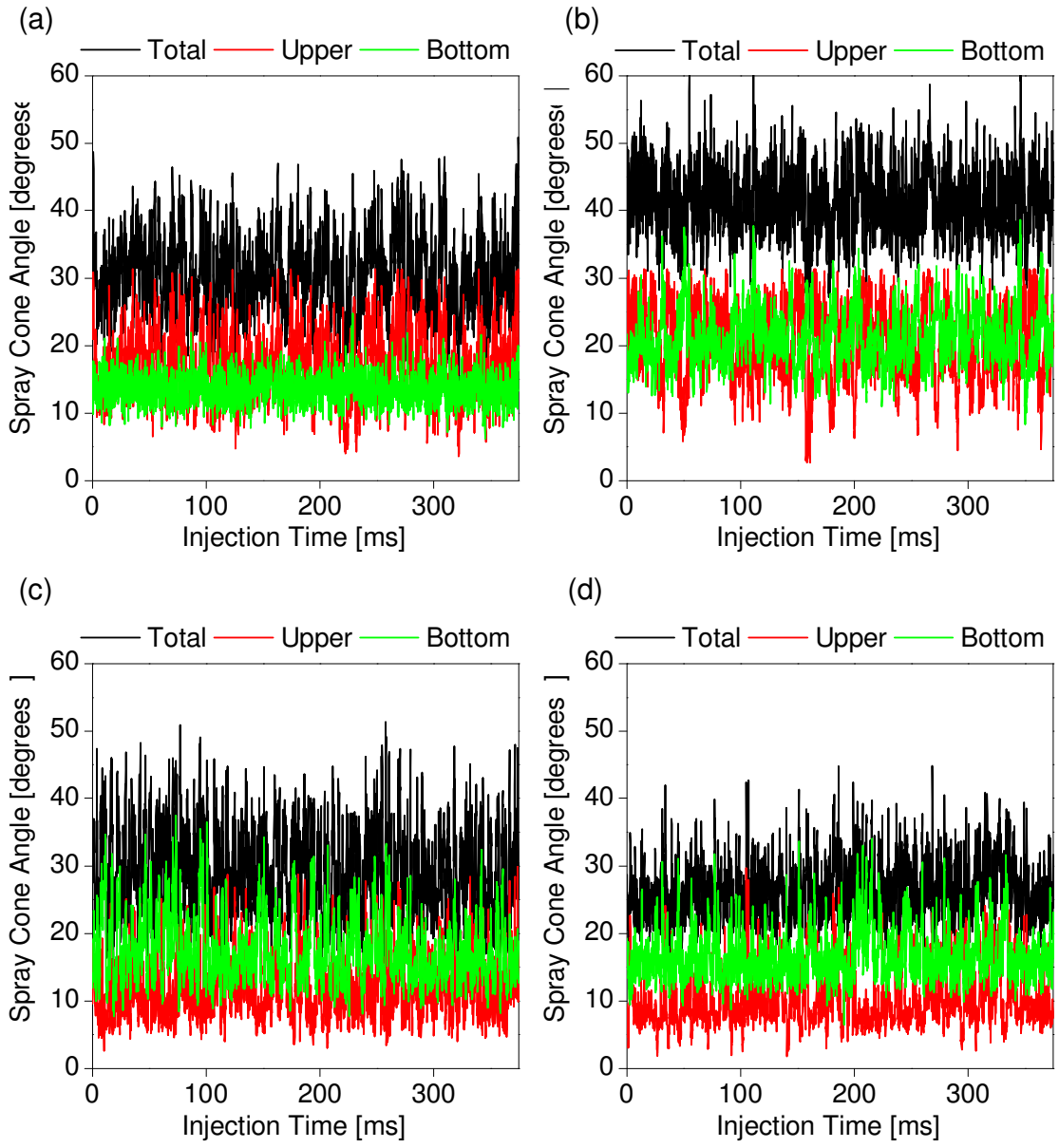

Figure 6-24: measured temporal variation of upper, bottom and total spray angle of the cylindrical single-hole nozzle for a) CN=1, b) CN=2, c) CN=4 and d) CN=7.

Also, since by increasing CN the cavitation intensity also increases and since cavitation is a highly fluctuating flow feature, the bottom spray angle is not within a confined range of values. In fact it spreads up to 20 degrees which is still lower thought than the spread of the upper spray cone angle which is in excess of 30 degrees. Finally it also interesting to observe that once CN increases the upper spray angle decreases compared to the values shown at the low CN case. This has not been addressed in past studies and a possible explanation may be the fact that as the vapour concentration to the lower part of the hole

increases, string cavitation favours that part of the hole. Apart from the existing vapour site, another possibility for this behaviour might be the axial velocity of the upstream nozzle flow which as CN increases, practically by increasing the injection pressure since the nozzle injects in atmospheric conditions, it also increases forcing the recirculation zone inside the sac volume to move downwards as well as increasing the percentage of flow entering directly from upstream through the upper part of the injection hole inlet.

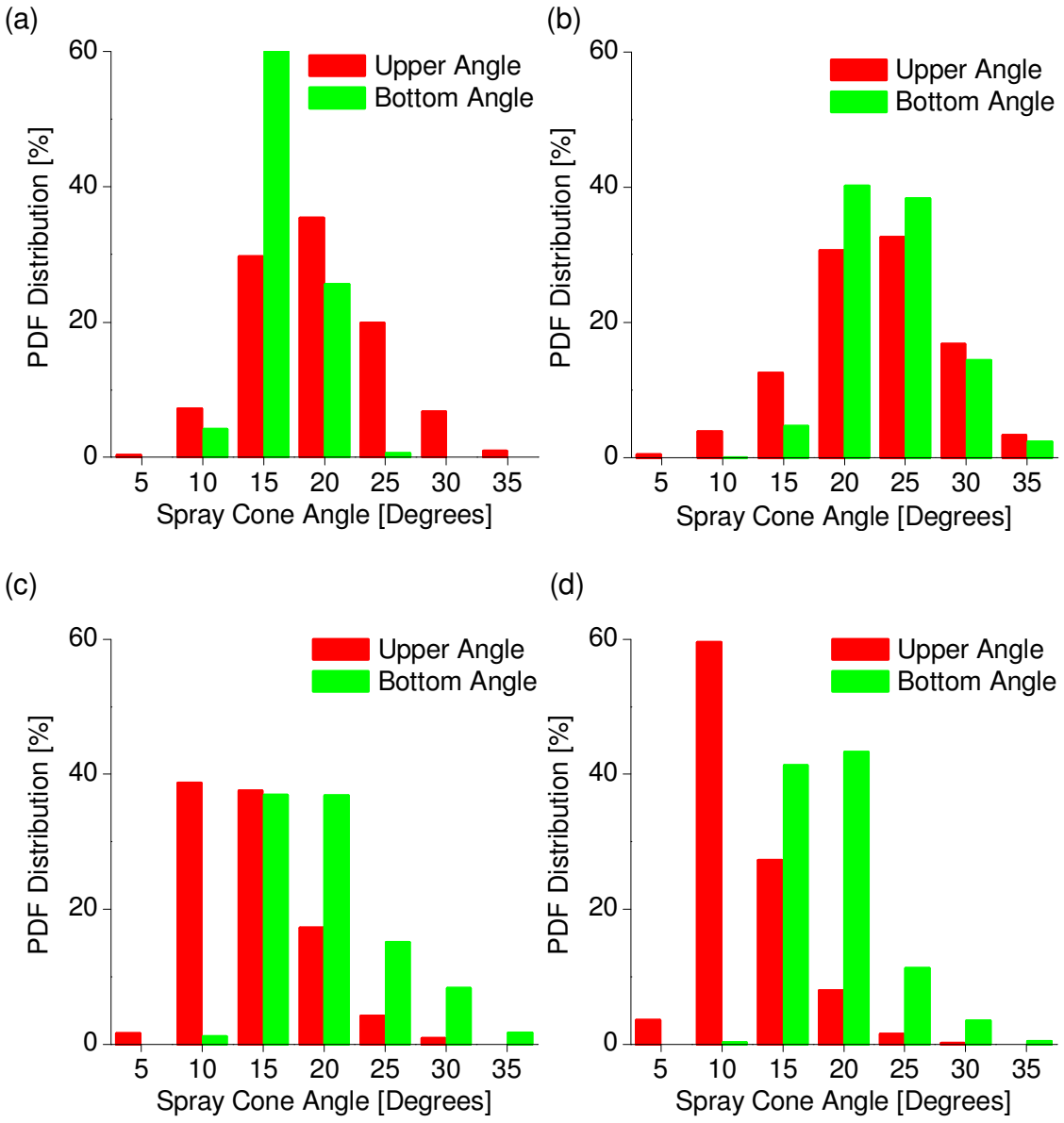

Figure 6-25: PDF distribution of upper and bottom spray angle of the cylindrical single-hole nozzle for a) CN=1, b) CN=2, c) CN=4 and d) CN=7.

The aforementioned observations regarding the upper and bottom spray cone angles can be also clearly seen in Figure 6-25 where the PDF distribution of upper and bottom spray angle for the same data sets are plotted. As CN increases the probability of having smaller upper spray angles increases and the probability of smaller bottom angles decreases. Also the range of the bottom spray angle is considerably increased, which can be realized by the more even probability distribution.

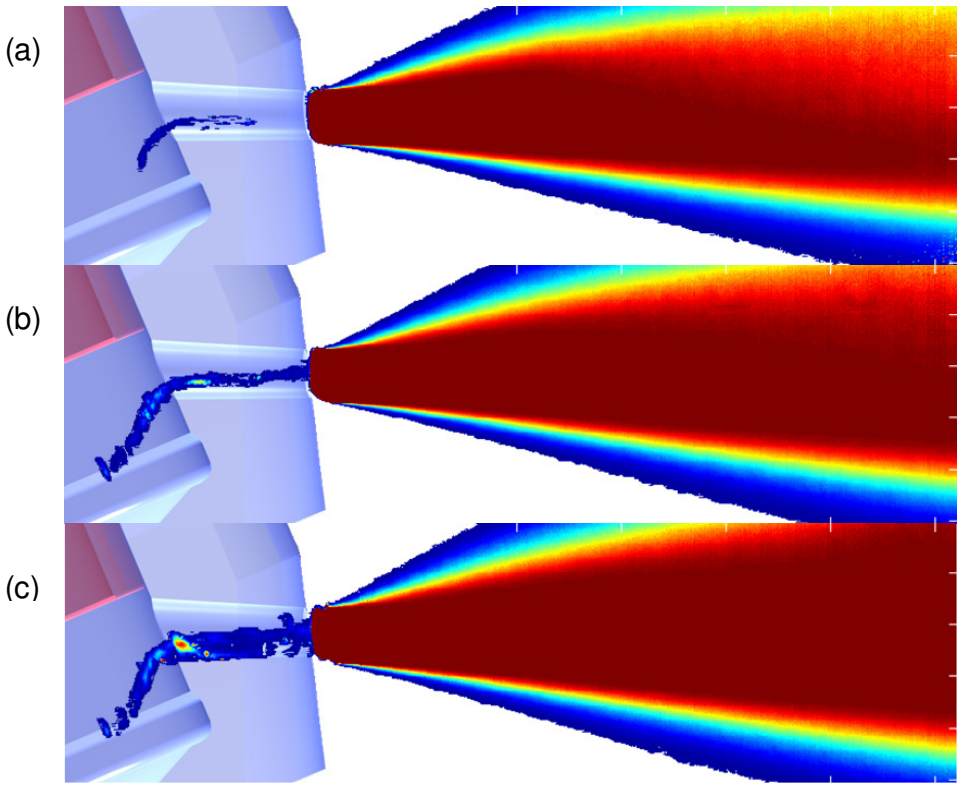

Figure 6-26: 2-D liquid probability, showing the effect of CN on spray dispersion for the Single Hole Tapered Nozzle. (a) CN=2, (b) CN=4 and (c) CN=7.

As mentioned before, apart from the single hole cylindrical nozzles, it was decided to investigate also the spray characteristics of the same nozzle design, this time with tapered hole. As it can be seen in Figure 6-26 at CN =2 and CN =4 there is only string cavitation. It can also be seen that for these two cases the bottom dispersion of spray is significantly smaller than the upper one, and comparing these mean images for the same CN for the cylindrical nozzle it can be seen that although the upper side has similar results, the lower one on the absence of hole cavitation is much different. By this observation it is further confirmed that hole cavitation enhances atomization while also the effect of string

cavitation mostly influences the upper spray cone angle. At a higher CN (=7), Figure 6-26 (C), there is also hole cavitation initiation, however it is still very weak in order to have a noticeable effect on the mean image results.

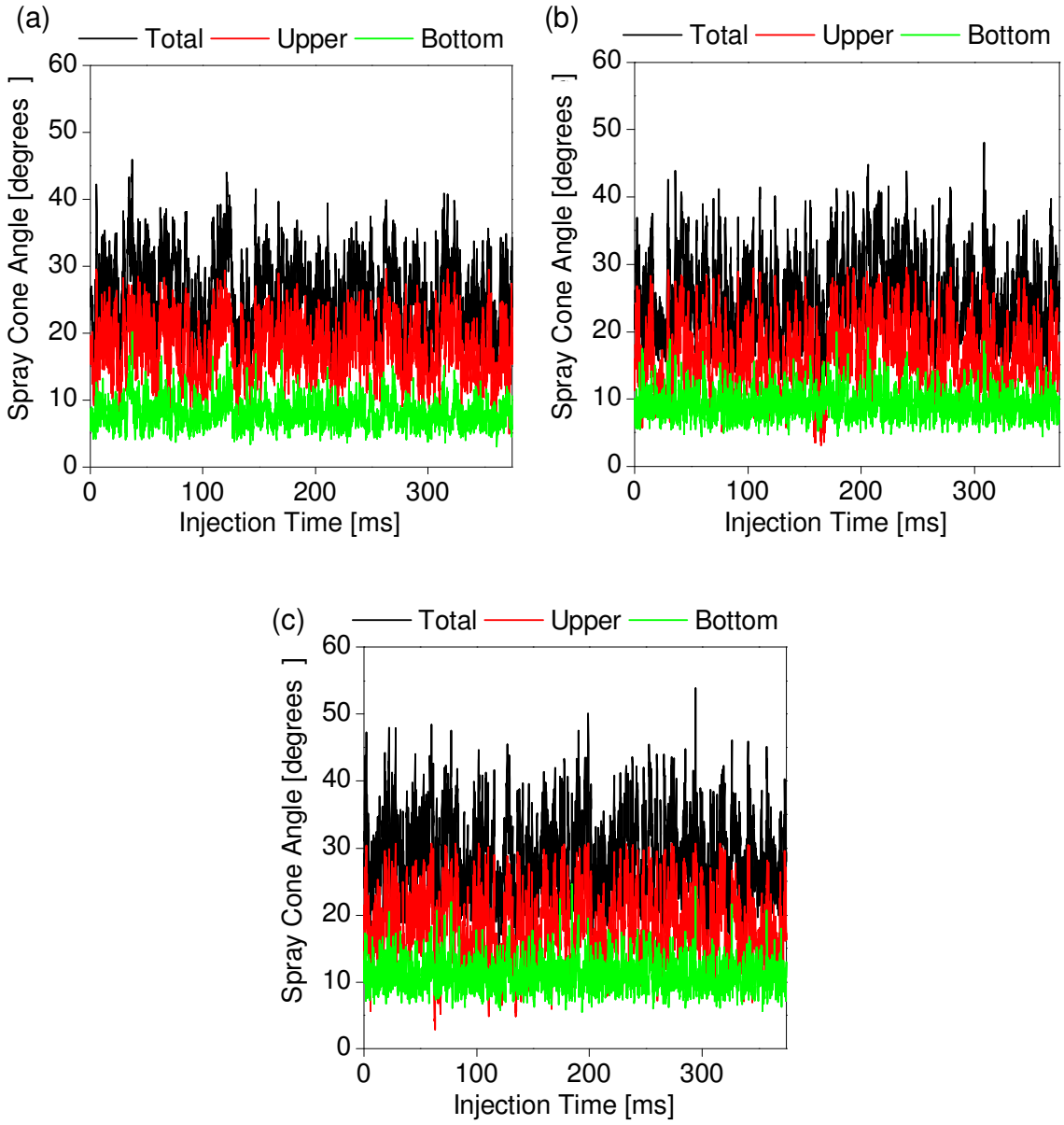

Figure 6-27: measured temporal variation of upper, bottom and total spray angle of the Tapered single-hole nozzle for a) CN=2, b) CN=4 and c) CN=7.

Proceeding into a more quantitative analysis of the results of the tapered nozzle, it can be seen from Figure 6-27 that for CN=2, 4 & 7 , the upper spray cone angle remains almost unchanged. It can also be seen from the shape of the line that it is highly fluctuating and takes a wide range of values, as it was also the case for the cylindrical nozzle. However,

contrary to the cylindrical nozzle, the upper spray cone angle does not decrease by increasing the CN, and by that it can be confirmed that there is an interaction between the effect of string cavitation and the pre-existing vapour due to geometrically induced cavitation.

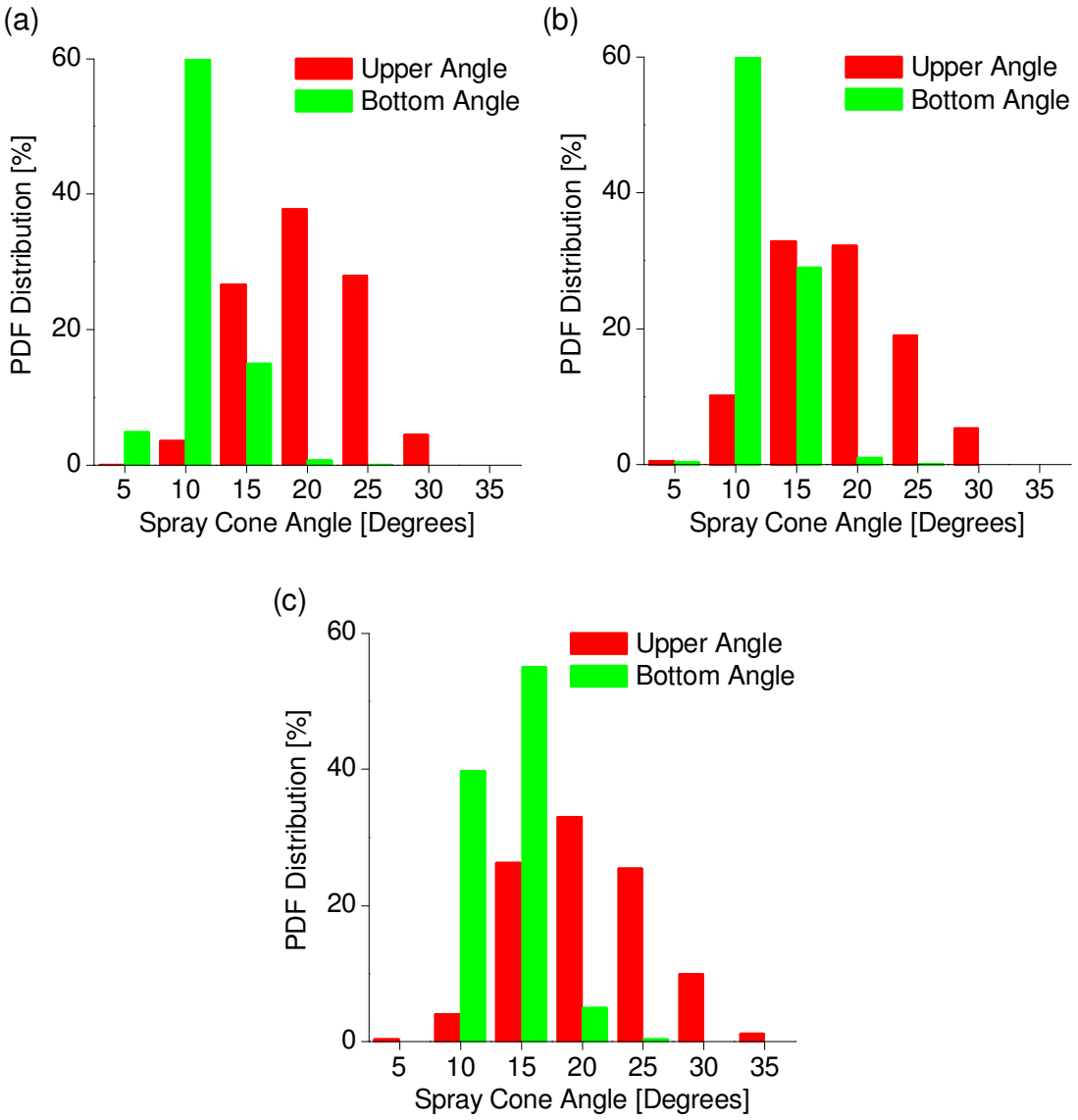

Figure 6-28: PDF distribution of upper, bottom and total spray angle of the Tapered single-hole nozzle for a) CN=2, b) CN=4 and c) CN=7.

It also has to be mentioned that the total spray cone angle is comparable to the one produced by the cylindrical nozzle and also the fact that for a range of CN values the cone angle remains unchanged, makes tapered nozzles suitable for injection systems that need to

be operable for a wide range of operating conditions. Regarding the bottom spray angle, it can be seen that is almost half of the values found in the cylindrical nozzle. It also interesting to point out the smoothness of the bottom spray angle, which can be realized by the dense green line. All bottom spray angles take values within an 8-9 degrees range. This comes in line with the fact that even if hole cavitation is a well predictable and relatively steady flow feature, once fully developed, it still produces relatively highly fluctuating cone angles. Finally, although when examining the mean images shown in Figure 6-26, the effect of hole cavitation could not be realized, in Figure 6-27(c) (CN =7) the bottom spray cone angle has been increased by at least 8 degrees on average.

By observing Figure 6-28, where the PDF distribution of the angles produced by the tapered nozzle are plotted, it can be concluded that at CN below 4, which is the operational point of the nozzle in real conditions and at which no initiation of hole cavitation is present, almost 60% of the bottom cone angles are at the region of 10o degrees. Regarding the upper spray angle, it can be seen that it takes values similar to those seen at low CN in the cylindrical nozzle. Moreover, contrary to the cylindrical nozzle, the distribution of angles seems to be independent of the CN, confirming that hole cavitation affects the upper spray angle by interacting with the strings formed inside the nozzle.

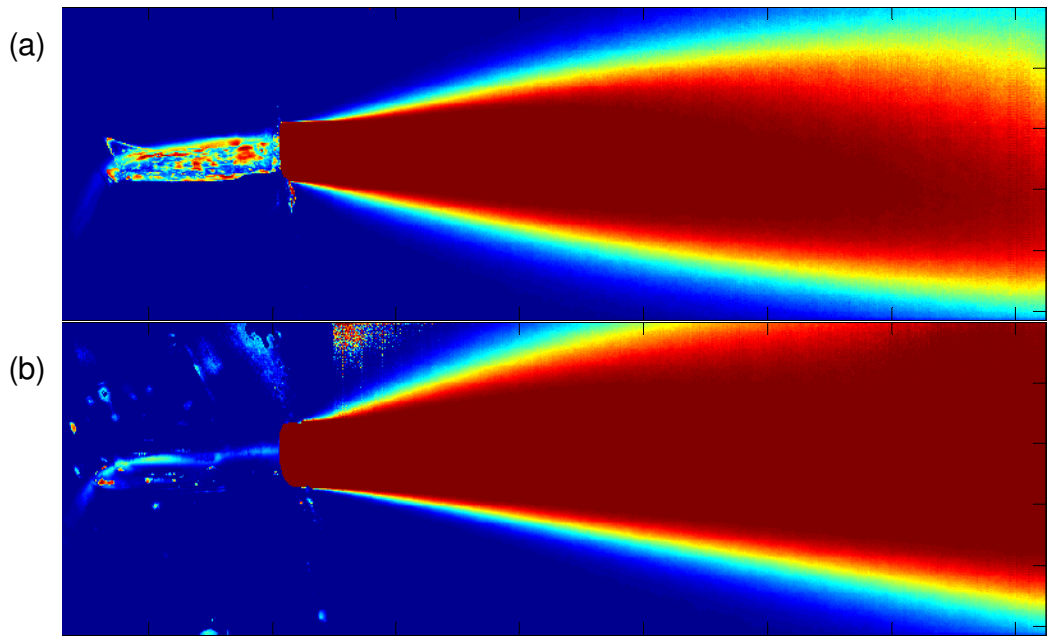

Figure 6-29: 2-D liquid probability, showing the effect of lower needle lift on spray dispersion for the Single Hole Nozzle. (a) Cylindrical, (b) Tapered. [CN=4]

Having examined the effect of CN and hole design on the spray dispersion and cone angle, the next step was to investigate the effect of needle lift. As it can be seen by the mean images presented in Figure 6-29 for both nozzle hole designs at CN=4, it is not possible to identify a clear effect compared to the full lift case. It has to be mentioned that through this study it became clear that averaging cannot always provide the necessary information regarding the effect that various parameters have on the spray and for that reason it became clear that more detailed analysis had to be performed.

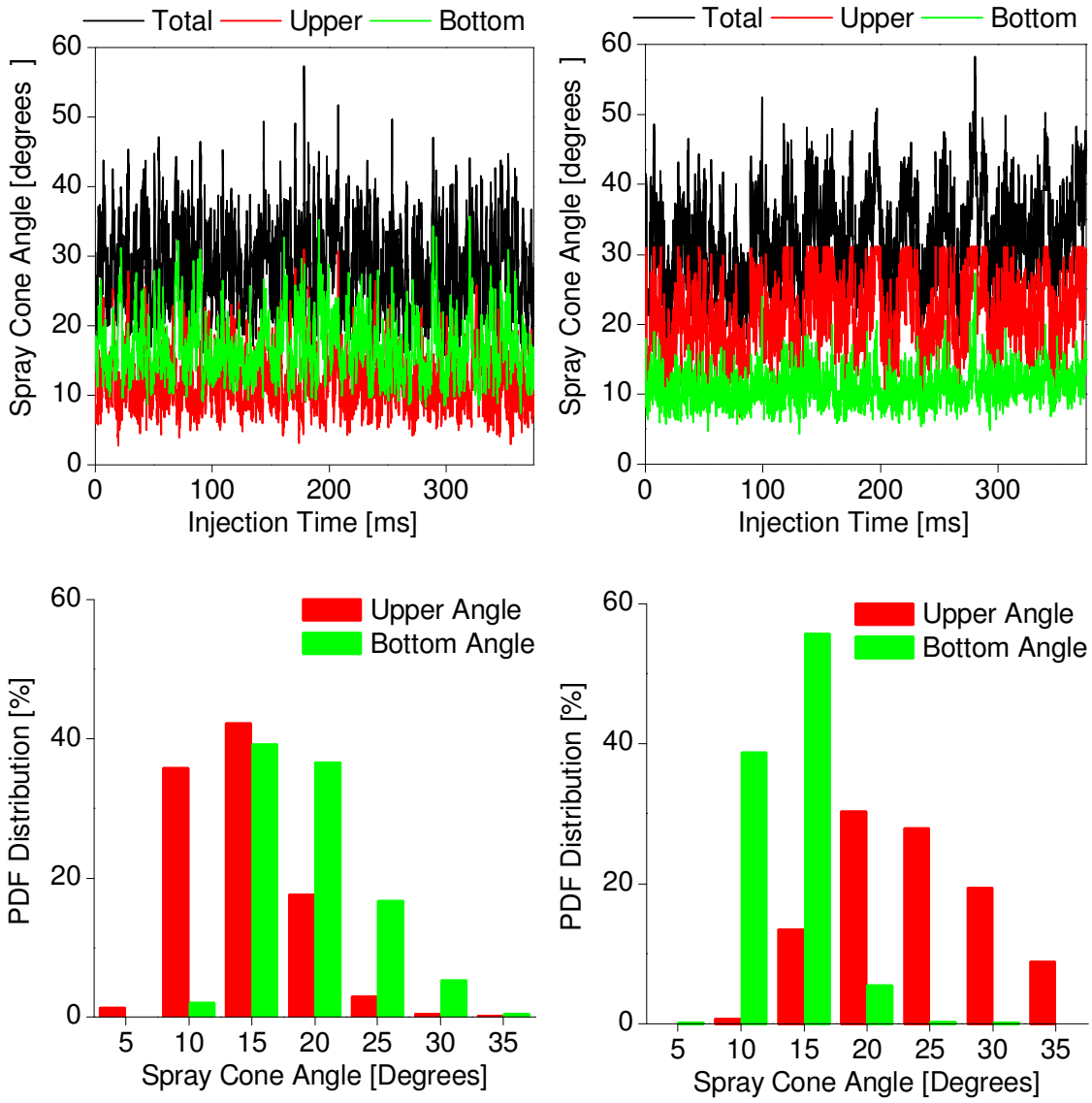

Figure 6-30: Measured temporal variation (Top Row) and PDF distribution (Bottom Row) of upper, bottom and total spray angle for the Single Hole Nozzle. (Left) Cylindrical, (Right) Tapered. [CN=4, Low Lift]

As it can be seen in Figure 6-30, the effect of needle lift is negligible for the cylindrical hole nozzle. Both the upper and the bottom cone angle take similar values as for the full lift case and only by examining the results in detail, it can be said that there is a slight increase of the percentages of higher upper cone angles and even smaller decrease of the higher bottom angle values percentage. Therefore it can be safely concluded that a 20% decrease in the needle lift is not likely to affect the initial spray characteristics. Looking at the right hand side, where the results of the conical nozzle are presented, it can be seen that that by lowering the needle lift the qualitative characteristics of spray formation have been preserved as in the full lift case. However it is evident that there is a small increase in both the upper and bottom spray angle. Proof of that can be given by observing the higher values that the total spray cone angle is reaching, black line, as well as by noticing that the percentages of having higher upper and bottom angles have both been increased. It has to be reminded that since this nozzle is tapered, it has a larger hole inlet diameter than the cylindrical one and since their orientation compared to the nozzle body has remained the same, a lower lifting the tapered nozzle brings the needle's edge closer to the upper side of the hole inlet.

6.11 Spray investigation –effect of imaging and measuring parameters on spray angle calculation

One of the limitations that have to be understood when considering high speed imaging is the resolution of the captioned image sequences. Even though for the current investigation the available equipment was the most technologically advanced system able to have high frame rates with high resolution, still mainly due to the size of the nozzle, a relative large amount of information was lost since the spray edge was lying outside the image boundaries once at 1 hole length from the exit plane of the injection hole.

Although it is widely acceptable that when studying the near hole exit spray structure one hole length is the suitable region to investigate, it was considered interesting to see how the spray angles vary at double this length. For that reason the resolution was increased by sacrificing the rate of image acquisition. A typical image with the spray cone angle measuring regions can be found in Figure 6-31.

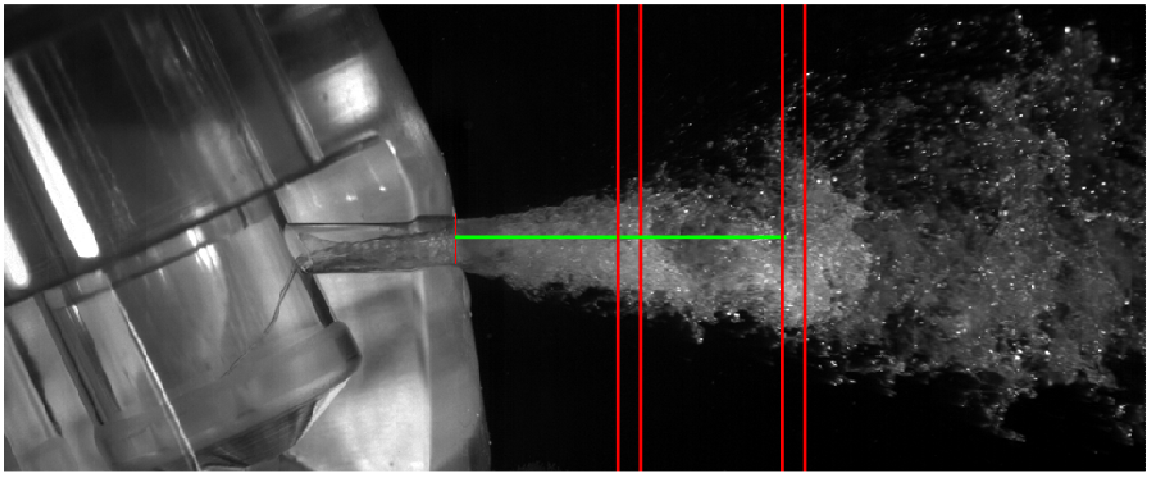

Figure 6-31: Typical spray investigation image showing the regions used to measured the cone angle at two hole lengths from the outlet.

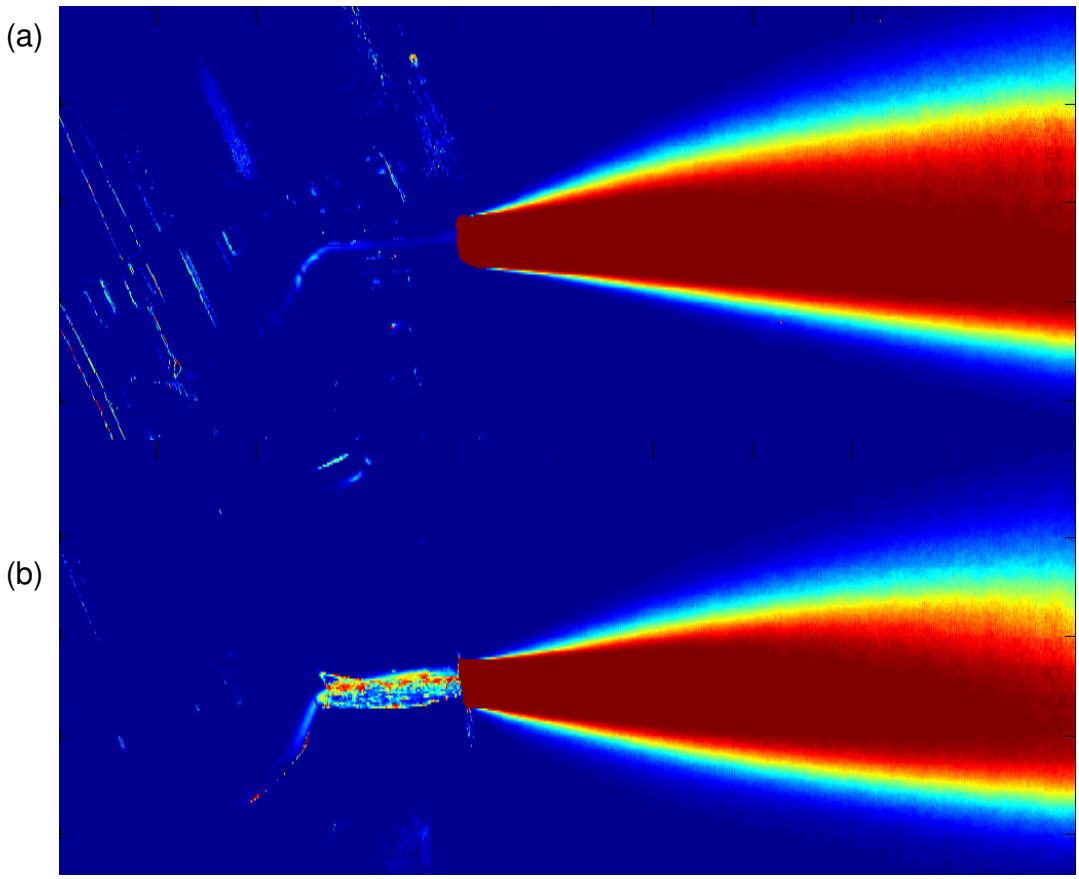

Figure 6-32: 2-D liquid probability of the Single Hole Nozzle with larger viewport. (a) Cylindrical, (b) Tapered [CN=4, Full Lift]

In Figure 6-32, the mean images that were derived by the lower frame rate, higher resolution, image sequences are presented for the operational CN=4 condition, for both the cylindrical and the tapered hole nozzle. It is interesting to mention that although with the smaller resolution it was difficult to draw clear conclusions regarding the spray dispersion, from these images it is much more information available and together with the correct colour scale that is used in order to highlight the differences, it is much more evident that the upper region where string cavitation dominates the atomization process, is much more extended than the bottom side. Also the fact that the colour bands are much wider at the top side, is a clear indication that there is more fluctuation than at the bottom side.

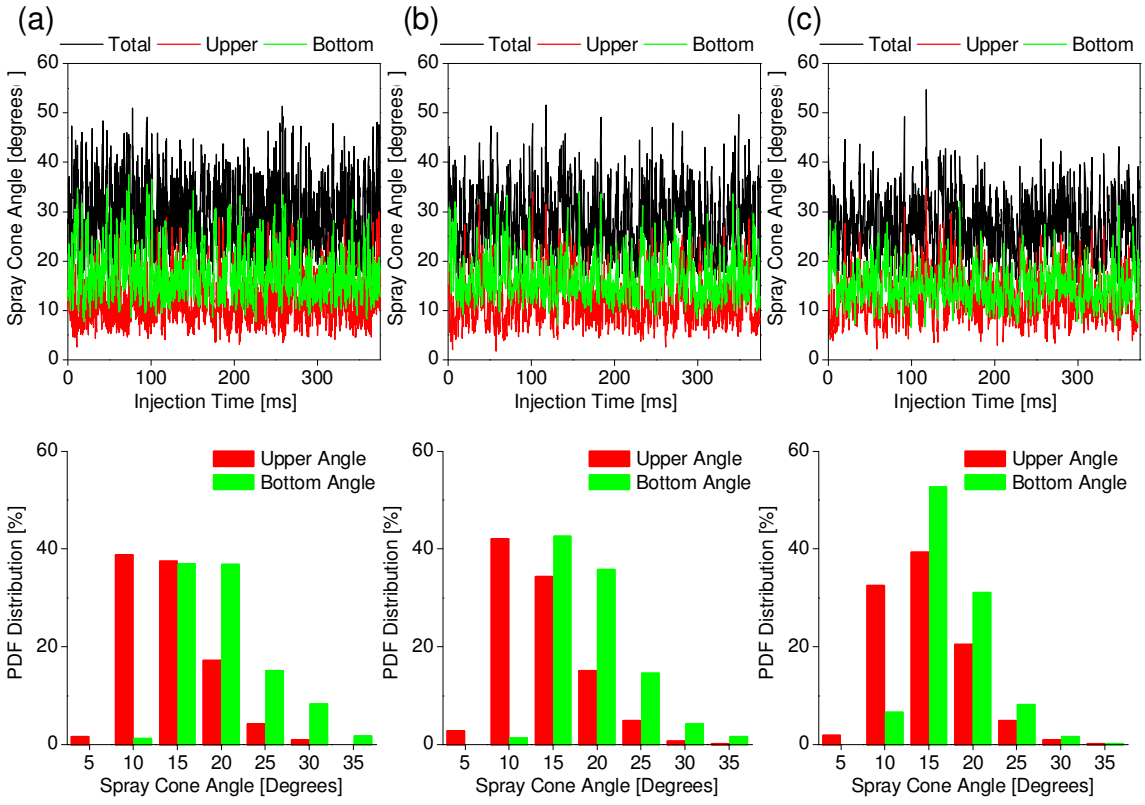

Figure 6-33: Measured temporal variation (Top Row) and PDF distribution (Bottom Row) of upper, bottom and total spray angle for the Single Hole cylindrical Nozzle. a) 1-hole length @ original resolution, b) 1-hole length @ increased resolution and c) 2-hole length @ increased resolution.[CN=4, Full Lift]

Since the aim of this investigation was to identify the effect of the distance at which spray cone angles are measured, Figure 6-33 provides a clear quantitative comparison between the resolutions and the measuring distances used. Figure 6-33 (a) is the baseline case which

was previously shown in Figure 6-23 (c), Figure 6-33 (b) shows the results from the increased resolution case for the same measuring distance as in Figure 6-33(a), while Figure 6-33(c) is at double the distance used for both Figure 6-33(a) and Figure 6-33(b). The first conclusion that can be drawn is that the qualitative characteristics that have been identified in the baseline case are the same for all other cases. This is important to mention, since due to the different frame rate, and given the time scales of the flow, these results could have been altered significantly.

In more detail, it can be said that although, by comparing Figure 6-33 (a) & (b), the upper angle takes almost the same values, the bottom angle which is dominated by the effect of the highly transient cavitation, has taken slightly smaller values. This confirms that unless a very high frame rate has been chosen, it is possible to fail capturing the effect of highly fluctuating flow characteristics. Therefore this can explain why some peaks of the bottom spray angle have been lost, hence decreasing the PDF of larger angles. On the other side, the upper side, where the periodicity of string cavitation is much larger than the interval between successive image acquisition, the effect of the frame rate is even less. Finally, by comparing Figure 6-33 (b) & (c), in order to find the effect of measuring distance, it can be seen that although the bottom angle does not show to be affected, the upper angle seems to fluctuate at larger intervals than before.

This can be realized by observing the bigger gaps between the dense regions of red lines. A possible explanation for this, is the combination of axial and the instantaneous increase of tangential velocity that is caused by the presence of string cavitation, which makes the spray droplets to travel at a distance having their original trajectory, before its direction changes. Nevertheless it can be safely concluded that the distance at which the cone angles will be measured has limited effect on the qualitative as well as quantitative characteristics.

6.12 Spray investigation – effect of hole geometry, string cavitation and CN on spray structure for all investigated nozzles

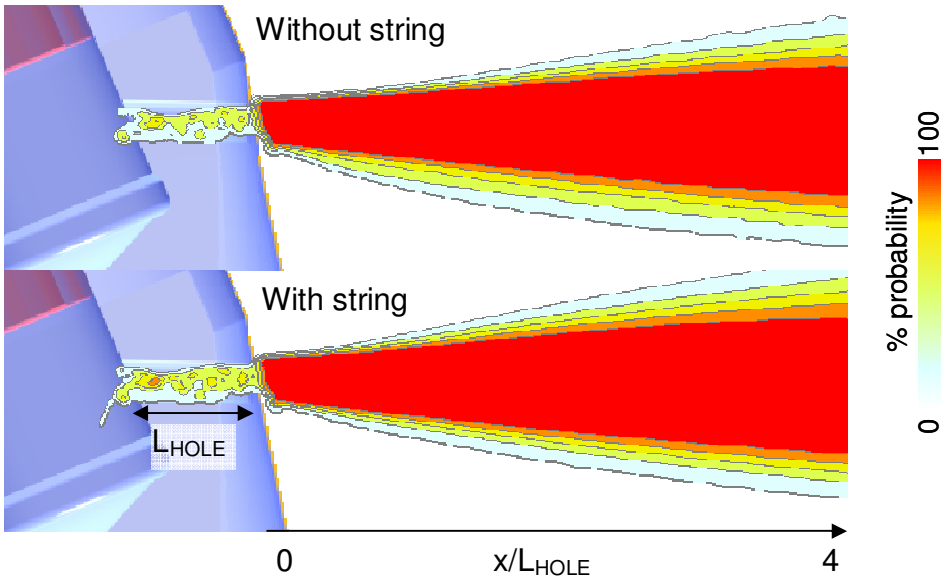

Figure 6-34: Projected on the 2-D viewing plane time averaged percentage liquid presence for the single-hole cylindrical nozzle with and without string cavitation [CN=4, Re=65,900, Nominal needle lift]

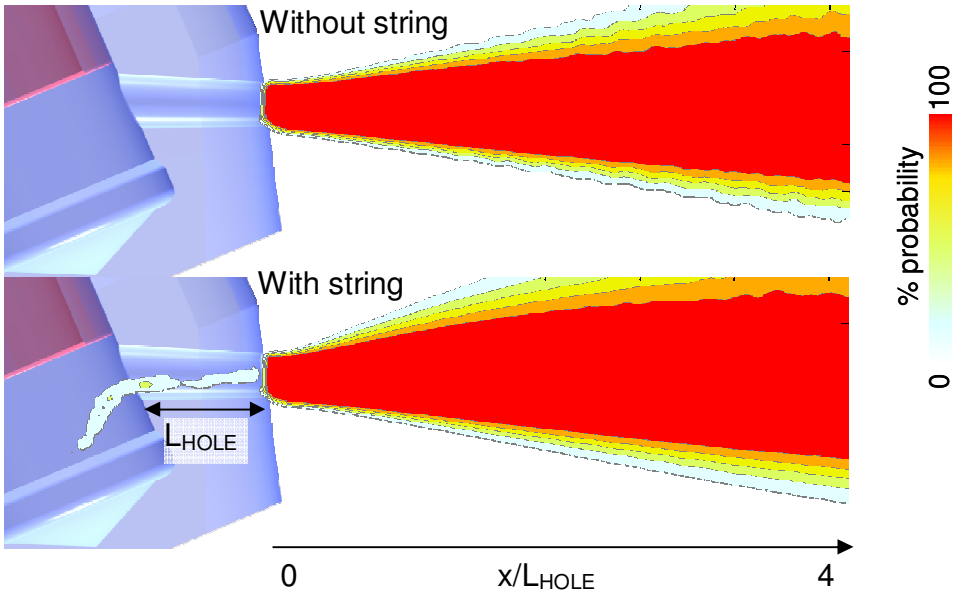

Figure 6-35: Projected on the 2-D viewing plane time averaged percentage liquid presence for the single-hole tapered nozzle with and without string cavitation [CN=4, Re=88,250, Nominal needle lift]

In order to summarize what it has been found through this study, Figure 6-34 and Figure 6-35 show the derived mean spray images for the cylindrical as well as the tapered single-hole nozzles, respectively. In each of them, the top row corresponds to the frames without string inside the nozzle hole, while the bottom row plots have been derived using all the acquired images. It is clear that the spray is much wider in the presence of strings. Subtraction of mean images gives a quantification of how much a specific location is covered by liquid on average as a result of string and/or geometric cavitation.

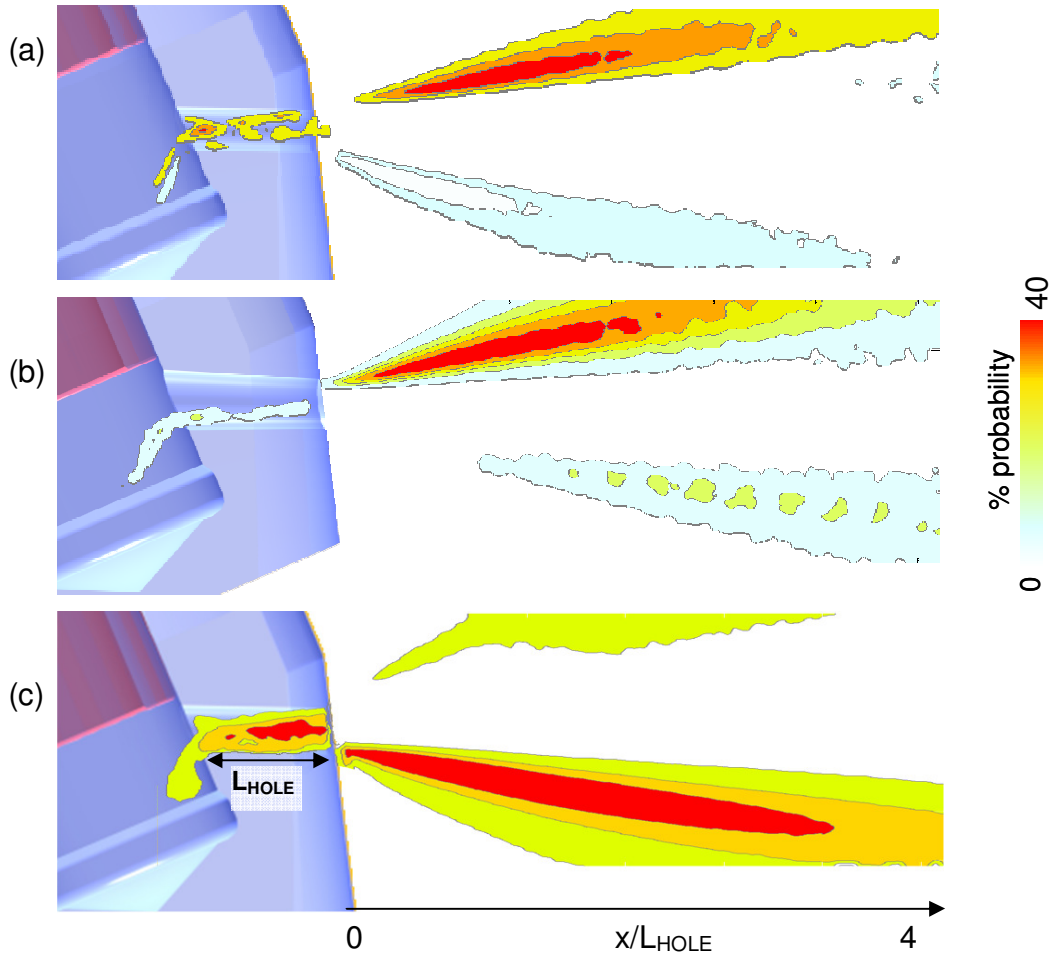

Figure 6-36: Subtraction between 2-D mean spray images for the single-hole nozzle, revealing: (a) effect of string cavitation in the cylindrical hole at Re=65,900 (b) effect of string cavitation in the tapered hole at Re=88,250 and (c) effect of geometric hole cavitation [CN=4, Nominal needle lift]

Three differences are shown in Figure 6-36. Figure 6-36(a) reveals the influence of string cavitation on the cylindrical single-hole nozzle. As clear, the bottom part, which

corresponds to the area of geometric cavitation inside the nozzle, remains almost unaffected, while a large difference up to 40% can be seen in the upper part. A similar result can be seen in Figure 6-36(b) but this time for the tapered nozzle. This time, the influence of string cavitation is more profound relative to that of the cylindrical nozzle. Finally, the last difference presented in Figure 6-36(c) has been obtained by subtracting the mean image of the cylindrical nozzle from the tapered nozzle; since the tapered hole is always free of geometric cavitation, this result may be interpreted as the influence of geometric-induced hole cavitation on the atomised liquid. It is clear now that mainly the bottom part of the spray is affected, as expected. The observed differences are as big as those observed for the string cavitation.

The final result to be reported addresses the effect of cavitation number (increased flow rate) on the mean spray angle of the different nozzles investigated. The latter has been estimated as the arithmetic mean from all images recorded irrespectively of the presence/absence of geometric and/or string cavitation. The obtained results can be seen in Figure 6-37 (a) for the cylindrical and Figure 6-37 (b) for the tapered holes, respectively. Two important observations can be made. The first one indicates that the mean spray angle of the two-hole nozzles is smaller compared to that of the single-hole nozzle. This is an expected result for this particular nozzle geometry; the frequency of cavitation string presence in one hole of the two-hole nozzle is reduced to almost half, since the vortex developing inside the nozzle switches location between the two holes. Thus, the increased spray angles observed with its presence in one hole take place less time and thus, the mean angle is decreased. The second comment that can be made refers to the different results observed between the cylindrical and the tapered holes. For the cylindrical holes it can be seen that increasing cavitation number beyond two, results to a decrease in the observed angle; the opposite is the case with the tapered holes, where a small increase has been recorded. The reason for that is related to the frequency of appearance of cavitation strings, which has been found to also increase with increasing flow rate. Increasing flow rate also results to formation of a fully developed cavitation inside the cylindrical hole. The results indicate that in the presence of a stable geometric-induced cavitation structure, the continuous presence of string cavitation becomes relatively less influential to the near-nozzle liquid disintegration. On the other hand, in the absence of geometric-induced

cavitation (tapered holes), the more frequent presence of cavitation strings inevitably results to the observed increase in the spray angle.

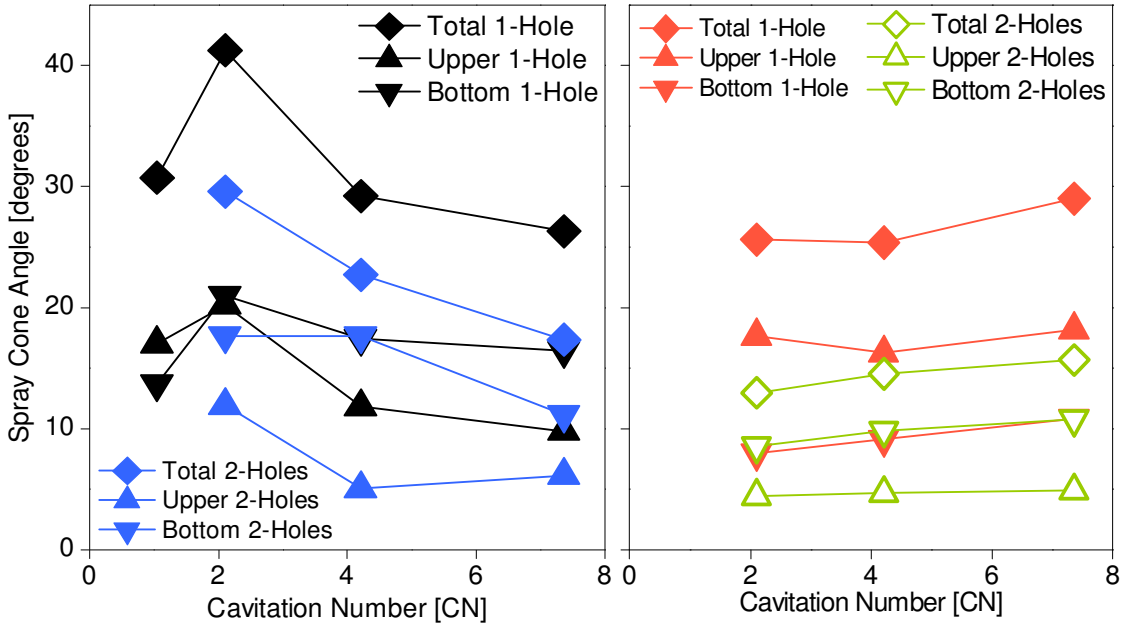

Figure 6-37: Mean spray angle (upper, bottom, and total) as a function of cavitation number for the one-hole and two-hole nozzles: (a) Cylindrical holes and (b) tapered holes (nominal needle lift).

6.13 Spray investigation – numerical investigation and interpretation of experimental results

Before closing this chapter, is worth to show some numerically obtained results that will help to further understand the mechanism through which string cavitation affects the initial spray structure. Nevertheless most experimental studies have been used as validating tools for CFD codes and it was considered a good opportunity to do the same for the in-house software. It has to be mentioned that this work is a joint effort together with other members within the research group and further details regarding the atomization model can be found in [143]& [162]. Figure 6-38 shows calculated results for the vapour volume fraction and the velocity flow field on the hole exit cross sectional area at two time instances. As it can be seen, cavitation is mainly concentrated at the bottom part of the injection hole, while at the same time a swirling motion is evident. The one profile selected for presentation

corresponds to a time instance where the nozzle volume vortex is facing this particular injection hole while the second profile refers to a time step with the vortex being away from this hole. The two calculations show significant time variation even in the absence of string cavitation which is not considered in the computational model.

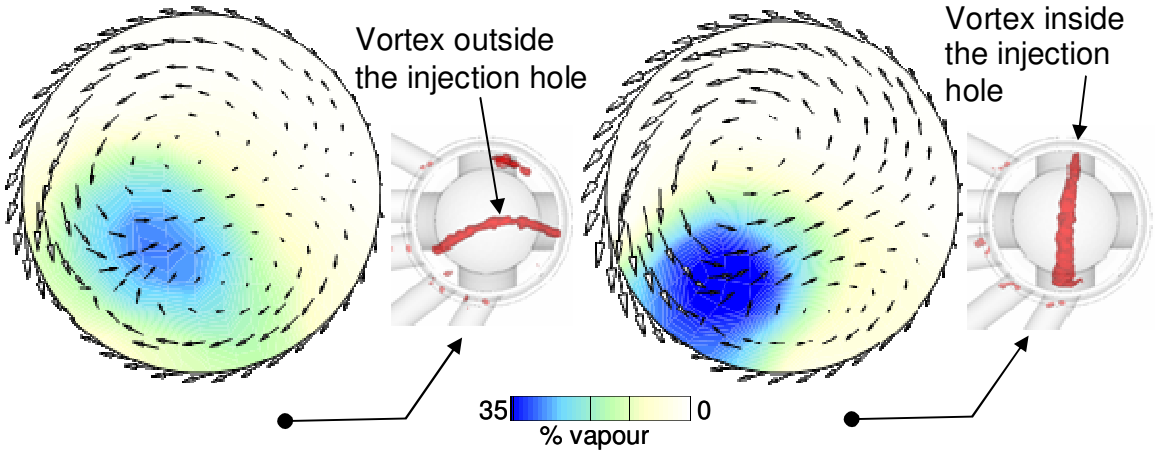

Figure 6-38: Predicted vapour volume fraction and flow field on the hole exit cross section at two time instances, revealing the calculated temporal variation of cavitation distribution due to the different location of the nozzle volume vortex

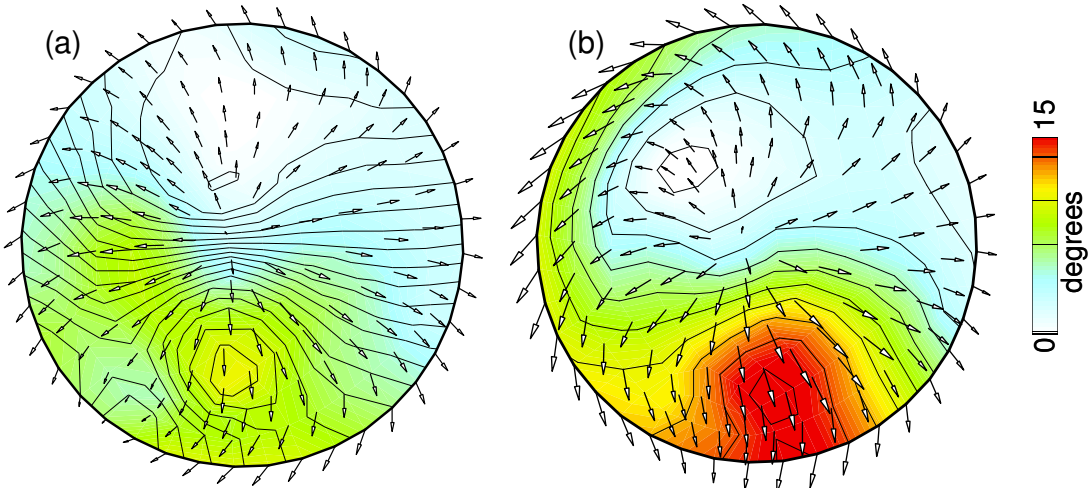

Figure 6-39: Predicted nozzle hole exit maximum injection angle of the cylindrical single-hole nozzle (a) large-scale and (a) real-size. The velocity vectors indicate the direction of the liquid once injected from the injection hole

Two more points require attention and will be addressed in the remaining last part of the chapter. The first refers to the comparison between the flow distribution inside the large-scale nozzle operating at low injection pressures and that of a real-size nozzle operating

under realistic engine conditions. As clear, all the analysis presented so far has been based to a large extend on the silent assumption that the conclusions from the visualisation studies presented can be extrapolated to the real life. Figure 6-39 shows the predicted mean maximum spray angle distribution on the nozzle exit cross sectional plane for the large-scale and the real-size cylindrical single-hole nozzle. The arrows plotted show the direction of the liquid once it leaves the nozzle hole.

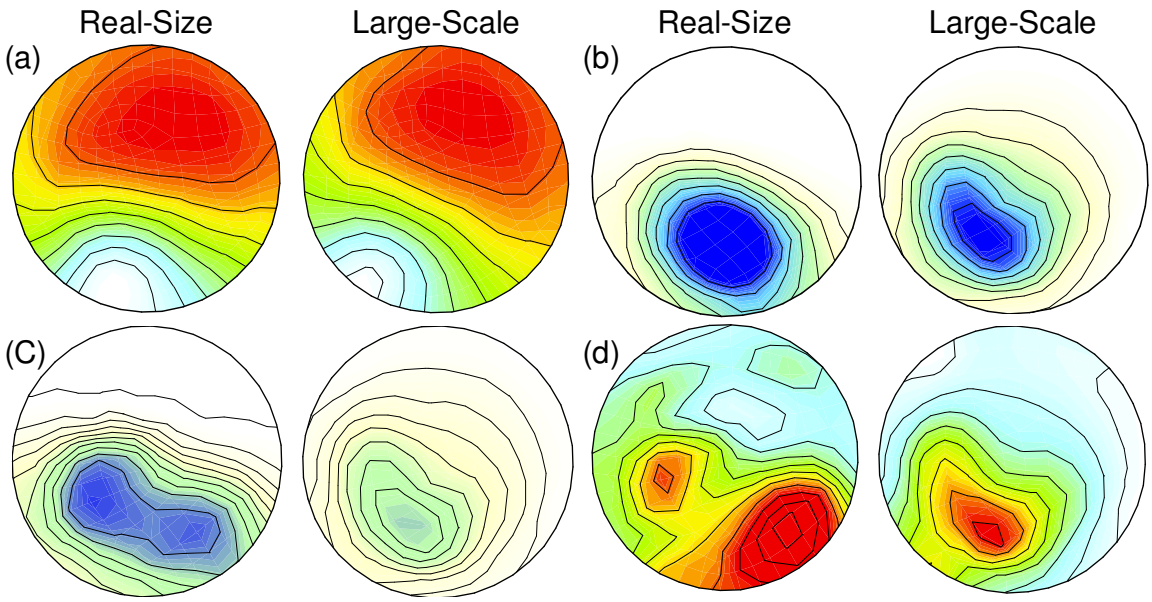

Figure 6-40: Comparison between the flow exit characteristics of the real-size and the large-scale single-hole nozzles (a) mean axial velocity, (b) mean vapour volume fraction, (c) vapour volume fraction standard deviation and (d) atomisation angle standard deviation. All scales are normalised with the maximum values.

More detailed comparison can be seen in Figure 6-40 for the axial velocity and cavitation volume fraction distribution, as well as for its standard deviation; the standard deviation of the maximum spray angle is additionally plotted. From this graph clear similarities can be identified although the profiles are not exactly the same. Differences are mainly attributed to cavitation which although similar in both nozzles it is does not scale exactly with the differences in the operating conditions.

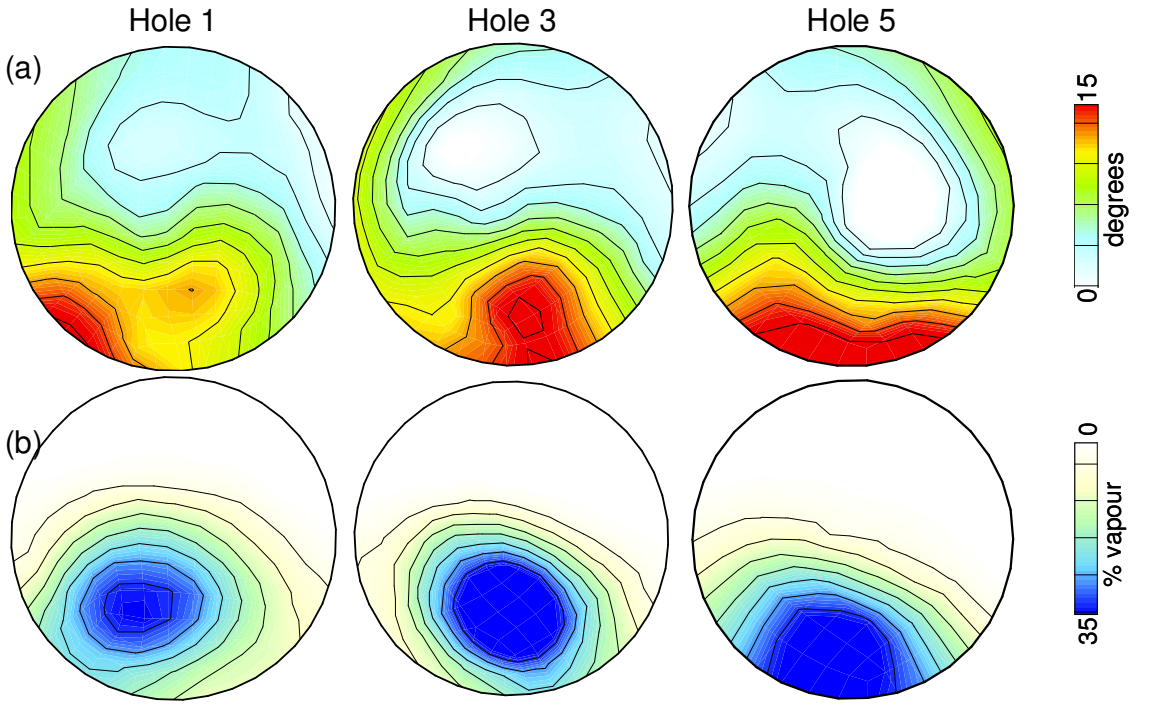

Figure 6-41: Predicted spatial distribution of (a) maximum magnitude of spray injection angle and (b) mean vapour volume fraction for three out of the five injection holes of the cylindrical real-size five-hole injector.

The remaining figures refer to model predictions for the real-size five hole nozzle operating under engine similar injection and back pressure conditions. Figure 6-41 shows the mean value over the injection period of the maximum spray angle and the cavitation vapour volume fraction spatial distribution on the nozzle hole exit plane for three out of the five injection holes, while Figure 6-42 shows the corresponding standard deviation. Comparison between the mean profiles of different injection holes can be interpreted as spray-to-spray variability over the whole injection duration event, while the standard deviation profile indicates the cycle-to-cycle variability of the spray injected from a particular injection hole. As expected, significant variations between the injected sprays are simulated, mainly for holes one and five. The plots indicate that not only spray-to-spray variations should be expected but also cycle-to-cycle ones, since calculated angle values may differ up to 10degres during the injection event.

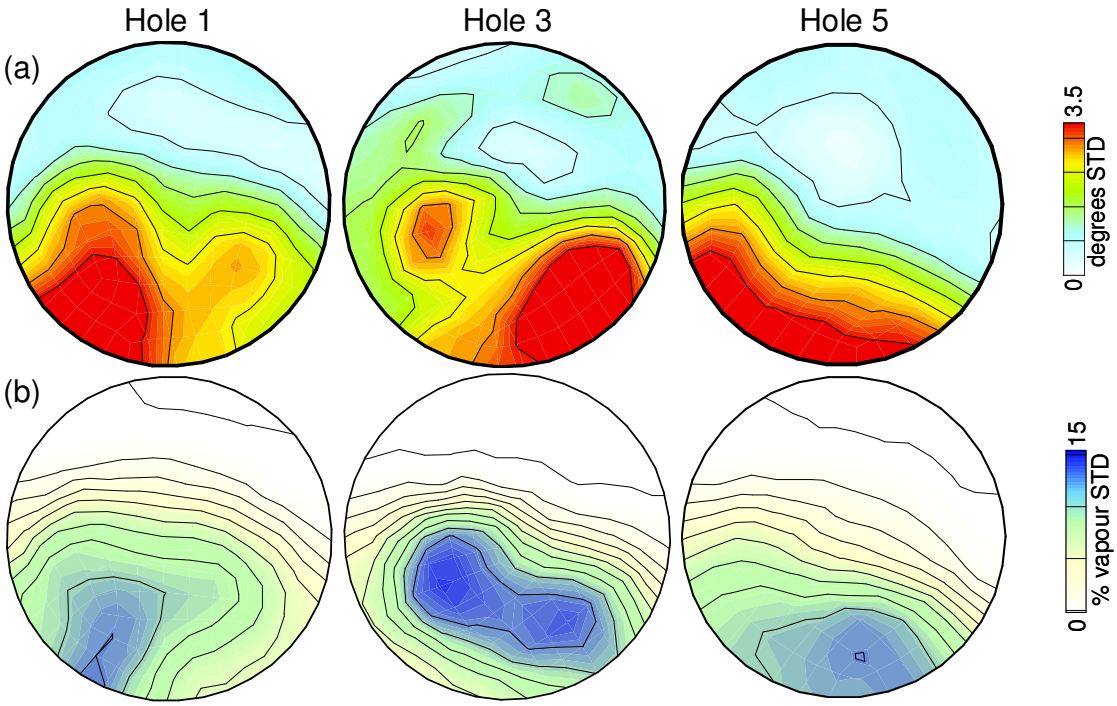

Figure 6-42: Predicted spatial distribution of the standard deviation of the (a) maximum magnitude of spray injection angle and (b) mean vapour volume fraction for three out of the five injection holes of the cylindrical real-size five-hole injector

6.14 Spray investigation – Conclusions

Effort has been made to investigate and quantify the role of nozzle flow and cavitation on the spray angle formed just at the exit of nozzle holes. For this reason, high speed visualisation has been performed in fully transparent replicas of nozzles used with low-speed two-stroke Diesel engines as well as multi-dimensional and multi-phase cavitating flow simulations have been used. The nozzles investigated incorporate one-, two- and five-hole designs with cylindrical as well as tapered-converging holes. Imaging has been performed simultaneously for the internal nozzle flow and the spray formed at the nozzle exit. The observed two-phase flow structures appear in two distinct forms, referred to as geometric-induced cavitation and dynamic or string cavitation.

Cylindrical holes induce geometric cavitation while tapered holes suppress it. String cavitation has been monitored in all nozzle types. Comparison of the obtained images between cylindrical and tapered nozzles in the absence of string cavitation has allowed the

influence of geometric cavitation to be quantified, while acquisition of high-speed images has allowed for comparison between images in the absence and presence of cavitation strings to be made. The results indicate a significant increase in the spray angle in the presence of cavitation strings which is more significant in the absence of geometric-cavitation. In addition, information has been provided for the variation of spray cone angle with time, expressed in terms of probability of finding dispersed liquid along the spray cone angle.

The range of the formed spray angles have been found to follow a probability distribution function which is function of the nozzle design and the two-phase flow regime formed inside the nozzle hole for a given operating condition.

Chapter 7
Experimental Results-Internal flow in Large scale Multi-hole nozzles

7.1 Introduction

Until this point all results presented were referring to asymmetric nozzles that are used mainly with large two-stroke marine engines. As it was shown apart from the well understood hole or geometric cavitation, another form of dynamic cavitation was also identified as been a key parameter affecting both the internal flow characteristic and the emerging spray structure.

It naturally follows that the next stage of this work would be to compare the previously reported results with a series of multi-hole nozzle geometries, which are used in a much wider range of internal combustion engines.

Although multi-hole nozzles have been extensively investigated, as can be also seen in Chapter 2, limited work has been done so far with respect to vortex cavitation, apart from studies considering propellers, hydraulic turbines and hydrofoils.

Apart from vortex cavitation during this stage of instigation the link between cavitation regimes existing in the nozzle sac volume and erosion problems will also be identified.

7.2 Cavitation structures inside VCO nozzle with cylindrical and tapered holes

The present section aims to provide new experimental data for the origin, formation, area of development and life time of the vortex-type or string cavitation observed in enlarged replicas of VCO Diesel injector nozzles incorporating tapered (converging) holes. The results of the tapered hole nozzle will be also compared to the cylindrical ones in order to allow comparison with the majority of previously published studies on cavitation visualisation in Diesel injectors. Through high speed images it will be shown that cavitation strings form not only from cavitation sites inside the injector but also from downstream air trapped to the vortical structures persisting up to the nozzle exit. Although this had been already reported in Chapter 5, investigating the flow inside the marine tapered nozzle, such observations are made for the first time for multi-hole nozzles and reveal the formation of a two-phase flow structure inside Diesel injectors not previously identified.

When needed the use of CFD simulations will provide information about the local flow field at the location where cavitation strings develop and therefore assist in the interpretation of the experimental images.

Cavitation visualisation has been performed in 15x enlarged transparent nozzle replicas details of which can be found in section 3.1.7. The design of the nozzle can be seen in Figure 7-1(a). Figure 7-1(b) shows a cross section at the symmetry plane of one injection hole. As mentioned before the nozzle is a VCO design which implies that the needle valve seals directly to the hole entry, thus eliminating the dead volume below the injection holes. As it will be shown later on, the nozzle with tapered holes have shown persistently formation of string cavitation. The images obtained have allowed detailed characterisation of this flow structure. The nominal hole diameter is 2.925mm (0.195μm in the real size injector). For both hole designs the radius of curvature at the hole entry has been ~0.3mm (approximately 20 μm in the real size nozzle).

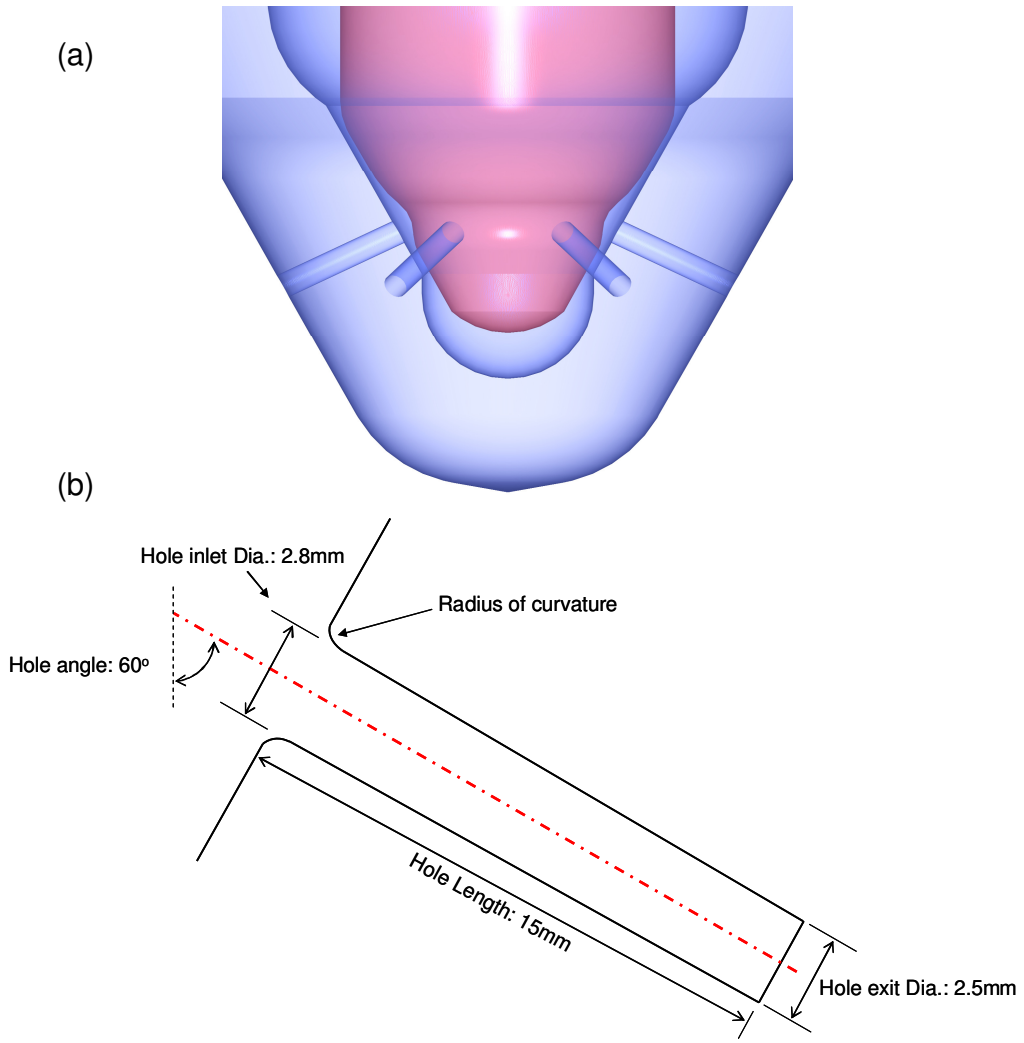

Figure 7-1: (a) 3-D CAD nozzle design of the VCO nozzle and (b) geometry of the injection hole.

Although the observed geometric-induced cavitation structures of the cylindrical holes are very similar to those observed in the majority of published data, the converging tapered holes greatly modify the pressure distribution within the nozzle, and as a result the formation of cavitation that depending on the degree of tapering might by fully eliminated. Figure 7-2(a) and Figure 7-2(b) shows the pressure distribution for the cylindrical and tapered nozzle hole shapes, respectively. Results are presented at 20 μm and 250μm equivalent needle lift, which will be referred to as low and high needle lift positions, respectively.

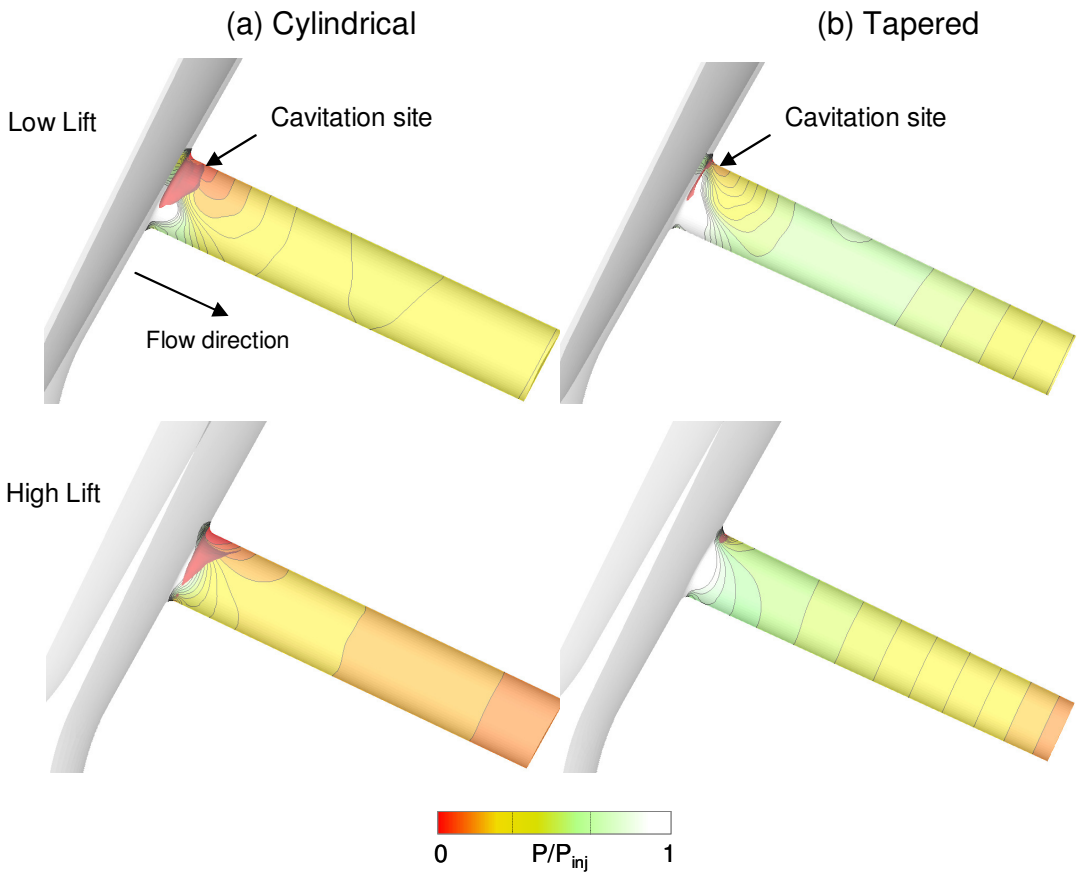

Figure 7-2: Predicted normalised pressure distribution of the VCO nozzle inside the (a) cylindrical and (b) the tapered injection hole at two different needle lifts .

As it can be seen tapered holes create a smooth pressure gradient along the hole length. The cavitation site is completely eliminated at high needle lift and only a very small region exists for low needle lifts. On the contrary, the computational results obtained for the cylindrical holes indicate a strong cavitation region at the top corner of the injection holes which is caused by the sharp pressure drop at the hole inlet.

The measured and calculated discharge coefficient can be seen in Figure 7-3 for the two nozzles and for the two needle lift sets investigated. The tapered hole nozzles have a much higher discharge coefficient, as expected also from the previously reported data.

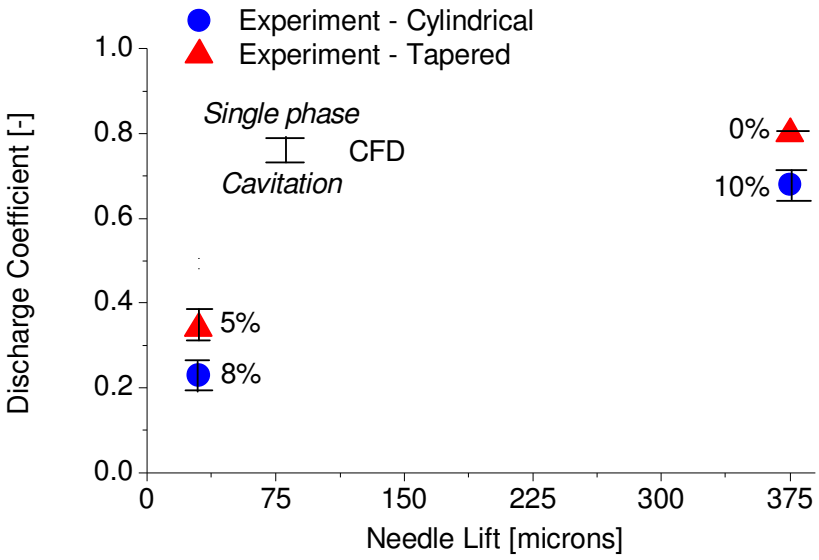

Figure 7-3: Measured and predicted VCO nozzle discharge coefficient as function of needle lift.

On the same plot, predictions from the CFD model are also included and these are indicated with two horizontal bars. The upper one corresponds to predictions obtained with the single phase flow solver and they are exhibiting values a little higher than those predicted using the cavitation model of [163]. This model accounts for the geometric-induced cavitation forming at the hole inlet due to the sharp pressure drop in this area. The model indicates that cavitation may be responsible for up to 5-10% reduction in the nozzle discharge coefficient at low needle lifts while its relative importance increases with the increased amount of cavitation. This is the case of the cylindrical hole nozzle at the highest needle lift setting. As mentioned, there is no cavitation for the same lift when tapered holes are employed, so in this case only one horizontal bar is depicted. Overall, model predictions are close to the experimental values and thus model predictions can be considered reliable for providing more detailed information of the flow distribution inside the nozzle.

The same steady-state flow test rig, that has been described in detail in section 3.2, has also been used in this investigation. By using both a delivery and a suction pump it was possible to reach high CN and Reynolds numbers. The operating conditions tested for the two large-scale transparent nozzles are listed in Table 7-1. As can be seen, cavitation numbers up to 13.5 have been tested, which are similar to those of the real-size injector operating under engine operating conditions. Imaging was performed for various combinations of the listed

parameters. The needle lifts positions chosen to be investigated were these corresponding to 20, 100 and 250 μm equivalent needle lift.

Eq. Needle Lift [μm]	Pressure [bar]		Cavitation Number	Reynolds Number	Equivalent P_{inj} [bar]
	Inlet	Back			
20	3.75	0.75	4.1	26,000	510
20	7	1.285	4.5	38,000	550
20	6.9	0.87	7.1	38,000	800
20	6.9	0.59	11.2	38,000	1200
100	6	1.1	4.5	65,000	550
100	5.9	0.52	11	66,000	1200
250	5.8	0.42	13.5	71,000	1450

Table 7-1: Range of operating conditions investigated for the transparent VCO type nozzle with tapered holes.

Figure 7-4 shows representative images of the observed cavitation regimes for all three needle lift positions investigated for both cylindrical and tapered injection holes. as it can be seen the difference between the two hole designs is evident. For the low needle lift case, the cylindrical hole nozzle exhibits mainly the formation of a cavitation cloud at the hole inlet, which occupies most of the hole inlet cross sectional area. The majority of the formed cavitation bubbles seems to collapse within the injection hole before reaching the hole exit. This regime has been referred to in past studies as incipient cavitation, for example see [144]. Increasing needle lift results to fully developed cavitation, which extends up to the hole exit. In addition to the geometric-induced cavitation, vortex or string cavitation has been observed, similar to [104]. The structure of cavitation is clear inside the tapered nozzle hole. There, string cavitation dominates the flow at low and intermediate lifts while both geometric and string cavitation disappears completely at high needle lifts. This type of cavitation structures have been observed in similar enlarged nozzle designs investigated over the last few years while limited evidence has been also reported in real size nozzle operating at realistic injection pressures and needle opening/closing events, as reported by [103], [37] and [104]. The similarity with the strings that were observed inside the marine nozzles previously presented in Chapter 5 is clear.

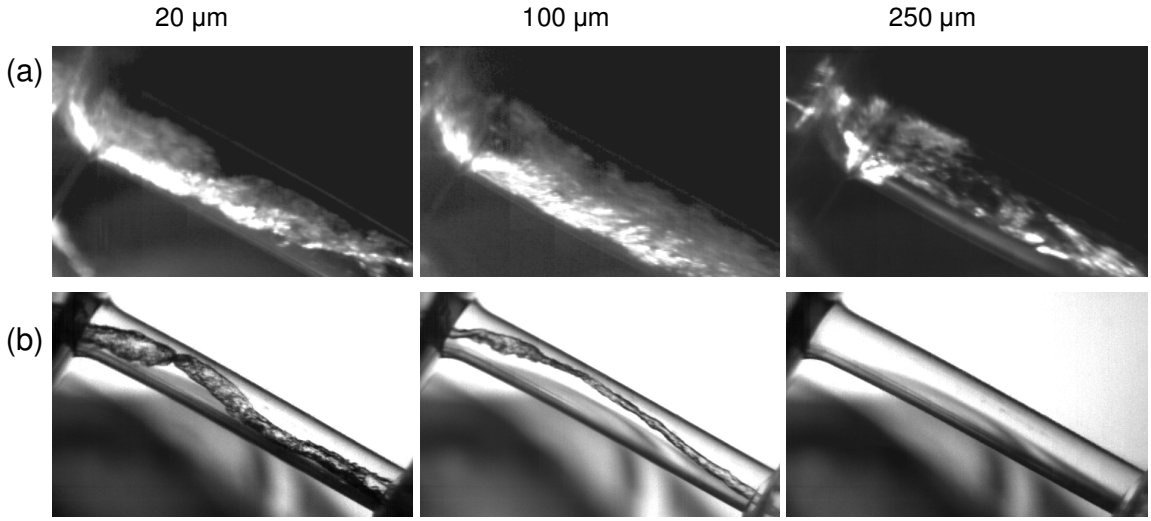

Figure 7-4: Sample representative images of cavitation structures formed in the injection hole of the VCO nozzle with grooved needle at three different needle lifts (a) cylindrical and (b) tapered hole, at the maximum Reynolds and cavitation numbers investigated.

The next figures will provide information regarding the origin and the mechanism of formation of these strings. Figure 7-5 shows the formation of a cavitation string as captured from the high speed camera at 16,000fps. For this particular operating condition, a weak geometric-induced cavitation bubble cloud is forming at the top corner of the injection hole. Cavitation bubbles found at locations closer to the axis of symmetry of the injection hole suddenly elongate and may take the shape of the observed strings within only a very small time interval.

Figure 7-6 shows a different origin or mechanism of string cavitation formation observed at the intermediate needle lift of 100 μm equivalent needle lift. This time, the increased needle lift combined with the tapered hole shape eliminates geometric induced cavitation sites pre-existing to the formation of string cavitation. Thus, initially, a single-phase liquid flow is present within the injection hole. Despite that, the sequence of high speed images indicates that downstream air may enter into the injection hole and propagate upstream, forming again the observed two-phase flow structure.

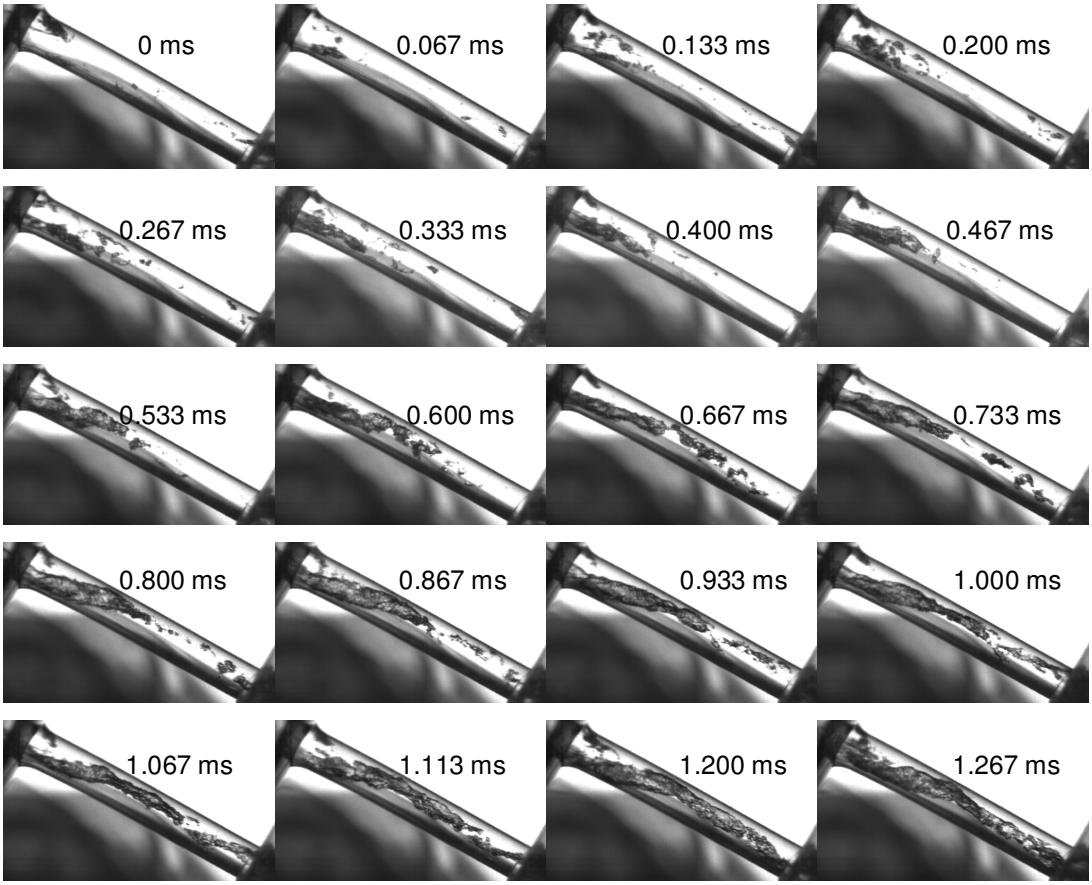

Figure 7-5: Sequence of events showing the formation of string cavitation from cavitation bubbles formed at the top corner of the injection holes feeding the vortical structure present inside the injection hole of the VCO nozzle [Eq. Needle Lift=20μm, Re=38,000, CN=11.2].

Although such a mechanism of formation had been identified n the marine nozzles, it is still surprising to observe that flow process, considering that the liquid towards the hole exit has almost an axial velocity component, as all past experimental and computational studies have indicated.

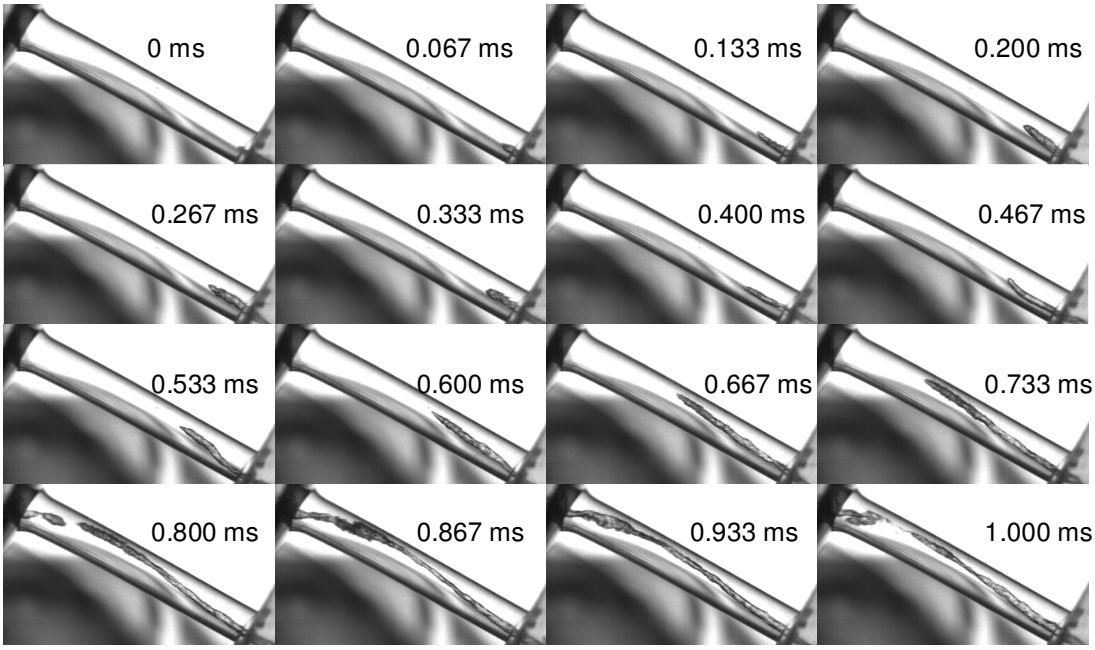

Figure 7-6: Sequence of events showing the formation of string cavitation originating from the air downstream of the injection hole and developing upstream inside the injection hole of the VCO nozzle [Eq. Needle Lift=100μm, Re=65,000, CN=4.5]

Cavitation strings have been observed not only inside the injection hole but also in the space between adjacent injection holes. The image of Figure 7-7(a) shows a cavitation string linking two adjacent holes. Averaging of all acquired images results to the picture of Figure 7-7(b); this can be interpreted as the probability of finding a cavitation string at a particular location in the space between two adjacent holes. The fact that the maximum levels of the plotted probability is less than 50% makes obvious that strings are not present continuously. In addition, their presence is more pronounced near the hole inlet rather than in the space between the hole inlet and exit. This is due to the mechanism of their formation and further development. As the pressure distribution plotted in the previous Figure 7-2 indicates, in the areas of formation of string cavitation the pressure is well above the vapour pressure of the flowing liquid, which is usually considered as the threshold for cavitation inception. Thus, cavitation strings do not form due to the local pressure drop but they rather represent a mechanism of vapour transport in these areas. This transport mechanism sometimes – but not always – results to a cavitation string linking the two adjacent holes. In most cases, two strings are formed, each one originating from the corresponding hole, but

disappear before coalescing and forming the continuous stream of vapour linking adjacent holes. This explains the lower levels of the plotted string probability of Figure 7-7 (b) at the central part of the injector. A scanning electron microscope (SEM) picture of the actual injector shown in Figure 7-7 (c) indicates that cavitation strings may also be responsible for cavitation erosion. As it can be seen the erosion pattern matches the shape and the orientation of the string.

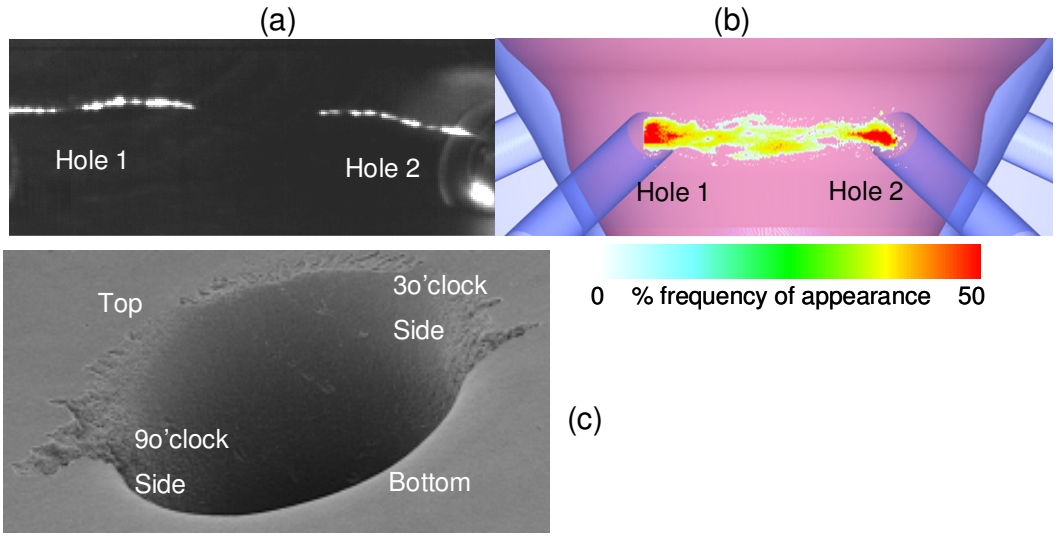

Figure 7-7: (a) Instantaneous image and (b) time-averaged probability of string cavitation appearance between two adjacent injection holes and (c) SEM image (by courtesy of [164]) of cavitation erosion at the entry to the injection hole, believed to be caused by string cavitation.

Since there are no available flow measurements in the areas of string cavitation development, the predicted flow field has been utilised to provide such evidence. Figure 7-8 shows predicted stream lines inside the nozzle volume as well as the injection holes for the low needle lift case. The plotted streamlines of Figure 7-8(a) are coloured according to the swirl number [137]. It is evident that in the space between the holes, a vortical structure is present. This is formed in the narrow space upstream of the injection holes due to the turning of the upstream flow in its path towards the discharge channels. Similarly, the flow distribution inside the injection hole, shown in more detail in Figure 7-8(b), has also a swirling pattern with a vortical structure formed around its central part. This originates from the non-uniform flow entering into the holes from the 3 and 9 o'clock sides. The observed flow non-uniformity may originate from the non-symmetric design of the feed

fuel pipe; other factors may be a small eccentricity of the needle lift which is known to affect the flow distribution in the narrow space between the needle and the injection holes as well as the transient development of the flow itself.

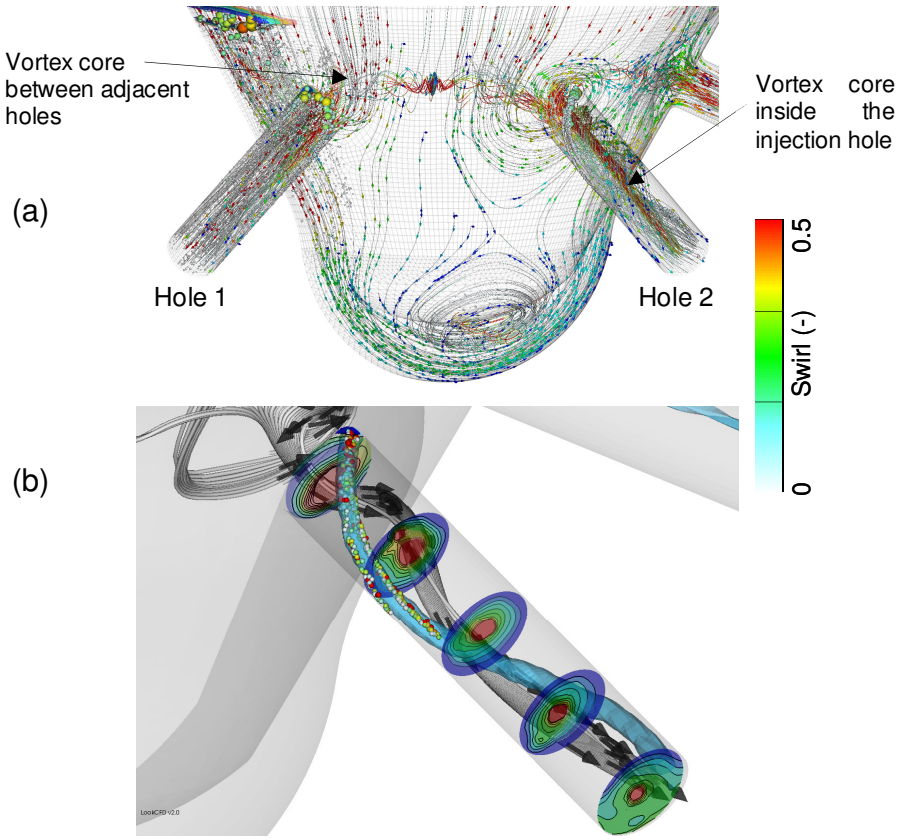

Figure 7-8: Model predictions for the original VCO nozzle using slightly eccentric needle position. Calculations indicate (a) formation of a strong vortex formed in-between adjacent holes and (b) the vortex core inside the injection hole can be linked with the area where string cavitation has been observed. (by courtesy of [164])

The latter may be attributed to flow turbulence but also to the instantaneous variation of the discharge coefficient of individual injection holes. This can be caused by the formation of the weak geometric cavitation at the top corner, which, instantly results to a reduction in the flow rate through that hole, as reported also in section 5.5 when considering the marine nozzle simulations and thus, creating a cross-flow between adjacent holes. Combination of the observed cavitation strings with the predicted flow vortices developing within the injector indicates that cavitation strings develop in the area of these vortices, effectively they represent a 'visualisation' of their presence, as supported by the trajectory of cavitation

bubbles specifically introduced into the flow and captured at the centre of the vortical structure, following closely its path towards the hole exit (Figure 7-8(b)).

7.3 VCO nozzle with cylindrical and tapered holes-Parametric studies

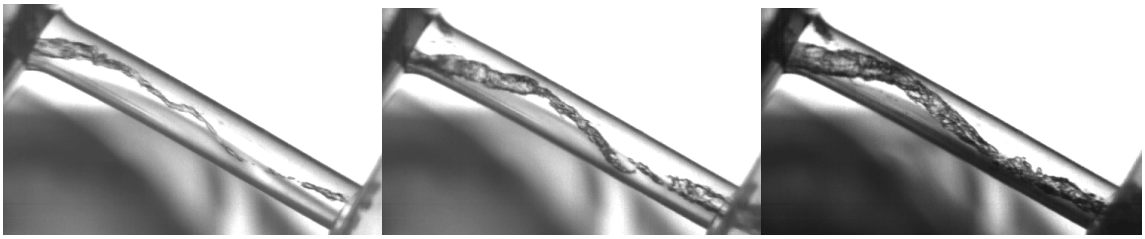

Figure 7-9: Effect of cavitation number of string cavitation structure inside the tapered injection hole of the VCO nozzle [Eq. Needle Lift=20μ, Re=38,000].

Having identified their origin and area of development, we proceed now to the last set of results which provide information on the temporal and spatial characteristics of string cavitation as function of the operating conditions. With the given experimental rig, the effect of cavitation number, Reynolds number and needle lift has been evaluated. Figure 7-9 depicts clearly the expected effect of increasing cavitation number keeping the flow rate through the rig constant and the needle at its lowest lift of 20 μm (equivalent). It can be seen that the formed strings are thinner at low cavitation numbers while no differences in their shape and extend can be observed with sufficient high CN.

In an effort to provide a visual representation of the thousand of the collected frames which show the dynamic development of the phenomenon at nominal quasi-steady state flow conditions, the following Figure 7-10 is presented.

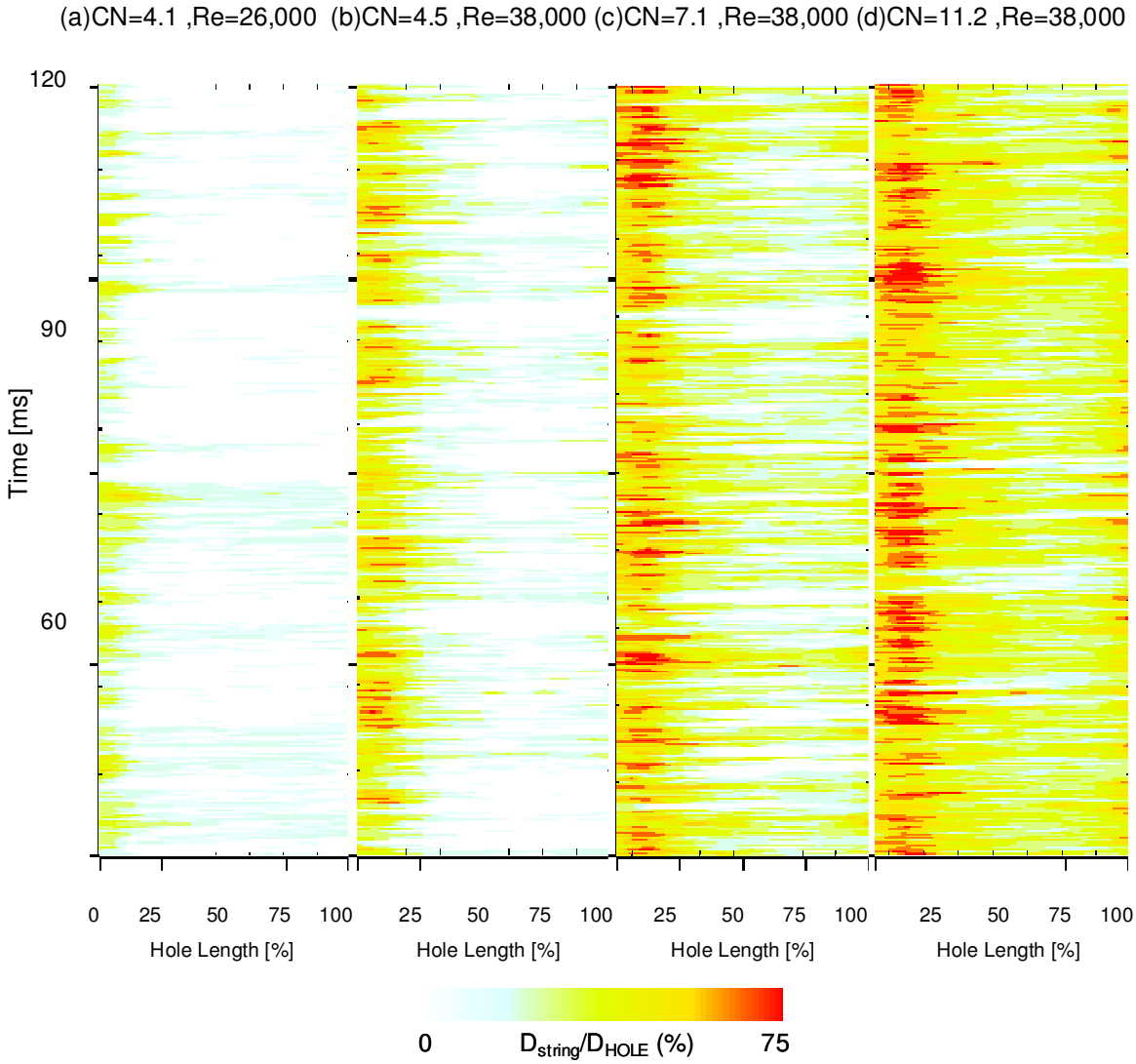

Figure 7-10: Spatial extent and temporal development of string cavitation inside the injection hole of the VCO nozzle as function of Reynolds and cavitation numbers for 20 μm equivalent needle lift; colour according to normalised string diameter.

On the plot, every horizontal line plotted indicates the instantaneous presence of string cavitation in the corresponding location along the injection hole. The colour used is according to the local diameter of the string at each location, normalised with the hole diameter. Thus, this graph allows for a convenient representation of the dynamics of string appearance and size for all individual frames collected. The last three plots (Figure 7-10 (a), (b) &(c)) indicate that the phenomenon is greatly affected by the cavitation number keeping the same Reynolds number (fixed flow rate). Increasing cavitation number results to more

frequent appearance of cavitation strings which gradually occupy the whole injection hole. Larger diameters can be found at the inlet and the exit of the injection hole while strings seem to become thinner and appear less at the central part. Comparison between Figure 7-10(a) and Figure 7-10 (b) indicates that the flow rate (Reynolds number) may also be an influential parameter but at low cavitation numbers.

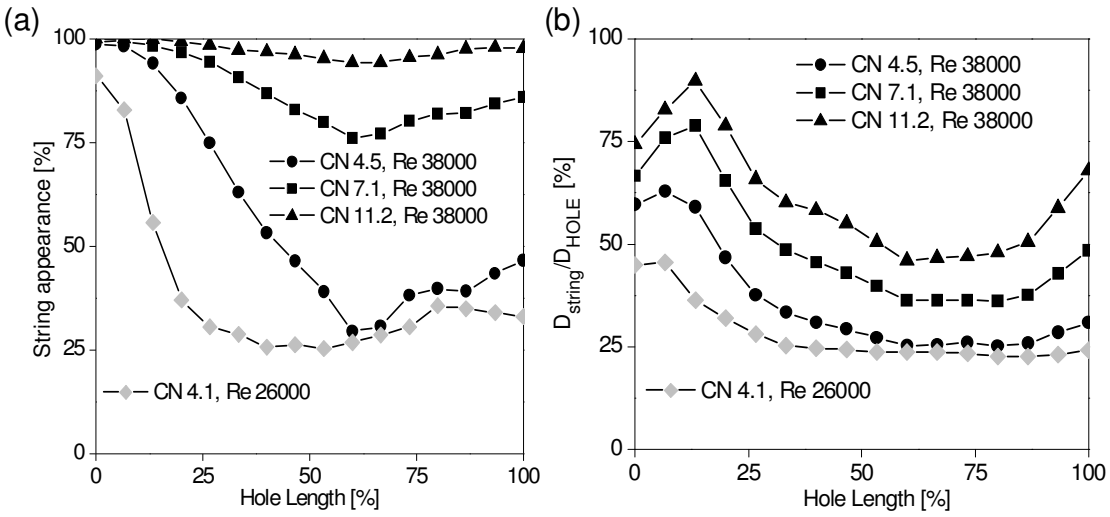

Figure 7-11: Effect of Reynolds and cavitation numbers on (a) string appearance along the hole length expressed as % of time and (b) normalised mean string diameter along the hole length [Eq. Needle Lift=20μ].

From these plots, the percentage of string appearance at a specific location within the injection hole and the temporal mean size have been estimated and shown in Figure 7-11 (a) and Figure 7-11 (b), respectively. The plots reveal that at the hole inlet, cavitation strings are always present but they disappear as they move inside the injection hole.

Towards the hole exit, string appearance increases again due to their formation from the downstream air, as explained previously. The decrease in their appearance is also linked with a decrease of their size. At the hole inlet, strings may occupy up to 75% of the hole cross sectional area while their size drops to 50% at the central part of the hole. This variation in size is also present even at sufficient high cavitation and Reynolds numbers which correspond to continuous presence of cavitation strings inside the injection hole.

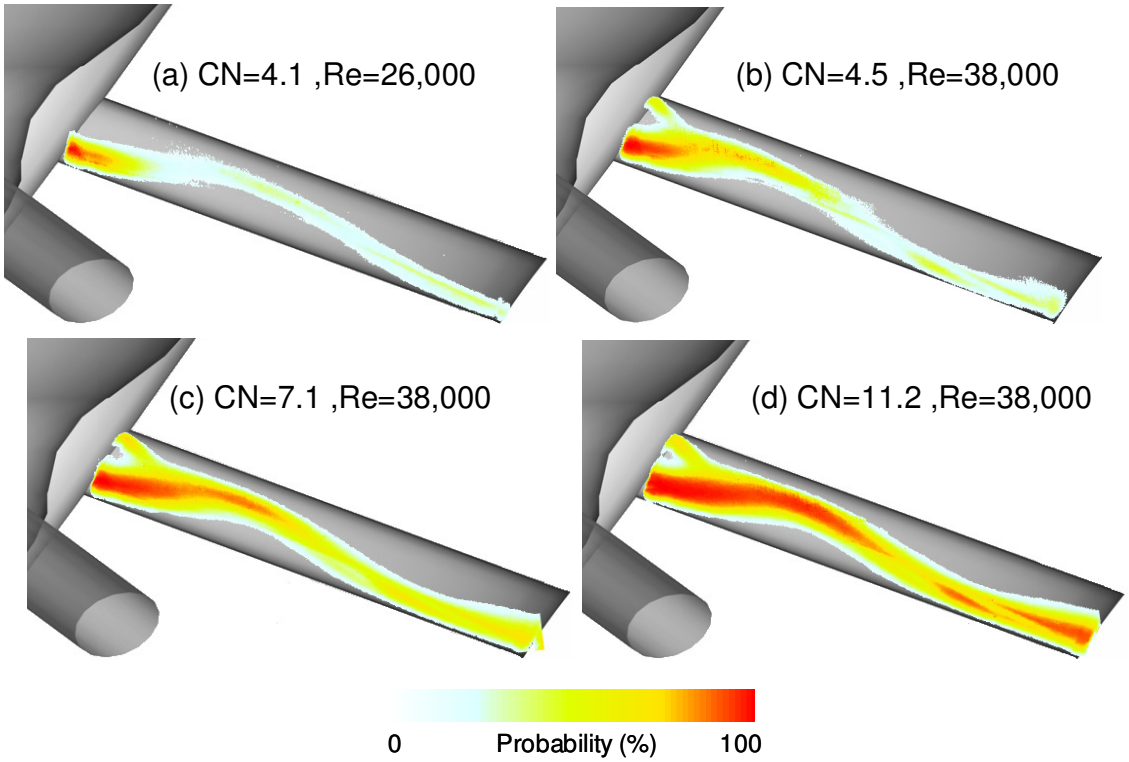

Figure 7-12: Effect of Reynolds and cavitation numbers on spatial probability of string cavitation location [Eq. Needle Lift=20μ]

Another visual representation of cavitation strings can be seen in Figure 7-12. This plot shows the effect of cavitation and Reynolds numbers on the temporal averaged string presence at a specific location on the 2-D viewing plane of the camera which can be interpreted as the probability of finding a cavitation string at a particular location along the hole length. The images reveal that strings originate mainly from the bottom part of the hole inlet or exit while they follow a path towards the upper part of the central hole region.

All previous results refer to the low needle lift case of 20 μm equivalent needle lift. Significant differences have been observed with increasing needle lift. A quantification of these differences between the low and intermediate needle lift cases is presented in the following figures. As already pointed out, the geometric-induced cavitation site is significantly reduced or even eliminated with increasing needle lift for the tapered nozzle hole geometry due to the differences in the pressure distribution inside the nozzle. As a result, much less cavitation strings have been observed; this can be seen by inspecting the instantaneous string appearance and size of Figure 7-13. For comparison, the corresponding

image obtained at the same cavitation number but for the low needle lift case is also re-plotted here.

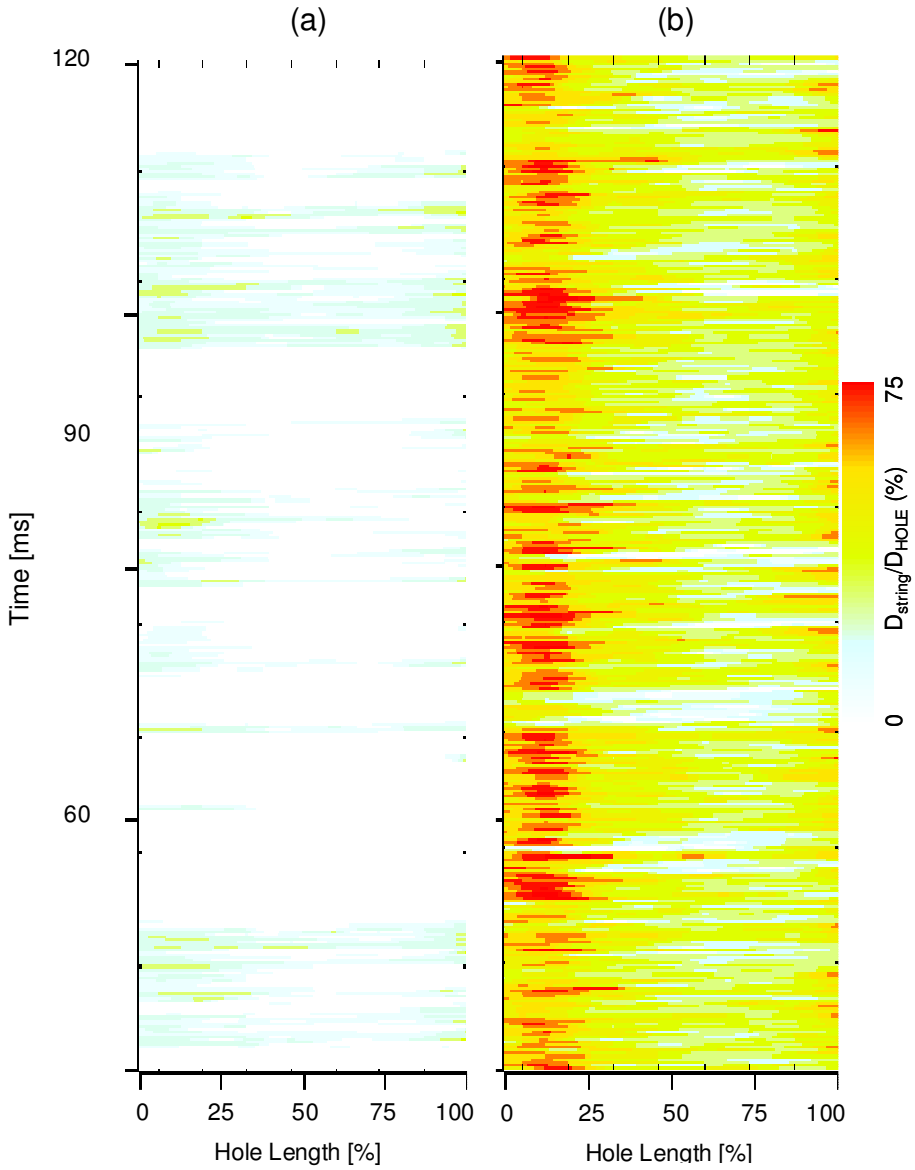

Figure 7-13: Effect of needle lift on spatial extent and temporal development of string cavitation inside the injection (a) Eq. Needle Lift=100μ, Re=66,000, CN≈11 and (b) Eq. Needle Lift=20μ, Re=38,000, CN≈11; colour according to normalised string diameter.

Figure 7-14 shows the comparison between the two needle lift cases on the % time of string appearance for the highest cavitation number. Increasing needle lift results to a gradual drop in the string appearance until they eventually disappear at the highest needle lift case investigated. Their size is also reduced to more than half compared to the lowest needle lift

case. This reduction is more profound at the hole inlet; as it can be seen, at this intermediate needle lift case the average string diameter remains almost constant along the injection hole with an increasing trend towards the hole exit.

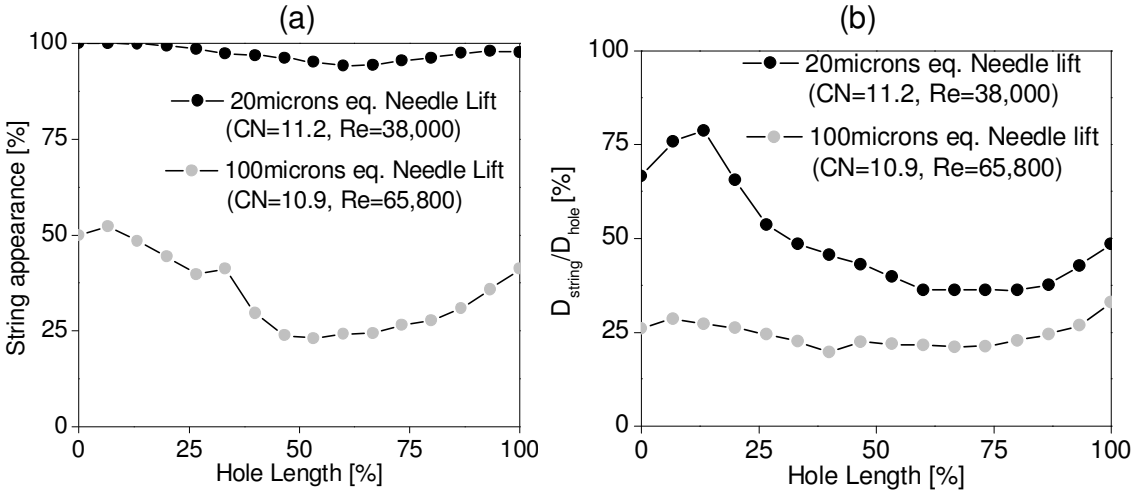

Figure 7-14: Effect of the needle lift on (a) string appearance along the hole length expressed as % of time and (b) normalised mean string diameter along the hole length.

Finally, Figure 7-15 indicates that some differences can be also appreciated in the probability of finding string cavitation at a specific location inside the injection hole. Strings now are occupying the upper surface of the injection hole towards its exit but they are still concentrated at the lower part at its inlet.

Closing, it has been considered useful to summarise the various findings of the observed flow regimes in flow maps that can be reconstructed by temporal and spatial averaging the instantaneous hole cavitation images at a specific operation point. Such averages are performed from every operating point and the corresponding results are shown in the contour plot of Figure 7-16. The two axes selected for plotting the results are the cavitation number and the needle lift, since these two are the most influential parameters. The contour levels represent normalised averages of the percentage hole area occupied by cavitation; from the previous results this parameter is expected to take values up to 50%. This is realised at low needle lifts and increased cavitation number. The cavitation inception number, of around 2, can be realised from this plots. Fully developed cavitation is realised for cavitation numbers above 5 as the horizontal shape of the plotted lines indicate.

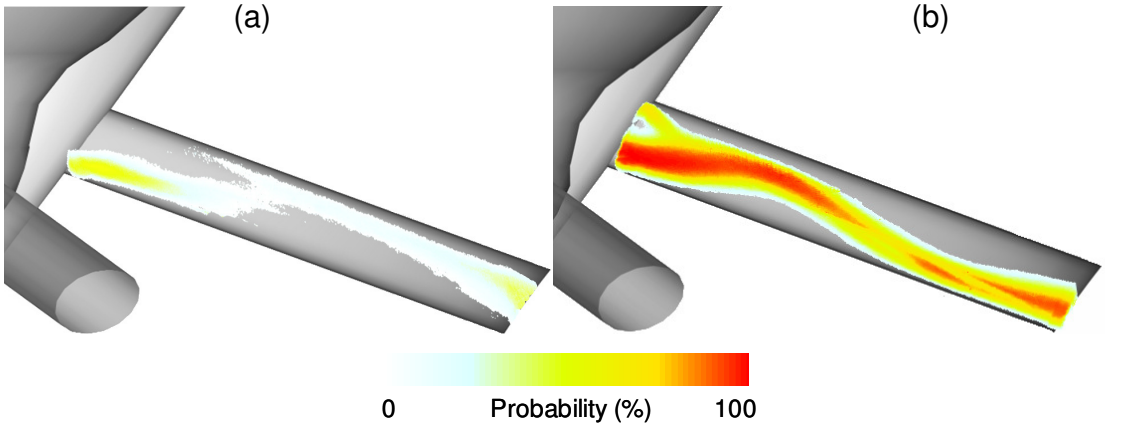

Figure 7-15: Effect of needle lift on spatial probability of string cavitation location (a) Eq. Needle Lift=100μ, Re=66,000, CN≈11 and (b) Eq. Needle Lift=20μ, Re=38,000, CN≈11.

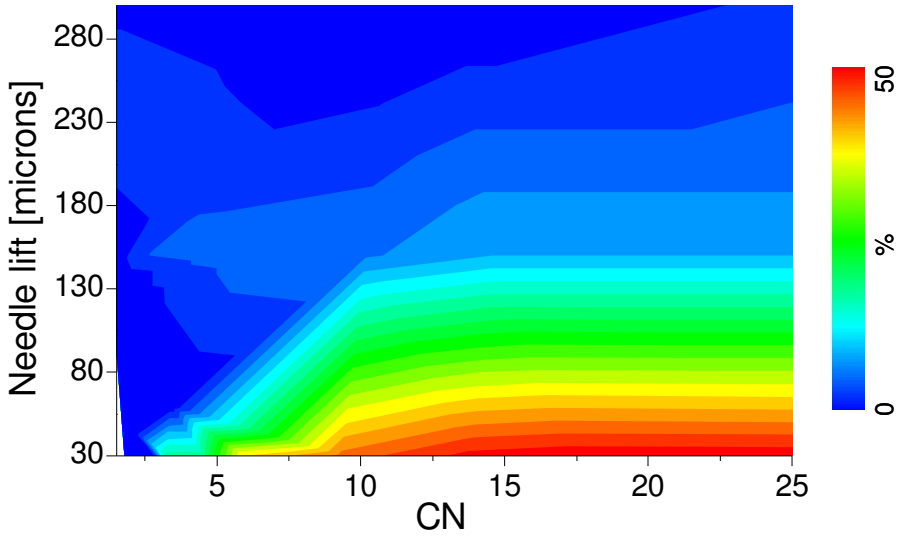

Figure 7-16: Flow map showing the normalised percentage hole area occupied by string cavitation as function of needle lift and cavitation number

7.4 Internal flow in large scale conventional multihole Sac-Type nozzle

Having investigated the flow regimes inside the VCO nozzles with both Cylindrical and tapered holes, the next chapter presents the experimental results from the internal nozzle flow investigation by using a Sac-Type nozzle. A 3-Dimensional schematic of the nozzle can be found in Figure 7-17(a), while a cross-section has been presented in Figure 3-19 in

Chapter 3. As done with the VCO nozzle, the same nozzle body was combined with different needle tips by using the adaptor described in Chapter 3 which can be seen in Figure 3-26. The needle designs investigated are shown in Figure 7-17(b).

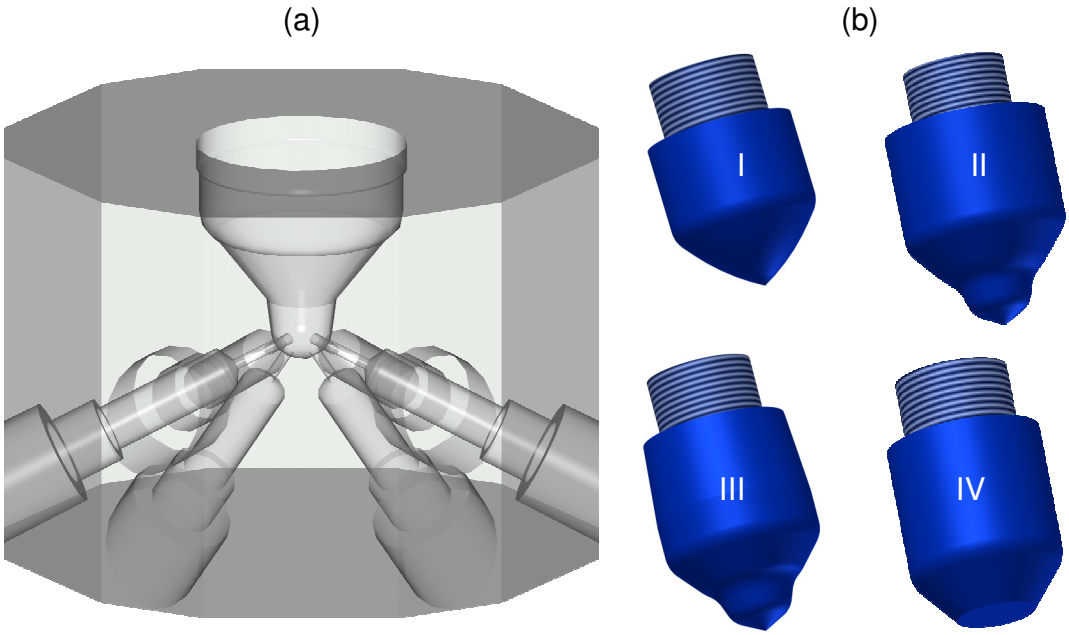

Figure 7-17: 3D schematic of a) the transparent large-scale model of a sac-type Diesel nozzle and b) four different needle tip designs.

7.4.1 Erosion & needle seat cavitation

As suggested by the nozzle manufacturer, it was found that the original design, which was formed by the nozzle body and the needle design (I), was particularly suffering from severe erosion at the region of the at the needle itself Figure 7-18(a) as well on the sac volume surface upstream of the hole inlet Figure 7-18(b). Contrary to what it was found in the VCO nozzle where erosion linked to the Hole-to-Hole strings between adjacent holes was evident, this nozzle type was found to be much less effected from erosion problems. It has to be mentioned that although the erosion site was found well above the injection holes, and therefore it could be said that there would not have been a significant effect on the flow inside them, the fact that the needle and the sac volume was eroded, led to improper sealing of the nozzle at closed needle position.

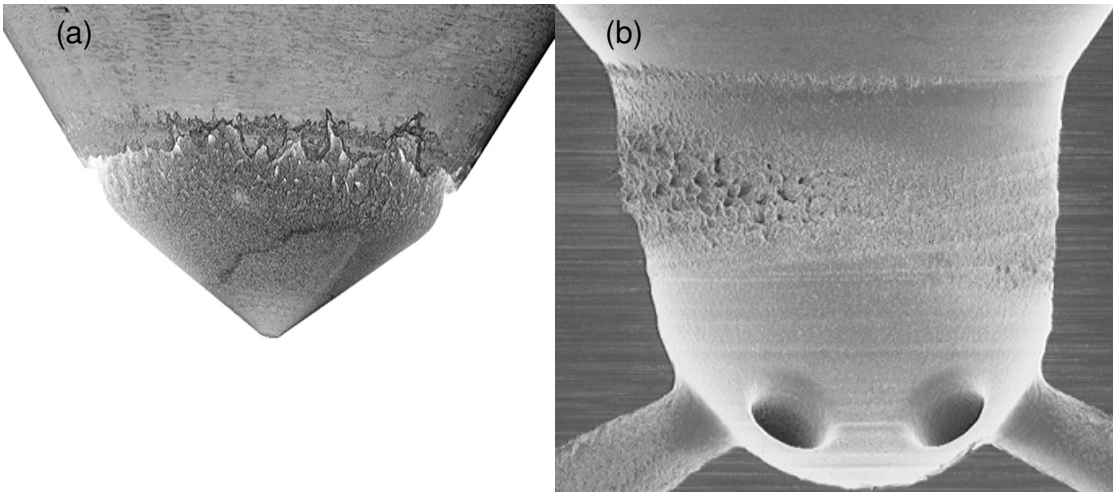

Figure 7-18: (a) picture of erosion damage of the needle and (b) erosion damage of the sac volume. (by courtesy of [164])

It has to be mentioned that the fact that erosion was concentrated close to the needle seat, the area where the needle seals with the nozzle body in order to cut fuel flow, gave rise to thoughts that the investigation had to be particularly focused at low lifts. Following table 1 shows the range of operating conditions that were used for this type of nozzle. The rig used is the same as the one used for the internal nozzle flow of the marine nozzle which is described in detail in section 3.2. It follows that, as before, the simultaneous use of a delivery and a suction pump allowed to achieve high CN values matching, or even in some cases exceeding, the operational one.

Needle lift (μm)	Pressure (bar)				CN		Re		Equivalent P_{INJ} (bar)	
	Inlet		Back							
	Min	Max	Min	Max	Min	Max	Min	Max	Min	Max
10	4	7	0.3	1	3	27	11000	23300	200	1400
20	4	8	0.2	1	3	52	22900	36700	200	2650
50	2	7	0.15	1	2	27	31400	61900	150	1400
150	3	7	0.3	0.65	11	27	45900	65000	600	1400
300	2	6	0.2	0.4	5	16	47000	80400	300	850

Table 7-2: Range of operating conditions investigated for the transparent sac-type nozzle

Before presenting processed results it is essential to show some raw images in order to identify the cavitation regimes existed in the nozzle at low lifts. As it shown in Figure 7-19, there are cavitation sites extending to the entire circumference of the needle. The cavitation pattern does not occupy uniformly the needle seat area. High-speed images have revealed that the location of the visualised black spots appear and disappear in a transient mode. Part of the vapour formed is moving inside the sac volume, where a large recirculation zone is present. Some bubbles manage to escape and exit from the injection holes while a substantial part of them collapses before entering into the sac volume.

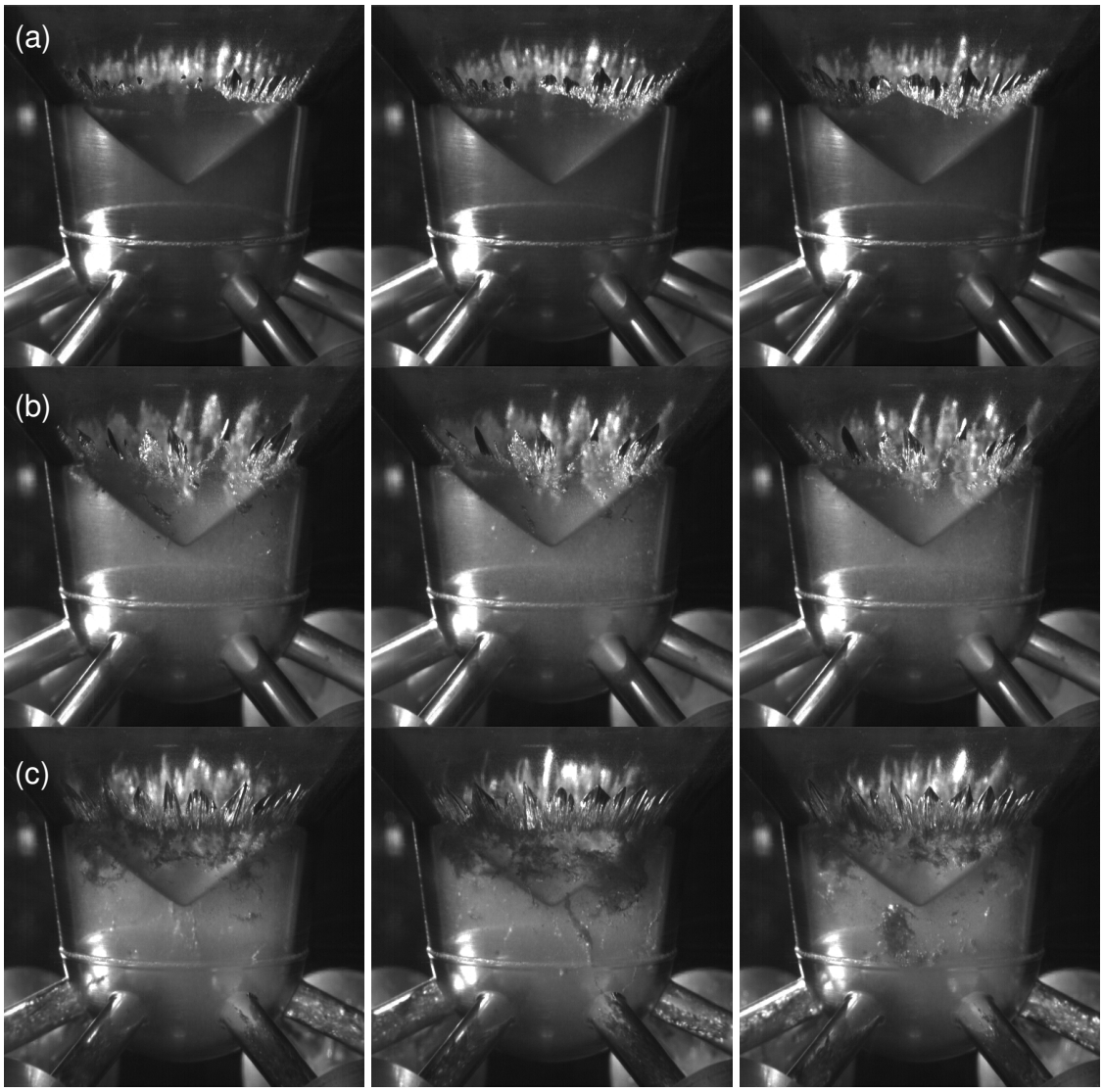

Figure 7-19: Side view of Sac-type nozzle with needle design I at 20μm equivalent needle lift for a) CN =3, Re=23300, b) CN =15, Re=23,300 and c) CN =52, Re=38,200.

Starting with a low CN and Re number, Figure 7-19(a), it can be seen that these small cavitation sites extend to a small degree and the bubbles produced break-up into a fine cloud and are almost uniformly mixed with the liquid inside the sac volume. It is also interesting to point out that these sites have small gaps between them while they have a rose spike shape with the tip been at the top of the flow direction. finally at CN=3 the injection holes are free of geometrically induced cavitation and additionally no visible strings are found inside the sac volume. Moving at a higher CN, CN=15 Figure 7-19 (b), keeping the same injection pressure, thus the same Re number, it can be seen that these cavitation structures are enlarged. Also the amount of vapour inside the nozzle starts to increase significantly, which can be realized by monitoring the difference in lightness of the sac volume region. The more vapour inside the liquid the whiter it becomes. However this is not the only change to observe. As it can be seen in the three representative images of this case, inside the sac volume there are some bright spots which where not present at lower CN. These bright marks are vapour bubbles that have not been collapsed into fine foam, and therefore are drifting away with the flow exiting through the injection holes. as we have seen in chapter 5, when vapour exists inside the injection holes, the near hole exit spray characteristics might change considerably. However it is expected that due to the limited amount of such undisolved bubbles there won't be a noticeable effect on spray formation. finally it has to be noticed that the number of sites (spikes) seem to be lower compared to the low CN case and the gap in between successive sites has been increased. Although more data points have been taken, moving to Figure 7-19 (c) the CN value has been increased to 52 and Re is almost two times greater than the one used in a&b. At this high CN number it can be seen that although the upper part of the cavitation sites has kept the same form as in case (b), the lower part which is the zone where the bubbles detach from the sites has been considerably extended. Also the amount of vapour produced has been significantly increased, and although the dissolved vapour in the liquid does not seem to have been increased noticeably, the amount of undisolved bubbles is much more than before. Looking at the third image it can be seen that entire bubble clouds having size equal or bigger to the hole diameter, have been detached and are present inside the sac volume without breaking up. This large vapour clouds are entering the injection holes and travel all the way to the exit. Also at this high CN all the injection holes show evidence of developed Hole cavitation and by a closer look it can be seen that there are also some strings forming. Interestingly enough, such strings can also be seen inside the sac volume, second image,

either detaching from the needle seat and travel to the injection holes or even connecting the vapour sites of the needle with those inside the injection holes. As model predictions of the internal nozzle flow have shown there are small and bigger recirculation sites existing inside the sac volume which vary in location and by dragging in bubbles from the two existing cavitation sites, since the pressure values in this region is considerably above vapour pressure, are forming these string like structures.

Volumetric Flow Rate (l/s)	P_{in} (bar)	P_{back} (bar)	Re	CN
0.33	4.0	0.3	23,300	15
0.33	4.0	1.0	23,300	3
0.38	5.0	0.3	26,900	19
0.38	5.0	0.5	26,900	10
0.38	5.0	1.0	26,900	4
0.47	7.0	0.3	33,200	27
0.47	7.0	1.0	33,200	6
0.54	8.0	0.2	38,200	52

Table 7-3: Range of operating conditions investigated for the transparent sac-type nozzle with needle design I at 20 μm equivalent needle lift.

Although the side images provide a good viewpoint in order to realize the extent and shape of those structures, it is not possible to perform further image processing since the background is constantly changing. For this reason it was chosen to further process the images acquired from the bottom view camera. It has to be mentioned that in most cases presented here the bottom and side view cameras were simultaneously recording and therefore it was possible to monitor how these cavitation structures evolve in a 3-dimensional perspective. The fact that the cameras were synchronized will be further exploited at a later stage. Table 7-3 above includes the operating conditions of all the investigated cases for needle design I at 20 μm equivalent needle lift. The first stage of processing was to perform time and space averaging of the binary bottom view images where pixels without needle seat cavitation had values of zero while those with vapour existing 1. this is the same concept as it has been used throughout the entire study both for internal nozzle flow and spray characterization. for the cases where hole cavitation was present it was considered useful to take into account these vapour regions as well in order t indicate which holes were experiencing negative pressure regions.

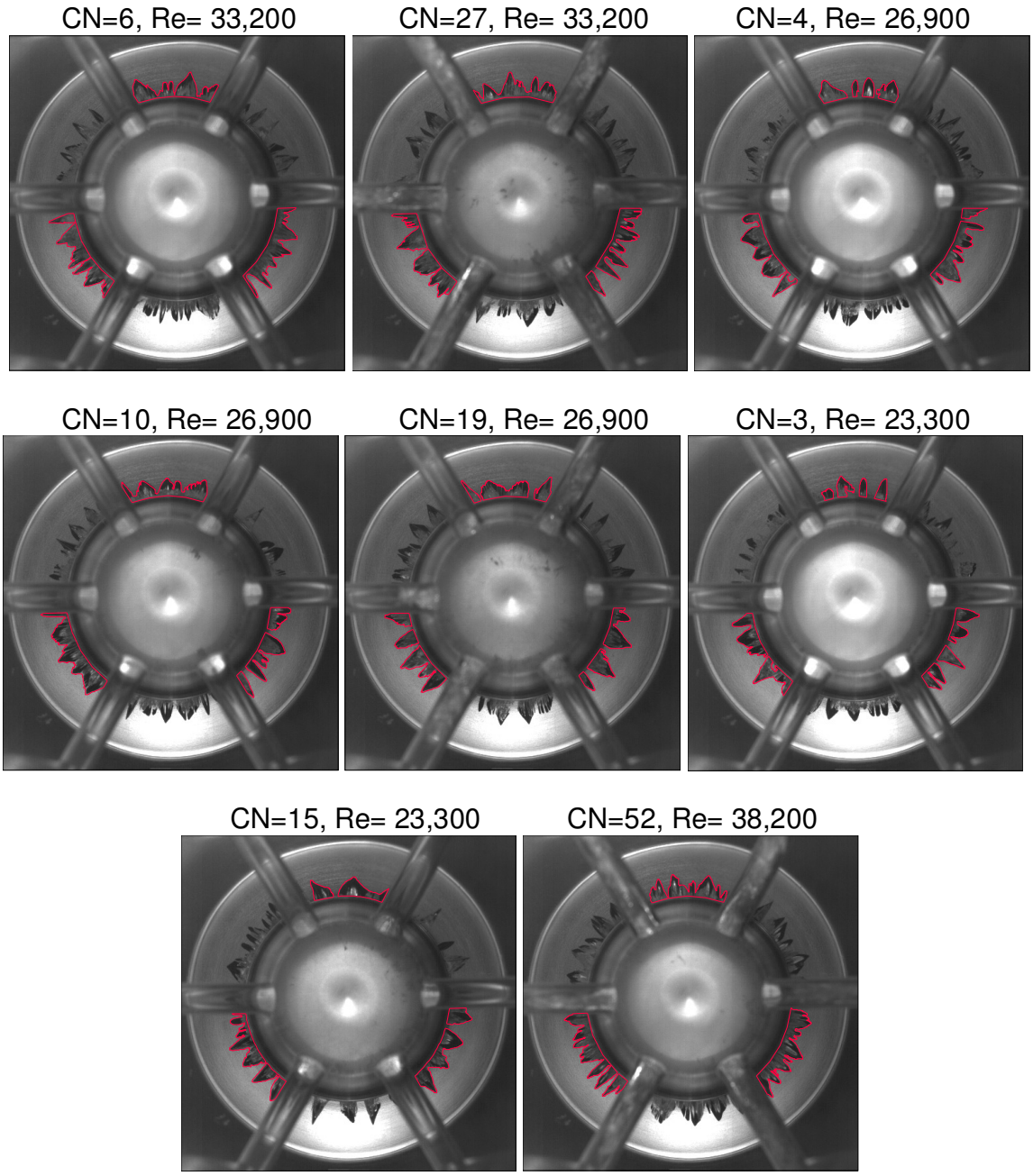

Figure 7-20: Typical bottom view images of the Sac-Type nozzle with needle design (I) at 20 μm equivalent needle lift.

Representative bottom view images of all the conditions tested at 20 μm equivalent needle lift with needle design I can be found in Figure 7-20. The red line represents the boundary of the needle seat cavitation regions in 3 representative sectors. As it can be seen the information that can be derived from this view is limited compared to the side one since the

vapour that extends to the vertical direction is not properly indicated. Nevertheless the mean images will show how this form of cavitation varies.

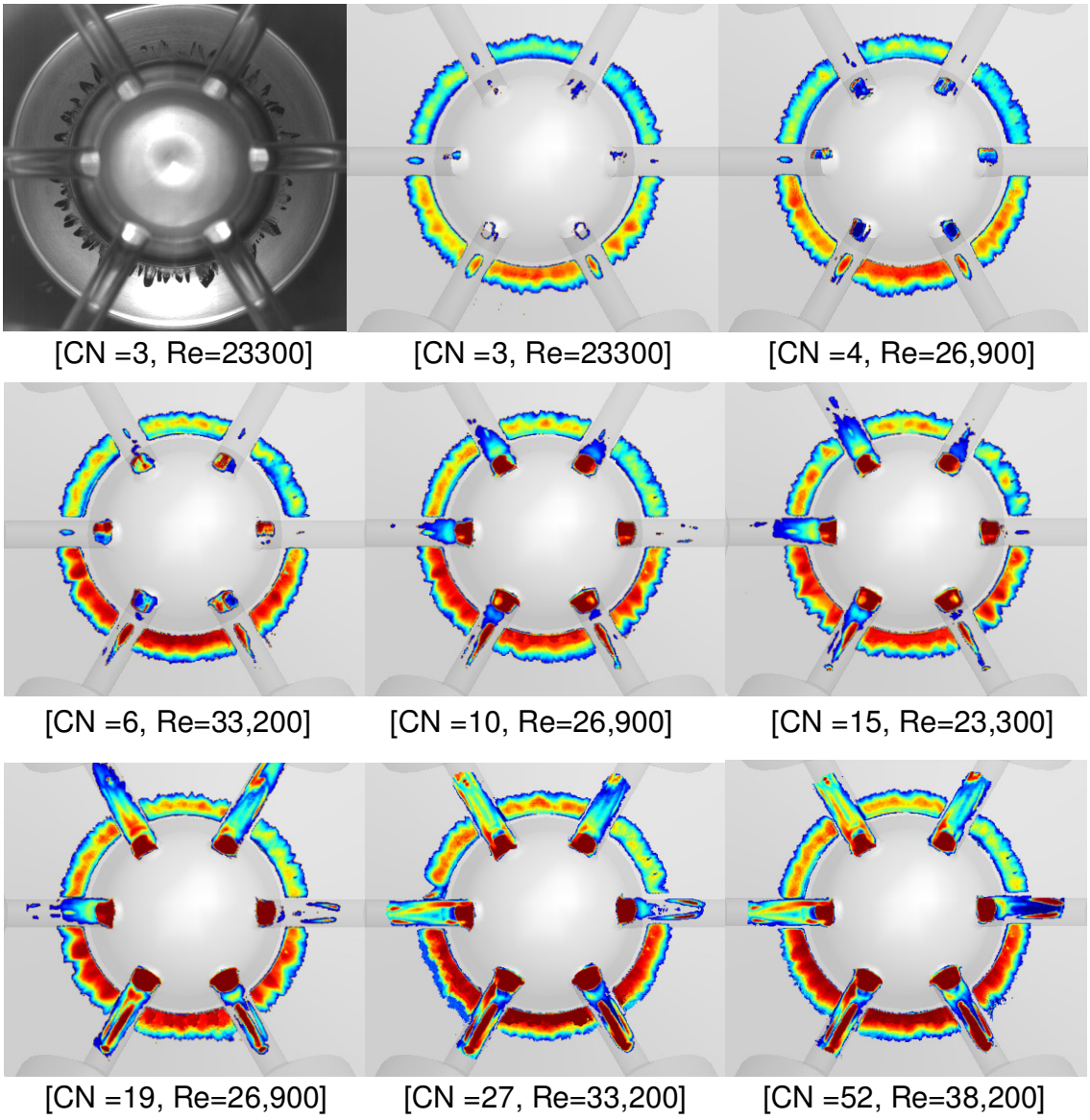

Figure 7-21: time averaged images for needle seat cavitation in sac-type nozzle with needle tip design (I) for different flow conditions. [20µm Needle Lift]

Representative mean images of the cases presented in Table 7-3 and Figure 7-20, are shown in Figure 7-21. Figure 7-21 shows mean images obtained by superimposing sufficient number of bottom-view images. Similar to the string cavitation presented earlier, the resulting image represents the probability of finding needle seat cavitation at a specific

location. As can be seen, for this low needle lift case, even a small needle eccentricity is enough to cause non-uniformity to the obtained results. During the experiment, it has been noticed that vibrations of the needle were imposed by the flow, despite the fact that for this nozzle a lower needle guide was present. The inherent instability of the flow can be captured by the computational model. As already described, local and instantaneous vapour formation modifies the pressure field, which may cause formation or collapse of cavitation. This, in turn, creates the observed fluctuations of the vapour formed. By carefully examining the various mean images, it can be concluded that needle seat cavitation is both affected by CN and Reynolds number. Increasing CN results in a higher probability of having vapour formed at the needle seat area. Similarly, although with lower effect, increasing Reynolds will also result in higher needle seat cavitation probability. Finally it s interesting to mention that the side of the nozzle which is associated with a higher needle sea cavitation probability, is also related with a higher hole cavitation probability. This is line with the fundamental mechanism of geometrically induced cavitation, which states that once impurities, such as dissolved bubbles, are introduced in a liquid it triggers the mechanism of cavitation formation. additionally it was found that the upper part of these spike like structure tend to change slightly location with time. This can be realized by the blue, lower probability region, ring that is present at that side. Moreover the similarity of the cavitation pattern shown both in Figure 7-20 and Figure 7-22 with the erosion marks as shown in Figure 7-18 is evident. Therefore it can be safely concluded that this form of cavitation severly affects the nozzle structure by eroding the components that are in its vicinity.

Volumetric Flow Rate (l/s)	P_{in} (bar)	P_{back} (bar)	Re	CN
0.12	4.0	0.3	8,500	15
0.12	4.0	1.0	8,500	3
0.16	5.0	0.3	11,300	19
0.16	5.0	1.0	11,300	4
0.25	7.0	0.3	17,700	27
0.25	7.0	1.0	17,700	6

Table 7-4: Range of operating conditions investigated for the transparent sac-type nozzle with needle design (I) at 10 μm equivalent needle lift.

A similar set of results for 10 μm equivalent needle lift and for the flow conditions listed in table 1-4 can be found in Figure 7-22 and Figure 7-23. as it can be seen the eccentricity effect, particularly at low CN and Reynolds, results in an even more non-uniform distribution of needle seat cavitation. Also , as expected, the location which these cavitation sites initiate have moved downwards since the needle has now less distance to the nozzle body.

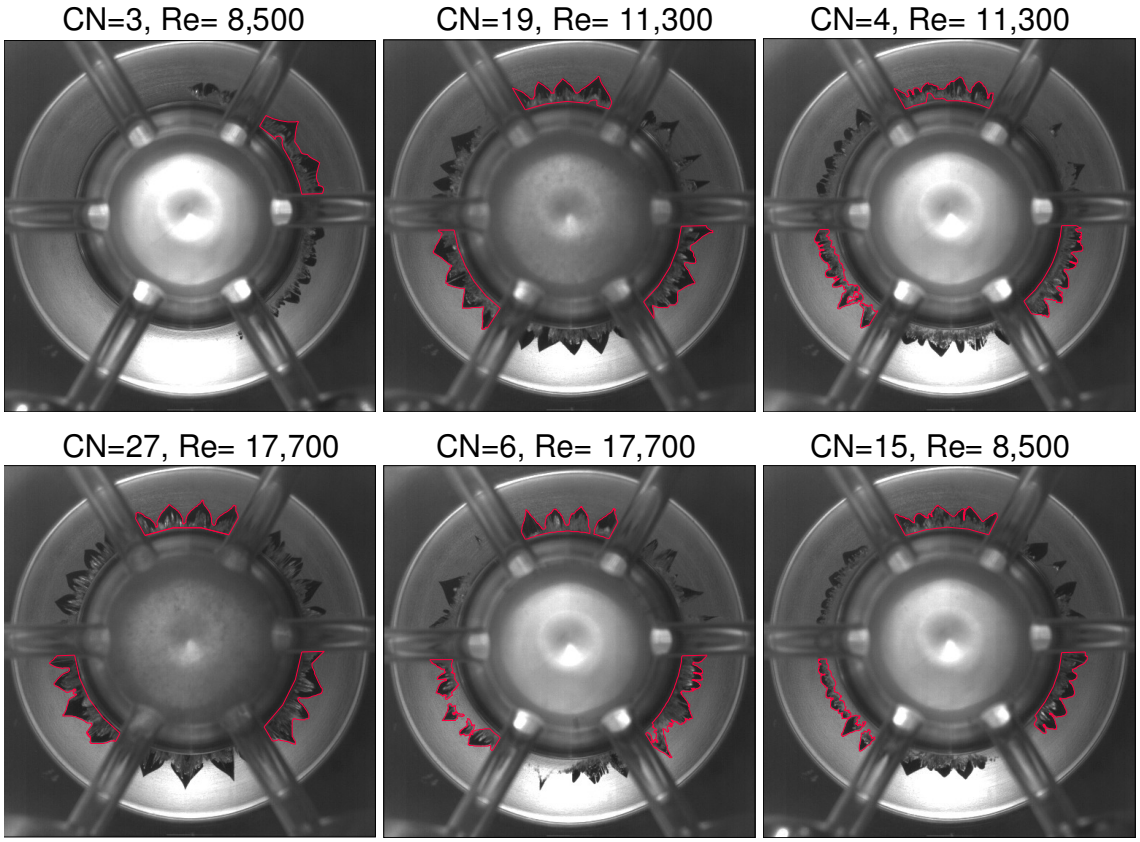

Figure 7-22: Typical bottom view images of the Sac-Type nozzle with needle design (I) at 10 μm equivalent needle lift.

Finally as it can be seen in Figure 7-23 below, for the same CN the probability of needle sa cavitation is increased compared to the 20 μm lift. This suggest that the lower the lift the more likely it is to have needle seat cavitation, which is true since after 30 μm needle lift the nozzle is free from this form of cavitation. Finally the fact that the probability distribution follows almost the same shape as the instantaneous images presented in Figure 7-22, suggests that the movement of these cavitation sites is more limited at lower lifts.

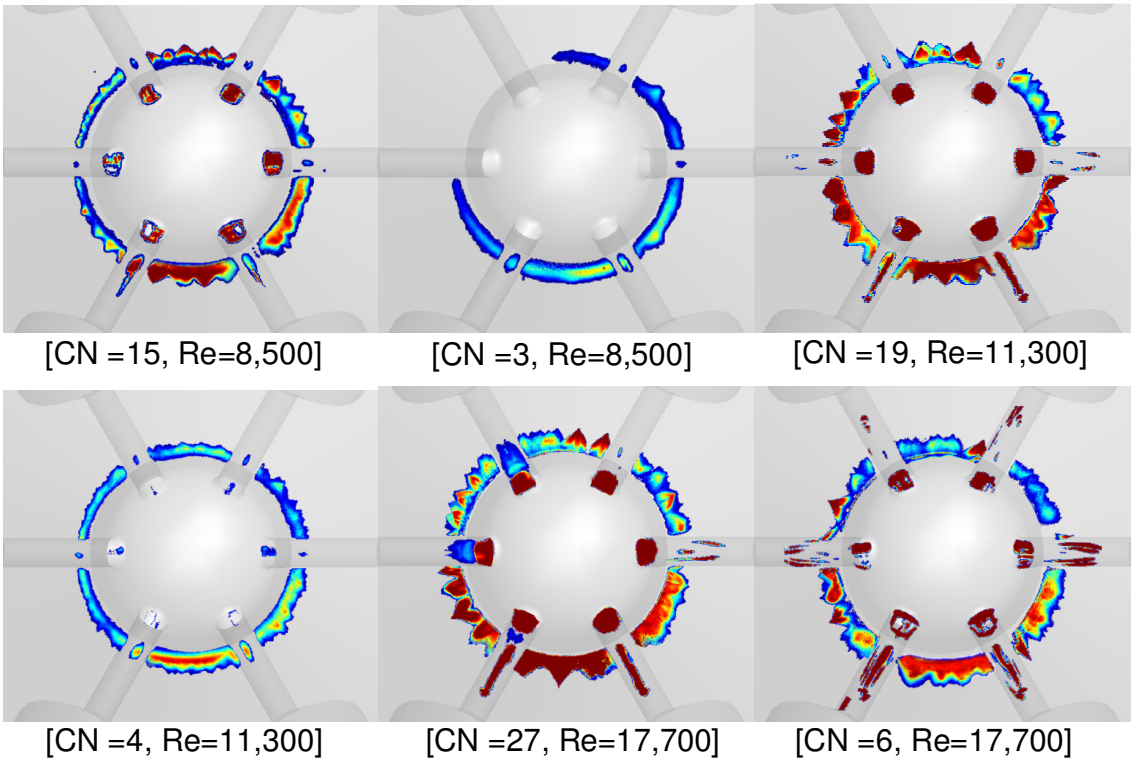

Figure 7-23: time averaged images for needle seat cavitation in sac-type nozzle with needle tip design (I) for different flow conditions. [10µm Needle Lift]

7.4.2 Needle seat cavitation quantitative analysis

By considering the limited amount of time that the needle is at close distance to the nozzle body, as it can be seen in Figure 7-24, it is impressive the amount of damage that can occur to the injection components by the mechanism of erosion due to cavitation bubbles collapse.

Therefore it becomes clear that this form of cavitation needs to be avoided and for that reason a series of other needle designs were tested. The reason to change only the needle is that it is much more difficult to change the shape of the nozzle downstream since there might be a significant change to the spray distribution, which is the key variable when considering the combustion chamber design.

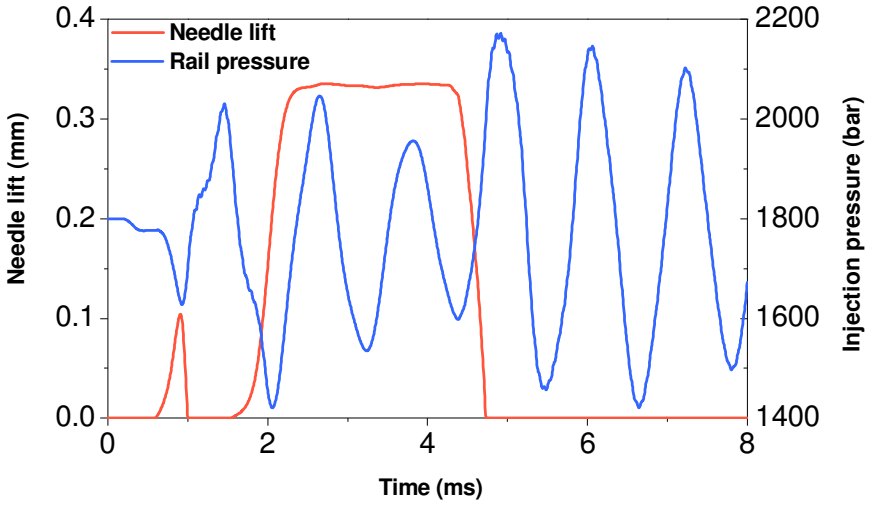

Figure 7-24: Injection pressure and needle lift diagram used for the real-size nozzle flow simulations for the sac-type nozzle.

By observing the sequence of images obtained through the entire investigation it soon became evident that there are many qualitative characteristics that could not be realized through a limited number of instantaneous images or even by the mean images derived for each case. The main reason for that, is the fact that cavitation is highly transient and unless a method of processing, that can instantly represent these rapid changes through time, is found, a large amount of useful information will be lost.

The next figures to be presented are results of the processing method described in section 3.4.5. The main concept was to divide the nozzle into radial sections, having 1 deg resolution, and within these sectors to monitor the percentage of vapour occupancy. The x-axis is the degrees of the circular area of the needle seat. The y –axis is the experimental time and the contour is coloured by the percentage of vapour existing inside its sector.

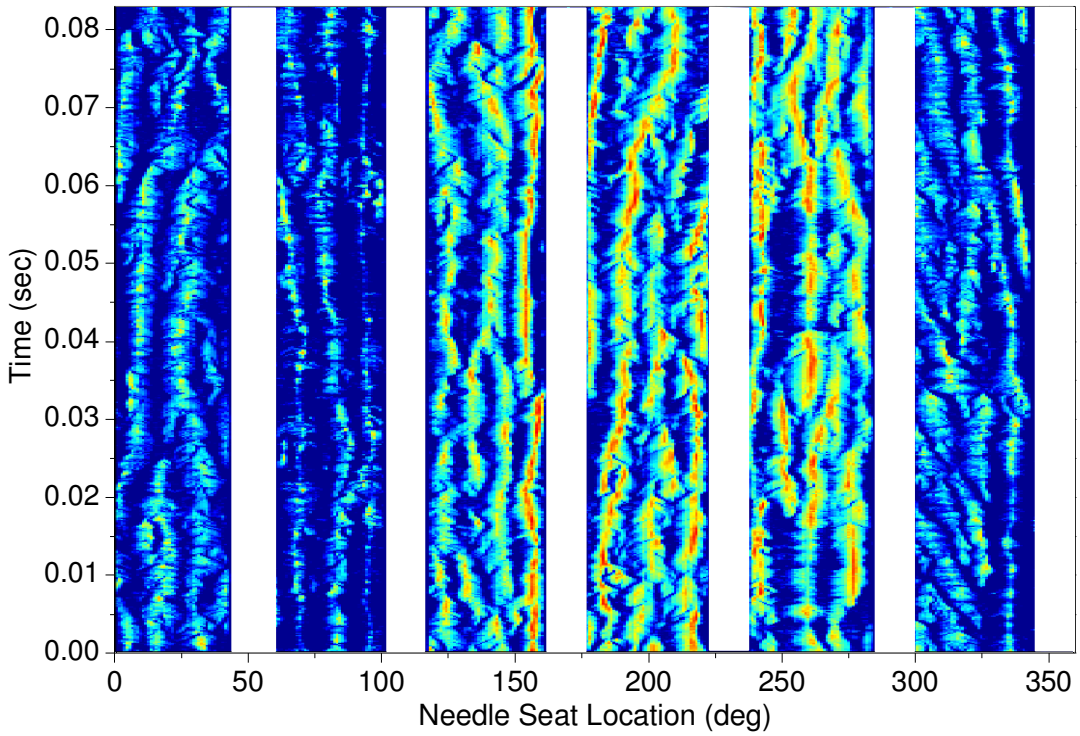

Figure 7-25: Needle seat cavitation intensity frequency [Eq. Needle Lift=20μ CN=15, Re=23,300]

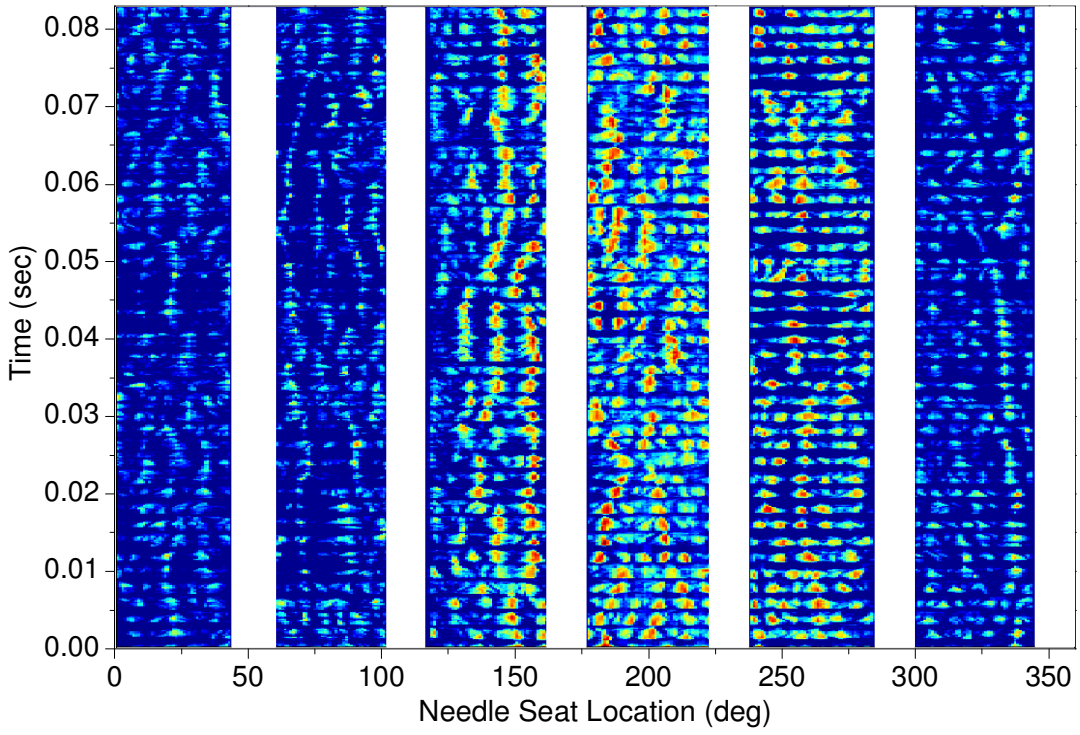

Figure 7-26: Needle seat cavitation intensity frequency [Eq. Needle Lift=20μ, CN=3, Re= 23,300]

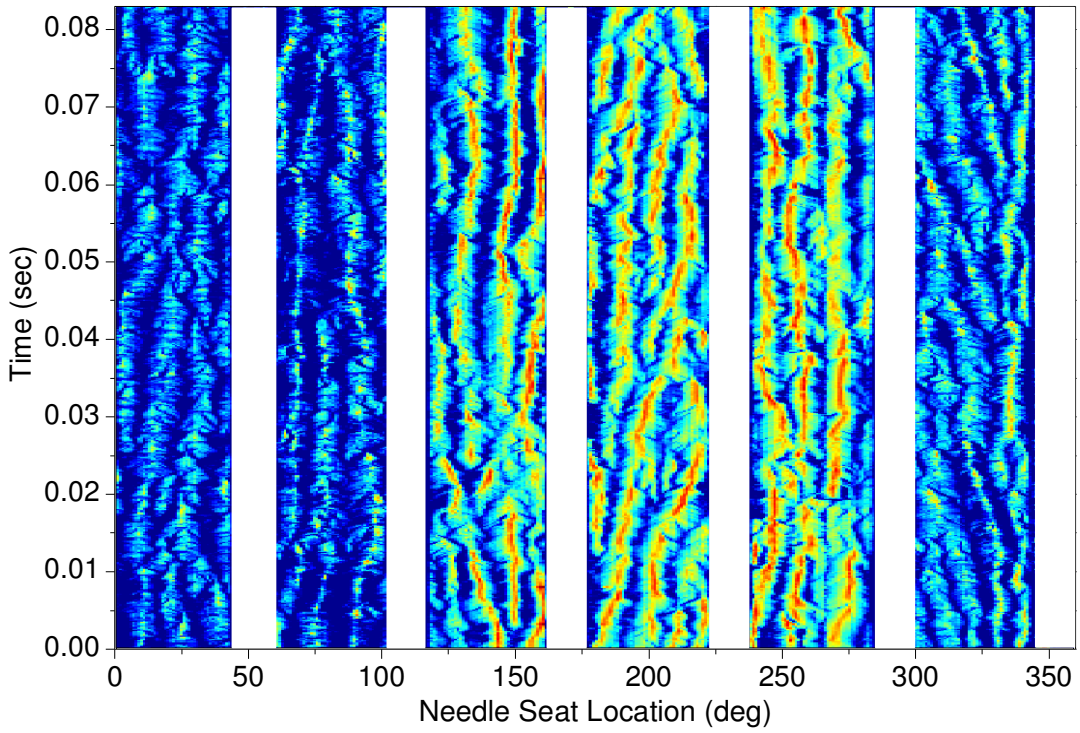

Figure 7-27: Needle seat cavitation intensity frequency [Eq. Needle Lift=20µ, CN=19, Re=26,900]

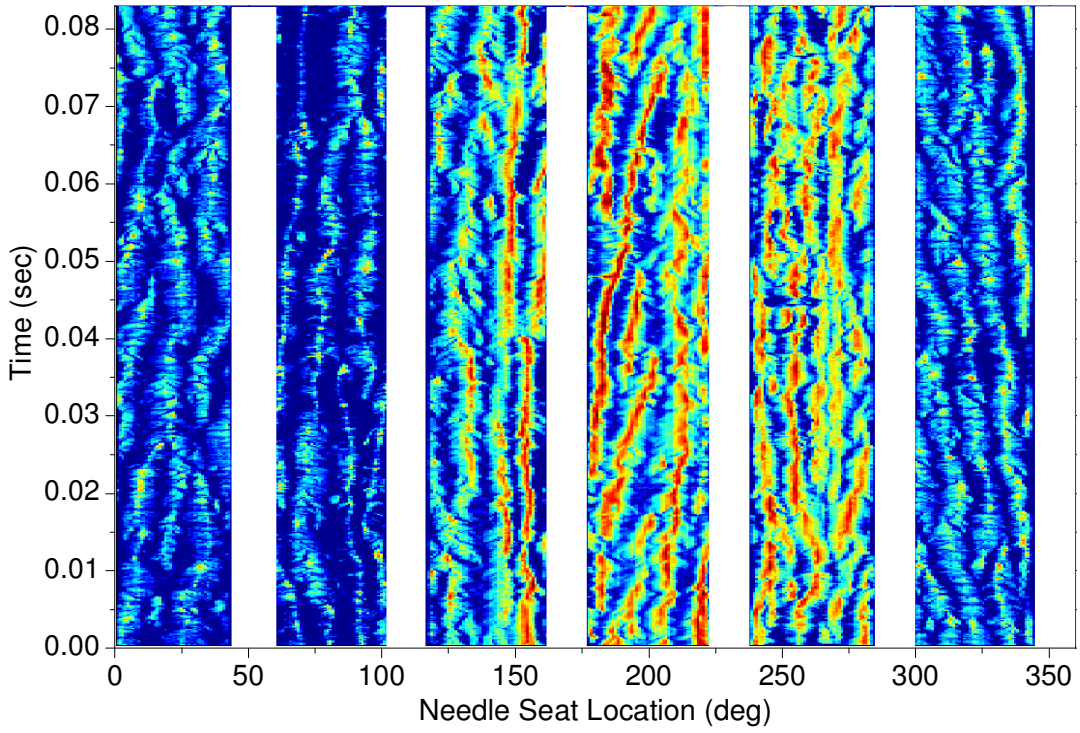

Figure 7-28: Needle seat cavitation intensity frequency [Eq. Needle Lift=20µ, CN=10, Re= 26,900]

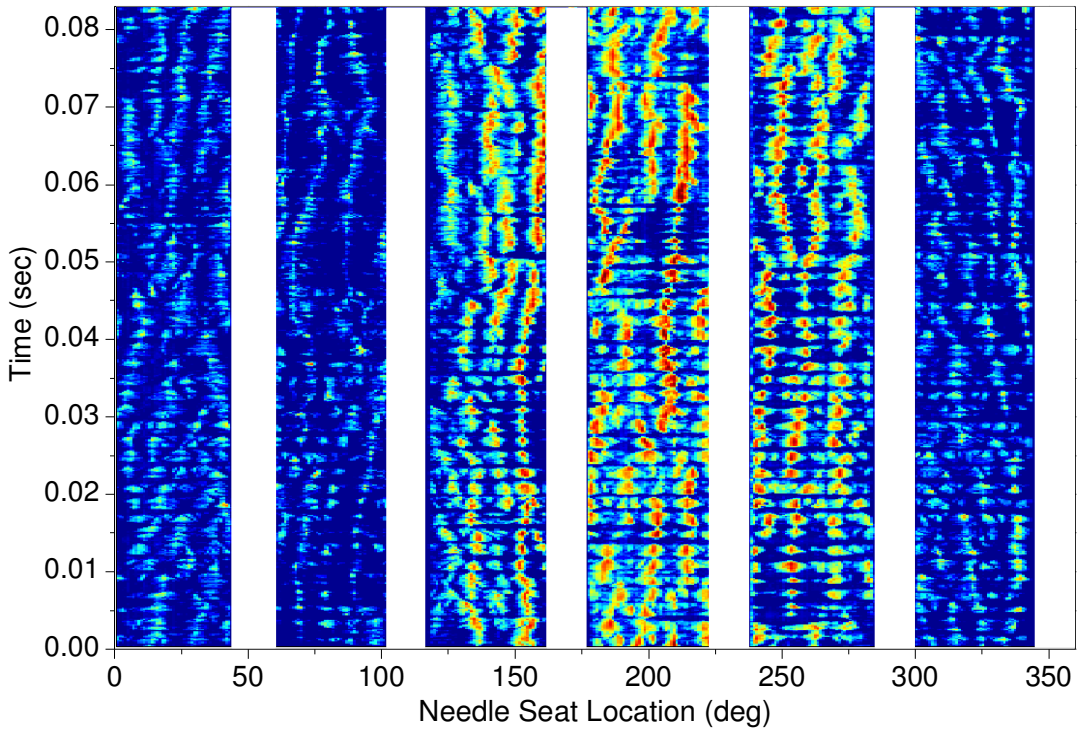

Figure 7-29: Needle seat cavitation intensity frequency [Eq. Needle Lift=20µ, CN=4, Re= 26,900]

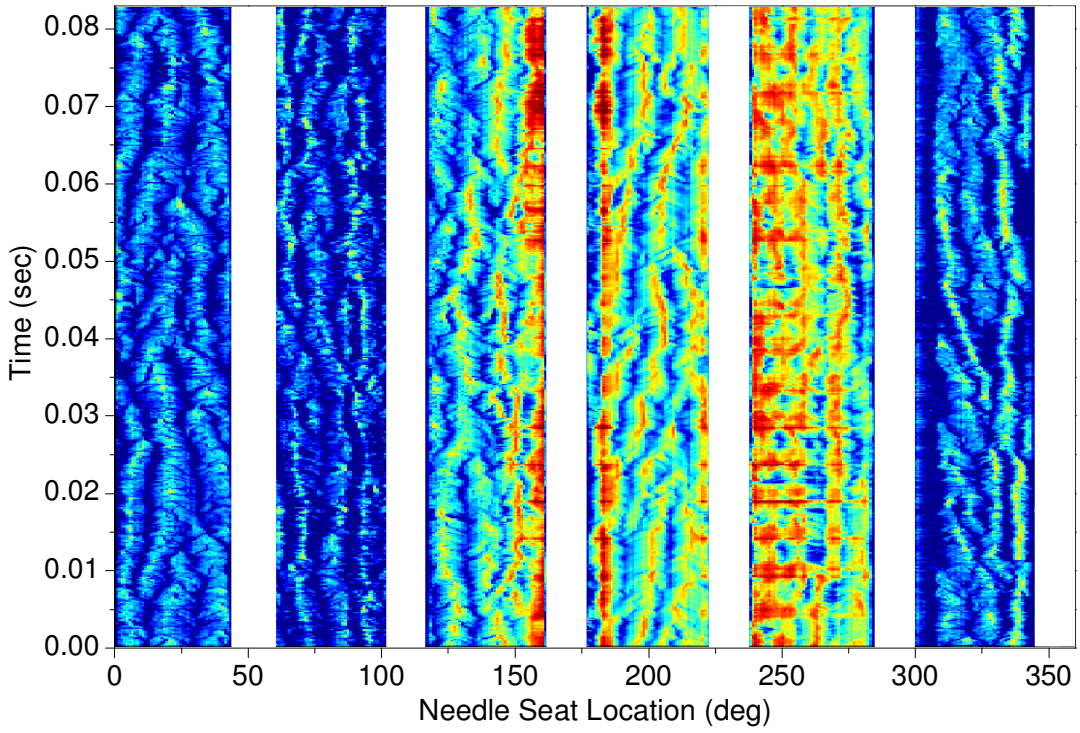

Figure 7-30: Needle seat cavitation intensity frequency [Eq. Needle Lift=20µ, CN=27, Re= 33,200]

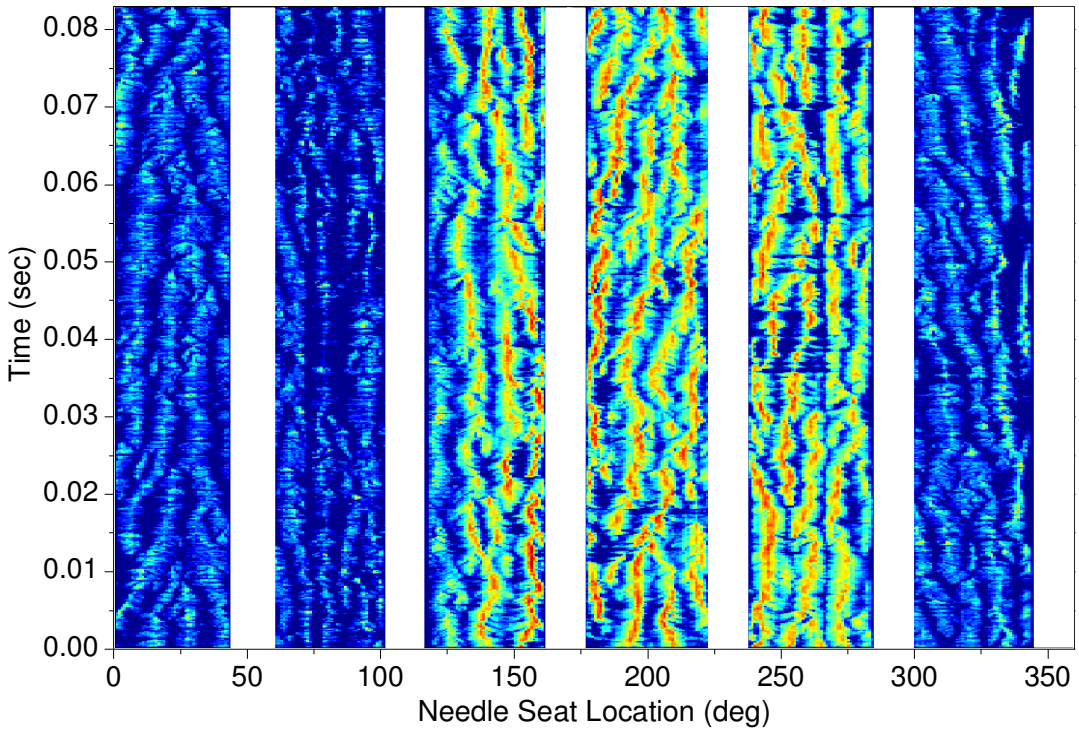

Figure 7-31: Needle seat cavitation intensity frequency [Eq. Needle Lift=20µ, CN=6, Re= 33,200]

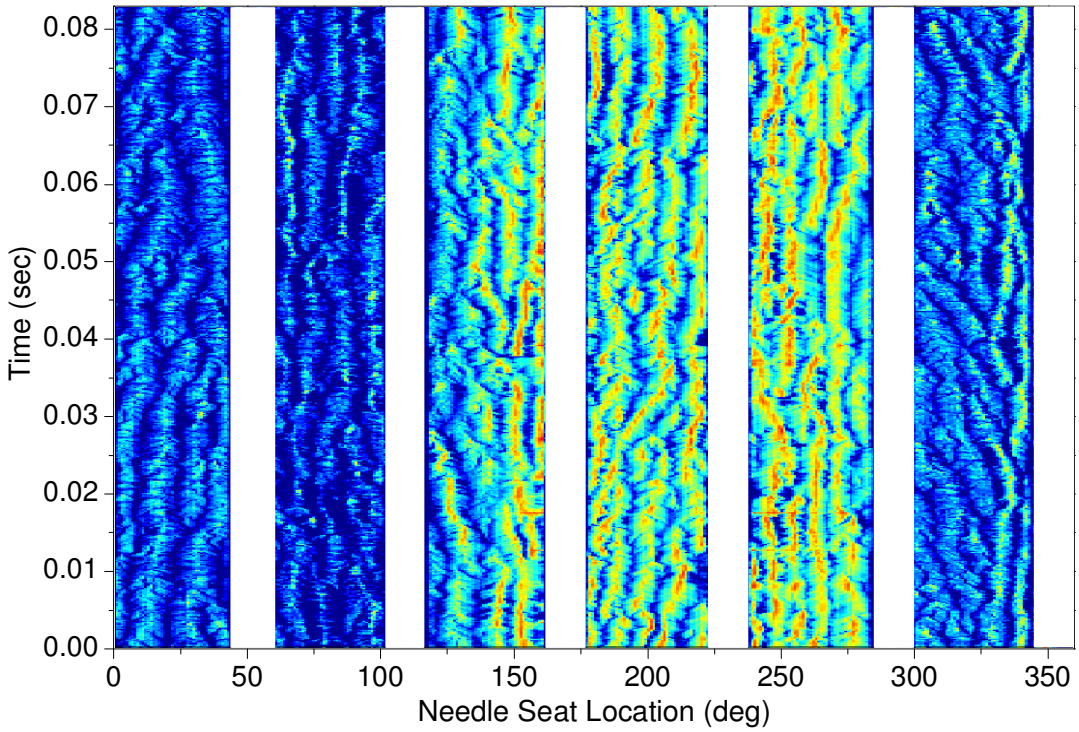

Figure 7-32: Needle seat cavitation intensity frequency [Eq. Needle Lift=20µ, CN=52, Re= 38,200]

By looking at Figure 7-25 through Figure 7-32, it can be seen that some wavy lines have been formed. These lines that, depending on the needle seat cavitation intensity, extend through a wide range of contour colour bands are separated by dark blue regions. As it can be understood, each one of these lines represents a needle seat cavitation site (spike). The centre of that spike like structure is at the location where the contour within the line is at its maximum value. This is due to the fact that because of the its shape, at the point of initiation the circular section is occupied the most from this vapour site. The wider the line, it denotes a wider cavitation site. The higher the contour value, it denotes a longer extent of these structures to the axial direction. The continuity of these lines in the y-axis indicates if the intensity of these cavitation structures vary with time. As it can be seen at low CN values the cavitation region lines are interrupted by dark blue lines almost breaking it completely in some regions. The physical meaning of this graphic feature is that In the particular case studied cavitation was not stable and it was fluctuating in intensity with time. Depending on the difference between the higher value of the continuous line contour and the contour value of the 'interruption' line, it can be concluded how heavily cavitation intensity varies. As it can be seen at high CN the line might go from bright red up to yellowish orange. This is an indication that these spike like structures were lightly varying with time. On the other side, at low CN, the line can go from bright red to dark blue. This means that at some point cavitation was almost extinct. It worth mentioning that even in the cases where cavitation fluctuates heavily, the transition from a high to a lower intensity occurs smoothly. This can be realized particularly to the low CN graphs where there is no transition from bright red to dark blue without having the intermediate colours of the contour in between. The larger this transition region the larger the fluctuation period. It can be said that these spikes vary in size by following the same movement as the medusa uses to propel at sea. Finally the fact that these lines are not straight, shows that these spikes were changing location with time. As it can be seen each spike moves in a different pattern. Some of the spikes are moving to one direction with a slight wavy motion, while other only undergo a wavy fluctuation around the same location. Finally even when a spike starts to move towards a direction once the gap with the other adjacent site increases and forms a cavitation free region, a new site appears and fills the gap. It has to be mentioned that such an analysis of such structure has not been presented before in literature and the closer resemblance to this cavitation structure has been seen in slit type injectors used in gasoline injectors.

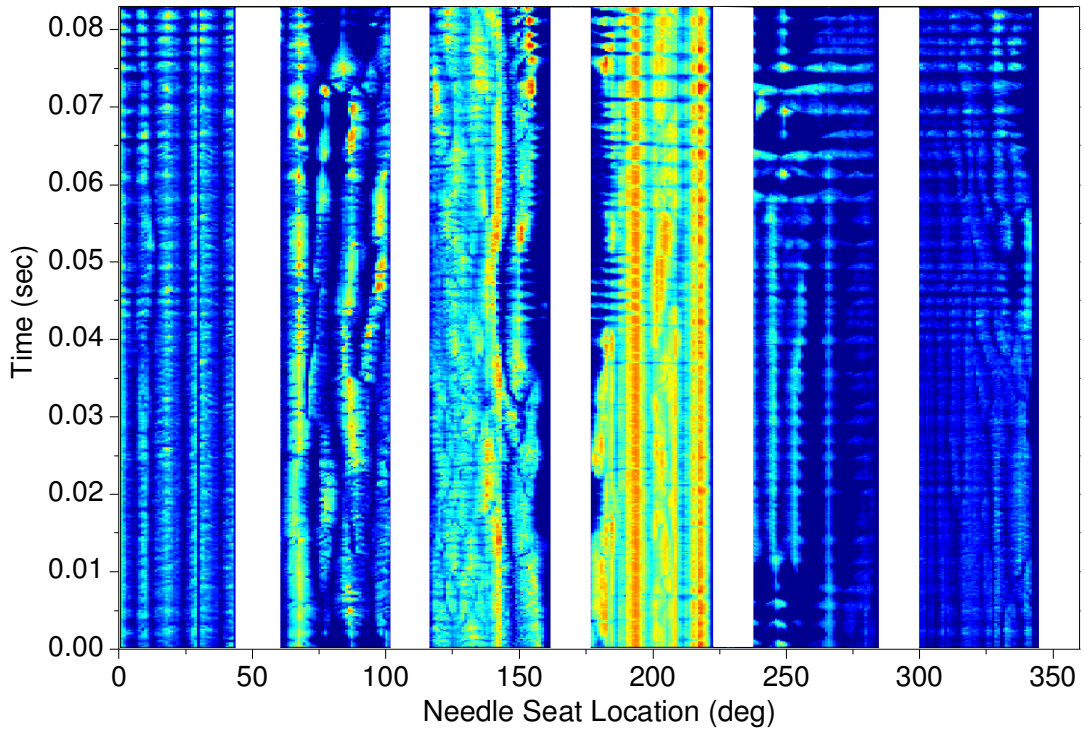

Figure 7-33: Needle seat cavitation intensity frequency [Eq. Needle Lift=10µ CN =15, Re=23,300]

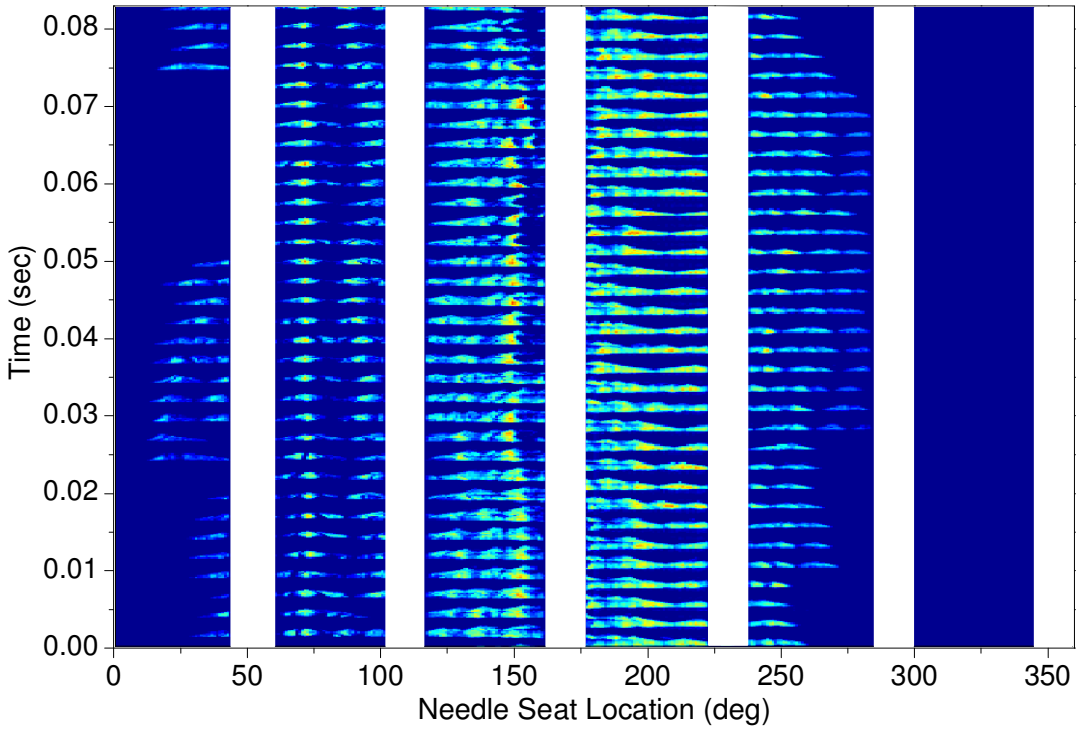

Figure 7-34: Needle seat cavitation intensity frequency [Eq. Needle Lift=10µ, CN=3, Re= 8,500]

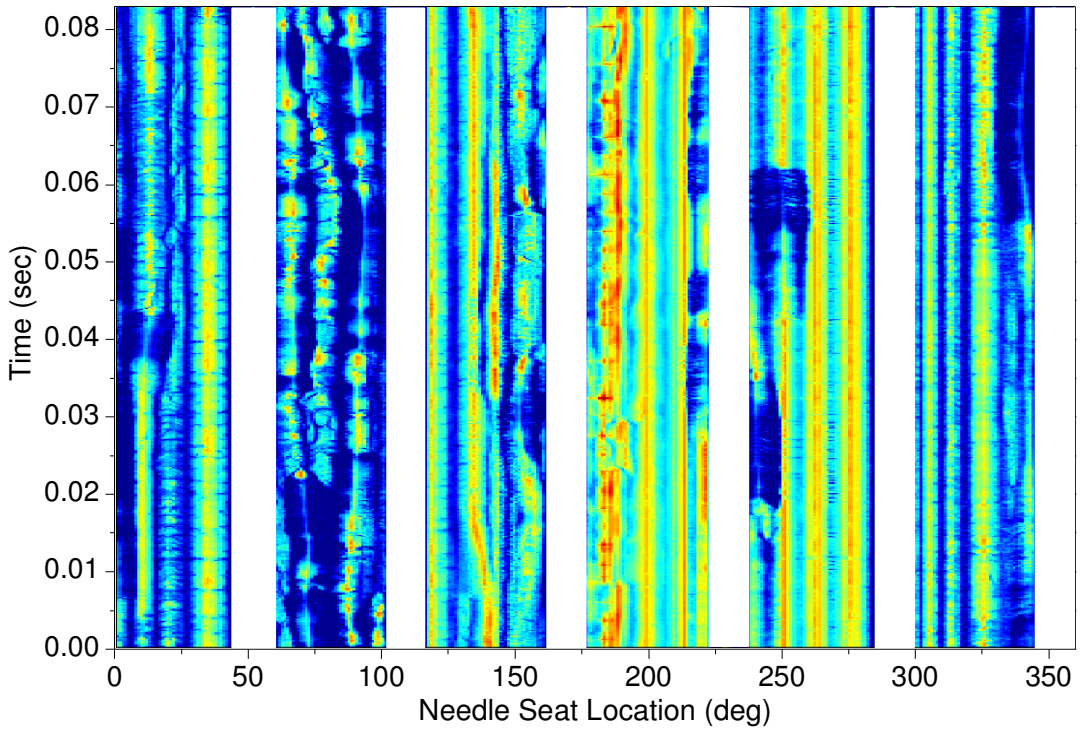

Figure 7-35: Needle seat cavitation intensity frequency [Eq. Needle Lift=10µ, CN=19, Re= 11,300]

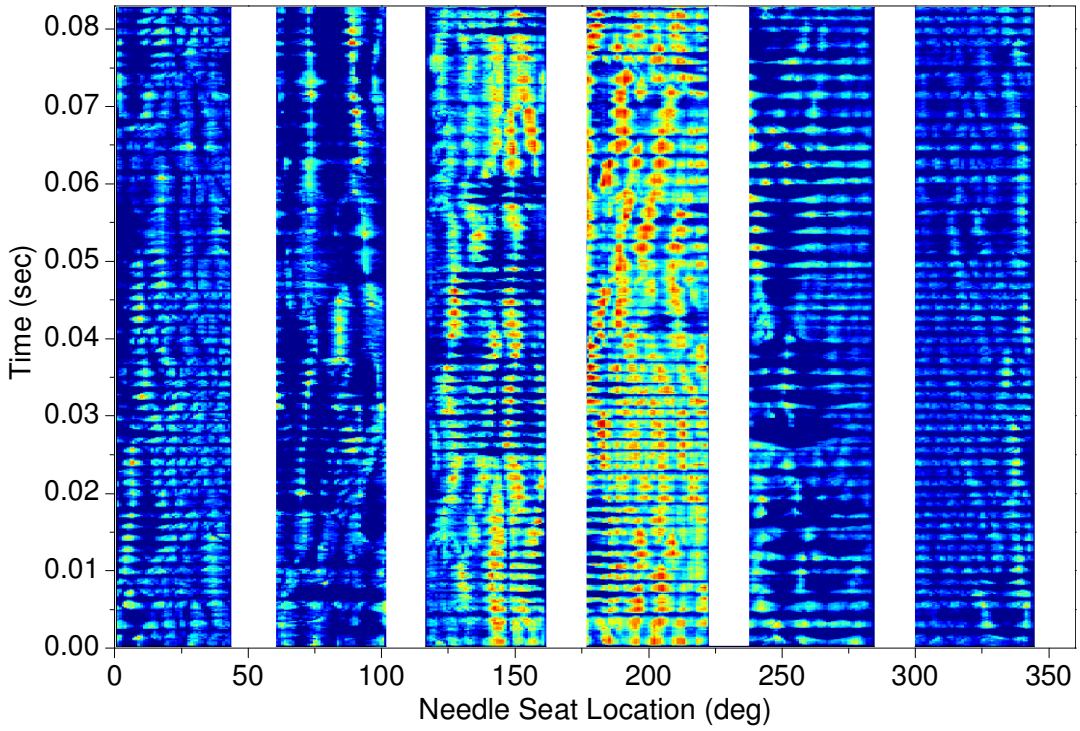

Figure 7-36: Needle seat cavitation intensity frequency [Eq. Needle Lift=10µ CN=4, Re= 11,300]

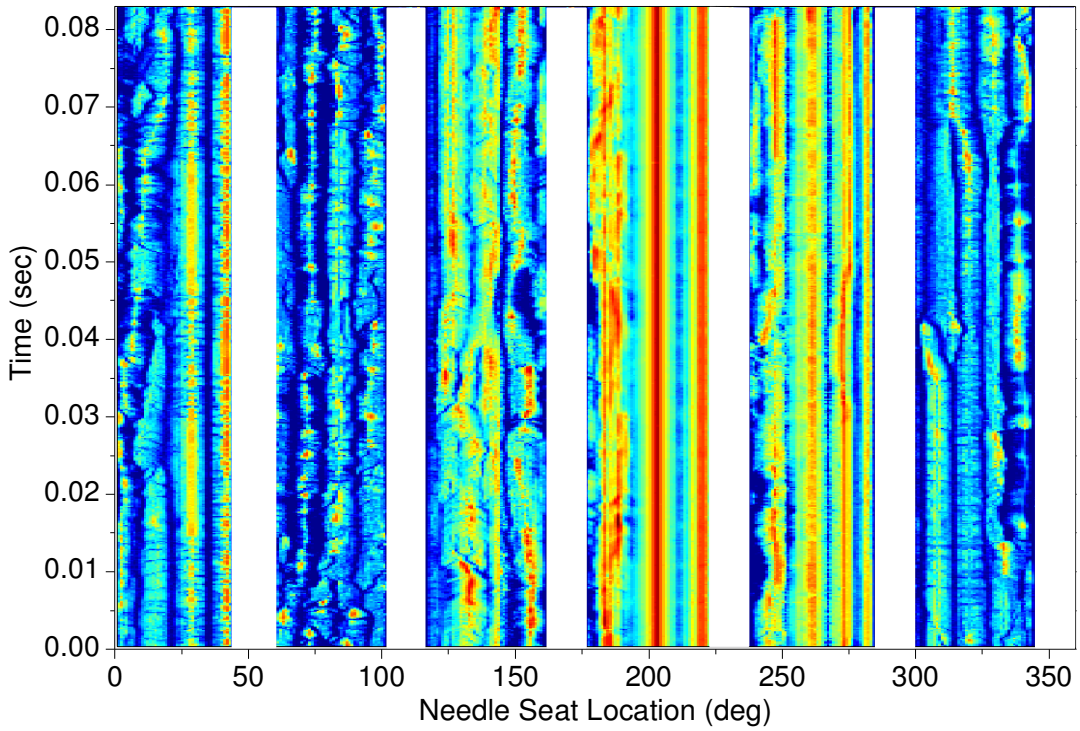

Figure 7-37: Needle seat cavitation intensity frequency [Eq. Needle Lift=10µ, CN= 27, Re= 17,700]

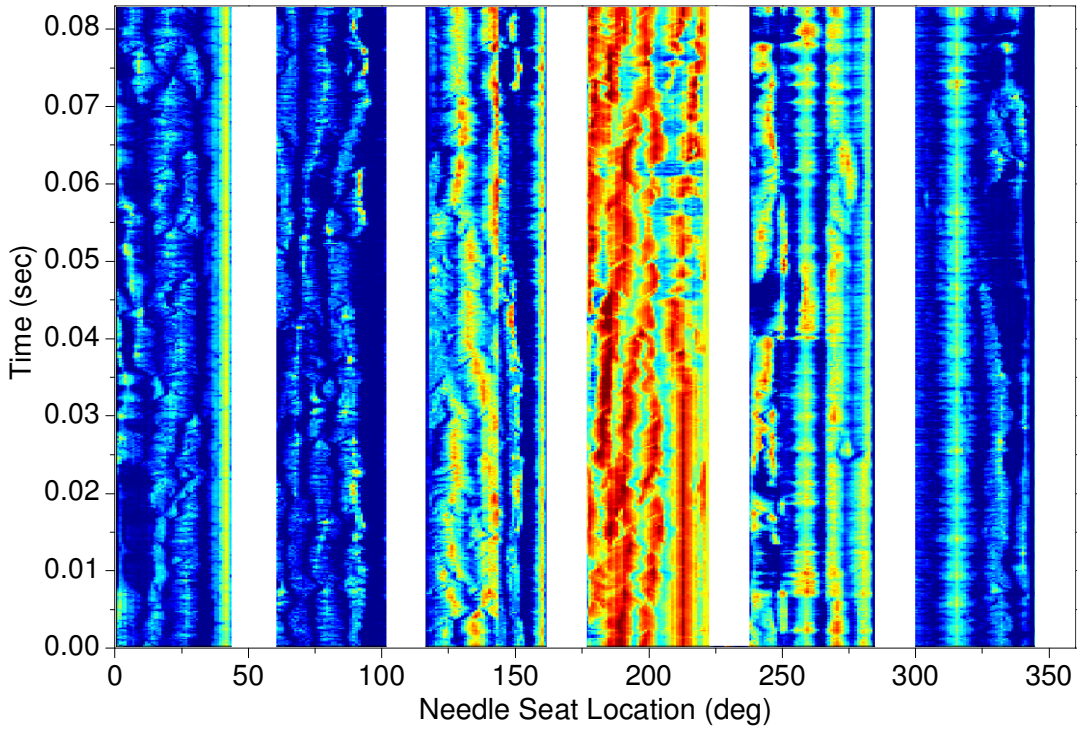

Figure 7-38: Needle seat cavitation intensity frequency [Eq. Needle Lift=10µ, CN=6, Re= 17,700

Figure 7-33 through Figure 7-38 show similar graphs for the 10 μm equivalent needle lift cases. The two main characteristics that are different to those of the 20 μm case, are the larger fluctuation of the cavitation intensity and the fact that the cavitation sites are almost anchored to the same location. It is particularly interesting to observe at the low CN case, Figure 7-34, that it seems like all the cavitation sites follow a wavy motion as a whole. This denotes a vibration to the needle which was mentioned that had been observed however it wouldn't have been possible to justify it without the aid of this type of analysis.

Volumetric Flow Rate (l/s)	P_{in} (bar)	P_{back} (bar)	Re	CN
0.19	4.0	0.3	13,500	15
0.19	4.0	1.0	13,500	3
0.28	5.0	0.3	19,800	19
0.28	5.0	1.0	19,800	4
0.38	7.0	0.3	26,900	27
0.38	7.0	1.0	26,900	6

Table 7-5: Range of operating conditions investigated for the transparent sac-type nozzle with needle design IV at 10 μm equivalent needle lift.

Volumetric Flow Rate (l/s)	P_{in} (bar)	P_{back} (bar)	Re	CN
0.32	4.0	0.3	22,600	15
0.32	4.0	1.0	22,600	3
0.40	5.0	0.3	28,300	19
0.40	5.0	0.5	28,300	10
0.40	5.0	1.0	28,300	4
0.46	7.0	0.3	32,500	27
0.46	7.0	1.0	32,500	6
0.50	8.0	0.2	35,300	52

Table 7-6: Range of operating conditions investigated for the transparent sac-type nozzle with needle design IV at 20 μm equivalent needle lift.

Having found that needle seat cavitation does cause erosion to the injection components it was suggested to study a series of different needle designs. The conditions examined for needle design IV can be found in Table 7-5 and Table 7-6 for 10 and 20 μm equivalent needle lift respectively. Following figures will show the same set of analysis as was done for the original needle design before.

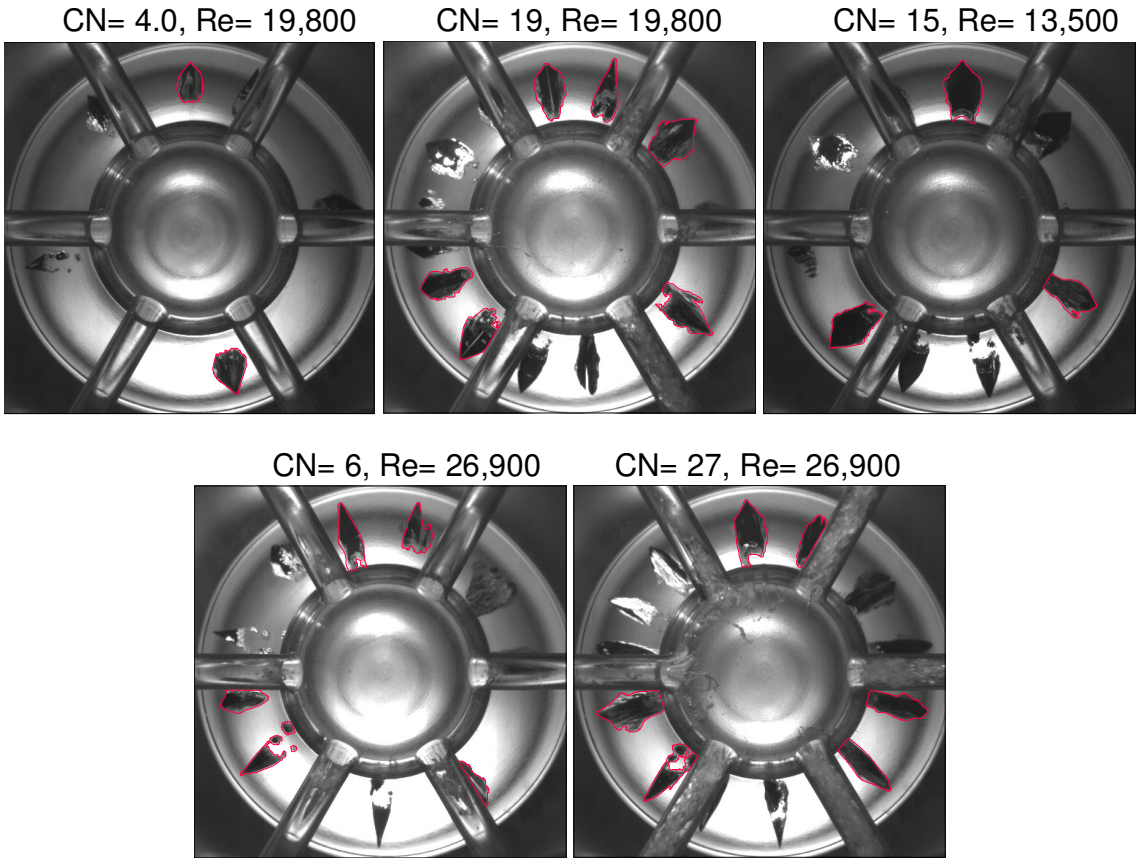

Figure 7-39: Typical bottom view images of the Sac-Type nozzle with needle design IV at 10 μm equivalent needle lift.

Even by looking at the first series of typical results from the modified needle design for 10 μm eq. needle lift, Figure 7-39, it can be seen that although needle seat cavitation is still present, its shape and intensity is totally different compared to the original design. It has to be mentioned that for this particular needle design the geometry of the nozzle body has also changed in order to bring the needle seat closer to the injection holes. as a result the cavitation sites are much more elongated than before and as the side view shows the end side of these structures are very close t the injection holes, which leaves limited time to the vapour to mix with the fluid present in the sac volume. Instead the detached bubble are directed by the flow and exit throw them also forming some cavitation strings that originate mainly from the injection holes.

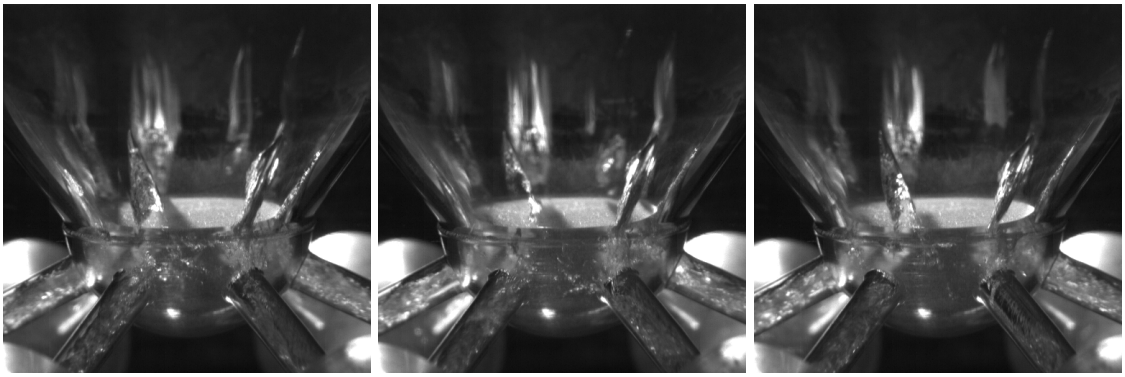

Figure 7-40: Side view of Sac-type nozzle with needle design IV at 10µm equivalent needle lift for CN =27, Re=26900.

Apart from the increased length of these structures, the other distinct difference is the space between the cavitation sites. Contrary to the original design the new arrangement leaves a space of almost two times the width of these cavitation spikes in between. It was also recorder that cavitation has a much higher fluctuation in its intensity even at high CN values. However these are to be discussed after presenting the processed data.

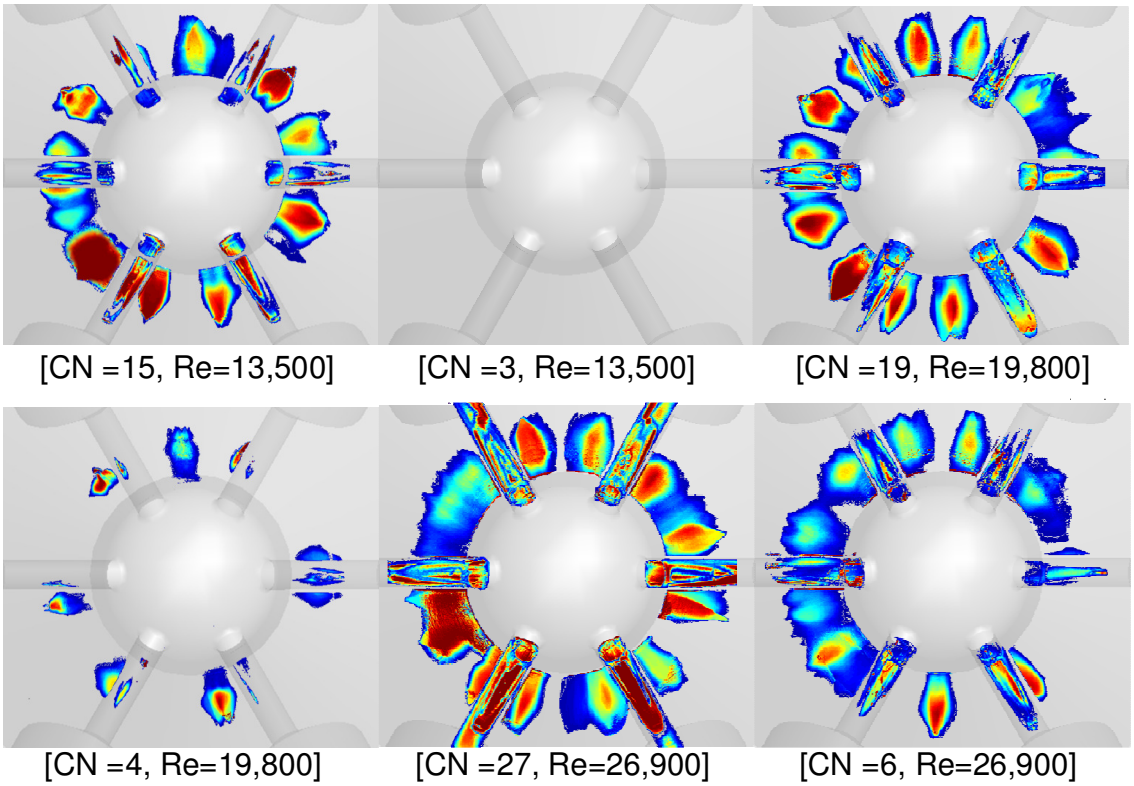

Figure 7-41: time averaged images for needle seat cavitation in sac-type nozzle with needle tip design (IV) for different flow conditions.[10 µm Needle Lift]

The concept behind time and space averaging has been explained in detail before. Figure 7-41 presents the mean images for the cases shown in Table 7-5. it becomes evident that the amount of vapour present at the needle seat is much more than that in the original design. Moreover the higher contour values at the centre of these structures suggests that the location of the cavitation sites does not change significantly with time. Instead, as also indicated by the extended colour bands around the core, the intensity of cavitation varies in an almost symmetrical way keeping the original shape of the spike. The effect of CN and Reynolds number is the same as to the original needle. An increase to either of these two characteristic flow numbers will result to an increase in cavitation intensity. Finally, as also seen for the original design, there is a slight eccentricity of the needle which results in, a moderate asymmetry of the vapour presence probability. Regarding the geometrically induced cavitation, it can be said that it starts at lower CN values than with the original needle which can be also attributed to the fact that large amounts of vapour bubbles are entering thought the injection holes.

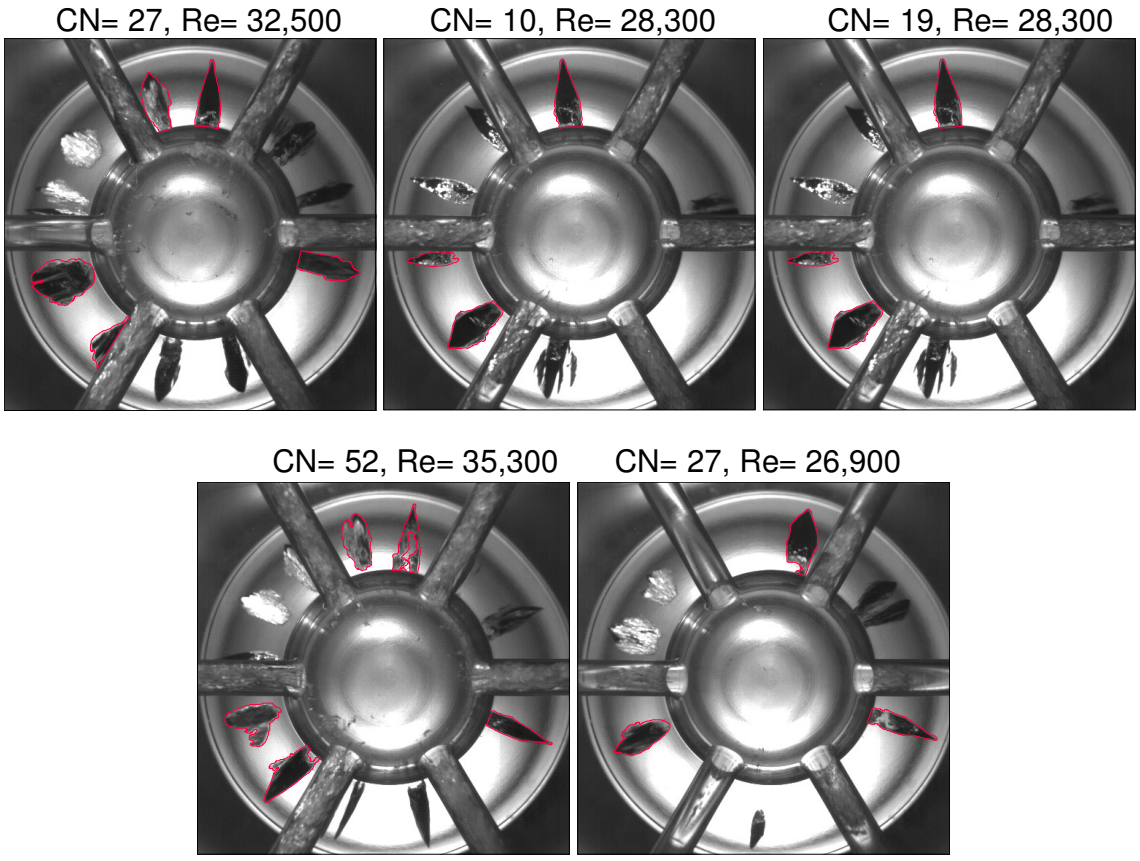

Figure 7-42: Typical bottom view images of the Sac-Type nozzle with needle design IV at 20 μm equivalent needle lift.

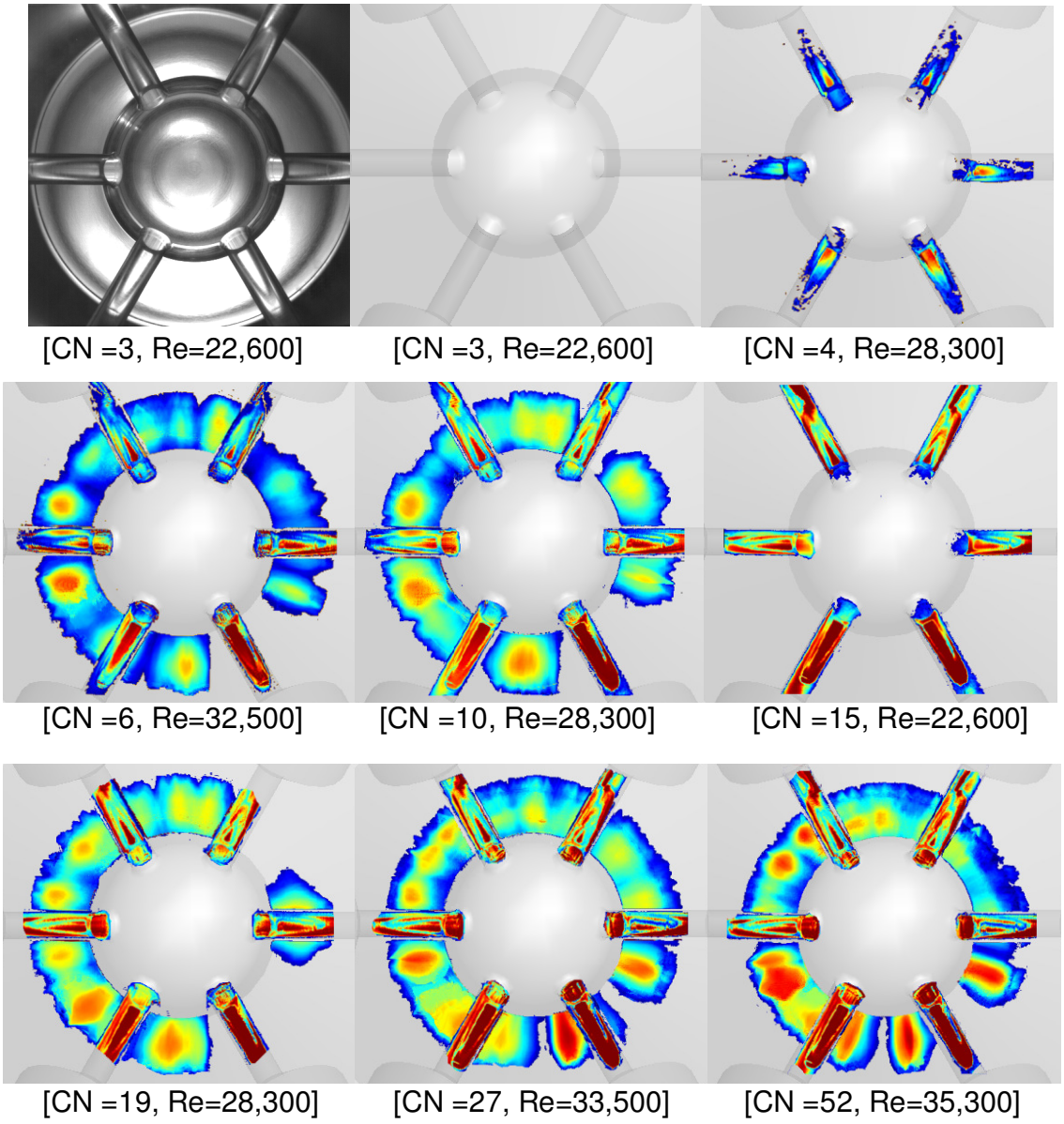

Figure 7-43: time averaged images for needle seat cavitation in sac-type nozzle with needle tip design (IV) for different flow conditions.[20 µm Needle Lift]

Comparing the results obtained for the higher lift for the new needle design, it can be concluded that increasing the needle lift will result into a reduced probability of having vapour produced due to needle seat cavitation. Unfortunately there are no available images of the real nozzle after operation in order to se if it also suffers from erosion problems.

Following figures, Figure 7-44 through Figure 7-53, are processed results showing the transient evolution of needle seat cavitation as was done for the original needle design. As it can be seen the first obvious difference is the fact that the lines indicating the location of

a cavitation spike are clearly defined without interfering with each other. The dark blue region that separates them in between is indication of needle seat cavitation free regions. The other feature to be mentioned is the indication of fluctuations in both the width of these spikes as well as in their length. It has to be pointed that such fluctuations were also existing in the original needle design however due to the small, or even no gap, between them it was not clearly seen. The increase and contraction in width can be realized by the diamond shape of the lines. The increase in length is realized by the increased contour levels. Similarly to what it was shown for the original needle design, at low CN values these fluctuations are much more evident than in higher CN. Another main difference is that the lines seem to follow an almost straight direction. This means that the cavitation spikes are anchored to their position. Also in some cases it can be seen that once the width of the line increases substantially it then brakes into two smaller ones. This means that once the cavitation site becomes too large it breaks into two smaller ones. In some cases it can also be seen that the lines are interrupted for a period of time and either they reaper or they simply fade out. This means that some of the cavitation sites stop producing vapour for a period of time until the flow conditions are suitable to generate them again. Finally once the needle lift increases to 20 μm equivalent needle lift, the lines seem to move more freely. This indicates that the spikes are now able to move along the radial direction of the needle seat, although the movement is still limited. Moreover it can be also seen that at higher lift and even at high CN values the fluctuations in the width and length are much more evident than at the lower lift condition.

Closing the discussion of the processed results it can be concluded that with the automated image processing it became possible to instantly show the entire evolution of the needle seat cavitation for the entire duration of the recording period by simply looking at a single figure.

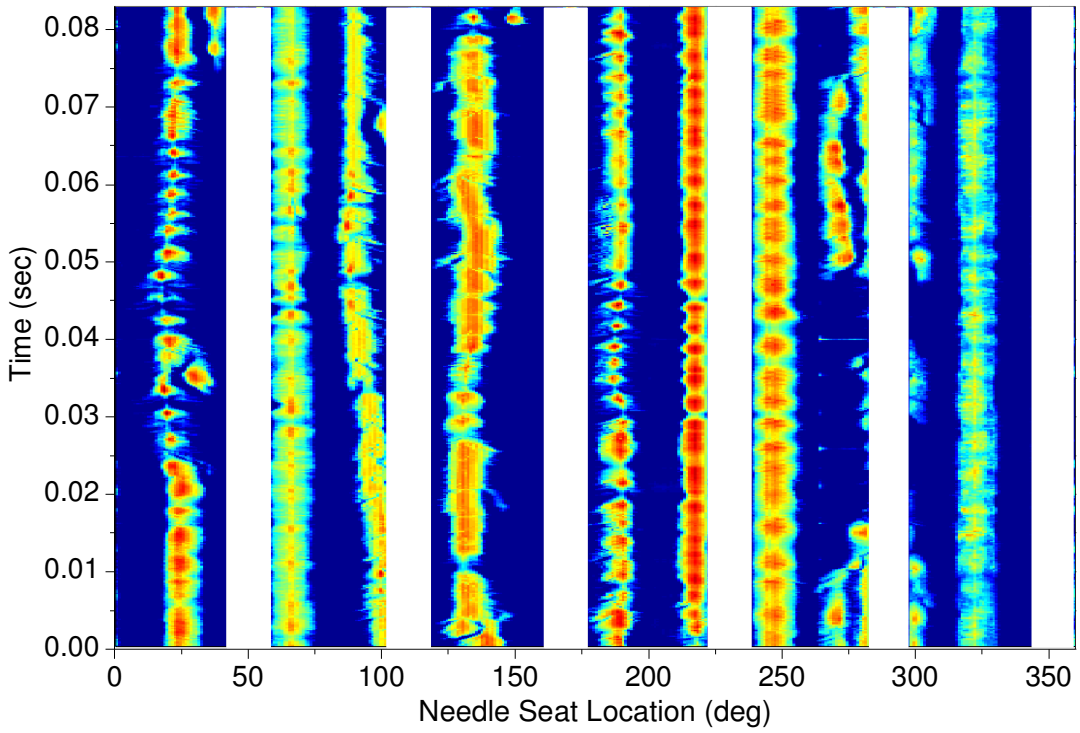

Figure 7-44: Needle seat cavitation intensity frequency [Eq. Needle Lift=10µm, CN= 15, Re= 13,500]

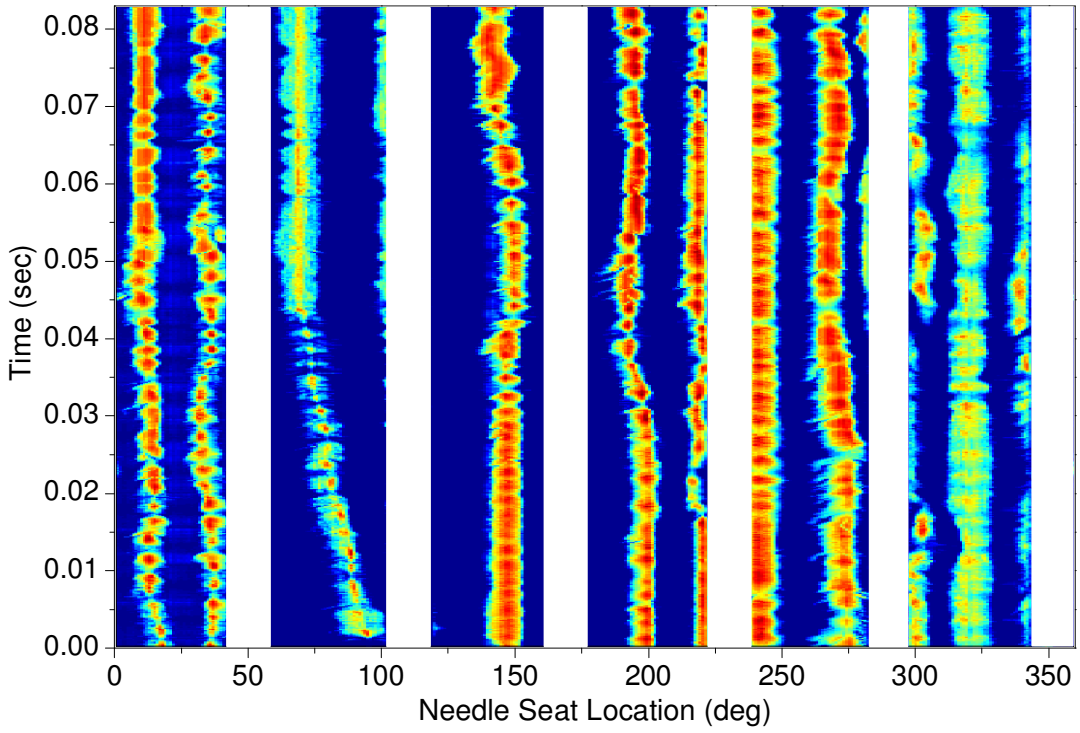

Figure 7-45: Needle seat cavitation intensity frequency [Eq. Needle Lift=10µm, CN= 19, Re= 19,800]

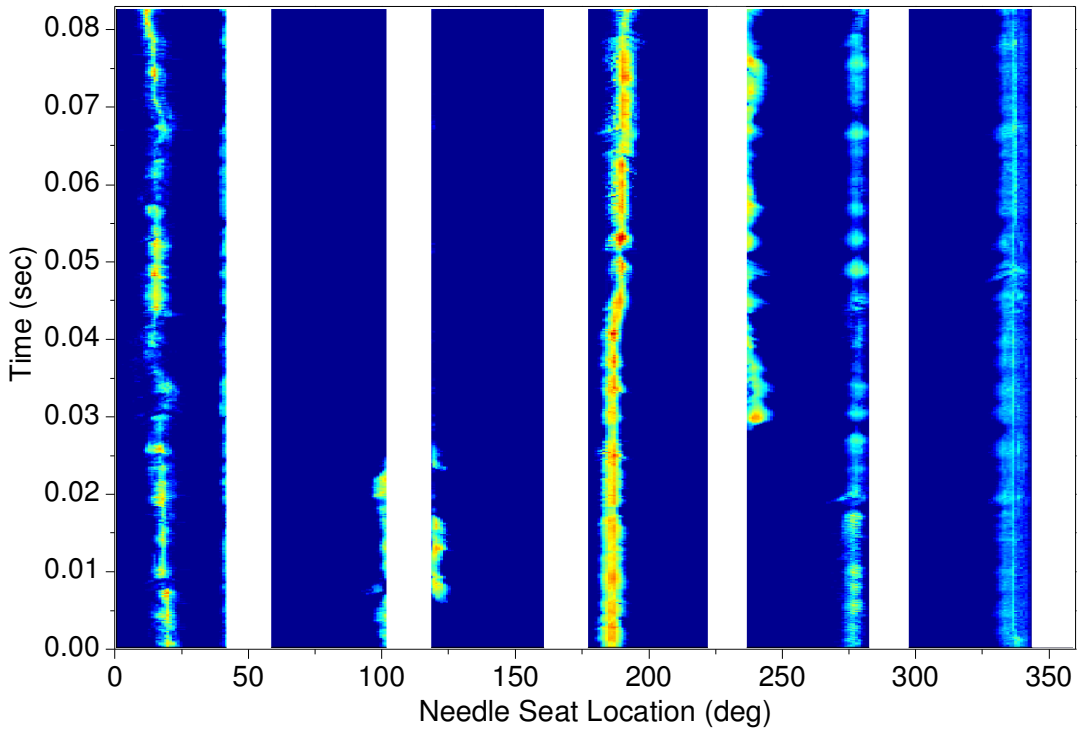

Figure 7-46: Needle seat cavitation intensity frequency [Eq. Needle Lift=10µm, CN= 4.0, Re= 19,800]

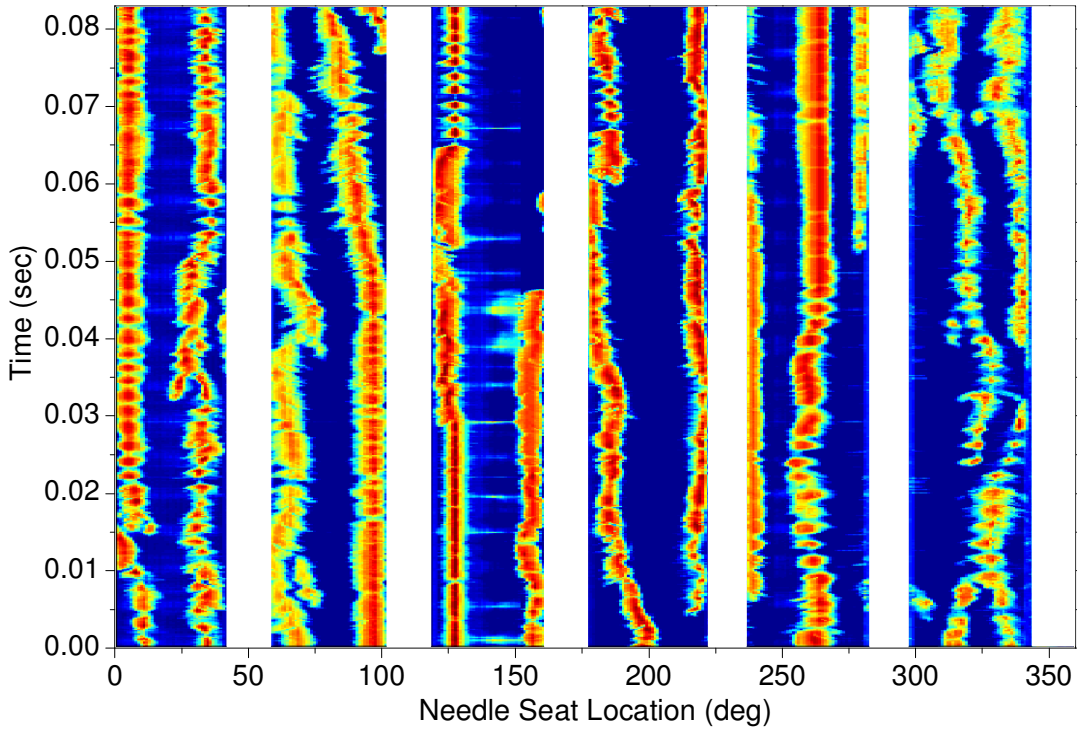

Figure 7-47: Needle seat cavitation intensity frequency [Eq. Needle Lift=10µm, CN= 27, Re= 26,900]

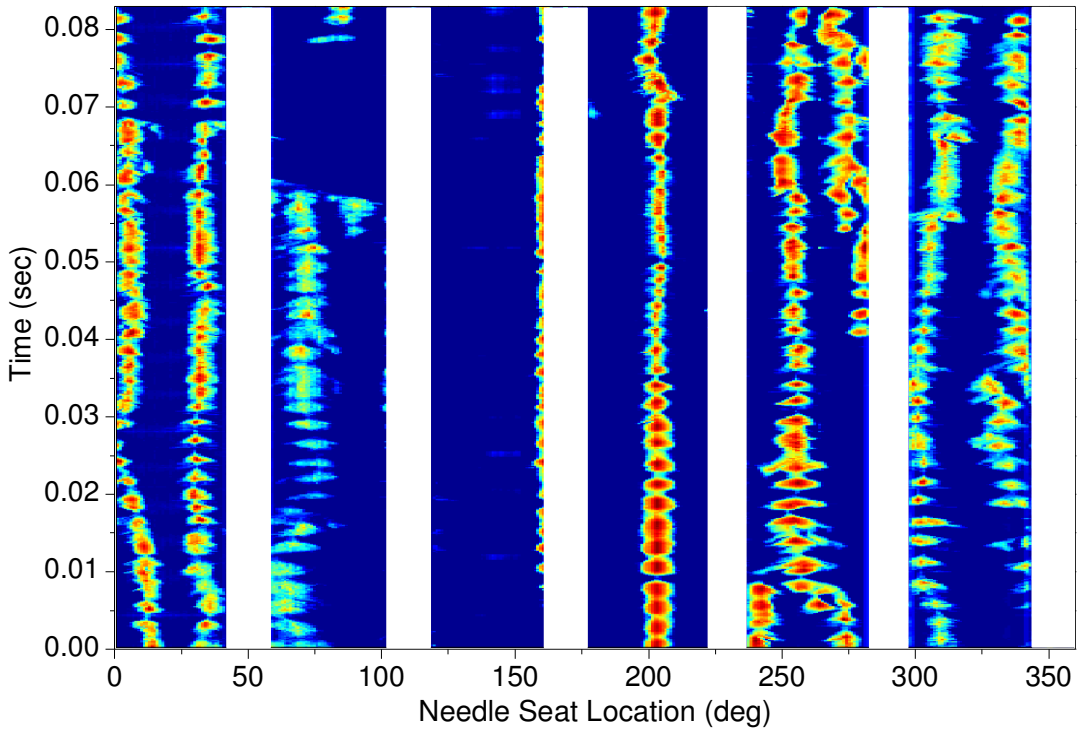

Figure 7-48: Needle seat cavitation intensity frequency [Eq. Needle Lift=10µm, CN= 6, Re= 26,900]

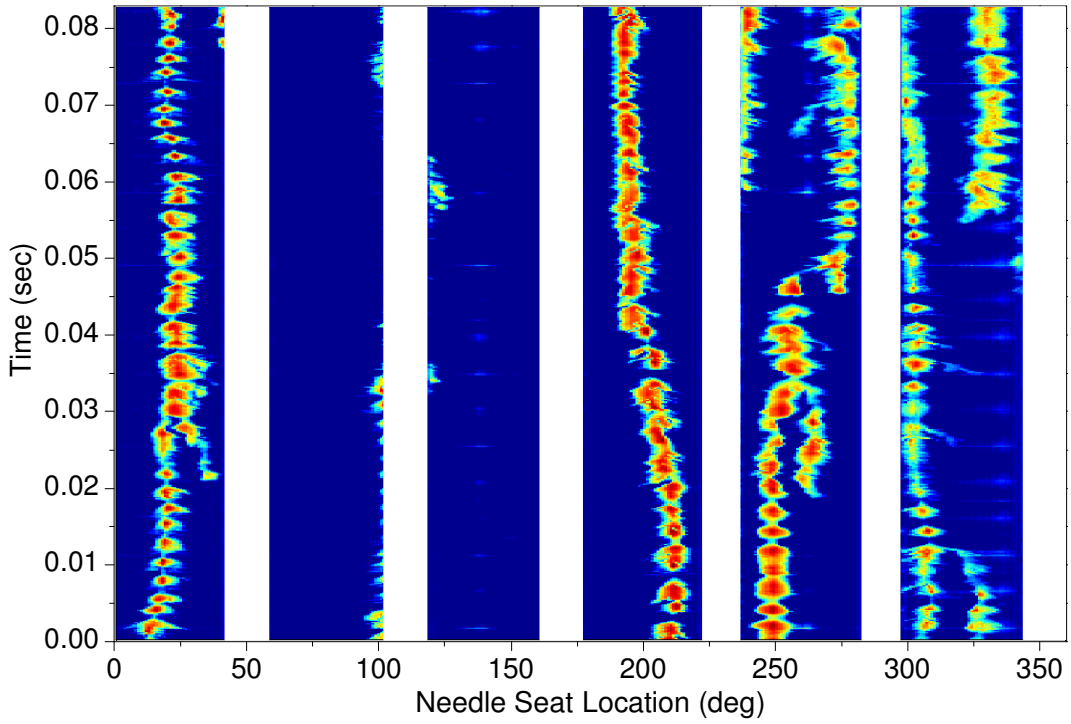

Figure 7-49: Needle seat cavitation intensity frequency [Eq. Needle Lift=20µm, CN= 19,
Re= 28,300]

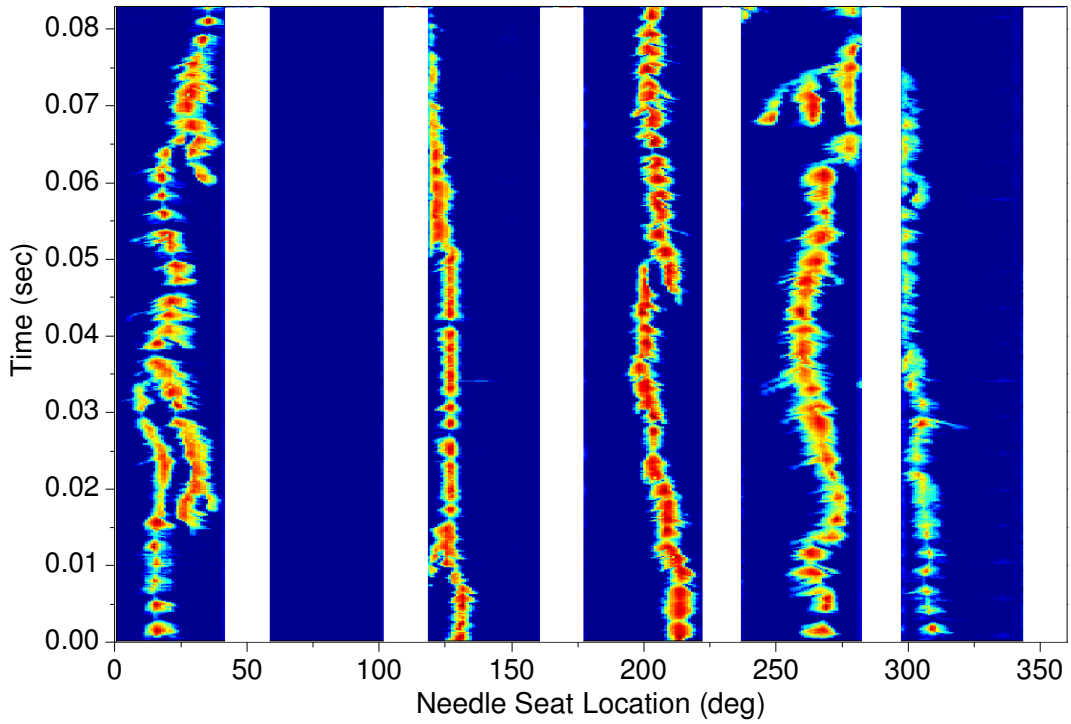

Figure 7-50: Needle seat cavitation intensity frequency [Eq. Needle Lift=20µm, CN= 10, Re= 28,300]

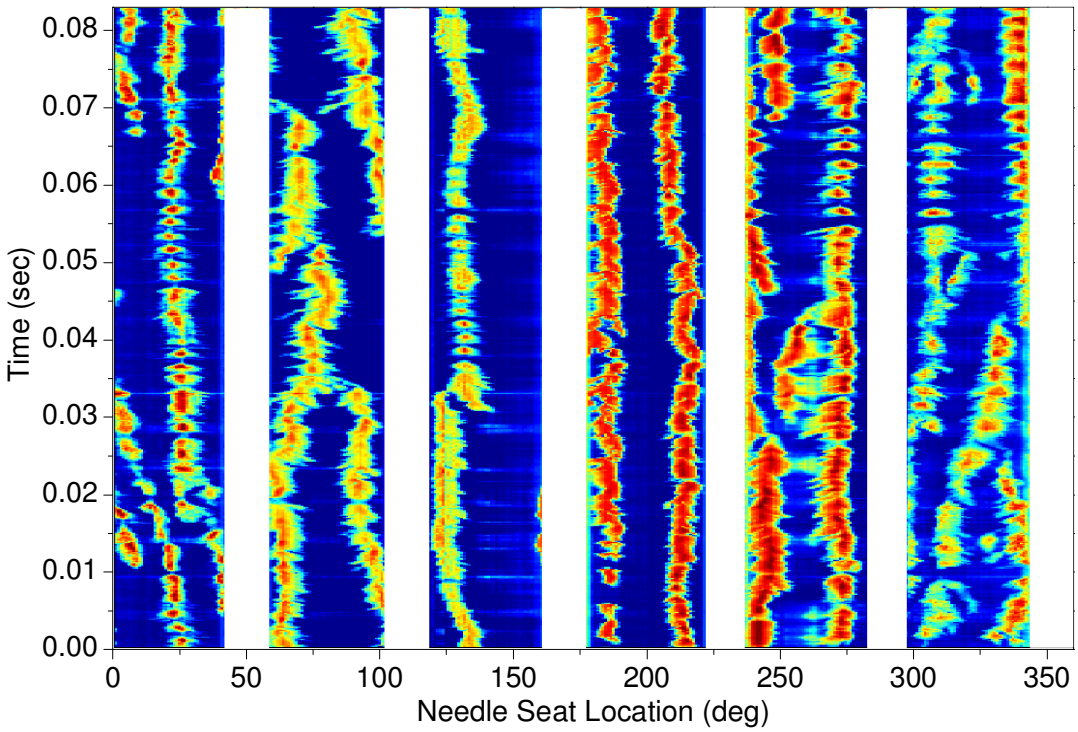

Figure 7-51: Needle seat cavitation intensity frequency [Eq. Needle Lift=20µm, CN= 27, Re= 32,500]

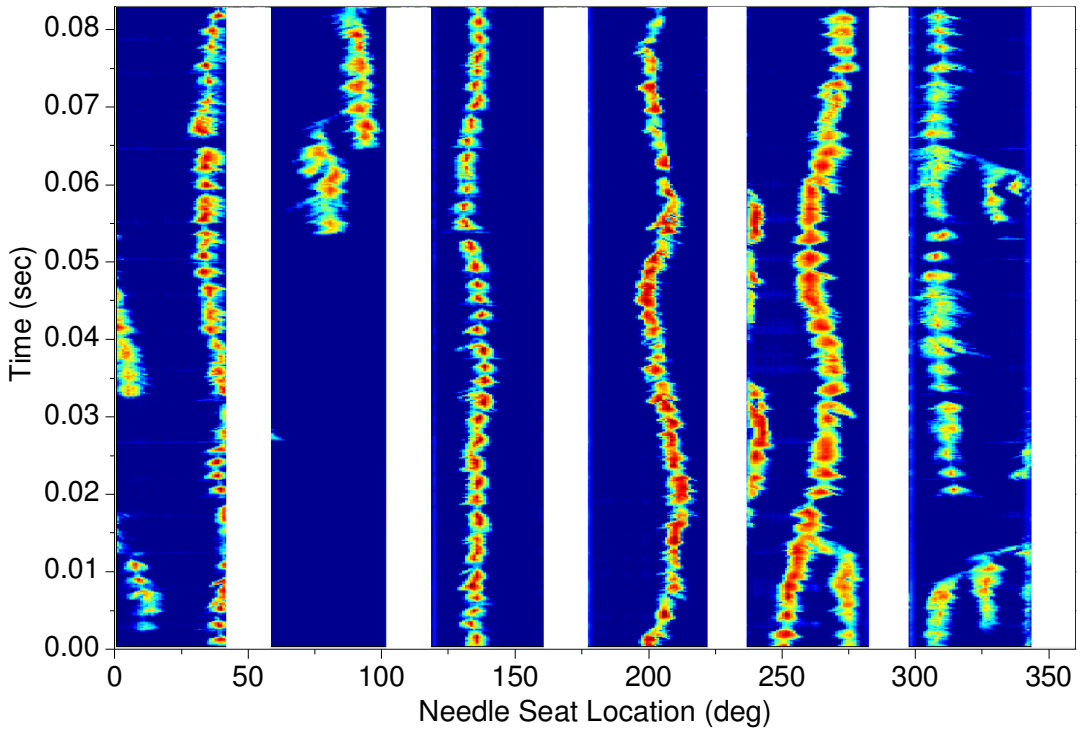

Figure 7-52: Needle seat cavitation intensity frequency [Eq. Needle Lift=20µm, CN= 6, Re= 32,500]

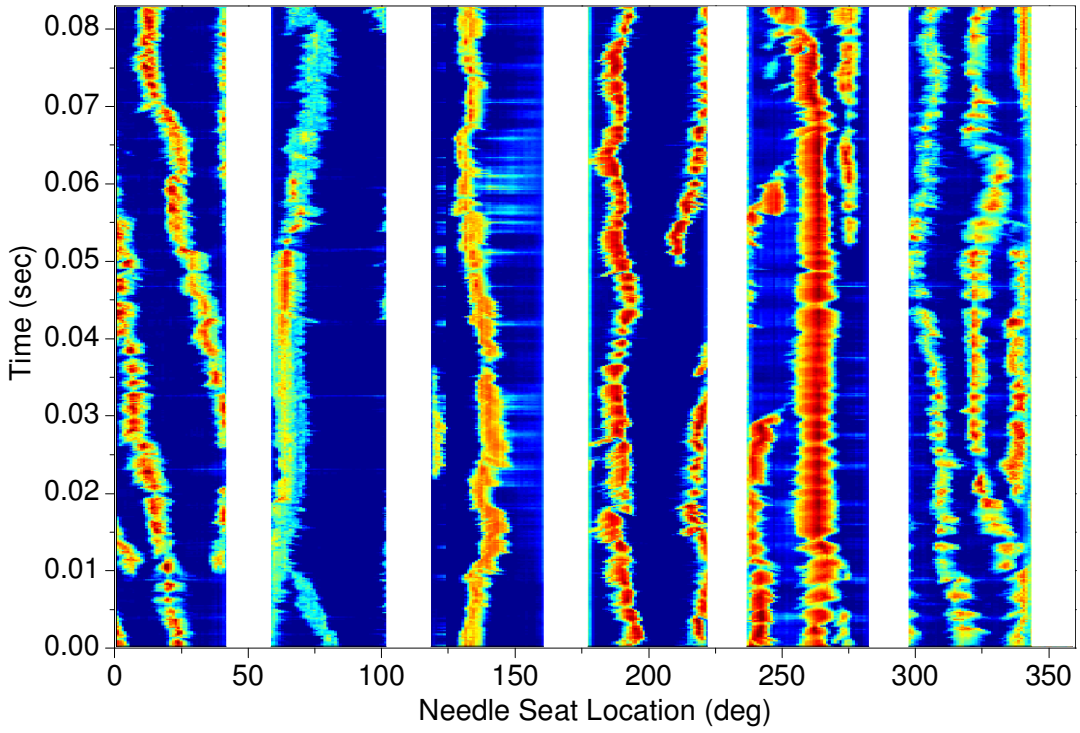

Figure 7-53: Needle seat cavitation intensity frequency [Eq. Needle Lift=20µm, CN= 52, Re= 35,300]

Apart from the two needle designs that have been presented so far, there was also a third design that was investigated. However from this case it was not possible to perform automated image processing. The reason was a problem with the electronic ballast of the flood light, which caused fluctuations in the light intensity and therefore it was impossible to have a background image to be used for the entire range of the recording period. Never the less, a comprehensive set of operating conditions were tested which can be found in Table 7-7, Table 7-8 and Table 7-9 for the 10, 15 and 20 μm needle lift respectively.

Volumetric Flow Rate (l/s)	P_{in} (bar)	P_{back} (bar)	Re	CN
0.10	2.0	0.4	7,000	5
0.17	4.5	1.0	12,000	4
0.19	5.0	1.0	13,500	4.5
0.23	7.0	0.3	16,000	27
0.25	7.0	0.2	17,500	48

Table 7-7: Range of operating conditions investigated for the transparent sac-type nozzle with needle design II at 10 μm equivalent needle lift.

Volumetric Flow Rate (l/s)	P_{in} (bar)	P_{back} (bar)	Re	CN
0.26	2.0	0.4	18.500	5
0.36	4.5	1.0	25,500	4
0.40	5.0	1.0	28,000	4.5
0.55	7.0	0.2	39,000	48
0.54	7.0	0.3	38,000	28

Table 7-8: Range of operating conditions investigated for the transparent sac-type nozzle with needle design II at 15 μm equivalent needle lift.

Volumetric Flow Rate (l/s)	P_{in} (bar)	P_{back} (bar)	Re	CN
0.24	2.0	0.4	17,000	5
0.25	2.0	0.35	17,000	7
0.41	4.0	0.35	29,500	15
0.51	5.0	1.0	36,000	4
0.59	7.0	0.2	41,500	48
0.58	7.0	0.3	41,000	28

Table 7-9: Range of operating conditions investigated for the transparent sac-type nozzle with needle design II at 20 μm equivalent needle lift.

The following series of figures (Figure 7-54 through Figure 7-57) show typical results from all the investigated cases for 10, 15 and 20 μm equivalent needle lift. As it can seen this time the cavitation spikes are even more elongated. This is due to the increased thickness of the needle which has moved the sealing point of the needle upwards. The eccentricity is also present in this case particularly for the two lower needle lift cases. Again as the CN and Reynolds increases the needle seat cavitation becomes stronger. The gap between the spikes is much smaller than it was in needle design VI. However at 10μm lift and increased CN the majority of the needle seat area is occupied by vapour. As lift increases the number of spikes and their intensity decrease similarly to other needle designs. It has to be mentioned that for this particular design at low CN values there were major vibrations on the needle. Although the mechanism that triggers these vibrations is not clear an attempt will be made to provide reasoning.

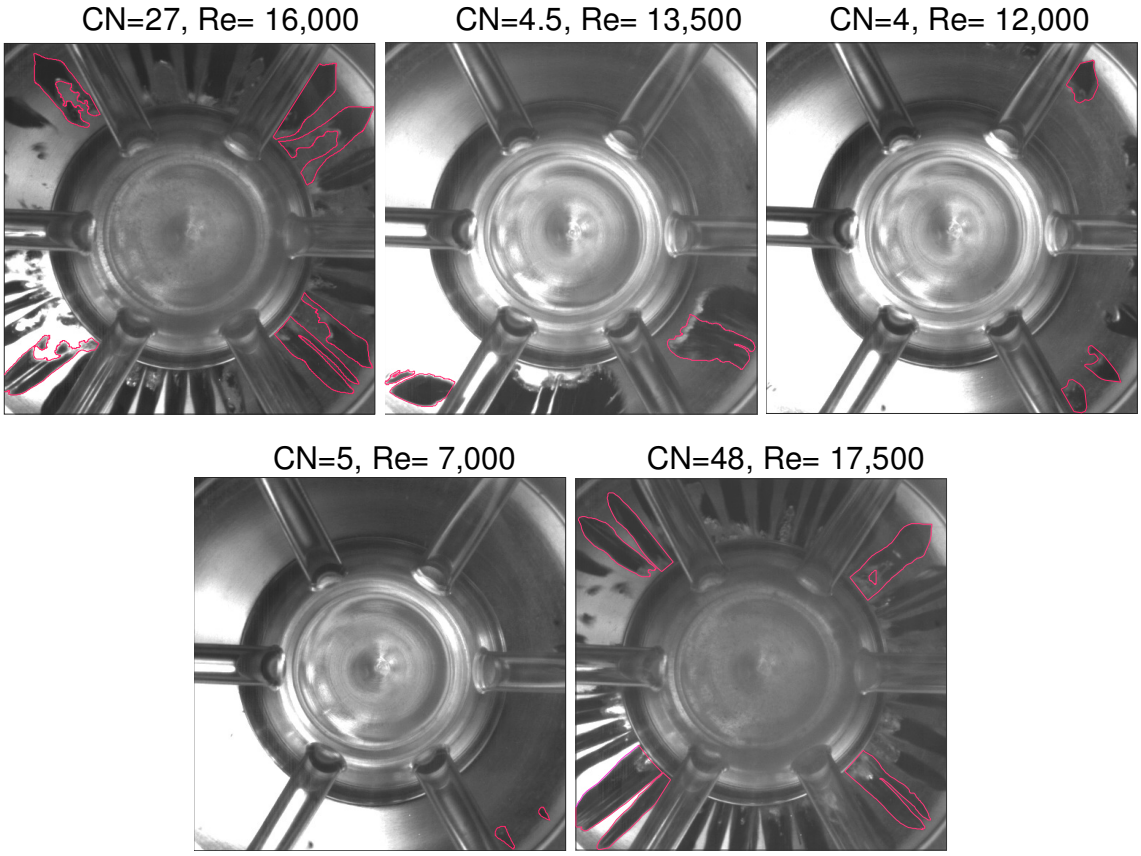

Figure 7-54: Typical bottom view images of the Sac-Type nozzle with needle design II at 10 μm equivalent needle lift.

At low lift the effect of eccentricity is increased. Once the flow conditions are such in order to trigger cavitation to occur at the needle seat area it is understood that the side having the smaller gap to the nozzle body will start to produce vapour first, since at this point the acceleration of the liquid will be higher. Once cavitation is established it will push the needle to the opposite direction. this will make the needle to vibrate in a circular pattern which in turn will trigger cavitation to different locations corresponding to the instantaneous smaller gap between the needle and the nozzle body. The fact that these vibrations occurred at low CN and Reynolds numbers, suggest that there is a critical value for this type of cavitation where it starts to initiate and is very sensitive to small flow and geometry changes. At higher CN the flow is capable to initiate cavitation at a much larger area of the needle seat and therefore there are counter reacting forces that stabilize the position of the needle.

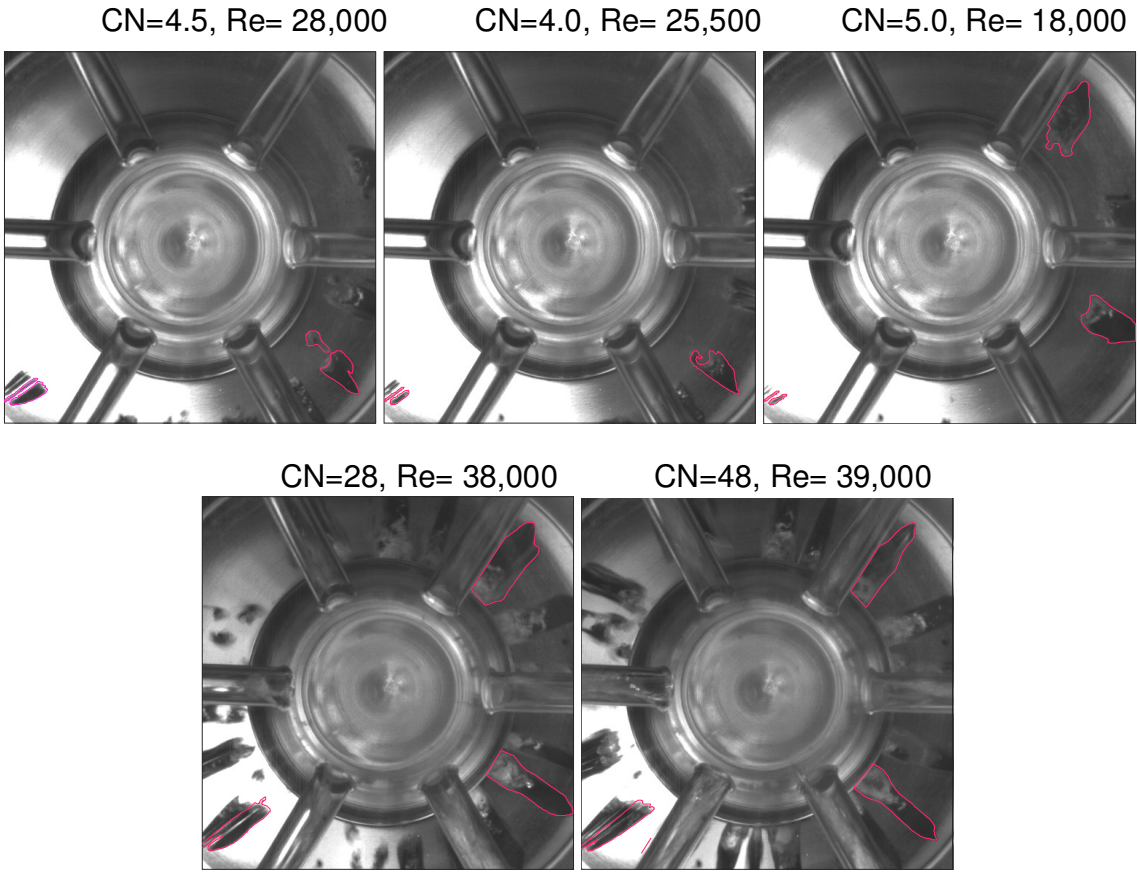

Figure 7-55: Typical bottom view images of the Sac-Type nozzle with needle design II at 15 μm equivalent needle lift.

It is widely acknowledged that needle vibrations, particularly for VCO nozzles, can occur due to the flow of the injecting liquid through the injection holes. in fact sometimes this vibrations are so intense that can cause big deflection to the needle and eventually damage the injection equipment. Needless to say that the asymmetry that is caused to the flow de to the needle eccentricity severely affect the spray characteristics of the nozzle. However these problems only apply to low needle lifts and are not expected to cause major differences to the combustion characteristics of the engine.

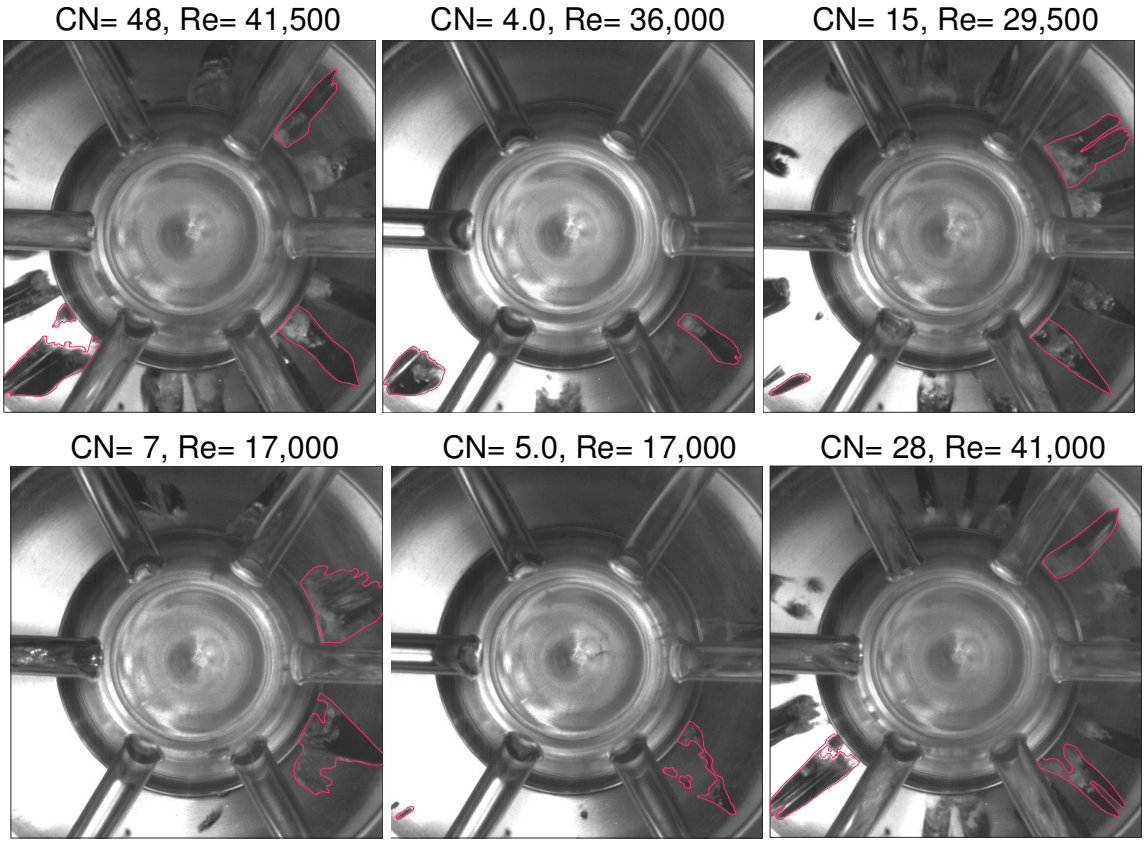

Figure 7-56: Typical bottom view images of the Sac-Type nozzle with needle design II at 20 μm equivalent needle lift.

Before closing the presentation of results for the last needle design, it is interesting to show typical images from two cases where a large cloud of vapour was trapped inside the nozzle's sac volume. As it can be seen in Figure 7-57, the vapour produced by needle cavitation was captured inside the recirculation zone existing right at the tip of the needle, and since the flow is weak in order to overcome the buoyancy of the bubbles in order to drift them towards the holes exit it remains concentrated under the needle and is slightly

rotating due to the circular component of the flow. This is a situation which is very unlikely to occur in real operating conditions, however since it was observed in the experiment it was considered interesting to report it as a possible flow regime.

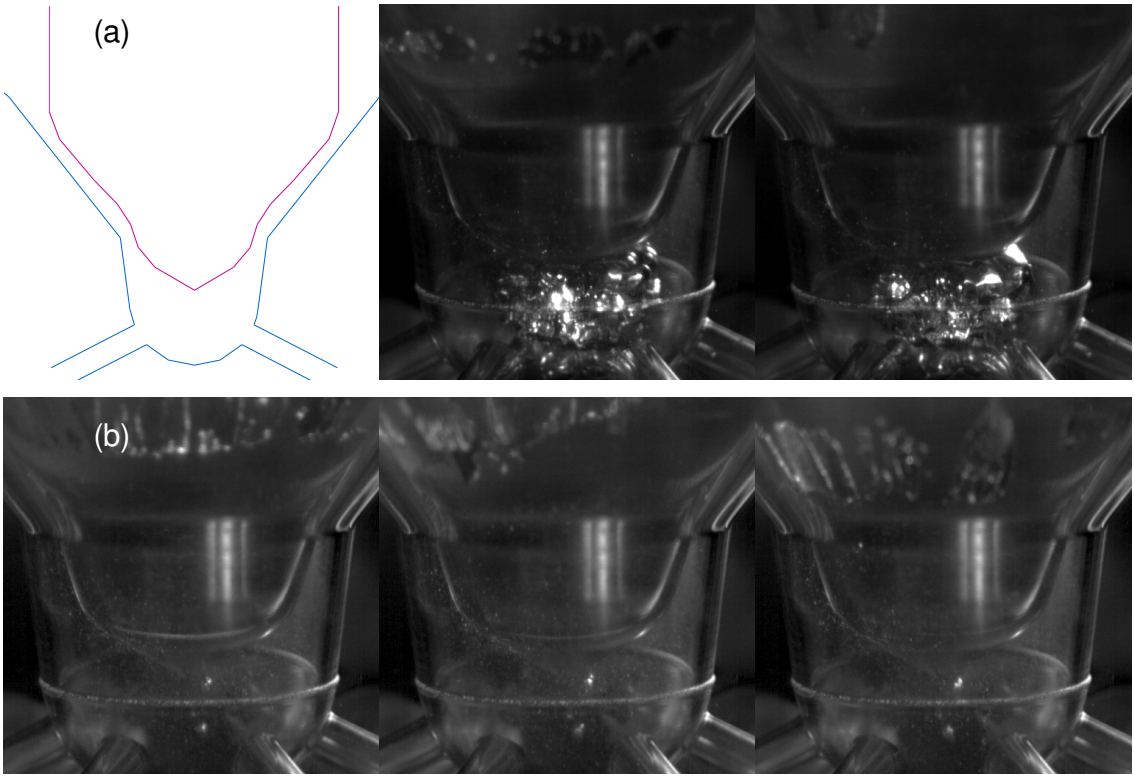

Figure 7-57: figure showing trapped vapour inside the sac-volume of the nozzle attached to the needle tip (design III) a) [CN=15, Re=3,000] and b) [CN=15, Re=8000]

7.4.3 Needle Seat Cavitation 3-D Reconstruction

The final results to be presented regarding needle seat cavitation is an attempt to combine the experimental findings with CFD simulations for the same geometries and operational conditions. As it was shown before, when considering the strings inside the sac volume of the marine nozzles, the best way to correlate the internal nozzle flow and the experimentally obtained cavitation regimes was through 3-dimensional reconstruction. the same concept was attempted to be applied for needle seat cavitation. The main aim was to confirm whether or not the computational model would show regions of volume under tension at the location where the spikes were originating. Combining the bottom and side

images from the same time instances and by describing the boundaries of the spikes, the red lines indicated on the sample images, it was possible to reconstruct them in the 3-dimensional space as volumes. The fact that the vapour was trapped between the two walls formed by the needle and the nozzle, made possible to form a fully asymmetric volume fully describing the real shape of the cavitation sites. The resulting vapour pockets where then inserted into their corresponding computational domains which had been firstly used in order to simulate the internal nozzle flow. The information chosen to be plotted were the streamlines of the total velocity along with the iso-surfaces of regions of negative pressure. The results of this processing are presented in Figure 7-58 through Figure 7-60figures 1-70 through 1-72 for all the three needle designs tested at operating conditions where needle seat cavitation was fully developed for four different views in order to enhance understanding.

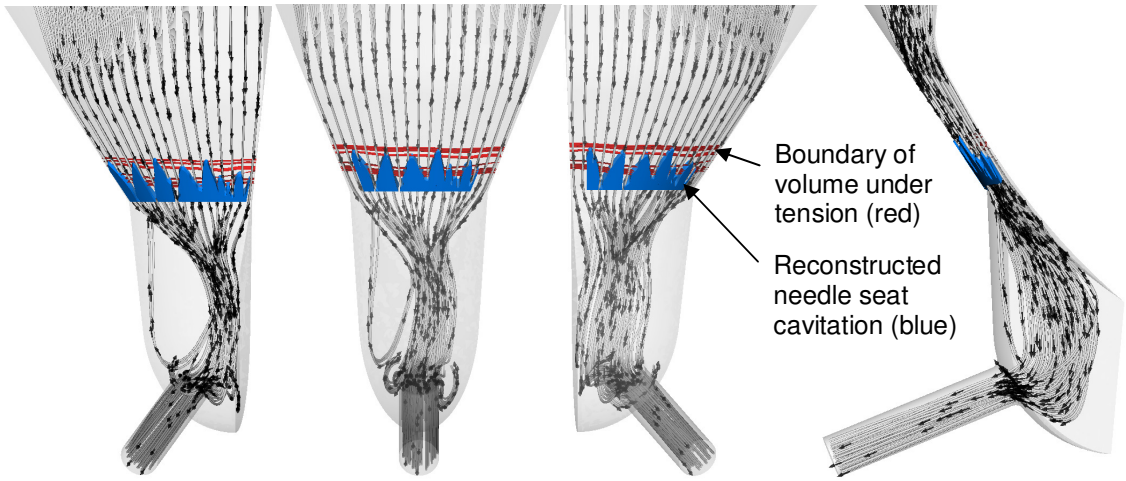

Figure 7-58: 3-Dimensional reconstruction of needle seat cavitation at 20 μm equivalent needle lift for needle design I.

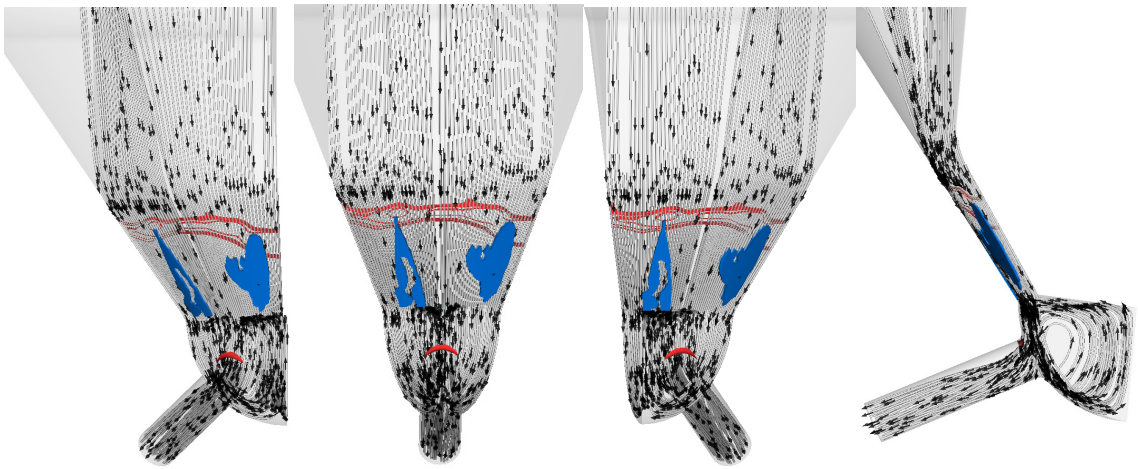

Figure 7-59: 3-Dimensional reconstruction of needle seat cavitation at 20 μm equivalent needle lift for needle design IV.

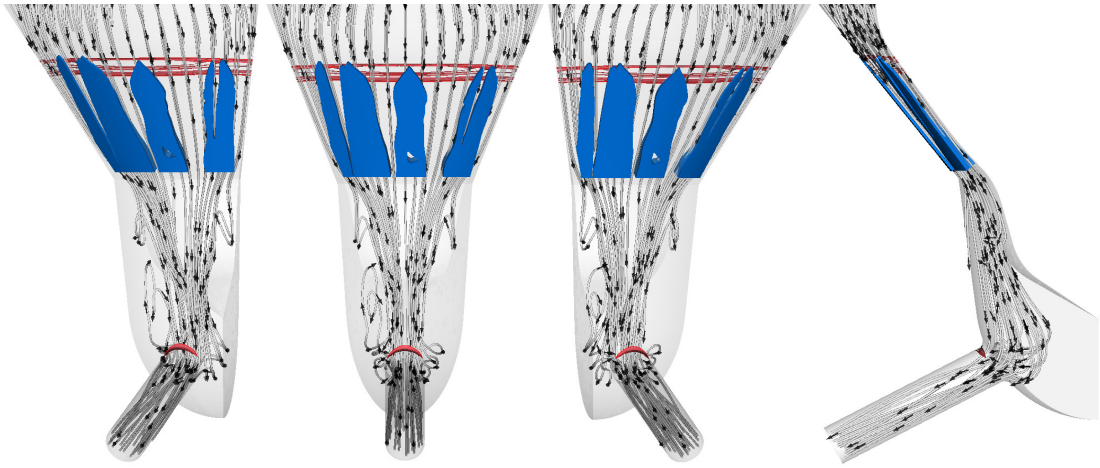

Figure 7-60: 3-Dimensional reconstruction of needle seat cavitation at 20 μm equivalent needle lift for needle design III.

As it can be seen the location where needle seat cavitation initiates lies between the region of negative vapour pressure which is visualized by the red iso-surface lines. This results proves that the mechanism of formation for this type of cavitation is based on the geometric characteristic of the narrow passage that causes the flow to accelerate dropping the pressure below the vapour one. This is the same mechanism that is responsible for hole cavitation and it can be successfully predicted by the in house CFD code. It has to be mentioned that such an analysis for needle seat cavitation has not been previously reported in literature.

7.5 String Cavitation inside the Sac-Type nozzle with cylindrical holes

Until this point of the current study, it has been shown that apart from hole cavitation there are other two, less investigated and understood, types of it. String cavitation and its mechanism of formation as well as its effect on the internal nozzle flow and the near hole exit spray structure has been thoroughly presented through a series of investigations that were conducted in the marine injector nozzles.

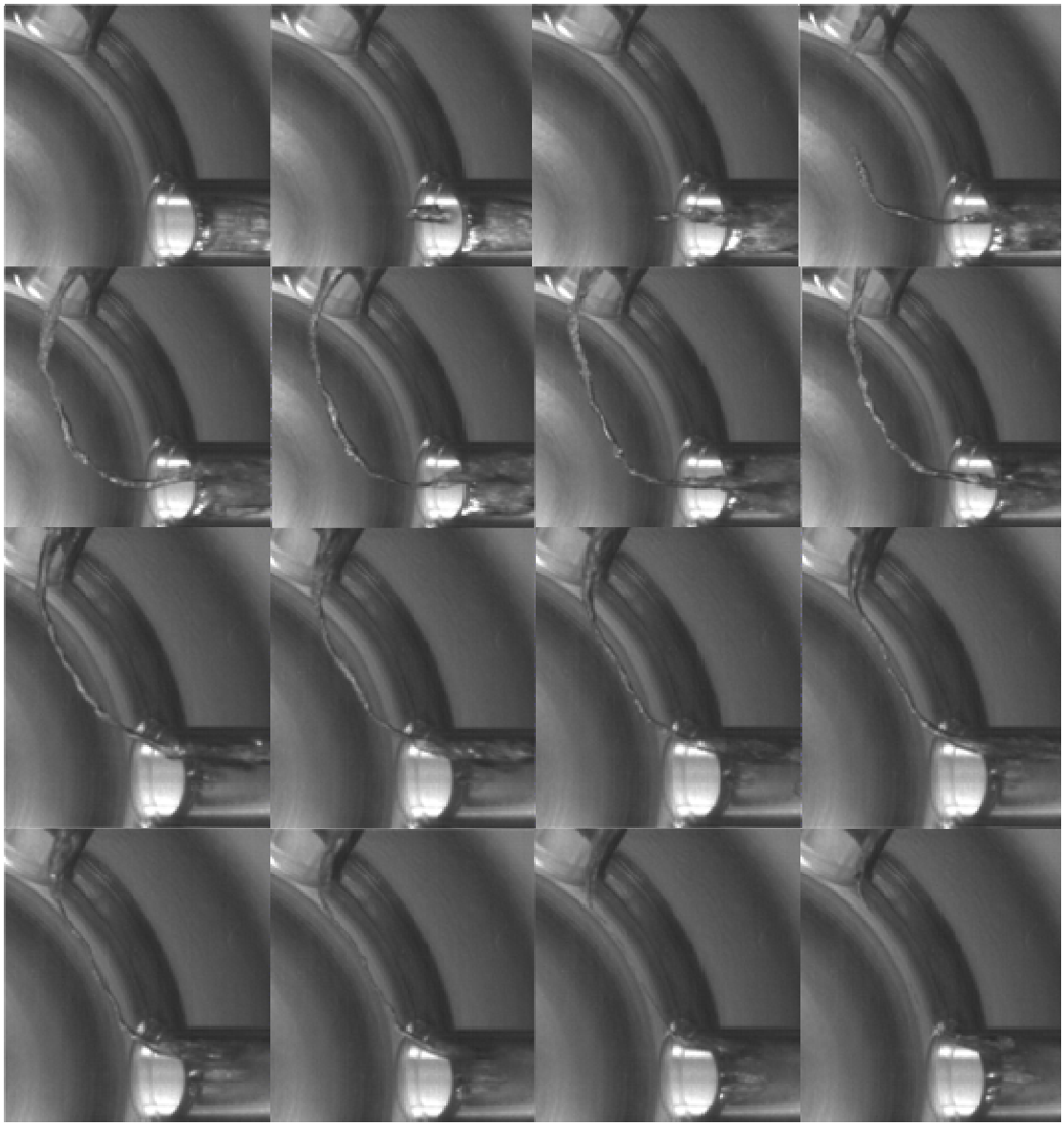

Figure 7-61: Sequence of events, 8ms interval, showing the formation of string cavitation originating from an injection hole and developing sideways inside the adjacent injection hole of the Sac-Type nozzle [Eq. Needle Lift=300μ, Re=44,500, CN=12]

Moreover it was also shown that in multihole VCO nozzles, particularly at low needle lifts, there are strings formed inside the injection holes that interact with the injector needle. Finally in Sac type nozzles and at very low lift it was found that needle seat cavitation can occur, which in turn leads into severe erosion problems on the injection equipment. The final part of this study will show the cavitation regimes inside the sac-type nozzle, however this time at higher needle lifts.

Figure 7-61 above shows a sequence of images for the needle design IV at 300 μm equivalent needle lift. As it can be seen there is a hole-to-hole string that initiates from one hole to the one next to it, it then stays connected to both holes for a period of time and then fades out. Since from the bottom view image it cannot be clearly seen the 3-dimensional shape of the string, for some of the investigated cases a side view camera was also used in order to record the string simultaneously similarly to what it was done with the marine nozzle before

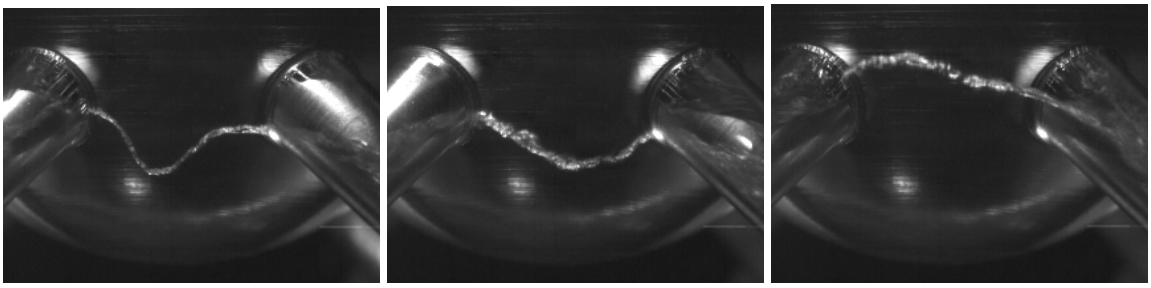

Figure 7-62: Typical images showing the formation of string cavitation from the side view Sac-Type nozzle [Eq. Needle Lift=300μm, Re=44,500, CN=12]

Figure 7-62 shows typical side view images from the same case where the sequence of Figure 7-61 was acquired. As it can be seen once the string is fully developed and links the two holes it is possible to vary in thickness and shape/location with time. So far we have seen that the string were forming inside the recirculation zones existing in the flow. Before confirming if this is the case for this type of nozzles, an extensive range of processed data will be shown, covering three different needle designs, three different needle lifts and many CN and Reynolds combination. The rig is the same as in all other internal nozzle flow investigations.

Starting from needle design I at 50 μm equivalent needle lift the following table shows the operating conditions tested.

Volumetric Flow Rate (l/s)	P_{in} (bar)	P_{back} (bar)	Reynold's	CN
0.47	2	0.15	33,200	19
0.6	3	0.5	42,400	6
0.77	5	0.5	54,400	10
0.92	7	0.3	65,000	27
0.91	7	0.5	64,300	14

Table 7-10: Range of operating conditions investigated for the transparent sac-type nozzle with needle design I at 50 μm equivalent needle lift.

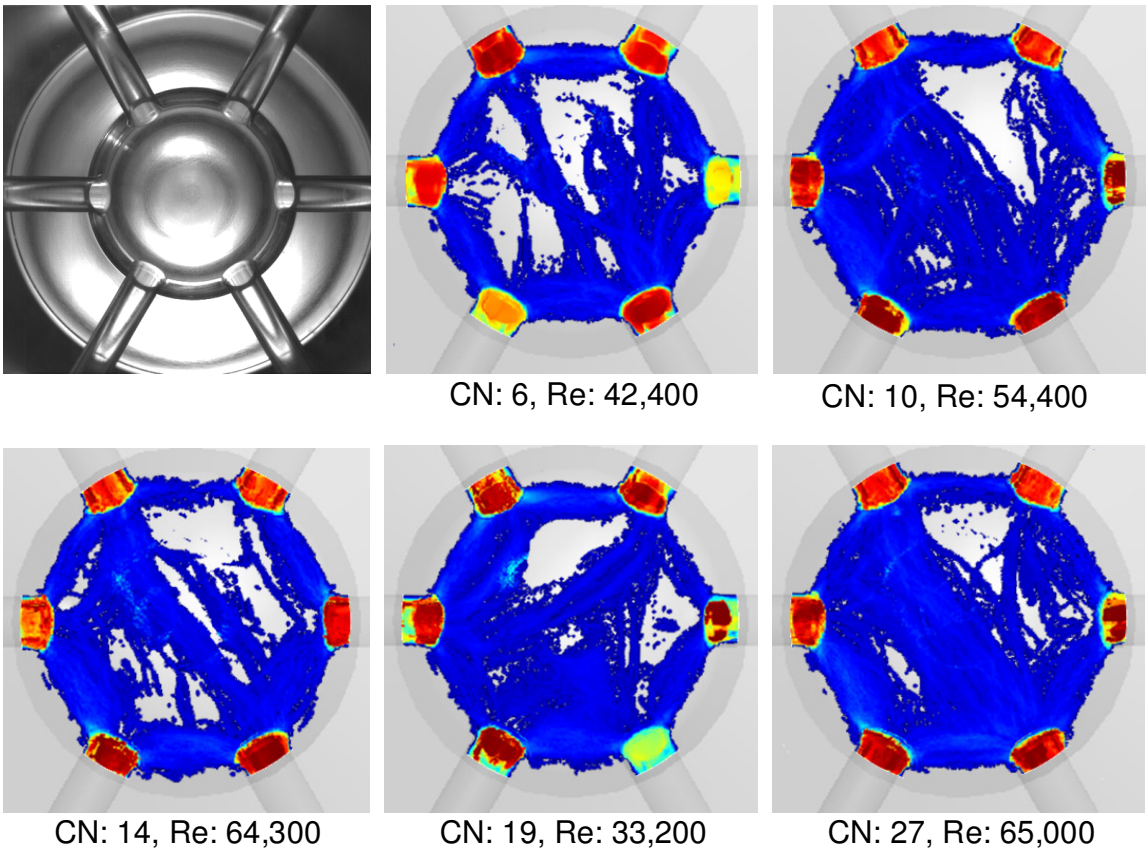

Figure 7-63: Averaged images for Vortex cavitation in sac-type nozzle with needle tip design (I) for different flow conditions. [50 μm equivalent needle lift]

Since mean images were proved to be a good method of comparing the qualitative and quantitative effects that changes in geometry and/or flow conditions have on the feature to

be examined, it was chosen to perform time and space averaging for almost all cases investigated.

Starting from Figure 7-63, the main conclusion is that for all the investigated cases there is less than 15-20% to have a frame where no string cavitation exists. Getting into a more detailed analysis, it can be said that the increase of CN and/or Reynolds increases the probability of string formation. This is in line with the previously reported results when considering the marine nozzle. Moreover it can be said, that although a slight eccentricity exists, the probability of having strings between adjacent holes is evenly distributed. Finally apart from hole-to-hole string connecting adjacent holes, it can be seen that there are strings connecting opposite holes as well one hole with one next to the adjacent one. It has to be mentioned that the shape and the location of the needle at the given lift is considered to play a major role for the allowable positions that the strings will be able to take.

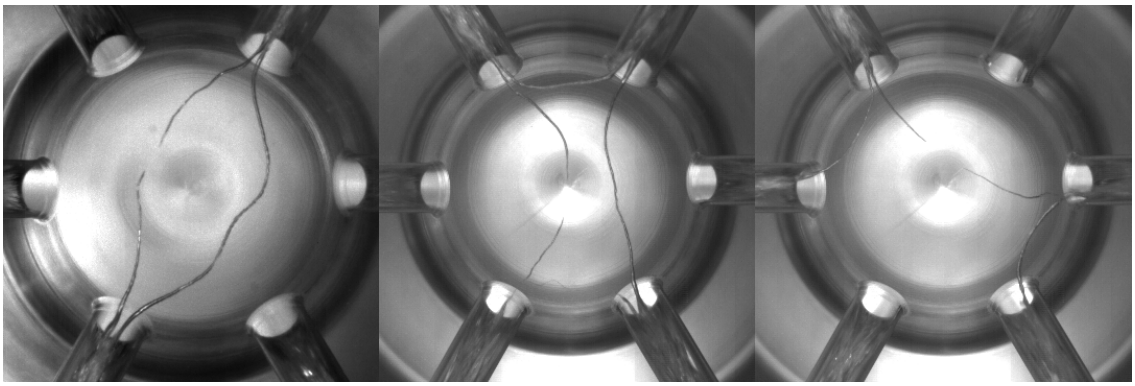

Figure 7-64: Typical bottom view images showing string cavitation structures inside the sac-type nozzle with needle design I [Eq. Needle Lift=50μm]

In order to explain how such asymmetrically distributed probabilities have been found, Figure 7-64 shows typical bottom view images indicating multiple strings existing between opposite, adjacent and side holes. It has to mentioned that existence of more than one strings at the same time was frequent. This was a new feature to be found since in the marine nozzle there was only one string at a given time.

Similarly to the previous results, Table 7-11 below and Figure 7-65, show the operating conditions and the mean images produced by the original needle design (I) this time at the maximum lift (300 μm equivalent). As it can be seen the probability of having strings has dropped dramatically. Also at lower CN the effect of slight eccentricity is highly noticeable. Finally strings are now almost solely formed between adjacent holes and almost every time at the same confined location. This can be realized by the narrow width of the blue regions in between the injection holes which were much thicker before.

Volumetric Flow Rate (l/s)	P_{in} (bar)	P_{back} (bar)	Re	CN
0.7	2	0.2	49500	12
0.7	2	0.4	49500	5
0.85	3	0.4	60100	7
0.95	4	0.3	67100	15
0.96	4	0.4	67800	10
1.06	5	0.4	74900	13
1.16	6	0.4	81900	16

Table 7-11: Range of operating conditions investigated for the transparent sac-type nozzle with needle design I at 300 μm equivalent needle lift.

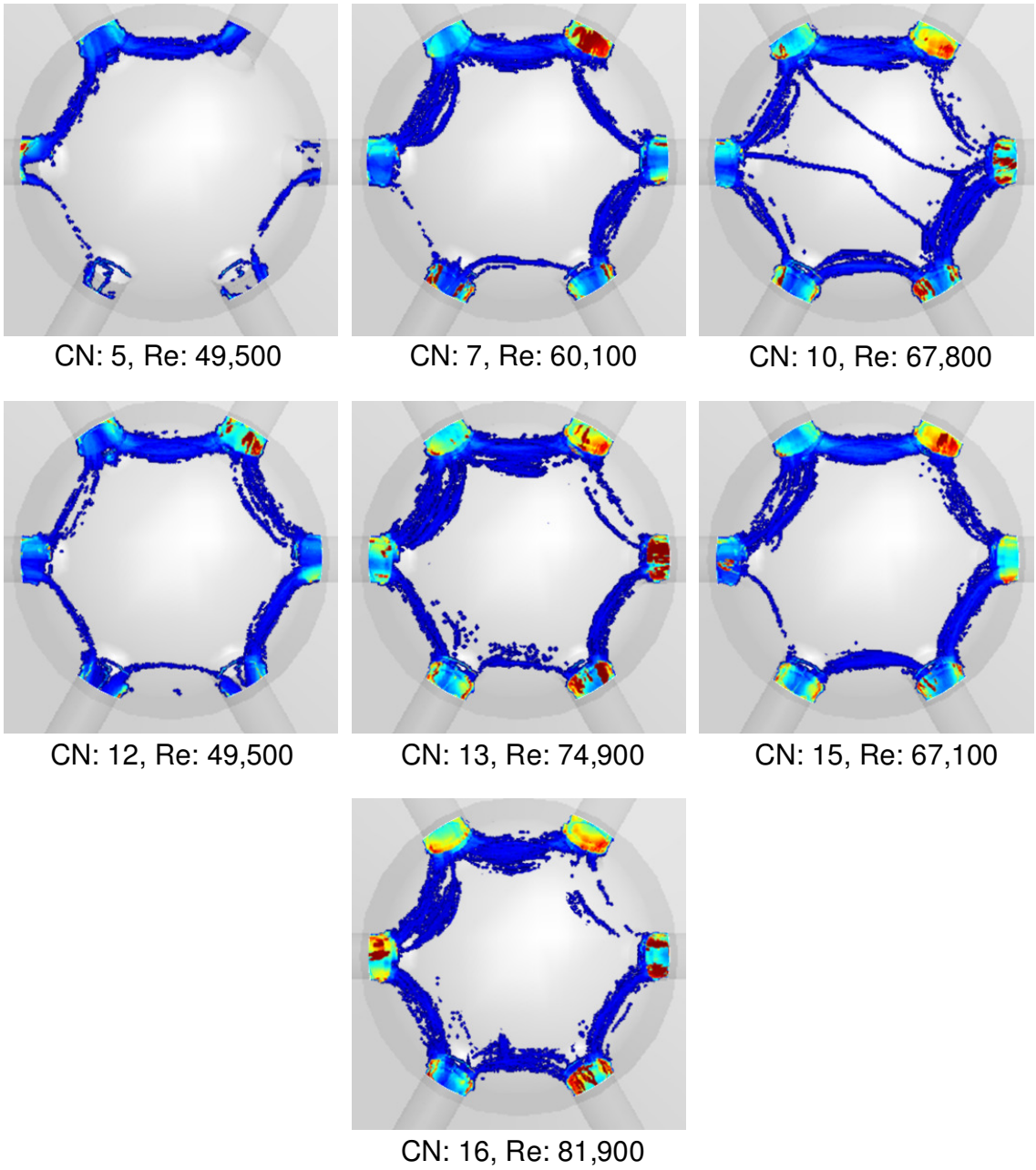

Figure 7-65: Averaged images for Vortex cavitation in sac-type nozzle with needle tip design (I) for different flow conditions. [300 µm equivalent needle lift]

Volumetric Flow Rate (l/s)	P_{in} (bar)	P_{back} (bar)	Re	CN
0.83	4.5	0.3	58500	17
0.83	4.5	0.65	58500	7
0.82	4.5	0.9	58000	4.5

Table 7-12: Range of operating conditions investigated for the transparent sac-type nozzle with needle design III at 50 µm equivalent needle lift.

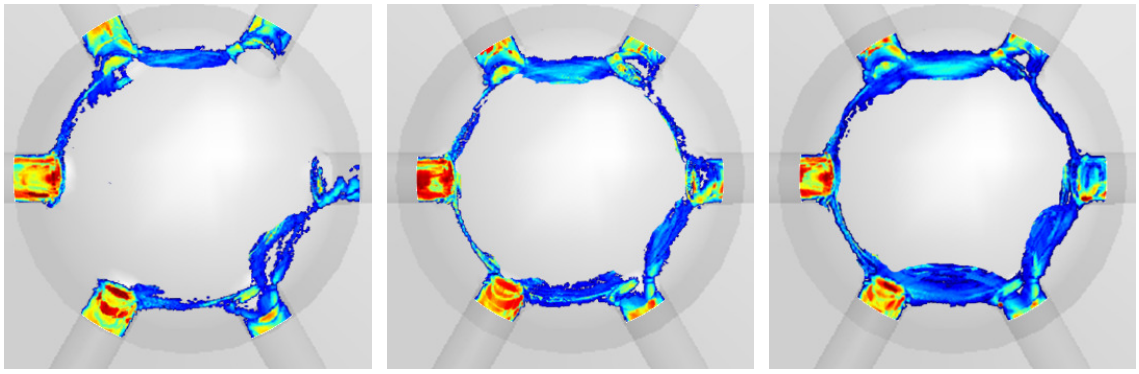

CN: 4, Re: 58,000 CN: 7, Re: 58,500 CN: 17, Re: 58,500

Figure 7-66: Averaged images for Vortex cavitation in sac-type nozzle with needle tip design (III) for different flow conditions. [50 μm equivalent needle lift]

Volumetric Flow Rate (l/s)	P_{in} (bar)	P_{back} (bar)	Re	CN
0.93	4	0.3	65500	15
0.92	4	0.8	65000	4.5

Table 7-13: Range of operating conditions investigated for the transparent sac-type nozzle with needle design III at 150 μm equivalent needle lift.

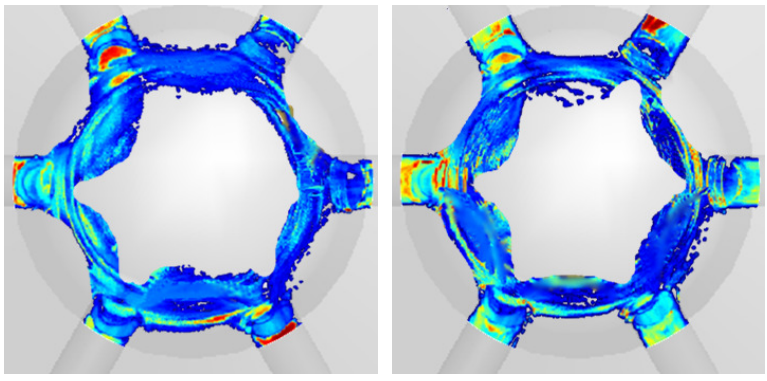

CN: 4, Re: 65,500 CN: 15, Re: 65,000

Figure 7-67: Averaged images for Vortex cavitation in sac-type nozzle with needle tip design (III) for different flow conditions. [150 μm equivalent needle lift]

Volumetric Flow Rate (l/s)	P_{in} (bar)	P_{back} (bar)	Re	CN
0.97	4	0.3	68500	15
0.6	1.5	0.1	42500	28

Table 7-14: Range of operating conditions investigated for the transparent sac-type nozzle with needle design III at 300 μm equivalent needle lift.

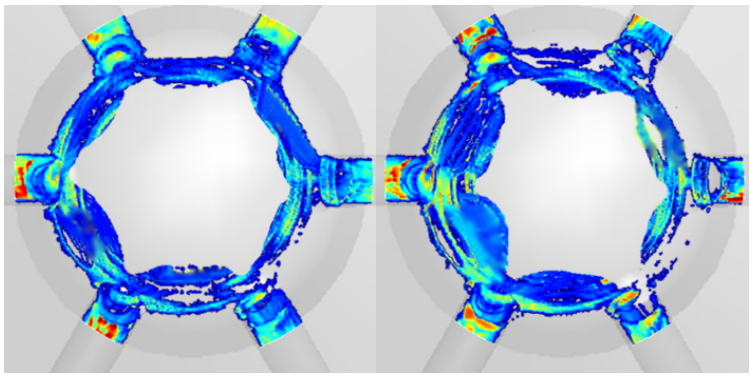

CN: 15, Re: 65,500 CN: 28, Re: 42,500

Figure 7-68: Averaged images for Vortex cavitation in sac-type nozzle with needle tip design (III) for different flow conditions. [300 μm equivalent needle lift]

The next tables and figure correspond to the needle design IV. This is the design where the needle is flat at its tip and once at low lifts is very close to the height of the injection holes. This time it was deliberately chosen to introduce a small eccentricity in order to see how the strings will be affected under such conditions.

Volumetric Flow Rate (l/s)	P_{in} (bar)	P_{back} (bar)	Re	CN
0.36	2	0.15	25500	19
0.43	3	0.3	30400	11
0.43	3	1	30400	2
0.59	5	0.5	41700	10
0.73	7	0.3	51600	27
0.72	7	0.5	50900	14

Table 7-15: Range of operating conditions investigated for the transparent sac-type nozzle with needle design IV at 50 μm equivalent needle lift.

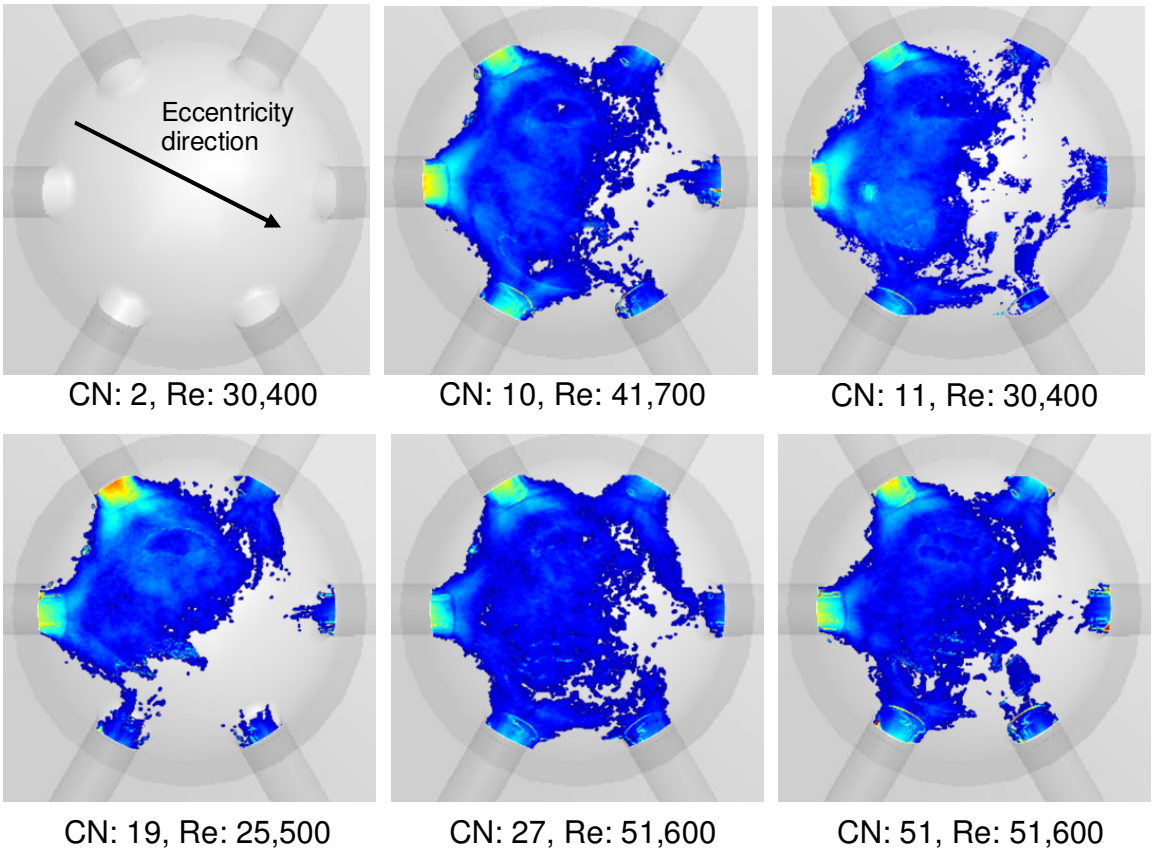

Figure 7-69: Averaged images for Vortex cavitation in sac-type nozzle with needle tip design (IV) for different flow conditions. [50 µm equivalent needle lift]

As it can be seen from Figure 7-69, the strings are concentrated to the side where the gap has been increase and therefore more flow is passing. Moreover it is interesting to see that the strings are not well defined and there is more like a uniform probability of having a vapour cloud in the sac volume rather than fully developed strings. Looking at the higher value region we can see that they lie on the sides of the injection holes. This means that the flow is similar to the one seen before and the strings originate from inside the injection holes with the same tendency to form hole-to-hole strings as we have seen before. However, most likely due to the flat surface of the needle which is very close to the hole inlets, the strings brake up and slide on the flat surface of the needle until they break up into smaller bubbles. This had been confirmed for all the low lift cases and it can also be recalled from the sample images presented when considering needle seat cavitation.

Volumetric Flow Rate (l/s)	P_{in} (bar)	P_{back} (bar)	Re	CN
0.36	3	0.3	45900	11
0.43	7	0.3	65000	27
0.43	7	0.65	65000	11

Table 7-16: Range of operating conditions investigated for the transparent sac-type nozzle with needle design IV at 150 μm equivalent needle lift.

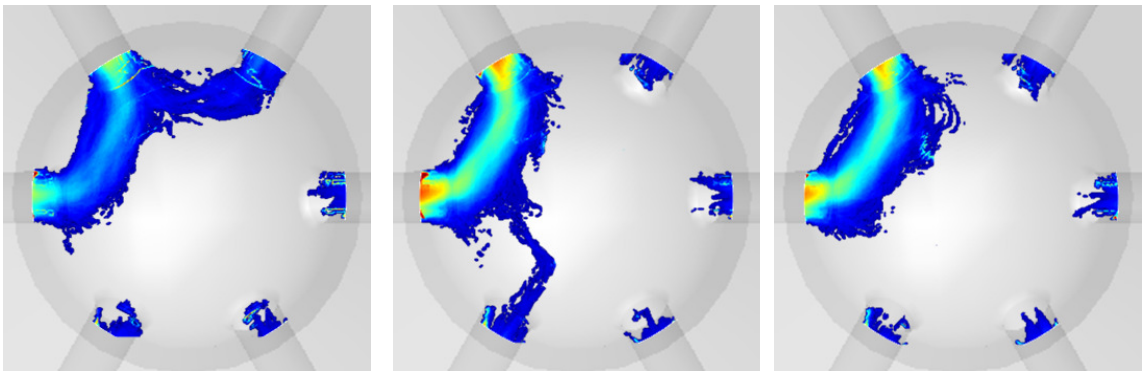

CN: 11, Re: 45,900 CN: 11, Re: 65,000 CN: 27, Re: 65,000

Figure 7-70: Averaged images for Vortex cavitation in sac-type nozzle with needle tip design (IV) for different flow conditions. [150 μm equivalent needle lift]

Moving at a higher lift for the same needle design and with the same amount of eccentricity it can be seen that the probability of having vapour in the sac volume is now much more defined and clearly indicates existence of fully developed hole to hole strings between the holes that lie under the wider passage of flow. Again the fact that higher value regions are found at the hole inlet, clearly indicates that strings originate from inside the holes and perhaps not always fully develop, and this is why the probability at the region in between the holes is lower. Finally the fact that all the strings are concentrated at one side has made more profound what is the effect of both Reynolds and CN number. Increasing Reynolds at the same CN increases the probability of string formation having a high CN and a High Reynolds and trying to increase CN further will not result in a noticeable difference. Finally apart from the bluish region, we can see that there is a much higher value region at the middle which denoted a clear preference of the vapour to concentrate there. This was not the case with the original nozzle design where the probability was evenly distributed both in the entire nozzle sac and in between the region of adjacent holes. It also has to be mentioned that will in all other cases the string were initiating from the sides of the

injection holes, this time the start from the middle. This should be caused due to the fact that the flow is mostly directed in that couple of holes making the side flow to their adjacent holes very weak.

Volumetric Flow Rate (l/s)	P_{in} (bar)	P_{back} (bar)	Re	CN
0.63	2	0.2	44500	12
0.64	2	0.4	45200	5
0.77	3	0.4	54400	7
0.88	4	0.3	62200	15
0.88	4	0.4	62200	10
0.99	5	0.4	69900	13
1.08	6	0.4	76300	16

Table 7-17: Range of operating conditions investigated for the transparent sac-type nozzle with needle design IV at 300 μm equivalent needle lift.

Finally the last set of results refer to the maximum needle lift for needle design IV, where the needle has been restored to its center position. As it can be seen the results are much more like those obtained for the original needle design at low lift. In fact the interaction of the needle, in terms of its distance from the holes is comparable. As it can also be seen there are only strings between adjacent holes and the probability is almost evenly distributed. Moreover the strings initiate from the sides of the injection holes and they have a wide range of movement in the sac volume. Although the differences are small, it is clear again that at higher CN and Reynolds the probability to have strings increases. Comparing the two needle design it can be concluded that the original one is much more resistant to this form of cavitation. This should be accounted to the needle designs which once at high lifts leaves the flow unguided to move towards the center of the sac volume thus reducing the side flow in between injection holes.

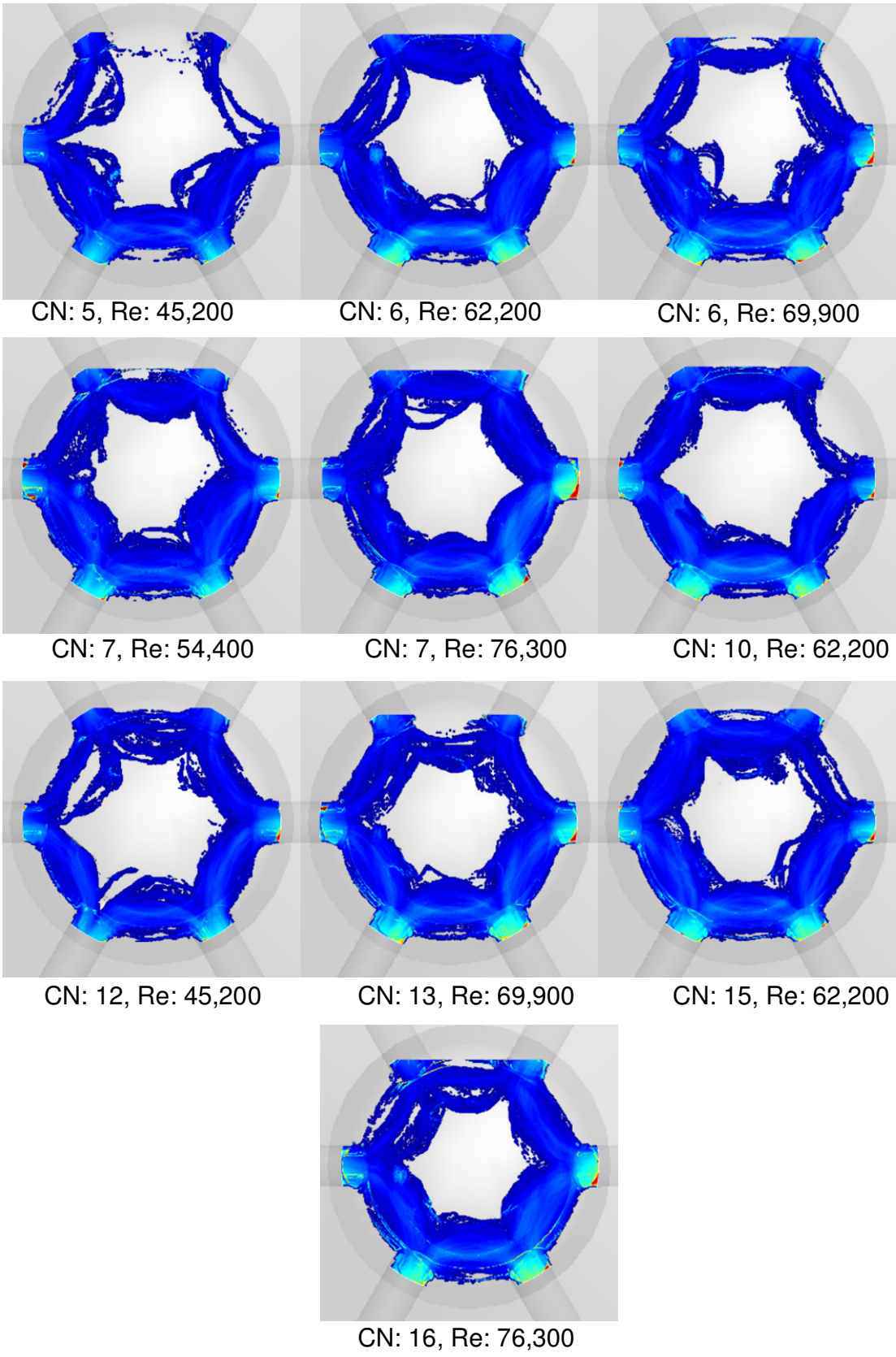

Figure 7-71: Averaged images for Vortex cavitation in sac-type nozzle with needle tip design (IV) for different flow conditions. [300 µm equivalent needle lift]

7.5.1 String Cavitation 3-D reconstruction

The final results to be presented in this study are from the multi-hole strings reconstructions and computational results. As mentioned throughout the investigation the aim of numerical results was to provide us with valuable information regarding the flow field inside the nozzle volume. One of the most interesting parameters that is plotted is the swirl intensity. At region where the values are high it is an indication that the flow is recalculating.

As it can be seen in Figure 7-72 the simulations have resulted into an accurate prediction of the recirculation zones since the experimentally obtained string were found at exactly the same locations having also the same arrangement.

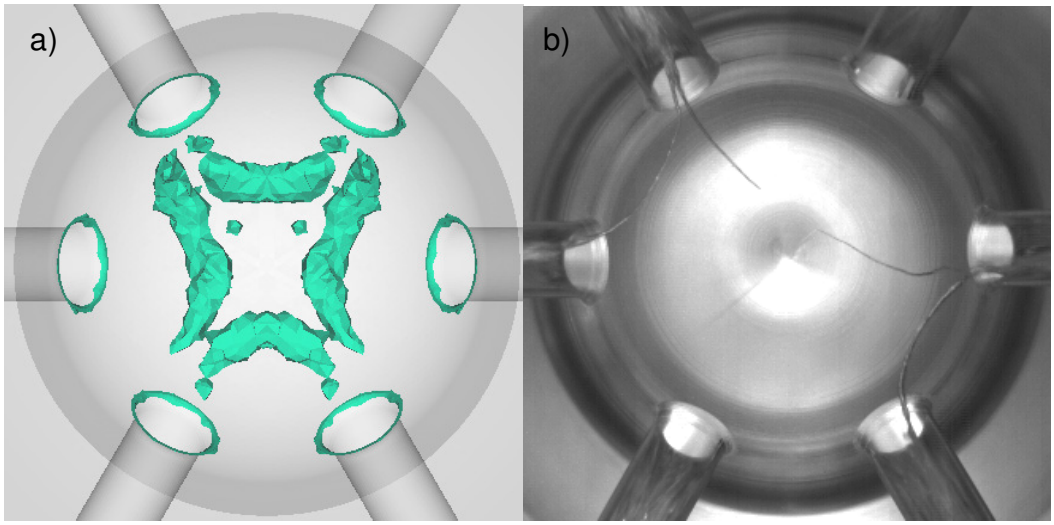

Figure 7-72: comparison between a) region of high swirl intensity (cyan) and b) experimentally obtained strings for the sac-type nozzle with needle design IV at 300μm equivalent needle lift [CN: 15, RE: 67,100]

Similarly to the above, Figure 7-73, show the same comparison for needle design IV at similar operating conditions and at the same needle lift as the original needle case. Again the results show total agreement confirming the good ability of the in house CFD code to predict accurately the complex flow inside the nozzles. It has to be mentioned that while in the original needle simulation there are predictions of high swirl regions between both adjacent holes and side holes, in the needle design IV there are only between adjacent holes. Since this was found to be the case from the experimental results, it has to pointed

that the code is capable to account for the changes induced to the flow due to the different geometry arrangement.

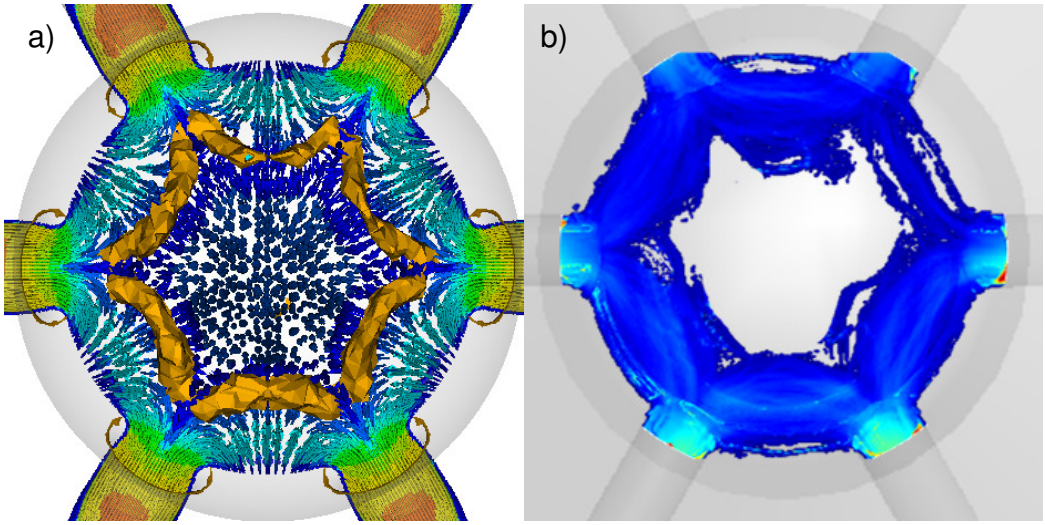

Figure 7-73: comparison between a) region of high swirl intensity (yellow) and b)experimentally obtained probability of strings for the sac-type nozzle with needle design IV at 300μm equivalent needle lift [CN: 15, Re: 62,200].

As shown in the previous two figures, Figure 7-72 & Figure 7-73, the CFD code is able to predict the core of the recirculation zones with good accuracy since the location and shape matches with the experimentally obtained strings. This is also in line with what it was shown before in Chapter 5 when examining marine nozzles.

The next step was to perform 3-D reconstruction using the method described in section 3.4.2. Similarly to the analysis presented in Chapter 5 the experimental strings were introduced in the numerically predicted flow field. A typical result of this process is shown in Figure 7-74. As it can be seen in the l-h-s where the contour of axial velocity is plotted, inside the sac, in the lower part downstream the injection holes, there is a recirculation zone indicated with red colour suggesting that the fluid moves in the opposite direction than the main flow. The fact that negative pressure region are predicted in the upper inlet of the hole is in line with what experiments and previous experience have shown. In the r-h-s the streamlines of the flow visualize the recirculation region. The experimentally obtained reconstructed string lies within the core of the predicted vortex. This is fully compatible with what it was found in the marine nozzles and confirms that strings are directly related with vortical flows.

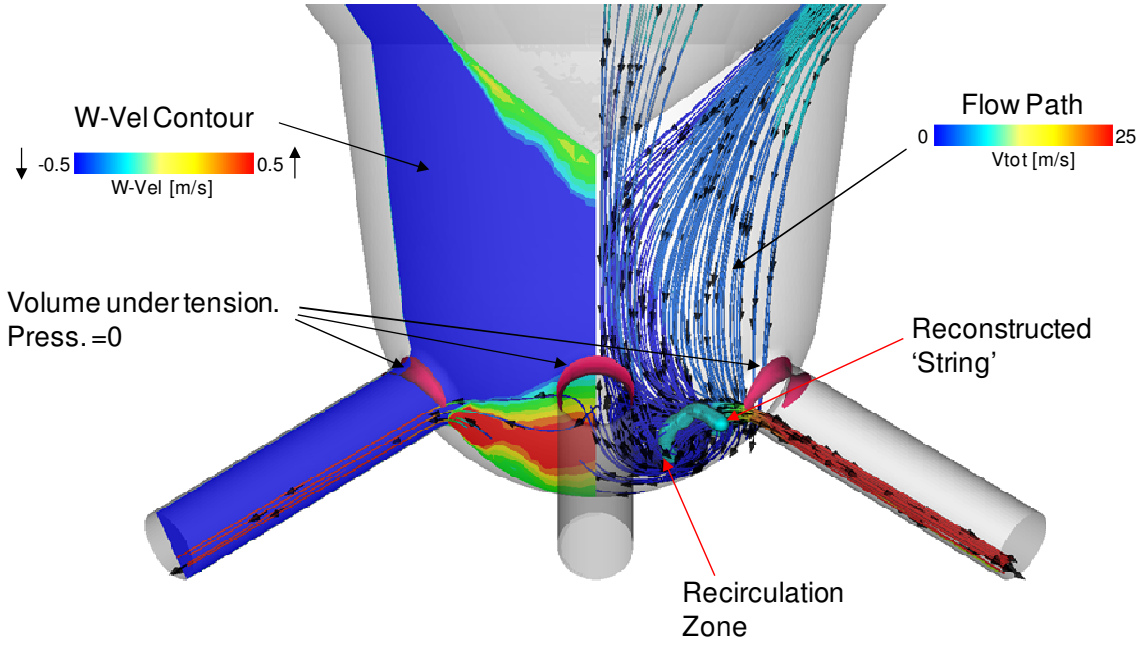

Figure 7-74: Predicted flow field inside sac-type nozzle with needle design I at 300µm equivalent needle lift along with a typical reconstructed string (cyan, side-view) and predicted regions of volume under tension (magenta) [CN: 15, RE: 67,100]

Similar to Figure 7-74, Figure 7-75 shows the front view of the reconstructed string. This time the flow lines, been coloured with total velocity, where chosen to initiate from the region of high swirl intensity. It is clear that all experimentally and numerically obtained vortical structures and string coincide. The string connects to adjacent holes and its shape and location matches with the regions that SEM images had shown to suffer from erosion in the VCO nozzle (Figure 7-7 (c))

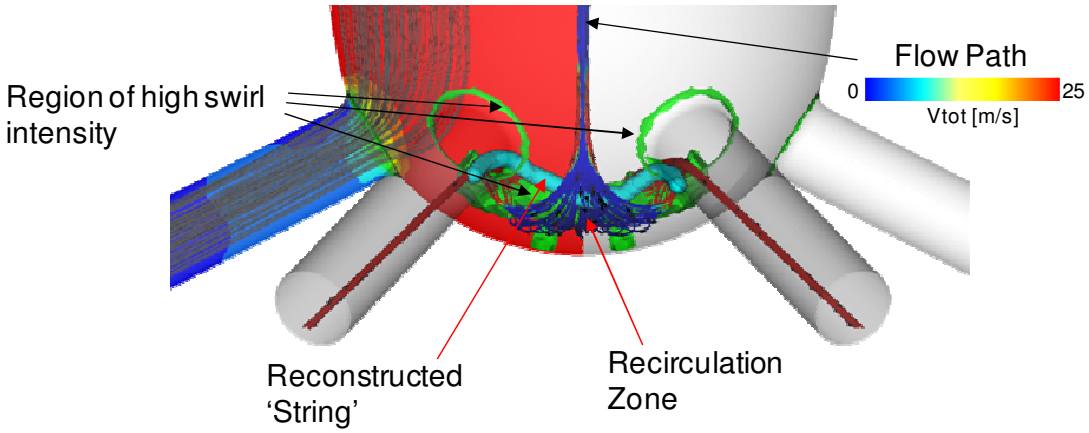

Figure 7-75: Predicted flow field inside sac-type nozzle with needle design I at 300µm equivalent needle lift along with a typical reconstructed string (cyan, front-view) and predicted regions of high swirl intensity (green) [CN: 15, RE: 67,100]

As previously show in Figure 7-62 the side camera was focusing between a set of adjacent holes. Performing 3-D reconstruction of string cavitation for a series of recorder bottom & side view images, for the same operating condition, and then inserting them in the simulated flow field results into Figure 7-76. In this case the design of the needle (IV) is such that at full lift the it is very close to the injection; almost inside the sac volume. This results into larger recirculation zones as suggested both by plotting the contour of axial velocity as well as the streamlines. As it can be seen for this particular case all strings related with the two visualized holes were reconstructed. Combining all the strings together will give the boundary inside which vortex cavitation can be formed for this particular operating conditions. The experimentally defined boundary superimposed on the predicted flow field can be found in Figure 7-77. As it can be seen the possibility to have a string formed is inside the core of the vortical flow. This concludes all the findings that have been shown so far and further supports the mechanism of vortex cavitation formation described in previous chapters.

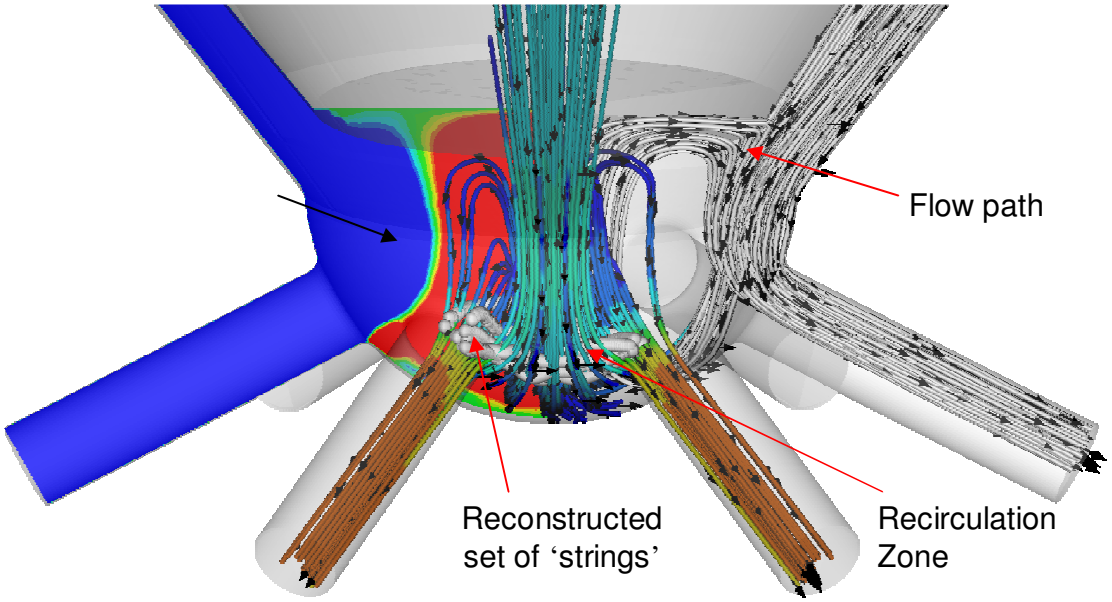

Figure 7-76: Predicted flow field inside sac-type nozzle with needle design IV at 300μm equivalent needle lift along with all reconstructed strings obtained between the monitored holes (gray, front-view) [CN: 15, Re: 62,200].

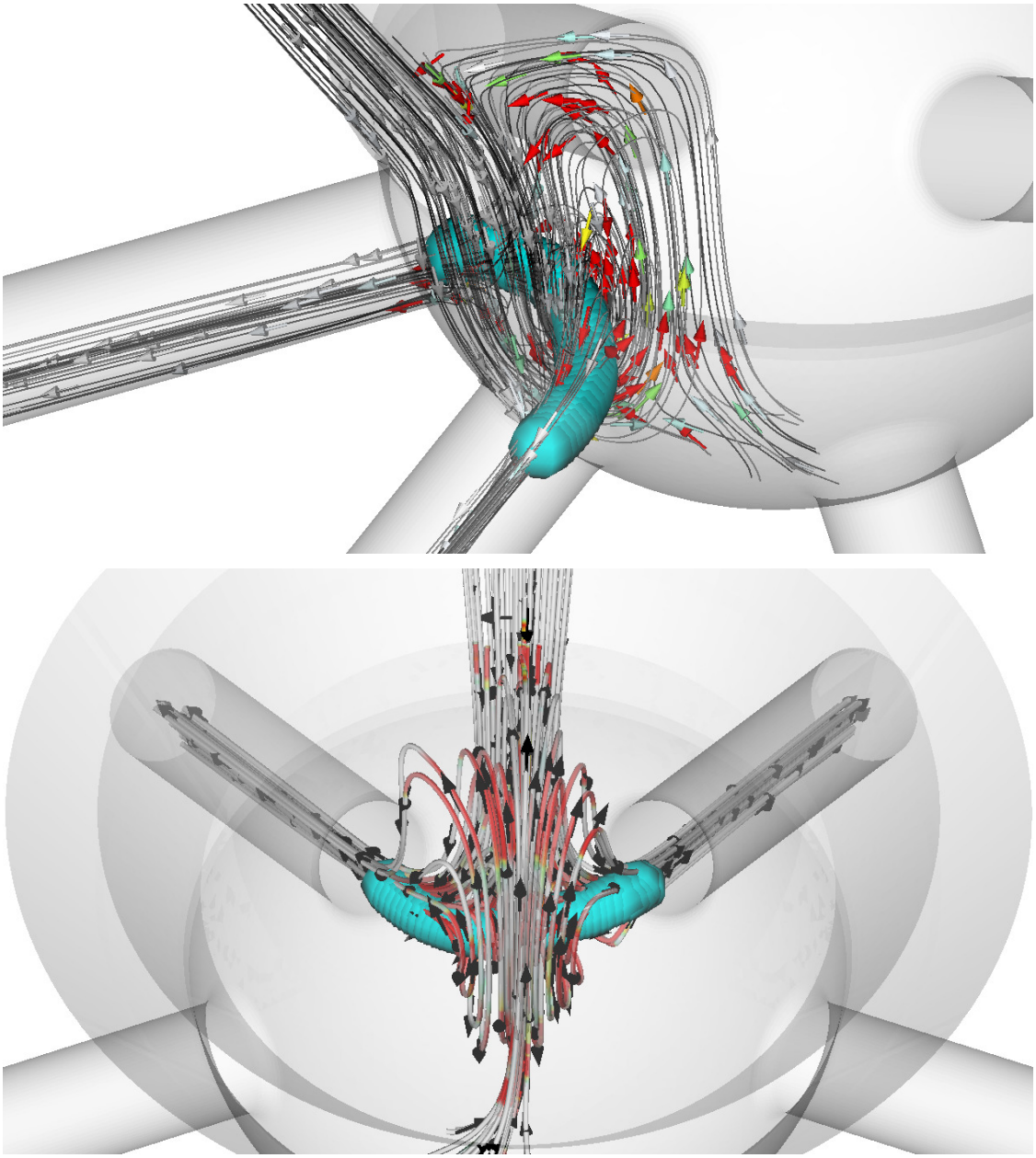

Figure 7-77: Predicted flow field inside sac-type nozzle with needle design IV at 300μm equivalent needle lift along with experimentally obtained boundary of string cavitation formation (cyan) [CN: 15, Re: 62,200].

7.6 Conclusions

In this chapter the results of the experimental investigation on the internal nozzle flow of multi-hole VCO and SAC type injectors were presented. String cavitation was identified in almost all investigated nozzles having both cylindrical and tapered, outwards converging, injection holes. A quantitative analysis was conducted in order to identify how flow parameter affect the geometric characteristics of string cavitation. It was found that as CN and Re number increase the strings become thicker and appear more frequently. The needle lift was also identified as a key parameter affecting string cavitation formation. For VCO nozzles low needle lifts resulted into higher probability of string formation due to the interaction of the needle being close to the injection hole inlet. For SAC type nozzles it was found that strings are formed between adjacent or even opposite holes and as before probability increases with CN and Re number. The SAC type was combined with different needle designs. The design of the needle affected the flow inside the nozzle sac volume and as a result the formation of strings. 3-D reconstruction of experimentally obtained strings and comparison with CFD predicted flow field showed that vortex cavitation is formed within the core of recirculation zones confirming the findings previously reported in Chapter 5 when considering marine nozzles. Furthermore, comparison of SEM images, showing damage at the inlet of the holes, with experimental findings identified string cavitation as a mechanism of erosion.

Apart from hole and string cavitation, inside the multi-hole mini-sac nozzles needle seat cavitation has been identified at low needle lifts due to the highly accelerated flow that the liquid is subjected. The intensity of needle seat cavitation was found to vary with CN number as well as with Re number. Higher CN and Re numbers produce more intense cavitation sites bubbles from which, for high CN numbers, can extend all the way to the sac volume and exit through the injection hole. For all needle designs tested, needle seat cavitation was extinct at lifts greater than 20 μm. An interesting feature of this form of cavitation was that at a critical condition of CN and Re numbers, where inception starts, the high fluctuating cavitation intensity can cause vibrations to the needle. Even more interestingly, comparison with SEM images of nozzle parts suggested that this form of cavitation can cause severe erosion at the area of needle seat within just a few hundred

operating hours. Finally, combining the simultaneously acquired side and bottom images of needle seat cavitation made possible reconstruction of its shape in the 3-D space. These experimentally identified vapour pockets were then inserted into the grid used with for numerical simulations. This analysis revealed that cavitation initiates within the boundary of the predicted volume under tension which is formed just downstream of the needle seat area.

Chapter 8
Conclusions & Recommendations for Future Work

The present Thesis has looked into various aspects of cavitation regimes used with marine, heavy duty and automotive Diesel injector nozzles. It has been performed in close links with major FIE manufacturers that require detailed knowledge of the flow phenomena taking place inside their injectors and the corresponding effects on the formed spray plumes; that represents the pre-requisite for the design of more sophisticated nozzles that will allow engines to meet future emission legislations.
As part of the work described in this Thesis, a number of phenomena have been thoroughly investigated in a wide range of nozzle geometries. The most important conclusions are summarised below, followed by recommendations for future work in this field.

8.1 Numerical investigation in marine nozzles

Numerical investigations were performed in both marine and multi-hole nozzles using the in house CFD code. The nozzles were examined under both real operational and experimental conditions. Comparison with experimental results for the same conditions revealed that internal nozzle flow and hole cavitation can be predicted accurately enough; that gives trust to model predictions for using it in other conditions. Particularly, for multi-hole nozzles it was found that apart from hole cavitation the code had also predicted needle seat cavitation. However, vortex or string cavitation can not at the time be predicted. On the other hand, the fact that the CFD code predicts the recirculation zones as well as their variation with time, it gives a good indication on where this dynamic form of cavitation may occur.

For the marine nozzles, a series of parametric studies were performed in order to become familiar with the special flow characteristics as well as with the factors affecting the predicted results. The needle geometry effect was investigated and it was found that it can

affect the inside nozzle flow structure significantly. Six new geometries were created and were compared with the standard nozzle design. Pressure values lower than the fluid's vapour pressure were at the bottom part of the hole inlet indicating the location of expected cavitation initiation. Differences in the flow rate and the mean exit velocity of individual injection holes were predicted; that indicates that under normal operating conditions some holes are over-fuelled and some are under-fuelled.

A large recirculation zone is formed inside the sac volume which indicates the possibility of vortex (string) cavitation to be present in the sac volume. Swirling motion inside the injection holes was identified with tangent velocities having magnitudes of 15%-20% of the corresponding axial velocity component.

The axial velocity profile at the hole exit plane is not symmetric which indicates that there might be a deviation from the designed injection direction. The hole interaction effect was investigated and it was found that when only one hole is allowed to inject, a portion of the flow is coming from the recirculation zone inside the sac volume even for holes that have never been associated with vortices in the sac volume. Moreover, the effect of hole length was investigated; it was found that, as the hole length increases, swirl is reduced and the velocity distribution at the hole exit plane becomes more uniform and symmetrical.

Finally the density of the grid was found to affect mostly the volume of the computational cells having pressure lower than the fluid's vapour pressure. Predictions obtained using the denser grid indicated presence of cavitation in all five holes, in line with experimental data. Moreover the grid size and different turbulence models gave similar results as far as recirculation zones and their location variation with time are concerned.

8.2 Internal nozzle flow patterns – Marine & Multi-hole nozzles

The main outcome from the experimental investigation on marine nozzles suggested that formation of cavitation strings is enhanced with increasing flow rate (and thus increasing cavitation number) while it is less sensitive to needle lift, although for multi-hole nozzles the effect can be significantly larger. Also clear evidence was provided that cavitation

strings may travel upstream the injection hole entry well inside the nozzle's sac volume but with a reduced frequency of appearance compared to their presence inside the injection hole. Moreover, interestingly enough, it was found that even when no existing vapour pockets exist inside the injection hole, the vortex can become strong enough to sac air from the injection hole exit, which then forms the same kind of string cavitation shape.

The present study has provided experimental data confirming the presence of string cavitation and addressing unresolved questions about its origin, area of formation, lifetime and influence on the nozzle hole flow. The visualization method employed has made simultaneous use of two high-speed cameras observing the two-phase flow structures forming inside transparent replicas of nozzles used in low-speed two-stroke Diesel engines. Interpretation of the obtained images has been assisted by computational fluid dynamics predictions of the nozzle and hole flow. The nozzle designs tested included both cylindrical and tapered holes operating at different fixed needle lift positions; nevertheless, the conclusions drawn for the observed flow mechanisms can be extrapolated to other nozzle designs where string cavitation is also present.

Images have revealed formation of an unsteady vapour structure upstream of the injection holes inside the nozzle volume, referred to as 'string cavitation'. From the images, it has been possible to reconstruct the location of the observed structures inside the nozzle volume. Combination of images with the simulated flow field has revealed that cavitation structures are found at the areas of flow circulation and they originate either from pre-existing cavitation sites forming at sharp corners inside the nozzle where the pressure falls below the vapour pressure of the flowing liquid, or even from suction of outside air downstream of the hole exit. This has been made possible by the manufacturing of nozzles with tapered holes which suppress the formation of geometric cavitation and thus have enabled data of string cavitation in controlled combination or in the absence of geometric cavitation to be obtained. Processing of the acquired images has allowed estimation of the mean location and probability of appearance of the cavitating strings inside the nozzle volume space, as a function of needle lift, cavitation and Reynolds numbers.

The frequency of appearance of strings has been correlated with the Strouhal number of the large-scale vortices developing inside the nozzle volume; the latter has been found to be

sensitive to the geometric characteristics of the nozzle, including the needle lift and the shape of the injection holes. Large variations in the instantaneous fuel injection quantity of individual injection holes have been recorded when a cavitation string is observed inside them. Combination with model predictions has revealed that the observed reduction in the individual hole flow rate is partially attributed to the increased vapour fraction inside the hole when a string is present; the vortex flow developing upstream of the hole entry is the main reason for the observed trend. Extrapolation based on model predictions for real-size injectors operating at realistic injection pressure indicates that cavitation strings are expected to appear within the time scales of typical injection events.

Finally, comparison of the location of experimentally identified strings with SEM images of the nozzles showed that hole-to-hole strings can cause erosion to the metal and severely damage the inlet of the injection hole.

8.3 Near hole exit spray characteristics

Effort has been made to investigate and quantify the role of nozzle flow and cavitation on the spray angle formed just at the exit of nozzle holes. For this reason, high speed visualisation has been performed in fully transparent replicas of nozzles used with low-speed two-stroke Diesel engines as well as multi-dimensional and multi-phase cavitating flow simulations have been used. The nozzles investigated incorporate one-, two- and five-hole designs with cylindrical as well as tapered-converging holes. Imaging has been performed simultaneously for the internal nozzle flow and the spray formed at the nozzle exit. The observed two-phase flow structures appear in two distinct forms, referred to as geometric-induced cavitation and dynamic or string cavitation.

Cylindrical holes induce geometric cavitation while tapered holes suppress it. String cavitation has been monitored in all nozzle types. Comparison of the obtained images between cylindrical and tapered nozzles in the absence of string cavitation has allowed the influence of geometric cavitation to be quantified, while acquisition of high-speed images has allowed for comparison between images in the absence and presence of cavitation strings to be made. The results indicate a significant increase in the spray angle in the

presence of cavitation strings which is more significant in the absence of geometric-cavitation. In addition, information has been provided for the variation of spray cone angle with time, expressed in terms of probability of finding dispersed liquid along the spray cone angle. In general increasing CN gives a wider spray angle. This was further explained by recording the spray angle of tapered nozzles that were hole cavitation free and had smaller dispersion. In addition, by recording the upper and lower spray angle for instances without string cavitation, it was clearly shown that the lower angle that was also emerging from the part of the hole mostly affected by hole cavitation was much wider than the upper were no bubbles were exiting. This unequal distribution of upper and lower angles results in an overall deflection of the emerging spray with respect to the geometric centreline defined by hole's direction.

The range of the formed spray angles have been found to follow a probability distribution function which is function of the nozzle design and the two-phase flow regime formed inside the nozzle hole for a given operating condition. Finally it was found that string cavitation entering in the an injection hole is not the only parameter to affect spray formation. It was concluded that the relative location of the string with hole cavitation can result to different effects on the spray cone angle; when a string is in the region that already hole cavitation exists the increase in spray cone angle is much smaller as when it is in a hole cavitation free region; this corresponds to the upper hole side for the marine nozzle.

8.4 Needle seat cavitation

Apart from hole and string cavitation, inside the multi-hole mini-sac nozzles needle seat cavitation has been identified. This type of cavitation is formed in the entire circumferential area of the needle seat (provided the needle is concentric and the flow fully developed) at low lifts; this is due to the highly accelerated flow that the liquid is subjected as it has to pass through a very narrow passage from the nozzle annulus towards the sac volume. The intensity of needle seat cavitation was found to vary with CN number as well as with Res number. Higher CN and Re numbers produce more intense cavitation sites bubbles from which, for high CN numbers, can extend all the way to the sac volume and exit through the injection hole; their presence has been found to enhance formation of hole cavitation. For

all needle designs tested, needle seat cavitation was extinct at lifts greater than 20 μm. An interesting feature of this form of cavitation was that at a critical condition of CN and Re numbers, where inception starts, the high fluctuating cavitation intensity can cause vibrations to the needle. Even more interestingly, comparison with SEM images of nozzle parts suggested that this form of cavitation can cause severe erosion at the area of needle seat within just a few hundred operating hours despite the fact that the needle stays at low lifts only for a small fraction of the whole injection period. Finally, by combining the simultaneously acquired side and bottom images of needle seat cavitation, reconstruction of its shape in the 3-D space has been made possible. These experimentally identified vapour pockets were then inserted into the grid used with for numerical simulations. This analysis revealed that cavitation initiates within the boundary of the predicted volume under tension which is formed just downstream but in the proximity of the needle seat area.

8.5 Recommendations for future work

Although this study provides useful conclusions on the understanding of string cavitation and its effects, the mechanism of its formation has to be better identified. Also, the fact that vortex location inside the sac volume varies with time and affects the individual flow rate of the injection holes also has to be quantified with higher precision. For future work, there could have been a more sophisticated rig with extremely fast pressure and flow transducers able to capture in real time and in combination with a high speed imaging system the flow rate of each hole, the pressure in the sac volume, in various location of interest, and the cavitation structure inside the sac volume as well as the injection holes. Having all this information combined and synchronized would give the answers in order to further understand how strings are formed.

Moreover the vortex core in flows that strings are known to be formed has to be identified before air bubbles be sucked into the nozzle hole. The intensity of the vortical flow has to be identified by using LDV, PIV or a similar non-invasive flow measurement technique. This will give an indication of the local pressure values and will allow more accurate comparison with numerical predicted results. Then it will be possible to assist towards the development and experimental validation of a new model able to predict string cavitation.

In the area of spray structure investigation, it would have been interesting to perform spray momentum calculations in order to capture the 3-D distribution of the emerged liquid. At the moment, using high speed imaging, made possible to distinguish the spray cone angle in a 2-D plane. As we have seen, string cavitation results into a hollow spray cone. However, this was only a qualitative conclusion that was drawn by observing the different light absorption on the spray. Having a more quantitative approach would enable to make more accurate spray models in order to improve the understanding on the atomization process and how is affected by internal nozzle flow and cavitation regimes.

Finally, it would have been interesting if more detailed investigations were done to explore the link between needle seat cavitation and erosion. Since needle seat cavitation occurs only in low lifts and given that erosion problems are reported after some hundred hours of operation, a large-scale model been able to operate steadily in low lifts would have been preferable. Then by applying special coatings, on both the needle and the nozzle body, that become detached when subjected to forces generated from bubble break-up, would enable to investigate and correlate how this form of cavitation may affect the real injector. Similar studies have been done with propellers but till now research on FIE is limited. Having a steady state rig, it will make possible to investigate how different levels of impurities in the fuel, different liquid temperatures and different surface roughness affect erosion process. It is worth mentioning that marine engines burn HFO which has high concentration of solids and metals and it can be predicted that such characteristics may accelerate the damage on the nozzle. Therefore, it is worth to be able to design nozzles that will be able to operate for prolonged periods without suffering from erosion.

References

1. European Environment Agency, *Greenhouse gas emission trends and projections in Europe 2007*. EEA Report, 2007. 5/2007.

2. Agency., E.E., *Greenhouse gas emission trends and projections in Europe 2007*. EEA Report, 2007. 5/2007.

3. Κυρτάτος, Ν.Π., *ΝΑΥΤΙΚΟΙ ΚΙΝΗΤΗΡΕΣ ΚΑΙ ΑΤΜΟΣΦΑΙΡΙΚΗ ΡΥΠΑΝΣΗ-ΝΟΜΟΘΕΣΙΑ, ΤΕΧΝΟΛΟΓΙΕΣ, ΠΡΟΟΠΤΙΚΕΣ*. 2007.

4. Essen, H.V., O. Bello, J. Dings, and R. Brink, *To shift or not to shift*. CE Delft, 2003.

5. The Danish Maritime Museum, *Online Internet Resources*, in www.maritime-museum.dk. 2008, Danish Maritime Museum, Elsinore, Denmark.

6. Roth, H., *Experimental and Computational Investigation of Cavitation in Diesel Injector Nozzles*. Imperial College, 2004. PhD Thesis.

7. Diesel, E., *Die erste Zündung*. 1939/41, Hamburg: Hanseatische Verlagsanstalt.

8. Diesel, E., *Die Geschichte des Diesel-Personenwagens*. 1955, Stuttgart: Deutsche Verlags-Anstalt.

9. Heywood, J.B., *Internal Combustion Engine Fundamentals*. 1988, New York: McGraw-Hill Book Company.

10. MAN B&W Diesel A/S, *K 98 MC-C Project Guide, Two-Stroke Engines*. 2nd ed. December 1999.

11. Brennen, C.E., *Cavitation and Bubble Dynamics*. 1995, New York; Oxford: Oxford University Press.

12. Knapp, R.T., J.W. Daily, and F.G. Hammitt, *Cavitation*. 1970, New York; London: McGraw-Hill.

13. Pearsall, I.S., *Cavitation*. 1972, London: Mills & Boon Limited.

14. Young, F.R., *Cavitation*. 1989, London: McGraw-Hill.

15. Wang, Y.-C., *Effects of Nuclei Size Distribution on the Dynamics of a Spherical Cloud of Cavitation Bubbles*. Journal of Fluids Engineering - Transactions of the ASME, 1999. 121(4): p. 881-886.

16. Reisman, G.E., J. Wang, and C.E. Brennen, *Observations of shock waves in cloud cavitation*. Journal of Fluid Mechanics, 1998: p. 355: pp. 255-283.

17. Mørch, K.A., *Cavitation nuclei and bubble formation - A dynamic liquid-solid interface problem.* Journal of Fluids Engineering-Transactions of the ASME, 2000: p. 122(3): pp. 494-498.

18. Zhen, H., S. Yiming, S. Shiga, H. Nakamura, and T. Karasawa, *The Orifice Flow Pattern, Pressure Characteristics, and Their Effects on the Atomization of Fuel Containing Dissolved Gas.* Atomization and Sprays, 1994. 4(2): p. 123-133.

19. Arcoumanis, C., M. Gavaises, and V. French, *Effects of Fuel Injection Processes on the Structure of Diesel Sprays.* SAE Paper 970799, 1997.

20. He, L. and F. Ruiz, *Effect of cavitation on flow and turbulence in plain orifices for high-speed atomization.* Atomization and Sprays, 1995. 5(6): p. 569-584.

21. Soteriou, C., M. Smith, and R.J. Andrews, *Diesel Injection - Laser Light Sheet Illumination of the Development of Cavitation in Orifices.* IMechE Paper C529/018/98, 1998.

22. Arcoumanis, C., M. Gavaises, J.M. Nouri, E. Abdul-Wahab, and R.W. Horrocks, *Analysis of the Flow in the Nozzle of a Vertical Multi Hole Diesel Engine Injector.* SAE Transactions Journal of Engines, 980811, 1998. 107-3.

23. Andriotis, A., M. Gavaises, and C. Arcoumanis, *Vortex flow and cavitation in diesel injector nozzles.* null, 2008. 610(-1): p. 195-215.

24. Andriotis, A. and M. Gavaises, *Visualization of String Cavitation Formation and Development inside Transparent Diesel Injector Nozzle Replicas.* in 22nd Conference on Liquid Atomization and Spray Systems (ILASS-Europe). 2008.

25. Gavaises, M., A. Andriotis, D. Papoulias, N. Mitroglou, and A. Theodorakakos, *Characterization of string cavitation in large-scale Diesel nozzles with tapered holes.* Physics of Fluids, 2009. 21(5): p. 052107.

26. Lefebvre, A.H., *Atomization and Sprays*. Combustion: An International Series. 1989: Hemisphere Publishing Corporation.

27. Arcoumanis, C., J.M. Nouri, and R.J. Andrews. *Application of Refractive Index Matching to a Diesel Nozzle Internal Flow*. in *Proc. IMechE Seminar on Diesel Fuel Injection Systems*. 1992, April 14-15. London, UK.

28. Soteriou, C., M. Smith, and R.J. Andrews, *Cavitation Hydraulic Flip and Atomization in Direct Injection Diesel Sprays.* IMechE Paper C465/051/93, 1993.

29. Yule, A.J., A.M. Dalli, and K.B. Yeong. *Transient Cavitation and Separation in a Scaled-Up Model of a VCO Orifice*. in *Proc. ILASS-EUROPE*. 1998, July 6-8. Manchester, UK.

30. Afzal, H., C. Arcoumanis, M. Gavaises, and N. Kampanis, *Internal Flow in Diesel Injector Nozzles: Modelling and Experiments.* IMechE Paper S492/S2/99, 1999.

31. Soteriou, C., R. Andrews, M. Smith, N. Torres, and S. Sankhalpara, *The Flow Patterns and Sprays of Variable Orifice Nozzle Geometries for Diesel Injection.* SAE Paper 2000-01-0943, 2000.

32. Roth, H., M. Gavaises, and C. Arcoumanis, *Cavitation Initiation, Its Development and Link with Flow Turbulence in Diesel Injector Nozzles.* SAE Transactions Journal of Engines, 2002-01-0214, 2002. 111-3: p. 561-580.

33. Scholz, J., K. Roetmann and V. Beushausen, *Influence of the internal flow conditions of slit nozzles on the stability of liquid sheets: Experimental results.* ICLASS 2003, 2003.

34. Nouri, J.M., E. Abo-Serie, A. Marchi, N. Mitroglou and C. Arcoumanis, *Internal and near nozzle flow characteristics from an enlarged model of an outward opening gasoline direct injector.* international Conference on Optical and Laser Diagnostics, 2005.

35. Sou, A., S. Hosokawa, A. Tomiyama, *Effects of cavitation in a nozzle on liquid jet atomization.* International Journal of Heat and Mass Transfer 50 (2007) 3575–3582, 2007.

36. Stegemann, J., J. Seebode, J. Baltes, C. Baumgarten, and G.P. Merker, *Influence of throttle effects at the needle seat on the spray characteristics of a multihole injection nozzle.* ILASS Europe, 2002.

37. Blessing, M., G. König, C. Krüger, U. Michels, and V. Schwarz, *Analysis of Flow and Cavitation Phenomena in Diesel Injection Nozzles and its Effect on Spray and Mixture Formation.* SAE Paper 2003-01-1358, 2003.

38. Arcoumanis, C., M. Gavaises, H. Flora, and H. Roth, *Visualisation of Cavitation in Diesel Engine Injectors.* Mécanique & Industries, 2001. 2(5): p. 375-381.

39. Karimi, K., *Characterisation of Multiple-Injection Diesel Sprays at Elevated Pressures and Temperatures. PhD Thesis*, in *School of Engineering*. 2007, University of Brighton in collaboration with Ricardo UK.

40. Bae, C.H. and J. Kang, *Diesel spray characterisation of common-rail VCO nozzle injector.* THIESEL 2000. Thermofluidynamic Processes in Diesel Engine, 2000.

41. Kim, J.H., K. Nishida, and H. Hiroyasu. *Characteristics of Internal Flow in a Diesel Injection Nozzle*. in *Proc. ICLASS*. 1997, August 18-22. Seul, Korea.

42. Spathopoulou, M., D. Papoulias, E. Giannadakis, M. Gavaises, and A. Theodorakakos, *Influence of the Spatially Resolved Nozzle Hole Exit Flow Distribution on Diesel Spray Development.* SAE Paper 2007-24-0025, Proc. 7th International Conference ICE2007 Internal Combustion Engines: Experiments and Modelling, Capri, Italy, Sept 17-20, 2007.

43. McGeogh, J., A.,, *Principles of Electrochemical Machining*. 1974, London: Chapman and Hall.

44. Rajurkar, K., P., *Electrochemical Machining*, in http://www.unl.edu/nmrc. 2003, University of Nebraska-Lincoln, Center for Non Traditional Manufacturing Research

45. Potz, D., W. Christ, and B. Dittus, *Diesel nozzle – The determining interface between injection system and combustion chamber.* ThieseL 2000, Valencia, Spain, 13-15 September, 2000.

46. Blessing, M., König, G, Krüger, C, Michels, U, Schwarz, V, *Analysis of Flow and Cavitation Phenomena in Diesel Injection Nozzles and its Effect on Spray and Mixture Formation.* SAE Paper 2003-01-1358, 2003.

47. Bae, C.H., J. Yu, J. Kang, J. Kong, and K.O. Lee, *Effect of nozzle geometry on the common-rail diesel sprays.* SAE Paper 2002-01-1626, 2002.

48. Baumgarten, C., *Mixture Formation in Internal Combustion Engines*. Heat and Mass Transfer. 2006: Springer.

49. Hsiao, C.-T., G.L. Chahine, and H.-L. Liu, *Scaling Effect on Bubble Dynamics in a Tip Vortex Flow: Prediction of Cavitation Inception and Noise*. 2000, Report 98007-1, Dynaflow Inc.

50. Arndt, R.E.A., *Cavitation if fluid machinery and hydraulic structures.* Annual review of fluid mechanics, 1981. 13: p. 273-328.

51. Ipp, W., V. Wagner, H. Kraemer, M. Wensing, A. Leipertz, S. Arndt, and A.K. Jain, *Spray Formation of High Pressure Swirl Gasoline Injectors Investigated by Two-Dimensional Mie and LIEF Techniques.* SAE 1999-01-0498, 1999.

52. Arndt, R.E.A., *Cavitation in vortical flows.* Annual review of fluid mechanics, 2002. 34: p. 143-175.

53. Batchelor, G.K., *The Theory of Homogeneous Turbulence*. 1953, Cambridge: Cambridge University Press.

54. Saffman, P.G., *Vortex Dynamics*. Cambridge publications, 1992.

55. Gilles-Birth, I., M. Rechns, U. Spicher, and S. Bernhardt, *Experimental investigation of the in-nozzle flow of valve covered orifice nozzles for gasoline direct injection.* Proceedings 7th International Symposium on Internal Combustion Diagnostics, 18-19 May, Kurhaus Baden-Baden, Germany, 2006.

56. Gavaises, M. and A. Andriotis, *Cavitation Inside Multi-hole Injectors for Large Diesel Engines and its Effect on the Near-nozzle Spray Structure.* SAE Transactions Journal of Engines, 2006-01-1114, 2006. 115-3: p. 634-647.

57. Nouri, J.M., N. Mitroglou, You You Yan, and C. Arcoumanis, *Internal Flow and Cavitation in a Multi-hole Injector for Gasoline Direct-Injection Engines.* SAE Paper 2007-01-1405, 2007.

58. Grogger, H.A. and A. Alajbegovic. *Calculation of the Cavitating Flow in Venturi Geometries using Two Fluid Model*. in *Proc. of FEDSM'98 - 1998 ASME Fluid Engineering Division Summer Meeting*. 1998. Washington, D.C., USA.

59. Marcer, R. and J.M. LeGouez. *Simulation of Unsteady Cavitating Flows in Diesel Injector with an Improved VOF Method*. in *Proc. ILASS-EUROPE*. 2001. Zurich, Switzerland.

60. Schmidt, D.P., C.J. Rutland, and M.L. Corradini, *A Fully Compressible, Two-Dimensional Model of Small, High-Speed Cavitating Nozzles.* Atomization and Sprays, 1999. 9(3): p. 255-276.

61. Singhal, A.K., M.M. Athavale, H.Y. Li, and Y. Jiang, *Mathematical basis and validation of the full cavitation model.* Journal of Fluids Engineering-Transactions of the ASME, 2002. 124(3): p. 617-624.

62. Giannadakis, E., *Modelling of Cavitation in Automotive Fuel Injector Nozzles*. 2005, PhD Thesis, Imperial College, University of London.

63. Fujikawa, S. and T. Akamatsu, *Effects of the non-equilibrium condensation of vapour on the pressure wave produced by the collapse of a bubble in a liquid.* Journal of Fluid Mechanics, 1980. 97(3): p. 481-512.

64. Momma, T. and A. Lichtarowicz, *A Study of Pressures and Erosion Produced by Collapsing Cavitation.* Wear, 1995. 186(2): p. 425-436.

65. Kimoto H. *An experimental evaluation of the effects of a water microjet and a shock wave by a local pressure sensor*. in *International ASME Symposium on Cavitation Research Facilities and Techniques*. 1987. FED 57, 217–224.

66. SAMSON AG, *Cavitation in Control Valves - L351*. 2003.

67. Okada, T., Y. Iwai, S. Hattori, and N. Tanimura, *Relation between Impact Load and the Damage Produced by Cavitation Bubble Collapse*. Wear, 1995. 184(2): p. 231-239.

68. Dular, M., B. Bachert, B. Stoffel, and B. Sirok, *Relationship between cavitation structures and cavitation damage*. Wear, 2004. 257(11): p. 1176-1184.

69. Bachert B., Stoffel B., Ludwig G., and Baumgarten S. *Comparison of Different Methods for the Evaluation of Cavitation Damaged Surfaces*. in *Proceedings of FEDSM2005*. 2005. Houston, TX, USA.

70. Arcoumanis, C., M. Badami, H. Flora and M. Gavaises, *Cavitation in Real-Size Multi-Hole Diesel Injector Nozzles.* SAE Paper 2000-01-1249, 2000.

71. Roth, H., M. Gavaises, and C. Arcoumanis, *Cavitation Initiation, Its Development and Link with Flow Turbulence in Diesel Injector Nozzles.* SAE Paper 2002-01-0214, 2002.

72. Asi, O., *Failure of a diesel engine injector nozzle by cavitation damage.* Engineering Failure Analysis, 2006. 13(7): p. 1126-1133.

73. Escaler, X., P. Dupont, and F. Avellan, *Experimental investigation on forces due to vortex cavitation collapse for different materials.* Wear, 1999. 235: p. 65-74.

74. Hattori, S., R. Ishikura, and Q.L. Zhang, *Construction of database on cavitation erosion and analyses of carbon steel data.* Wear, 2004. 257(9-10): p. 1022-1029.

75. Smith, R.L. and G.E. Sandland, *An Accurate Method of Determining the Hardness of Metals, with Particular Reference to Those of a High Degree of Hardness. Proceedings of the Institution of Mechanical Engineers*, 1922. Vol. I: p. p 623-641.

76. Chen, W.G., C.Q. Gu, K. Zhao, and F.S. Shen, *Correlation of cavitation erosion resistance and mechanical properties of some engineering steels.* Journal of Materials Science, 2006. 41(7): p. 2151-2153.

77. Steller, J., A. Krella, J. Koronowicz, and W. Janicki, *Towards quantitative assessment of material resistance to cavitation erosion.* Wear, 2005. 258(1-4): p. 604-613.

78. Bregliozzi, G., A. Di Schino, S.I.U. Ahmed, J.M. Kenny, and H. Haefke, *Cavitation wear behaviour of austenitic stainless steels with different grain sizes.* Wear, 2005. 258(1-4): p. 503-510.

79. Krella, A. and A. Czyzniewski, *Cavitation erosion resistance of Cr-N coating deposited on stainless steel.* Wear, 2006. 260(11-12): p. 1324-1332.

80. Hattori, S., Y. Goto, and T. Fukuyama, *Influence of temperature on erosion by a cavitating liquid jet.* Wear, 2006. 260(11-12): p. 1217-1223.

81. Payri, R., J.M. García, F.J. Salvador, and J. Gimeno, *Using spray momentum flux measurements to understand the influence of diesel nozzle geometry on spray characteristics.* 2005. 84: p. 551-561.

82. Soteriou, C., R.J. Andrews, and M. Smith, *Direct Injection Diesel Sprays and the Effect of Cavitation and Hydraulic Flip on Atomization.* SAE Paper 950080, 1995.

83. Payri, R., A. Gil, A.H. Plazas, and B. Gimenez, *Influence of Nozzle Seat Type on Internal Flow of Convergent Nozzles.* SAE Paper 2004-01-2010, 2004.

84. Smallwood, G.J. and O.L. Gulder, *Views on the structure of transient diesel sprays.* Atomization and Sprays, 2000. 10(3-5): p. 355-386.

85. Tamaki, N., M. Shimizu, and H. Hiroyasu. *Enhanced Atomization of a Liquid Jet by Cavitation in a Nozzle Hole*. in *Proc. ICLASS*. 2000, July 16-20. Pasadena, CA, USA.

86. Tamaki, N., M. Shimizu, and H. Hiroyasu, *Enhancement of the atomization of a liquid jet by cavitation in a nozzle hole.* Atomization and Sprays, 2001. 11(2): p. 125-137.

87. Stepowski, D. and O. Werquin, *Measurement of the liquid volume fraction and its statistical distribution in the near development field of a spray*. Atomization and Sprays, 2004. 14(3).

88. Paciaroni, M., M. Linne, T. Hall, J.-P. Delplanque, and T. Parker, *Single-shot two-dimensional ballistic imaging of the liquid core in an atomizing spray.* Atomization and Sprays, 2006. 16(1): p. 51-70.

89. Desantes, J., R. Payri, J. Pastor, and J. Gimeno, *Experimental characterization of internal nozzle flow and Diesel spray behavior. Part I: non-evaporative conditions.* Atomization and Sprays, 2005. 15(5).

90. Kyubok Ahn, Junghoon Kim, and Youngbin Yoon, *Effects of orifice internal flow on transverse injection into subsonic crossflows: cavitation and hydraulic flip.* Atomization and Sprays, 2006. 16(1): p. 15-34.

91. Tanner, F., Feigl K.A., S.A. Ciatti, C.F. Poweel, Cheong S.K, J. Liu, and J. Wang, *Structure of High Velocity Dense Sprays in the Near Nozzle Region.* Atomization and Sprays, 2006. 16: p. 579-597.

92. Yong Yue, Christopher Powell, Ramesh Poola, Jin Wang, and Johannes Schaller, *Quantitative measurements of Diesel fuel spray characteristics in the near-nozzle region using x-ray absorption*. 13th International Multidimensional Engine Modeling User's Group Meeting, Detroit, MI., pp. 1-6, March 2, 2001. 11(4).

93. Reitz, R.D. and F.V. Bracco, *Mechanism of Atomization of a Liquid Jet.* Physics of Fluids, 1982. 25(10): p. 1730-1742.

94. Huh, K.Y., E.J. Lee, and J.Y. Koo, *Diesel spray atomization model considering nozzle exit turbulence conditions.* Atomization and Sprays, 1998. 8(4): p. 453-469.

95. Soteriou, C., R. Andrews, and M. Smith, *Further Studies of Cavitation and Atomization in Diesel Injection.* SAE Paper 1999-01-1486, 1999.

96. Chaves, H., M. Knapp, A. Kubitzek, and F. Obermeier, *Experimental Study of Cavitation in the Nozzle Hole of Diesel Injectors Using Transparent Nozzles.* SAE Paper 950290, 1995.

97. Chaves, H., C. Kirmse, and F. Obermeier. *The Influence of Nozzle Inlet Curvature on Unsteady Cavitation in Transparent Diesel Injection Nozzles*. in *1st International Colloquium on Microhydrodynamics*. 2000. Paris, France.

98. Badock, C., R. Wirth, S. Kampmann, and C. Tropea. *Fundamental Study of the Influence of Cavitation on the Internal Flow and Atomization of Diesel Sprays*. in *Proc. ILASS-EUROPE*. 1997, July 8-10. Florence, Italy.

99. Badock, C., R. Wirth, A. Fath, and A. Leipertz, *Investigation of cavitation in real size diesel injection nozzles.* International Journal of Heat and Fluid Flow, 1999. 20(5): p. 538-544.

100. Feng Li-yan, Long Wu-qiang, Du Bao-gu, Tian Hua, and Obokata Tomio, *Experimental research on spray and combustion characteristics of the third generation conical spray* Journal of Marine Science and Application, 2005. 4(1): p. 44-49.

101. Soteriou C, Lambert M, Zuelch S, and Passerel D, *The flow characteristics of high efficiency Diesel nozzles with enhanced geometry holes.* Proc. THIESEL International Conference on Thermo- and Fluid Dynamic Processes in Diesel Engines. Valencia, Spain, 2006.

102. Nouri J.M, Mitroglou N, You You Yan, and Arcoumanis C, *Internal Flow and Cavitation in a Multi-hole Injector for Gasoline Direct-Injection Engines.* SAE 2007-01-1405, 2007.

103. Arcoumanis, C., M. Badami, H. Flora, and M. Gavaises, *Cavitation in Real-Size Multi-Hole Diesel Injector Nozzles.* SAE Transactions Journal of Engines, 2000-01-1249, 2000. 109-3.

104. Roth, H., E. Giannadakis, M. Gavaises, C. Arcoumanis, K. Omae, I. Sakata, M. Nakamura, and H. Yanagihara, *Effect of Multi-Injection Strategy on Cavitation Development in Diesel Injector Nozzle Holes.* SAE Transactions Journal of Engines, 2005-02-1237, 2005. 114-3: p. 1029-1045.

105. Soteriou, C., R.J. Andrews, N. Torres, M. Smith, and R. Kunkulagunta. *Through the Diesel Nozzle Hole - A Journey of Discovery II.* in *Proc. ILASS-Europe*. 2001. Zurich, Switzerland.

106. Bergwerk, W., *Flow Pattern in Diesel Nozzle Spray Holes.* Proceedings of the Institution of Mechanical Engineers, 1959: p. 173(25): pp. 655-660.

107. Spikes, R.H. and G.A. Pennington, *Discharge Coefficient of Small Submerged Orifices.* Proc. Inst. Mech. Engrs., 1959. 173(25): p. 661-665.

108. Nurick, W.H., *Orifice Cavitation and its effects on spray Mixing.* Journa of Fluids Engineering, 1976: p. 98: pp. 681-687.

109. Chaves, H. and F. Obermeier. *Correlation between Light Absorption Signals of Cavitating Nozzle Flow within and outside of the Hole of a Transparent Diesel Injection Nozzle*. in *Proc. ILASS-EUROPE*. 1998. Manchester, UK.

110. Gilles-Birth I, Rechns M, Spicher U, and Bernhardt S, *Experimental investigation of the in-nozzle flow of valve covered orifice nozzles for gasoline direct injection.* Proceedings 7th International Symposium on Internal Combustion Diagnostics, 18-19 May, Kurhaus Baden-Baden, Germany, 2006.

111. Chahine, G.L. and R. Duraiswami, *Dynamical Interactions in a Multi-Bubble Cloud.* Journal of Fluids Engineering - Transactions of the ASME, 1992. 114(4): p. 680-686.

112. Chahine, G.L. and K.M. Kalumuck. *Simulation of Surface Piercing Body Coupled Response to Underwater Bubble Dynamics Utilizing 3DYNAFS, a Three-Dimensional BEM Code*. in *Proc. IABEM 2002 - International Association for Boundary Element Methods*. 2002. Austin, Texas, USA.

113. Andriotis, A., M. Spathopoulou, and M. Gavaises, *Effect of Nozzle Flow and Cavitation Structures on Spray Development in Low-speed Two-Stroke Diesel Engines.* Proceedings CIMAC 2007, Vienna, May 2007, 2007.

114. Roth, H., *Experimental and Computational Investigation of Cavitation in Diesel Injector Nozzles. PhD Thesis*. 2004, Imperial College, University of London.

115. Mitroglou, N., *Multihole Injectors for Direct-Injection Gasoline Engines. PhD Thesis*, in *School of Engineering and Mathematical Sciences*. 2006, City University London.

116. Kampanis, N., *Flow, Mixture Distribution and Combustion in Five-Valve Gasoline Engines.* Imperial College, 2003. PhD Thesis.

117. Giannadakis, E., *Modelling of Cavitation in Automotive Fuel Injector Nozzles. PhD Thesis*. 2005, Imperial College, University of London.

118. Badock, C., R. Wirth, and C. Tropea. *The Influence of Hydro Grinding on Cavitation inside a Diesel Injection Nozzle and Primary Break-Up under Unsteady Pressure Conditions*. in *Proc. ILASS-EUROPE*. 1999, July 5-7. Toulouse, France.

119. Photron, Photron USA Inc (www.photron.com), San Diego, USA.

120. PCO, PCO AG (www.pco.de), Kehlheim, Germany.

121. Matlab, *Matlab R2006a*. 2006, The MathWorks Ltd.

122. Berckmueller, M., *A Study of Mixture Formation in a Lean Burn Research Engine Using Laser Fluorescence Imaging, in Mechanical Engineering Department.* Cranfield University, Bedfordshire, 1999.

123. Berckmueller, M., N.P. Tait, R.D. Lockett, D.A.-C.U. Greenhalgh, K. Ishii, Y. Urata, H. Umiyama, and K.-H.R.D.C.L. Yoshida, *In-Cylinder Crank-Angle-Resolved Imaging of Fuel Concentration in a Firing Spark-Ignition Engine Using Planar Laser-Induced Fluorescence.* The Combustion Institute, 25th International Symposium on Combustion, 1994, 1994: p. 151-156.

124. Gonzales, R.C., R. E. Woods and S. L. Eddins, *Digital Image Processing Using MATLAB* 1st ed. 2004, Upper Saddle River, New Jersey: Pearson Prentice Hall.

125. LookCFD, *LookCFD v1.0 Scientific Visualization*. 2007, www.lookcfd.com.

126. Tecplot, *Tecplot 360*. 2006, Tecplot Inc.

127. Goudanis, S., *Post GFS*. 2005, Fluid Research.

128. Fluent Inc., *GAMBIT 2.3.**.* 1988-2008, ANSYS Inc.: Pennsylvania, USA.

129. Ferziger, J.H. and M. Peric, *Computational Methods for Fluid Dynamics*. 2nd ed. ed. 1996, Berlin Heidelberg: Springer-Verlag.

130. Perry, R.H. and D.W. Green, *Perry's Chemical Engineers' Handbook*. 7th ed. ed. 1998: McGRAW-HILL.

131. Arcoumanis, C., Flora, Gavaises, M Kampanis, N, *Investigation of Cavitation in a Vertical Multi-Hole Injector.* SAE Paper 1999-01-0524, 1999.

132. Badock, C., Wirth, R, Fath, A, Leipertz, A. *Application of Laser Light Sheet Technique for the Investigation of Cavitation Phenomena in Real Size Diesel Injection Nozzles*. in *Proc. ILASS-EUROPE*. 1998, July 6-8. Manchester, UK.

133. Goney, K.H.a.M.L.C., Isolated Effects of Ambient Pressure, Nozzle Cavitation, and Hole Inlet Geometry on, *Isolated Effects of Ambient Pressure, Nozzle Cavitation, and Hole Inlet Geometry on Diesel Injection Spray Characteristics.* SAE Paper 2000-01-2043, 2000.

134. Bosch, Robert Bosch GmbH (FV/SLE), Stuttgart, Germany.

135. Salvador, F.J., Desantes J.M, Payri. R and Gimeno. J, *Measurements of Spray Momentum for the Study of Cavitation in Diesel Injection Nozzles.* SAE Paper 2003-01-0703, 2003.

136. Payri, R., X. Margot, and F.J. Salvador, *A Numerical Study of the Influence of Diesel Nozzle Geometry on the Inner Cavitating Flow.* SAE Paper 2002-01-0215, 2002.

137. Jeong, J. and F. Hussain, *On the identification of a vortex.* Journal of Fluid Mechanics, 1995. 285: p. 69-94.

138. Launder, B.E. and S. D.B, *The Numerical Computation of Turbulent Flows.* Computer Methods in Applied Mechanics and Engineering, 1974. 3: pp. 269-289.

139. Yakhot, V., S.A. Orszag, S. Thangam, T.B. Gatski, and C.G. Speziale, *Development of turbulence models for shear flows by a double expansion technique.* Physics of Fluids A, 1992. 4(7): p. 1510-1520.

140. Shyy, W., S. Thakur, H. Ouyang, J. Liu, and E. Blosch, *Computational Techniques for Complex Transport Phenomena*. 1997, New York: Cambridge University Press.

141. Yuan, W., J. Sauer, and G.H. Schnerr. *Modeling and Computation of Unsteady Cavitation Flows in Injection Nozzles*. in *1st International Colloquium on Microhydrodynamics*. 2000. Paris, France.

142. Giannadakis, E., M. Gavaises, H. Roth, and C. Arcoumanis. *Cavitation Modelling in Single-Hole Diesel Injector Based on Eulerian-Lagrangian Approach*. in *Proc. THIESEL International Conference on Thermo- and Fluid Dynamic Processes in Diesel Engines*. 2004, September 8-10. Valencia, Spain.

143. Tonini, S., *Fuel Spray Modelling in Direct-Injection Diesel and Gasoline Engines.* City University, London., 2006. PhD Thesis.

144. Arcoumanis, C., H. Flora, M. Gavaises, N. Kampanis, and R. Horrocks, *Investigation of cavitation in a vertical multi-hole injector.* SAE Transactions Journal of Engines, 1999-01-0524, 1999. 108-3.

145. Nouri, J.M., N. Mitroglou, Y. Yan, and C. Arcoumanis, *Internal flow and cavitation in a multi-hole injector for gasoline direct injection engines.* SAE 2007, 2007.

146. Gopalan, S., J. Katz, and O. Knio, *The flow structure in the near field of jets and its effect on cavitation inception.* Journal of Fluid Mechanics, 1999. 398: p. 1-43.

147. Gopalan, S. and J. Katz, *Flow structure and modeling issues in the closure region of attached cavitation.* Physics of Fluids, 2000. 12(4): p. 895-911.

148. Soteriou, C., M. Lambert, S. Zuelch, and D. Passerel, *The flow characteristics of high efficiency Diesel nozzles with enhanced geometry holes.* Proc. THIESEL International Conference on Thermo- and Fluid Dynamic Processes in Diesel Engines. Valencia, Spain, 2006.

149. Andriotis, A. and M. Gavaises, *Influence of Vortex Flow and Cavitation on Near-nozzle Diesel Spray Dispersion Angle.* Atomization and Sprays, 2008.

150. Andriotis, A., M. Spathopoulou, and M. Gavaises. *Effect of Nozzle Flow and Cavitation Structures on Spray Development in Low-speed Two-Stroke Diesel Engines.* in *25th CIMAC World Congress, International Council on Combustion Engines, Paper No 262*. 2007. Vienna, Austria, 21-24 May.

151. Giannadakis, E., D. Papoulias, M. Gavaises, C. Arcoumanis, C. Soteriou, and W. Tang, *Evaluation of the predictive capability of diesel nozzle cavitation models.* SAE Paper 2007-01-0245, 2007.

152. Soteriou C., A.R.J., Torres N., Smith M., and Kunkulagunta R. *Through the Diesel Nozzle Hole - A Journey of Discovery.* in *Proc. ILASS America, 14th Annual Conference on Liquid Atomization and Spray Systems*. 2001. Dearborn, Michigan, USA.

153. Arcoumanis, C., Gavaises, M., Roth, H., Choi, Y.S., and Theodorakakos, A. *Nozzle Flow and Spray Characteristics from VCO Diesel Injector Nozzles.* in *Proc. THIESEL International Conference on Thermo- and Fluid Dynamic Processes in Diesel Engines*. 2002, September 10-13. Valencia, Spain.

154. Mitroglou, N., Nouri, J.M., Gavaises, M., and Arcoumanis, C., *Spray structure generated by multi-hole injectors for gasoline direct-injection engines.* SAE 2007, 2007.

155. Mitroglou, N., Nouri, J.M., Gavaises, M., and Arcoumanis, C., *Spray Characteristics of a multi-hole Injector for Direct-Injection Spark-Ignition Engines.* International Journal of Engine Research, 2006. vol.7(issue 3).

156. Arndt, S., K. Gartung, and D. Brueggemann, *Spray Structure of High Pressure Gasoline Injectors : Analysis of Transient Spray Propagation and Spray-Gas Momentum Transfer.* ILASS Europe, Zurich 2-6 Sep. 2001, 2001.

157. Skogsberg, M., P. Dahlander, R. Lindgren, and I. Denbratt, *Effects of Injector Parameters on Mixture Formation for Multi-Hole Nozzles in a Spray-Guided Gasoline DI Engine.* SAE 2005-01-0097, 2005.

158. Landenfeld, T., A. Kufferath, and J. Gerhardt, *Gasoline Direct Injection - SULEV Emission Concept.* SAE 2004-01-0041, 2004.

159. Honda, T., M. Kawamoto, H. Katashiba, M. Sumida, M. Fukutomi, and K. Kawajiri, *A Study of Mixture Formation and Combustion for Spray Guided DISI.* SAE 2004-01-0046, 2004.

160. Gashi, S., Y.-Y. Yan, R.D. Lockett, and C. Arcoumanis, *Mixture Distribution in a Spray-Guided Direct Injection Spark Ignition (DISI) Engine using Planar Laser Induced Fluorescence (PLIF).* International Journal of Engine Research, 2006.

161. Karaiskos, E., *Spray Structure and Mixture Distribution in Direct-Injection Gasoline Engines.* Imperial College, 2005. PhD Thesis.

162. Gavaises, M., *Modeling of Diesel Fuel Injection Processes*, in *Department of Mechanical Engineering*. PhD Thesis, 1997, Imperial College London: London.

163. Giannadakis, E., M. Gavaises, and C. Arcoumanis, *Modelling Cavitation in Diesel Injector Nozzle Holes.* J. Fluid Mechanics, 2008.

164. Gavaises, M., D. Papoulias, A. Andriotis, E. Giannadakis, and A. Theodorakakos, *Link between cavitation development and erosion damage if Diesel fuel injector nozzles.* SAE Paper 2007-01-0246, 2007.